950656
64-161

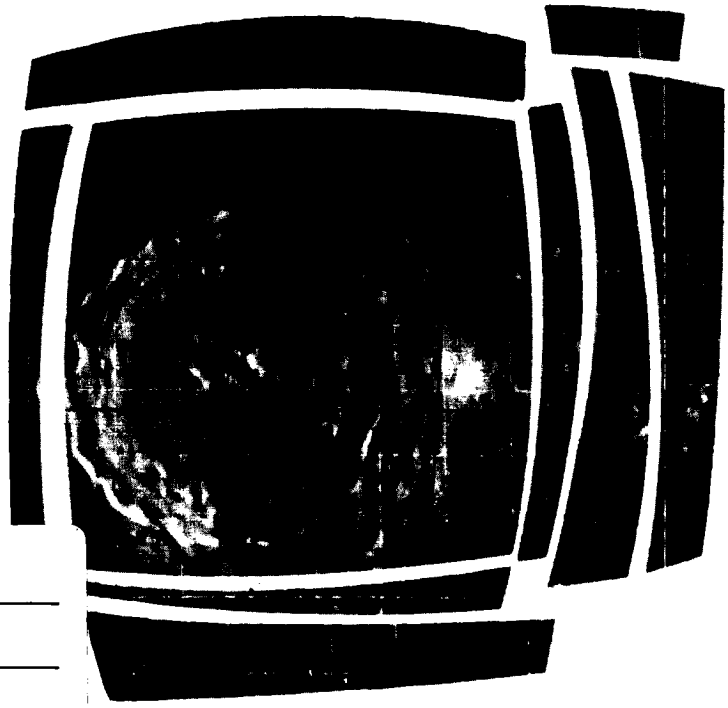

FINAL TECHNICAL REPORT

N66-15483

(ACCESSION NUMBER) (THRU)

373 1

(PAGES) (CODE)

CR 69397 11

(NASA CR OR TMX OR AD NUMBER) (CATEGORY)

FACILITY FORM 602

Surveyor Lunar Roving Vehicle, Phase I

BSR-903

Volume III PRELIMINARY DESIGN AND SYSTEM DESCRIPTION

Book 2 Validation of Preliminary Design

Bendix SYSTEMS DIVISION

SURVEYOR
LUNAR ROVING VEHICLE, PHASE I

BSR-903

FINAL TECHNICAL REPORT

SUBMITTED TO

JET PROPULSION LABORATORY
CALIFORNIA INSTITUTE OF TECHNOLOGY

JPL CONTRACT
950656
under NAS. 7-100, JPL

VOLUME III
PRELIMINARY DESIGN AND SYSTEM DESCRIPTION

BOOK 2:
VALIDATION OF PRELIMINARY DESIGN

APRIL 1964

Bendix SYSTEMS DIVISION

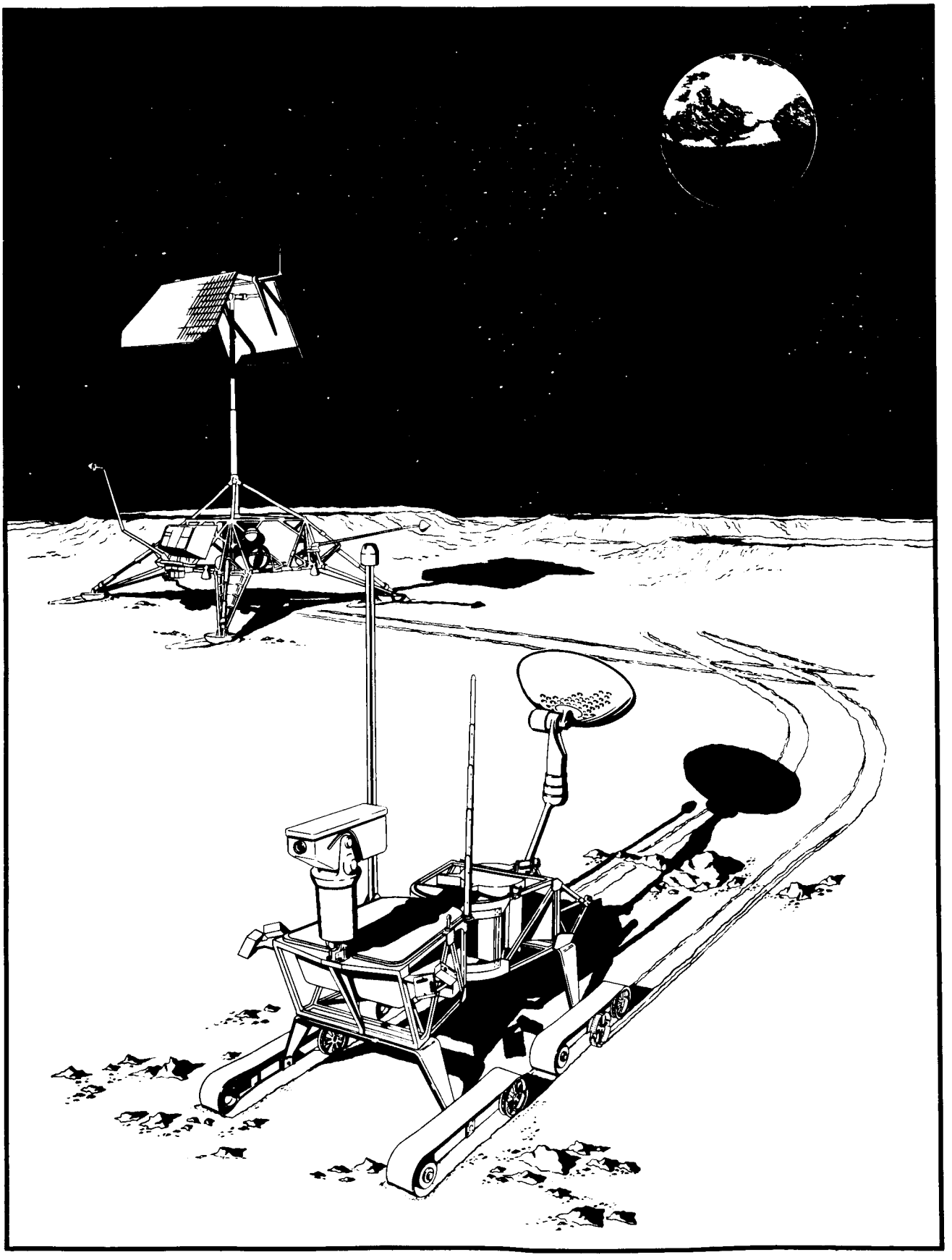

FOREWORD

As part of the continuing program of unmanned exploration of space, and to increase the effectiveness of the manned space program for exploring the moon, the Jet Propulsion Laboratory of the California Institute of Technology issued six-month study contracts to investigate the feasibility of a small, unmanned, lightweight, remotely controlled roving vehicle to be incorporated in the surveyor spacecraft to extend its data-gathering capabilities on the lunar surface. Specifically, the study program was to determine the feasibility of a 100-lb Surveyor Lunar Roving Vehicle (SLRV) system in gathering sufficient scientific information by surveying the lunar surface near the Surveyor spacecraft landing point to certify the area, in terms of specific hazards, as a potential Apollo LEM landing site.

This Final Technical Report, submitted in five volumes, presents the results and conclusions of the study program conducted by The Bendix Corporation under JPL Contract No. 950656. The volumes are organized to correspond to the specific objectives of the program: to conduct an analysis, to generate a preliminary design, and to fabricate and demonstrate an engineering test model in support of the over-all program objectives.

The results of Bendix's study show that the SLRV concept is not only feasible, but can make substantial contributions to the unmanned exploration of the moon in support of the manned Apollo program. The SLRV characteristics, the problems, and the initial trade-offs have been determined in sufficient detail to permit the definition of specific objectives and criteria for a follow-on development program. Program conclusions and recommendations are included in Volume V.

LIST OF VOLUMES

VOLUME I – PROGRAM SUMMARY

VOLUME II – MISSION AND SYSTEM STUDIES

VOLUME III – PRELIMINARY DESIGN AND SYSTEM DESCRIPTION

Book 1 – System Description and Performance Characteristics

→ Book 2 – Validation of Preliminary Design

VOLUME IV – RELIABILITY

VOLUME V – SYSTEM EVALUATION

THE DOCUMENT YOU ARE READING IS INDICATED BY THE ARROW

TABLE OF CONTENTS

		Page
1.	INTRODUCTION	1-1
2.	MOBILITY	2-1
2.1	TRACTION DRIVE ASSEMBLY	2-3
2.1.1	Track and Rim Design	2-3
2.1.2	Traction Drive Mechanism	2-14
2.1.3	TDA, Strut, and Idler Wheels	2-47
2.2	STEERING LOCK ASSEMBLY	2-50
2.2.1	Lock Operation	2-53
2.2.2	Lock Mechanism Analysis	2-54
2.3	VEHICLE BRAKING	2-56
2.4	STEERING AND MOBILITY CONTROL	2-58
2.5	VEHICLE PERFORMANCE	2-63
2.5.1	Vehicle Maneuverability	2-63
2.5.2	Vehicle Static Stability	2-64
2.5.3	Torque and Coefficient of Friction Requirements	2-70
2.5.4	Vehicle Dynamics	2-72
2.5.5	Crevice Crossing	2-72
2.6	SUMMARY	2-75
3.	STRUCTURE	3-1
3.1	STRUCTURAL DESIGN LOAD CRITERIA	3-1
3.2	BODY STRUCTURE DESIGN	3-15
3.3	FLOATING PIVOT DESIGN	3-17
3.4	VEHICLE SUPPORTS - STOWAGE	3-18
3.5	COMPONENTS INSTALLATION	3-25
3.6	STRUT DESIGN	3-25

TABLE OF CONTENTS (CONT.)

		Page
3.7	MATERIALS	3-27
3.7.1	Environment	3-28
3.7.2	Metals	3-28
3.7.3	Polymers	3-51
3.8	SUMMARY	3-56
3.9	REFERENCES	3-59
4.	DEPLOYMENT	4-1
4.1	DESIGN LOADS	4-1
4.2	DESIGN REQUIREMENTS	4-1
4.3	DEPLOYMENT SEQUENCE	4-2
4.4	SUBSYSTEM DESIGN AND ANALYSIS	4-2
4.5	STRUT VIBRATIONAL MODES	4-9
4.5.1	Flexural Mode	4-10
4.5.2	Torsional Mode	4-15
4.6	DEPLOYMENT DYNAMICS	4-17
4.6.1	Spring Action on the Vehicle	4-17
4.6.2	Pure Rotation About the Hinge	4-20
4.6.3	Plane Motion After Unlatching	4-20
4.6.4	Impact During Deployment Landing	4-24
4.6.5	Landing Stability	4-28
4.7	SUMMARY	4-35
5.	FOLDING AND ERECTION MECHANISMS	5-1
5.1	TV CAMERA SUPPORT AND ERECTION MECHANISM	5-1
5.1.1	Description	5-1
5.1.2	Actuation	5-2
5.1.3	Design	5-2
5.2	DIRECTIONAL ANTENNA SUPPORT AND ERECTION MECHANISM	5-11

TABLE OF CONTENTS(CONT.)

		Page
6.	APOLLO SUPPORT SCIENTIFIC EXPERIMENTS	6-1
6.1	MAPPING AND SITE VERIFICATION	6-1
6.1.1	Photogrammetric Analysis	6-1
6.1.2	Determination of Lunar Slopes by Photometric Technique	6-40
6.2	PENETROMETER	6-55
6.2.1	Summary	6-55
6.2.2	Operation	6-59
6.2.3	Interfaces	6-60
6.2.4	Parametric Studies	6-62
6.2.5	Preliminary Design	6-64
6.2.6	Engineering Prototype Penetrometer Tests	6-77
6.2.7	Modes of Partial Operation	6-98
6.2.8	Conclusions	6-98
6.3	BEARING STRENGTH EXTRAPOLATION STUDIES	6-100
6.3.1	Summary	6-100
6.3.2	Soil Properties	6-101
6.3.3	Experimental Investigation in Atmosphere	6-104
6.3.4	Penetrometer and Footing Tests in Vacuum	6-112
6.3.5	Results	6-115
6.4	CORRELATION PROCEDURES FOR SURFACE PROPERTIES	6-143
7.	NAVIGATION	7-1
7.1	NAVIGATION SYSTEM REQUIREMENTS	7-1
7.2	NAVIGATION CONCEPT TRADE-OFFS	7-1
7.3	NAVIGATION SYSTEM DESCRIPTION	7-4
7.3.1	Intrapoint Navigation Procedure	7-6
7.3.2	Intrapoint Navigation Procedure	7-10
7.3.3	Computations	7-12
7.4	CONCEPT VALIDATION	7-16

TABLE OF CONTENTS (CONT.)

		Page
7.5	NAVIGATION SENSORS	7-29
7.5.1	RF Ranging Unit	7-31
7.5.2	Inclinometer	7-46
7.5.3	Solar Aspect Sensor	7-63
7.5.4	Odometer	7-68
8.	VEHICLE CONTROL AND DISPLAY	8-1
8.1	CONTROL CONCEPTS	8-1
8.1.1	Autonomous Operation - Remote Operator Control	8-1
8.1.2	Programmed Command - Incremental Command	8-1
8.1.3	Selected Concept	8-3
8.2	CONTROL DISPLAY CONCEPTS	8-4
8.2.1	TV Profile Driving Display	8-4
8.2.2	Topographic Map Driving Display	8-4
8.2.3	Selected Display Concept	8-5
8.3	CONTROL AND DISPLAY DESCRIPTION	8-5
8.4	SYSTEM CONSIDERATIONS	8-12
8.4.1	Stereo Display	8-12
8.4.2	Operator Decision Time	8-14
8.4.3	Solar Angle Effects	8-14
8.4.4	Degraded Mode Operation	8-16
8.4.5	Continuous Control	8-16
9.	TELEVISION	9-1
9.1	INTRODUCTION AND SUMMARY	9-1
9.2	SYSTEM DESIGN STUDY	9-8
9.2.1	Optics and Exposure	9-8
9.2.2	Light Sensor and Resolution	9-15
9.2.3	Digital Techniques	9-17

TABLE OF CONTENTS (CONT.)

	Page
9.3 TV PRELIMINARY DESIGN DATA	9-21
9.3.1 Optics Design	9-21
9.3.2 Exposure Control	9-26
9.3.3 Tube Application	9-30
9.3.4 Circuitry	9-33
9.3.5 Electronics Packaging	9-72
9.3.6 Motion Control	9-72
9.3.7 Structural and Mechanical Design	9-89
10. TELECOMMUNICATIONS	10-1
10.1 TELECOMMUNICATION FUNCTIONS AND REQUIREMENTS	10-1
10.1.1 Data Collection	10-1
10.1.2 Data Handling	10-2
10.1.3 Signal Processing	10-2
10.1.4 Signal Radiation and Reception	10-2
10.2 TELECOMMUNICATION PERFORMANCE REQUIREMENTS	10-2
10.3 TELECOMMUNICATION PERFORMANCE ANALYSIS	10-4
10.4 TELECOMMUNICATIONS SUBSYSTEM PRELIMINARY DESIGN	10-10
10.4.1 Data Handling	10-14
10.4.2 Data Link Transmitter	10-68
10.4.3 Command Receiver	10-89
10.4.4 Antennas	10-112
10.4.5 Mobility Control	10-140
11. PRIMARY POWER SUPPLY	11-1
11.1 SELECTION AND LOAD DISTRIBUTION	11-1
11.2 INTEGRATION	11-10
11.2.1 Operation of RTG	11-13
11.2.2 Operation of Converter-Regulator	11-15

TABLE OF CONTENTS (CONT.)

	Page
11.3 RTG TRADE-OFF ANALYSIS	11-16
11.3.1 Fuel Selection	11-23
11.3.2 RTG Design Analysis	11-24
11.4 CONVERTER-REGULATOR DESIGN	11-34
11.4.1 Converter Circuit Description	11-34
11.4.2 Regulators	11-40
12. THERMAL CONTROL	12-1
12.1 THERMAL ENVIRONMENT	12-1
12.1.1 Prelaunch	12-1
12.1.2 Launch	12-1
12.1.3 Transit	12-1
12.1.4 Landing	12-1
12.1.5 Lunar	12-2
12.2 DESIGN PHILOSOPHY	12-2
12.3 ANALYTICAL TECHNIQUES	12-3
12.4 SUBSYSTEM DESIGN AND DESCRIPTION	12-5
12.4.1 Electronic Compartment	12-5
12.4.2 Tracks, Structure and Antennas	12-6
12.4.3 Traction Drive Modules (TDM)	12-6
12.4.4 TV Camera	12-9
12.5 DESIGN CONSIDERATIONS	12-15
12.6 EVALUATION	12-16
12.6.1 Lunar Day-Night Conditions	12-16
12.6.2 Transit	12-22
12.7 THERMAL COATINGS	12-36
12.8 TELEMETRY REQUIREMENTS	12-37
12.9 SUMMARY	12-38

TABLE OF CONTENTS (CONT.)

	Page
13. DSIF/SFOF	13-1
13.1 FUNCTIONAL REQUIREMENTS	13-1
13.1.1 Mission Planning	13-2
13.1.2 Mission Direction	13-4
13.1.3 Navigation	13-5
13.1.4 Vehicle Control (Driving)	13-5
13.1.5 Survey Data Collection and Landing Point Verification	13-5
13.1.6 Vehicle Performance Monitoring and Control	13-7
13.1.7 Communications and Data Handling	13-8
13.1.8 Scientific Analysis of Survey Data	13-8
13.2 OPERATIONAL CONFIGURATION	13-9
13.2.1 TM and TV Data Recovery	13-13
13.2.2 Control Consoles	13-20
13.2.3 SLRV Command Generation	13-35
13.2.4 Data Analysis Equipment	13-37
13.2.5 Data Recording	13-37
13.3 STANDBY STATUS MONITORING CONFIGURATION	13-37
13.4 GROUND COMPUTATION REQUIREMENTS	13-37
13.4.1 On-Line Requirements	13-39
13.4.2 Off-Line Requirements	13-46
13.4.3 Remote Station Computer Requirements	13-48
13.5 MULTIPLE VS SINGLE DEEP SPACE STATION UTILIZATION	13-49
13.6 GROUND OPERATIONS FLOW AND "DECISION TIME" ESTIMATES	13-57

LIST OF ILLUSTRATIONS

Figure	Title	Page
1-1	SLRV Configuration	1-2
2-1	Traction Drive Assembly	2-5/2-6
2-2	Rim Geometry	2-7
2-3	Rim Deflection Geometry, 2-Inch Radius of Curvature	2-10
2-4	Rim Deflection Geometry, Sharp Load	2-11
2-5	Tread Design Concepts	2-13
2-6	AC-DC Motor Comparison	2-16
2-7	Motor Characteristics	2-16
2-8	Motor Power Distribution	2-18
2-9	Motor Parameters	2-18
2-10	Transmission Trade-off	2-19
2-11	Layout of SLRV Traction Drive Mechanism	2-20
2-12	Forces on Shaft Due to Bearing Loads	2-24
2-13	Motor Performance Characteristics	2-37
2-14	Layout of Nutator Transmission and Drive Unit Demonstration Model	2-44
2-15	Nutator Transmission and Drive Unit Demonstration Model with Plastic Housing	2-45
2-16	Nutator Transmission and Drive Unit Demonstration Model Components	2-45
2-17	Nutator Transmission Test Schematic	2-46
2-18	Nutator Transmission Test Setup	2-46
2-19	Transmission Demonstration Performance Curve	2-48
2-20	Steering Lock Assembly	2-51/2-52
2-21	SLRV Braking Characteristics	2-59
2-22	Vehicle Center-of-Gravity Trajectory for 90° Right Turn	2-65
2-23	CG Height vs CG Longitudinal Location	2-66
2-24	SLRV Static Stability	2-68
2-25	Vehicle Stability Determination	2-69
2-26	Torque and Coefficient of Friction Parameters	2-71
2-27	Torque and Coefficient of Friction Requirements, $\alpha = 30^{\circ}$	2-73
2-28	Torque and Coefficient of Friction Requirements, $\alpha = 45^{\circ}$	2-74

PRECEDING PAGE BLANK NOT FILMED.

LIST OF ILLUSTRATIONS (CONT.)

Figure	Title	Page
3-1	SLRV Structure Assembly, Sheet 1 of 3	3-5/3-6
3-2	SLRV Structure Assembly, Sheet 2 of 3	3-7/3-8
3-3	SLRV Structure Assembly, Sheet 3 of 3	3-9/3-10
3-4	SLRV-Surveyor Integration Stress Analysis, Sheet 1 of 4	3-11
3-5	SLRV-Surveyor Integration Stress Analysis, Sheet 2 of 4	3-12
3-6	SLRV-Surveyor Integration Stress Analysis, Sheet 3 of 4	3-13
3-7	SLRV-Surveyor Integration Stress Analysis, Sheet 4 of 4	3-14
3-8	SLRV Rear Support Structure Stress Analysis	3-19/3-20
3-9	Deflection of Articulated Joint, Stress Analysis	3-21/3-22
3-10	Lower Deployment Structure and Upper Support Structure Stress Analyses	3-23/3-24
3-11	Strut Configuration	3-26
3-12	Shock Strut Stress Analysis	3-29/3-30
3-13	Tensile Strength vs Temperature for AZ31B Magnesium	3-31
3-14	Tensile Strength vs Temperature for AZ61A Magnesium	3-32
3-15	Tensile Strength vs Temperature for 2014-T6 Aluminum	3-34
3-16	Tensile Strength vs Temperature for 2024-T6 Aluminum	3-35
3-17	Tensile Strength vs Temperature for 6061-T6 Aluminum	3-36
3-18	Tensile Strength vs Temperature for 7075-T6 Aluminum	3-37
3-19	Tensile Strength vs Temperature for Type 302 Stainless Steel Annealed	3-39
3-20	Tensile Strength vs Temperature for Type 316 Stainless Steel, Annealed	3-40
3-21	Strength-Weight Ratio vs Temperature for Various Metals	3-41
3-22	Tensile Strength vs Temperature for T1-6AL-4V Titanium, Annealed	3-42
3-23	Tensile Strength vs Temperature for T1-5AL-2.5 SN Titanium, Annealed	3-44
3-24	Sublimation Rate vs Temperature for Various Materials in Hard Vacuum ($\simeq 10^{-6}$ Mm Hg)	3-45
3-25	Rates of Weight Loss vs Temperature for Organic Materials Tested	3-53
3-26	Effect of Sample Thickness on Rates of Weight Loss	3-54
4-1	SLRV Deployment Subsystem, Sheet 1 of 2	4-3/4-4
4-2	SLRV Deployment Subsystem, Sheet 2 of 2	4-5/4-6
4-3	Strut vs Vibration Body	4-11

LIST OF ILLUSTRATIONS (CONT.)

Figure	Title	Page
4-4	Schematic Diagram of Strut	4-14
4-5	SLRV in Stowed Position	4-18
4-6	Deployment on 15° Slope, Uphill or Downhill	4-23
4-7	Orientation vs Vehicle Dropping Distance	4-25
4-8	Linear Velocity vs Dropping Distance	4-26
4-9	Impact Force During Lunar Landing of Roving Vehicle	4-29
4-10	Angular Velocity after Impact, Front Tracks Hitting	4-30
4-11	Linear Velocity after Impact, Front Tracks Hitting	4-30
4-12	Geometry of Vehicle During Deployment	4-33
4-13	Geometry of Vehicle after Rebound	4-33
5-1	TV Camera Erection Mechanism	5-3/5-4
5-2	Ideal TV Camera System Design Loads	5-5
5-3	Ideal TV Camera System Stowed Configuration	5-7
5-4	Linear Torsion Spring Design	5-10
5-5	Antenna Support and Erection Mechanism	5-13/5-14
6-1	Angular Relationships for Leveled Photograph	6-3
6-2	Angular Relationships for Inclined Photograph	6-5
6-3	Intersection with Convergent Camera Axes	6-7
6-4	Image Measurement Error (11 x 11 Mm Format)	6-22
6-5	Image Measurement Samples, Sheet 1 of 2	6-23
6-6	Image Measurement Samples, Sheet 2 of 2	6-24
6-7	Error Coefficient for Normal Horizontal Case	6-29/6-30
6-8	Evaluation of $\Delta\delta/Y$	6-31
6-9	Error Coefficients of $\Delta Xi/Y$, $\Delta\psi/Z_iY$ for 50° Lens, 15° Convergence	6-32
6-10	Error Coefficient $\Delta\lambda/ZY$ for 50° Lens, 15° Convergence	6-33
6-11	Error Coefficient $\Delta\delta/Y$ for 50° Lens, 15° Convergence	6-34
6-12	Error Coefficient $\Delta X/Y$, $\Delta\psi_i/Z_iY$ for 50° Lens, 30° Convergence	6-35
6-13	Error Coefficient of $\Delta\lambda_1/Z_1Y_1$ for 50° Lens, 30° Convergence	6-36
6-14	Error Coefficients of $\Delta\lambda_2/Z_2Y_2$ for 50° Lens, 30° Convergence	6-37
6-15	Error Coefficient of $\Delta\delta/Y$ for 50° Lens, 30° Convergence	6-38
6-16	Lunar Photometric Simulation Model	6-41
6-17	Theoretical Photometric Function	6-43

LIST OF ILLUSTRATIONS (CONT.)

Figure	Title	Page
6-18	TV Photometry on Simulated Lunar Surface Material	6-44
6-19	Empirical Photometric Function	6-47
6-20	Photometric Functions for i = +50°	6-49
6-21	Vidicon Calibration Format	6-51
6-22	Photometric Reference Axes	6-53
6-23	Penetrometer Schematic Diagram	6-56
6-24	Penetrometer Subsystem	6-57
6-25	Penetrometer Block Diagram	6-58
6-26	Penetrometer Circuit Diagram	6-61
6-27	Power Module Assembly	6-67/6-68
6-28	Probe Tube Module	6-69/6-70
6-29	Probe Tip Assembly	6-72
6-30	Probe Payout Records Obtained in Four Tests with no Resistive Load	6-78
6-31	Typical Curves Showing Power Required During Extension and Retraction Phases of Operation, Test A, Run 1	6-80
6-32	Load vs Penetrometer Payout Obtained in Four Test Runs under Loading Conditions (B)	6-81
6-33	Typical Curve Showing Power Required During Extension and Retraction Phases of Operation, Test B, Run 2	6-82
6-34	Load vs Penetrometer Payout Obtained in Three Test Runs under Loading Conditions (C)	6-84
6-35	Force Per Unit Area vs Ratio of Penetration to Perimeter (F/A vs X/C), Run 2	6-86
6-36	Force Per Unit Area vs Ratio of Penetration to Perimeter (F/A vs X/C), Run 3	6-87
6-37	Typical Curve Showing Power Required During Extension and Retraction Phases of Operation, Test C, Run 4	6-89
6-38	Load vs Penetrometer Payout Obtained in Four Test Runs under Loading Conditions (D)	6-90
6-39	Typical Curve Showing Power Required During Extension and Retraction Phases of Operation, Test D, Run 3	6-91
6-40	Load vs Penetration Payout Obtained in Four Test Runs Under Loading Conditions (E)	6-93
6-41	Typical Curve Showing Power Required During Extension and Retraction Phases of Operation, Test E, Run 3	6-95

LIST OF ILLUSTRATIONS (CONT.)

Figure	Title	Page
6-42	Load vs Penetrometer Payout Obtained in Test Conducted Under Loading Condition (G)	6-97
6-43	Grain Size Accumulation Curve for Silica Flour	6-102
6-44	Penetrometer Tips Used	6-105
6-45	Typical Load Cell Output for Penetrometer Test in Atmosphere	6-106
6-46	Force vs Penetration for Various Cone Angles	6-107
6-47	Force as a Function of Penetration for Various Rates of Penetration	6-109
6-48	Penetration as a Function of Time	6-110
6-49	Time/Penetration as a Function of Time	6-111
6-50	Bearing Pressure as a Function of Penetration for Footings	6-113
6-51	Force/Penetration (F/X) as a Function of Penetration (X)	6-116
6-52	Typical F/A vs X/C Curves for 60° Penetrometer	6-119
6-53	Typical XA/FC vs X/C Curves for 60° Penetrometer	6-120
6-54	Graphical Representation of Equation	6-121
6-55	Slope and Intercept as Functions of Porosity (60° Cone)	6-123
6-56	a_f/a_p as a Function of d_f/d_p	6-124
6-57	b/b_p as a Function of d/d_p	6-125
6-58	F/A vs X/C for General Case of Footing on Soil	6-127
6-59	XA/FC vs X/C for General Case of Footing on Soil	6-127
6-60	Computed and Actual Bearing Capacity of 1.5-Inch Footing	6-131
6-61	Computed and Actual Bearing Capacity of 3-Inch Footing	6-132
6-62	Computed and Actual Bearing Capacity of 6-Inch Footing	6-133
6-63	Computed and Actual Bearing Capacity of 9-Inch Footing	6-134
6-64	Computed and Actual Bearing Capacity of 12-Inch Footing	6-135
6-65	Graphical Representation of Equation	6-137
6-66	F/A vs X/C for Penetrometer Tests in Vacuum	6-138
6-67	XA/FC vs X/C for Penetrometer Tests in Vacuum	6-140
6-68	Actual and Computed Bearing Capacity of 3-Inch Footing in Vacuum	6-141
6-69	Actual and Computed Bearing Capacity of 12-Inch Footing in Vacuum	6-142
7-1	Triangulation Between Known Landmarks, Relative Geometry Known	7-8
7-2	Triangulation Between Known Landmarks, Relative Geometry Unknown	7-9

LIST OF ILLUSTRATIONS (CONT.)

Figure	Title	Page
7-3	Coordinate Convention	7-13
7-4	Navigation Geometry for Three-Wheeled/Tracked Vehicle	7-15
7-5	Effect of Azimuth Measurement Error on True Azimuth	7-17
7-6	Effect of Elevation Measurement Error on True Azimuth	7-18
7-7	Effect of Inclinometer Error on True Azimuth	7-19
7-8	Solar Azimuth Uncertainty vs Subsolar Point Distance	7-20
7-9	Triangulation Accuracy	7-23
7-10	Navigation Geometry, Surveyor at Site Center	7-24
7-11	Navigation Geometry, Surveyor at Site Edge	7-26
7-12	Elevation Error vs Slope for Various Odometer Errors	7-28
7-13	Point Photogrammetry Operations for Elevation Profile Matching	7-30
7-14	Surveyor Transponder and SLRV RF Ranging System	7-32
7-15	RF Ranging Unit	7-42
7-16	Inclinometer Sensor	7-47
7-17	Open-Loop Inclinometer	7-49
7-18	Inclinometer Electronics	7-50
7-19	Typical Dynamic Situation	7-55
7-20	Integrating Technique	7-59
7-21	Solid-State Integrator Block Diagram	7-61
7-22	Waveform Timing Chart for Solid-State Integrator	7-62
7-23	Solar Aspect Sensor Electronics Logic Diagram	7-66
7-24	Solar Aspect Sensor Electronics Assembly	7-67
7-25	Solar Aspect Sensor Prototype Model	7-68
7-26	Odometer Assembly	7-73/7-74
7-27	Odometer Electronics	7-75
8-1	Control Loop Flow Diagram	8-5
8-2	Angle Subtended by Crevice and Step of 0.2 Unit Dimension vs Distance for Camera Height of Unit Length	8-7
8-3	Driving Display - Initial View (No Video Shown)	8-8
8-4	Driving Display Path Description	8-10
8-5	Vehicle Operator's Control Console	8-13
8-6	Relationship Between Interaxial Distance, Nearest Object, and Farthest Object for Comfortable 3-Dimensional Viewing	8-15

LIST OF ILLUSTRATIONS (CONT.)

Figure	Title	Page
9-1	Television Functional Block Diagram	9-2
9-2	SLRV TV Displays	9-5/9-6
9-3	Exploded View of TV Configuration	9-7
9-4	Full-Scale Model of TV Subsystem, Left Side Without Insulation	9-9
9-5	Full-Scale Model of TV Subsystem, Right Side Without Insulation	9-10
9-6	Elevation Geometry	9-13
9-7	256 x 256 Elements, Low-Resolution Performance	9-20
9-8	512 x 512 Elements, High-Resolution Performance	9-20
9-9	Possible Optical Configuration Layout	9-23
9-10	Sketch of Possible Optical Configuration	9-24
9-11	Normal Galilean Telescope	9-24
9-12	The 0.444 Position	9-24
9-13	Optic Train	9-27
9-14	Exposure Control Circuit	9-29
9-15	TV Camera Circuitry Block Diagram	9-35/9-36
9-16	Over-All Timing Diagram	9-37/9-38
9-17	Horizontal and Vertical Sweeps and Controls	9-41/9-42
9-18	Timing Diagram Details	9-43/9-44
9-19	Vidicon Video Amplifier and Power Supply	9-47/9-48
9-20	Simplified D/A Converter	9-49
9-21	D/A and Deflection Amplifiers	9-51/9-52
9-22	Roberts Generator Using Signetics Logic	9-54
9-23	Plot of Picture Gray Scale	9-55
9-24	Encoder Block Diagram	9-55
9-25	Encoder Circuit Diagram	9-61/9-62
9-26	Line and Frame Sync Generator	9-63/9-64
9-27	Azimuth Drive Block Diagram	9-75
9-28	Elevation Drive Block Diagram	9-75
9-29	Elevation Drive Arrangement	9-77
9-30	Bridge Amplifier Schematic	9-77
9-31	Layout of Components in Standard Drive	9-88
9-32	Standard Drive for Azimuth, Tilt, and Lens Turret Axes	9-88
9-33	TV Camera Package and Support Structure	9-91
10-1	Telecommunications Block Diagram	10-11/10-12
10-2	Command Format	10-15
10-3	Command Decoder Block Diagram	10-17
10-4	Address Decoder A Logic Diagram	10-19
10-5	Switching Control Logic Diagram	10-21
10-6	Communications and Penetrometer Decoder Logic Diagram	10-22
10-7	Television Decoder Logic Diagram	10-24
10-8	Mobility Decoder Logic Diagram	10-25

LIST OF ILLUSTRATIONS (CONT.)

Figure	Title	Page
10-9	Command Decoder Assembly	10-32
10-10	Mobility Logic	10-33
10-11	SLRV Operational Modes	10-36
10-12	SLRV Operational Directions	10-38
10-13	Telemetry Processor Block Diagram	10-41
10-14	Telemetry Word and Frame Formats	10-42
10-15	A/D Converter Block Diagram	10-44
10-16	Analog Switch	10-47
10-17	A/D Converter (A and B)	10-50
10-18	Programmer Clock Divider Logic Diagram	10-53
10-19	Programmer Word Selection Matrix	10-54
10-20	Output Multiplexer	10-55
10-21	Telemetry Processor Assembly Arrangement	10-66
10-22	Telemetry Processor Assembly Cutaway View	10-67
10-23	SLRV Antenna Gain vs Bit Rate Capability for Various Transmitter Power Levels	10-71
10-24	Transmitter Capability as Function of Weight	10-74
10-25	Transmitter Assembly Arrangement	10-78
10-26	Transmitter Assembly Cutaway View	10-79
10-27	Transmitter Block Diagram	10-80
10-28	Transmitter Schematic Diagram	10-81
10-29	Command Receiver Block Diagram	10-91
10-30	Command Receiver Assembly Arrangement	10-95
10-31	Command Receiver Assembly Cutaway View	10-96
10-32	Command Receiver RF Section	10-103/10-104
10-33	Crystal IF Filter Response	10-105
10-34	Command Receiver Logic Section	10-107-10-108
10-35	Command Receiver Data Filter	10-109
10-36	Spherical Coordinate System	10-113
10-37	Square Hybrid, Schematic Form	10-116
10-38	General Schematic of RF Circuitry	10-117
10-39	S-Band Omnidirectional Antenna	10-119
10-40	Pointing Error Loss for Misaligned Antenna	10-121
10-41	Crossed Dipole Feed	10-122
10-42	17-db Pointed Antenna	10-123
10-43	17-db Directional Antenna Assembly	10-127
10-44	Gimbal Drive Electronics	10-130
10-45	Antenna Drive Electronics	10-131

LIST OF ILLUSTRATIONS (CONT.)

Figure	Title	Page
10-46	Earth-Sun Coordinates	10-133
10-47	Geometry of SLRV-Earth-Sun Selenographic Positions	10-137
10-48	Mobility Control Assembly	10-141
10-49	Traction Drive Mechanism Directional Control	10-142
10-50	Traction Drive Mechanism Speeds	10-145
10-51	SLRV Speed Control	10-146
10-52	SLRV Speed Control, Expanded Scale	10-147
10-53	Traction Drive Mechanism Speed Control, SCR Phase Control	10-148
10-54	Secondary Speed Control (Digital)	10-149
10-55	Steering Lock Control	10-151
10-56	Mobility Power Control	10-152
11-1	Summary of RTG Requirements	11-5/11-6
11-2	RTG Configuration	11-7
11-3	Schematic Diagram of Converter-Regulator	11-8
11-4	Configuration of Converter-Regulator	11-9
11-5	RTG Equivalent Circuit	11-14
11-6	RTG Output Voltage vs Output Current and Power Output	11-14
11-7	Martin Co. RTG Design	11-18
11-8	Atomics International RTG Design, Sheet 1 of 3	11-19
11-9	Atomics International RTG Design, Sheet 2 of 3	11-20
11-10	Atomics International RTG Design, Sheet 3 of 3	11-21
11-11	General Atomics RTG Design	11-22
11-12	Comparison of Isotopes	11-25/11-26
11-13	Method of Generating Data Used to Compare Isotopes	11-27
11-14	Gamma Exposure Rates at One Meter vs Thermal Output for Equilateral Right Cylinder Power Sources	11-28
11-15	Neutron Exposure Rates at One Meter vs Thermal Output for Equilateral Right Cylinder Power Sources	11-29
11-16	Thermal Output vs Time for Indicated Isotopes	11-30
11-17	Converter Efficiency vs Input Voltage	11-35
11-18	Converter Schematic Diagram	11-36
11-19	Converter-Regulator Block Diagram	11-37
11-20	Diode Efficiency vs Output Voltage	11-39
11-21	Power Regulator Circuit Diagrams	11-42
11-22	Precision Regulator Circuit Diagram	11-44
11-23	Oven Control Circuit Diagram	11-45

LIST OF ILLUSTRATIONS (CONT.)

Figure	Title	Page
12-1	Electronic Compartment	12-7
12-2	Electronic Mounting Plate Temperature Variation	12-8
12-3	SLRV Used in Thermal Analysis	12-10
12-4	Electrical Power Density vs Radiator Temperature for Various Solar Angles	12-11
12-5	Semiactive Thermal Control Concept	12-13
12-6	Radiator Temperatures vs Power Level Operating Envelope	12-14
12-7	RTG Lunar Surface Model	12-17
12-8	Lunar Surface Temperature Under RTG	12-18
12-9	Stowed SLRV During Transit	12-29
12-10	Radiating Surfaces for RTG	12-31
12-11	Alternate RTG Configuration	12-33
13-1	GOE Configuration for Single-Station Operation	13-11/13-12
13-2	Approaches for Routing TM and TV Data to SFOF	13-15
13-3	Data Reconstruction Unit	13-14
13-4	Data and Clock Waveforms	13-17
13-5	Driver's Main Display Block Diagram	13-27
13-6	Vehicle Control Console	13-29
13-7	Survey Control Console	13-32
13-8	DSS Configuration for SLRV Stand-By Status Monitoring	13-38
13-9	Available DSIF Network Capabilities	13-51
13-10	Approximate DSIF Station Lunar Coverage	13-54
13-11	GOE Configuration for Remote DSS Operation	13-55/13-56
13-12	Interpoint Operations Flow Diagram	13-59
13-13	Intrapoint Operations Flow Diagram	13-60

LIST OF TABLES

Table	Title	Page
2-1	Mobility Parameters	2-2
2-2	Preliminary Specifications	2-22
2-3	Results of Transmission Efficiency Tests	2-47
2-4	Vehicle Maneuverability Characterisitcs for Various Heading Change (ϕ)	2-64
3-1	Mechanical Input Vibration	3-2
3-2	Service Conditions vs Equipment Status	3-3/3-4
3-3	Load Summary Limit on SLRV-Surveyor Integration	3-16
3-4	Oxide Removal Temperatures for Various Metals	3-49
4-1	Maximum and Minimum Dropping Distance and Vehicle Orientation in Landing of the Roving Vehicle	4-28
6-1	Component Errors for Normal Case, Line Sight Horizontal	6-26
6-2	Required Instrumentation	6-52
6-3	LRV Photometry Mission Input Data Requirements	6-54
6-4	Time, Distance and Velocity Data Obtained in Test B	6-83
6-5	Time, Distance and Velocity Data Obtained in Test C	6-85
6-6	Time, Distance and Velocity Data Obtained in Test D	6-92
6-7	Time, Distance and Velocity Data Obtained in Test E	6-94
6-8	Modes of Partial Operation	6-99
7-1	Basic Navigation Concepts	7-2
7-2	Dead Reckoning Augmentation Methods	7-3
7-3	Azimuth Measurement Methods	7-5
7-4	Estimated Power Budget — SLRV Ranging System	7-43
7-5	Summary of Inclinometer Requirements	7-52
9-1	Television Design Weight Summary	9-4
9-2	TV Optical Performance Data	9-11
9-3	Exposure Data	9-16
9-4	Encoded and Decoded Gray Scale Signal Levels Using Roberts Modulation	9-56
9-5	First 40 Steps of Roberts Generator	9-58
9-6	TV Modes" Power Requirements	9-69

LIST OF TABLES (CONT)

Table	Title	Page
9-7	TV Telemetry Points	9-70
9-8	TV Command Inputs	9-71
9-9	TV Weight and Volume Breakdown	9-73
9-10	Miniature Digital Encoder Characteristics	9-87
9-11	SLRV-TV Weight Summary	9-92
10-1	Communications Subsystem Performance Requirements	10-5
10-2	System Bit Rate as a Function of DSIF Station Antenna and SLRV Antenna Utilized in Various Modes for 2W Transmitter Output Power	10-7
10-3	SLRV to Earth Direct Link Design Chart For a DSIF Using 210' Dish Antenna	10-8
10-4	Earth to SLRV Command Link Design Chart 210' Reflector	10-9
10-5	Telecommunication Hardware, Size, Weight and Power	10-13
10-6	SLRV Telemetry List	10-56
10-7	Transmitter Capability for Various Transmitter Designs	10-73
10-8	Survey of TWT in the 2.4 kMc Frequency Range with an Output Power Capability of 1 to 10 W Using ppm Focusing	10-75
10-9	Breakdown of Power Consumption for the 314 H Hughes TWT at P_{out} = 2w	10-76
10-10	Weight and Power Consumption Breakdown for the Proposed 2W-TWT Transmitter	10-89
10-11	Earth to SLRV Command Link Design Chart — 210-ft Reflector	10-93
10-12	Command Receiver Power Table	10-110
11-1	Power Supply Comparisons	11-2
11-2	Design Summary	11-3
11-3	Converter Output Power Distribution (A)	11-4
11-4	Converter Output Power Distribution (B)	11-11/11-12
11-5	AEC Projections for Typical Fuels	11-31
11-6	Possible Influence of Typical AEC Nuclear Safety Requirements on Design	11-32

LIST OF TABLES (CONT)

Table	Title	Page
12-1	Trajectory Parameters	12-3
12-2	Surface Models	12-3
12-3	Electrical Power Distribution	12-21
12-4	RTG Radiating Surface Temperatures	12-34
12-5	Gray Body View Factor (B_{ij}) for the Electronics Package Thermal Plate	12-35
12-6	LRV Temperatures	12-36
13-1	Ground Operating Equipment and Facilities for SLRV Missions	13-10
13-2	Display Presentation Techniques	13-24
13-3	Video Storage Techniques	13-26
13-4	Summary of Worst Case SLRV Computation Functions (Vehicle Moving)	13-40
13-5	Summary of Worst Case SLRV Computation Functions (Vehicle Stopped)	13-42
13-6	Summary of Worst Case SLRV Computation Functions (Vehicle-Stopped-Penetrometer Working)	13-44
13-7	SLRV Computing Requirements	13-45
13-8	Intrapoint Survey Activity (Along Critical Time Path)	13-61
13-9	Interpoint Driving Activity (Along Critical Time Path)	13-63

SECTION 1

INTRODUCTION

This volume of the Final Technical Report presents the results of the SLRV Phase I study program in accordance with Article 1, Section (a) (1) (ii) of the Statement of Work of JPL Contract No. 950656, Modification No. 1, which states:

> "Prepare a preliminary design and system description for the proposed configuration, which shall include, but not necessarily be limited to, the following:
>
> (A) Configuration, including all subsystems and instrumentation
>
> (B) Weight breakdown, including center of gravity and moments of inertia
>
> (C) Power profile
>
> (D) Operational sequence
>
> (E) Ground operational equipment".

This book (Book 2) of Volume III presents the validation of the feasibility of the preliminary 100-lb vehicle design described in Book 1 of Volume III, and demonstrates the extent to which it is practical and realistic to implement a 100-lb SLRV that can satisfy the mission objectives. The design and evaluation of vehicles in excess of 100 lb are given in Volumes II and V, respectively.

For reference purposes in the subsequent subsystem discussions, the SLRV configuration is presented in Figure 1-1.

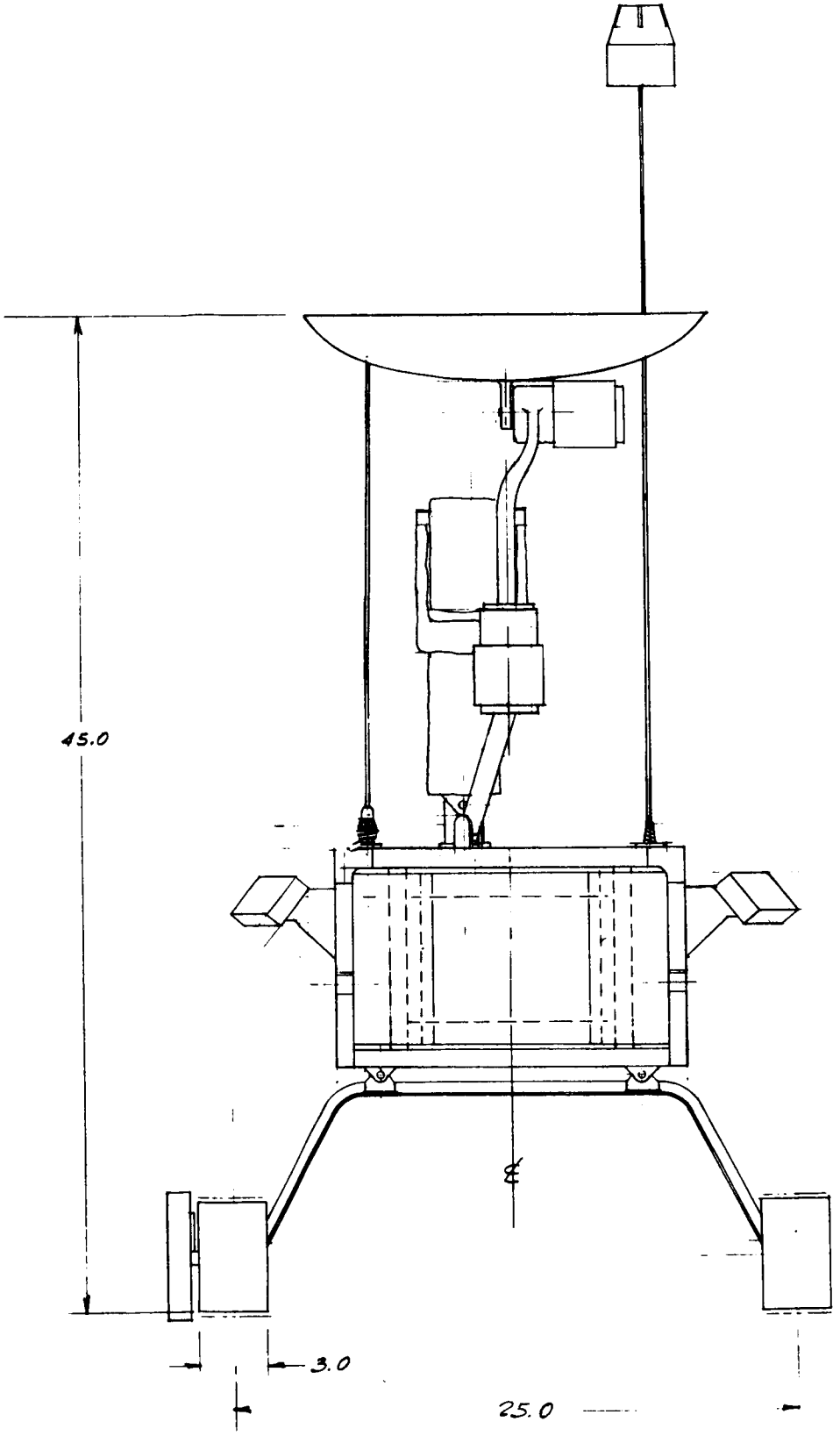

Figure 1-1 SLRV Configuration (Sheet 1 of 4)

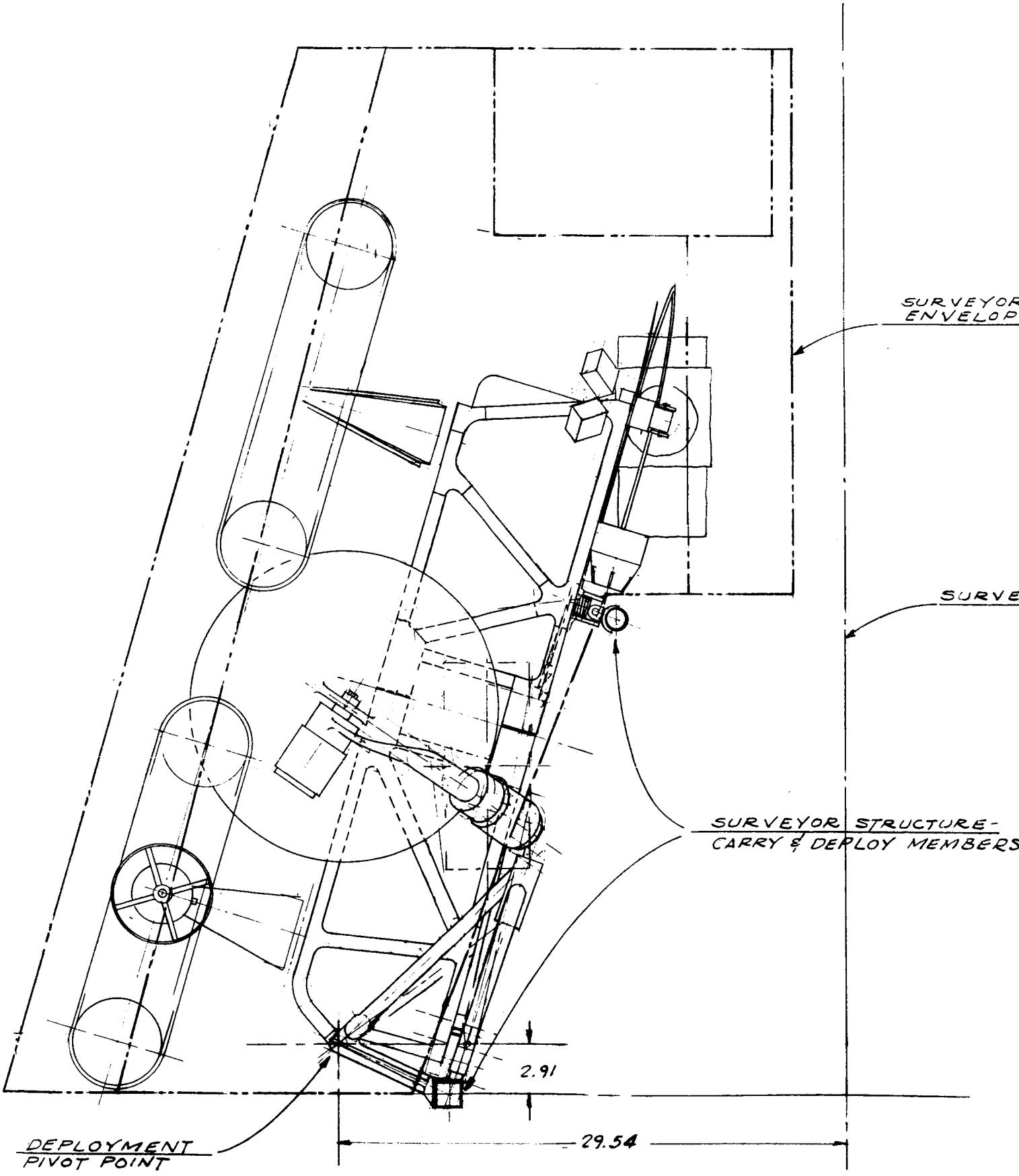
SURVEYOR
ENVELOP
SURVE
SURVEYOR STRUCTURE-
CARRY & DEPLOY MEMBERS
2.91
29.54
DEPLOYMENT
PIVOT POINT

#1

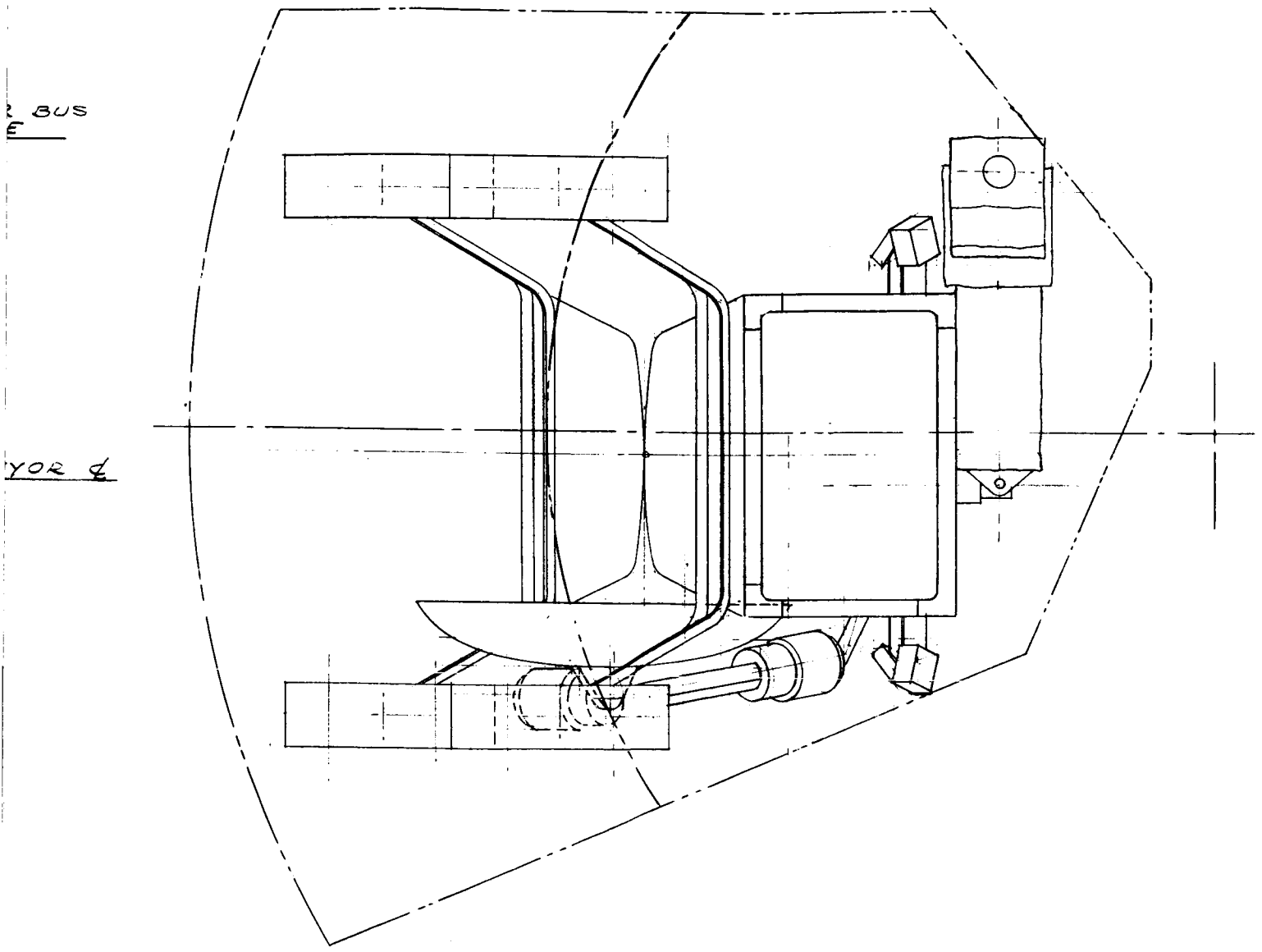

Figure 1-1 SLRV Configuration (Sheet 2 of 4)

#2

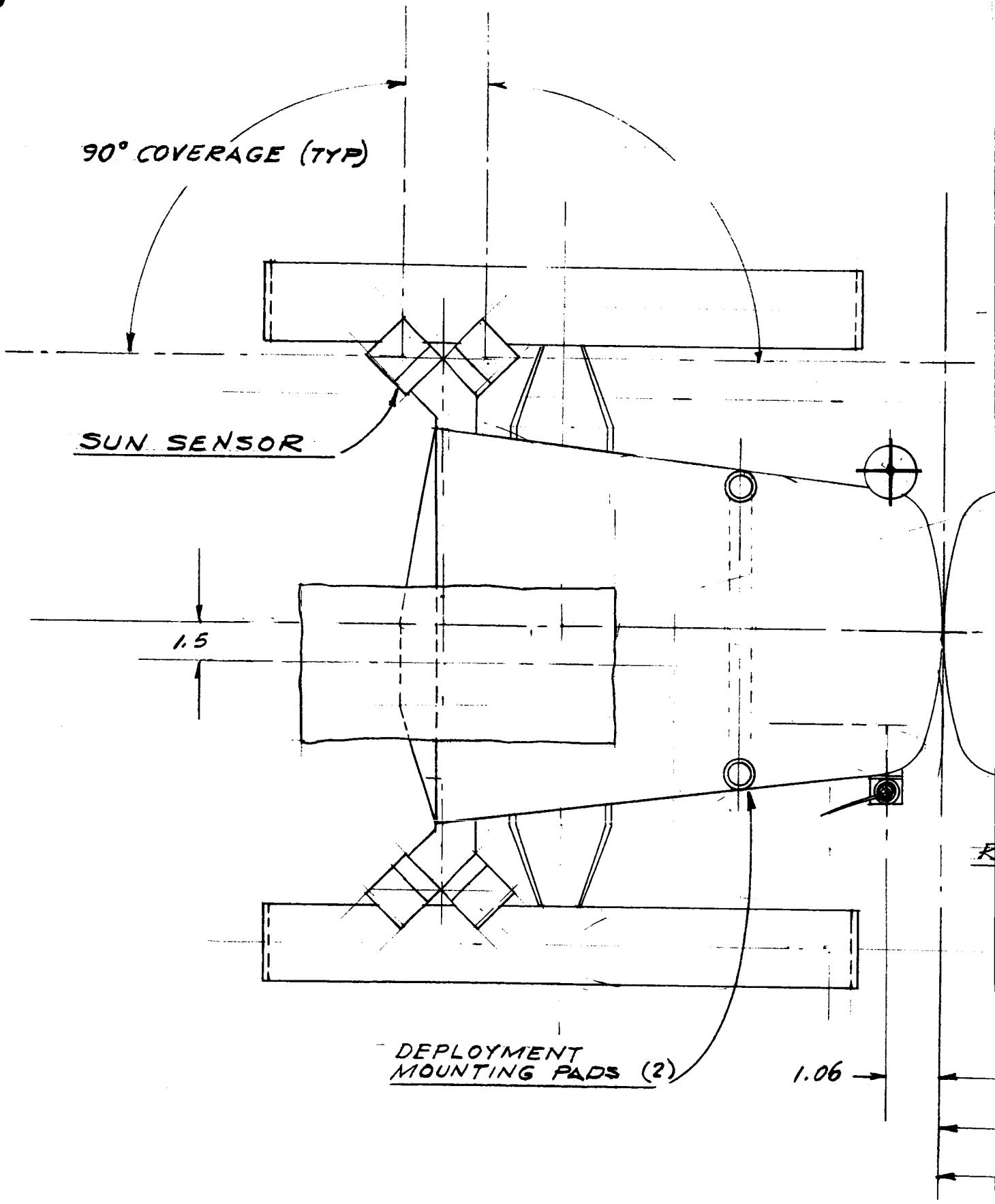
90° COVERAGE (TYP)
SUN SENSOR
1.5
DEPLOYMENT
MOUNTING PADS (2)
1.06

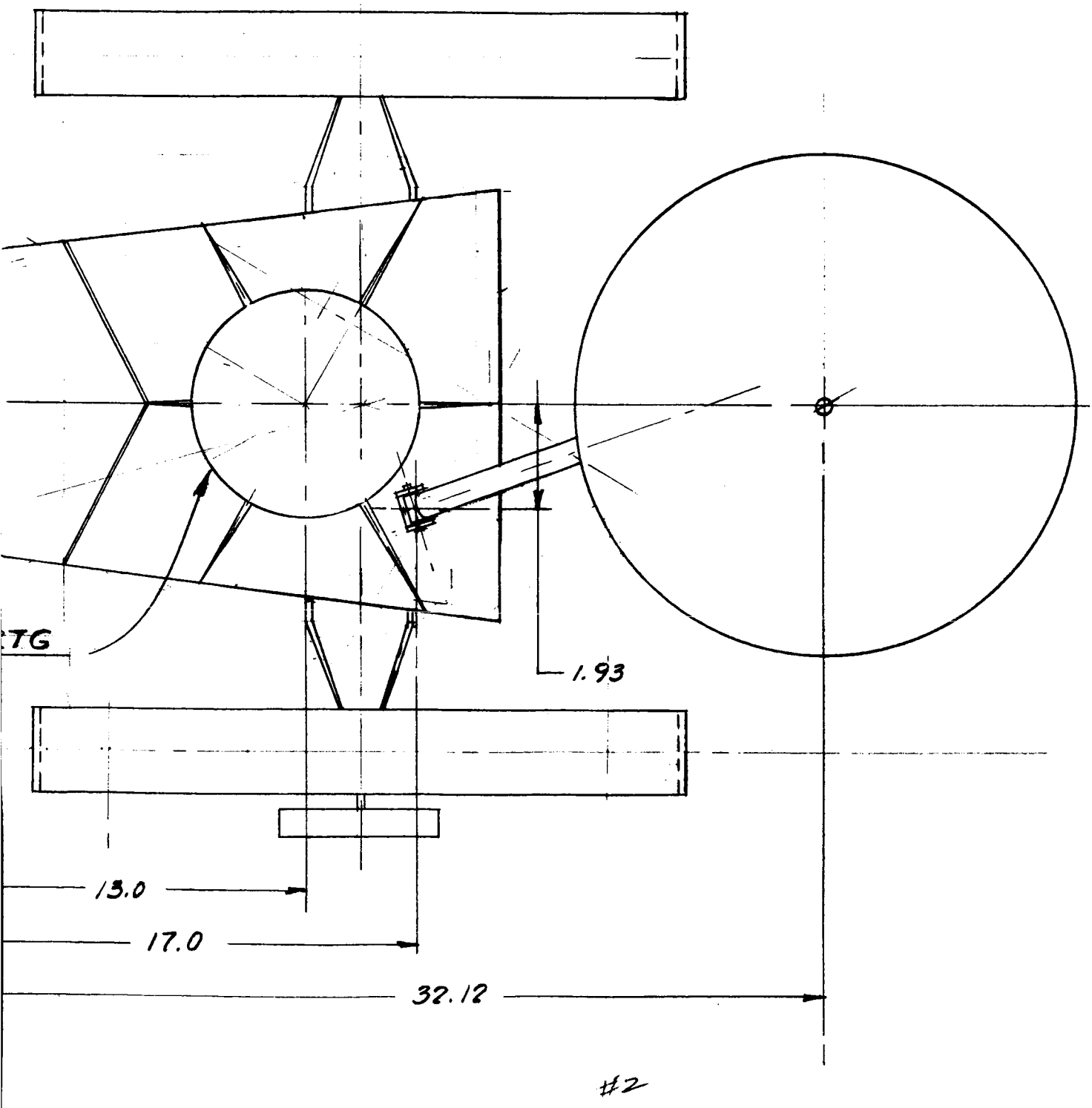

Figure 1-1 SLRV Configuration (Sheet 3 of 4)

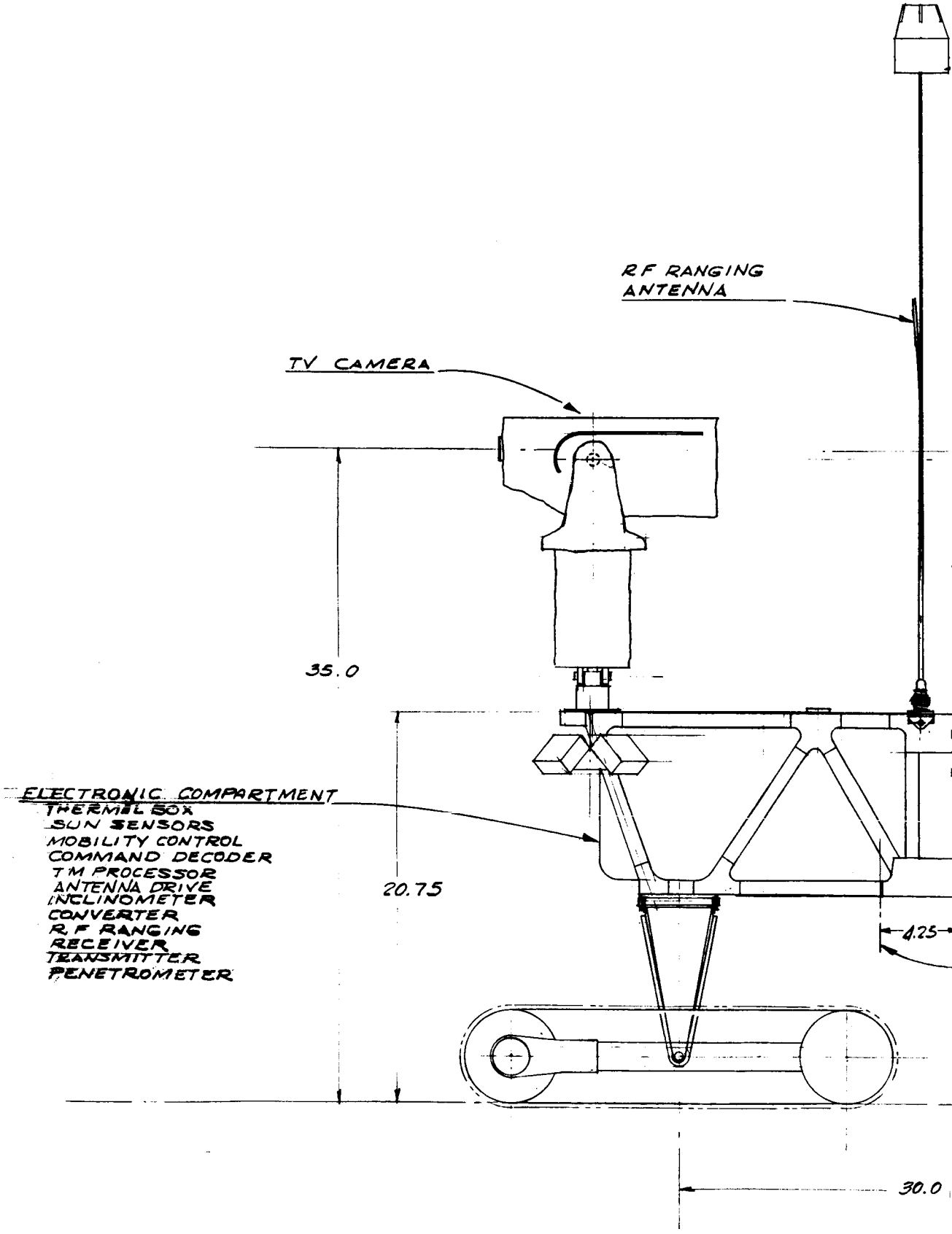
RF RANGING ANTENNA
TV CAMERA
35.0
ELECTRONIC COMPARTMENT
THERMAL BOX
SUN SENSORS
MOBILITY CONTROL
COMMAND DECODER
TM PROCESSOR
ANTENNA DRIVE
INCLINOMETER
CONVERTER
R.F RANGING
RECEIVER
TRANSMITTER
PENETROMETER
20.75
4.25
30.0

#1

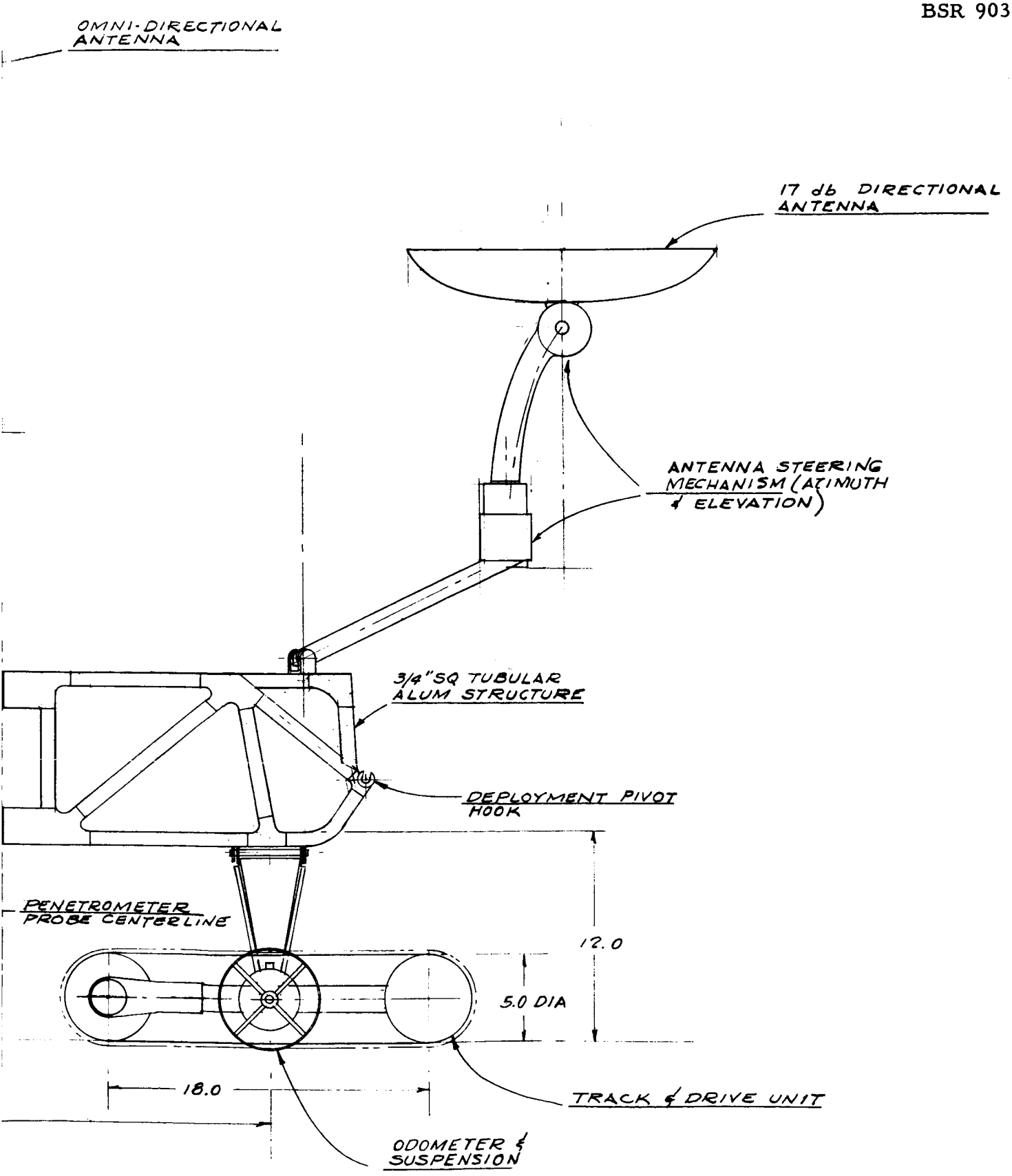

Figure 1-1 SLRV Configuration (Sheet 4 of 4)

#2

SECTION 2

MOBILITY

This section presents the SLRV mobility subsystem preliminary design (Figure 1-1, Section 1). Preceding final selection of this design, an extensive parametric study was conducted evaluating several different concepts and overall capabilities in the light of the requirements set forth in Volume II, Section 3 (1 meter obstacle capability desired). The volume limitations imposed by Hughes Document HAC 239503, Rev. C; the weight and power limits imposed; and other factors which affect mobility to varying degrees. The results of the parametric studies are summarized in Volume II, Section 4. 2.

The mobility subsystem hardware consists of four traction drive assemblies (TDA) and the steering lock. Additional equipment items which mount, space and/or control these basic items are of equal importance to the overall mobility capability of the SLRV. Thus the "mobility" discussions account for all the factors which influence vehicle performance.

The target values and the design values of the various mobility parameters are shown in Table 2-1. The target values shown are those specified by System Engineering as the best compromise between competing factors. The design values are those incorporated in this preliminary design.

All the parameters shown in Table 2-1 are self explanatory with the possible exception of the three speeds. The vehicle will at all times operate at one of the constant speeds specified. The speed at any one time depends on the torque requirements; i. e., during minimum torque requirements the vehicle will move at the highest speed (V_1): conversely, it will move at the lowest speed (V_3) when maximum torque is required. The intermediate speed (V_2) provides an intermediate torque range. In addition, V_1 and V_2 speeds are in a specific ratio to permit minimum scuffing as the vehicle executes a steady-state turn (see Section 1. 4). Additionally, the use of constant speed operation provides the best compromise between vehicle performance and speed control mechanization. Constant speed operation also furnishes a convenient distance measurement back up to the odometer.

TABLE 2-1

MOBILITY PARAMETERS

Mobility Parameter	Target Value	Design Value
Vehicle Configuration		
Track Base	30 in.	30 in.
Track Span	25 in.	25 in.
Ground Clearance	12 in.	10.7
Steering Lock Position	--	0, ±14.5°
Track Pitch Angle	±30°	±30°
Performance		
Obstacle	30 cm	30 cm[1]
Crevice	30 cm	29.2 cm
Slope Climbing	15° (soft soil)	22°[2]
Turn Radius	60 in.	60 in.
Speed		
V_1	--	0.16 mph
V_2	--	0.105 mph
V_3	--	0.03 mph
Power — Maximum	6 watts	8 watts[3]
Weight	17.7 lb	12.9 lb

[1] Demonstrated 43 cm with track pitch angle at 45° on ETM.

[2] Demonstrated with ETM in 7.5 lb/ft^3 perlite.

[3] Only 5.46 watts required; additional power allocated for energy losses in tracks, track slippage, etc.

2.1 TRACTION DRIVE ASSEMBLY (TDA)

The traction drive assembly (Figure 2-1) consists of a support structure pivoted to the vehicle axle at its center with a 5-in. diameter drive drum traction drive mechanism (TDM) at one end and a pair of 5-in. diameter idler wheels at the opposite end. Center distance from TDM to idler wheel is 18 in. A stainless steel continuous rim 3-in. wide is driven by the TDM and supported by the idler wheels (Figure 2-1). A limit stop is provided to limit rotation of the TDA about the axle to $\pm 30^{\circ}$ from the horizontal.

2.1.1 Track and Rim Design

The basic track geometry has resulted from the requirements: of (1) climbing a 30-cm obstacle, and (2) supporting the vehicle on a soil of 1 psi/ft bearing strength. Consequently, the distance between centers of the idler and traction drive mechanism (TDM) is 18 in., and the track is 3-in. wide. Thus, each track has a flat plate area of 54 square inches which gives a peak pressure under the tracks of 0.0816 psi with a maximum sinkage of 0.98 inch and a rolling resistance of 0.12 pound per track.

The track, as shown in Figure 2-1, is supported from the vehicle by an axle, and is free to rotate $\pm 30^{\circ}$ from the horizontal after the lock pins are removed prior to deployment. The TDM is located inside the pre-stressed rim, and drives the rim through a silicon-rubber-covered crowned pulley. The silicon rubber provides a high friction contact for the driving surface, prevents metal-to-metal contact in the lunar environment, and precludes cold welding effects. The crowned pulley operates as a self-centering device to maintain the rim on the drive when used in conjunction with dual idler wheels. The combination of the crowned pulley and dual idler wheels acts as a three-point support for the rim. Each idler has a guide flange which is a backup to ensure that the rims will not "walk off" the drive and idler.

A high friction contact between the rim and the lunar surface is provided by a foamed silicone rubber tread. The present concept uses a 0.25-in. thick reinforced foamed tread covered by a 0.020 in. vulcanized sheet on the running surface. However, a thorough investigation of the effect of tread thickness on the vehicle performance and life will be conducted in Phase II for final selection of the material and its thickness.

The rim of the track is constructed of 17-7 pH stainless steel and is heat treated to its full hard condition after it has been formed into a 3-in. radius. After heat treat, the rim is electron beam welded on scarf. This process has been selected to minimize the annealing effect of the joint, and to distribute the discontinuity of the joint over a large segment of the rim, thereby minimizing stress concentrations in the rim.

The formed, or prestressed, rim concept was developed to eliminate additional track idlers while maintaining a rigid support structure under the track. Under the worst case loading conditions (i.e., when the track runs over a knife-edge object) the loaded portion of the track acts as a rigid beam and does not buckle. This then eliminates the high end loads on the idler and traction drive mechanism which result from deflection of a conventional rim.

2.1.1.1 Rim Analysis

Supporting data are available to show that a design analysis of the prestressed rim has been completed. The major considerations in the rim design are: (1) the determination of the radius of transverse curvature to minimize pretensioning of the rim, (2) the stresses developed as a result of rolling the prestressed rim over the drive and idler wheels, and (3) the sinkage and rolling resistance of the track in soft soil. These three quantities are determined for the design shown in Figure 2-2.

The radius of curvature is derived from

$$\left(\frac{R}{r}\right)^3 = \frac{3}{2}\frac{[1 - \pi/4]}{\phi^2}$$

For r = 2.5 in. and $\phi = 38.4^{\circ}$, the value of R is found to be 2.24 in.

To facilitate manufacturing and provide for some slight pretensioning of the rim, the design value of r was increased to 3 in.

The axial stress is derived by

$$\sigma_y = \frac{Et}{2r}$$

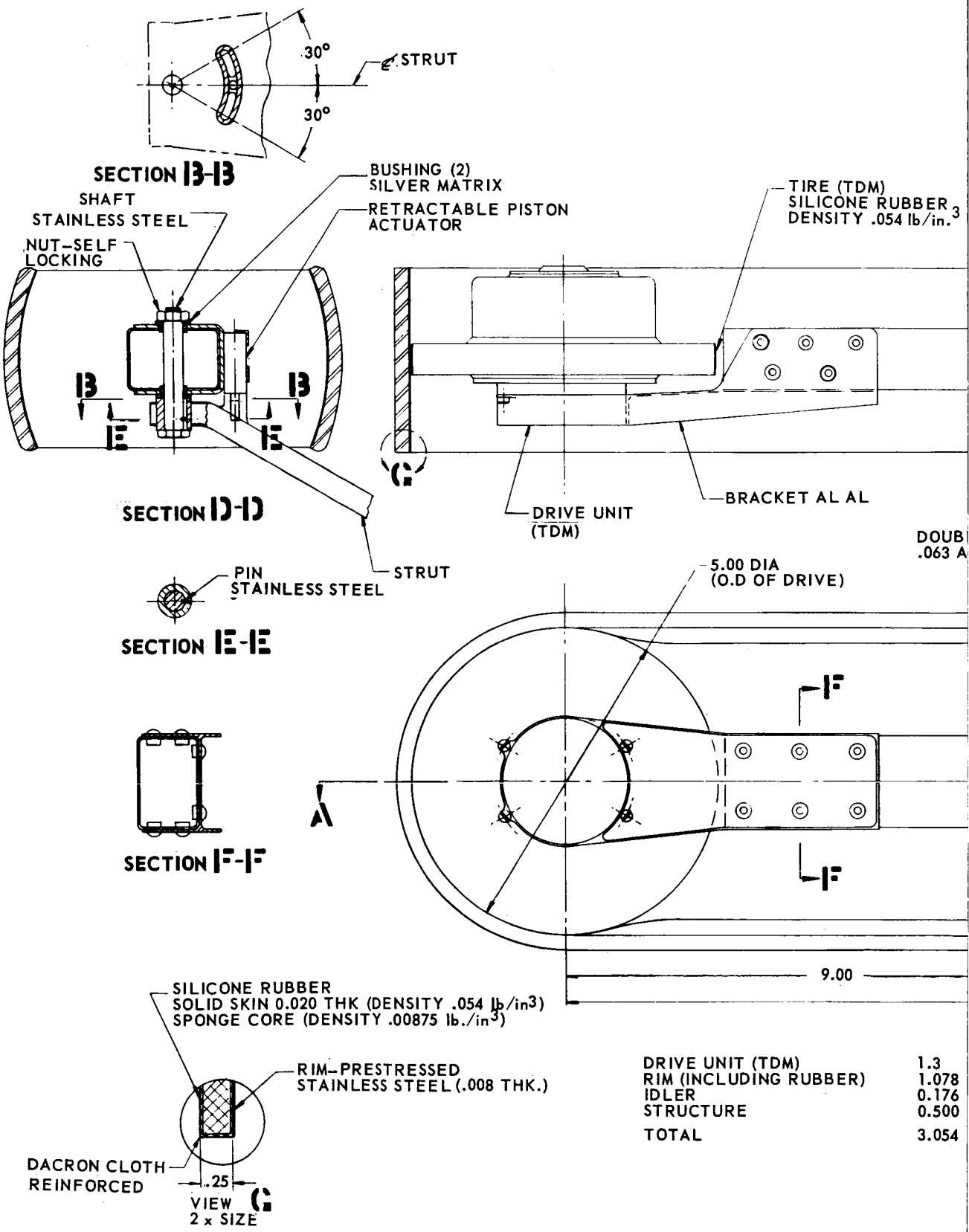

DRIVE UNIT (TDM)	1.3
RIM (INCLUDING RUBBER)	1.078
IDLER	0.176
STRUCTURE	0.500
TOTAL	3.054

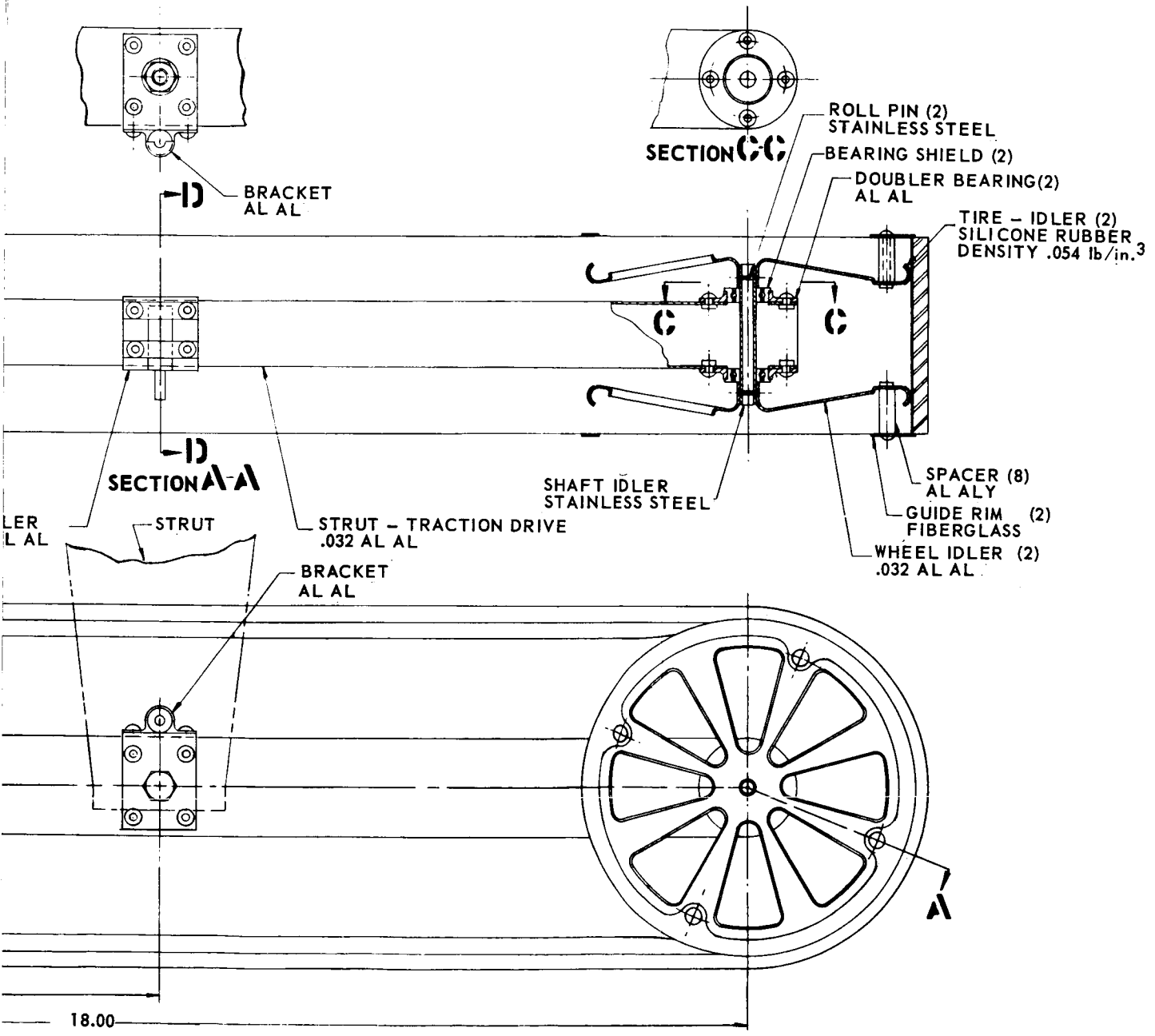

lb
lb
lb
lb
lb

Figure 2-1 Traction Drive Assembly

#2

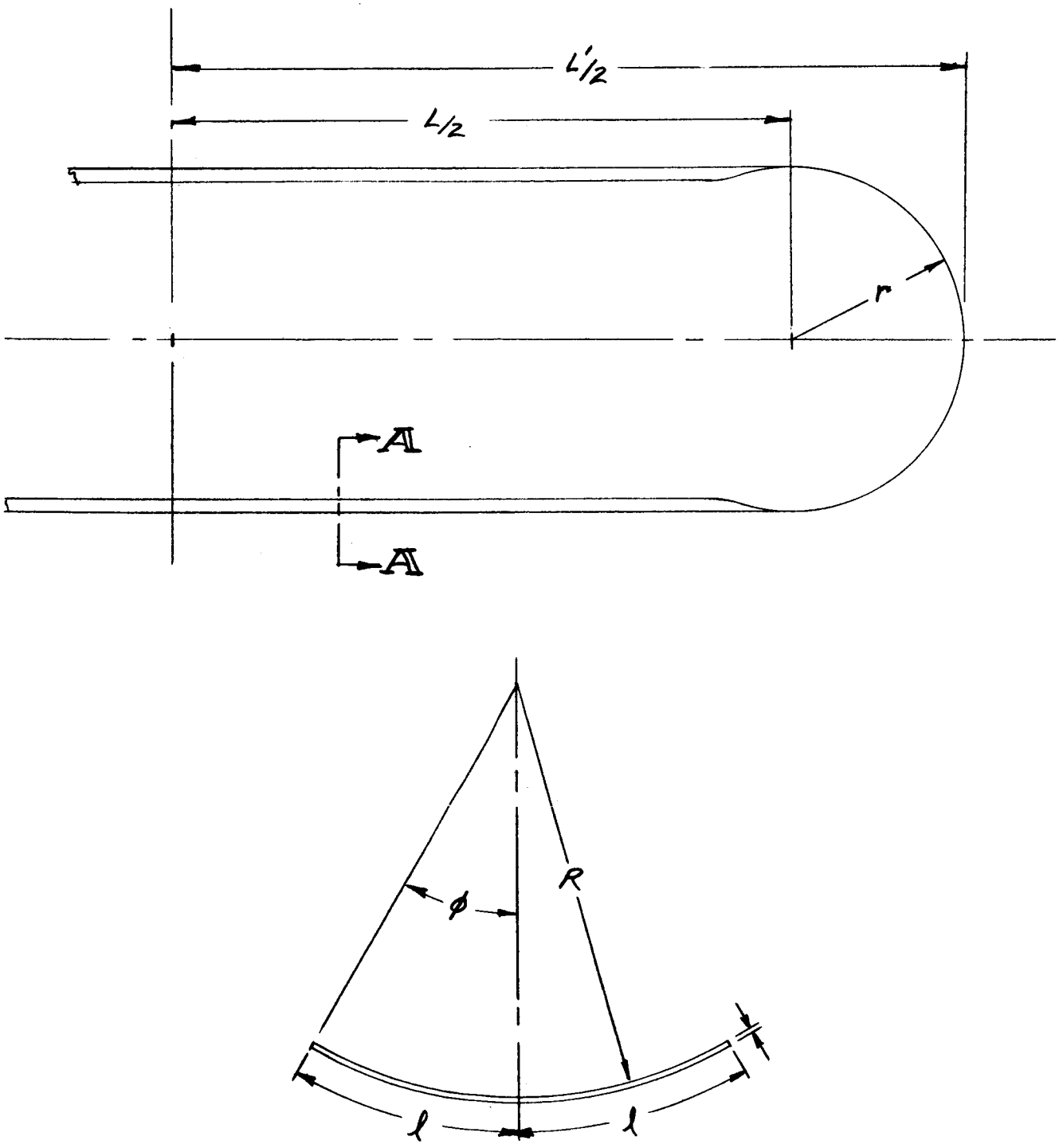

Figure 2-2 Rim Geometry

For $E = 30 \times 10^6$ psi, $t = 0.008$ in. and $r = 3.0$ in., the value of $\sigma_y = 40,000$ psi.

The transverse stress yields

$$\sigma_x = \frac{Et}{2R} = 48,000 \text{ psi}$$

for $R = 2.5$ in.

The maximum shear stress is

$$\tau_{max} = 1/2(\sigma_x + \sigma_y) = 44,000 \text{ psi}$$

Some additional stress will be experienced as a result of pretensioning and loading the rim. However, this increase is estimated to be much less than 4000 psi.

The sinkage of any one track is calculated from

$$Z_o = R\left[1 - \frac{\dfrac{W}{2\left(2KR\phi^{2/3} - L'\right)k_\phi R^2} + \dfrac{1}{4}\sin 2\phi + \phi/2}{\sin\phi}\right] = 0.98 \text{ in.}$$

where

$R = 2.5''$

$W = \dfrac{100.0}{6 \times 4}$ = lunar wt per track

$K = \dfrac{2}{3(1 - \pi/4)}$ = constant

$\phi = 28.65^\circ = 0.5$ rad

$L' = 23$ in. = track length

$k_\phi = 0.083$ lb/in.^{3} = friction modulus

The rolling resistance is derived as follows

$$R_R = k_\phi R \phi Z^2$$

$$= 0.12 \text{ lb/track for the 100-lb vehicle}$$

Comparing these results with those obtained for an equivalent flat rim (3 in. x 18 in.), the increase for the prestressed rim is 3.2% in track sinkage and 10% in rolling resistance.

A study was made of deflection of a flat rim ($R = \infty$) under load. (Figures 2-3 and 2-4.) A load applied through a 2-in. radius of curvature (fairly concentrated) stresses in the rim would not be excessive. To ensure that this result will be valid, a wide variation of loading conditions were investigated. No effect of stress concentrations caused by irregularities was considered.

In computing the deflection, the strain energy equation for the rim was set up and differentiated with respect to the applied load W. The prestressed rim will deflect less than a flat rim because of the much higher EI value. Once the prestressed rim has buckled, its behavior should approach that of a flat rim.

No tread was considered in this study. The silicon rubber tread (Figure 2-1) should have a significant effect in terms of storing energy and spreading a concentrated load over a larger area.

2.1.1.2 Tread Design

Several materials and concepts were considered for the SLRV tread design. The basic parameters against which these concepts have been evaluated are:

1. Friction augmentation between the track and lunar surface, (maximum coefficient of friction required between obstacle and track is 0.62).

2. Maximum bearing pressure on soft soil of 0.1 psi.

3. Ability of tread to attach or conform to rigid obstacle.

PREPARED BY J.H.O CHECKED BY REVISED BY	ENGINEERING REPORT THE Bendix CORPORATION BENDIX SYSTEMS DIVISION ANN ARBOR, MICHIGAN	DATE 1-14-64 PAGE 1 REPORT No. MODEL SLRV

DEFLECTION OF RIM

GEOMETRY

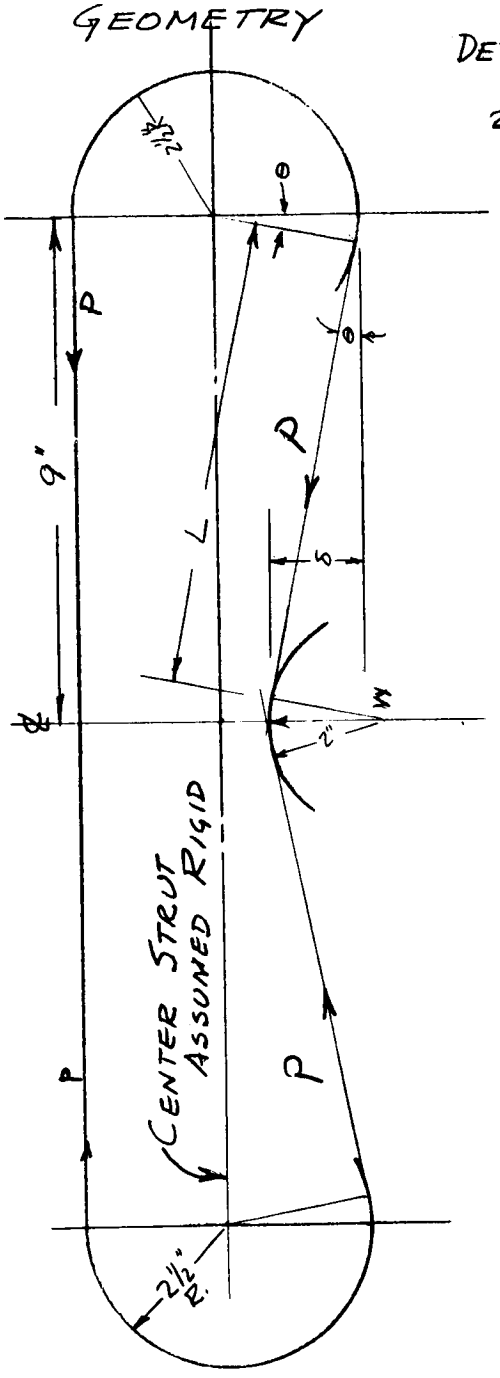

DETERMINE L & δ IN TERMS OF θ

$$2\sin\theta + L\cos\theta + 2.5\sin\theta = 9$$

$$L = \frac{9 - 4.5\sin\theta}{\cos\theta}$$

$$\delta = 4.5 - 4.5\cos\theta + L\sin\theta$$

$$\delta = 4.5(1-\cos\theta) + \left(\frac{9-4.5\sin\theta}{\cos\theta}\right)\sin\theta$$

θ_1	L	δ
10'	8.987	.026
20'	8.974	.052
30'	8.961	.078
40'	8.948	.104
50'	8.935	.1295
1-00°	8.921	.1570
1-10'	8.908	.1560
1°-20'	8.895	.2070
1°-30'	8.882	.2330
1°-40'	8.869	.2690
1°-50'	8.856	.2840
2°-00	8.843	.3090
2°-30'	8.804	.3830
3°-00'	8.764	.4600
3°-30'	8.725	.5320
4°-00'	8.686	.6070
4°-30'	8.646	.6800
5°-00	8.620	.7520
6°-00°	8.590	.9270
7-00°	8.520	1.0800
8-00°	8.460	1.1900
9-00°	8.400	1.3700

BS 268

Figure 2-3 Rim Deflection Geometry 2-Inch Radius of Curvature

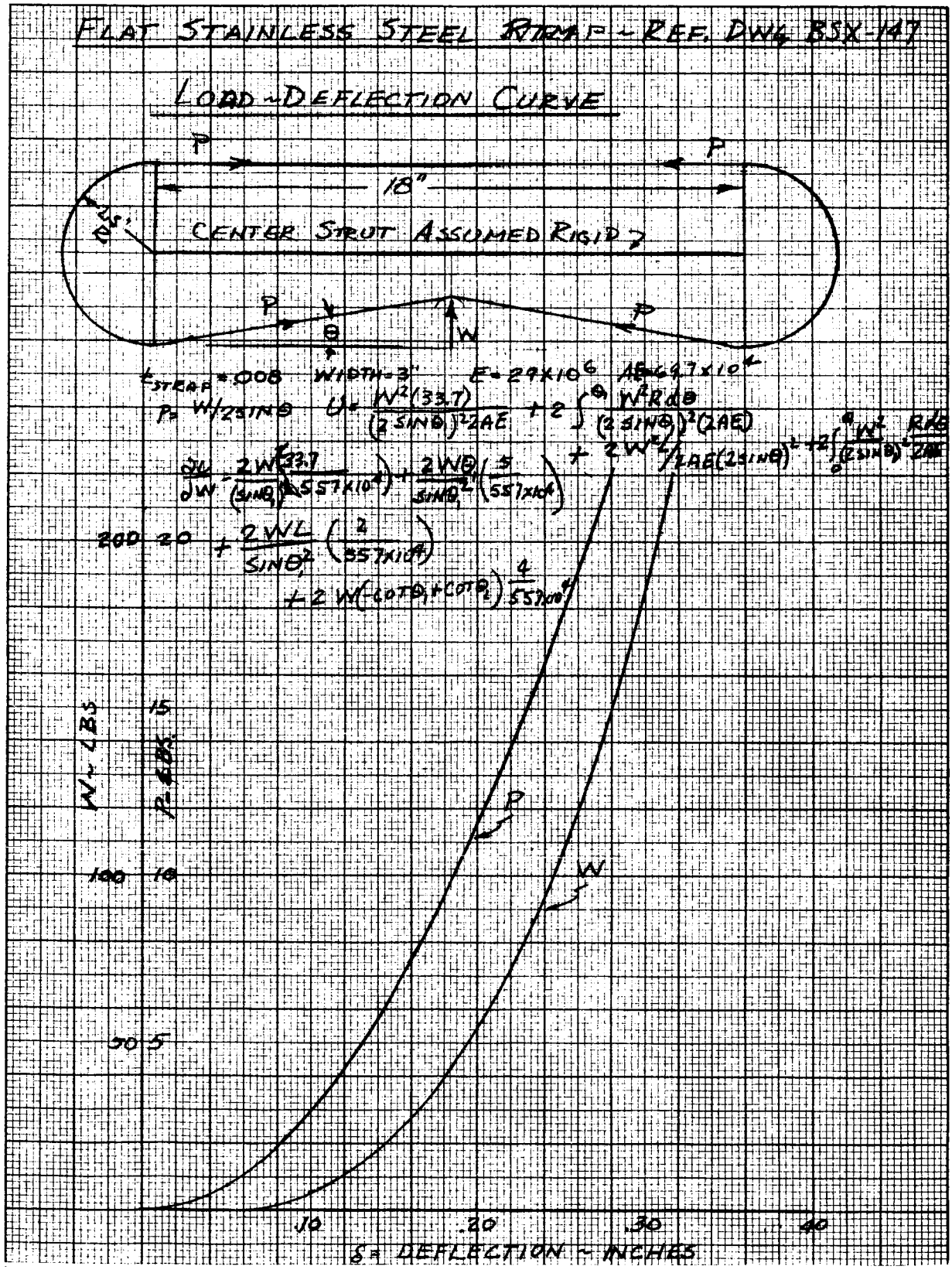

Figure 2-4 Rim Deflection Geometry. Sharp Load

4. Ability to operate in high temperature and vacuum environment and to survive the low temperatures of lunar night.

5. Operational life of 30, 000 meters at 0. 16 mph max.

The three basic concepts compared are shown in Figure 2-5. Figure 2-5(a) uses a metallic cleat or grouser. This concept would give additional thrust capability in soft soil. However, this type of cleat would not be practicle on a hard surface while the vehicle is trying to climb an obstacle.

Figure 2-5(b) shows a rubberized cleat which: (1) augments the coefficient of friction between the surface and the track on soft and smooth surfaces, and (2) provides a mechanical engagement with irregular surfaces. The rolling resistance of the track is increased by locally increasing the sinkage in the area of the cleat.

Figure 2-5(c) shows the selected design. The tread is foamed silicone rubber with a vulcanized skin having a thickness of 0. 020 in. dacron fabric re-enforced. This design develops the necessary friction, forms itself to an obstacle, and maintains approximately the same rolling resistance as the solid rim. The wearability of this material at elevated temperatures will be investigated further.

An alternative construction for the SLRV tread is a silicone rubber impregnated wire cloth. This process has been successfully used by Bendix for drive belt applications, but would require further development and study to assess its total feasibility for use as a rim.

The process uses 6-mil diameter wire flattened to 2/3 of its thickness. The wire would be woven to approximately a 100-mesh screen and brazed. The cloth would then be impregnated with a silicone rubber to improve the shear strength of the section and provide a suitable layer of tread material. Preliminary estimates of this type of construction indicate that a net reduction of 1 to 2 lb may be achieved for the mobility subsystem. The principal problems requiring further investigation are:

1. Determine that this could be used as a formed rim, or that it would be necessary to use it as a flat band.

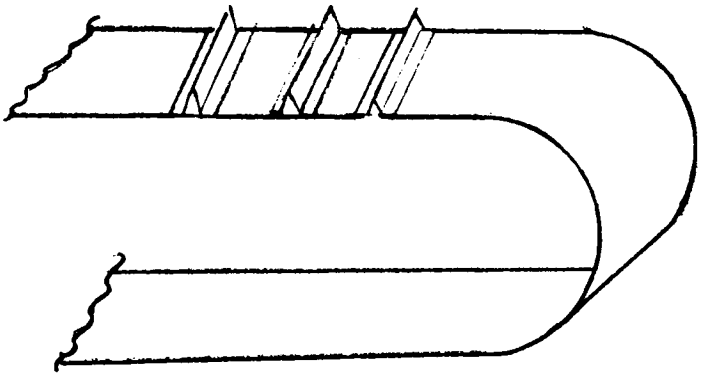

(a)

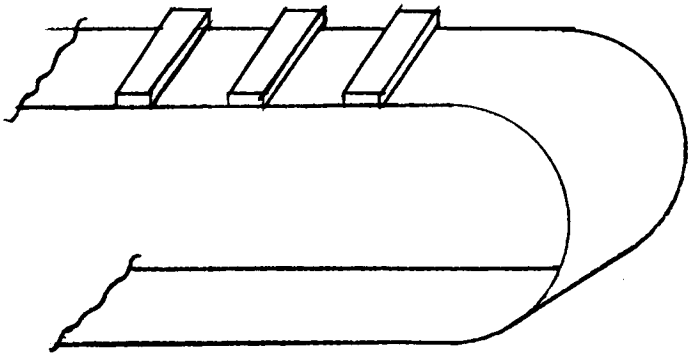

(b)

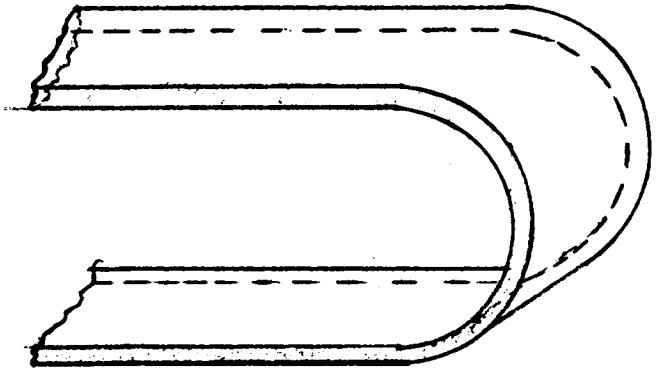

(c)

Figure 2-5 Tread Design Concepts

2. Determine the applicability of using a 3-point support loading of the wire cloth rim versus redesigning the drive wheel and idler.

3. Determining strength of the brazed cloth under high temperature operating conditions.

2. 1. 2 Traction Drive Mechanism

The major elements of the traction drive design consist of a 5-oz permanent magnet DC drive motor, a nutator type transmission with 87:1 gear reduction ratio, hermetically sealed chamber using a bellows flexible member, dust seal, drive drum, and an explosive type decoupler located between the drive drum and the nutator transmission. For optimization of the drive mechanism, system reliability was the prime consideration.

2. 1. 2. 1 Design Analysis

Drive Motor Trade-Off Study

A preliminzary survey of electric motors was conducted to determine the most suitable drive motor for the SLRV-traction drive requirements. In the motor trade-off study, the performance characteristics of each type of motor were analyzed in light of SLRV specifications.

Both AC and DC motors were considered for SLRV-TDM application during the trade-off study. However, the only AC motor types whose speed can be conveniently controlled are induction motors and series (universal) motors. A given series motor is more efficient when operated on DC. Thus, the only AC motor type which might be seriously considered is the induction motor.

DC motors include those with field windings and those with permanent magnet fields. Both types have brushes and commutators, which present problems with respect to brush wear when operated in a vacuum. These problems can be eliminated by operating the motor in a gas-filled chamber. At a maximum power level of 5 watts or less, the wound-field type has no advantages to offset its greater complexity as compared to the permanent magnet type.

Figure 2-6 is a plot of input power at stall versus the product of no-load speed and stall torque for representative small induction motors and permanent magnet field DC motors; the DC motor gives superior performance for a given power level.

A permanent magnet field DC motor typically has linear torque-speed and torque-surrent curves, as shown in Figure 2-7. The shaded area in Figure 2-8 shows the power distribution at any motor speed and developed torque.

Transmission Trade-Off Study

The design parameters used in conducting the transmission trade-off study were primarily based on the motor trade-off study and the general SLRV specifications. Because of the drive unit power requirements and the environments dictated by lunar surface conditions, two types of hermetically sealed transmissions were considered: harmomic drive and nutator drive.

Harmonic drive transmissions are suitable for high ratios, becoming marginal at about 60:1. Nutator transmissions in which the flexible element is a diaphragm are also marginal at about the same ratio. When the flexible element is a bellows, much lower ratios are practical. Either type is suitable for a ratio as high as 217 in a single stage. The ratio of a planetary transmission is rarely over 8:1. Thus, two or three stages would be required. Spur gearing has no definite limits, but weight and space considerations usually result in ratios less than 8:1 for each stage.

For long brush life, good heat transfer, and reliable insulation the motor will benefit from being enclosed in a gas-filled chamber. Efficient lubrication of bearings is also simplified if they need not operate in a vaccum. Thus, a great advantage of harmonic drive or nutator transmissions is the fact that they can trasmit power through a flexible wall of a completely sealed chamber, within which are all the high-speed bearings. Since perhaps only minimal advantage in efficiency would result from the use of any other transmission type, only these two types will be considered further.

The torque required to drive the transmission at no load will depend on bearing preloads, lubrication, and other design factors. Substantial bearing loads are inherent in the wave generator of the harmonic

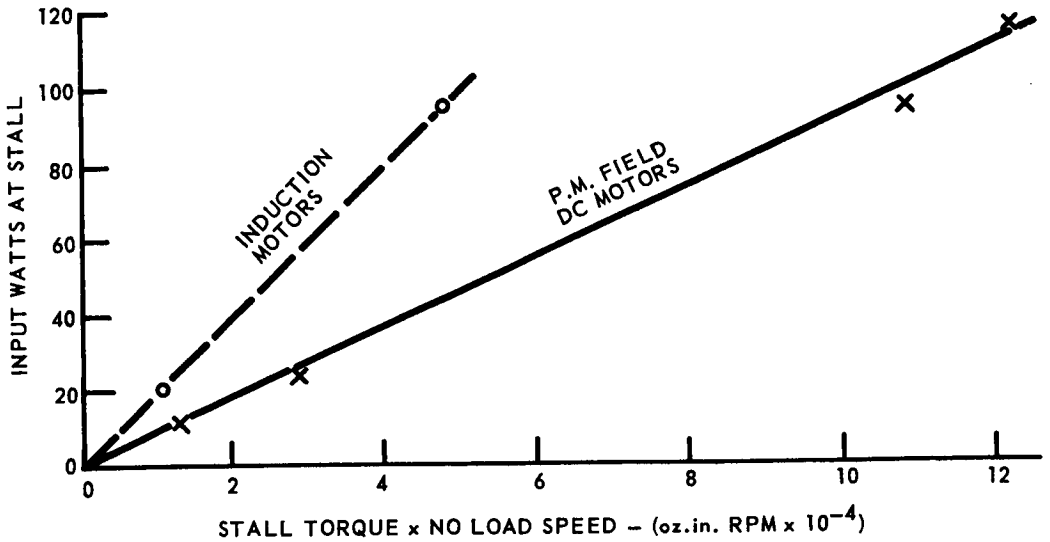

Figure 2-6 AC-DC Motor Comparison

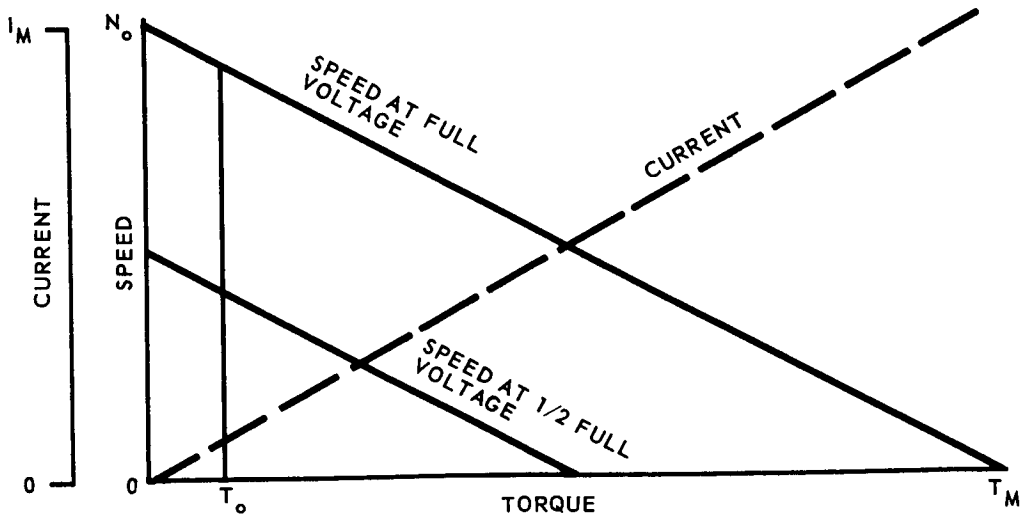

T_o = TORQUE DUE TO BRUSH & BEARING FRICTION

T_m = STALL TORQUE

N_o = NO-LOAD SPEED

I_m = ARMATURE CURRENT

Figure 2-7 Motor Characteristics

drive, particularily for low ratios, since these bearings must provide the forces to distort the flexible gear and its torque-transmitting sleeve or cup. The nutator transmission for low torque outputs does not require heavy bearing loads, because its gears are not distorted, and the torque-transmitting bellows can have a very low spring rate in bending.

The results of the transmission trade-off study are presented in Figures 2-9 and 2-10. The motor parameters m (negative slope of S-T) and T_o (motor friction) are assumed to be a function of the motor weight, W, as shown in Figure 2-9. Interface with other subsystems will establish the other parameters, such as P_m (maximum input power), r (pitch radius), F (traction force) and d (distance traveled). Choice of motor weight and transmission type and design, in combination with these parameters, will determine all the other parameters, through equations as plotted in Figure 2-10.

SLRV-TDM Preliminary Design

The design analysis and description of the SLRV traction drive preliminary design (Figure 2-11) is presented in the following paragraphs.

The unit is powered by an Inland motor, model T-1321A specially wound for high temperature service. The motor shaft is supported by two ball bearings in the motor housing.

The transmission is of the nutator type, in which a nutating internal bevel gear with 88 teeth is meshed with a rotating external bevel gear of 87 teeth. The nutating gear carrier is supported on an extension of the motor shaft by two ball bearings. The axis of the extension is at a small angle to the axis of rotation, so that shaft rotation causes the internal bevel gear to "wobble", or nutate. The gear carrier is connected to the housing by a bellows. This prevents gear rotation. In each nutation cycle the gear tooth contact travels once around the nutating gear, engaging 88 teeth on each gear. Thus, the other gear is forced to rotate through 1/87 of a revolution in a direction opposite to that of the motor shaft. The transmission ratio is therefore 87 to 1. This transmission ratio is applicable for the final SLRV-TDM design. Prior to the final design, the traction drive transmission ratio was determined for the initial design parameters. This transmission was calculated to be 78 to 1. The majority of the design analyses were based on this ratio; however, in Section 2.5 both transmission ratios are discussed.

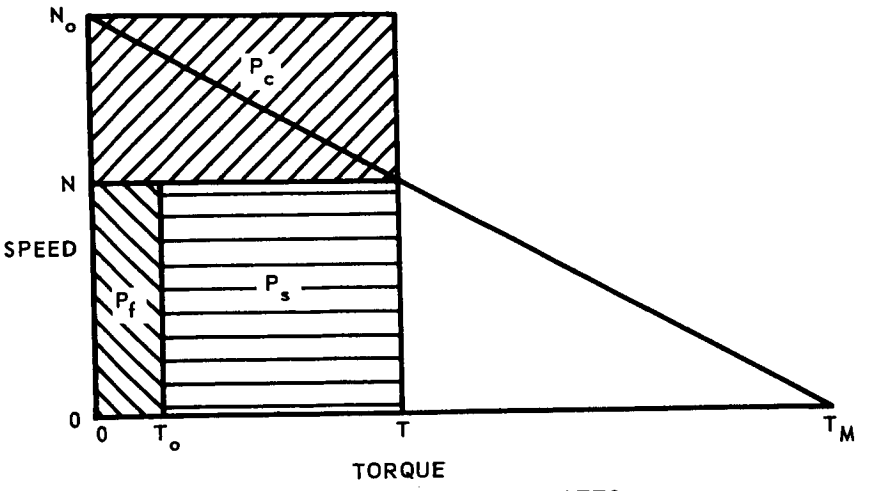

P_c = ELECTRICAL (COPPER) LOSS, WATTS

P_f = FRICTION LOSS, WATTS

P_s = SHAFT POWER, WATTS

Figure 2-8 Motor Power Distribution

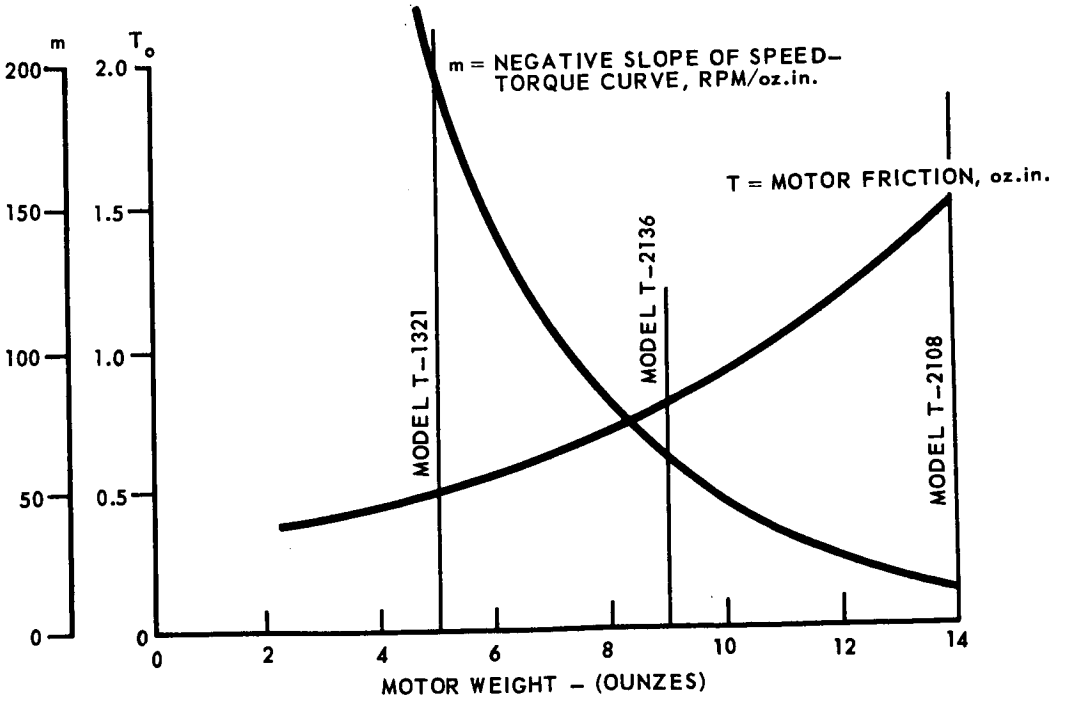

Figure 2-9 Motor Parameters

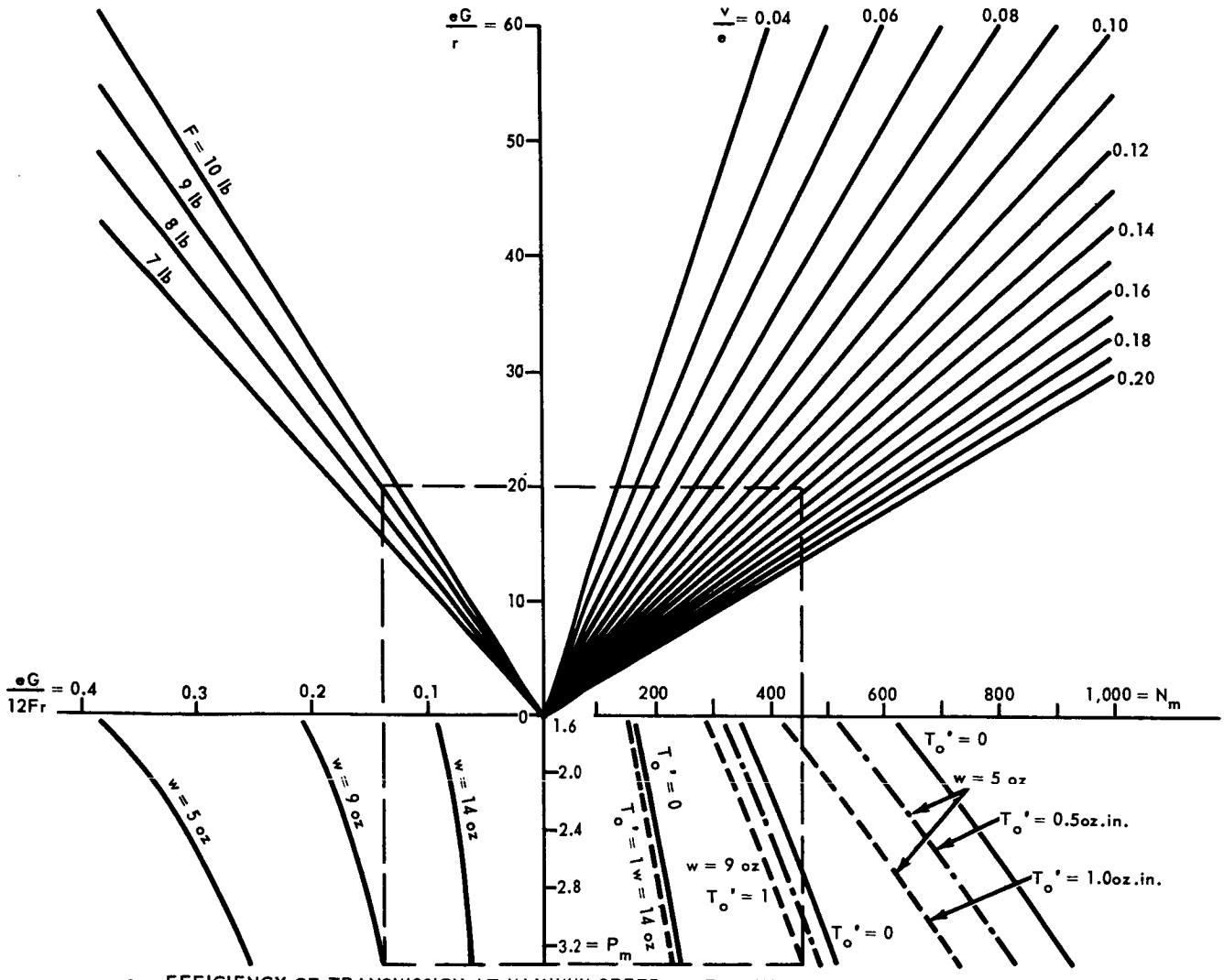

e = EFFICIENCY OF TRANSMISSION AT MAXIMUM SPEED
G = GEAR RATIO
r = DRIVE DRUM PITCH RADIUS, INCHES
V = VEHICLE SPEED, MPH
F = MAXIMUM RATED FORCE AT PITCH RADIUS, LB
N_m = MOTOR SPEED, RPM
w = MOTOR WEIGHT, OUNCES
P_m = MAXIMUM INPUT RATED POWER, WATTS

Figure 2-10 Transmission Trade-off

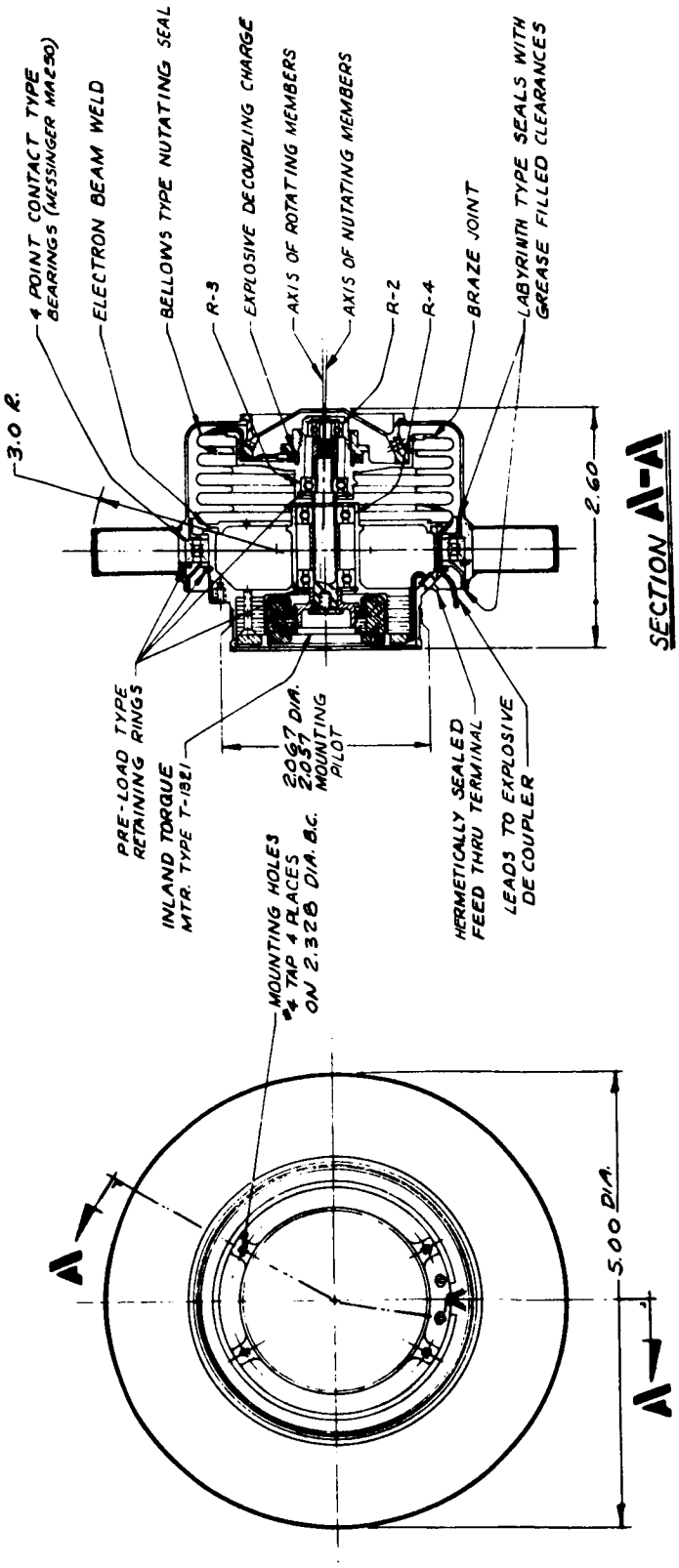

Figure 2-11 Layout of SLRV Traction Drive Mechanism

The motor housing, bellows, and carrier of the nutating gear combine to form a hermetically sealed enclosure for the motor and the bearings on the motor shaft. An atmosphere within the enclosure improves motor winding reliability, extends brush life, and permits the use of the best lubricants for the shaft bearings.

The final output member of the tractive drive unit is a drive drum which engages a thin metallic belt, or "track". The drum is supported by a single ball bearing, located centrally with respect to the track width. This bearing is of the 4-point contact type, slightly preloaded to eliminate both radial and axial clearance.

The drum bearing is mounted on the motor housing between two spacers. The spacers are shaped to provide small radial clearances of extended length between their outer diameters and the inside of the hub. These clearances will be filled with a non-volatile grease to protect the bearing from contamination by dust. The gears will also be protected, since they are within a cup-like extension of the drum hub.

As the ambient pressure drops during launch, air enclosed between the sprocket hub and the hermetically sealed chamber will escape through a small groove in the motor housing wall, under the drum bearing and its spacers.

An explosive decoupler will be actuated from earth in the event of any failure which results in either loss of power to the drive drum or resistance to free rotation of the drive drum by external means. Actuation will explode a charge contained in the carrier of the nutating gear. The explosion will shear the web from the hub, driving the web toward the motor and eliminating contact between the two gears. A slight taper on the hub will ensure sufficient friction to prevent the return of the web to its initial position. The gas generated by the explosion will escape through the same groove mentioned above. The electrical leads to the explosive will be threaded through this groove, and also through a channel between the nutating gear and its carrier. Table 2-2 indicates the preliminary specifications.

The bellows is a modification of one manufactured by Bridgeport Thermostat Division of Robertshaw-Fulton Controls Company. It resembles their part no. 790, with the following modifications:

Material - stainless steel #321	instead of phosphor bronze
No. convolutions - 4-1/2	instead of 15
Thickness - 0.008 in.	instead of 0.00925 in.

TABLE 2-2

PRELIMINARY SPECIFICATIONS

	Initial Design	Final Design
Envelope		
Drive Drum Diameter	5 in.	5 in.
Axial Length	2-3/4 in.	3 in. max
Weight	15 oz min to 21 oz max	21 oz max
Rated Torque	9.4 lb in. (150 in.-oz)	220 in.-oz
Speed at Rated Torque	1-1/3 rpm	2.0 rpm
Power Input at Rated Torque	1-1/2 watts	2.6 watts
Speed at No-Load	7-1/4 rpm	———
Power Supply	8.44 VDC	3 to 18 VDC

With these modifications, the spring rate will be 121 lb/in. and the maximum rated stroke will be 0.275 in. The effective area will remain 4.35 in.^{2}, and the mean radius is 1.18 in.

The maximum rated bend is

$$\frac{0.275}{1.18} = 0.234 \text{ rad.}$$

The spring rate in bending is found from

$$k = \frac{121}{2\pi} \int_{\theta}^{2\pi} (1.18 \sin \theta)^2 d\theta = 83.5 \text{ lb-in./radian}$$

The bending imposed on the bellows is 0.0272 radian. The "minimum" life (90% survival) is, according to the manufacturer's data, extrapolated beyond 10^8 cycles,

$$\bar{n} = 40,000 \left(\frac{0.234}{0.0272}\right)^{12} = 6.6 \times 10^{15} \text{ cycles}$$

This may be regarded as infinite life.

The bearings on the motor shaft are loaded by the gear tooth forces, (which are proportional to output torque), by force caused by atmospheric pressure acting on the bellows, and by forces caused by deflection of the bellows.

Figure 2-12 shows the forces on the shaft caused by bearing loads. The shaft is represented by two center-lines, intersecting at the vertex of the gear pitch cones. The bearing locations are given as distances from this vertex. The forces are represented by radial components in the vertical plane, radial horizontal components, and by axial thrust components.

The gears have a pressure angle of 14°. The angle between the axis of the nutating gear and the elements of its pitch cone is 65°. The cone length, from vertex to point of application of resultant tooth force, is 0.88 in. Then, at 9.4 lb-in. of output torque, the equations of equilibrium give the following loads caused by torque:

$H_1 = 8.4$	$H_2 = 3.6$	$H_3 = 26.1$	$H_4 = 13.9$
$V_1 = 4.5$	$V_2 = 3.2$	$V_3 = 5.9$	$V_4 = 4.6$
	$A_2 = -2.7$	$A_3 = -2.7$	

The effective area of the bellow is 4.35 in.^{2} and the pressure difference is 1.0 psi. The resulting thrust load is

$$A'_2 = A'_3 = 4.35 \text{ lb}$$

The bellows is 0.92-in. long, and is bent 0.0272 radians. Its stiffness in bending is 83 lb-in./radian.

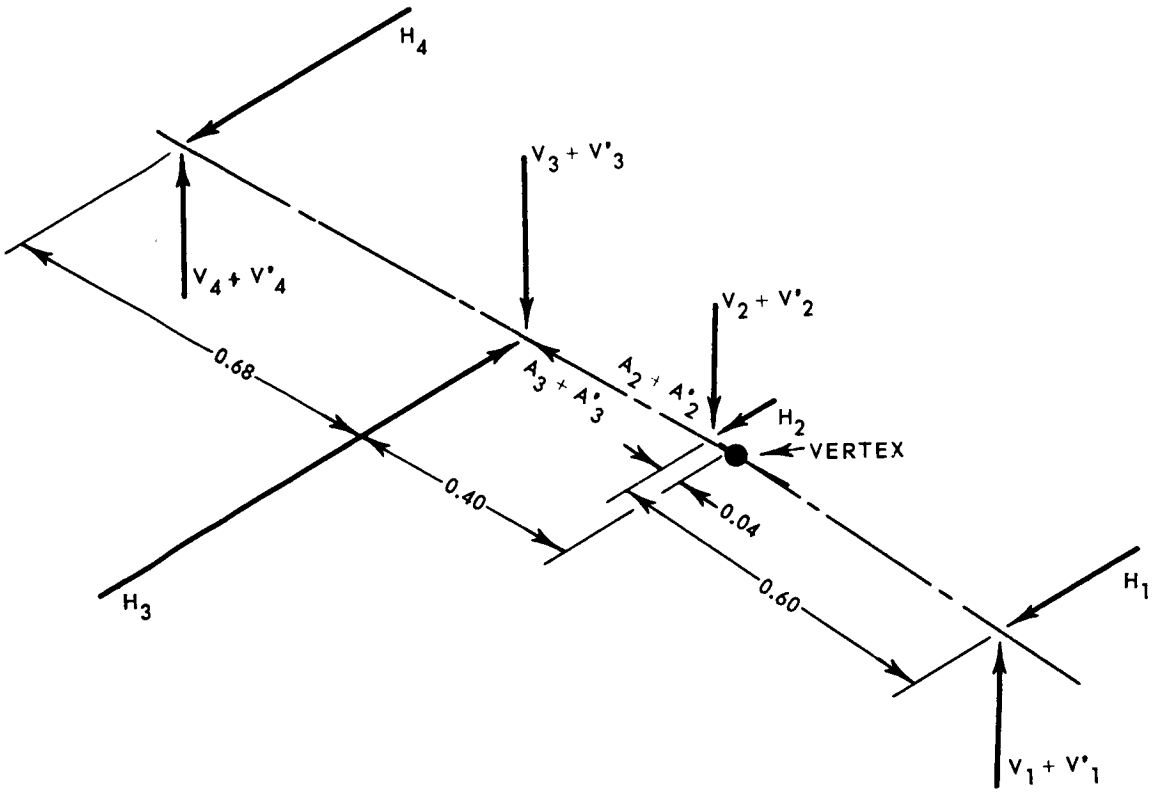

Figure 2-12 Forces on Shaft Due to Bearing Loads

Then the bending moment is

$$M_b = \left(83 + \frac{0.92}{2} \times 4.35\right) \times 0.0272$$

$$= 2.3 \text{ lb-in.}$$

The loads on the bearings caused by bellows deflection are

$$V'_1 = V'_2 = 3.8 \qquad V'_3 = V'_4 = 3.4$$

The total radial load on a bearing is

$$R = \sqrt{H^2 + (V + V')^2}$$

Evaluating the loads on each bearing gives

$$R_1 = 11.8 \text{ lb} \qquad R_2 = 7.9 \text{ lb} \qquad R_3 = 27.7 \text{ lb} \qquad R_4 = 16.0 \text{ lb}$$

$$A_2 + A'_2 = 1.65 \text{ lb} \qquad A_3 + A'_3 = 1.65 \text{ lb}$$

The following listing gives the rated capacity of the bearings for 3800-hr average life at 1000 rpm, their maximum effective radial loads, and the average life in revolutions for the maximum effective loads, per New Departure Catalog, 1961.

Bearing Number	1	2	3	4
Size	R - 2	R - 3	R - 4	R - 4
Rated Capacity, lb	17	40	43	43
Effective radial load	11.8	8.4	28.0	16.0
Life in revolutions	9.8×10^8	1170×10^8	12.8×10^8	118×10^8

The bending moment at bearing number 2 (above) is

$$M_2 = 0.60 \text{ in.} \times 11.8 \text{ lb} = 7.07 \text{ lb-in.}$$

The diameter of the shaft at this location is 0.1875 in.; thus the bending stress is

$$S_2 = \frac{32 \times 7.07}{\pi \times (0.1875)^3} = 10,900 \text{ psi}$$

Similarily, the bending stress at bearing number 3 is

$$S_3 = \frac{32 \times 0.68 \times 16.0}{\pi \times (0.250)^3} = 7,100 \text{ psi}$$

To simplify the calculations, the effective diameter of the shaft is assumed to be 0.1875 in. between bearings number 1 and number 2, and 0.250 in. for the rest of its length. Then there are two moments of inertia,

$$I_1 = \frac{\pi}{64} \times (0.1875)^4 = 0.609 \times 10^{-4} \text{ in}^4$$

and

$$I_2 = \frac{\pi}{64} \times (0.250)^4 = 1.92 \times 10^{-4} \text{ in}^4$$

Assume the deflection is zero at bearings number 3 and number 4. Let the deflection at bearing number 1 caused by the force H_2 be denoted by $1\,\Delta_{H_2}$, etc. Then $1\,\Delta_H = 1\,\Delta_{H_1} + 1\,\Delta_{H_2}$ is the total horizontal deflection at bearing number 1.

$$1\,\Delta_{H_1} = \int_{\text{number 1}}^{\text{number 4}} \frac{M^2 H_1\, dl}{H_1 E I} = \int_0^{0.60} \frac{H_1 x^2\, dx}{E I_1}$$

$$+ \int_{0.60}^{0.96} \frac{H_1 x^2\, dx}{E I_2} + \left(\frac{0.96}{0.68}\right)^2 \frac{H_1 y^2\, dy}{E I_2} = \frac{3270 H_1}{E}$$

Similarly,

$$1\,\Delta_{V_1} = \frac{3270(V_1 + V'_1)}{E}$$

$$1\,\Delta_{H_2} = \int_{\text{number 2}}^{\text{number 4}} \frac{M_{H_2} M_{H_1}\, dl}{H_1 E I}$$

$$= \int_{0.60}^{0.96} \frac{H_2 (x - 0.60)\, x\, dx}{E I_2} + \int_0^{0.68} \left(\frac{0.96}{0.68}\right)\left(\frac{0.36}{0.68}\right) \frac{H_2 y^2\, dy}{E I_2}$$

$$= \frac{693 H_2}{E}$$

$$1\,\Delta_{V_2} = -\frac{693(V_2 + V'_2)}{E}$$

$$2\,\Delta_{H_1} = \frac{693 H_1}{E}$$

$$2\,\Delta_{V_1} = \frac{693(V_1 + V_1)}{E}$$

$$2\,\Delta_{H_2} = \int_{\text{number 2}}^{\text{number 4}} \frac{M_{H_2}^{\;2}\,dl}{H_2 E I} = \int_0^{0.36} \frac{H_2 x^2\,dx}{E I_2}$$

$$+ \int_0^{0.68} \left(\frac{0.36}{0.68}\right)^2 \frac{H_2 y^2\,dy}{E I_2} \; \frac{234\,H_2}{E}$$

$$2\,\Delta_{V_1} = -\frac{234(V_2 + V'_2)}{E}$$

Then

$$1\,\Delta_H = \frac{3270\,H_1}{E} + \frac{693\,H_2}{E} = \frac{29400}{E}$$

$$1\,\Delta_V = \frac{3270}{E}(V_1 + V'_1) - \frac{693}{E}(V_2 + V'_2) = \frac{22,200}{E}$$

$$2\,\Delta_H = \frac{693\,H_1}{E} + \frac{234\,H_2}{E} = \frac{6640}{E}$$

$$2\,\Delta_V = \frac{693(V_1 + V'_1)}{E} - \frac{234(V_2 + V'_2)}{E} = \frac{4110}{E}$$

For stainless steel, $E = 2.8 \times 10^7$, then

$$1\,\Delta_H = 0.00107 \qquad 1\,\Delta_V = 0.00079$$

$$2\,\Delta_H = 0.00024 \qquad 2\,\Delta_V = 0.00015$$

Denote displacement of the vortex of the nutating gear by O Δ. Then,

$$0\ \Delta_H = 2\ \Delta_H + \frac{0.04}{0.60}\ (1\ \Delta_H - 2\ \Delta_H) = 0.00029$$

$$0\ \Delta_V = 0.0019$$

Denote angular displacement of the axis of the nutating gear by θ. Then,

$$\theta_H = \frac{1\ \Delta_H - 2\ \Delta_H}{0.60} = 0.00138$$

$$\theta_V = 0.00107$$

This displacement changes the nutation angle. The original angle is 0.0272 radian. The final angle is

$$\gamma = \sqrt{(0.0272 - 0.0011)^2 + 0.00138^2}$$

$$= 0.0262$$

The effect of shaft deflection on the gear mesh is analogous to an increase in center distance for spur gears. Backlash and pressure angle are slightly increased, and working depth is decreased about 0.0009 in. These changes are not excessive.

Let S_b = beam stress on gear tooth

f = face width = 0.12 inch

y = Lewis form factor

$G + 1$ = 79

The Lewis equation for beam stress in bevel gears can be put in the form

$$S_b = \frac{9.4/0.88 \sin 65^\circ}{\frac{2\ \pi \times 0.88 \sin 65^\circ}{79} \times 0.12 \times \frac{0.88 - 0.12}{0.88}\ y}$$

$$= \frac{1790}{y}$$

From a layout of tooth shape, y is found to be 0.14.

Therefore,

$$S_b = 12,800 \text{ psi}$$

when,

$$T_2 = 9.4 \text{ lb-in.}, \text{ the motor speed is 100 rpm.}$$

Then the tooth mesh velocity is 42 ft per minute. At this low speed dynamic loading will be negligible, and the maximum beam stress will be approximately 13,000 psi.

General simplifying assumptions were made in the analysis of stresses in the traction unit drive drum.

Assuming the maximum drive drum load of 400 lb[1] uniformly distributed on the section of the housing supporting the drive drum bearing, the shear stress in this section will be,

$$S_s = \frac{400}{\frac{\pi}{4}(2.5^2 - 2.34^2)} = 646 \text{ psi.}$$

The bending stress at the section at the mounting plane will be,

$$S_b = \frac{400 \times 0.65 \times 3.06}{\frac{\pi}{32}(3.06^4 - 2.94^4)} = 623 \text{ psi.}$$

These stresses are moderate, ensuring that the actual stresses will not be excessive for materials with yield strength of the order of 30,000 psi or higher.

The rated load on the drive drum bearing is 570 lb for a 3000-hr life at 100 rpm. The life at 400-lb load is,

$$\bar{n} = \left(\frac{570}{400}\right)^3 \times 18 \times 10^6 = 52 \cdot 10^6 \text{ revolutions.}$$

[1] Final design calls for approximately 100 lb.

The 90% survival point is $n_{90} = 10.4 \times 10^6$ rev. This corresponds to a travel of 4,060 km.

The motor parameters are given in the following listing:

DC resistance	40 ohms
Torque sensitivity	16.5 oz-in./amp
Back emf	0.0122 volt/rpm
Total friction	0.5 oz-in.

The input power at 85% of stall torque is specified as 1.5 watts. At constant voltage operation the power at stall will be,

$$\frac{1.5}{0.85^2} = 1.77 \text{ watts.}$$

Therefore the stall current will be,

$$I_M = \sqrt{\frac{1.77}{40}} = 0.211 \text{ amp}$$

The stall torque will be,

$$T_M = 16.5 \times 0.211 = 3.48 \text{ oz-in.}$$

The applied voltage will be,

$$V = 40 \times 0.211 = 8.44 \text{ volts.}$$

At 85% of stall torque, the torque is,

$$T = 2.96 \text{ oz-in.}$$

and the speed is,

$$N = (1 - 0.85) \times \frac{8.44}{0.0122} = 104 \text{ rpm.}$$

At this operating point, the output torque is required to be 9.4 lb-in., or 150 oz-in., as indicated in the initial specification.

Assuming that the friction torque in a bearing is,

$$0.0025\ R\ r_b,$$

where R is the effective radial load and r_b is the radius of a circle through the centers of the balls, the total friction torque caused by the shaft bearings is,

$$T' = 0.0025\ (11.8 \times 0.125 + 8.4 \times 0.172 + 28.0 \times 0.218 + 16.0 \times 2.18)$$

$$= 0.031 \text{ lb-in.} = 0.50 \text{ oz-in.}$$

Assuming a gear and drive drum bearing efficiency of 0.98, the required gear ratio is,

$$G = \frac{150}{0.98\ (2.96 - 0.5 - 0.50)} = 78$$

The drive drum speed at 9.4 lb-in. torque will be,

$$\frac{N}{G} = \frac{104}{78} = 1.33 \text{ rpm.}$$

At no load, the bearing friction torque will be,

$$T' = 0.0025\ (3.8 \times 0.125 + 4.7 \times 0.172 + 4.3 \times 0.218 + 3.4 \times 0.218)$$

$$= 0.0074 \text{ lb-in.} = 0.12 \text{ oz-in.}$$

Then the motor speed will be,

$$N_M = \left(1 - \frac{0.5 + 0.12}{3.48}\right) \frac{8.44}{0.0012} = 568.$$

The no-load drive drum speed will be,

$$\frac{568}{78} = 7.28 \text{ rpm.}$$

The performance can be summarized by a torque-speed equation for the drive drum:

$$N_S = 7.28 - .634\ T_S$$

where N_S is drive drum rpm, and T_S is drive drum torque in lb-in.

The initial design of the traction drive mechanism (TDM) was based on the following design parameters:

Maximum rated torque	9.4 lb-in. (150 oz-in.)
Input power at rated torque	1.5 watts

The initial specification was revised so the TDM unit is to be driven at any of three controlled speeds, as follows:

N_1 = 10.8 rpm

N_2 = 7.2 rpm

N_3 = 2.0 rpm.

At N_3, the torque is to be 220 oz-in. with a power input of 2.6 watts. This requirement represents a new specification for the traction drive unit. The final design is based on this requirement, and it represents the final design parameters and configuration for the SLRV drive unit.

The requirement for a torque of 220 oz-in. and a speed of 2.0 rpm at a power 2.6 watts can be met by increasing the transmission ratio. The controlled speeds are not a function of the TDM design, but of the means employed to drive it.

The required change in gear ratio is found as follows. Calculation of friction torque at various values of output torque indicates that the total friction torque on the input shaft is:

$$T_f = 0.00272\ T_s + 0.60 \text{ oz-in.}$$

where T_s is output (drive drum) torque. Assuming 98% efficiency for the gear mesh and drive drum bearing, the geat ratio must be:

$$G = \frac{T_s}{0.98\,(T - T_f)}$$

where T is motor developed torque. When $T_s = 220$,

$$T = \frac{224 + 1.2\,G}{G}.$$

The torque developed at stall by the Inland motor T-1321-A is:

$$T_m = \frac{16.5}{40}\,V = 0.413\,V$$

where V is applied voltage.

The theoretical no-load speed of this motor is:

$$N_m = \frac{V}{0.0122}$$

The power input at developed torque T is:

$$P = \frac{N_m\,T}{1350}, \text{ in watts.}$$

The motor speed at T is:

$$N = \frac{T_m - T}{T_m}\,N_m, \text{ in rpm.}$$

The drive drum speed is:

$$N_s = \frac{N}{G}.$$

Solving these equations for G, when $P = 2.6$, $N_s = 2.0$, and $T_s = 220$, gives:

$$2.4\,G^3 - 2775\,G^2 + 107{,}000\,G + 10{,}000{,}000 = 0.$$

The smallest positive root of this equation is 86.7. Therefore, the transmission ratio selected is 87:1. The performance of the TDM is then defined by these equations:

$$N = \frac{T_m - T}{T_m} N_m$$

$$= \frac{0.413\ V - T}{0.413 \times 0.0122} = 199\ (0.413\ V - T).$$

$$N_s = \frac{N}{87}$$

$$T_s = 0.98 \times 87\ (T - 0.60 - 0.00272\ T_s)$$

Therefore,

$$T = \frac{T_s}{85.2} + 0.00272\ T_s + 0.60$$

$$= \frac{T_s}{69.3} + 0.60$$

Therefore,

$$N_s = \frac{199}{87}\left(0.413\ V - 0.60 - \frac{T_s}{69.3}\right)$$

$$= 0.945\ (V - 1.45) - 0.0330\ T_s.$$

Also:

$$P = \frac{N_m\ T}{1350}$$

$$= \frac{V}{0.0122 \times 1350} \times \left(\frac{T_s}{69.3} + 0.60\right)$$

Therefore,

$$T_s = 1140\ \frac{P}{V} - 41.6.$$

Figure 2-13 is a plot of N_s versus T_s at various voltages, with limiting curves for P = 1.5, 2.6, and 8.0 watts. The motor current, which is a linear function of T_s is also plotted.

No change will be made between the initial design and final design configurations, except to increase the number of teeth in the bevel gears from 78 and 79 to 87 and 88, and to decrease the nutation angle from 0.0272 radian to 0.0244 radian.

The bending stress on the bellows is reduced by the factor (0.0244/0.0272) = 0.90. The maximum stress on the bearings and shaft is increased by the factor (220/150) = 1.47. This is within the capacity of the bearings, and will not affect the life calculation, since the extreme load is applied infrequently. The shaft bending stress is 16,000 psi, a safe value for low-alloy steel.

The gear tooth stress is increased by the factor (87/78) (220/150) = 1.64, to 21,300 psi. This is a conservative stress for heat-treated steel gears.

In view of the intention to control the speed by varying the effective voltage, there is no longer a single rated voltage. Pulse-modulated DC is a practical power source, if a diode shunt is used to maintain motor current during the short periods when voltage is not applied, and also provided that these periods are short relative to the inductive time constant of the motor. Under these conditions, the motor current will be nearly constant during steady-state operation. This is required for satisfactory brush life.

Major factors in material selection are:

1. Temperature range in the lunar environment from -118°F minimum to 272°F maximum requires that differences in coefficient of thermal expansion between mating parts, (and particularly between ball bearings and their mountings) be minimized.

2. Integrity of the hermetic seal requires that all components of the wall of the sealed chamber be compatible for joining by gas-tight welding, brazing or hard-soldering.

3. Weight must be minimized to the extent possible without compromising reliability.

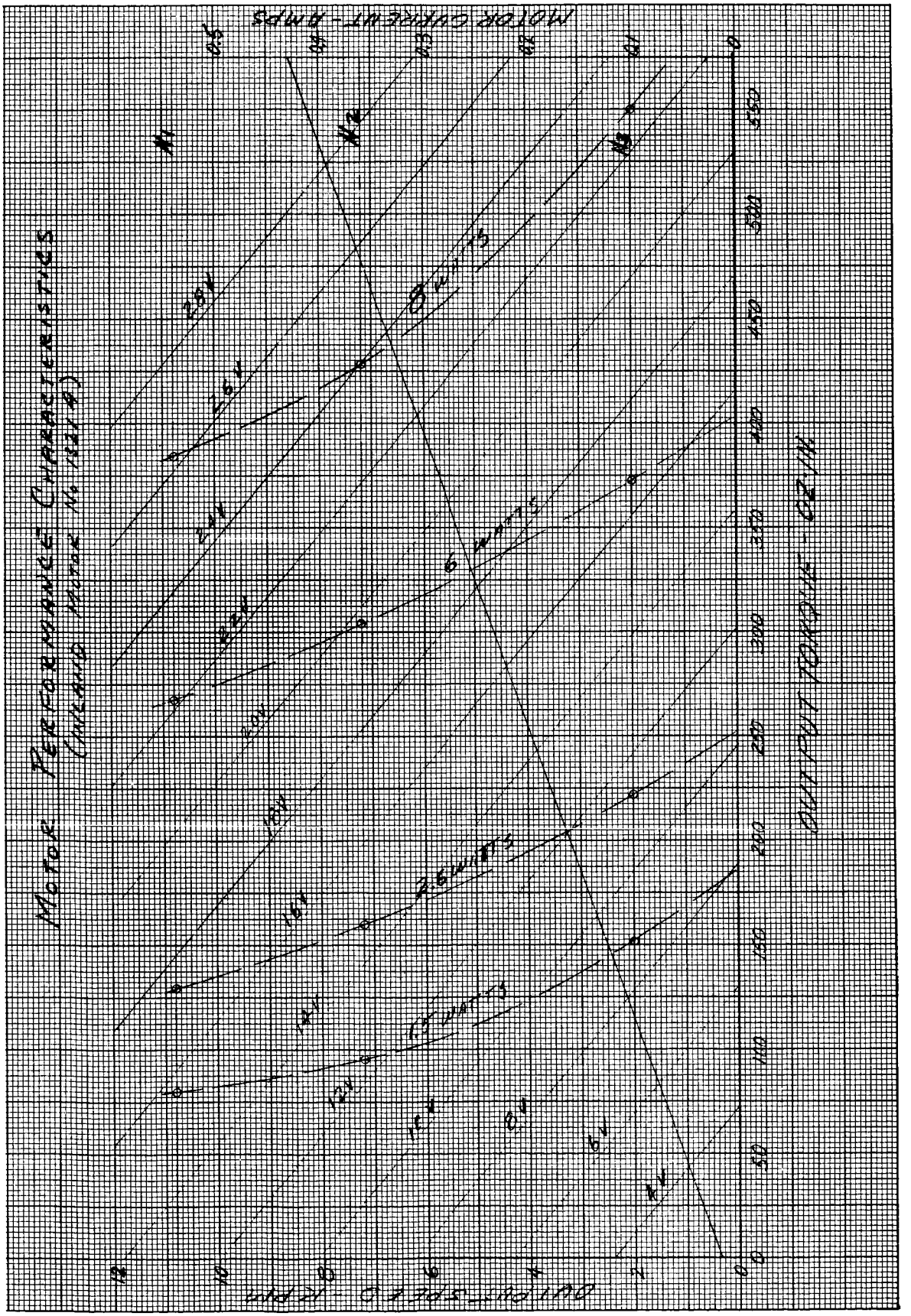
MOTOR PERFORMANCE CHARACTERISTICS
Underwood Motor No 1221 A
MOTOR CURRENT - AMPS
OUTPUT TORQUE - OZ/IN
MOTOR SPEED - RPM
0.5
0.4
0.3
0.2
0.1
0
50
100
150
200
250
300
350
400
450
500
550
0
2
4
6
8
10
12
14
16
18
20
22
24
26
28
30
32
34
36
38
40
42
44
46
48
50
52
54
56
58
60
62
64
66
68
70
72
74
76
78

4. Stresses caused by loads are moderate for all parts other than the ball bearings.

5. The motor housing must be nonmagnetic.

The best material for the ball bearings is the manufacturer's standard steel since it has the highest endurance available in the anticipated temperature range.

Because of the importance of minimum weight, beryllium will be used where practical. Its coefficient of thermal expansion is 6.8×10^{-6} per°F, very nearly identical to that of the ball bearing material.

The motor shaft and gears will be made of a low-alloy steel with low notch sensitivity.

The bellows will be made of a material suitable for hydraulic forming, such as phosphor bronze or one of the 300 series stainless steels. The final choice will be based on compatibility for hermetically joining to the gear carrier and the end disc of the motor housing, for which beryllium is perferred. If no solder is suitable for these joints it may be necessary to make the gear carrier, the motor housing, and both its end plates for type 310 stainless steel. Stainless steel construction will result in a weight of 1.31 lb.

Study of Commutated Motor Brushes

Since commutated type DC motors have been selected as the drive motors in the SLRV preliminary design, a study of motor brushes was conducted. The purpose of this study is to determine generally the effects of various atmospheres and a vacuum on the operational life of commutated motors.

The primary area of concern in the operational life of commutated motors is brush wear. Under normal atmospheric pressure, brush wear rates are a function of the type of commutator surface, where effective lubrication is obtained by the absorption of materials present under normal operating and environmental conditions. However, when the environment materials are absent, as in the case of a vacuum environment, a much higher brush wear rate takes place.

Investigation of commutated motor brush life, as reported in published literature, indicates that the wear rate of graphite brushes on copper is determined by the type of surface on the copper. Also, the type of surface on the copper is determined by brush pressure, surface speed, contact area, and current. At high speeds and heavy brush loads, the wear rate is relatively high and unaffected by the magnitude of the current. At this condition, a continuous layer of transferred graphite is formed on the commutator resulting in a relatively high brush wear rate.

However, at low speeds and light loads, a surface film of cuprous oxide (Cu_2O) is developed which prevents the transfer of graphite and thus reduces the wear rate. Since high current breaks down the oxide film, which results in the transfer of graphite, the wear rate then increases with current. At high current, the transferred layer of graphite becomes continuous, approaching the condition of heavy loads and high speeds. The significance of this study indicates that the conditions that tend to produce severe wear rates are normally encountered in vacuum operations, where a lubricating film is not allowed to develop on the commutator surface.

The problem of extremely high wear rates of motor brushes may be resolved by providing standard motors with a lubricant adequate for vacuum operation.

Several orbiting satellites use commutated motors that are operating satisfactorily at lunar environment. The satellite has two torque motors aboard operating as follows:

	Azimuth Drive Motor	Elevation Drive Motor
Inland Torque Motor	T-4006 A	T-2907 B
Operating Time, hours	7900	7900
Total Revolutions	15.8×10^6	null-seeking mode
Pressure, mm Hg	1×10^{-8}	1×10^{-8}
Speed, rpm	30 - 40	null-seeking mode
Temperature, ^oC	5 - 10	-3
Armature Current	Average 185 ma	0 - 300 ma (Average 100 ma)

Also, the S-17 satellite torque motor (Inland, type T-4009 A) had completed 4800 hr at 60 rpm at 5×10^{-8} mm Hg and has accumulated 17.3×10^{6} rev with no apparent deterioration of performance. The above information was reported at the "Proceedings of the First Symposium on Direct Drive Torque Motors in Precision Servo Systems, May 1963".

The lubricant used in these satellites, called Vac Kote, was developed by Ball Brothers Research Corporation. This lubricant was also used successfully in other satellite applications such as bearings and slip rings.

It was also reported that to determine the effects of the Vac Kote process under normal conditions, two identical units, Inland type T-2108 E, one treated with Vac Kote and one not treated, ran 17.4×10^{6} rev at 1800 rpm, 250-ma armature current, and at ambient pressure with no significant difference in wear rate.

Additional test information is available on other lubricants proved to be effective under vacuum conditions. CBS Laboratories technique of vapor depositing extremely thin films of various materials on the surfaces to be protected proved to be successful. The vapor deposit process consists of several layers of nickel, chromium, silver, and a top layer of molybdenum-disulfide. A slip ring test was conducted by CBS using silver graphite brushes and successive layers of vapor deposited nickel, chromium, and lead sulfide. Twenty amps were continuously passed at 1/12 rpm for 50 minutes on and 10 minutes off for 15 days at temperatures of 0, 25, and 70°C at 10^{-9} mm Hg and a brush pressure of 150 to 180 grams. At the conclusion of the test, no increase in contact resistance was noted and no gross surface damage had resulted.

In the Orbiting Solar Observatory (OSO), the brush material was composed of 75% coin silver (90% Ag, 10% Cu), 20% graphide, and 5% MoS_2. The slip ring material was coin silver and lubricated with Apiezon c oil and 5% special additive, vacuum impregnated into the ring.

NASA Marshall Space Flight Center (Space Lubrication Conference, May 1963) reported that hot pressed, sintered cermet brush materials have proved to be successful on DC motors operating under vacuum environment. Brushes made from molybdenum disulfide, silver, and silver sulfide have operated up to 3700 hr at 2000 rpm, 10 amps. cm^2, and at 10^{-7} mm Hg. Brush wear and arcing were negligible.

In the proposed SLRV-TDM design, an Inland type T-1321 A, DC motor will drive the lunar vehicle. This is a 5-oz motor that will operate in an inert atmosphere at 1-psia pressure and in a hermetically sealed chamber. Maximum vehicle loads require the motor to operate at approximately 8 volts (17% of rated (48 v) voltage), up to 500 - 700 rpm, and 17% of rated (1.21 amps) current.

The 1-psia atmospheric environment present in the sealed chamber becomes essentially inert (N_2) after a brief period of operation, since a chemically active atmosphere containing 0_2 becomes inert after the 0_2 has been consumed.

The predicted mean brush life of the 5-oz T-1321 A motor for SLRV application is given as 225 km, based on motor rotation of 200,000 rev/km. This gives a total brush life of 45×10^6 revolutions.

For a 30-km mission, the motor accumulates a total of 6.0×10^6 rev (30 km x 2000,000 rev/km). This is only 13.3% of the predicted mean brush life. Comparing the 45×10^6 revolutions to the number of revolutions of the torque motors that are operating in (OSO) indicates that the predicted performance of the SLRV motor is within reasonable values.

The azimuth (T-4006 A) drive motor or OSO accumulated 15.8×10^6 rev as of 13 May 1963. This is approximately 2.6 times the operating revolutions of the SLRV motor and 35% of its predicted brush life. As of this date, OSO satellite is still orbiting and has probably accumulated an additional 10×10^6 revolutions without motor failure.[1] Also, the elevation motor (T-2907 B) experienced the same operating conditions as the azimuth motor except this motor operated in a null-seeking mode.

The torque motor (T-4009 A) of the S-17 satellite also accumulated 17.3×10^6 rev which is almost three times the operating revolutions of the SLRV motor and 38.5% of its predicted brush life without failure.

These motors operate at only a fraction (15 to 20%) of rated power. The SLRV motor projected performance indicates that it will also operate at a fraction of power at maximum load. However, the speed of this motor is higher than the motors aboard the satellites cited above.

---

[1] Telephone conversation, Mr. Frank Josephs, Inland Motors.

During a discussion with Inland Motors on commutated motor brush life in a vacuum environment, the following was reported.

1. For all motors that operate at an altitude up to 100,000 ft (0.16 psia), the brushes are given the altitude treatment. (This treatment is a proprietary process provided by the brush manufacturer, Metallized Carbon, Yonkers, N.Y., and is called H-21.)

2. Brush composition for these motors is 50% silver and 50% graphite.

3. In the motors used in OSO, both the brushes and the commutator were treated with Ball Brothers Vac Kote process. All other motors that operate in a vacuum environment are also treated with this process.

4. The latest reports indicate that OSO has operated successfully for 18 months.

5. No arcing problems were encountered, since these motors are operating at a relatively low voltage resulting in no ionization.

Arcing the ionization are normally encountered in systems operating at high voltage and pressure. At a low system voltage and vacuum environment, ionization, and arcing problems are essentially absent.

Vacuum lubrication is required for commutated motors operating in lunar environment to extend motor brush life. The most effective lubricant appears to be the Ball Brothers Vac Kote process. Brushes made of silver, graphite, and MoS_2 are satisfactory for vacuum application. However, consideration must be given to other materials used in lunar environments. These materials may exhibit unwanted properties such as outgassing or expansion caused by entrapped pressure. Also, qualification tests should be conducted on critical components under environment conditions simulating operational requirements.

2.1.2.2 Description and Design

The SLRV nutator transmission demonstration model is shown in Figure 2-14. One of the two test models that were fabricated is shown in Figures 2-15 and 2-16. Figure 2-15 shows a completely assembled SLRV-TDM unit, with a plastic body to view the nutating transmission and bellow. Figure 2-16 shows an exploded view of the components that are used in assembling the transmission and the drive unit. The basic design of this unit is similar to the preliminary TDM design as described in Section 2.1.

Besides the nutating transmission, this unit also uses the Inland 5-oz drive motor, T1321A (and T1321C for the second unit), the transmission ratio of 75:1, which was arbitrarily selected early in the program, and a hermetically sealed chamber using a bellows flexible member. Other components such as shaft bearings and drive drum bearings are also similar to the SLRV design in size and type. The transmissions for the demonstration models were designed early in the program because of the lead time required to fabricate the gears. The hermetically sealed chamber permits this unit to operate at both room conditions and vacuum environment. A provision was incorporated in the design to evacuate the hermetically sealed chamber to 1 psia during vacuum environment tests.

Limited performance tests of test models were conducted. Both models were tested in normal atmospheric environment; serial number 1 was additionally tested in vacuum. Figures 2-17 and 2-18 show a photograph and schematic of the test set up.

2.1.2.3 Test Results

The results of the efficiency tests are summarized in Table 2-3. A typical performance curve is shown in Figure 2-19.

The efficiency when operating within a vacuum slightly exceeded its atmosphere operation. This may be explained in part by reduction of windage losses.

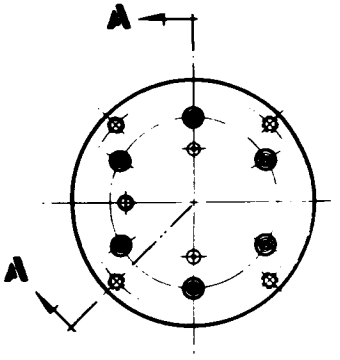

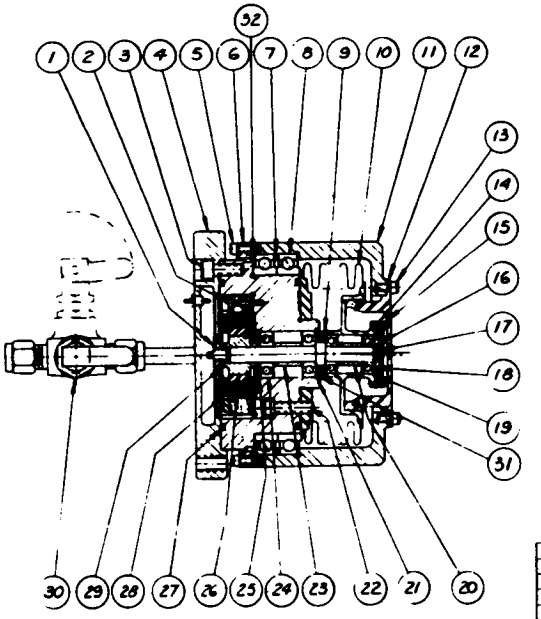

SECTION A-A

1	2154366-2	SPACER			32
1	2154358	HOUSING TORQUE MTR			31
1	STOCK	VALVE-TOGGLE	HOKE #1245 303 SST		30
1	2154371	WASHER TAB LOCK			29
1	STOCK	TORQUE MOTOR	INLAND TYPE T-1921		28
2	STOCK	"O"RING PARKER #2-35	2.239 I.D. x .070 C.S.		27
1	2154367	HUB-MOTOR ROTOR			26
1	STOCK	SNAP RING-BOWED, INT	TRUARC #N5001-75		25
2	STOCK	BEARING	R4A - ABEC 5		24
1	2154365-2	SPACER			23
6	STOCK	SCR-HEX SOC HD CAP	#8-32 NC x .62 LG		22
1	STOCK	SNAP RING-INTERNAL	TRUARC N5000-75		21
1	2154365-1	SPACER			20
1	STOCK	"O" RING PARKER #2-16	.614 I.D. x .070 C.S.		19
2	STOCK	BEARING	R4 — ABEC 5		18
1	2154357	SHAFT-NUTATING GEAR			17
1	STOCK	SNAP RING-BOWED, EXT	TRUARC #5101-25		16
6	STOCK	SCR-HEX SOC HD CAP	#0-80 NF x .18 LG		15
1	2154361	CAP-GEAR CARRIER			14
8	STOCK	SCR HEX SOC HD CAP	#4-40 NC x .31 LG		13
1	2154280	GEAR-BEVEL			12
1	2154863	DRUM-DRIVE WHEEL			11
1	2154359	BELLOWS ASSY			10
1	STOCK	SNAP RING-INTERNAL	TRUARC N5000-62		9
2	STOCK	BEARING-SPLIT BALL BRG	TCF 41-52 P ABEC 3		8
1	2154366-1	SPACER			7
1	2154862	RING-BRG RETAINER			6
8	STOCK	SCR-HEX SOC HD CAP	#4-40 NC x .50 LG		5
1	2154364	COVER-MOTOR HSG			4
6	STOCK	SCR HEX SOC HD CAP	#10-24 NC x .50 LG		3
4	STOCK	SCREW FLAT HD	#2-56 NC x .50 LG		2
1	STOCK	NUT HEX #10-32			1
QTY REQ'D	PART NO	DESCRIPTION	MATERIAL DESCRIPTION & SPECIFICATION	CODE IDENT	ITEM NO

Figure 2-14 Layout of Nutator Transmission and Drive Unit Demonstration Model

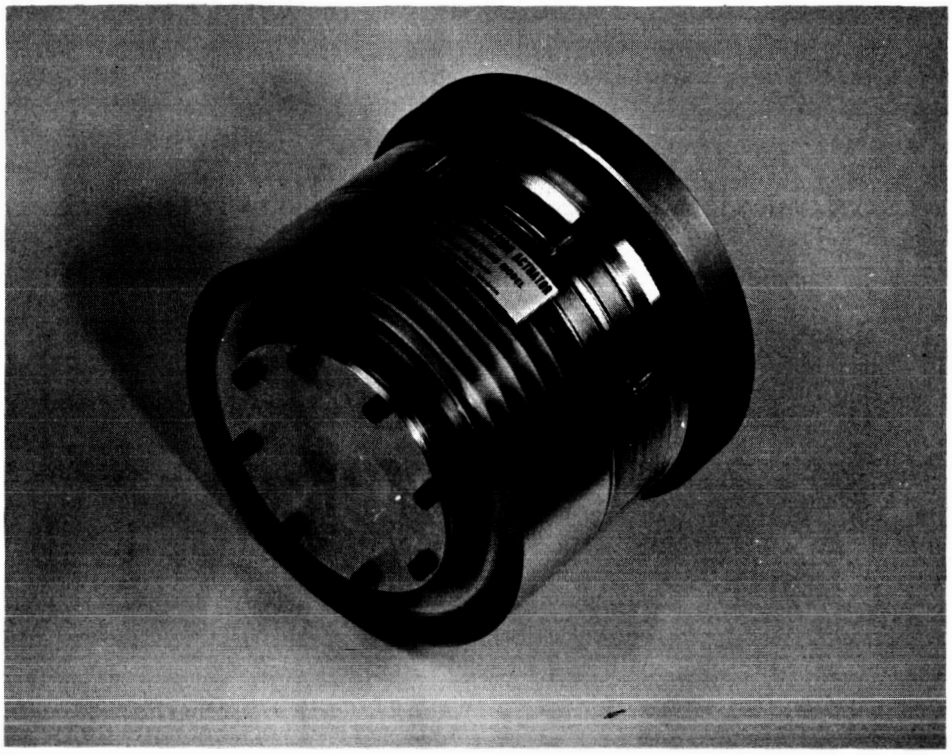

Figure 2-15 Nutator Transmission and Drive Unit Demonstration Model with Plastic Housing

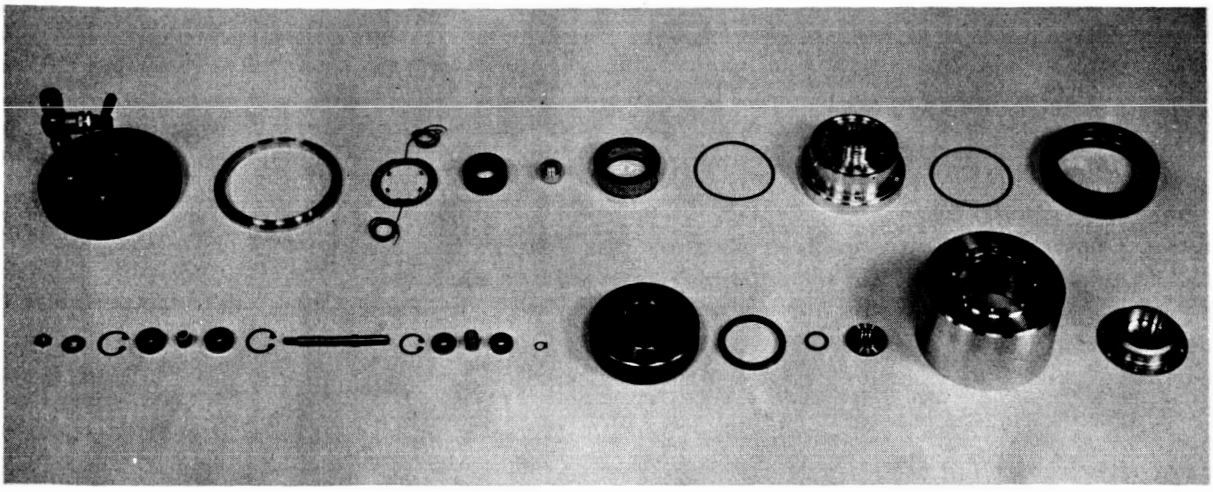

Figure 2-16 Nutator Transmission and Drive Unit Demonstration Model Components

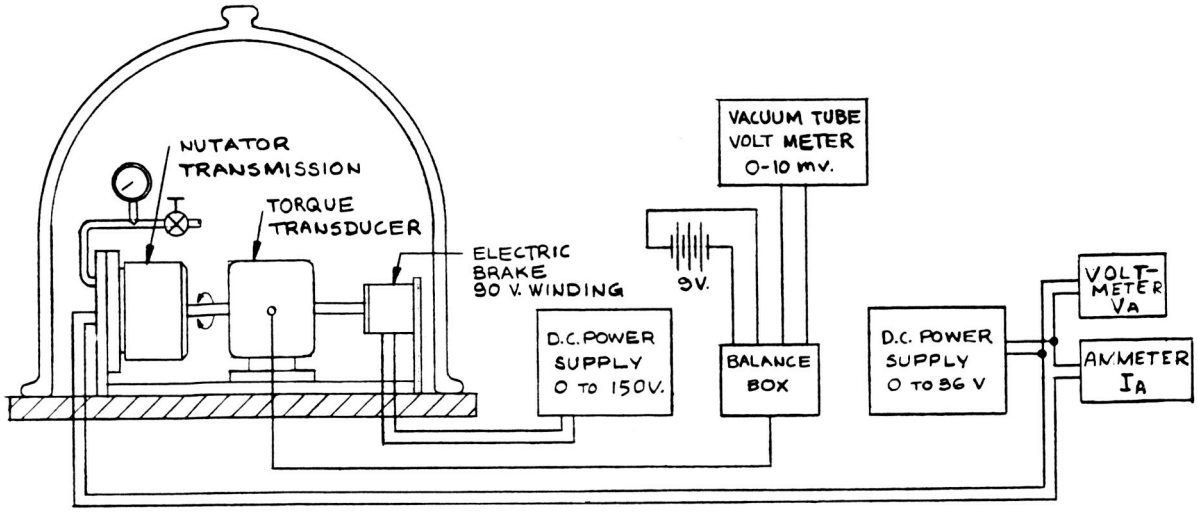

Figure 2-17 Nutator Transmission Schematic

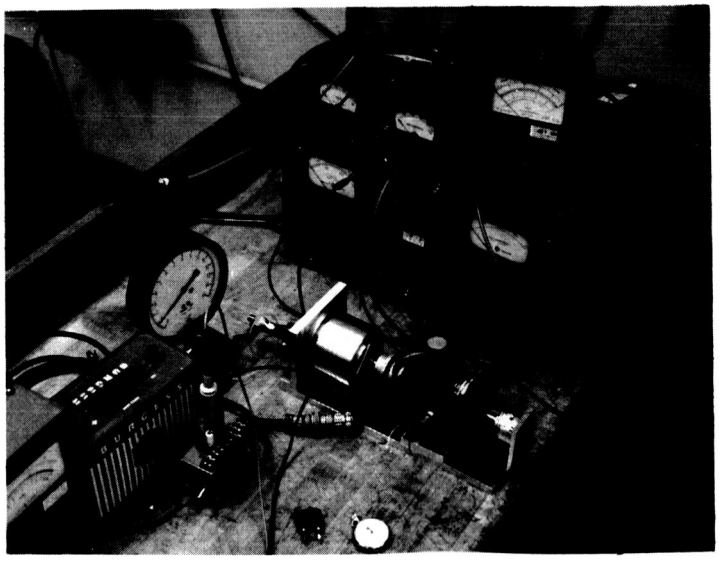

Figure 2-18 Nutator Transmission Test Setup

TABLE 2-3

RESULTS OF TRANSMISSION EFFICIENCY TESTS

Output Torque	Serial Number 1 (Atmospheric) Average	Serial Number 1 (Atmospheric) Average	Serial Number 2 (Atmospheric) Average
2 lb-in	81.8	87.2	71.5
4 lb-in.	82.5	92.3	69.3
6 lb-in.	90.0	93.2	80.8
8 lb-in.	93.0	94.7	83.5
10 lb-in.	92.8	93.5	82.0
12 lb-in.		95.8	

2.1.2.4 Conclusions

The results of these tests indicate that the nutator transmission and the drive assembly are operating satisfactorily. The 5-oz drive motor, flexible bellows, and the shaft and drive drum bearings operated smoothly. The efficiency of both transmissions compared favorably with the 80% efficiency used as a conservative value in the analysis.

2.1.3 TDA, Structure, and Idler Wheels

The main strucutre of the TDA is a 1.0 x 1.5 x 0.032 aluminum alloy tube (Figure 2-1). An aluminum bracket for mounting the TDM is riveted to one end of the tube, and a pair of bearing supports is attached to the opposite end. Two shielded ball bearings (with appropriate environmental treatment) support the common shaft for the two idler wheels. The idler wheels are pressed from sheet aluminum and contain flanged lightening holes for stiffness and weight reduction. The outside diameter of the wheel is rolled to a small radius crown and covered with a thin layer of silicone rubber to prevent metallic contact between the idler wheel and the rim. A rim guide circular flange is attached to each idler wheel by riveted spacers such that the rim is channeled between the flanges as it passes around the idler wheels. These guides, plus the slightly crowned silicone rubber tire on the TDM drive drum, keep the rim centered on the TDA.

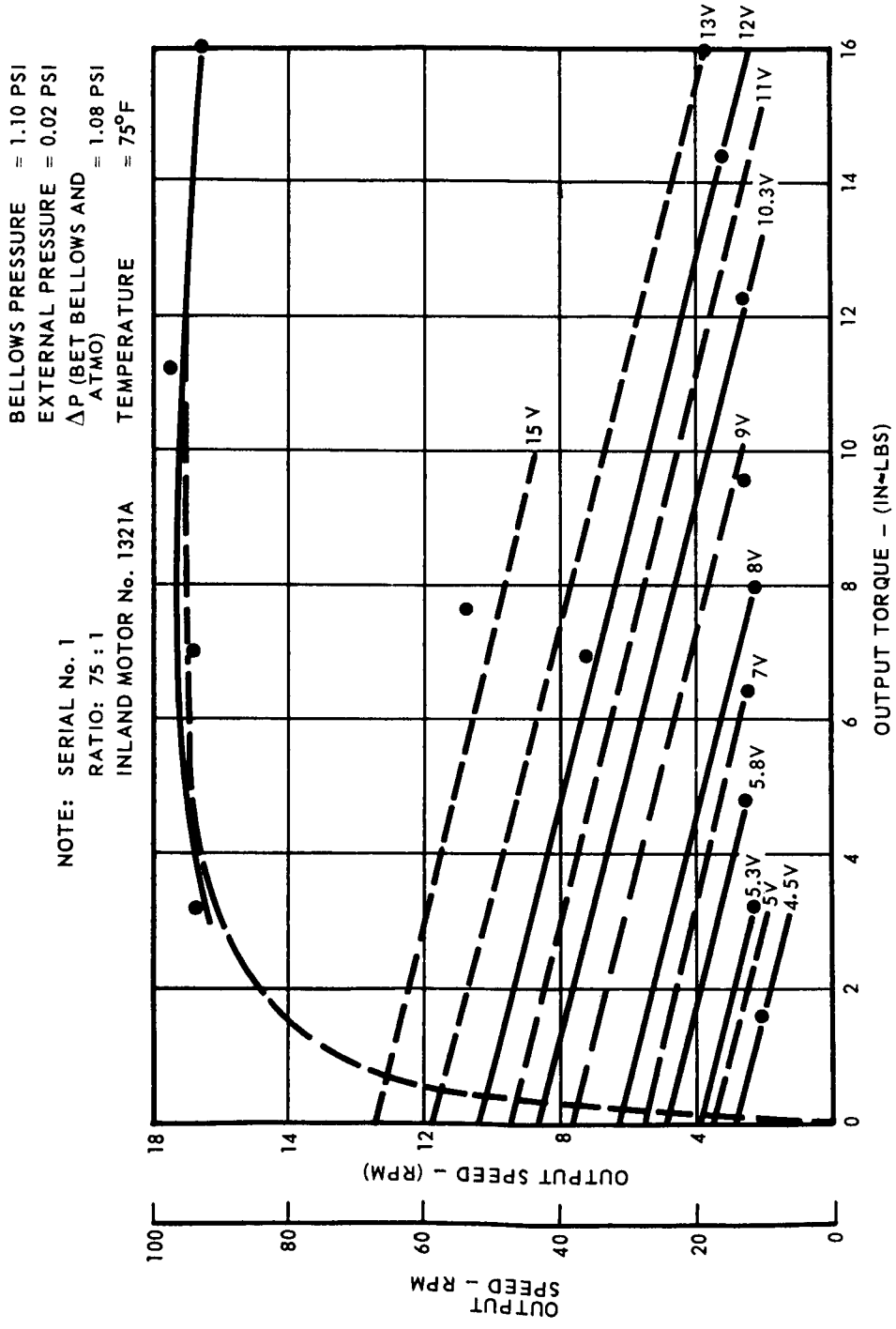

Figure 2-19 Transmission Demonstration Performance Curve

The TDA pivots about the axle on two self-lubricated bushings through the structure at its longitudinal center. The retractable piston actuator which locks the TDA to the suspension strut prior to deployment becomes the limit stop pin after it is actuated at deployment. The retracted actuator pin remains captive in the strut slot (Figure 2-1), and the rotation of the TDA relative to the suspension strut is limited to $\pm 30^{\circ}$.

There must be enough initial tension in the track to assure reliable torque transmission from the TDM to the track under maximum thrust conditions.

While developing the friction drive for the ETM it was experimentally found that a longitudinal spreader bar compressive load of 200 lb was not enough to avoid slippage under maximum load conditions. When the compressive loading was increased to 400 lb, the friction drive transmitted maximum load without noticeable slippage.

Since ETM torque was scaled to six times SLRV torque, it is reasonable to assume satisfactory SLRV operation with one-sixth the ETM track tension. This assumption implies that a minimum compressive load of 67 lb would be adequate.

As a check on the validity of the above assumptions, consider a flat belt and drive pulley analysis as shown in the engineering sketch below.

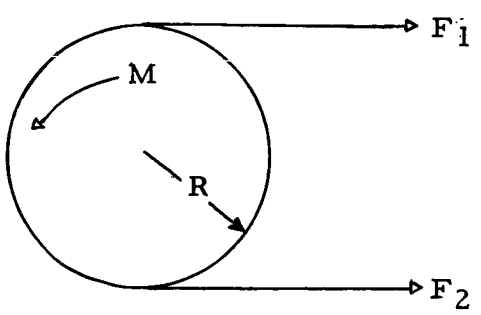

Let the track represent a flat belt driven by a 5-in. diameter pulley. Let the torque M to be transmitted be 550 oz-in. (TDM torque at N_3 speed and 8 watt total input to the four units). Assume a conservative value of $\mu = 0.2$ for the friction coefficient (actual $\mu \sim 1$) between the TDM silicone rubber tire and the stainless steel rim. Then:

$$F_1 - F_2 = \frac{M}{R} = \frac{550}{2.5} = 220 \text{ oz} = 13.8 \text{ lb}$$

It can be shown that $\frac{F_1}{F_2} = e^{\mu \theta}$ where θ is the belt wrap in radians.

So,

$$F_1 = F_2 (e^{0.2 \pi}) \quad = F_2 (1.87)$$

$$F_1 - F_2 = 1.87 F_2 \quad - F_2 = 0.87 F_2 = 13.8$$

$$F_2 = \frac{13.8}{0.87} = 15.9 \text{ lb}$$

$$F_1 = 1.87 F_2 = (1.87)(15.9) = 29.7 \text{ lb}$$

$$F_1 + F_2 = 15.9 + 29.7 = 45.6 \text{ lb}$$

The sum of the belt tensions (45.6 lb) is the compressive load on the TDA strut. This value is essentially in agreement with the earlier assumption, and indicates the magnitude of the loads.

The present design philosophy assumes the required preload be built into the TDA at assembly. No analysis has been made of the effects of differential thermal expansion on the preload, but such analysis is anticipated prior to final design.

A possible failure mode for the TDA might be track breakage caused by wedging of foreign material between the drive or idler wheel and the rim. Although the present design does not include a method of avoiding this possibility, a solution to this problem may be the addition of lightweight deflectors similar to locomotive cow catehrs to each end of the TDA. The specific design requirements will be based on the size range of foreign objects to be shielded against, since some objects will be too large to become wedged, and some are so small that they may be passed safely between the track and wheel.

2.2 STEERING LOCK ASSEMBLY

The steering lock assembly (Figure 2-20) consists of the lock tonque attached to the front body section of the vehicle and protruding into the rear section across the floating pivot joing; the lock mechanism, which includes the actuator and position sensors, mounted on the rear section; and the supporting structure.

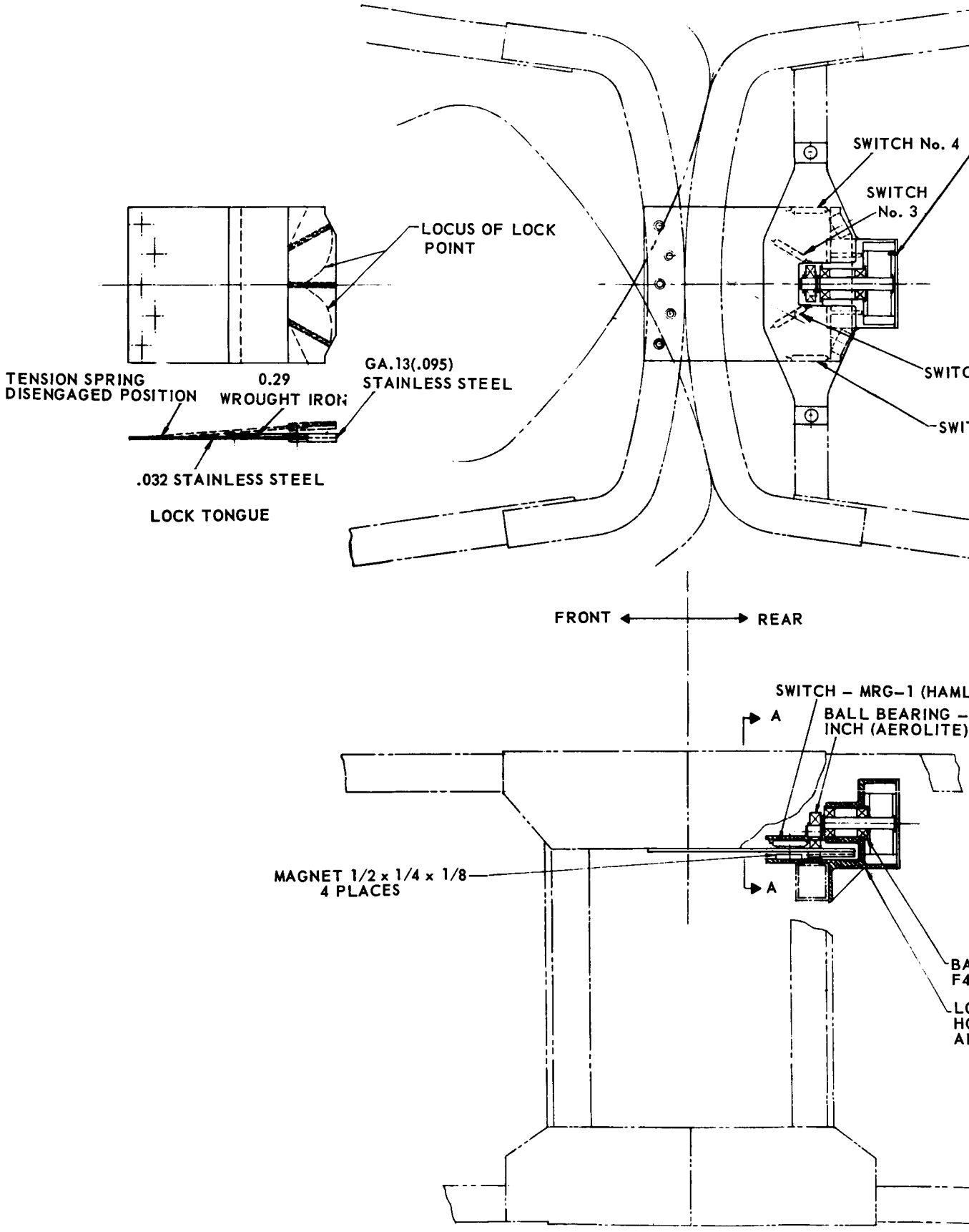
LOCUS OF LOCK POINT
TENSION SPRING DISENGAGED POSITION
0.29 WROUGHT IRON
GA.13(.095) STAINLESS STEEL
.032 STAINLESS STEEL
LOCK TONGUE
SWITCH No. 4
SWITCH No. 3
FRONT
REAR
SWITCH – MRG–1 (HAML
BALL BEARING –
INCH (AEROLITE)
A
A
MAGNET 1/2 x 1/4 x 1/8
4 PLACES

#1

LIMIT PIN (MOUNTED ON HOUSING COVER)
SEE MOTOR LAYOUT BELOW

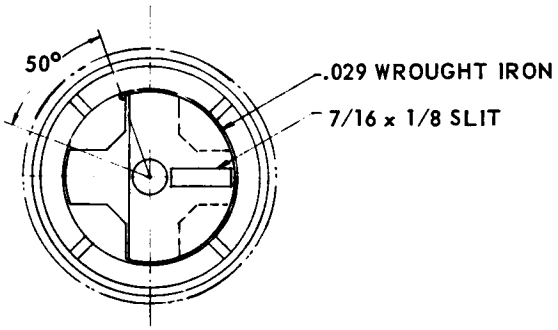

H No. 2

CH No. 1

TORQUER MOTOR OUTLINE
TQ-2 (AEROFLEX LAB.'S)
SCALE : 2/1

SWITCH No. 5 - MRG-1 (HAMLIN INC.)

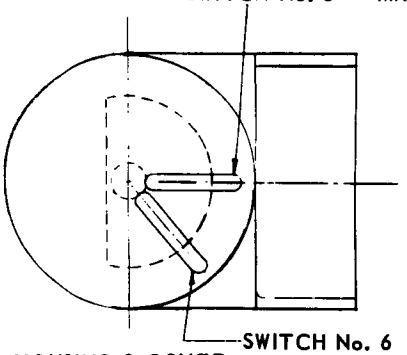

SWITCH No. 6

HOUSING & COVER
SCALE: 2/1

IN INC.)

SINGLE ROW RADIAL
SERIES - SIK (FAFNIR CO.)

TOOTH ENGAGEMENT .040
MATERIAL:
SILVER MATRIX IMPREGNATED
WITH DRY FILM LUBRICANT

.180 (REF)

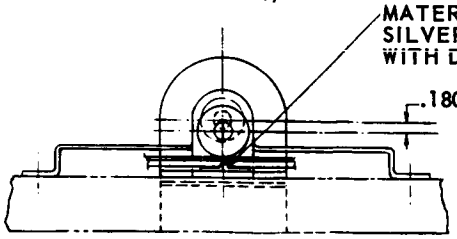

VIEW A-A

LL BEARING (FLANGED) SERIES
OD (FAFNIR CO.) 2 PLACES

CK MECHANISM
USING & COVER -
UMINUM

CALCULATED WEIGHT	
ADDITIONAL STRUCTURE	.09 lb
LOCK TONGUE	.22 lb
LOCK MECHANISM	.59 lb
TOTAL	.90 lb

#2

Figure 2-20 Steering Lock Assembly

2.2.1 Lock Operation

The lock tongue is a flat spring, cantilevered from the front body structure and having three notches corresponding to the three steady-state steering positions (center, 14.5° left and 14.5 right) on one side of its free end. The free end of the lock tongue is positioned in the slot of the lock mechanism. One side of this slot contains a single tooth designed to mesh with a notch in the lock tongue. On the other side of the slot is an eccentric roller cam which deflects the lock tongue into engagement with the lock tooth. The eccentric cam is driven from one of its bi-stable positions to the other by an Aeroflex TQ-2 torque motor.

The cam is stable in the locked position because of a 5° over-center travel against the stop pin. In the unlocked position, the torque motor rotor is held aginst the stop pin (50° from the locked position) by the spring force of the lock tongue.

All bearings will be lubricated to withstand the lunar environment for the duration of the mission. The lock tooth will be constructed of self-lubricating material of sufficient strength to withstand dynamic loads while providing a low friction surface for engagement with the lock tongue notches.

Position sensing of the vehicle chassis orientation is accomplished by the four glass encapsulated reed switches which are normally closed by permanent bias magnets below each switch. The lock tongue, however, has a section of magnetically soft steel sheet attached. The steel sheet acts as a flux shutter, such that when it is positioned between a reed switch and its bias magnet, the magnetic flux which would normally operate the switch is shunted through the steel, and the switch opens.

In the center position (Figure 2-20) the flux shutter shields all the switches from their associated magnets, and all switches are open. As the vehicle starts into a left turn, the lock tongue moves right relative to the lock mechanism and exposes Switch No. 1 to its bias magnet and the switch closes. When the body has turned to the left steady-state position, Switch No. 2 becomes exposed and closes. Similarly, for a right turn, Switch No. 4 is operated as the vehicle goes into a right transient, and Switch No. 3 actuates at the right steady-state position. These four switches develop the body position feedback signals required as inputs to the mobility logic for automatic control.

Lock mechanism attitude is sensed by Switches No. 5 and 6. These glass reed switches are attached to the rear cover of the lock mechanism and are operated by leakage flux from the permanent magnet rotor of the torque motors. A soft steel shutter fastened to the rotor aligns a flux slot with one of the switches in each of the bi-stable positions, while shielding the other switch. Operation of Switch No. 5 signals a lock condition while Switch No. 6 develops the unlock signal.

The torque motor is a two-terminal device which requires current reversal for torque reversal. Thus, current flow in one direction transfers the cam from lock to unlock, and current flow in the opposite direction causes operation from unlock to lock. Power is required only during the transfer and there is no power drain in switching because lock operation is performed by the mobility control subsystem.

2.2.2 Lock Mechanism Analysis

The torque output of the Aeroflex TQ-2 motor with an input of 8 watts is 6.06 oz-in.

With 5° over-center travel of the eccentric cam, the start of the lock operation occurs with the cam 45° from vertical. For a cam eccentricity of 0.180 in., the cam lift will be:

$$y = 0.180\,(- - \cos 45^{\circ}) = 0.180 \times 0.293 = 0.053 \text{ in.}$$

Cam force available at the beginning of lift is:

$$F = \frac{\text{torque}}{\text{moment arm}} = \frac{6.06}{0.18\,(\sin 45)} = \frac{6.06}{0.138} = 44 \text{ oz} = 2.74 \text{ lb}$$

The pressure angle (θ) of the lock tooth must be greater than the maximum friction angle ϕ of the tooth material ($\tan \phi = \mu$ = coefficient of friction). For the silver matrix material selected, $0.17 > \mu > 0.14$ in. vacuum.

To assume unlocking, $\tan \theta$ must be larger than μ max. Therefore $\theta \geq 9.7^{\circ}$.

During locking, the effective wedge angle γ will be $\theta + \phi$ max. For an arbitrarily selecged pressure angle of 14.5° the effective wedge angle will be 24.2°.

The minimum locking forces in the plane of the steering moment will be:

$$S = \frac{F}{\tan\gamma} = \frac{2.75}{0.85} = 6.12 \text{ lb}$$

This force is developed 12.5 in. from the rear axle, resulting in a locking moment of 76.8 lb-in. which can be shown to be in excess of the maximum moment imposed on the vehicle during manual operation.

2.3 VEHICLE BRAKING

The use of friction losses in the TDM as a means of providing vehicle braking has been investigated. Retarding torque (T_R) at the output of the TDM will be:

$$T_R = \frac{T_b \cdot G}{N}$$

where

T_b = motor torque caused by brush friction = 0.5 oz-in.

G = transmission gear ratio = 87:1

N = transmission efficiency, estimated at 90%

For these values, the ratarding torque will be 48.5 oz-in. Braking force (F_b) available at the track will be:

$$F_b = \frac{T_R}{R} = 19.4 \text{ oz}$$

where

R = drive drum radius = 2.5 in.

This value of braking force is conservative since the effects of losses in the rest of the TDA have been neglected.

For a simplified analysis, in which weight distribution changes produced by shift are neglected, the vertical loads (F_v) per axle are:

$$F_v = \frac{W_v}{4}\left(\frac{g_m}{g_e}\right) = 3.83 \text{ lb} = 61 \text{ oz}$$

When

W_v = vehicle earth weight = 92 lb

$\frac{g_m}{g_e}$ = ratio of lunar gravity to earth gravity = 1/6

The limiting slope at which braking will be effective may be determined by equating the braking force to the tangential force component of the vertical load:

$$F_b = F_T = F_v \sin\theta$$

$$\theta - \sin^{-1}\frac{F_b}{F_v} = \sin^{-1}\frac{19.4}{61} = \sin^{-1} 0.318 = 18.5^o$$

From catalog data for the Inland T-1321-A motor, the viscous damping with a zero impedance source is 0.05 oz-in./rad/sec. This occurs when the motor terminals are shorted together and the motor is driven as a generator. Viscous damping (C_o) at the drive drum will then be:

$$C_o = C_i G^2 = 0.05 \times (87)^2 = 378 \text{ oz-in./rad/sec}$$

where

C_i = viscous damping at input = 0.05 oz-in./rad/sec

G = gear ratio = 87:1

Critical slope angle for pitch stability is:

$$\theta = \tan^{-1}\left(\frac{h/2}{h-r}\right) = \tan^{-1}\frac{15}{(19.7-2.5)} = 41^o$$

At this slope, all the vehicle's weight is on the downhill axle and the load per axle will be $2F_v$ = 2(61 oz) = 122 oz. The component of this load, tangent to the slope will be:

$$F_T = F_v \sin\theta = 122 \sin 41^o = 81.6 \text{ oz}$$

The tangent force is opposed by the retarding force made up of friction and viscous drag.

$$F_T = F_b + F_d$$

$$81.6 = 19.4 + F_d$$

$$F_d = 81.6 - 19.4 = 62.2 \text{ oz}$$

Track velocity at a viscous drag force of 62.2 oz will be:

$$N = \frac{F_d}{C_o} = \frac{62.2 \text{ oz}}{378 \text{ oz-in./sec}} = 0.165 \text{ in./sec} = 0.0094 \text{ mph}$$

So, with drive motors shorted, the vehicle will have a downhill speed limit of 0.165 in./sec at the steepest slope on which it could survive without longitudinal pitchover. At shallower slopes the speed will be less, as shown in Figure 2-21. Because of the simplifying assumptions used in the analysis, it is anticipated that the braking effect will be considerably better than the results shown here.

2.4 STEERING AND MOBILITY CONTROL

Steering will be accomplished by relative rotation of the two vehicle segments about a floating pivot point using torque developed by differential speed control of the traction motors.

In order to steer the vehicle, the individual speeds of all four drive motors must be controlled. It can be shown that two different motor speeds, N_1 and N_2, which have the proper ratio, will allow full maneuverability.

The ratio of speed N_1 to N_2 is determined by vehicle geometry and turn radius. For a vehicle of track span W and turn radius R (to body centerline at the axle), the relation between outside track speed N_1 and inside track speed N_2 is:

$$N_2 = N_1 \left(\frac{(R/W - 1/2)}{(R/W + 1/2)} \right)$$

The SLRV has a track span W of 25 in. and a turn radius R of 60 in. For these values, $N_2 = 0.656\ N_1$.

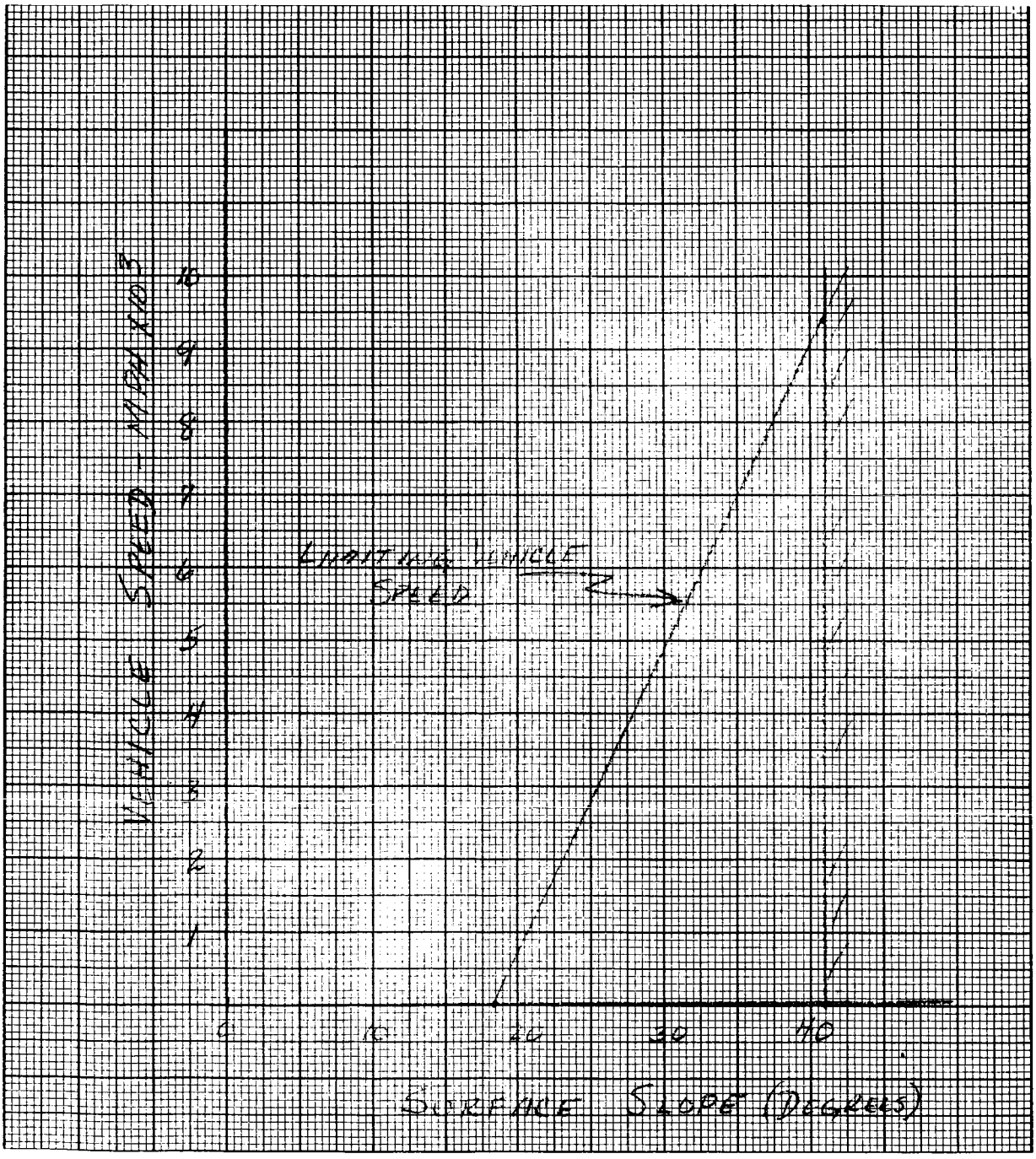

Figure 2-21 SLRV Braking Characteristics

The control requirements for the SLRV traction drive mechanism have been established as follows.

The sum of the powers being consumed by the four TDM's will be limited to 8 watts. If 8 watts are exceeded, the vehicle will be automatically shut down, and will require an earth command for reactivation.

Figure 2-13 shows operational conditions of SLRV TDM's. The control system will provide for three constant vehicle speeds which may be commanded from the earth. These speeds (referred to as V_1, V_2, V_3) are as follows:

V_1 = 0.16 mph (N_1 = 10.8 rpm)
Normal operating speed of SLRV when it is on flat and relatively smooth surfaces, or up slopes on hard surfaces. Highest speed of steady state turn.

V_2 = 0.105 mph (N_2 = 7.2 rpm)
Alternative operational speed for rough surface operation. Lowest speed of steady state turn.

V_3 = 0.03 mph (N_3 = 2 rpm)
Creeper speed for climbing large obstacles.

The mobility control unit will accept command signals from the earth through the information and control subsystem. It will also accept control signals generated by the steering lock. In turn, it will supply the proper lock actuator signals and motor pulses such that the vehicle executes the desired maneuvers. Mobility control will thus consist of vehicle sensors, logic, and power control electronics.

During automatic logic control of the vehicle, speeds are limited to V_1 for straight trajectories, and V_1 and V_2 for turns. The turn maneuver consists of a change from a steady-state condition through a transient to a new steady-state condition. An automatic steering maneuver is accomplished by operating a pair of diagonally opposite tracks at speed V_1, and the other pair of diagonally opposite tracks at speed V_2. This maneuver is defined as a "long transient". A "short transient", in which one pair of diagonal tracks is driven in the opposite direction from the other diagonal pair, is achievable only by manual earth control.

Use of speeds V_2 and V_3 as operational speeds is limited to manual control.

With bang-bang steering, three steady-state vehicle attitudes are possible: (1) straight ahead (S_{ss}), (2) full right turn (R_{ss}), or (3) full left turn (L_{ss}). The dynamic process of going from a full left turn to straight ahead, or from straight ahead to full right, or from full left to full right is defined as a right transient (R_t). A left transient (L_t) is defined as vehicle rotation in the opposite sense, as produced when going from full right to straight, straight to full left, or full right to full left.

Three steering commands and five feedback signals are sufficient to perform all steering maneuvers.

Let steering commands be:	Feedback signals:
L_c - Left command	L_f - Left feedback
S_c - Straight command	S_f - Straight feedback
R_c - Right command	R_f - Right feedback
	L_{t_f} - Left transient
	R_{t_f} - Right transient

Using Boolean notation in which AB = A and B and A + B = A or B, the steady state conditions are defined by the combinations:

$$L_{ss} = L_c L_f$$

$$S_{ss} = S_c S_f$$

$$R_{ss} = R_c R_f$$

Initiation of the right transient: $R_t\,(SET) = R_c S_f + R_c L_f + S_c L_f$

Initiation of the left transient: $L_t\,(SET) = L_c S_f + L_c R_f + S_c R_f$

Completion of either transient: $R_t\,(RESET) + L_t\,(RESET) = L_{ss} + S_{ss} + R_{ss}$

Steering commands are earth generated and processed through the command decoder. Feedback signals are developed on the vehicle by the steering lock switches as follows:

	S_1	S_2	S_3	S_4
L_f	X	X	O	O
S_f	O	O	O	O
R_f	O	O	X	X
L_{t_f}	X	O	O	O
R_{t_f}	O	O	O	X

The function of Switches S_1 and S_4 is to maintain a feedback signal during the transient, to avoid loss of control if a steering command is changed during the transient. If the four tracks of the vehicle are powered by motors number 1, 2, 3, and 4, the motor speeds required for execution of the various maneuvers are:

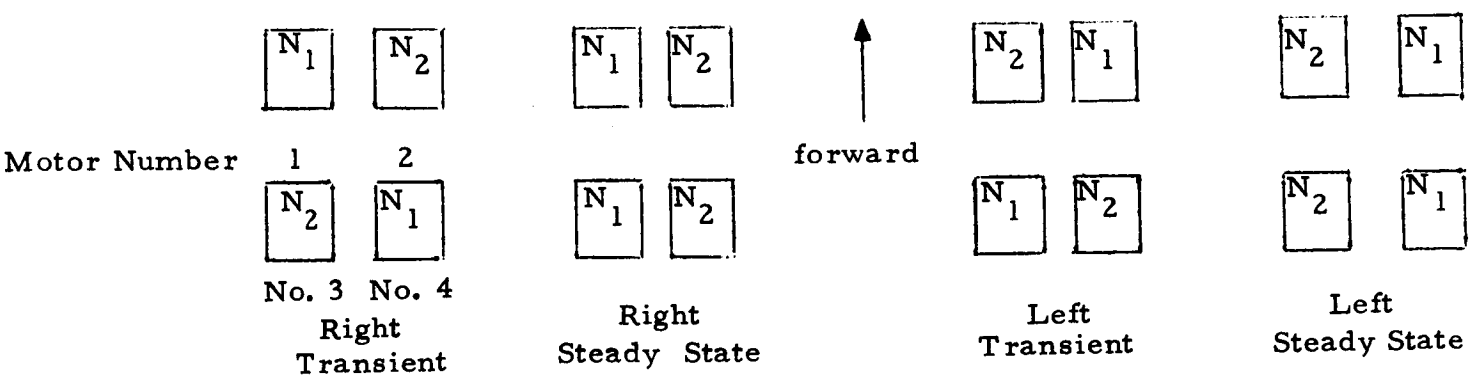

Straight steady-state operation requires all motors to run at speed N_1 (normal speed). The logical requirements to produce the lower speed (N_2) on each motor are:

Motor Number 1	$L_{ss} + L_t$
Motor Number 2	$R_{ss} + R_t$
Motor Number 3	$R_{ss} + L_t$
Motor Number 4	$L_{ss} + R_t$

Switches S_5 and S_6 on the steering lock assembly generate lock feedback signals which are used in conjunction with the lock commands to control lock operation. The lock commands are developed as follows:

$$\text{Unlock} = (R_t + L_t + R_{t_f} + L_{t_f})(\text{lock feedback})$$

$$\text{Lock} = (R_{ss} + S_{ss} + L_{ss})(\text{unlock feedback})$$

2.5 VEHICLE PERFORMANCE

Various mobility concepts were investigated before selecting the four tracked articulated vehicle with overall dimensions shown in Figure 1-1, Section 1. Although the gross performance characteristics of the vehicle were established at an early date, detail performance evaluation could not begin until the major design of all subsystems was completed. This evaluation, and considerations for extending the performance are presented in the succeeding paragraphs.

2.5.1 Vehicle Maneuverability

Maneuverability (see Table 2-4) of the preferred design is determined by the following:

Vehicle track base	L	= 30 in. (center to center)
Vehicle track span	W	= 25 in. (center to center)
Vehicle turn radius	R	= 60 in. (to middle of track span)
Vehicle top speed	V_1	= 0.16 mph

At the completion of a turning transient, the trajectory becomes the arc of a circle of 60-in. radius (steady-state turn). To accomplish a heading angle change of $\Delta\phi$, arriving at a straight-ahead condition, an entry transient, steady turn, and exit transient are generally required. For large values $\Delta\phi$, the steering maneuver consists of a transient $\Delta\phi_E$ from constant heading angle ϕ_1, a steady-state turn $\Delta\phi_{ss}$ at constant $\dot{\phi}$, and another transient $\Delta\phi_t$ from the steady-state turn to the new heading angle ϕ_2. Heading angle change $\Delta\phi_t$ during the steering transient is 7.25° and requires 6.45 sec

to accomplish. The steady-state turn rate $\dot{\phi}_{ss}$ (i.e., longitudinal velocity divided by the turn radius) is 2.25°/sec. For heading changes greater than $2\Delta\phi_t$ (14.5°) a steady-state turn $\Delta\phi_{ss}$ is required. The value of $\Delta\phi_{ss}$ is $(\phi_2 - \phi_1) - 2\Delta\phi_t$. Thus a 90° turn would consist of a transient lasting 6.45 sec for a heading change of 7.25°, a steady-state turn of (90° - 14.5°) = 75.5° lasting 33.5 sec, and another 6.45-sec transient be executed in 46.4 sec with an offset of 67.87 in. (See Figure 2-20.)

TABLE 2-4

VEHICLE MANEUVERABILITY CHARACTERISTICS FOR VARIOUS HEADING CHANGE (ϕ)

Heading Change	Time to Complete Maneuver (sec)	Offset (inches) Longitudinal	Offset (inches) Lateral	Arc Length (in.)	Remarks
14.5°	12.90	29.6	3.8	30.0	No steady-state turn
30	19.8	36.5	9.8	46.2	15.5° steady-state turn
60	33.1	41.1	33.4	77.6	45.5° steady-state turn
90	46.4	67.9	67.9	109.0	75.5° steady-state turn
180	86.2	0	135.3	203.0	165.5° steady-state turn

The above values are based on an initial straight-ahead configuration followed by a turn maneuver and ending with a straight-ahead configuration in the new direction.

2.5.2 Vehicle Static Stability

A static stability analysis was conducted. The vehicle was assumed to be making an uphill turn on a 15° slope with the uphill tracks climbing an obstacle. The results of this analysis (Figure 2-23) indicate the centers of gravity of the two vehicle halves should lie on the axle centers.

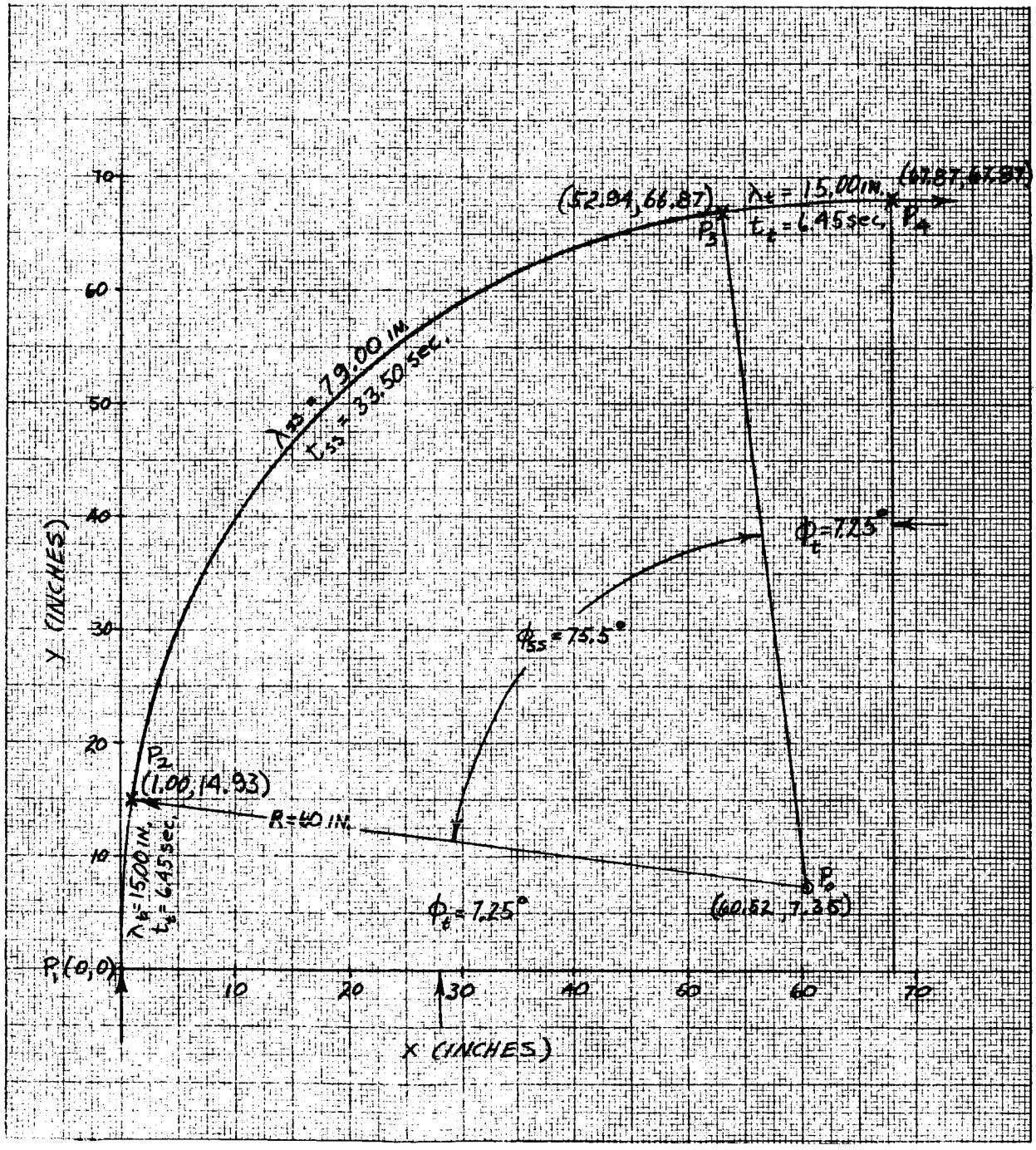

Figure 2-22 Vehicle Center-of-Gravity Trajectory for 90° Right Turn

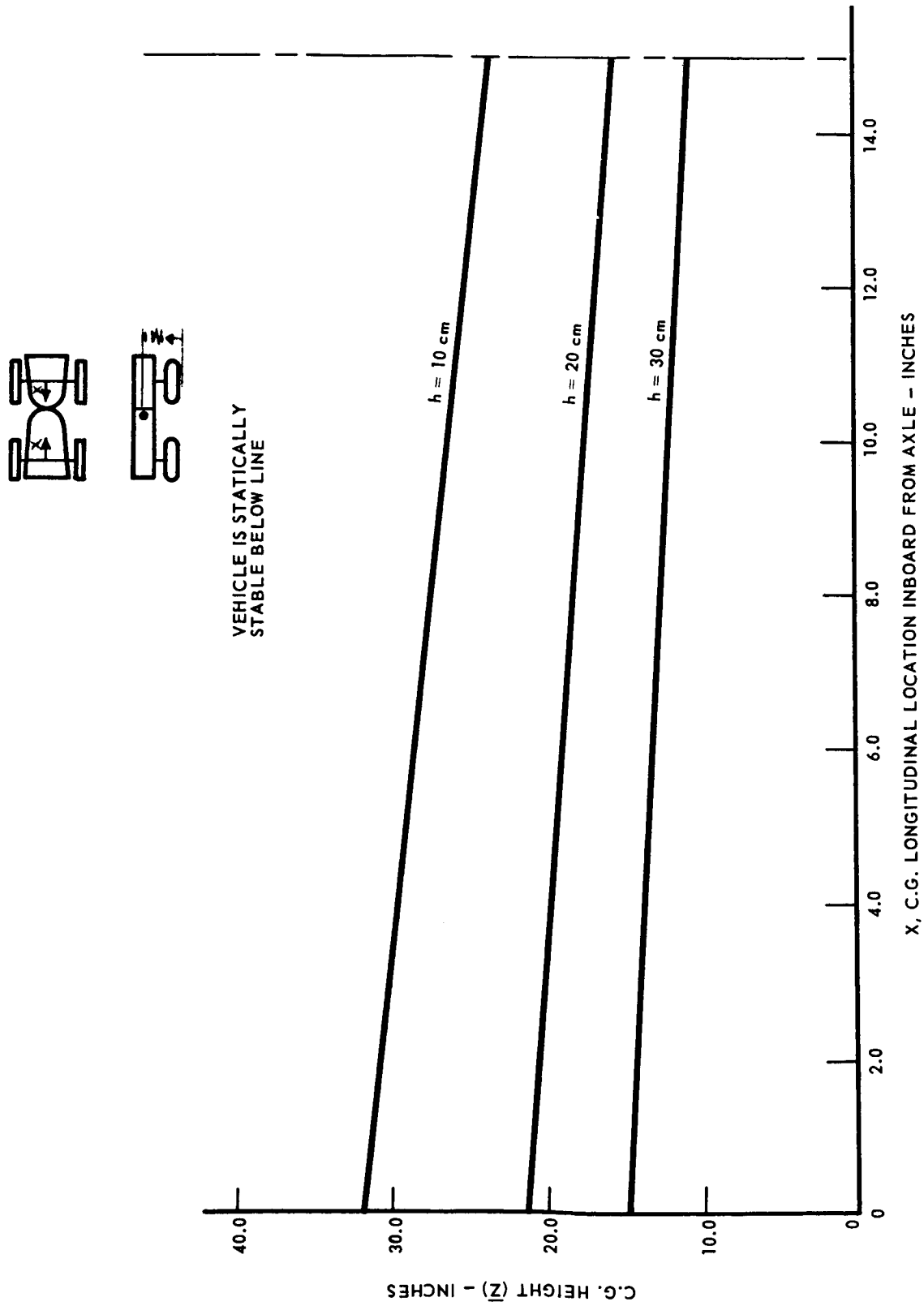

Figure 2-23 CG Height vs CG Longitudinal

To determine the static stability of the vehicle when traversing a side slope consider the sketch below.

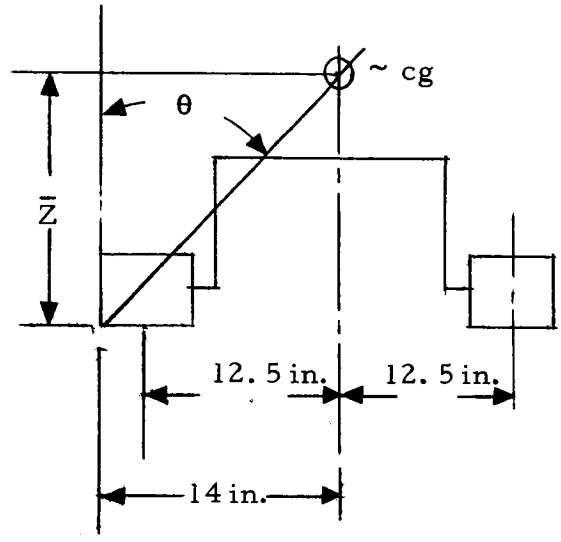

The angle (θ) defines the angle through which the vehicle can rotate before reaching neutral equilibrium, as a function of the vehicle cg height ($\overline{Z}$).

$$\theta = \arctan^{-1}\left(\frac{14}{\overline{Z}}\right)$$

This relationship makes the tacit assumptions that the cg is on the x-axis and the vehicle perfectly rigid. The first assumption will probably be realized; the second tends to underestimate the actual stability limit. The results are shown in Figure 2-24.

The fore and aft vehicle static stability was determined in a similar manner (see Figure 2-25).

The critical inclination of the vehicle as a function of cg height ($\overline{Z}$) is given as:

$$\gamma_{CR} = \arctan\left(\frac{2L}{2\overline{Z} - d}\right)$$

The results are shown in Figure 2-24. Again the assumption was made that the vehicle is perfectly rigid and the cg is at the center of the

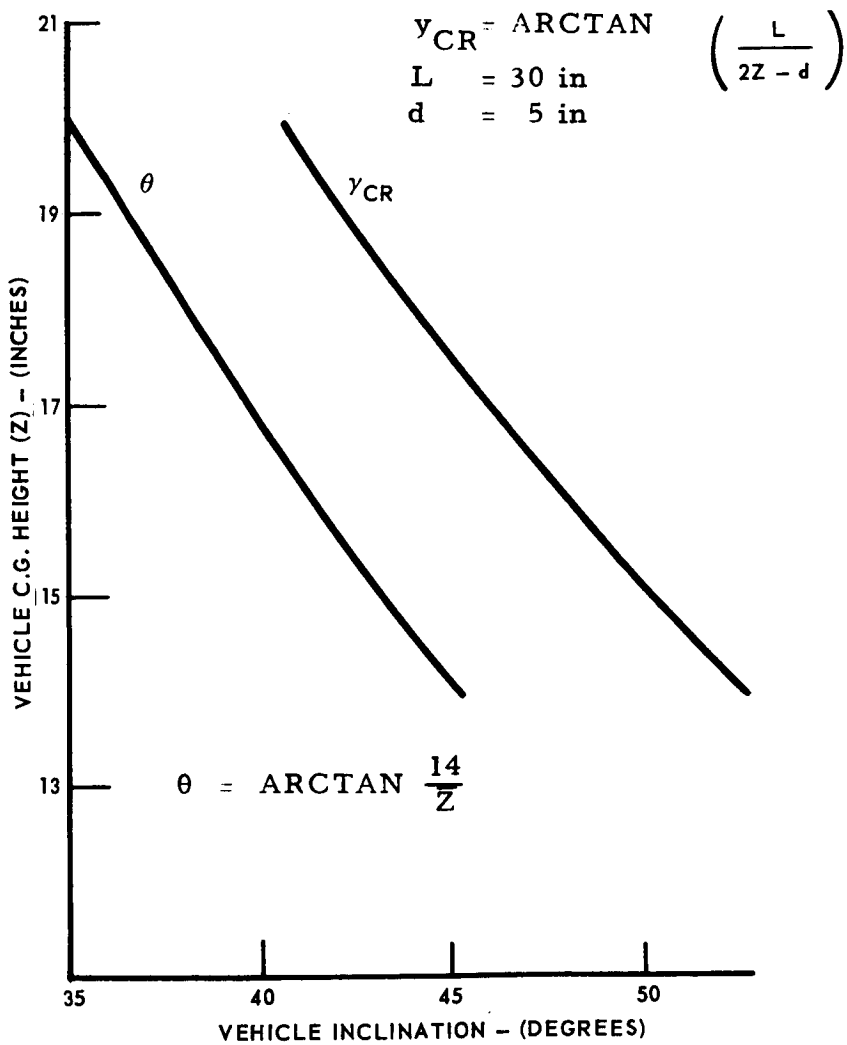

Figure 2-24 SLRV Static Stability

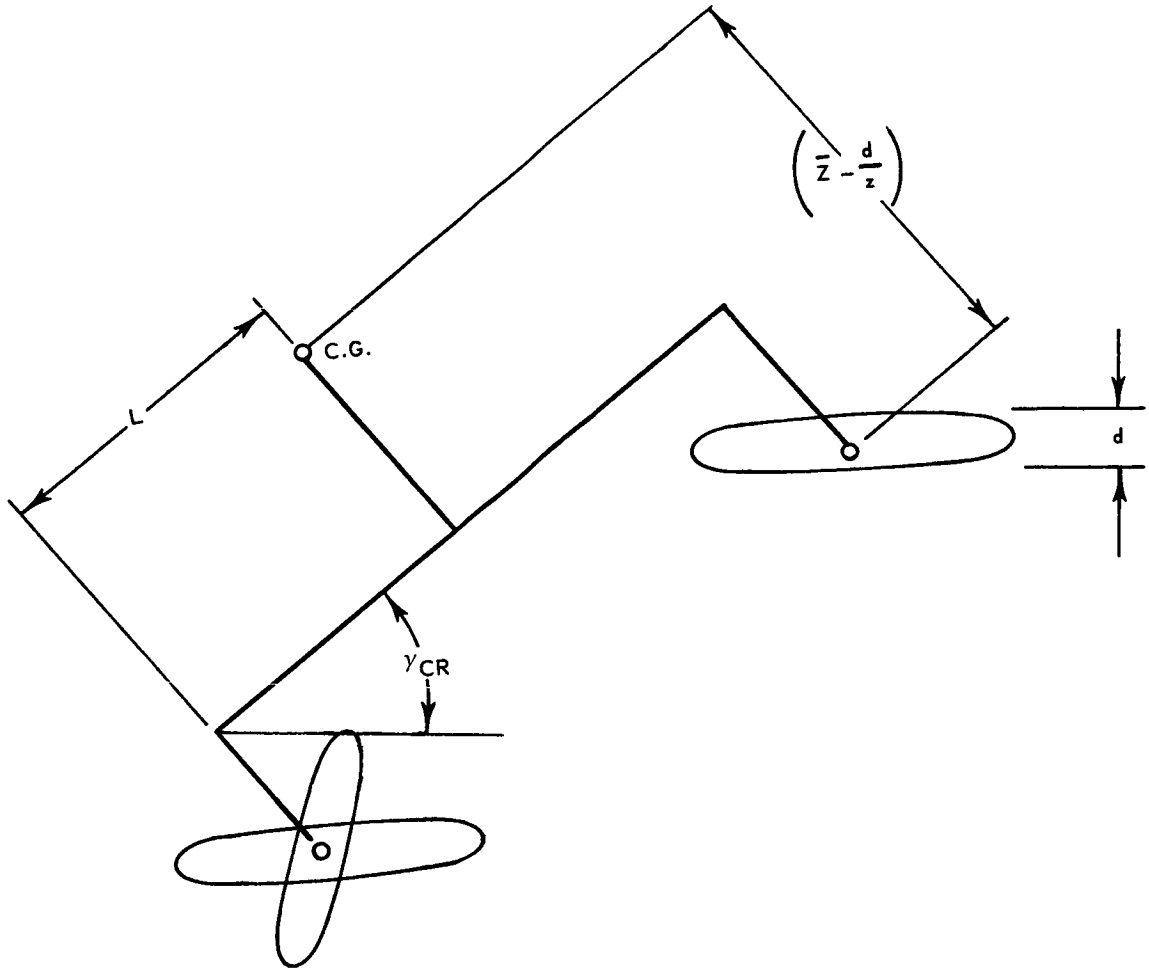

Figure 2-25 Vehicle Stability Determination

vehicle. Although it is less likely that the actual cg will be at the center of the vehicle for this situation, it may readily be shown that γ_{CR} is only a weak function of L, for small changes in L.

2.5.3 Torque and Coefficient of Friction Requirements

To provide a basis for the design of the mobility subsystems, and in particular of the TDA, a study was conducted to determine the minimum torque and coefficient of friction required to climb an obstacle as a function of various vehicle parameters. Most of these parameters are shown in Figure 2-26. They are:

x - location of cg on x-axis

$\overline{Z}$ - cg height

α - maximum pitch angle of track

Many of the vehicle dimensions had been fixed at the time of this study as a result of trade-offs made between available space, power available, tread size for minimum sinkage, etc. The fixed dimensions are listed below:

$c \sim 10$ in.

$d = 5$ in.

$\ell = 23$ in.

$L = 30$ in.

$W = 16.5$ lb (lunar wt assumed)

$S = 25.0$ in.

$b = 3.0$ in.

There are many possible positions that the vehicle may assume as it first engages an obstacle and subsequently climbs that obstacle. Initially, this study considered six different relative geometries between the vehicle and obstacle. For $\overline{x} = 15$ in., $\overline{Z} = 3$ in., and $\alpha = 30$ degrees, the worse

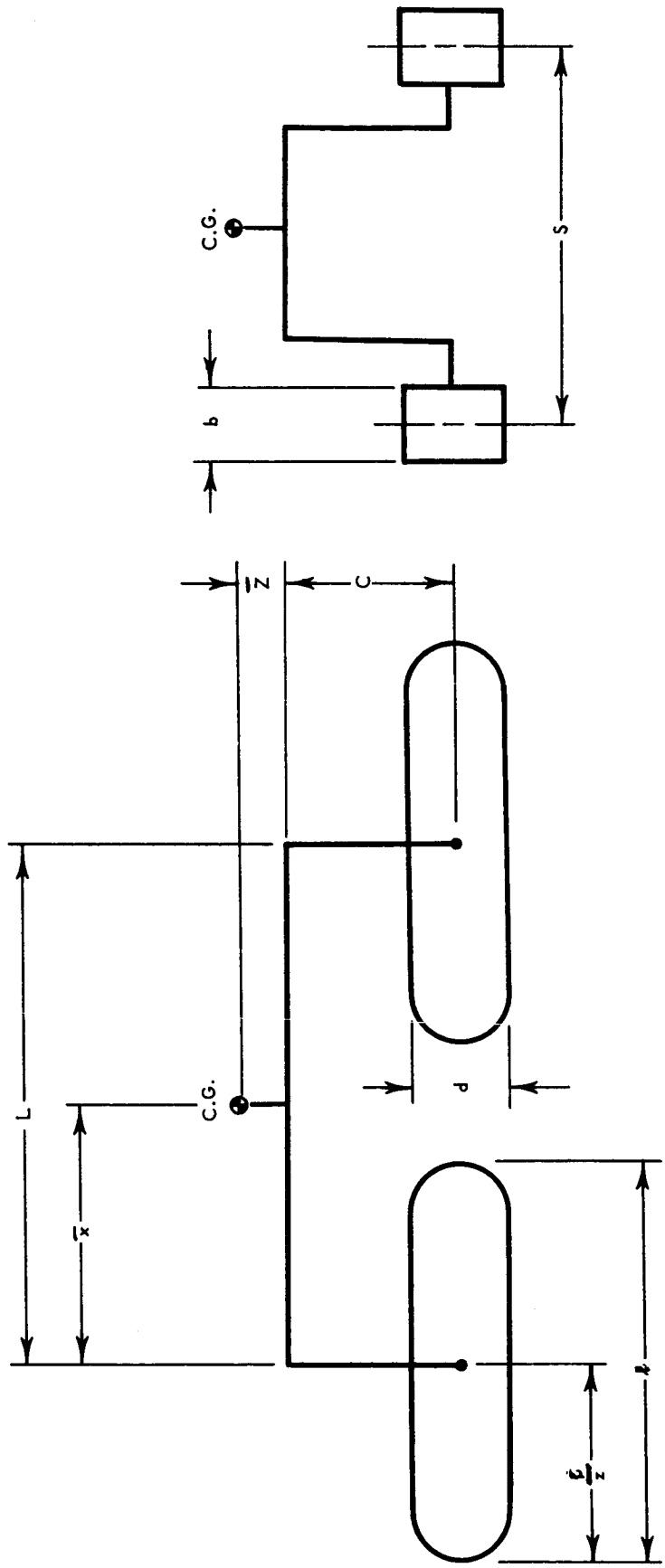

Figure 2-26 Torque and Coefficient of Friction Parameters

case requirements for minimum coefficient of friction (μ_{min}) and minimum torque (T_{min}) required to climb a 30-cm obstacle are 0.62 and 13.8 in.-lb. This torque is required at only two of the four tracks. However, because of the varying vehicle-obstacle geometry, and complete mobility symmetry, this torque must be available at all four tracks.

Subsequently, this study was extended to include the effects of changing cg height ($\overline{Z}$), and increasing obstacle height. The results of this further study are presented in Figures 2-24 and 2-25 for $\alpha = 30^{o}$ and $\alpha = 45^{o}$.

2.5.4 Vehicle Dynamics

The dynamic behavior of the LRV was analyzed for a postulated operational environment. The vehicle was assumed to be travelling at 0.18 mph[1] on a horizontal surface in the lunar gravitational field when the right rear track encounters a ramp-type obstacle. The vehicle pitch, roll, and vertical translation degrees of freedom are considered.

The vehicle was assumed to be a rigid body suspended on linear elastic springs with velocity dependent dampers. The spring constant is 3 lb/in. and the damping factors of the three- and four-track configurations are 0.166 and 0.207 lb-sec/in. These values correspond to damping ratios of 0.163 and 0.235.

The values of forward velocity and the cg height used in the simulation are both greater than subsequent design values. This tends to make the predicted dynamic behaviour worse than the actual case.

With an assumed soft suspension system, lunar surface irregularities had no adverse effect on the stability of the vehicle moving with maximum possible velocity. The actual suspension system is quite rigid; the spring stiffness for each vehicle strut is approximately 480 lb/in. The greater stiffness corresponds to a higher natural frequency and higher dynamic stability than the low natural frequency suspended vehicle. The detail analysis and results were reported in the Second Bimonthly Progress Report.

2.5.5 Crevice Crossing

The maximum crevice width that can be crossed is 29.2 cm, when the vehicle approaches the crevice at right angles. This width is equal to half the TDA length.

[1] Maximum design speed is 0.16 mph

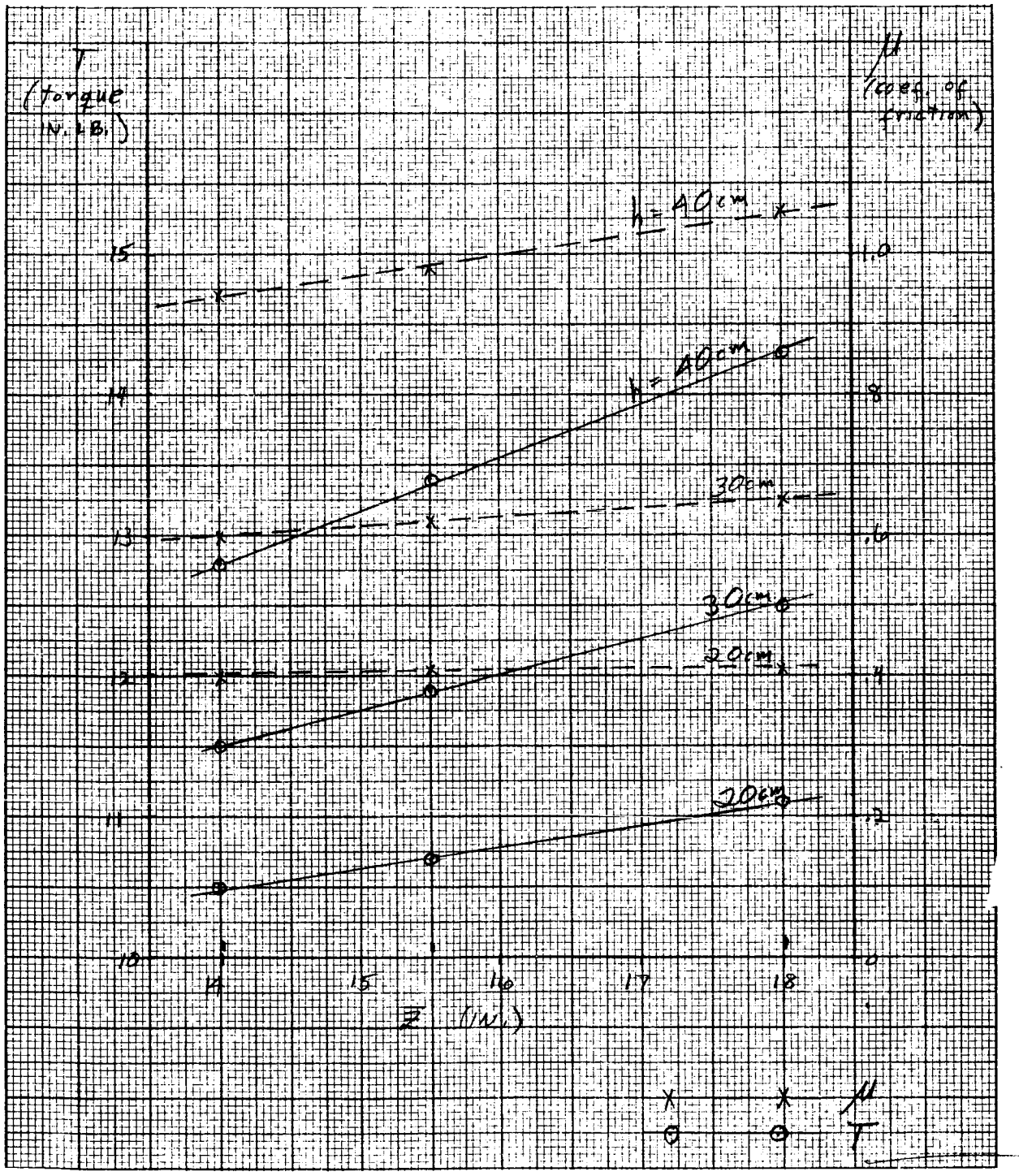

Figure 2-27 Torque and Coefficient of Friction Requirements. $\alpha = 30^{\circ}$

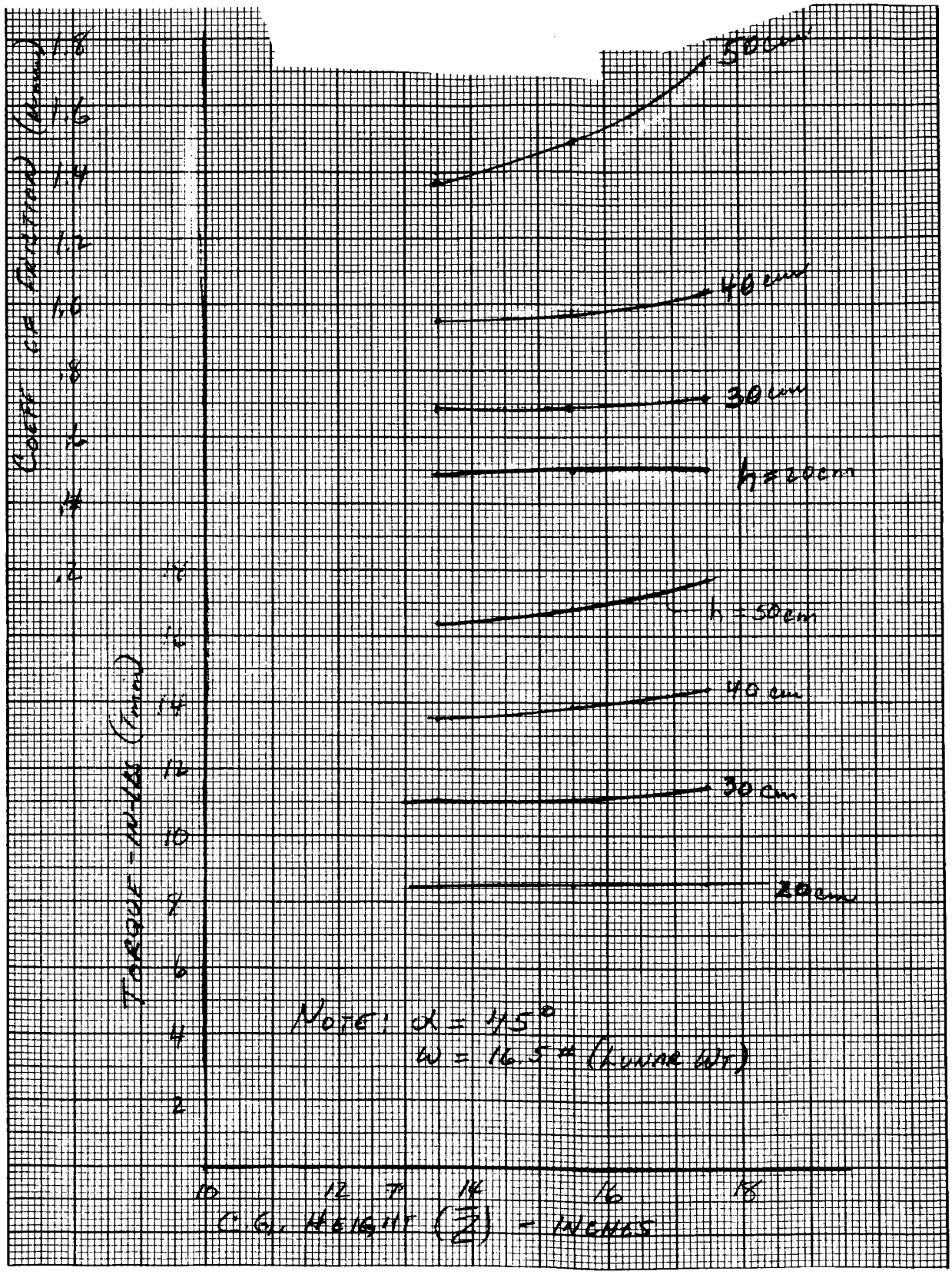

Figure 2-28 Torque and Coefficient of Friction Requirements. $\alpha = 45^{\circ}$

2.6 SUMMARY

The mobility subsystem design summarized in Table 2-1 and the supporting analyses indicate that the subsystem is capable of meeting the SLRV mobility requirements. The performance analyses presented in this section were based on conservative values where assumptions were necessary. Thus, as the detailed design of the subsystem evolves and the hardware development progresses, increased performance capabilities and/or decreased weight may be achieved.

SECTION 3

STRUCTURE

The SLRV body structure is the basic vehicle framework, and provides mounting surfaces and attachments for the track struts, electronics compartment, RTG power supply, transmitting and receiving antennas, TV camera, and deployment fittings. It consists of two modules having an open framework of square tubular members with riveted joints. The two modules are connected at the steering pivot joint as shown in Figures 3-1, 3-2, and 3-3.

The design philosophy for the body structure is to provide an efficient and simple structural design within the present state of the art which meets the equipment packaging, thermal, and load requirements and is within the allocated structural weight. The design was augmented by a study of the effect of the lunar environment on both metallic and nonmetallic materials, a complete description of which appears in Section 3.7.

3.1 STRUCTURAL DESIGN LOAD CRITERIA

The SLRV design load criteria reflect the design conditions imposed by all operational phases of the flight: launch, transit, deceleration, lunar landing, deployment to the lunar surface, and lunar operation. The launch, flight, and landing load and environmental criteria were established on the basis of definitions provided by the Basic Bus Contractor. In addition, deployment conditions when the SLRV makes lunar contact we re-established and investigated. Not only the structure and deployment subsystems were analyzed for these design load criteria, but also the other SLRV subsystems and components.

Table 3-1 is a summary of the mechanical input vibration spectrum, and Table 3-2 provides a summary of the loads and environmental conditions used for design purposes. Figures 3-4 through 3-7 define the axes and geometry used in establishing the loads. The design values given for mechanical vibration and shock are those which occur at the Surveyor-Centaur interface. In accordance with Specification HAC 239503, the SLRV

TABLE 3-1

MECHANICAL INPUT VIBRATION

Input Direction	Frequency	Vibration Level	Flight Phase
	5-40 cps	2.5 g O-P VFSW* (Max. amplitude 1.0 in. P-P)	Throughout powered flight
	40-2000 cps	2.0 g O-P VFSW*	Throughout powered flight
Axial	100-1500 cps	White Gaussian acceleration 2.0 g rms	Throughout powered flight except during liftoff, maximum q, and/or Mach 1
	100-1500 cps	White Gaussian acceleration 4.5 g rms	During liftoff, maximum q, and/or Mach I
	1-2.5 cps	2.0 in. O-P VFSW* (1.28 g maximum)	Throughout powered flight
	2.5-40 cps	1.25 g O-P VFSW*	Throughout powered flight
	40-2000 cps	2.0 g O-P VFSW*	Throughout powered flight
Lateral	100-1500 cps	2.0 g rms white Gaussian noise	Throughout powered flight except during liftoff, maximum q and/or Mach 1
	100-1500 cps	4.5 g rms white Gaussian noise	During liftoff, maximum q and/or Mach 1

NOTE: Values occur at Surveyor - Centour interface
Reference: HAC 239503, Revision C

T

SERVICE CONDITIONS

Service Condition \ Equipment Status	Column A: Service Conditions to which SLRV and its Subelements Will Be Subjected During Laboratory Usage and Test — Operating	Column A — Non-Operating	Column B: Service Conditions to which Shipping Container is Subjected — Non-Operating	Column C: Storage Conditio — Non-Operating
1. TEMPERATURE a. Inside Elect. Compartment	-45°F to +125°F	-45°F to +185°F	-10°F to +145°F	+20°F to +145°F
b. External to all Subsystems	-45°F to +600°F	-300°F		
2. PRESSURE	17.5 psia to hard vacuum(10^{-13} mm Hg)	Same as "Operating"	Sea Level to 25000 ft	Sea Level to 1000 ft
3. MECHANICAL VIBRATION	Must operate after being subjected to loads of "A" Non-Op.	Qual. test to 1.5 times levels of Table I & F.A.T. to 1.1 times these levels.	Will not exceed 5 g during air transport 0-300 cps	NA
4. SHOCK	Must operate after being subjected to conditions of Columns B, D and E.	Same as Columns B, D and E.	Exposure to shocks of 10 g magnitude of 20±2 millisecond duration.	NA
5. ACCELERATION	Must operate after being subjected to conditions under "Non-Operating."	Long. +8.9 g, −16.2 g Lat. ± 1.15 g	Negligible	NA
6. HUMIDITY	Must operate after being subjected to conditions under "Non-Operating."	RH up to 95±5% with condensation taking place.	Same as "A" Non-Operating	NA
7. ACOUSTIC VIBRATION	Designed to meet the levels of Column E		NA	NA
8. RFI	Required to perform in accordance with MIL-I-26600 (Class Ib) and MIL-E-6051.		Same as "A"	Same as "A"
9. EXPLOSIVE ATMOSPHERE	Must meet requirements of MIL-E-5400 by proper design precautions with subassemblies subjected as nec. to justify design.		Same as "A"	NA
10. STORAGE TIME	Minimum of 120 days		Same as "A"	Same as "A"
11. COMBINED ENVIRONMENT	Shall meet operational requirements after being subjected to natural service condition combinations of the specified environments.		Same as "A"	NA

#1

ABLE 3-2

VS EQUIPMENT STATUS

	Column D	Column E	Column F	Column G	Column H
s	Service Conditions during Handling and Assembly	Service Conditions while Aboard Surveyor	Service Conditions during Deployment to the Lunar Surface	Service Conditions during Lunar Day Operation	Service Conditions during Lunar Night
	Operating or Non-Op.	Non-Operating	Non-Operating	Operating	Non-Operating
	$+32^{o}F$ to $+145^{o}F$	$-45^{o}F$ to $+185^{o}F$	$-45^{o}F$ to $+185^{o}F$	$-45^{o}F$ to $+125^{o}F$	$-45^{o}F$ min.
		$+500^{o}F$ max.	$+500^{o}F$	$+400^{o}F$	$-280^{o}F$
	Same as "C"	17.5 psia to 10^{-13} mm Hg	10^{-13} mm Hg	Same as "F"	Same as "F"
	NA	See Table I	NA	NA	NA
	Free drops up to 1" & pivotal drops up to 4" (or 30°) on a hard flat surface.	25 g Long. t = 0.005 sec 15 g Lat. t = 0.005 sec	Design to ensure these do not exceed Column "E"	Same as "F"	NA
	NA	Long. +5.9g, −10.8 g Lat. ± 0.75 g	NA	Lunar Gravity	NA
	Same as "A" Non-Operating	95% max. 30% min.	NA	NA	NA
	NA	145 db from 20 to 10 kc	NA	NA	NA
	Same as "A"	Same as "A"	Same as "A"	Same as "A"	NA
	NA	Same as "A"	NA	NA	NA
	NA	8 days on launch pad	NA	NA	NA
	Same as "A"	Same as "A"	Same as "A"	Same as "A"	Same as "A"

#2

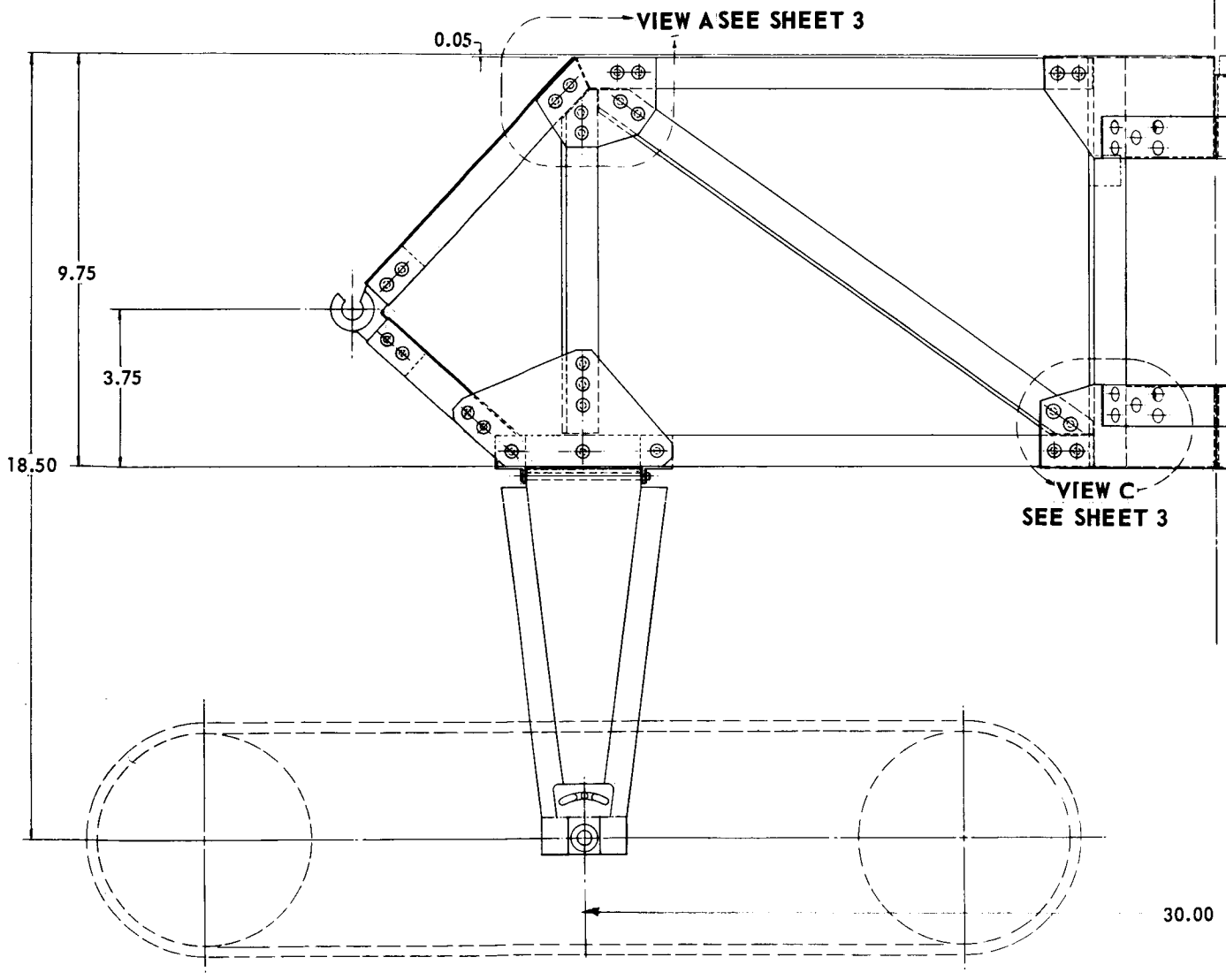

#1

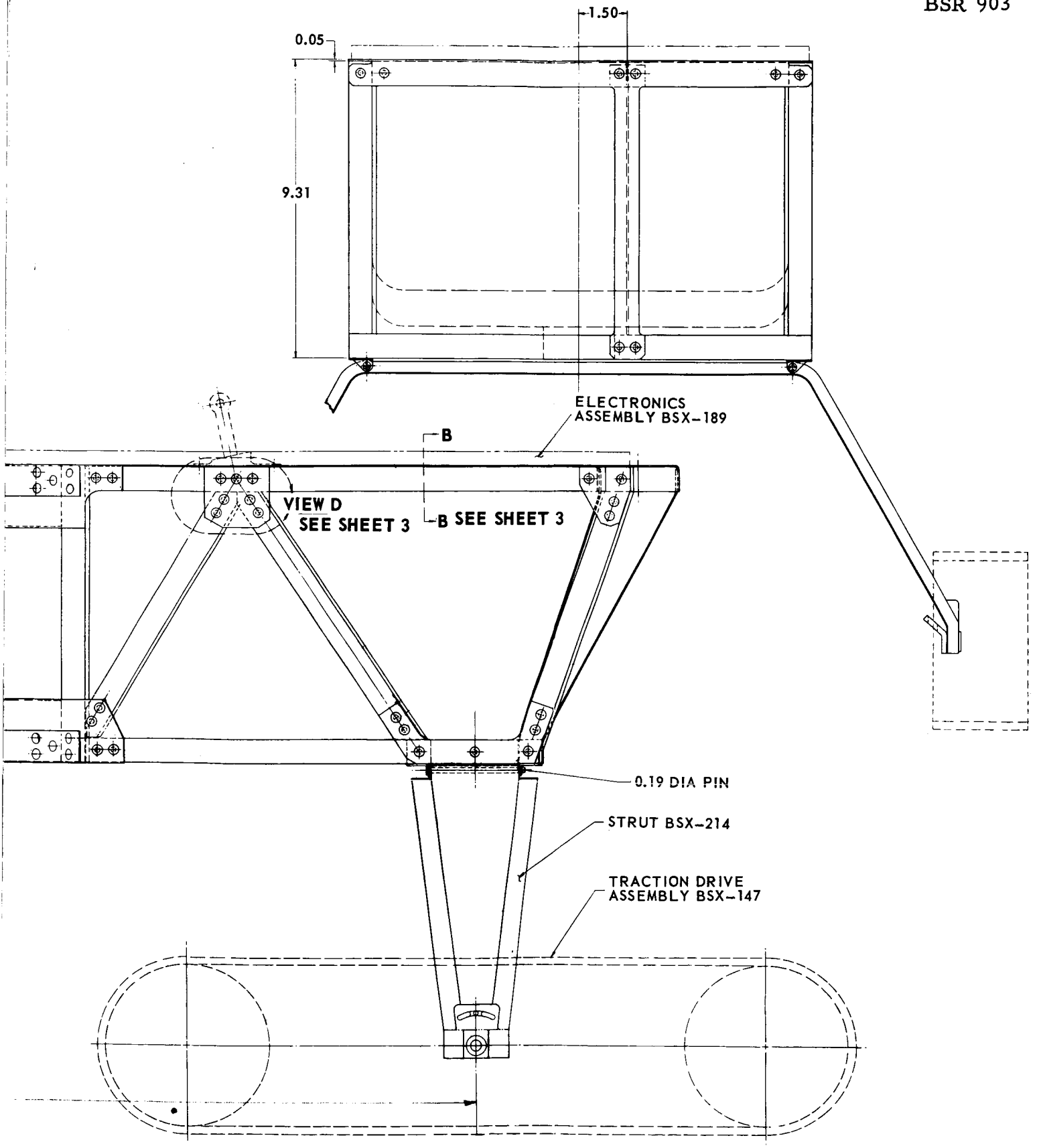

Figure 3-1 SLRV Structure Assembly (Sheet 1 of 3)

#2

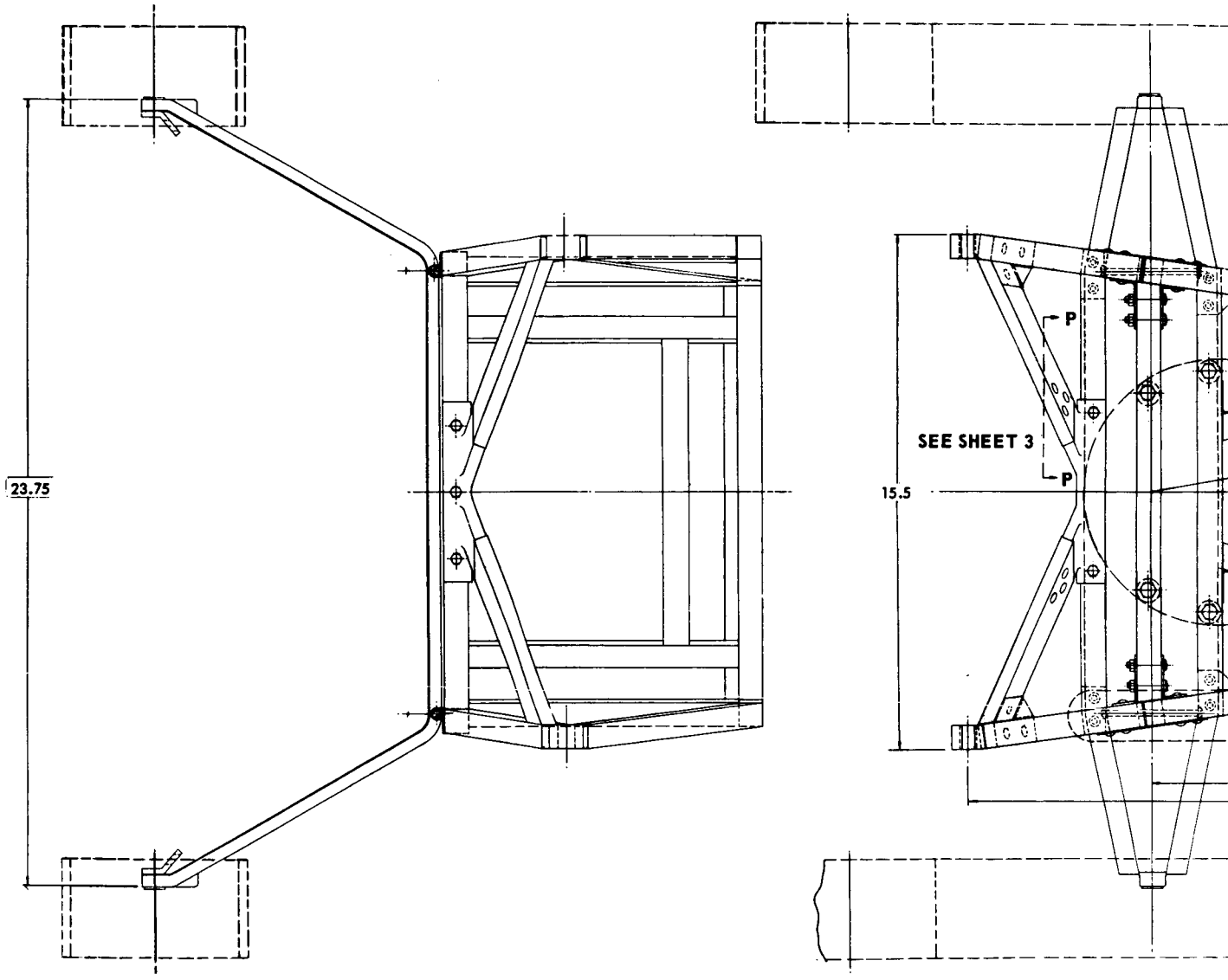
23.75
15.5
P
P
SEE SHEET 3

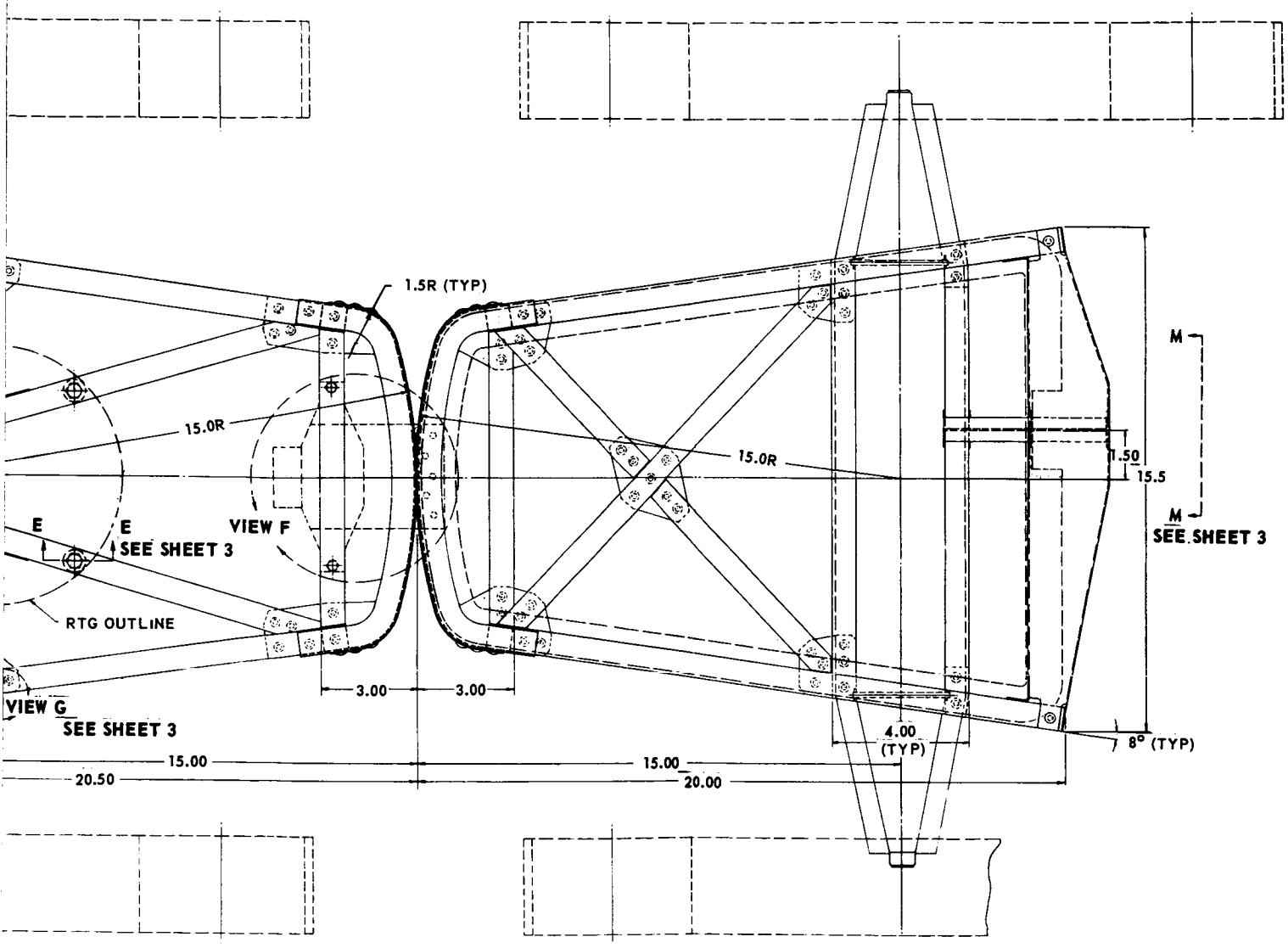

Figure 3-1 SLRV Structure Assembly (Sheet 2 of 3)

#2

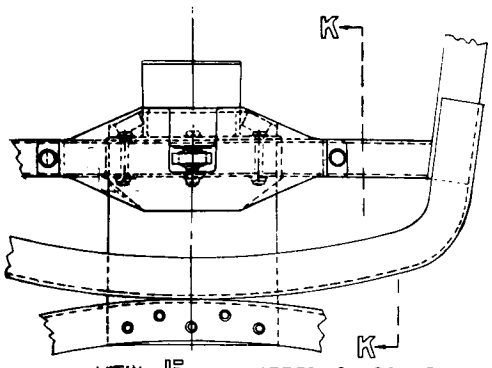

VIEW F STEERING LOCK DETAIL

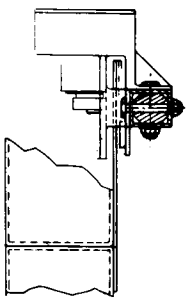

SECTION K-K

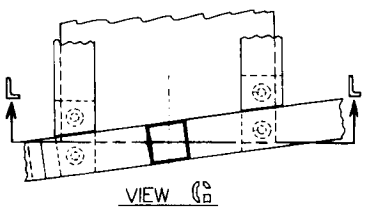

VIEW G
STRUT ATTACHMENT

SECTION L-L

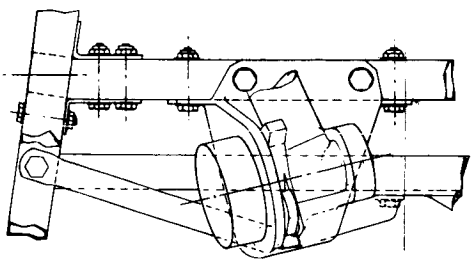

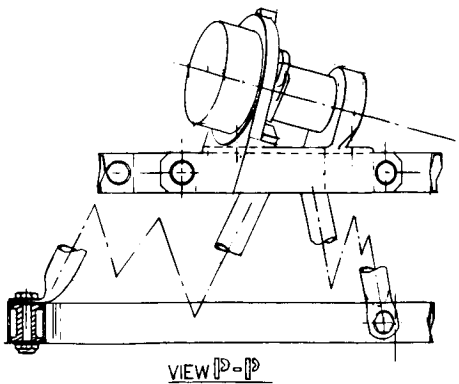

VIEW P-P

R.T.G.

DEPLO

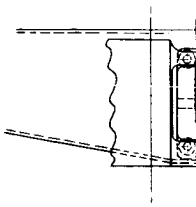

VIE

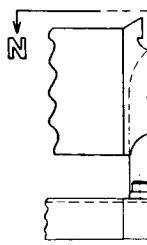

VIEW
TV CAME

#1

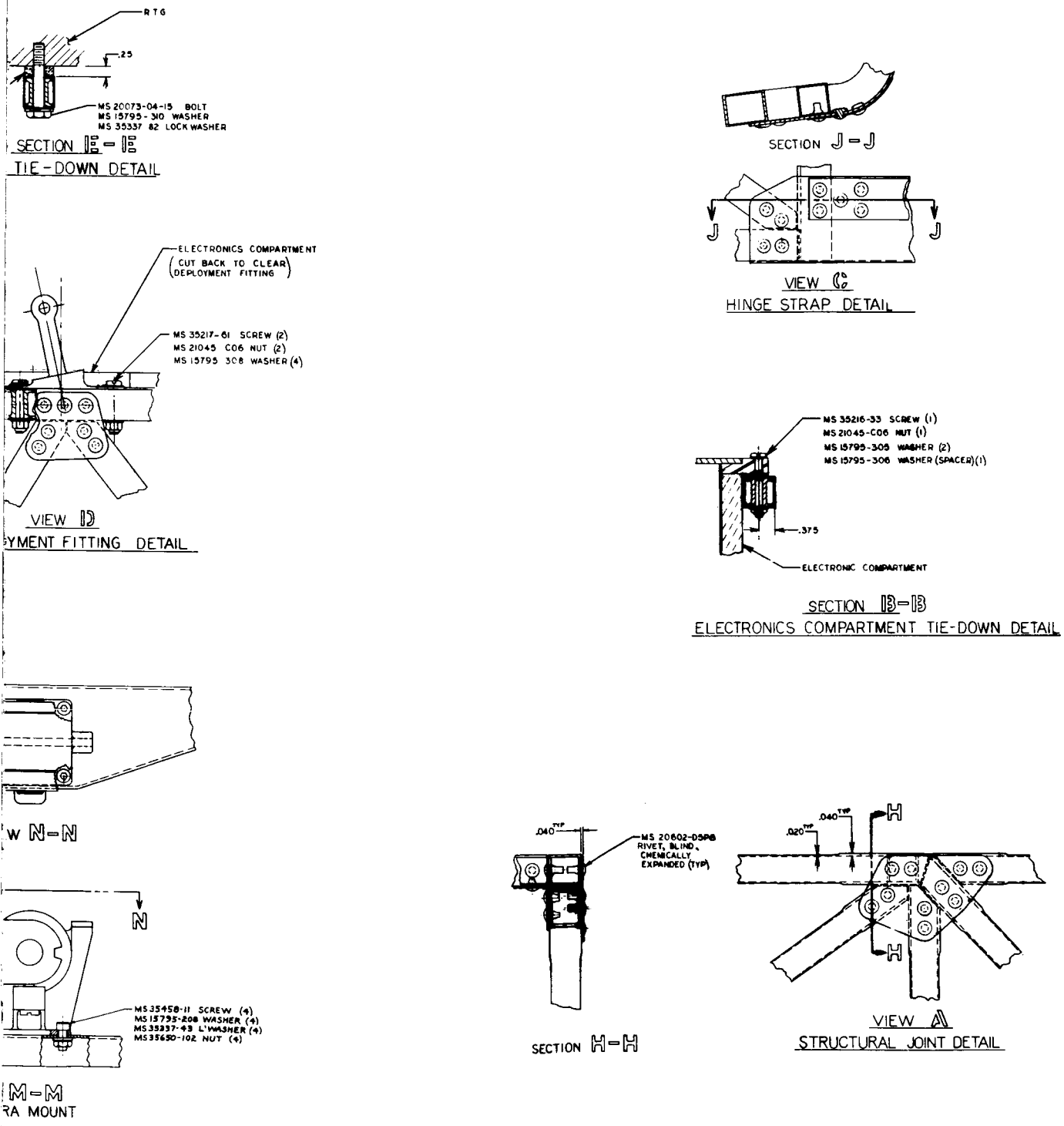

Figure 3-1 SLRV Structure Assembly (Sheet 3 of 3)

#2

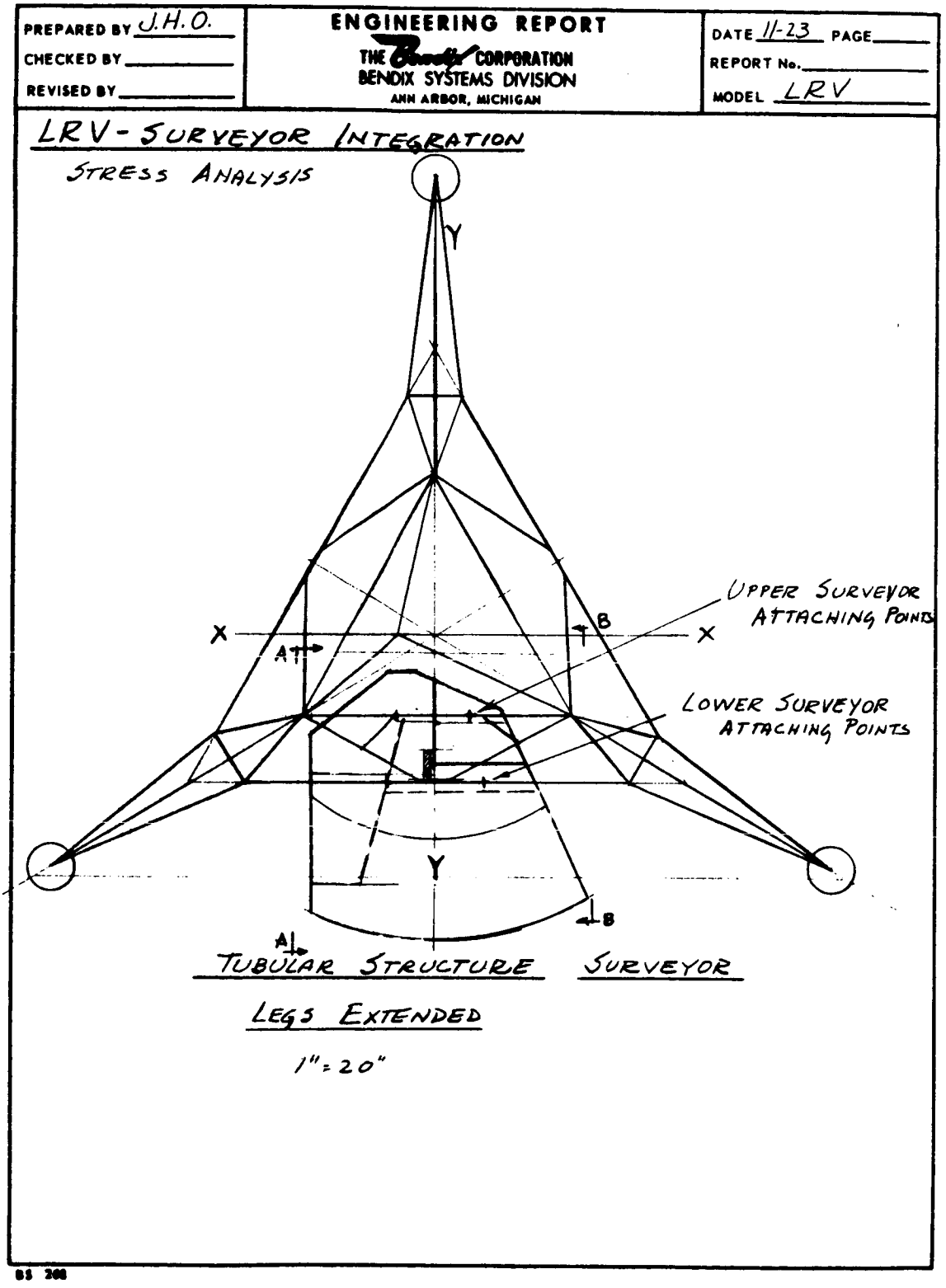

Figure 3-4 SLRV-Surveyor Integration Stress Analysis, Sheet 1 of 4

PREPARED BY J.H.O.	ENGINEERING REPORT	DATE 11-23 PAGE
CHECKED BY	THE BENDIX CORPORATION	REPORT No.
REVISED BY	BENDIX SYSTEMS DIVISION	MODEL LRV
	ANN ARBOR, MICHIGAN	

LRV SURVEYOR INTEGRATION

STRESS ANALYSIS

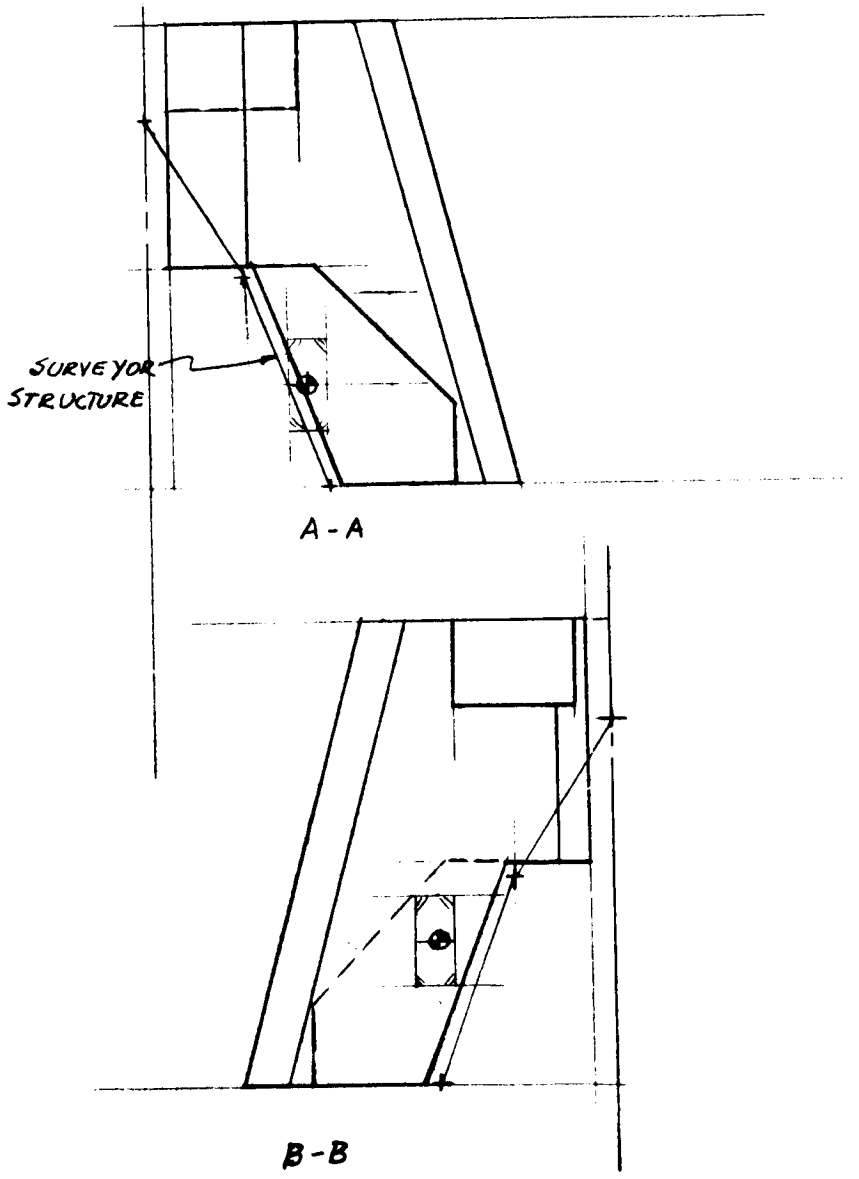

Figure 3-5 SLRV-Surveyor Integration Stress Analysis, Sheet 2 of 4

PREPARED BY ____	ENGINEERING REPORT	DATE ____ PAGE ____
CHECKED BY ____	THE Bendix CORPORATION	REPORT No. ____
REVISED BY ____	BENDIX SYSTEMS DIVISION ANN ARBOR, MICHIGAN	MODEL ____

LRV ~ SURVEYOR INTEGRATION

STRESS ANALYSIS

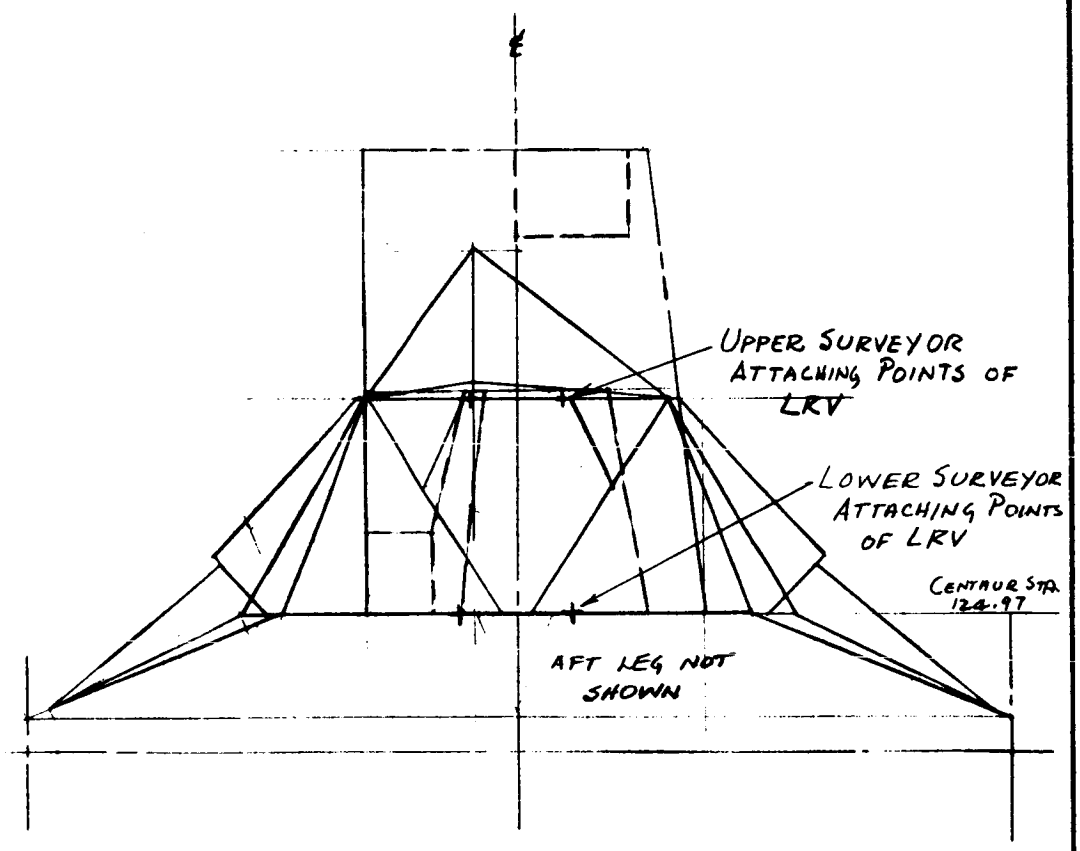

TUBULAR STRUCTURE

ELEVATION LEGS EXTENDED

1" = 20"

BS 268

Figure 3-6 SLRV-Surveyor Integration Stress Analysis, Sheet 3 of 4

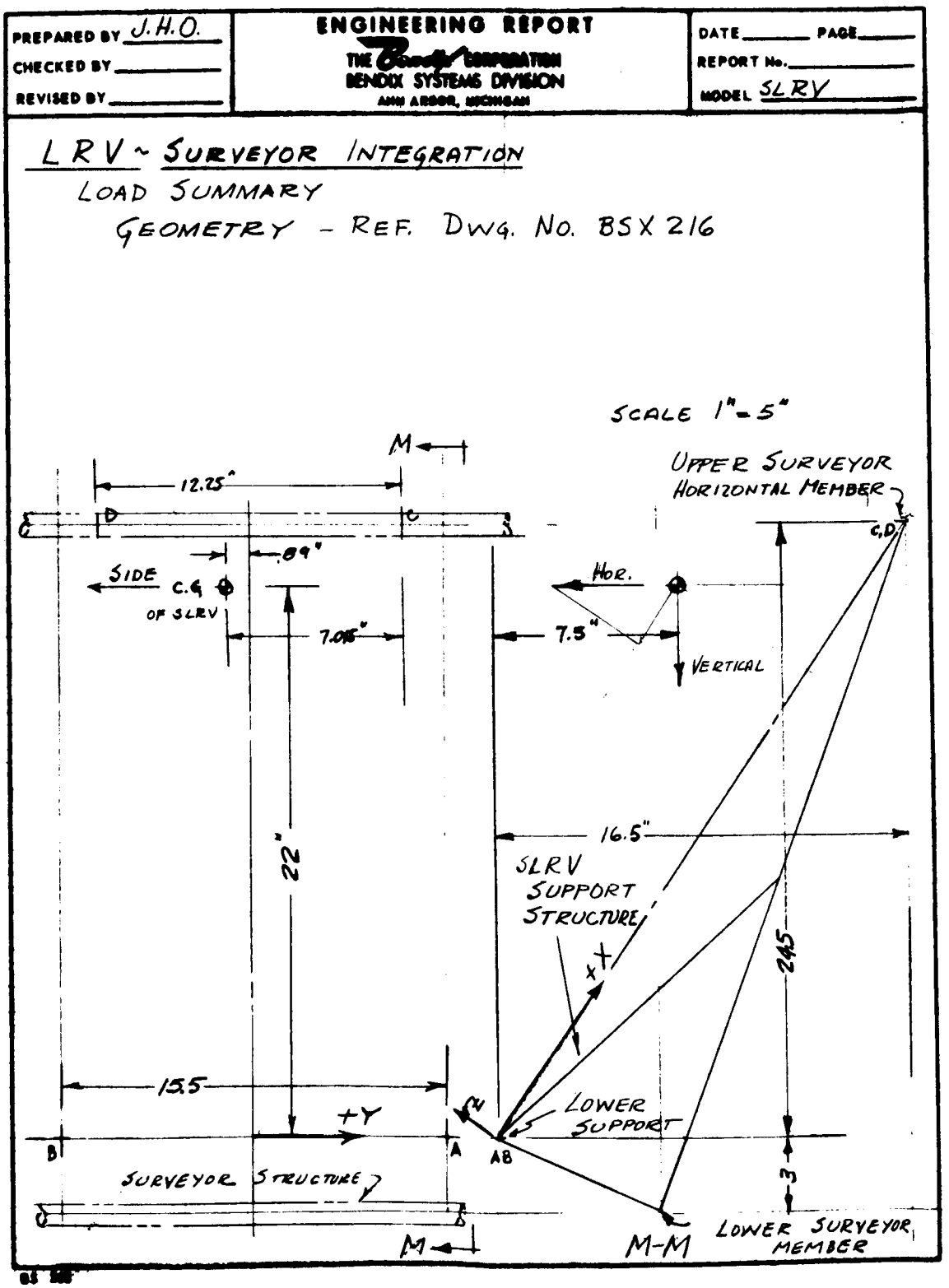

Figure 3-7 SLRV-Surveyor Integration Stress Analysis, Sheet 4 of 4

response to the variable-frequency sine wave was assumed to be 8 times the values given in Table 3-1. The vehicle may have an individual response of the same order, but the final design would minimize this problem by providing that the vehicle response does not occur at the same frequency as the Surveyor response.

The over-all loading for the attaching points of the SLRV to the Surveyor is given in Table 3-3. Only maximum conditions are considered. Certain simplifying assumptions have been made. The loads have been computed assuming that only one of the upper attachment points (C or D) is acting at any given time. This is conservative because the two attachments tend to share the load; however, either one might approach 100% of the total. Therefore, the design is not overpenalized by the assumption.

The upper support points C and D (Figure 3-7) were assumed to react only pure tension or compression loads in the Z direction. All loads in the X and Y direction (see Figure 3-7 and Table 3-3) are assumed reacted at lower points A and B.

Conservatively, all side loads are assumed to be taken by bearing on either Support A or B. The loose sliding fits of these joints make this a valid assumption.

3.2 BODY STRUCTURE DESIGN

The body structure is a space framework of square tubular members with riveted joints. An open framework was chosen, rather than a shell structure, for the following reasons:

1. Greater accessibility to equipment
2. Better thermal radiation paths
3. Ease of mounting equipment.

The use of square tubing provides flat surfaces for simple joint attachments. Riveted joints are used in preference to welding because they offer better structural damping. Also, welded aluminum joints tend to be brittle and pose problems of distortion. All joints are gusseted to increase over-all stiffness through reduced joint rotation and to be more compatible with the thermal radiation requirements for the RTG.

TABLE 3-3

LOAD SUMMARY LIMIT ON SLRV-SURVEYOR INTEGRATION

(IN PLANE AND ⊥ TO ABCD, PT. C ASSUMED INACTIVE)

	25g Vert			20g Vert			15g Horiz			Σ			20g Vert			15g Side			Σ		
Pt	X	Y	Z	X	Y	Z	X	Y	Z	X	Y	Z	X	Y	Z	X	Y	Z	X	Y	Z
A	940	0	495	750	0	397	-364	0	-460	386	0	-53	750	0	397	-145	0	-578	605	0	-181
							364	0	460	1114	0	857				145	-1500	578	895	-1500	975
B	1180	0	208	947	0	167	-460	0	-315	487	0	-148	947	0	167	145	1500	580	1092	1500	747
							460	0	315	407	0	482				-145	0	-580	802	0	413
D	0	0	617	0	0	493	0	0	1080	0	0	1573	0	0	493	0	0	0	0	0	493
							0	0	-1080	0	0	-587				0	0	0	0	0	493

(PT D ASSUMED INACTIVE)

	25g Vert			20g Vert			15g Horiz			Σ			20g Vert			15g Side			Σ		
Pt	X	Y	Z	X	Y	Z	X	Y	Z	X	Y	Z	X	Y	Z	X	Y	Z	X	Y	Z
A	940	0	305	750	0	397	-364	0	-470	386	0	-73	750	0	397	-145	0	-578	605	0	-181
							364	0	470	1114	0	867				145	-1500	578	895	-1500	975
B	1180	0	655	947	0	167	-460	0	608	487	0	775	947	0	167	145	1500	580	1092	1500	747
							460	0	-608	1407	0	-441				-145	0	-580	802	0	-413
C	0	0	617	0	0	493	0	0	1080	0	0	1573	0	0	493	0	0	0	0	0	493
							0	0	-1080	0	0	-587				0	0	0	0	0	493

The square tubular truss structure selected for this design is shown in Figures 3-1, 3-2, and 3-3. Figures 3-1 and 3-2 show the front, side, and top views of the structure, while Figure 3-3 shows pertinent structural details of the vehicle. To maximize design efficiency, a major consideration in the design of the structure was to minimize load path eccentricities by having the load paths of the various members pass through the centroid of the joint (see Figure 3-3, View A). As shown in this view, the tubing is 0.020-inch wall, 3/4-inch square with 0.040-inch wall thickness at joints. The excess 0.020 -inch wall thickness is removed by machining on the outside between joints. The joint design is conventional for aircraft construction, consisting of a riveted tube cluster reinforced by a gusset plate. An analysis is shown for the primary backup members to the reaction points in Figure 3-8.

3.3 FLOATING PIVOT DESIGN

The two tubular structure modules making up the main vehicle structure are connected by a floating pivot. This feature is shown in Figures 3-1 and 3-2, and a detail in View C of Figure 3-3. The floating pivot consists of an upper and lower channel section riveted to the body structure and a pair of stainless steel hinge straps across each channel section. A steering lock at the floating pivot is described in detail in Section 2.3. The steering lock is shown installed in Figure 3-1, and an installation detail is shown in View F, Figure 3-3. To protect the floating pivot against "cold welding" in the lunar vacuum conditions, an oxide coating will be formed on the surface of the channel sections. The choice of an oxide coating over a meterial like Teflon was based on long-term stability considerations.

The stainless steel hinge straps are riveted to the channel section. The design requirements satisfied by this attachment are as follows:

1. A simple, lightweight, and reliable mechanical attachment

2. An attachment which would maintain the straps at the proper tension level

3. A tensioning procedure which would not require an integral tensioning device (e.g., turnbuckles, tensioning screws, etc.)

4. Provide for replacement of straps, if necessary, without replacing adjacent structural members.

The floating pivot was studied for deflection due to moments about the y-y axis (Figure 3-7) by setting up the equation for the work done by the strap and differentiating with respect to the applied load. The number of variables in the equation required a trial and error solution. The results of these calculations are shown in Figures 3-9.

To prevent excessive deflections and vibrations of the floating pivot while installed in the Surveyor, a jettisonable lock is installed which provides another load path across the base of the vehicle (see Section 4.4).

3.4 VEHICLE SUPPORTS - STOWAGE

The deployment system (described in Section 4) operates through attach and release fittings integral to the SLRV structure.

Lower Hinges

An open half-hinge fitting is located on each side of the structure at the aft end of the vehicle (see Figures 3-5 and 3-6). As the vehicle deploys, these fittings rotate about a fixed hinge line on the Surveyor Bus. During the launch, transit, and landing phases, these fittings transfer loads between the vehicle and Bus.

Upper Attachment

In the forward half of the vehicle are two attach and release fittings, one on each upper edge of the structure (Figures 3-2 and 3-3, View D) which also transfer loads during the launch, transit, and landing phases. In addition, they contain the spring-loaded ejection device which provides the impulse for deployment of the vehicle to the lunar surface (see Section 4.6).

The aft hinge fitting is a machined member riveted into the tubular framework (see Figures 3-1 and 3-3) to form a rigid truss-type structural joint which can withstand applied loads about all three axes. The attachment fittings on the forward vehicle section, together with the mating fittings on the Surveyor Bus, form a load-carrying member capable of transmitting loads primarily along the LRV Z axis (see Figure 3-7). Only limited load transferral along the X and Y axes is possible at the forward fittings; hence, the major portion of these loads will be carried by the aft hinge fittings. An analysis is shown in Figure 3-10.

#1

SLRV REAR SUPPORT STRUCTURE

REF DWGS BSX215, BSX216

MEM	X'	Z'	Y'	Σ
BH	-.82X	+.60Z	0	-.82X+.60Z
BG	-.48X	-.87Z	±.375Y	-.48X-.87Z±.375Y
BJ			±1.142Y	±1.142Y

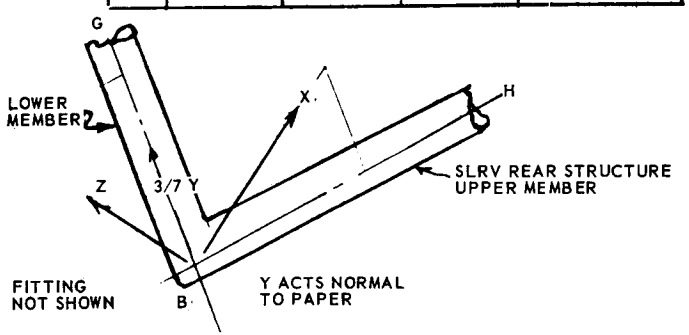

MEMBER	Σ(X'+Z'+Y')	20g VERT. + 15g HORIZ.	20g VERT + 15g SIDE
BH	-.82X+.60Z	-1150-264=	-895-447= -1342
BG	-.48X-.87Z±.375Y	-676-384=	-525-650-562=1737
BJ	±1.142Y	0	±1715

ANALYSIS OF MEMBERS

SLRV REAR SUPPORT STRUCTURE

ANALYSIS OF MEMBERS

BH P=-1342# LIM. FOR .020 WALL 3/4" TUBE
P_{ALLOW} = 1570# (REF. PG)

$M.S. = \frac{1570}{1342} - 1 = .17$ LIMIT

BG P= -1737# FOR .025 WALL A = .073
F_{cy} = 42000#/□" P_{ALL} = .073 X 42000
= 3070#

$M.S. = \frac{3070}{1737} - 1 = .77$

BJ P = -1715

$M.S. = \frac{3070}{1715} - 1 = .79$

NOTE: ~ DUE TO PRELIMINARY NATURE OF DESIGN EFFECTS OF ECCENTRICITIES ARE NEGLECTED. A LATER MORE RIGOROUS ANALYSIS WILL INCLUDE ALL SECONDARY EFFECTS.

BUCKLING OF THIN SQUARE TUBES

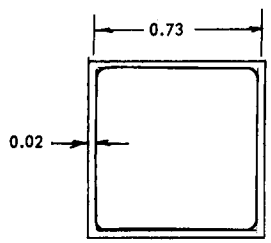

REF. AIRPLANE STRUCTURAL ANALYSIS AND DESIGN SECHLER & DUNN Pg. 180

$b/h = 1 \qquad \frac{t_b}{t_h} = 1.0 \qquad K = 4.0$

$$\sigma_{CR} = K \frac{\pi^2 E}{12(1-\mu^2)} \left(\frac{t_h}{h}\right)^2$$

$$= 4 \frac{9.85 \times 10^7}{12 \times .91} \left(\frac{.02}{.73}\right)^2 = 27000 \#/\square''$$

$P_{ALLOW} = .73 \times 4 \times .02 \times 27000$

$= \underline{1570}\#$

$A = .0585 \ \square''$

$$I = \frac{.71 \times .02 \times .73^2}{2} + \frac{.75^3 \times .02 \times 2}{12} = .00378 + .00141 = .00519$$

$$\rho = \sqrt{\frac{I}{A}} = \sqrt{\frac{.00519}{.0585}} = .298 \qquad L = 9'' \text{ FOR COLS. OVER STRUTS}$$

$L/\rho = 9/.298 = 30.2$ APPROXIMATELY $40{,}000 \#/\square''$

CHECK WITH MARTIN STRUCTURAL ALLOWABLES

ER 10228-1

$\sqrt{K_1} = 1.9 \qquad \frac{b}{t\sqrt{K}} = \frac{.73}{.020(1.9)} = 19$

$\sigma_{CR} = 26000 \#/\square''$ CHECK

CRIPPLING ALLOWABLES FOR 3/4" SQUARE TUBES

$$\sigma_{CR} = \frac{K \pi^2 E}{12(1-\mu^2)} \left(\frac{t_h}{h}\right)^2 = \frac{4 \times 9.85 \times 10^7}{12 \times .91} \left(\frac{t}{.75-t}\right)^2 = 8.6 \times 10^7 \left(\frac{t}{.75-t}\right)^2$$

$K = 4 \quad E = 10^7$

REF. "AIRPLANE STRUCTURAL ANALYSIS & DESIGN" SECHLER & DUNN Pg. 180

$t = .020$	$\sigma_{CR} = 27000 \#/\square''$
$t = .030$	$\sigma_{CR} = 62000 \#/\square'' > F_{cy}$
$t = .025$	$\sigma_{CR} = 43000 \#/\square''$
$t = .022$	$\sigma_{CR} = 33000 \#/\square''$

Figure 3-8 SLRV Rear Support Structure Stress Analysis

#2

#1

DEFLECTION OF ARTICULATED JOINT
INCLUDING CHANGE OF LOAD DUE TO DEFLECTION GEOMETRY

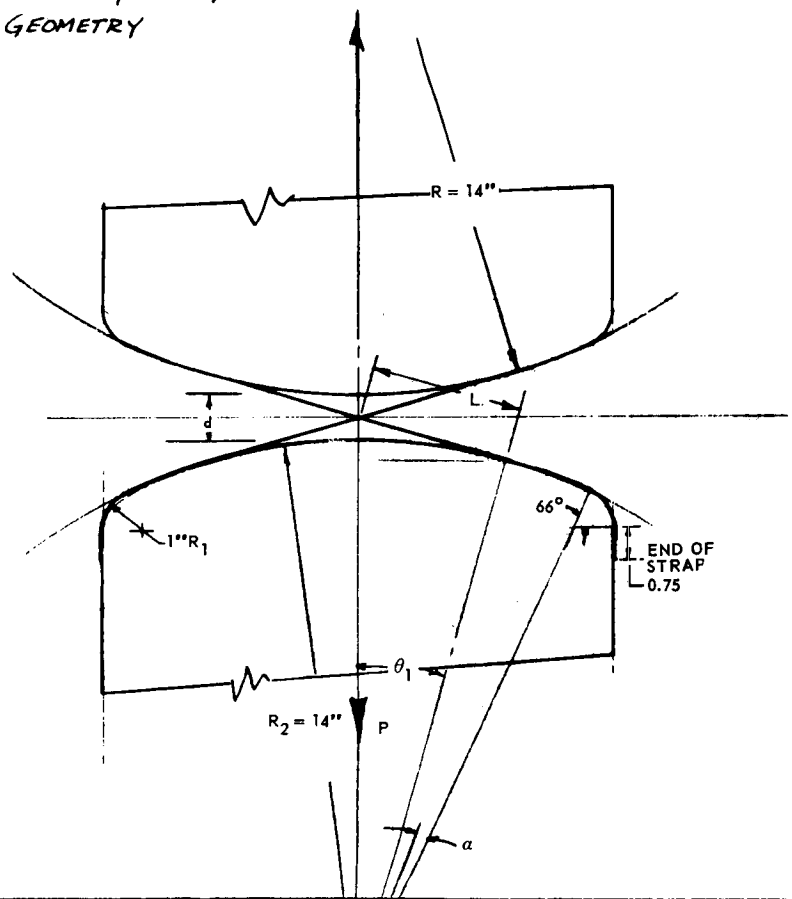

VARIATION OF L AND SIN θ WITH d

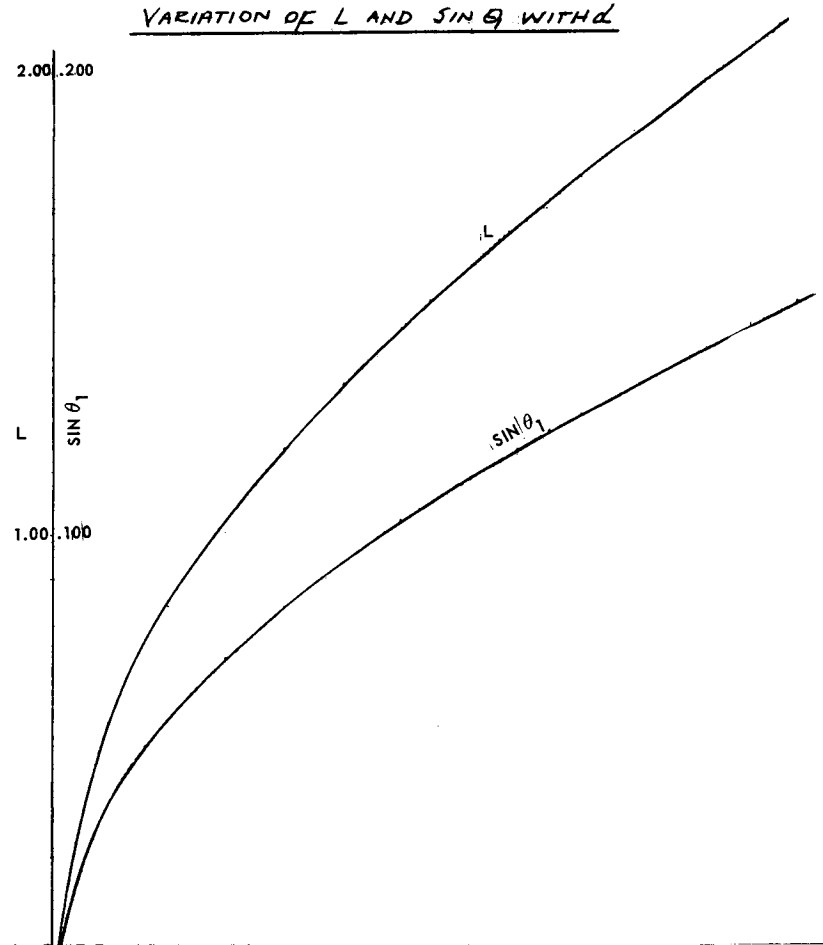

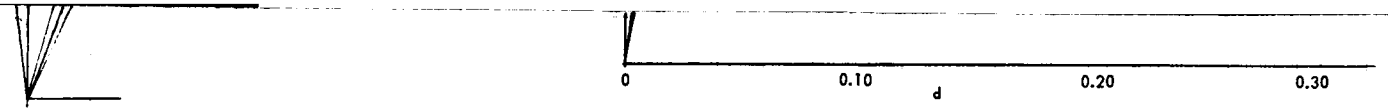

DEFLECTION OF ARTICULATED JOINT

GENERAL EQUATION FOR STRAP DEFLECTION DUE TO LOAD P

$$W = \frac{2(PK_1)^2 .75}{2AE} + 2\int_0^{65^\circ}\left(\frac{PK_1}{\cos\theta}\right)^2 \frac{R_1\,d\theta}{2AE} + 2\int_{\theta_1}^{25^\circ}\left(\frac{PK_1}{\sin\alpha}\right)^2 \frac{R_1\,d\alpha}{2AE} + 2\left(\frac{PK_1}{\sin\theta_1}\right)^2 \frac{L}{2AE}$$

$$+ \frac{2(PK_2)^2 .75}{2AE} + 2\int_0^{65^\circ}\left(\frac{PK_2}{\cos\theta}\right)^2 \frac{R_1\,d\theta}{2AE} + 2\int_{\theta_1}^{25^\circ}\left(\frac{PK_1}{\sin\alpha}\right)^2 \frac{R}{2AE}\,d\alpha + 2\left(\frac{PK_2}{\sin\theta_1}\right)^2 \frac{L}{2AE}$$

$$\frac{\partial W}{\partial P} = \frac{1}{AE}\left[1.5K_1^2P + 2K_1^2\int_0^{65}\left(\frac{P}{\cos^2\theta}\right)d\theta + 2\theta K_1^2\int_{\theta_1}^{25}\left(\frac{P}{\sin^2\alpha}\right)d\alpha + \frac{2PK_1^2}{(\sin\theta_1)^2}L\right.$$

$$\left. + 1.5K_2^2P + 2K_2^2\int_0^{65}\left(\frac{P}{\cos^2\theta}\right)d\theta + 2\theta K_2^2\int_{\theta_1}^{25}\frac{P}{\sin^2\alpha}\,d\alpha + \frac{2PK_2^2}{(\sin\theta_1)^2}L\right] = d$$

W = WORK

P = APPLIED LOAD

θ, α, θ_1

A = AREA OF STRAP = 2.75 X .016 = .044 $\square''$

$E = 29 \times 10^6$

K_1, K_2 = % OF LOAD ON EACH STRAP ASSUME $K_1 = K_2 = .50$

L, d, R_1, R_2

$$\frac{1}{AE}(K_1^2 + K_2^2)\left\{1.5P + 2\left[P\tan\theta\right]_0^{65^\circ} + 2\theta\left[P(-\cot\theta)\right]_{\theta_1}^{25} + \frac{2PL}{(\sin\theta_1)^2}\right\} = d$$

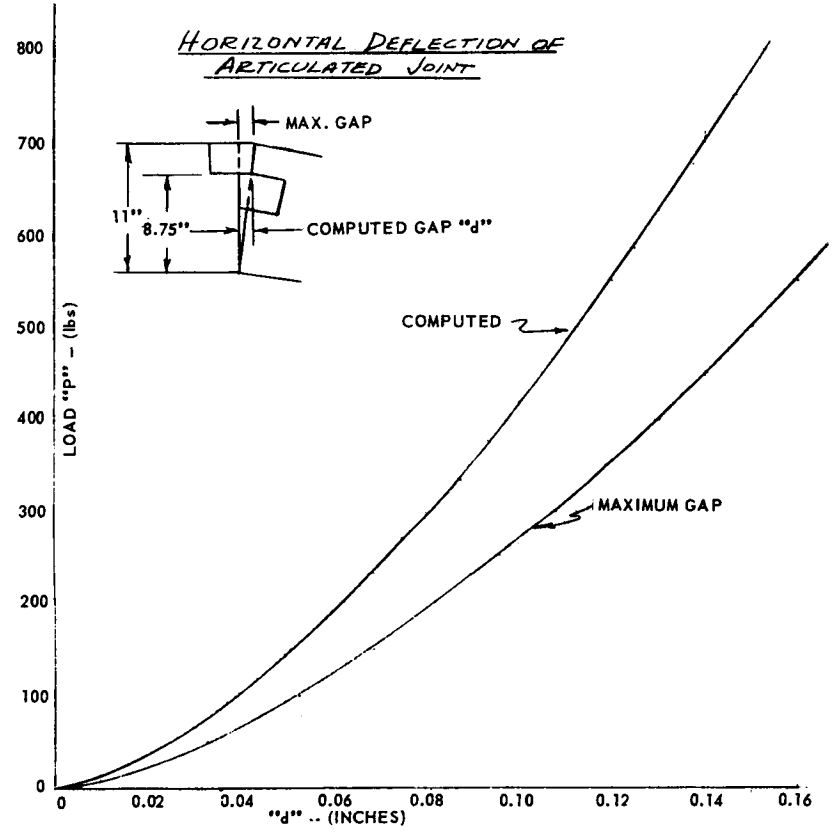

Figure 3-9 Deflection of Articulated Joint, Stress Analysis

#2

LRV- SURVEYOR INTEGRATION
LOWER DEPLOYMENT STRUCTURE

REF. DWG. NO. BSX216

MEM.	X'	Z'	Σ
BF	1.06X	.182	1.06X+.182
BE	-.25X	-1.012	-.25X-1.012

Y LOADS CARRIED IN BENDING BY BE

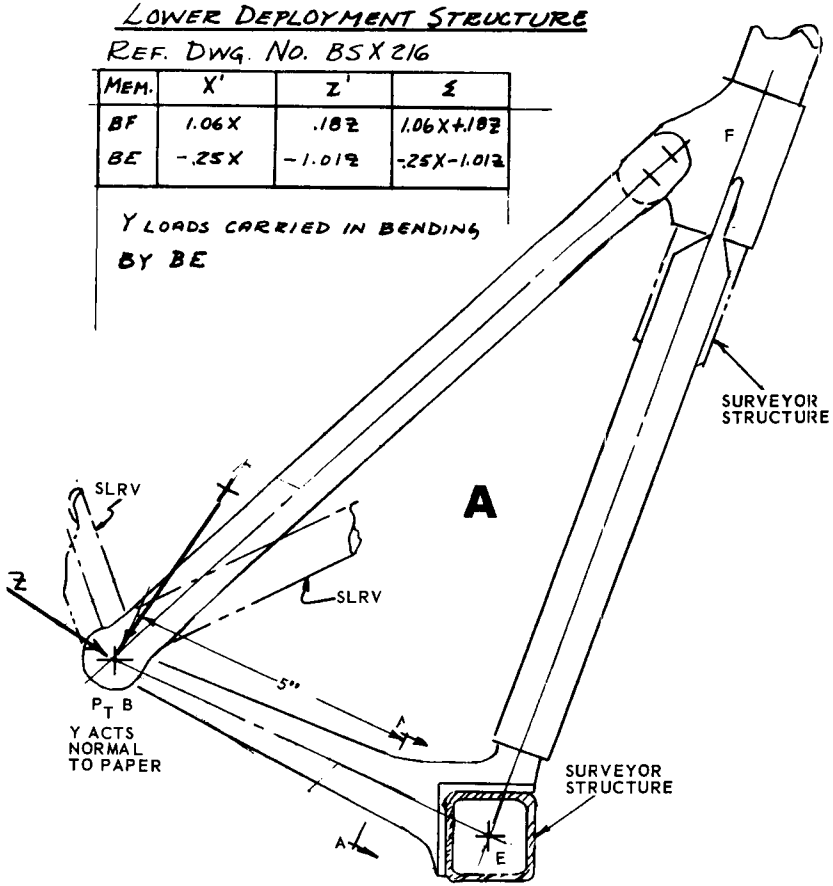

NOTE:- ONLY STRUCTURE SHOWN IS THAT REQUIRED FOR DEPLOYING SLRV. NO MODIFICATIONS HAVE BEEN MADE TO SURVEYOR STRUCTURE TO REACT THESE LOADS.

LRV ~ SURVEYOR INTEGRATION
LOWER DEPLOYMENT STRUCTURE

LOADS IN LOWER STRUCTURE

MEMBER	Σ(X'+Z')	20g VERT + 15g HORIZ	20g VERT + 15g SIDE
BF	1.06X+.182	1490 + 87 = 1577	1160 + 134 = 1294
BE	-.25X-1.012	-352 - 486 = -838	-273 - 755 = -1028

ANALYSIS OF MEMBERS

BF $P = 1294^{\#}$

ASSUME 3/4 x .028 WALL TUBE $A = .0635 \text{ in}^2$

$\frac{P}{A} = \frac{1294}{.0635} = 20400 \#/\text{in}^2$ **B**

ASSUME 24ST TUBING $F_{ty} = 42000 \#/\text{in}^2$

$M.S. = \frac{42000}{20400} - 1 = 1.06$ LIMIT

BE

SECT. A-A

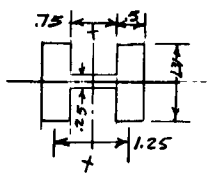

$P = -1028^{\#}$ LIMIT $B.M. = 1500 \times 5 = 7500 \text{ in}^{\#}$ LIMIT

AREA: $.50 \times 1.31 \times 2 + .75 \times .25$

$= 1.31 + .188 = 1.50 \text{ in}^2$

$I = \frac{.5 \times 1.31 \times 1.25^2}{2} + \frac{.75^3 \times .25}{12}$

$= .51 + .009 = .519$

$f_b = \frac{7500 \times .875}{.519} = 12600 \#/\text{in}^2$ $F_{ty} = 42000$

$\frac{P}{A} = \frac{1028}{1.5} = \frac{700}{13300 \#/\text{in}^2}$ $M.S. = \frac{42000}{13300} - 1$

$= 2.15$

SLRV UPPER SUPPORT STRUCTURE

REF DWG NO. BSX 216

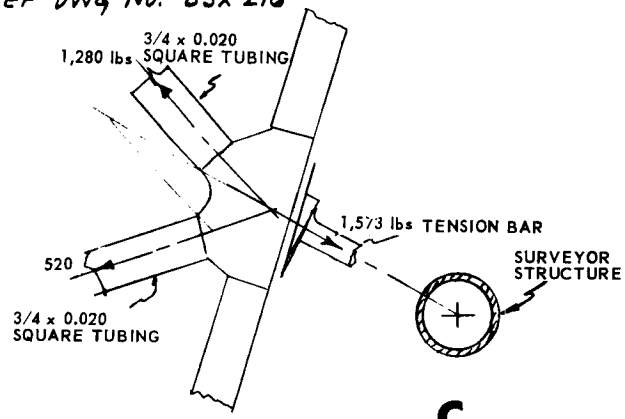

C

ANALYSIS OF MEMBERS

3/4 x .020 TUBE $P = 1280^{\#}$ $P_{ALLOW} = 2530^{\#}T$ FOR $F_{cy} = 42000^{\#}/\square''$

$$M.S. = \frac{2530}{1280} - 1 = .98$$

TENSION BAR

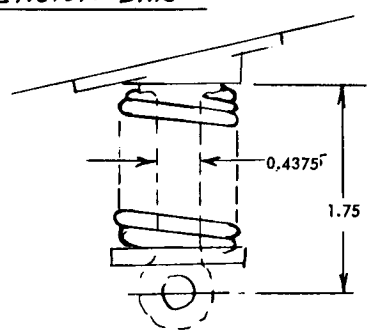

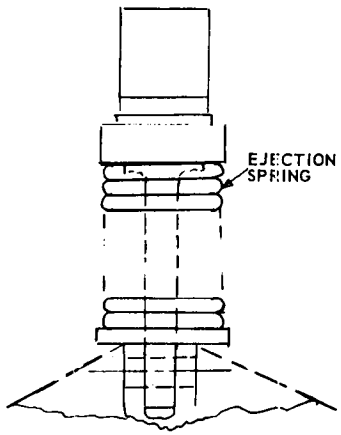

SLRV UPPER SUPPORT STRUCTURE

TENSION BAR (CONTINUED)

CONSERVATIVELY ASSUME 60% OF 1500 x .75 ON ONE STRAP

$P = 1500 \times .75 \times .60 = 675^{\#}$

$B.M. = 675 \times 1.75 = 1180^{in\#}$

$$f_b = \frac{Mc}{I} = \frac{1180 \times .219}{.001797} = 144000^{\#}/\square''$$

$F_{by} = 132000 \times 1.7 = 225000^{\#}/\square''$

$$M.S. = \frac{225000}{144000} - 1 = .56$$

D

Figure 3-10 Lower Deployment Structure and Upper Support Structure Stress Analyses

#2

3.5 COMPONENTS INSTALLATION

The forward structural module houses the electronics compartment (including the thermal plate) and provides a television camera mount. The electronics compartment and thermal plate comprise a subassembly box which is bolted to the upper structural members. A typical detail of this attachment appears in Section B-B, Figure 3-3. Attachment is through an insulating ring provided on the box to avoid a thermal conductive path.

For attachment of the television camera, a mounting flange is connected to the upper forward structural member and stiffened by means of an I-section which extends to the lower forward structural members. The TV camera mounting flange is 1.50 inches to the left of the vehicle centerline of symmetry, and the camera folds to the right in the stowed position (directions as seen from the rear). A tie-down fitting is provided on the right-hand side of the structure to restrain the TV camera during flight.

The RTG power supply and directional antenna are installed in the aft structural module. The RTG is mounted slightly forward of the aft track strut and bolted to upper and lower structural cross members (see Figures 3-1 and 3-2). A detail of this attachment appears in Section E-E, Figure 3-3. If the RTG were mounted directly over the track strut, eccentric loads in the structure would have been minimized; however, the present location is the result of a trade-off between structure, fin radiation area, accessibility, and vehicle center of gravity location.

A mounting bracket for the directional antenna is located on the aft structural module at the upper left, near the corner. An explosive latch pin fitting on the left side of the structure restrains the antenna in the stowed position; its operation will be described in Section 5.

3.6 STRUT DESIGN

To complete the SLRV structure, two strut assemblies (which connect to the mobility track units) are attached to the vehicle body at the forward and aft ends as shown in Figures 3-1 and 3-2. Details of the strut and its attachment appear in Figure 3-11 and View G of Figure 3-3, respectively. The strut design provides the shock absorption necessary during deployment. As shown in Figure 3-11, the tapered struts have a closed cross section made up of a hat section riveted along the flanges to flat

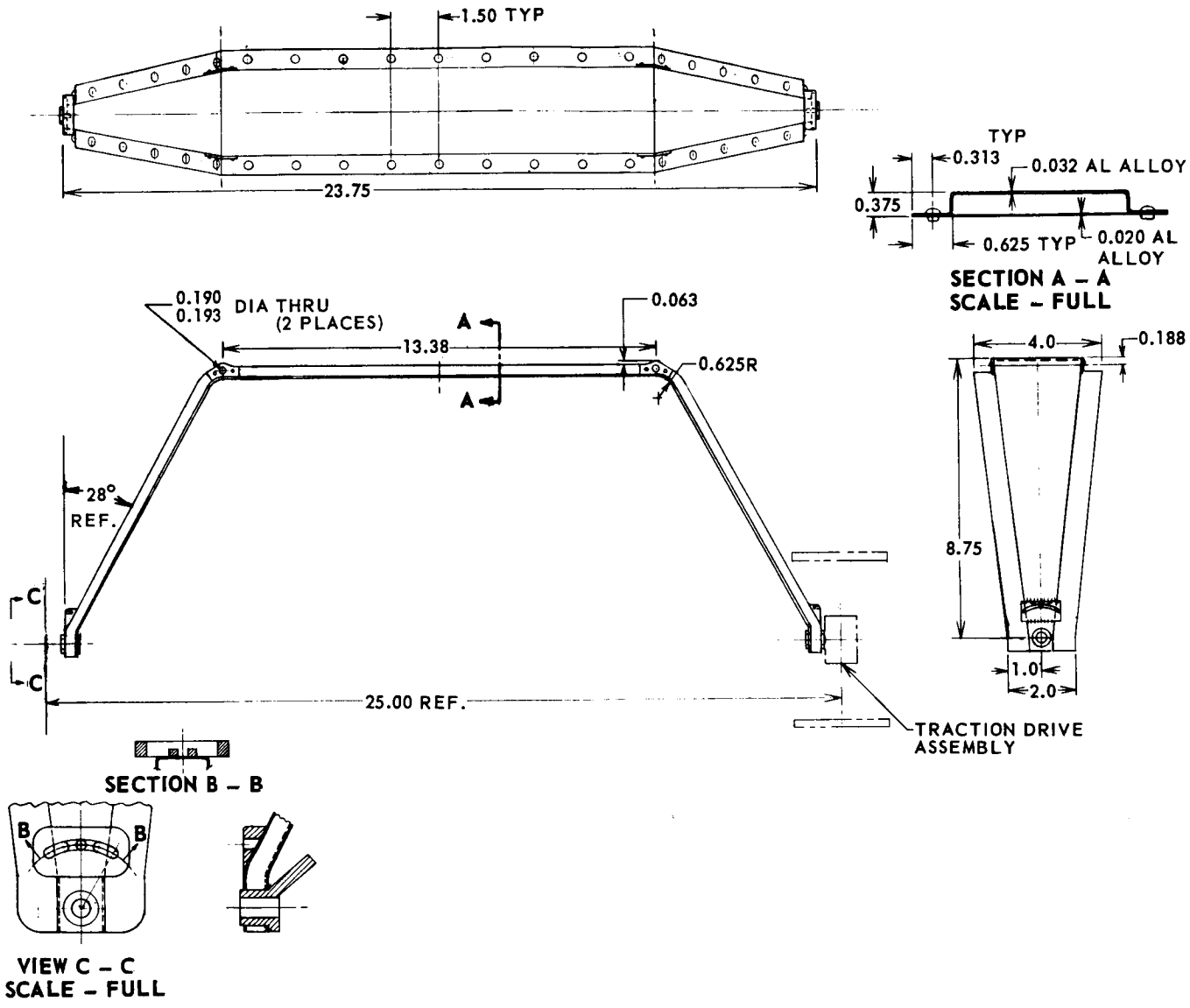

Figure 3-11 Strut Configuration

sheets. The struts are attached to the body by pin joints, thus permitting rotation of the strut and alleviating the deployment shock loads that would be transmitted to the vehicle structure by a rigid attachment. This design is conservative, because it is based on an early analysis which did not account for the energy loss due to the angular momentum imparted to the vehicle. A later analysis in Section 4.6 shows that the energy to be absorbed at impact is much less. The stress analysis for the strut is given in Figure 3-12.

3.7 MATERIALS

A materials study was conducted to examine the properties of both metallics and nonmetallics with respect to the postulated lunar environment. On the basis of existing state-of-the-art information, general and, in some cases, specific recommendations have been made regarding material classes to be used for SLRV.

The lunar environment as described in document EPD-98 is summarized as follows:

1. Temperature: $-280^{\circ}F$ to $+260^{\circ}F$
2. Vacuum: 10^{-12} to 10^{-13} mm Hg
3. "The effects of certain factors in the lunar environment will be small and shall not be considered as design conditions. These factors are: (a) meteorite particles, (b) magnetic and electric fields, (c) electromagnetic radiation, except for the range of values that affect heat balance, and (d) corpuscular radiation."

When considering polymeric materials for structural purposes, radiation effects cannot be ignored. Consequently, electromagnetic radiation was considered as a design requirement insofar as polymeric materials were concerned. Corpuscular radiation levels are sufficiently low to be neglected.

The materials considered during the course of this study were:

1. Aluminum
2. Beryllium
3. Magnesium
4. Titanium
5. Stainless steel
6. Polymeric materials (general).

Because of the numerous varieties and types of polymers, reference to specific materials is made in the text as the discussion warrants.

3.7.1 Environment

The materials used in SLRV will experience extreme temperature variations on the lunar surface; consequently, careful consideration must be given to the temperature effects on materials. Temperature control techniques employed in the vehicle design will minimize these effects in various areas of the vehicle, but in the areas outside the temperature control system, careful attention must be given to the variations in mechanical and physical properties of the materials which are sensitive to large temperature fluctuations.

Another environmental extreme to which SLRV materials will be subjected is that of hard vacuum, which usually manifests itself in solid materials through evaporation or sublimation of constituent elements or absorbed gases.

Radiation damage to materials in the lunar environment will come primarily from solar sources. Cosmic radiation is of low enough intensity that it may be ignored. Since there is no appreciable lunar atmosphere, there will be little or no shielding against solar radiation. The damage to materials will be principally from electromagnetic radiation.

It will not be possible to discuss extensively the interaction effects of vacuum, temperature, and radiation on materials since little theoretical or experimental data exist on combined effects.

3.7.2 Metals

Within the temperature variations described for the lunar environment, the materials discussed herein do not appear to exhibit any sudden changes or discontinuities in properties with the exception of, perhaps, magnesium. This peculiarity appears around - 110°F as shown in Figures 3-13 and 3-14 (plotted from data taken from Reference 3-1*). No explanation is offered for this phenomenon, because the low-temperature properties of magnesium have not been thoroughly investigated as yet.

---

*References are given in Section 3.9.

SHOCK STRUT INVESTIGATION REF. DWG BSX214

ASSUME A TAPERED FLAT PLATE

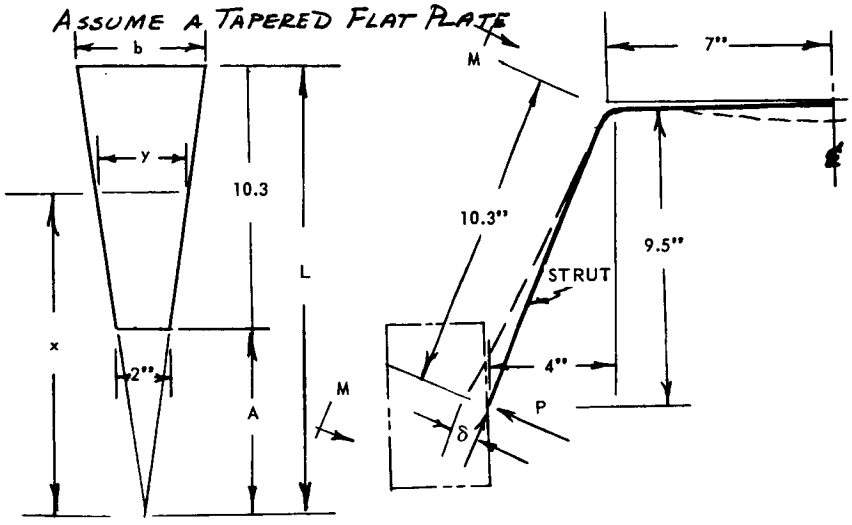

M-M

$y = \frac{xb}{L}$ $I_x = \frac{bx}{L}\frac{t^3}{12} = \frac{bt^3x}{12L}$ $M = P(x-A)$

STRAIN ENERGY IN TAPERED STRUT $= \int \frac{M^2 dx}{2EI}$

$$= \int_A^L \frac{P^2(x-A)^2 dx}{2Ebt^3x/12L} = \frac{12LP^2}{2bt^3E}\int_A^L \frac{x^2-2Ax+A^2}{x}dx = \frac{6LP^2}{bt^3E}\int_A^L \left(x-2A+\frac{A^2}{x}\right)dx$$

$$= \frac{6LP^2}{bt^3E}\left[\frac{x^2}{2}-2Ax+A^2\log_e x\right]_A^L = \frac{6LP^2}{bt^3E}\left[\frac{L^2}{2}-2AL+A^2\log_e L-\frac{A^2}{2}+2A^2-A^2\log_e A\right]$$

$$= \frac{6LP^2}{bt^3E}\left[\frac{L^2}{2}-2AL+A^2\left(\log_e L-\log_e A+\frac{3}{2}\right)\right] = \frac{6LP^2}{bt^3E}\left[\frac{L^2}{2}-2AL+A^2\left(\log_e\frac{L}{A}+\frac{3}{2}\right)\right]$$

TOTAL STRAIN ENERGY $= \int_0^7 \frac{(P(L-A))^2 dx}{E\frac{bt^3}{12}} + \frac{6LP^2}{Ebt^3}\left[\frac{L^2}{2}-2AL+A^2\left(\log_e\frac{L}{A}+\frac{3}{2}\right)\right] =$

$$84\left[\frac{P^2(L-A)^2}{Ebt^3}\right] + 6LP^2/Ebt^3\left[\frac{L^2}{2}-2AL+A^2\left(\log_e\frac{L}{A}+\frac{3}{2}\right)\right]$$

KINETIC ENERGY OF IMPACT $= \frac{1}{2}MV^2$ $M/_{WHEEL} = \frac{25}{386} = .0647$

$V = 8'/SEC. = 96''/SEC.$ ASSUMING 25#/WHEEL

$KE = \frac{1}{2} \times .0647 \times \overline{96}^2 = 298''^{\#}$

ENERGY ABSORPTION OF
SLRV SHOCK STRU

ASSUME $b = 4''$ $L = 20.$

$U = 84\left[\frac{P^2\,\overline{10.3}^2}{E(4)t^3}\right] + \frac{6(2}{E(4}$

$= \frac{2230P^2}{Et^3} + 30.9\frac{P^2}{Et^3}[2$

$U = \frac{2230P^2}{Et^3} + \frac{632P}{Et^3}$

ASSUME $P_{MAX} = 125^{\#}$

$\frac{2862P^2}{Et^3} = 298$

$\delta = \frac{\partial U}{\partial P} = \frac{2(2862)P}{Et^3}$

$\sigma_b = \frac{6M}{bd^2} = \frac{6 \times 10.3}{4 \times .2}$

NOTE: -THE ABOVE CAL
THIS ACCORDING TO LAT
KEEPING $t = .25$

$\sigma_b = \frac{6 \times 10.3 \times 64}{4 \times .25^2} =$

#1

PLATES

6" $A = 10.3"$ $L-A = 10.3"$

$.6)P^2 \left[\frac{\overline{20.6}^2}{2} - 2(10.3)(20.6) + \overline{10.3}^2\left(\log_e \frac{20.6}{10.3} + \frac{3}{2}\right)\right]$

$)t^3$

$3-426+106(.6931+1.5)]$

$= \frac{2862 P^2}{Et^3}$ $U = 298"^{\#}$ (CONSERVATIVE)

FIND t $E = 10^7$ FOR ALUMINUM

$\frac{2862(125)^2}{298 \times 10^7} = t^3$ $t^3 = .015$ $t = .246"$ OR .25"

$= \frac{5724 \times 125}{10^7 \times .\overline{25}^3} = 4.6"$

$\frac{125}{2} = 30800^{\#}/\square"$

CULATIONS ARE BASED ON $U = 298"^{\#}$

ST ESTIMATES SHOULD BE $75"^{\#}$

$= \frac{75(Et^3)}{2862} = \frac{75 \times 10^7 \times .\overline{25}^3}{2862} = 4080$

$= 64^{\#}$

$6300^{\#}/\square"$ $\delta = \frac{5724 \times 64}{10^7 \times .\overline{25}^3} = 2.36"$

SLRV SHOCK STRUT

IN ORDER TO REDUCE WEIGHT A BUILT UP SECTION SHALL BE USED WITH AN I EQUAL TO A 1/4" PLATE.

REF. DWG. NO. BSX 214

$I_{PLATE} = \frac{4 \times .\overline{25}^3}{12} = .0052$

SIMULATED SECTION

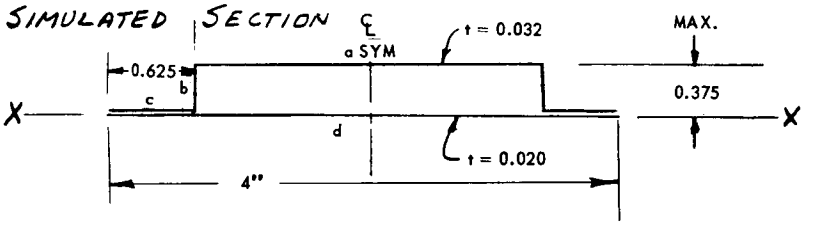

ITEM	A	h	Ah	Ah^2	I_o
a	.088	.349	.03070	.010700	NEG.
b	.0186	.1875	.00349	.000653	.000131
c	.040	.0260	.00104	.000027	NEG
d	.080	0	0	0	NEG.
	.2266	.1552	.03523	.011380	.000131

$I = .011380 + .000131 - .2266(.1552)^2$

$= .011380 + .000131 - .00545 = \underline{\underline{.00606}}\ IN^4$

#2

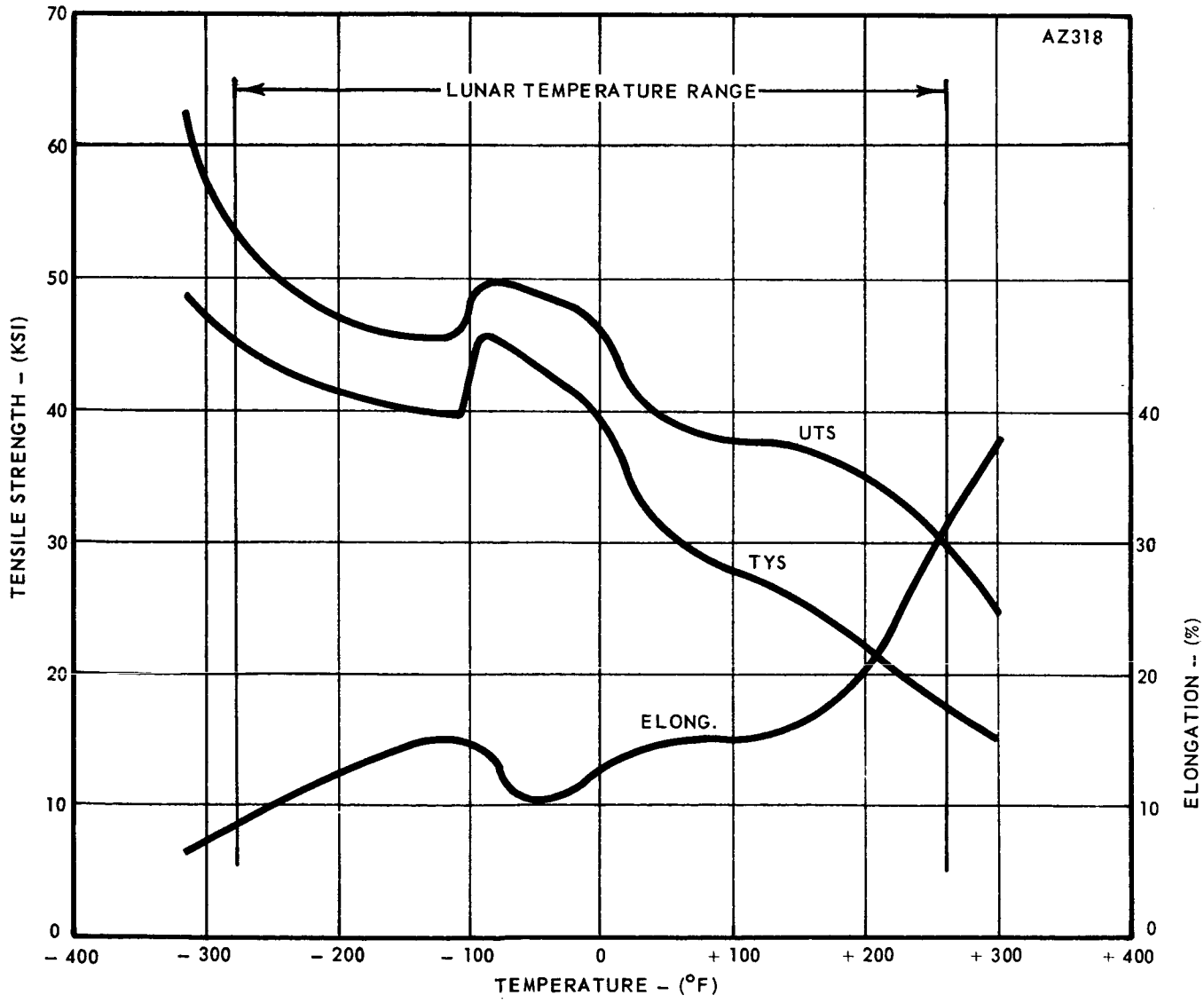

Figure 3-13 Tensile Strength vs Temperature for AZ31B Magnesium

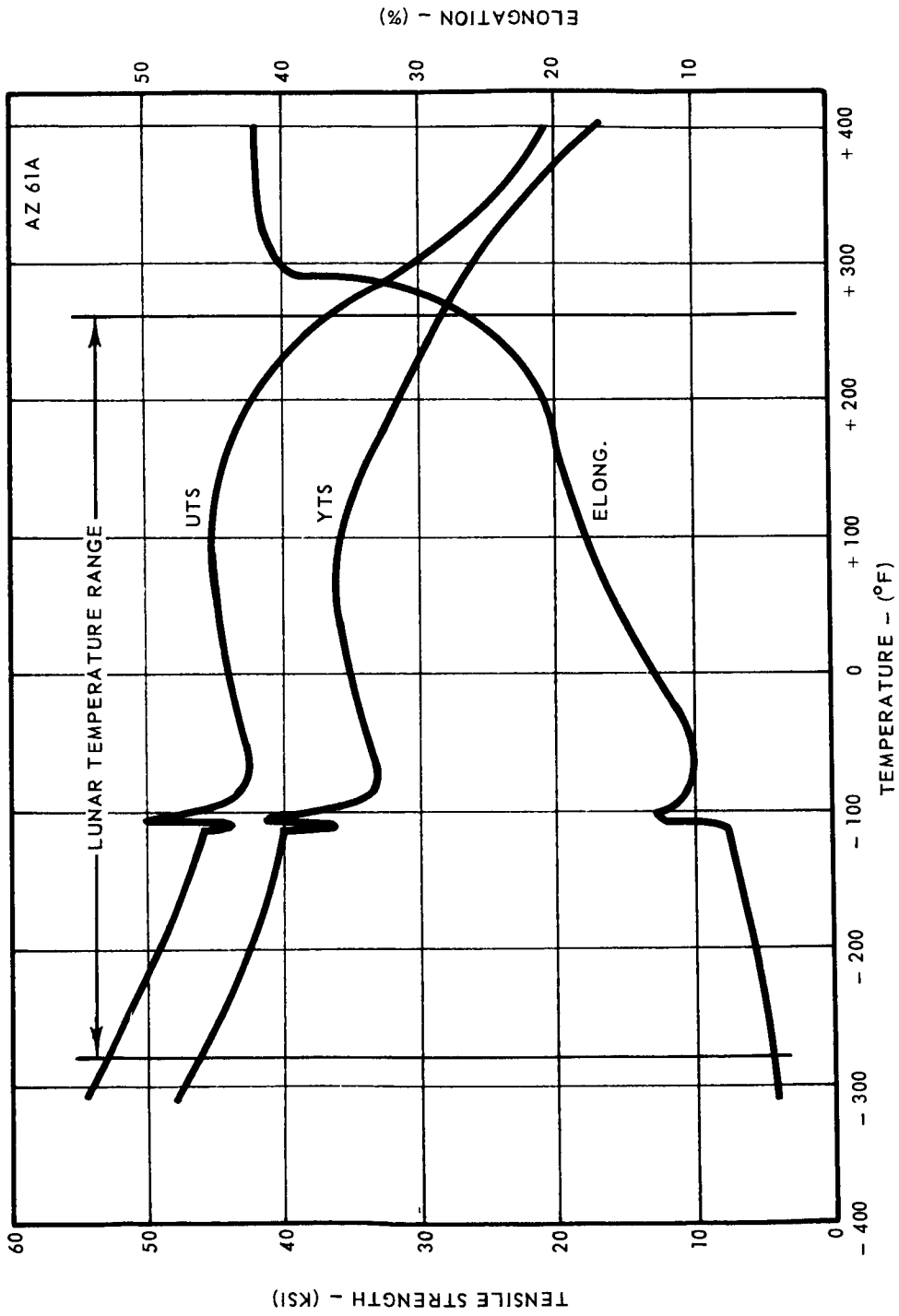

Figure 3-14 Tensile Strength vs Temperature for AZ61A Magnesium

The properties shown in Figures 3-13 and 3-14 are representative test results only and do not necessarily indicate typical values. Magnesium has been briefly discussed with respect to temperature effects. This discussion will be pursued further when other environmental factors are considered. In general, mechanical properties of metals and polymers, which are discussed in a later section, show a tendency to degrade with increasing temperature and either maintain or improve over room temperature properties with decreasing temperature (Ref. 3-2). Specifically, though, particular properties are sometimes adversely affected at various temperatures; consequently, the need to evaluate each application on the basis of individual requirements.

Some of the other materials investigated, such as beryllium, will now be discussed. Most beryllium used today is hot-pressed beryllium block and is used when the application does not require unusually high mechanical properties. Cross-rolled beryllium sheet is beginning to appear and posses better mechanical properties than the hot-pressed block (Ref. 3-3 and 3-4). Unfortunately, minimum guaranteed properties do not warrant the wide-spread use of this material in primary structural applications. As more experience is gained, guaranteed properties will no doubt increase. Furthermore, beryllium still has a difficult brittleness problem. Little or nothing is known about its low temperature properties. Although beryllium has some rather attractive properties, such as high modulus-to-density ratio and low density, its usage is limited by the previously mentioned shortcomings.

3.7.2.1 Aluminum Alloys

Aluminum alloys are one class of materials for which extensive engineering data are available. Aluminum alloys find a place in structures from moderately elevated temperatures down through cryogenic temperature ranges for several reasons. Besides attractive mechanical properties, the use of aluminum results in considerable reduction in weight with no loss of strength; aluminum structures require a minimum of maintenance, and they offer an advantage in their ease of fabrication.

Figures 3-15 through 3-18 show results of tensile tests over the expected lunar temperature range for four selected aluminum alloys (data plotted from Ref. 3-5 and 3-6). These alloys were selected as representative of the more commonly used aluminum alloys. Almost all the aluminum alloys become stronger and tougher as the temperature decreases. Not all are well-suited to elevated temperature applications. Consequently,

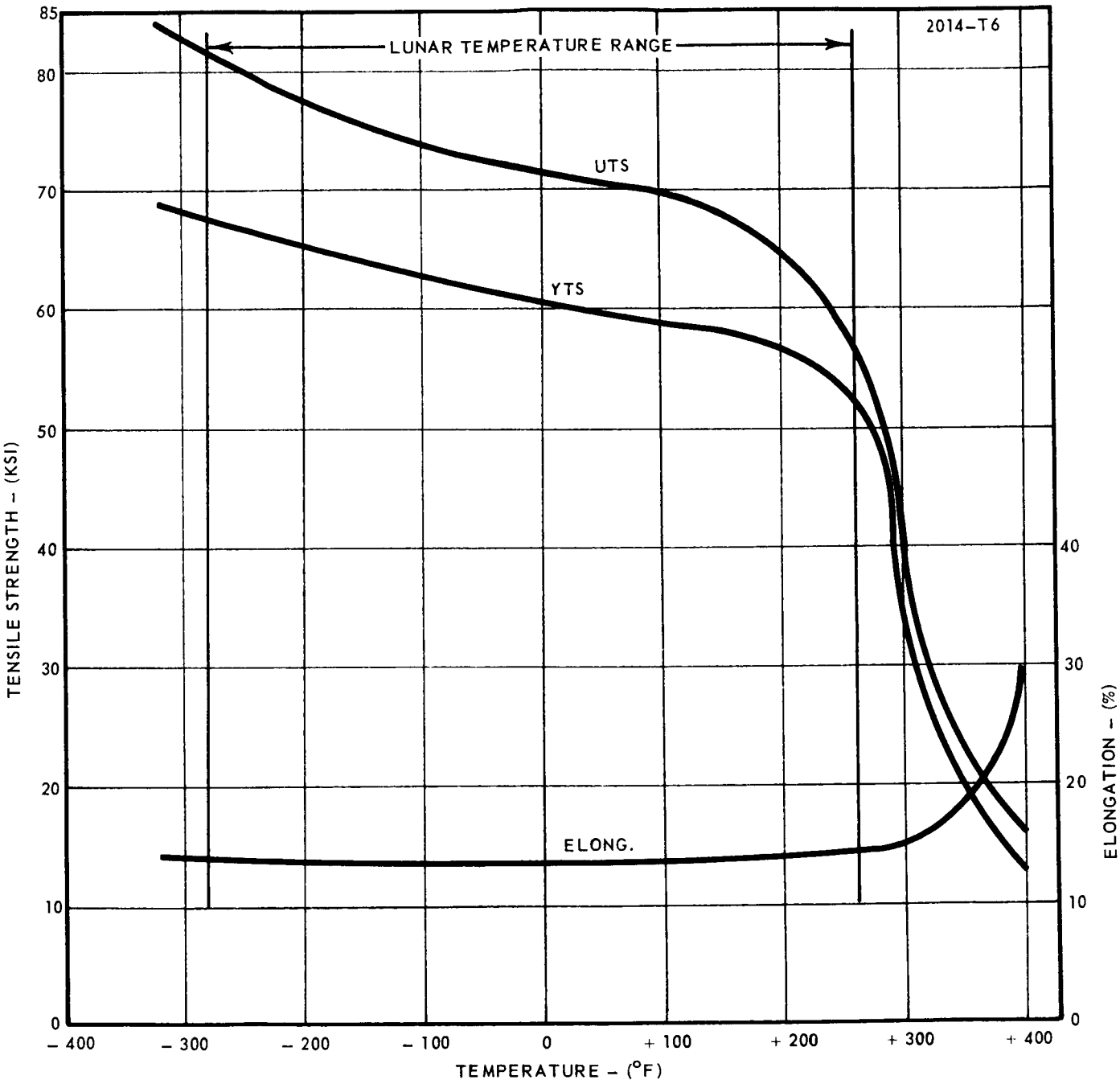

Figure 3-15 Tensile Strength vs Temperature for 2014-T6 Aluminum

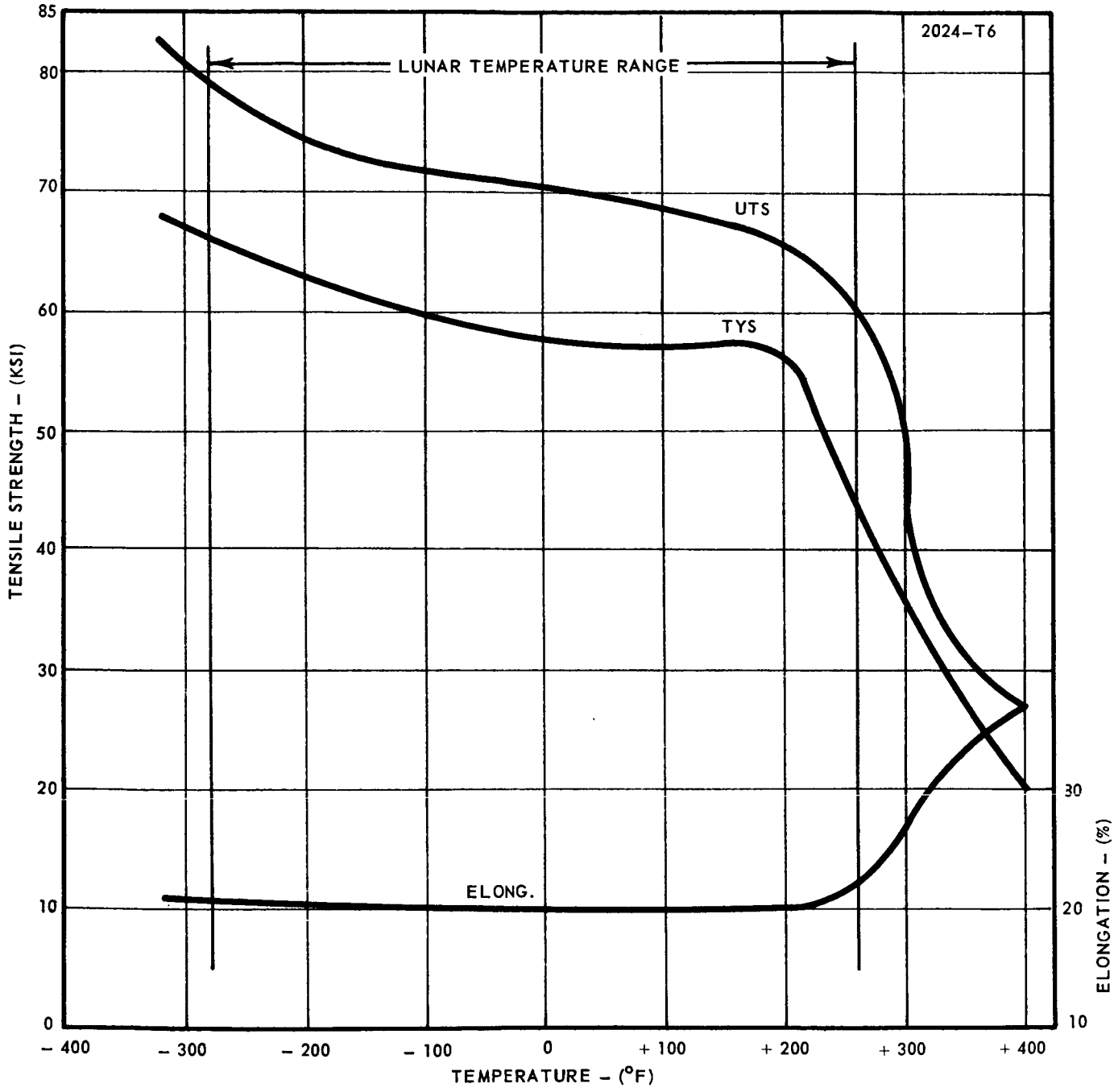

Figure 3-16 Tensile Strength vs Temperature for 2024-T6 Aluminum

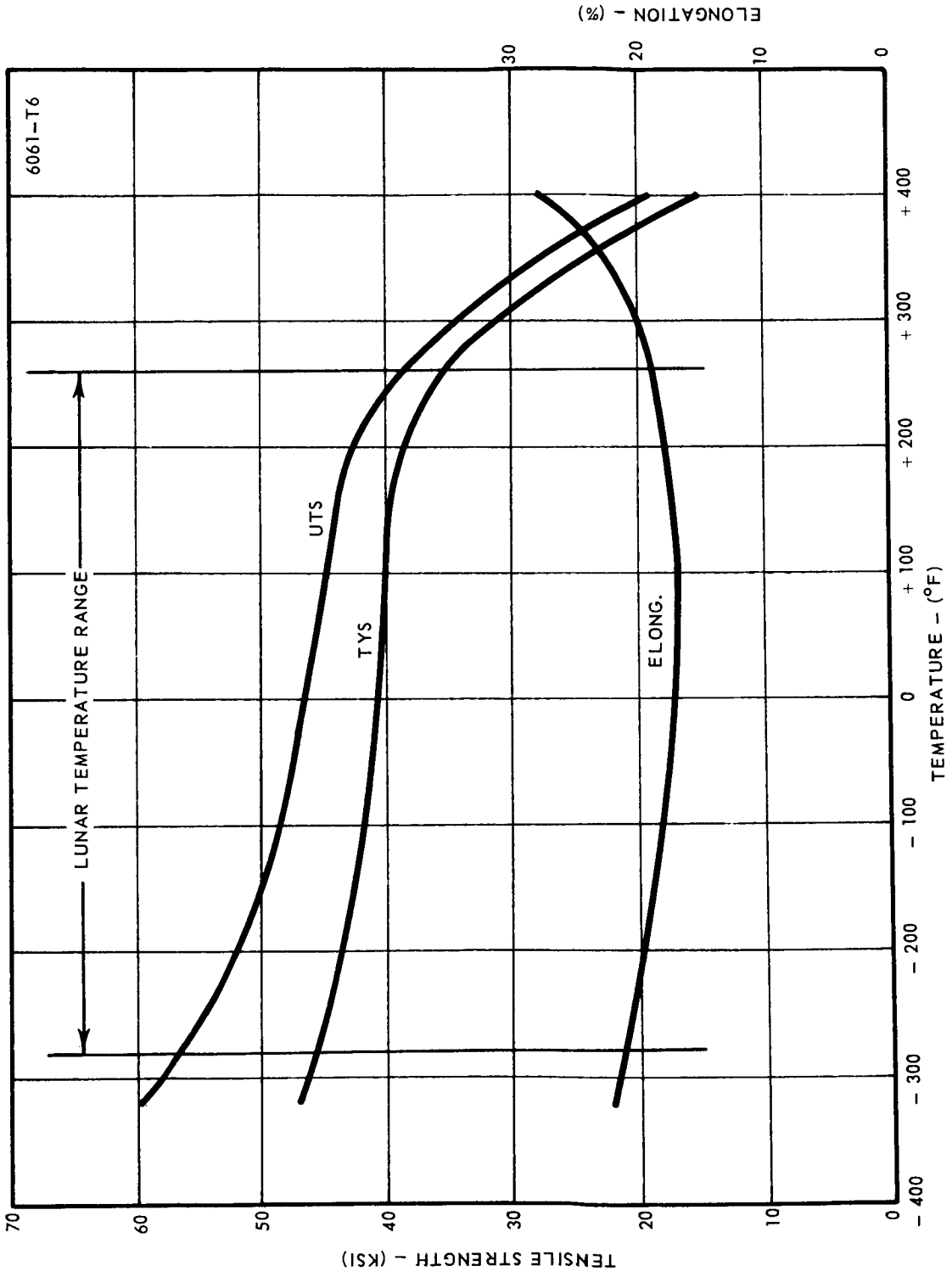

Figure 3-17 Tensile Strength vs Temperature for 6061-T6 Aluminum

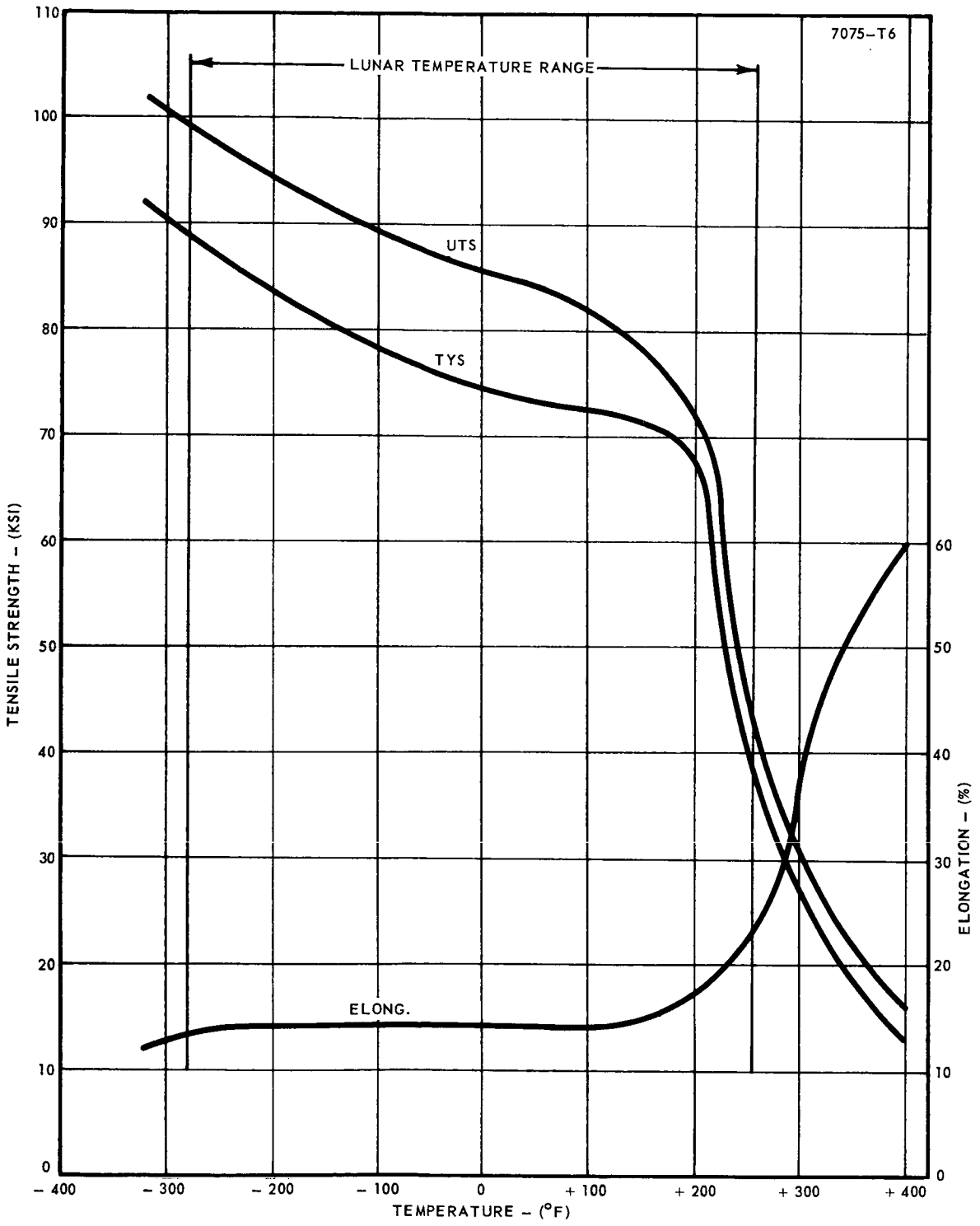

Figure 3-18 Tensile Strength vs Temperature for 7075-T6 Aluminum

for use in temperature ranges exceeding 150°F, care should be exercised in the selection of the alloy. For instance, of the four alloys selected for this study, 7075 would require care in its application since it exhibits a sharp drop in tensile properties beyond 200°F and a tendency toward brittleness at reduced temperatures.

The information presented in Figures 3-15 through 3-18 can be used to approximate temperature effects on other properties by the rule that shear and bearing ultimate strengths are governed by the same percentages as ultimate tensile strength, whereas compressive, shear, and bearing yield strengths are governed by the same percentages as tensile yield strength.

Fatigue tests at reduced and elevated temperatures show an increase of approximately 25% above room temperature fatigue strengths at -300°F and a decrease of 25% below room temperature values at +300°F (Ref. 3-6).

3.7.2.2 Stainless Steel

The stainless steel family is another group of materials about which considerable data are known. A wide range of structural properties are available over the temperature range of interest in this study. The stainless steel family possesses excellent mechanical properties in the room and elevated temperature regimes. When considering the low-temperature properties, one must be a bit more selective. The type 400 series of stainless steel has marked transition temperatures where the material goes from ductile to brittle at lower temperatures. This occurs in the neighborhood of -80°F. Consequently, type 400 series stainless steels are not considered when low temperatures are involved.

The type 300 series are important because they retain a large portion of their room temperature structural qualities at temperatures as low as -423°F. Their tensile and yield strengths increase about 100% from room temperature to -320°F (Figures 3-19 and 3-20), and the modulus of elasticity also increases as the temperature decreases. The fatigue strength increases, but the amount of increase does not seem to be proportional to the increase in tensile strength (Ref. 3-7).

3.7.2.3 Titanium

Titanium is 44% lighter than stainless steel, exhibits excellent strength-to-weight ratios, as shown in Figure 3-21, and has excellent tensile properties over the temperature ranges of interest (Figures 3-22

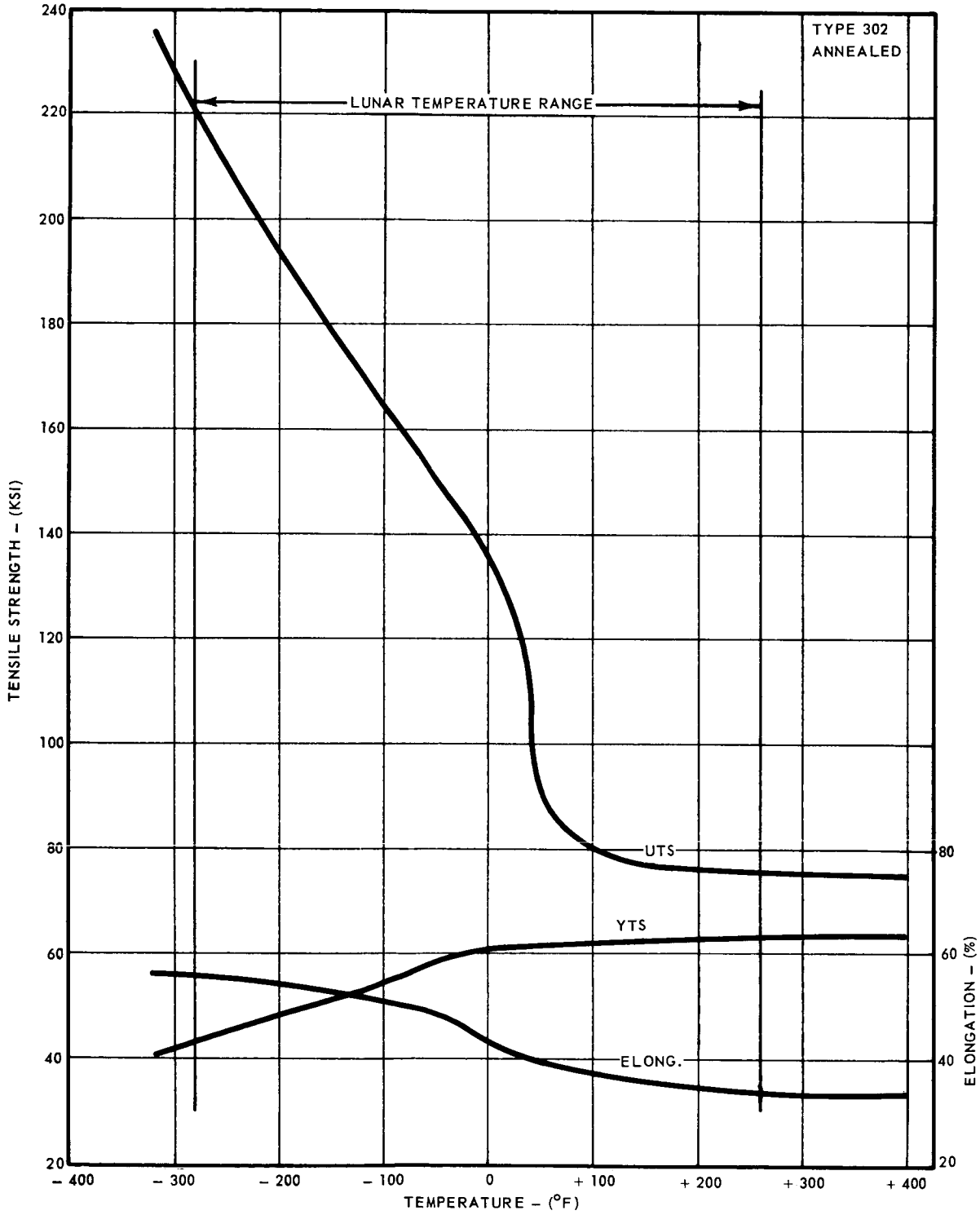

Figure 3-19 Tensile Strength vs Temperature for Type 302 Stainless Steel, Annealed

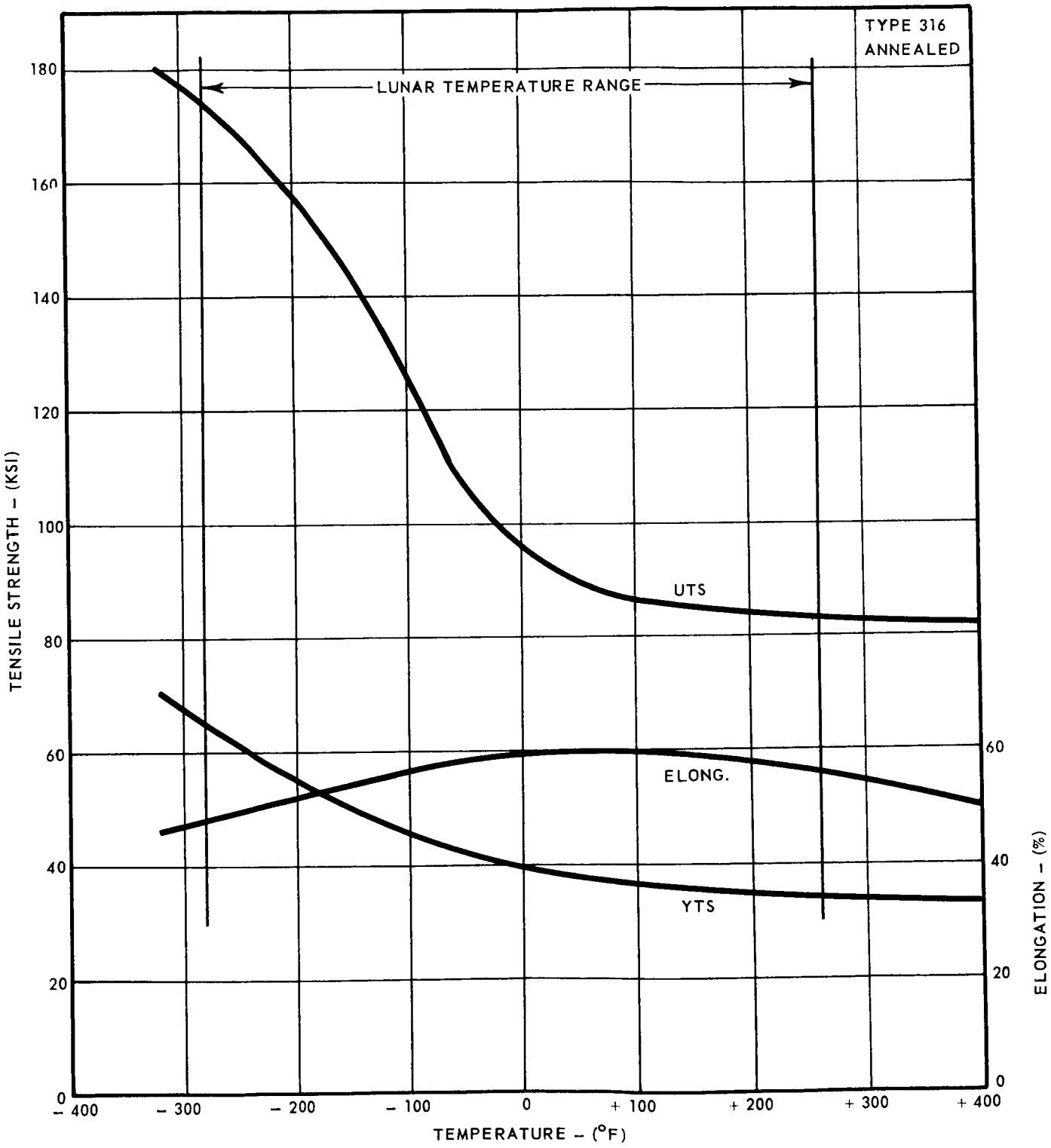

Figure 3-20 Tensile Strength vs Temperature for Type 316 Stainless Steel, Annealed

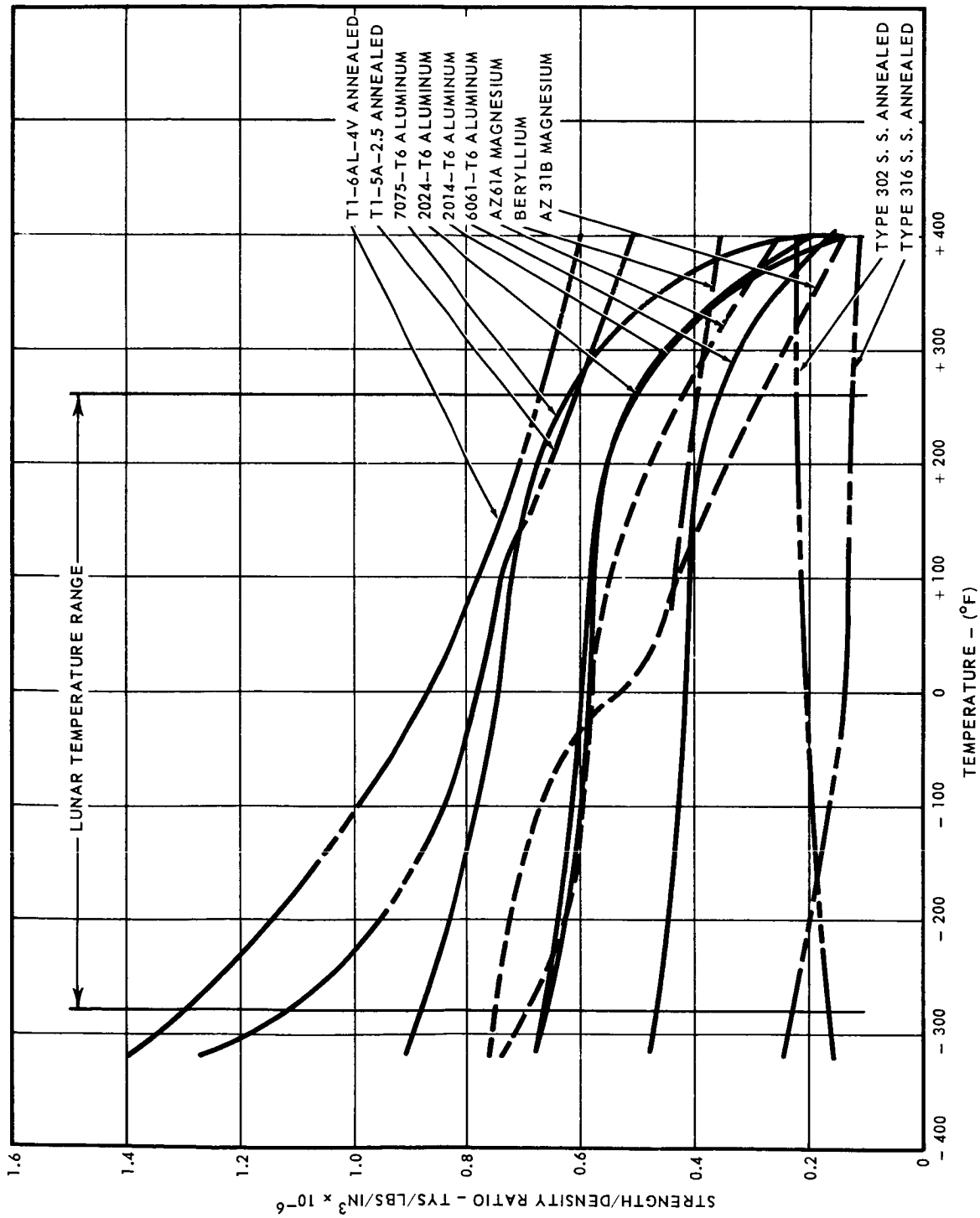

Figure 3-21 Strength-Weight Ratio vs Temperature for Various Metals

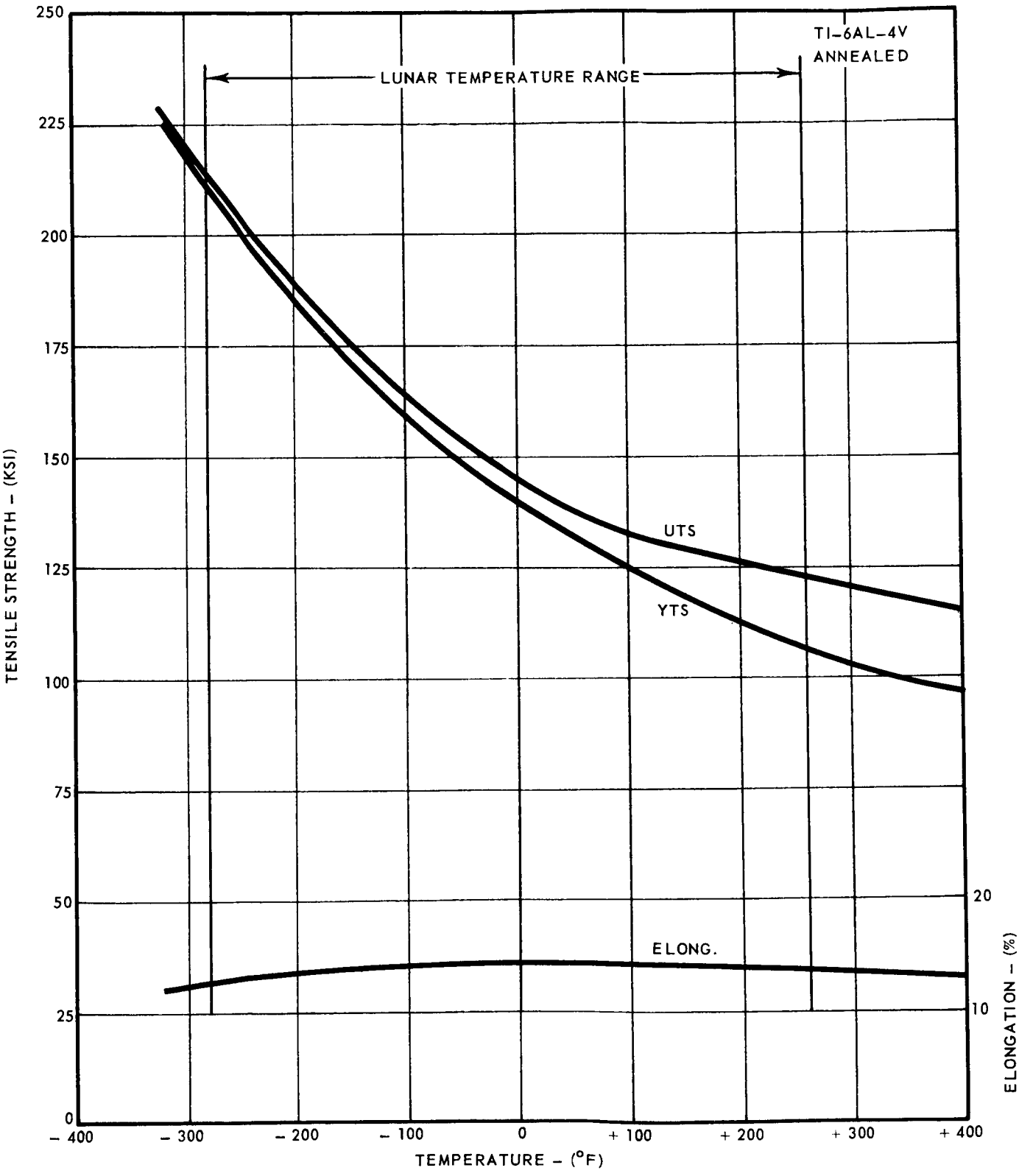

Figure 3-22 Tensile Strength vs Temperature for T1-6AL-4V Titanium, Annealed

and 3-23). The two alloys chosen for this study (Ti6Al-4V and Ti5Al-2.55n) were selected on the basis of having other desired properties in addition to those already mentioned. These alloys have excellent elevated temperature properties, are metallurgically stable in annealed and heat-treated conditions under stresses up to 950°F, are weldable, and are available in a wide range of mill products and sizes. These alloys also exhibit good ductility and notch sensitivity down to -320°F when reasonable control on impurities is exercised. If good ductility and notch sensitivity are desired beyond the -320°F range, closer control of the interstitial content is required (oxygen, nitrogen, carbon, and hydrogen). This results in a series of alloys known as ELI titanium (extra low interstitial). The main element controlled in this process is oxygen (Ref. 3-8, 3-9, and 3-10).

3.7.2.4 Vacuum Effects On Metals

Metals and alloys generally exhibit excellent stability in a space vacuum, particularly over the temperature ranges of interest. Figure 3-24 shows some of the more common alloying elements and their rates of sublimation per year. As can be seen from this figure, the only elements that might give trouble are cadmium and zinc. The temperature at which magnesium would sublime and become troublesome would be of such magnitude that the structural properties would be degraded by temperature alone.

It should be kept in mind that these sublimation rates are for elemental metals, which are not used for structural applications but rather alloys. The effect of loss of bulk material from an alloy is difficult to predict, because the rate of vaporization cannot be predicted solely on the basis of the vapor pressures of the constituent elements. Some knowledge of the diffusion coefficients of the elements also is necessary. Furthermore, unless the temperature is high enough to permit diffusion of the volatile elements through the solid alloy, the loss will, in all probability, occur only at the surface layers. For significant diffusion to occur from inside the alloy, the alloy must be in an elevated temperature situation where creep would become a significant factor. This temperature is on the order of 250°F for aluminum base alloys and 1000°F for steels. Even there, the loss will be less than the pure metal in proportion to composition of the alloy. Although experimental data are meager, indications are that loss of volatile alloying elements is many orders of magnitude less than for the pure elemental material. The data also indicate that the loss of yield and ultimate tensile strength will be less than 10%. Again,

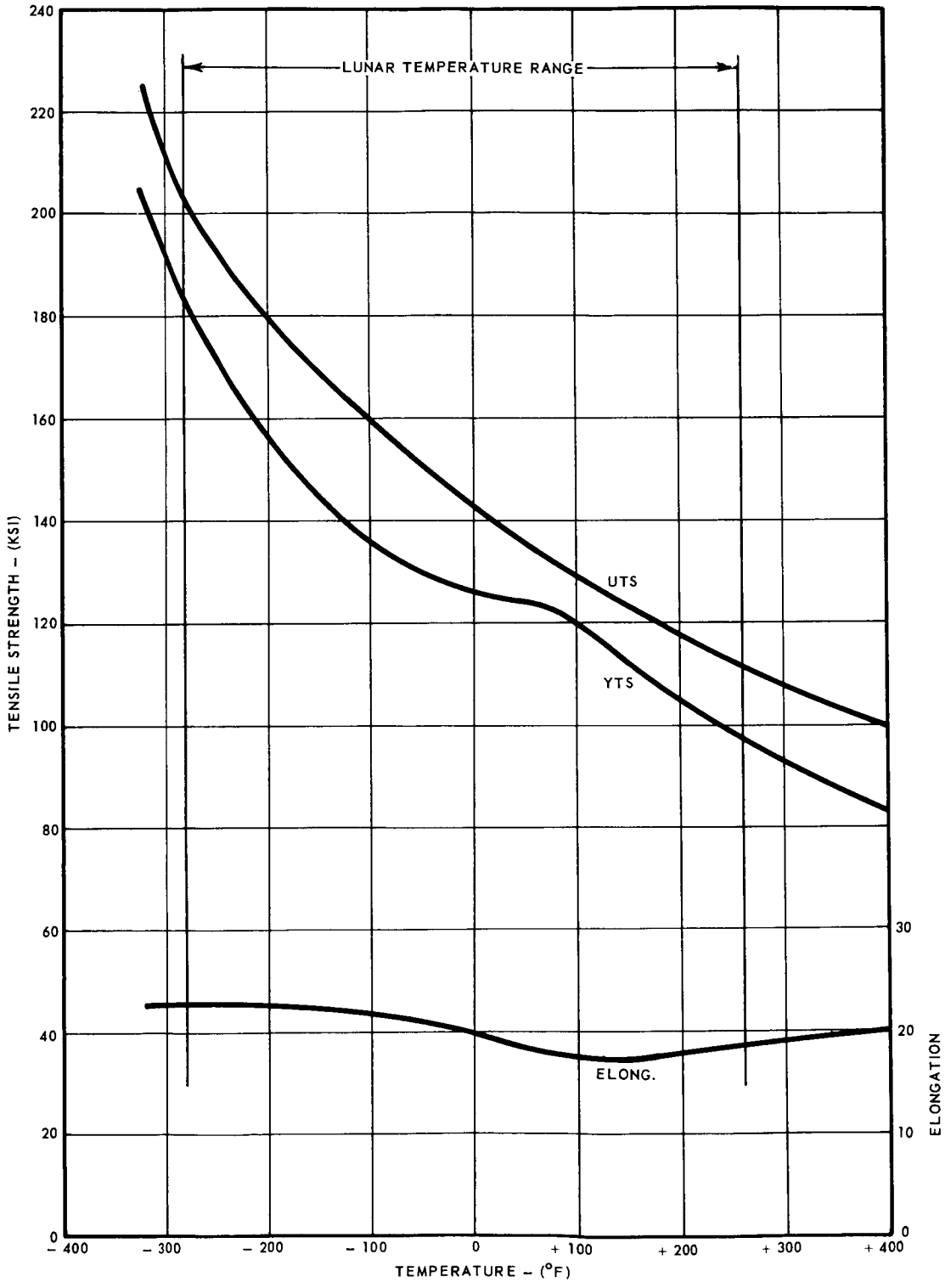

Figure 3-23 Tensile Strength vs Temperature for T1-5AL-2.5 SN Titanium, Annealed

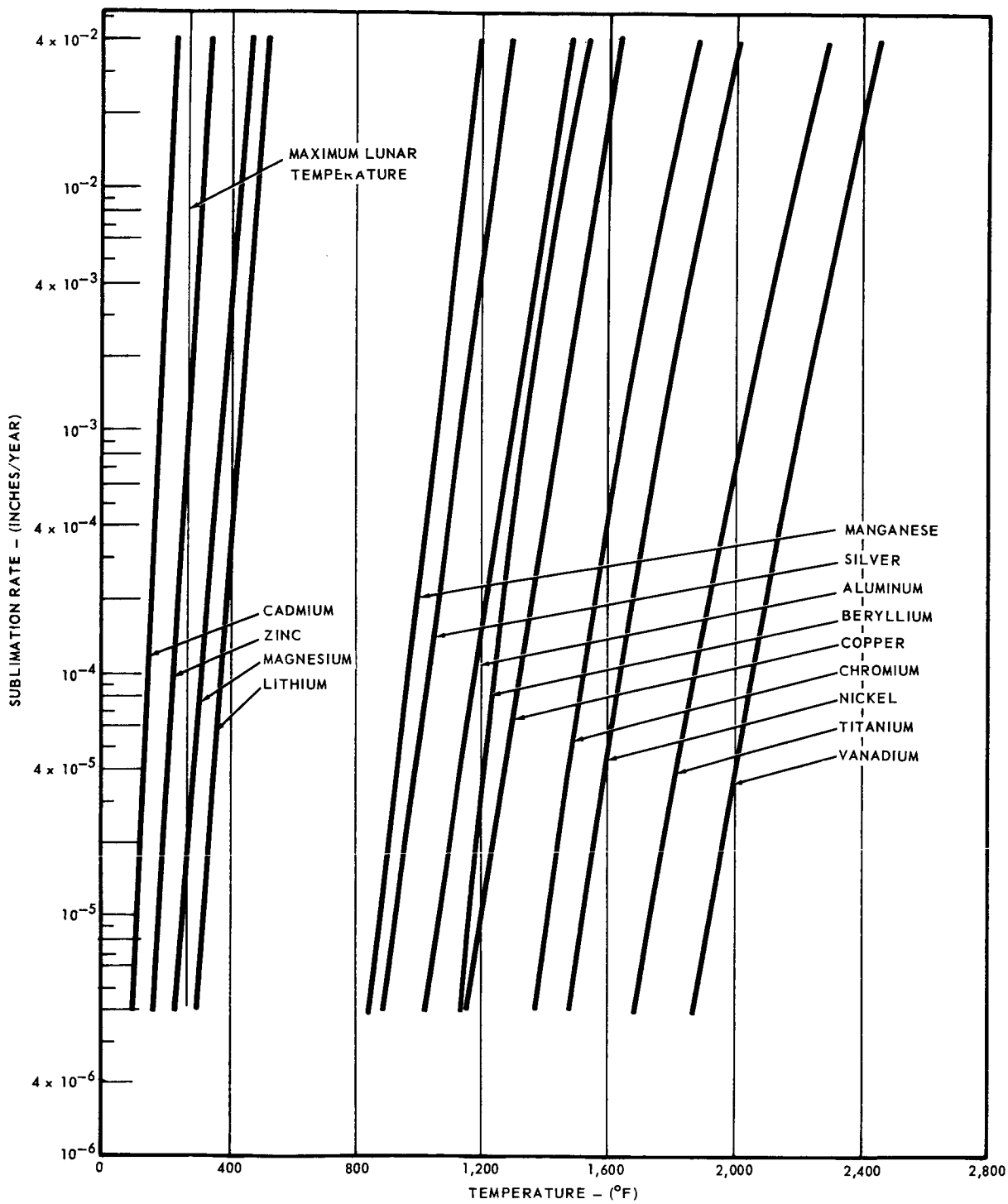

Figure 3-24 Sublimation Rate vs Temperature for Various Materials in Hard Vacuum ($\simeq 10^{-6}$ Mm Hg)

some caution should be exercised in the use of this information since it is based on short time tests (approximately 24 hours), and a very limited number of alloys (X-2020 aluminum, Dow LA 142 magnesium, copper, platinum and gold). It could also be argued that vacuum effects on tensile strength are not a prime consideration on anything but thin sections. (Ref. 3-11.)

Fatigue and creep rupture data are also scarce, but the available information indicates that at high temperatures and low stresses creep-rupture specimens are stronger in air than in vacuum. On the other hand, at lower temperatures and high stresses there is a reversal and the materials tested exhibit greater creep-rupture strength in vacuum (copper; 80 nickel - 20 chromium; 76 nickel - 19 chromium - 4 Al; Type 316 stainless steel; commercially pure nickel). It was observed that when the metals are stronger in a vacuum, the differences are small. Fatigue data obtained on nickel and Type 316 stainless steel indicate similar behavior. At low cycles per second the strength reduction in air is more pronounced as compared with vacuum for an increasing amplitude of vibration. At low cycles and low amplitudes a reversal appears to take place (Ref. 3-11 and 3-12).

A second important effect of hard vacuum on solid materials is the partial or complete removal of the surface film of gas which covers all material in the earth environment. After prolonged exposure to the space vacuum environment, the character of the gas layer on the surface of exposed material will change from its earth condition.

It has been observed that in a terrestrial environment, exposed solid surfaces quickly absorb films of ozygen and water vapor. It has also been observed that when these surfaces are clean and free of absorbed films and subjected to combinations of hard vacuum (below 10^{-7} torr), temperature, contact pressure, and time in contact, cold welding occurs. Surfaces become "clean" by losing adsorbed gases into a vacuum, by dissolving in the material and diffusing inward, and by mechanical wear between mating surfaces. Preliminary data from recent studies have been reported by the National Research Corporation on specimens of various materials broken in a vacuum (Ref. 3-13).

The materials were copper, 1018 steel, and hard 52100 steel. The following conclusions were made based on the work done:

1. The maximum cohesion at room temperature obtained for clean surfaces of the metals studies are:

Copper	65%
1018 Steel	19%
Hard 52100 Steel	0%

Cohesion appears to be a function of physical properties as well as surface cleanliness. Although surface cleanliness is not the only criterion for cold welding, no cold welding of copper surfaces occurred which had not been effectively precleaned.

2. Cold welding is temperature-dependent, increasing as temperature increases; e.g.;

Copper (752°F)	= 75%
1018 Steel (916°F)	= 100%

3. Time in contact is an important factor at high temperatures but not at low temperatures. The effect noted is one of increased cold welding with longer time in contact.

It should be noted that these experiments represent values in which clean surfaces were achieved by breaking a specimen in a vacuum and not by the methods which would actually occur in a practical application. Furthermore, they were subjected to compressive loads during contact which did not go below 25% of the compressive yield strength of the original material. In most cases the compressive load to which these specimens were subjected was 50% or better of the original material values. Time in contact was another variable which fluctuated from a few minutes to a few hours; hence, it is difficult to apply these cold welding results to a particular space application.

Since the data discussed to this point are representative of the state-of-the-art of cold welding, the remainder of the discussion will be from a somewhat theoretical standpoint.

Cold welding under vacuum conditions has first been noticed on metals. The reason for this is that because of the plasticity of metals and their high self-diffusion coefficient, stronger adhesion would be observed

with them than with other materials under identical conditions. However, it would be shortsighted to assume that increase in adhesive forces under vacuum occurs only with metals.

Experiments carried out by Arthur D. Little, Ineo, and Air Force Cambridge Research Laboratories indicate strong adhesive forces between particles of silica at 10^{-10} torr. The adhesion of SiO_2 to copper containers has also been observed. The adhesive forces measured were larger than could be accounted for by electrostatic forces. Varian Associates have reported qualitative observations on the adhesion of basalt particles to each other and to metal components. These reports indicate that it would be well to consider the adhesion of oxides to each other as well as the adhesion of oxides to metals as potential problem areas.

For study purposes the lunar soil has been assumed cohesionless or almost cohesionless; it is quite probable that this is not a valid assumption. No matter what material the soil is made of, the adhesive forces between the lunar dust particles should be considerable at the ultrahigh vacuum conditions existing at the lunar surface. The adhesive forces between the soil particles will be competing between the adhesive forces between the soil particles and the wheels or tracks of lunar vehicles. At present, the lack of data does not even allow a guess as to the amount of soil that might be built up on the wheels or even an answer to the question of whether or not a vehicle or an astronaut will get "stuck" to the surface. Considerable experimental work is needed to evaluate the seriousness of these problems and, if the adhesive forces are expected to be great, to work out solutions. Adhesive forces between some metals and some oxides might be negligible compared to others. The laws that govern adhesion of materials in ultrahigh vacuum not only are not understood, but have not even been speculated upon.

The processes by which materials lose their surface films are all temperature-dependent. The minimum temperatures at which metal surface films are removed over a period of one year by decomposition or evaporation of oxide films in a perfect vacuum can be estimated from thermodynamic data and gas kinetic theory. Estimated temperatures for removal of oxide layers from some typical metals and alloys are given in Table 3-4 (Ref. 3-14). These temperatures are conservatively low, being based on removal of a film 100 Å thick (approximately 4×10^{-7} inches).

TABLE 3-4

OXIDE REMOVAL TEMPERATURES FOR VARIOUS METALS

Metal	Temperature, °F	Mechanism Assumed
Cobalt	1560	Oxide dissociation
Copper	950	Oxide dissociation
Iron	1860	Oxide dissociation
Nickel	1472	Oxide dissociation
Titanium	572	Oxygen diffusion
Zirconium	580	Oxygen diffusion
Molybdenum	1920	Oxide dissociation
Mo-C alloy	356	Carbon reduction
Fe-C alloy	212+	Carbon reduction
1018 Steel (Mn)	212+	Carbon reduction
4140 Steel (Cr-Mo)	212+	Carbon reduction
52100 Steel (Cr)	212+	Carbon reduction
Cu-Be alloy	950	Carbon reduction

These calculated data imply that for some of the more common metals and alloys, the loss of their natural films of oxide, etc., is indeed a slow process, even after a year in a perfect vacuum. In a real situation in space, the metals exist in an environment at low partial pressures. There is then a situation where the surface film could conceivably be getting thinner by one of the removal processes previously discussed above a certain temperature or getting thicker (or not changing) below this temperature as a result of impingement, adsorption, and reaction of gas molecules with the metal surface.

It could be concluded from this discussion that most metal surfaces exposed to a space vacuum are not likely to become clean enough for cold welding to take place in any reasonable period of time. There is one other mechanism of cleaning which may accelerate surface layer removal and produce clean surfaces in a much shorter time; i.e., impingement of radiation (both electromagnetic and particulate) on the metal surface. It is assumed that radiations of this nature are to be ignored as specified in document EPD-98, then only effects of time, temperature, vacuum, and mechanical abrasion between surfaces must be considered.

To solve some of the problems of adhesion in ultrahigh vacuum, a company-sporsored research program is underway at the Bendix Systems Division designed to study the adhesion between oxides and metals at pressures of 10^{-11} torr. Initially, the adhesion between oxides and aluminum silicates and metals will be studied quantitatively as a function of contact pressure and time of contact.

Examples of pairs of materials to be studied are:

Al_2O_3 - Al, Al_2O_3 - Cu, Al_2O_3 - Ti, SiO_2 - Al, and SiO_2 - Cu.

Crystal orientation and method of surface cleaning will be other experimental variables.

A preliminary literature search in related areas has already been carried out. To date, work done in the areas of ceramic-to-metal seals, thin film adhesion to substrates, and ceramic-metal composites give strong indications that oxide-metal (ceramic-metal) adhesion is expected under an ultrahigh vacuum condition, but that these forces will be very specifically dependent on the nature of the materials.

3.7.2.5 Radiation Effects on Metals

It is anticipated that metals and alloys will not be affected by the radiation levels encountered at the lunar surface for the time periods involved.

3.7.2.6 Effects of Combined Envirments

Combined environment data for metals are meager. The available thermal-vacuum data were presented in the discussion of vacuum effects. Combined temperature, vacuum, and radiation environmental test data are completely lacking.

3.7.2.7 Selection of Metals for SLRV

Of the metals discussed, aluminum, stainless steel, and titanium would be satisfactory in the lunar environment for this application. Magnesium is a possible fourth choice, but its use is not recommended where impact loading at low temperatures would be critical or fatigue life would be important. A primary structural application of beryllium is not recommended because of the uncertainty in guaranteed mechanical properties, a tendency toward brittleness, and lack of low-temperature data.

3.7.3 Polymers

The next class of substances to be discussed have a wide range of properties and their terrestrial uses are diverse. Some of the materials are soft and rubbery, others are soft and plastic, others are hard and rigid, and still others are tough and flexible. Although their properties are varied, these substances have one thing in common: they are all polymers formed by combining smaller molecules (monomers). Polymers include not only plastics, but fibers, rubbers, surface coatings, and adhesives.

In molecular structure, polymers may be (1) straight chain (linear) compounds in which the molecules are joined in an extended series or (2) cross-linked compounds, which involve a three-dimensional network.

The linear types of polymers are represented by fibers, rubbers, etc. The cross-linked polymers are represented by the infusible, hard plastics.

From the practical point of view, plastics fall into two main categories: (1) thermo-setting, those which harden into infusible, insoluble materials on heating; (2) thermo-plastics, whose which soften on heating and can be reshaped repeatedly, such as polyvinyl resins.

3.7.3.1 Vacuum Effects on Polymers

Numerous experimental programs have investigated the evaporation rates of organic materials in a vacuum environment. Most of these experiments have been conducted at such high temperatures that a large part of the test specimen was quickly volatilized. Relatively few experiments on organic materials have been conducted at temperatures of engineering interest for space applications. For this reason, much of the lower temperature data in the literature are extrapolated from results of pyrolysis experiments at high temperatures. The validity of these extrapolations has not been clearly established.

NASA-Ames (Ref. 3-15) measured weight loss rates of organic materials in a vacuum at temperatures between 80° and 500°F for time periods up to 48 hours and vacuum levels of 3×10^{-6} to 3×10^{-7} torr.

The materials tested were polytetrafluoroethylene (Teflon) and polycarbonate (Lexan), two relatively pure thermoplastic materials; nylon-phenolic and silica-phenolic, two typical high-temperature composite materials; and epoxy (Epon 821), a relatively pure thermosetting material.

Weight loss rates for Teflon at temperatures below 500°F were found to be many orders of magnitude higher than would be predicted from an extrapolation of pyrolysis data obtained by other investigators at temperatures above 700°F. It was also indicated that the degradation mechanism at temperatures up to about 600°F may be different from that which occurs at higher temperatures.

Material thickness did not affect the rate of weight loss of Teflon at a surface temperature of 300°F for thicknesses ranging from 0.05 to 0.25 inches. It was concluded that at this temperature the reaction is effectively a surface phenomenon. The rates of weight loss of Lexan, epoxy, nylon-phenolic, and silica-phenolic were found to increase significantly with decreasing material thickness, indicating that the diffusion of the reaction products through the bulk of the material was a controlling factor in the weight loss process of these materials. These conclusions tend to contradict conclusions reported by earlier investigators (Ref. 3-12).

Finally, these test results indicate that material loss may be significant at reasonable spacecraft temperatures, and the rates of weight loss may be especially high for thin films. However, tests of several hundred hours duration are needed to establish these points.

Weight losses from the above tests are shown in Figures 3-25 and 3-26 as a function of temperature and thickness, respectively.

Information on vacuum effects is usually reported in terms of weight loss because, weight losses of 1 or 2% generally, do not produce important property changes, while weight losses approaching 10% are accompanied by considerable changes in engineering properties. An exception to this general statement must be made for plastics and elastomers containing plasticizers that are volatile in vacuum. In some cases, loss of less than 10% of the plasticizer from a polymer may significantly embrittle the material. Other conditions to be considered when using data on polymers in a design include the following:

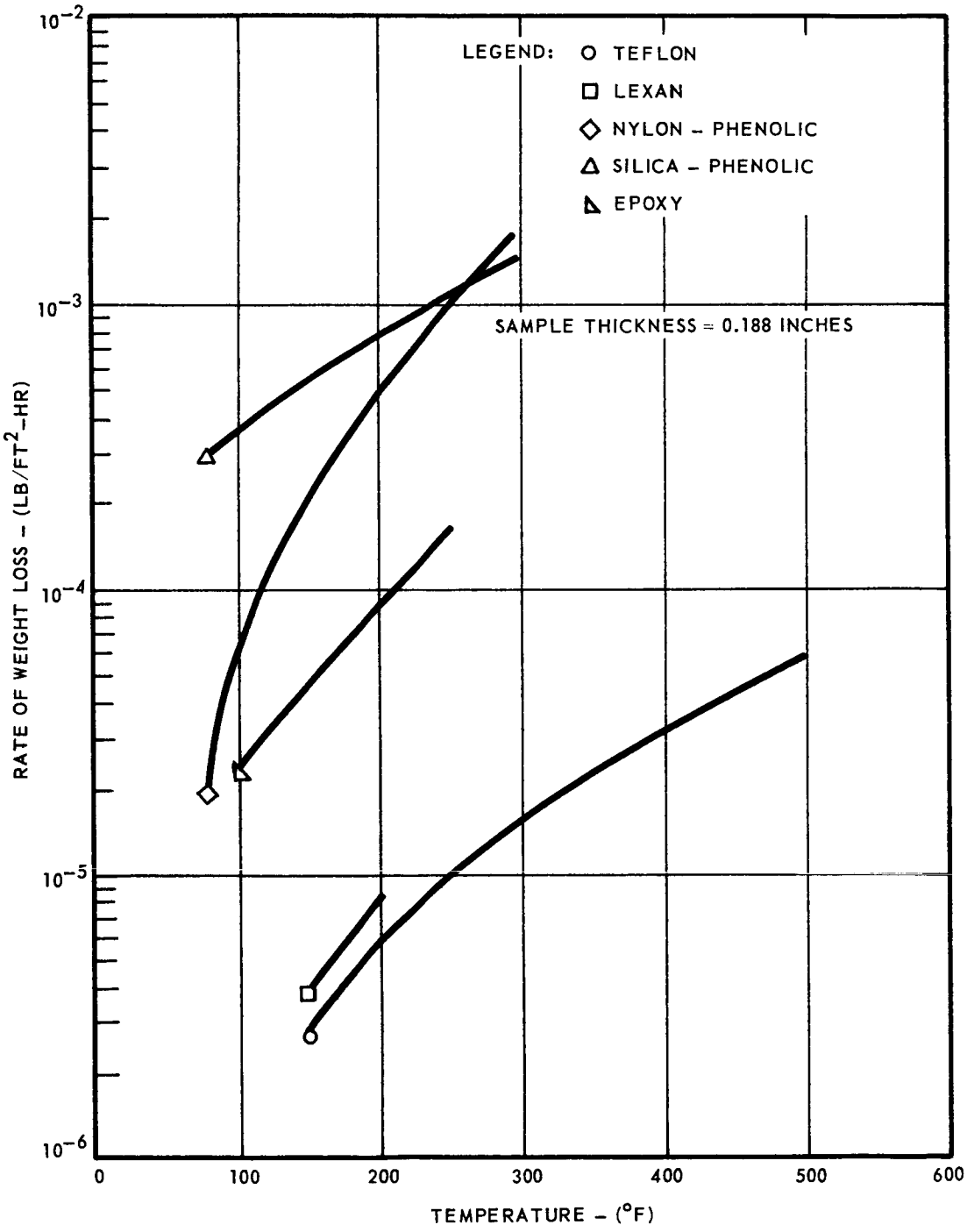

Figure 3-25 Rates of Weight Loss vs Temperature for Organic Materials Tested

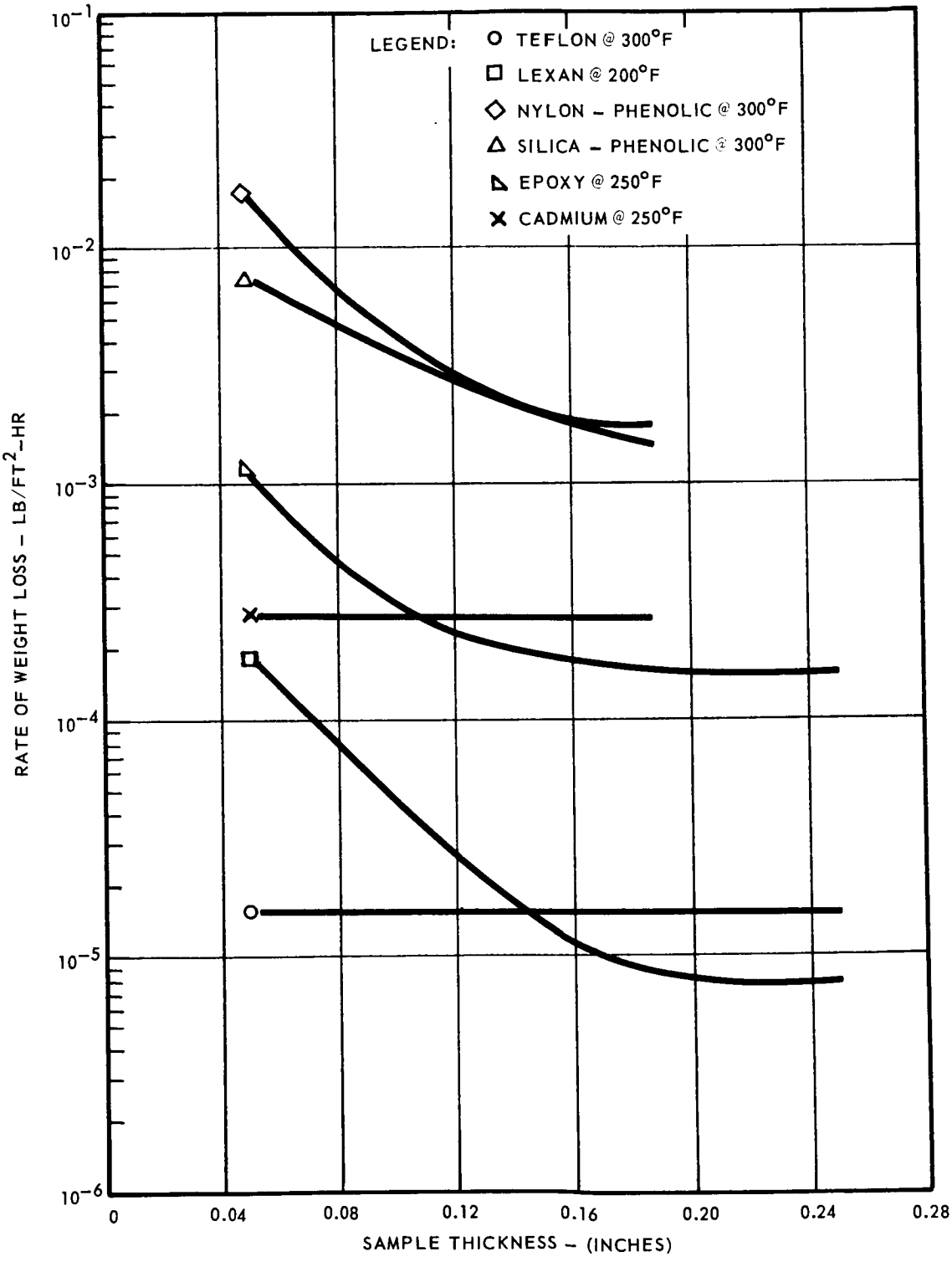

Figure 3-26 Effect of Sample Thickness on Rates of Weight Loss

1. Designations may refer to polymers made from whole classes of monomers. Further subdivision could often be made in terms of the particular monomer or monomers used.

2. The chain length (molecular weight), branching, and cross-linking affect decomposition characteristics.

3. Small amounts of impurities and additives often accelerate decomposition in a vacuum.

4. Plasticizers and mold lubricants are highly detrimental to stability in a vacuum.

5. The particular formulation and curing procedure may have important effects on vacuum stability.

3.7.3.2 Radiation Effects on Polymers

When polymeric materials are exposed to electromagnetic radiation from the sun, the ultraviolet portion of the spectrum affects their properties. Depending on wavelength, damage can occur on the outer layers of the material or deeper. The changes produced in polymers by utraviolet radiation are (1) decomposition (scission) and (2) cross-linking. Decomposition results in breaking of the polymer chains into smaller fragments; cross-linking is a polymerization process. Decomposition is usually accompanied by loss of mechanical strength and elastic deflection. The process is retarded in reduced pressure environment; e.g., space vacuum. Cross-linking, up to a point, increases mechanical strength, but reduces elastic deflection. If continued, it eventually embrittles polymers to the point where surface flaking and fractures occur.

No direct experiments have been reported on irradiation of polymers in the far ultraviolet and X-ray region of the spectrum, and irradiation in a vacuum in the near ultraviolet is reported only in a limited fashion. Reported experiments involving films of commerical phenyl silicone, vinyl chloride, and methyl methacrylate polymers underwent appreciable cross linking on exposure equivalent to a few days in space sunlight; at 160°F, natural rubber underwent considerable cross linking in less than a day. At exposures corresponding to one or two weeks in

space, polyethylene, polyethylene terephthalate (mylar), polyvinyl chloride, and, in some tests, polytetrafluorethylene, lost much of their mechanical strength and flexibility. At exposure equivalent to a month to a year in space, a phenyl methyl silicone (at 200°F) suffered severe loss of bend flexibility.

3.7.3.3 Effects of Combined Environments on Polymers

Data on the effects of vacuum-temperature and vacuum-radiation environments on polymers are just starting to appear. Published data on a combined environment of vacuum-radiation-temperature do not exist (Ref. 3-12 and 3-16 through 3-22).

3.7.3.4 Selection of Polymers for SLRV

Because of the wide variations in behavior which may be expected for any particular polymeric material, and because of the difficulty in determining the reliability of current published test data, if organics are considered for SLRV structural materials, it will be necessary to perform careful experiments with particular formulations and curing procedures, in the environment of interest.

3.8 SUMMARY

The structure of SLRV has been designed for simplicity and high reliability within specified weight and volume limits.

The most critical area of the structure is the aft end where the vehicle is supported on the Surveyor Bus. The tubular structure in this area was designed on the basis of loading conditions rather than practical minimum gauges. Consequently, when the RTG-induced temperature environment is more completely defined, it may be necessary to consider other structural materials for the aft structure, such as titanium.

2024-T4 aluminum alloy was selected as the primary structural material because of its high strength-to-weight ratio and excellent damping properties, in addition to the requirements for reliability and ease of fabrication. There is also a wealth of knowledge on the physical and mechanical properties of aluminum under various environmental conditions. The thermal environment caused by the RTG during the launch phase is

above the normal operating temperature range for aluminum (on the order of 350°F), but the loss in tensile strength for a soak period of 100 hours is 20% or less depending on the alloy temper. The total elapsed time from launch to lunar landing is 66 hours; consequently, the structure can be designed to accommodate this order of strength loss. During operation on the lunar surface, the vehicle structure may experience temperatures as high as 340°F (lunar high noon), but the load levels on the vehicle are so low during the lunar operation that adequate margins of safety can be maintained in the structure, even through the materials will be at a reduced level of tensile strength.

The straps in the floating pivot are stainless steel. This material was selected, rather than aluminum, to minimize the thermal expansion and resultant high deflection in the straps. Analysis showed that high deflections are possible and must be minimized through (1) choice of material, (2) careful manufacturing and installation methods, and (3) locking the fore and aft ends together during the flight and landing phases of the mission.

The design of the struts (between body and tracks) is complicated by uncertainty in the degree of fixity at the frame and track, by nature of the lunar surface, coefficient of friction between track and surface, energy absorbed by the track, etc. The deflection of the strut is sufficient to approach nonlinearity; although, for the range considered, the non-linear effects are small (Ref. 3-23). Since the analysis performed in this area is conservative, the closed hat section design and the strut installation method should be capable of absorbing sufficient energy to keep shock loads in the SLRV within safe limits.

Section 3.7 emphasized the effects of lunar environment on materials in terms of structural applications. Recommendations for the use of specific materials are not universal since each application will have peculiar requirements and should result in a unique selection.

For nonstructural applications, the selection will also be based on the individual requirements because several of the materials, not especially recommended for structural use, find use where particular properties are desirable; e.g., electrical, optical, thermal, etc.

The materials study, is far from exhaustive, but it indicated that correlated investigations at all levels are needed to provide information on the effect of the space environment on the behavior of materials.

Without considering basic research areas, the following is a partial list of recommendations for laboratory measurements for the purpose of data compilation:

1. Vaporization rates and partial pressures of alloys

2. Physical and mechanical properties of alloys subjected to long-term vacuum environment

3. Physical and mechanical properties of polymeric materials subjected to long-term vacuum environment

4. Evaporation and decomposition rates of polymers in a vacuum up to maximum usable temperatures

5. Combined environmental effects on physical and mechanical properties of metals and polymers.

3.9 REFERENCES

3-1 Low Temperature Mechanical Properties--Beryllium, Private Communication from M.I. Jacobson, Lockheed Missiles & Space Company, Palo Alto, California.

3-2 Besserer, C. W., Missile Engineering Handbook, D. Van Nostrand Company, Inc., Princeton, N. J., 1958.

3-3 Beryllium Design Data, Lockheed Missiles and Space Division, Sunnyvale, California.

3-4 Beryllium in Aerospace Structures, The Brush Beryllium Co., Cleveland, Ohio.

3-5 Alcoa Aluminum Handbook, Aluminum Company of America, Pittsburgh, Pennsylvania.

3-6 Alcoa Data Sheets, Cryogenic and Elevated Temperatures, Aluminum Company of America, Pittsburgh, Pennsylvania.

3-7 Stainless Steel Handbook, Allegheny Ludlum Steel Corporation, Pittsburgh 22, Pennsylvania.

3-8 Properties of Ti-6 Al-4V, Titanium Metals Corporation of America, 233 Broadway, New York 7, N. Y.

3-9 Review of Current Data on the Tensile Properties of Metals at Very Low Temperatures, DMIC Report 148, Defense Metals Information Center, Battelle Memorial Institute, Columbus, Ohio, 14 February 1961.

3-10 Tensile Properties of Titanium Alloys at Low Temperatures, DMIC Report 107, Defense Metals Information Center, Battelle Memorial Institute, Columbus, Ohio, 15 January 1959.

REFERENCES (CONT)

3-11 Clauss, T. J. (ed.) Surface Effects on Spacecraft Materials, John Wiley and Sons, Inc., New York, N. Y., 1960.

3-12 Jaffe, L. D. and Rittenhouse, J. B., Behavior of Materials in Space Environments, ARS Journal, March 1962, Vol. 32, pp. 320-346.

3-13 Ham, John L., Investigation of Adhesion and Cohesion of Metals in Ultrahigh Vacuum, Preliminary Unpublished Data, September 1962.

3-14 Ham, John L., Mechanisms of Surface Removal from Metals in Space, Aerospace Eng., 20, 5, page 20; 1961.

3-15 Initial Weight Loss of Plastics in a Vacuum at Temperatures from 80° to 500°F, NASA TND-1329, December 1962.

3-16 Delayed Action, Foam-In-Place Polyurethane for Use in an Aerospace Environment, ASD Technical Report TDR 62-416, March 1963.

3-17 Deterioration of Textile Materials by Ultraviolet Light, WADD Technical Report 60-510, October 1960.

3-18 Investigations of Combined Effects of Radiation and Vacuum and of Radiation and Cryotemperatures on Engineering Materials, Volume I: Radiation - Vacuum Tests, FZK-116-1, Nuclear Aerospace Research Facility, General Dynamics/Forth Worth, Texas, 5 January 1963.

3-19 Ultraviolet Effects on Space Vehicle Operation in Ultrahigh Vacuum Environment, AEDC-TDR-62-17, January 1962.

3-20 Vacuum Considerations of Space Environment, Bell Aerosystems Company, Report No. 8500-920002, 15 January 1962.

3-21 Vacuum Volatility of Organic Resins, WADD Technical Report No. 59-268, September 1959.

3-22 Research on Elastomeric and Compliant Materials for Aerospace Sealants, ASD Technical Report TDR-62-709, August 1962.

REFERENCES (CONT)

3-23 Bishop, K. E., and Drucker, D. C., Large Deflections of Cantilever Beams, Quarterly of Applied Mathematics, October 1945.

3-24 Data Sheet, Crucible Steel Company of America, Issue 2, Pittsburgh, Pennsylvania.

3-25 Effect of Vacuum Environment on the Mechanical Behavior of Materials, Air Force Office of Scientific Research, AFOSR 2139, October 1961.

3-26 Materials Evaluation under High Vacuum and Other Satellite Environmental Conditions, Lockheed Missiles and Space Division, Sunnyvale, California, ASTIA 270279, January 1962.

3-27 Physical Properties of Magnesium and Magnesium Alloys, The Dow Metal Products Company, Midland, Michigan, September 1962.

3-28 Studies of Magnesium Alloys for Use at Moderate Temperatures, RI 6078, Bureau of Mines, 1962.

SECTION 4

DEPLOYMENT

The deployment subsystem is shown in Figures 4-1 and 4-2. The subsystem consists of the lower hinge bracket assembly, the spring-loaded lock assembly, the auxiliary strut support assembly, and the interface structural modifications to the Surveyor spaceframe. This subsystem serves as the means of removing the SLRV from the Surveyor Bus and depositing it on the lunar surface. It also restrains and supports the SLRV on the Surveyor Bus during the launch, transit, and landing phases of the mission.

4.1 DESIGN LOADS

The design load criteria utilized in the stress analysis of the deployment subsystem are discussed in Section 3.1 and are not repeated here.

4.2 DESIGN REQUIREMENTS

The deployment subsystem is designed to meet the following requirements:

1. Restrain and support the SLRV on the Surveyor Bus during the launch, transit, and landing phases of the mission within the allocated stowage volume and specified center of gravity location

2. Integrate the deployment subsystem design into the Surveyor Bus spaceframe and recommend the necessary changes to the Surveyor Bus structure to accomplish the integration

3. Provide auxiliary support for the SLRV struts and tracks during the launch, transit, and landing phases of the mission. This support must be removed prior to deployment of the SLRV to the lunar surface

4. Deploy the SLRV from the Surveyor Bus to the lunar surface

5. Release the tie-downs on the TV camera and antennas which are used to hold these items in the stowed position during flight and landing phases

6. Provide a thermal radiation shield between the SLRV and the Surveyor Bus to minimize the heat transfer between the two vehicles

7. Make provisions for an umbilical connection.

The design shown in Figure 4-1 meets all the above objectives.

4.3 DEPLOYMENT SEQUENCE

The sequence of deployment events which occur after the Surveyor Bus lands on the lunar surface are as follows:

1. Release and eject the auxiliary strut support assembly

2. Release track locks

3. Release the two upper vehicle lock fittings. This causes the vehicle to rotate about the lower support hinge. At a nominal position of 45° between the x-axis of SLRV and the local horizontal, the SLRV will disconnect completely from the Surveyor Bus (see Section 4.6)

4. Concurrent with Item 3, the steerable antenna is released at the tie-down, and permitted to erect partially before the vehicle contacts the lunar surface

5. The umbilical connection is released during the vehicle separation

6. Release the TV camera and whip antennas tie downs permitting these devices to erect.

7. The deployment of the steerable antenna is then completed.

4.4 SUBSYSTEM DESIGN AND ANALYSIS

The deployment subsystem consists of the lower hinge bracket assemblies, the upper spring-loaded lock assemblies, the auxiliary strut support

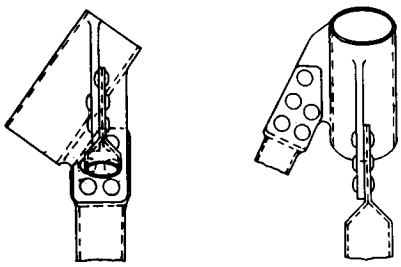

DETAIL C
SCALE 1 = 1

SECT

SECTI

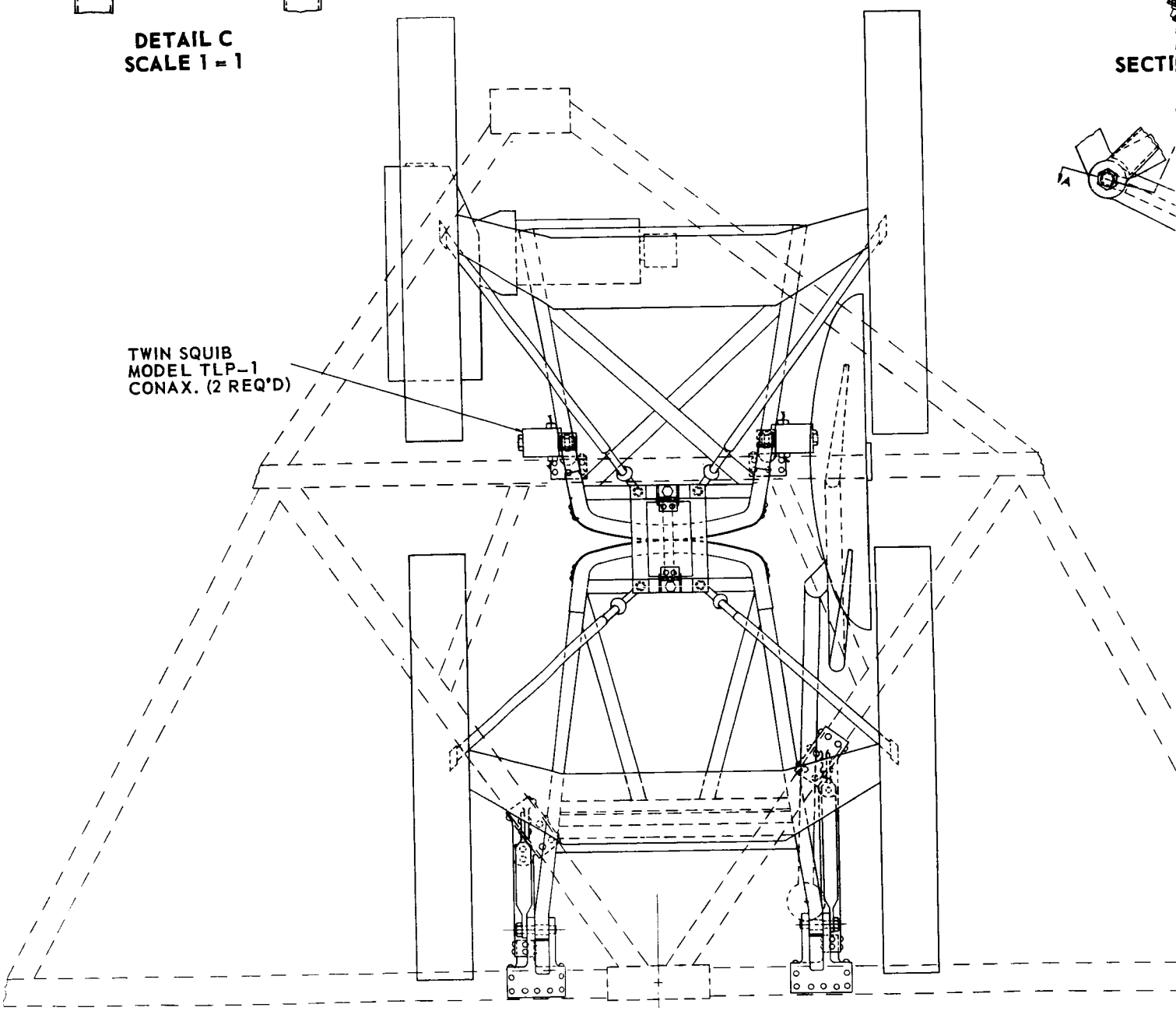

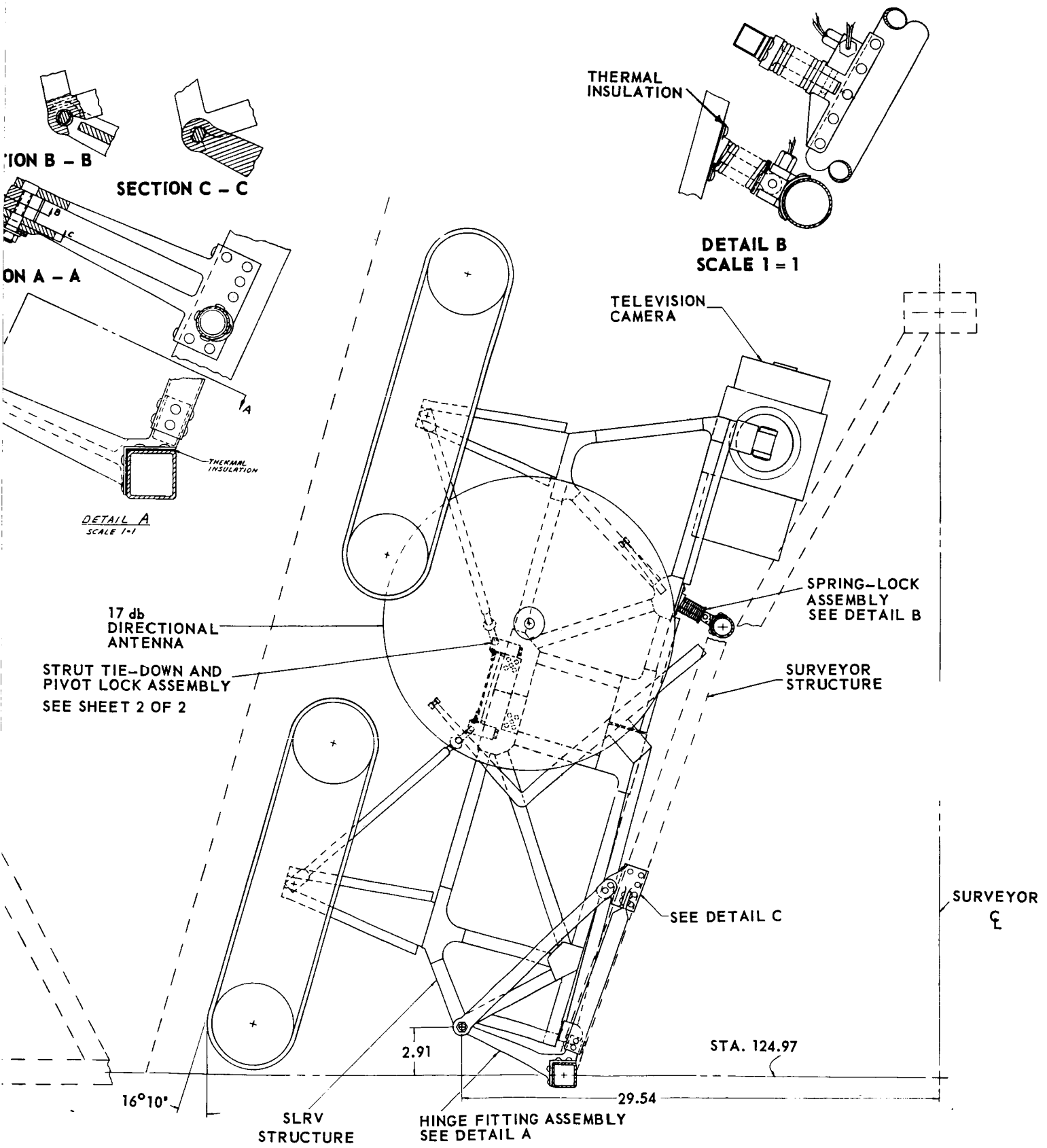

Figure 4-1 SLRV Deployment Subsystem (Sheet 1 of 2)

#2

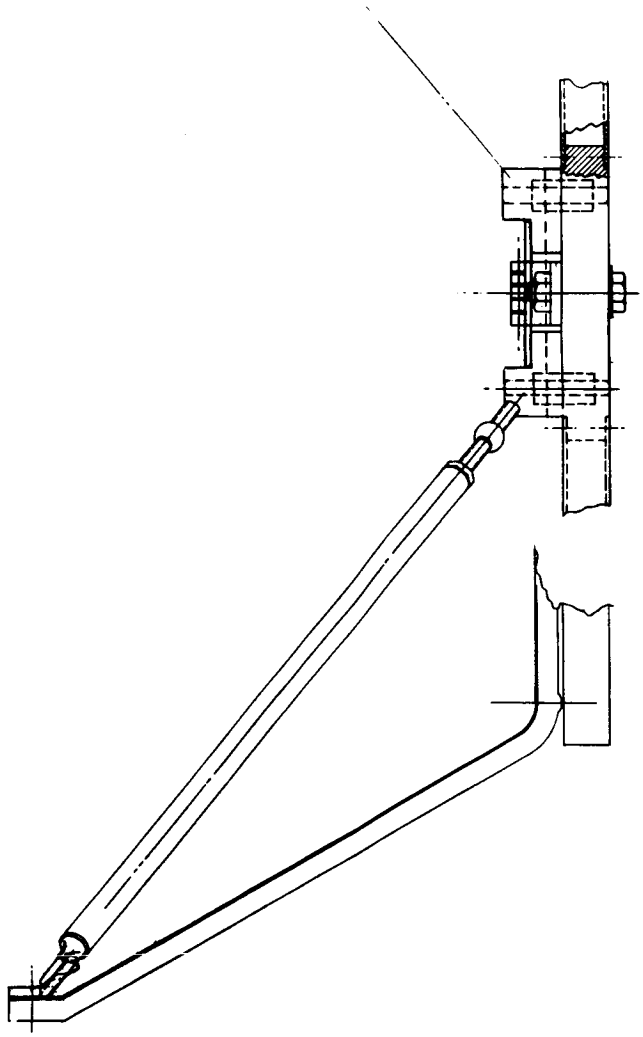

TUBE – AL ALLOY
0.50 Dia x 0.06 WALL x 14.44 LON
(4 REQ'D)

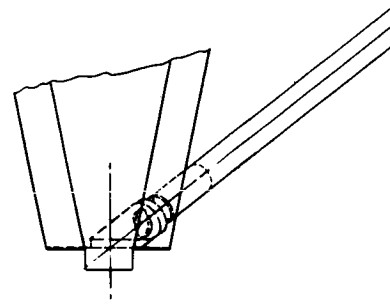

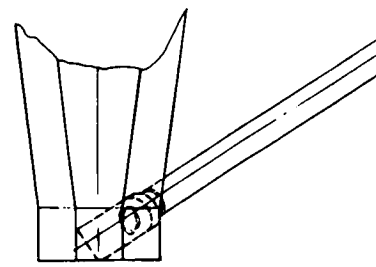

#1

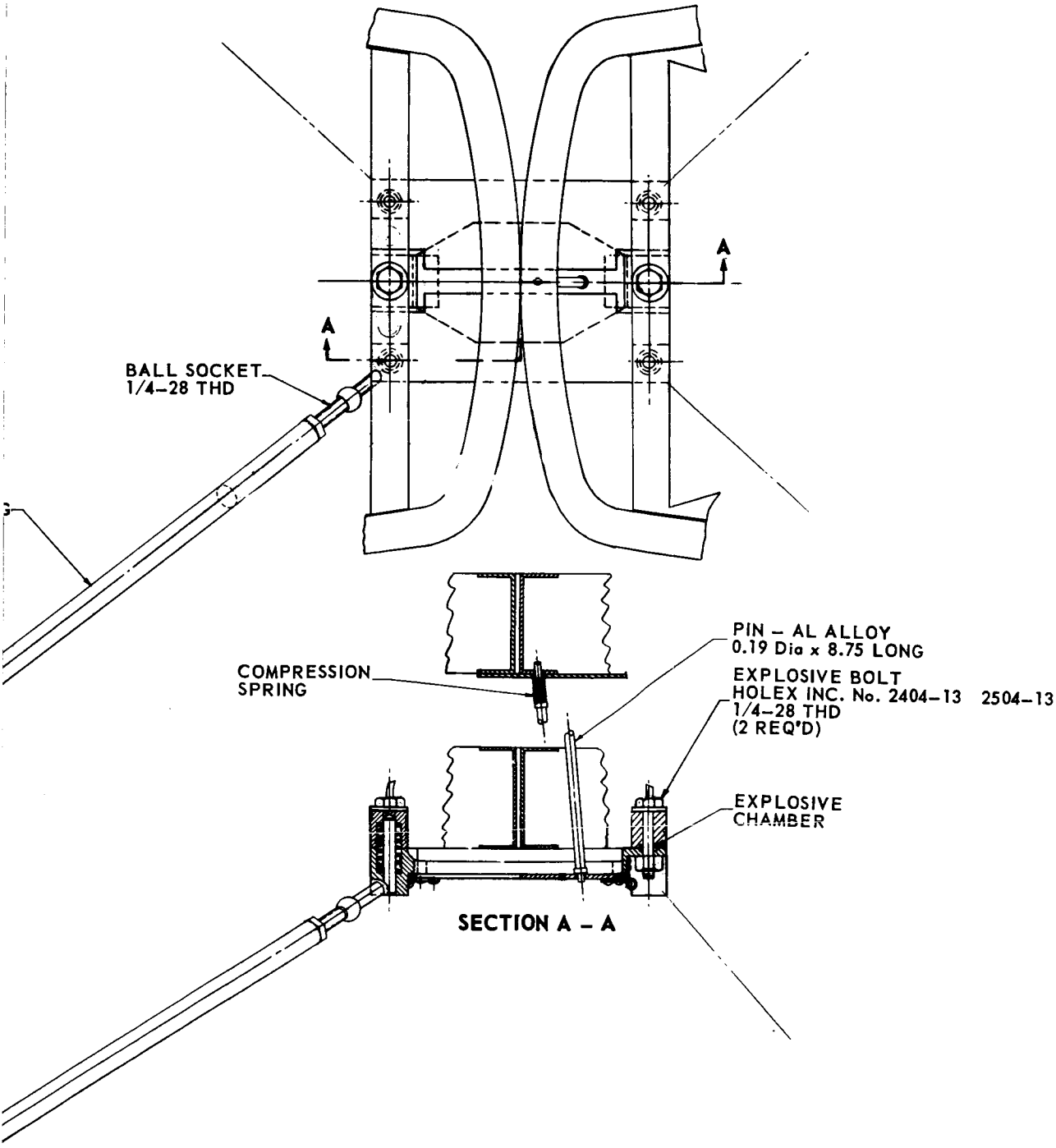

Figure 4-1 SLRV Deployment Subsystem (Sheet 2 of 2)

assembly, and the necessary interface structural modifications to the Surveyor Bus spaceframe. In addition, there are tiedown disconnects for such equipment as the TV camera, antennas, tracks, and umbilical connection.

The lower hinge bracket consists of a two-part assembly. The female fitting is an integral part of the SLRV vehicle structure (see Section 3.4), and a one-piece male fitting is riveted to the Surveyor structure.

The upper spring-loaded lock assembly is a clevis-type fitting. The male fitting is attached to the SLRV structure. The female portion of the fitting is riveted to the upper tube member of the Surveyor spaceframe. The deployment spring is fastened to the female fitting by means of a spring seat attached to the end of the fitting and remains with the Surveyor Bus after SLRV deployment. The male fitting feeds through the center of the deployment spring, which compresses the spring. The assembly is locked by an explosive pin puller. Dual bridge circuits are used in the pin puller for high reliability. The hinge point location on the vehicle is designed to ensure that the vehicle will drop free of the Surveyor Bus and clear a 10-cm obstacle beneath the tracks. The stress analysis of the deployment attach points appears in Section 3.4.

To secure the deployment hardware certain modifications must be made in the Surveyor Bus structure. Additional tubular structure is added for greater rigidity at the hinge point and for better load distribution (see Figure 4-1). In all cases where attachment to the Surveyor is necessary, flange-type fittings and riveted attachments are used to minimize dynamic loading effects.

A strut tiedown assembly alleviates the dynamic loading problem and acts as a stiffening member for transmitting loads between the fore and aft sections of the vehicle (see Figure 4-2). This assembly includes a base plate and four tubular braces. A brace extends from the base plate to each of the four track struts. The base plate consists of two individual pieces, each piece connected to the fore and aft structure sections by means of spring-loaded dowel pins. A fifth spring-loaded pin extends from the base plate to the steering lock. The two plate sections are held rigidly in place by a hinged spanner strap connected to the vehicle structure with two explosive bolts. This design has high reliability in that the failure of one explosive bolt still permits the spanner strap to rotate away and release the connector plate. The tubular braces are joined to the plate through a swivel

joint and to each of the four track struts with a hook designed so that when the connector plate is released, the hooks drop free. The momentum imparted to the connection plate by the spring-loaded dowel pins carry the strut tie-down assembly away from the vehicle in two halves.

A brief analysis was made to determine if the loads imposed in the tubular braces were excessive. It was assumed that the leg of the track strut acted as a cantilever beam:

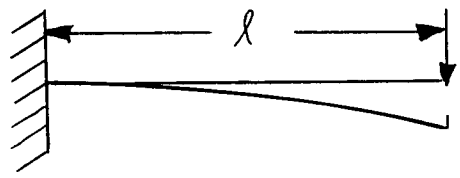

where

ℓ = strut length between vehicle attachment point and hook attachment point

P = inboard load applied by deflecting strut to install tubular brace

δ = deflection of strut

The length (ℓ) is 9.65 in.

It was assumed that the strut would be deflected inboard 2 inches (prestressed) to mate with the tubular brace installation. Therefore, $P = 3\delta EI/\ell^3$.

An average value of the moment of inertia of the strut was calculated to be 5.9×10^{-3} in.^{4}. The force normal to the strut to achieve a 2-inch deflection is:

$$P = \frac{3 \times 2 \times 10 \times 10^6 \times 5.9 \times 10^{-3}}{(9.65)^3} = 394 \text{ lb}$$

When this load is resolved into the angle taken by the tube, P' = 962 lb.

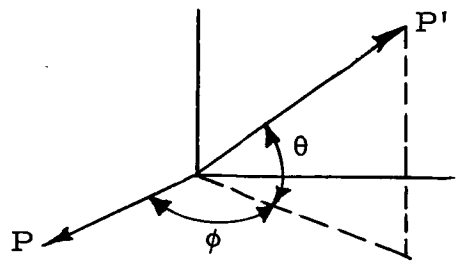

Assuming a 2024 aluminum tube with d = 0.50 in.; wall thickness = 0.20 in.

Area of tube $= 0.0314 \text{ in.}^2$

$$S = \frac{P'}{A} = \frac{962}{0.0314} = 30,600 \text{ psi}$$

Allowable stress = 42,000 psi

$$\text{M.S.} = \frac{42,000}{30,600} - 1 = (1.375 - 1)\,100 = 37.5\%$$

The determination of the natural frequency of the strut with and without the auxiliary strut support is given in Section 4.5. The tiedown assembly discussed here provides support for the strut, but the torsional vibration analysis indicates that further support may have to be provided for the track during the flight phase.

Provisions are made for attachment to the structure of the tiedown disconnects (each requiring an explosive device for actuation) for the TV camera, antenna, and umbilical connector. Detailed descriptions of these mechanisms appear in Section 5.

4.5 STRUT VIBRATIONAL MODES

The track mass at the end of the strut results in inherently low natural frequencies; consequencly, the following analysis was conducted both to verify this fact and to show how the addition of the auxiliary strut support increases the natural frequency.

Approvimate methods are used to find the natural frequencies of the struts in the fundamental flexural and torsional modes. One end of the strut is fixed on the vehicle while the other end carries the weight of the tracks. The cross-sectional area and moment of inertia are assumed to be varying linearly along the length of the strut (Figure 4-3).

4.5.1 Flexural Mode

According to Rayleigh's principle, the fundamental frequency can be obtained by equating the maximum kinetic energy and the maximum potential energy of the system; i.e.,

$$K.E._{max} = P.E._{max} \tag{4-1}$$

Assuming a parabolic variation of the motion, it follows that

$$\begin{aligned} y &= \bar{y}\,(x/\ell)^2 \sin pt \\ \dot{y} &= p\bar{y}\,(x/\ell)^2 \cos pt \\ \frac{d^2g}{dx^2} &= 2\,(\bar{y}/\ell^2) \sin pt \end{aligned} \tag{4-2}$$

where p is the frequency and $\bar{y}$ is the amplitude at $x = \ell$. The kinetic energy consists of two parts. The first part is due to the motion of the strut, and the second part to the motion of the track. Thus,

$$K.E. = \int_0^\ell \frac{1}{2}\, m\, \dot{y}^2\, dx + \frac{1}{2}\frac{W}{g}\, \dot{y}_\ell^2 \tag{4-3}$$

where $\dot{y} = dy/dt$, W is the weight of the track, $\dot{y}_\ell$ is $\dot{y}$ at $x = \ell$, and m is the mass of the beam per unit length. The potential energy of the beam is

$$P.E. = \frac{1}{2}\int_0^\ell EI\left(\frac{d^2y}{dx^2}\right)^2 dx. \tag{4-4}$$

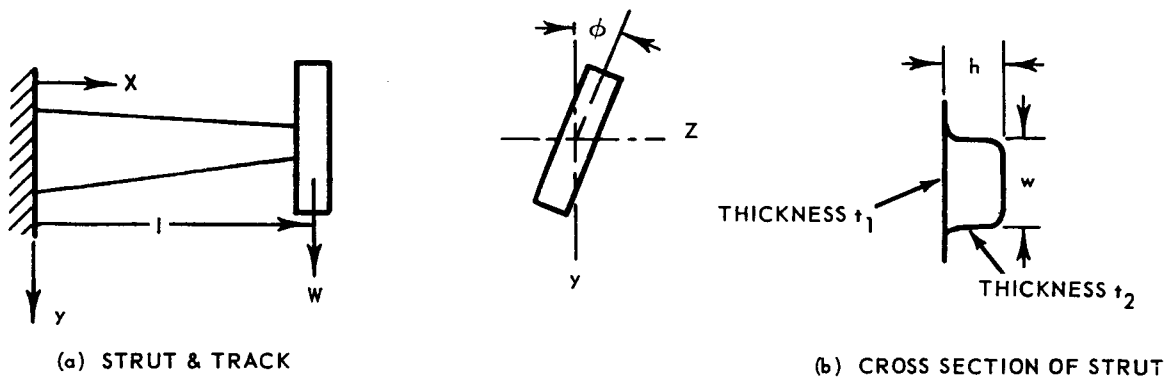

Figure 4-3 Strut as a Vibration Body

As functions of x, the mass and moment of inertia are respectively

$$m = \frac{\gamma}{g}(A_o - \frac{x}{\ell}\Delta A) \tag{4-5}$$

$$I = I_o - \frac{x}{\ell}\Delta I \tag{4-6}$$

where $\Delta A = A_o - A_\ell$, $\Delta I = I_o - I_\ell$, subscript o refers to the end section, subscript ℓ refers to the tip section, and γ is the specific weight.

Substituting Equation (4-2) and (4-5) into Equation (4-3) and taking the maximum results in

$$K.E._{max} = \frac{p^2 \bar{y}^2}{2g}\left[W + \gamma\ell\left(\frac{Ao}{5} - \frac{\Delta A}{6}\right)\right] . \tag{4-7}$$

Substituting Equation (4-6) and (4-2) into Equation (4-4) and taking the maximum results in

$$P.E.\ max. = \frac{2E\bar{y}^2}{\ell^3}\left(I_o - \frac{\Delta I}{2}\right). \tag{4-8}$$

Equating Equation (4-7) and (4-8) yields

$$p^2 = \frac{4Eg\left(I_o - D\frac{\Delta I}{2}\right.}{\ell^3\left[W + \gamma\ell\left(\frac{Ao}{5} - \frac{\Delta A}{6}\right)\right]} . \tag{4-9}$$

For an aluminum strut with $I_o = 59 \times 10^{-4}$ in.^{4}, $I_\ell = 22 \times 10^{-4}$ in.^{4}, $\ell = 9.65$ in., $W = 4.4$ lb, $\gamma = 0.1$ lb/in.^{3}, $E = 10^7$ psi, $A_o = 0.229$ in.^{2}, and $A_\ell = 0.125$ in.^{2}. Equation (4-9) gives

$$p = 124 \text{ rad/sec} = 19.7 \text{ cps}. \tag{4-10}$$

While the LRV is stowed in the Surveyor, the struts behave like cantilever beams with a load concentrated at the free end. This load is the weight of the track. It has been shown that the first mode natural

frequency of this cantilevered strut-leg due to bending is 19 cps. In order to increase this value, the strut-leg will be stiffened during flight by a temporary structure which will be ejected before LRV deployment. This structure will connect to the strut-leg at a point near the track. If the system shown schematically in Figure 4-4 represents the strut-leg of length L, loaded at the free end by the mass of the track (m), and supported rigidly with respect to vertical displacement at the point $x = \ell$, then the first mode natural frequency is

$$f_n = \frac{\sqrt{3EI/mL}}{2\pi(L - \ell)} \quad . \tag{4-11}$$

The weight of the beam is considered to be negligible compared to the weight of the track. This equation cannot be used directly, because the beam has a variable moment of inertia and the derivation of the equation assumes a constant moment of inertia. But the important point is that f_n is inversely proportional to $(L - \ell)$. Now if $\ell = 0$, the system represents the cantilevered strut unsupported except at $x = 0$.

According to Equation (4-10), the natural frequency for this case is 19 cps. Since

$$\frac{(f_n)_{\ell_2}}{(f_n)_{\ell_1}} = \frac{(L - \ell_1)}{(L - \ell_2)} , \tag{4-12}$$

it follows that

$$f_n = \frac{19L}{(L - \ell)} \quad . \tag{4-13}$$

Now if $L = 9.65$ in. and $\ell = 8.65$ in., then

$$f_n = 183 \text{ cps} \tag{4-14}$$

The system analyzed here differs from the actual system in two ways. First, the support at $x = \ell$ is not rigid. This effect would lower f_n. Second, the support at $x = 0$ is not pinned, but is nearly "built-in". This difference would increase the natural frequency of the actual system.

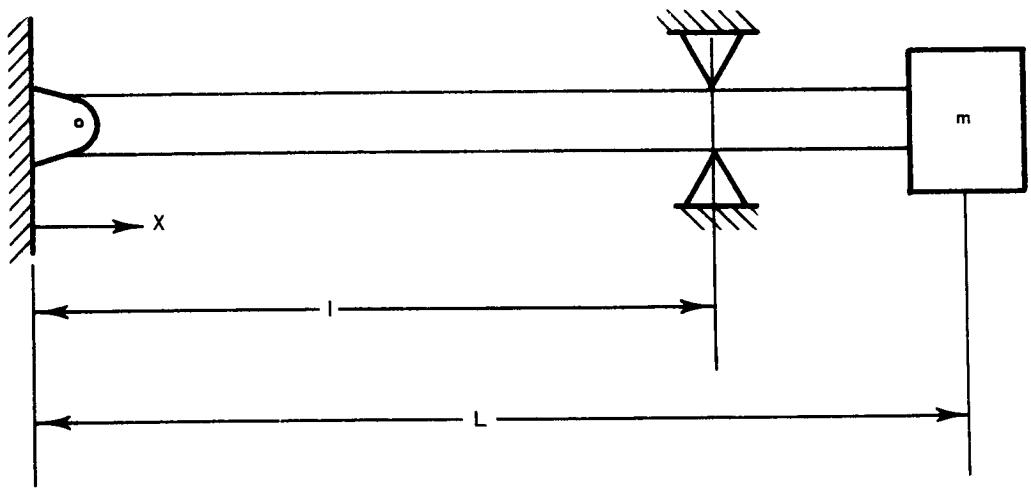

Figure 4-4 Schematic Diagram of Strut

It is concluded that the temporary support structure (if it is reasonably stiff) will increase the natural frequency above the goal value of 100 cps.

4.5.2 Torsional Mode

The equation governing the torsional vibration is

$$I_P \ddot{\theta} + k\phi = 0 \tag{4-15}$$

where I_P is the mass moment of inertia of the wheel-track combination with respect to the axis of twist and k is the torque required to twist the track a unit angle of ϕ. Thus, the natural frequency of twist is

$$p_t = \sqrt{\frac{k}{I_P}} \ . \tag{4-16}$$

For a hollow shaft with a variable cross section, the angle of twist of a length dx when a torque T is applied is expressed by[1]

$$d\phi = \frac{T}{4GA_1^2 \int \frac{dw}{t}} \tag{4-17}$$

where G is the shear modulus and A_2 is the cross-sectional area.

For the cross section shown in Figure 4-3(b) and if the edges are neglected, it follows that

$$\int \frac{dw}{t} = \frac{2h}{t_2} + \frac{w}{t_1} + \frac{w}{t_2} = \frac{2t_1 + w\,(t_1 + t_2)}{t_1 + t_2} \tag{4-18}$$

and

$$A_1 = w\,h$$

$$w = w_o - \frac{x}{\ell}\,(w_o - w_\ell) = w_o - \frac{x}{L}\,\Delta w \tag{4-19}$$

[1] See R. J. Roark, "Formulas for Stress and Strain", p. 170, Table IX, No. 10.

where

$$w_o = w \text{ at } x = o, \text{ and } w\ell = w \text{ at } x = \ell \tag{4-20}$$

Now

$$\phi = \int d\phi = \frac{T}{4G} \int \frac{dx}{A_1^2 \oint \frac{dw}{t}} \tag{4-21}$$

Substituting (4-18), (4-19), and (4-20) into (4-21) and integrating results in

$$\phi = \frac{T}{4Gh^2 t_1 t_2} \left[\frac{2t_1 h \ell}{w_o w_\ell} + \frac{\ell(t_1 + t_2)}{\Delta w} \log \frac{w_o}{w_\ell} \right]. \tag{4-22}$$

Since k is defined as the torque T to make an angle $\phi = 1$ rad,

$$k = 4Gh^2 t_1 t_2 \left(\frac{2t_1 h\ell}{w_o w_\ell} + \frac{\ell(t_1 + t_2)}{\Delta w} \log \frac{w_o}{w\ell} \right). \tag{4-23}$$

For $G = 4 \times 10^6$ psi, $t_1 = 0.02$ in., $t_2 = 0.03$ in., $h = 0.375$ in., $\ell = 9.65$ in., $w_o = 2.75$ in., and $w_\ell = 0.75$ in., Equation (4-23) yields

$$k = 3450 \text{ in.-lb/rad} \tag{4-24}$$

Assuming that the masses of the track are concentrated at the two wheel centers,

then

$$I_P = 2m_1 d_1^2 \tag{4-25}$$

where m_1 is half of the whole mass of the track and d_1 is the distance between the strut and the wheel center. Using $m_1 = 2.1$ lb and $d_1 = 9$ in.,

it follows that

$$I_P = 0.88 \text{ slug-in.}^2 \tag{4-26}$$

Substituting the above values for I_P and k into Equation (4-16) reveals that

$$p_t = 62.6 \text{ rad/sec} = 9.97 \text{ cps.}$$

4.6 DEPLOYMENT DYNAMICS

Two dynamical problems are posed by the landing of the lunar roving vehicle on the lunar surface during deployment: (1) how large is the impact force? , and (2) is there any possibility of overturning during landing? In considering these two problems, the dynamics (angular and linear velocity) of landing is studied first.

The lunar roving vehicle is connected to the surveyor by two hinges at the bottom and two spring-loaded locks at the top (Figure 4-5). The springs are precompressed to store the energy for pushing the vehicle off the Surveyor. The hinges are so constructed that at a certain rotational position, the vehicle will unlatch from the Surveyor pivot axis. Since the construction of the vehicle is nearly symmetrical, motion can be approximated as two-dimensional. To further simplify the analysis, the motion is separated into three steps: (1) the spring energy pushes the vehicle around the hinged joint from the stowed position up to the vertical position such that the cg (center of gravity) is aligned with the local vertical, (2) the vehicle rotates about the hinged joints from the vertical position to the position where unlatching occurs, and (3) after unlatching, the vehicle drops to the ground with a plane motion (translation plus rotation). Details are given below.

4.6.1 Spring Action on the Vehicle

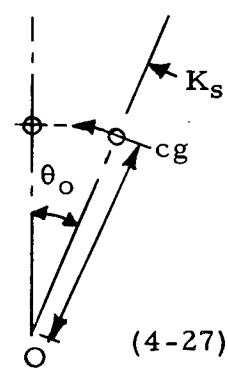

Due to the released spring energy K_s, the vehicle is pushed up to the vertical position; i.e., its cg is aligned with the local vertical. If the friction loss is neglected and the work energy principle is used, it follows that

$$K_s = m g_m x_c (1 - \cos \theta_o) + \frac{1}{2} I_o \dot{\theta}_o^2 \tag{4-27}$$

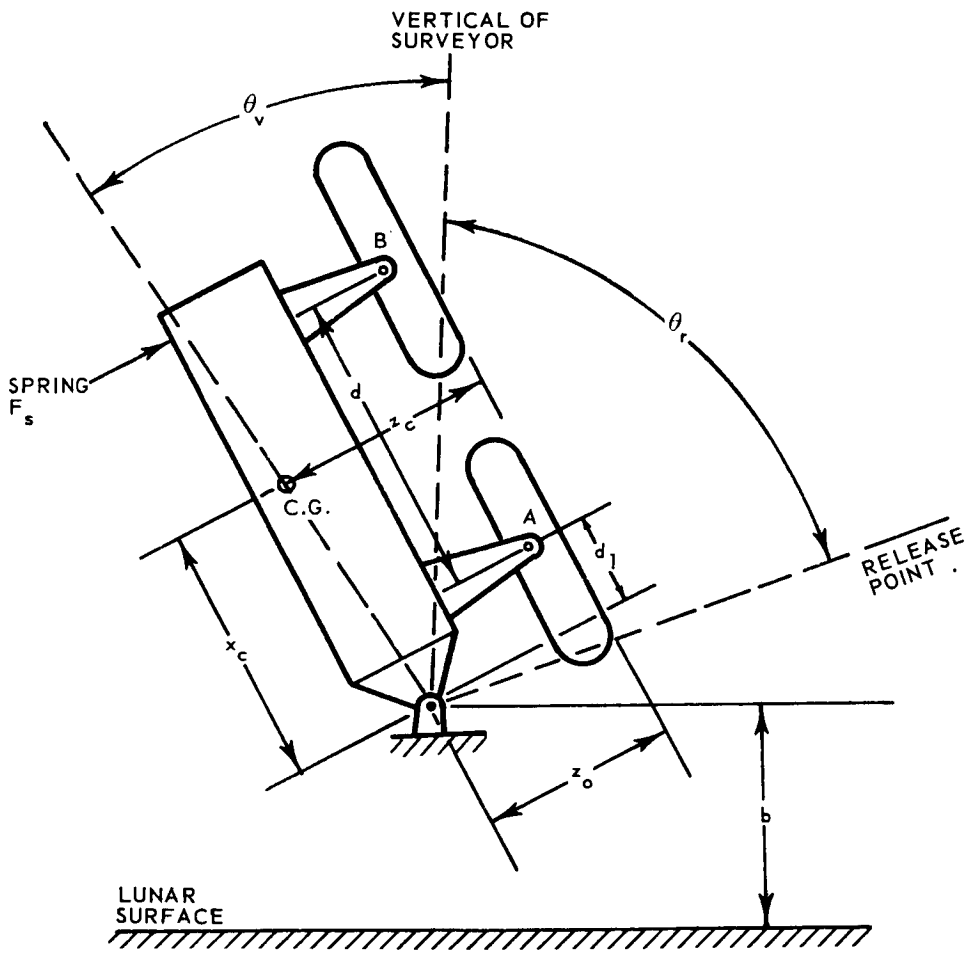

Figure 4-5 SLRV in Stowed Position

where

K_s $= \frac{1}{2} k \delta^2$ = stored energy of the spring

m = mass

g_m = lunar gravity

x_c = distance of the cg from the hinge point

I_o = mass moment of inertia about the hinge

$\dot{\theta}_o$ = angular velocity when the vehicle reaches the top.

Considering that the Surveyor may land on a slope, the lunar roving vehicle deployment can be either uphill, downhill, or sidehill. Maximum slope is assumed to be 15°. Among all these cases, the uphill condition requires maximum spring energy. Hence, the spring energy shall be set to just push the vehicle in the maximum uphill position (15°). If the initial angle (θ_o) for the 15° uphill position is $\overline{\theta}_o$ and $\dot{\overline{\theta}}_o = 0$ then the spring energy required is

$$\overline{K_s} = mg_m x_c (1 - \cos \overline{\theta}_o) \tag{4-28}$$

As $m = 3.1$ slugs, $g_m = 5.37$ ft/sec^2, $x_c = 23.2$ in., and $\overline{\theta}_o = 36^o$, Equation (4-28) gives

$$\overline{K_s} = 73.7 \text{ in.-lb.} \tag{4-29}$$

For any other θ_o values (sidehill or downhill), the initial angular velocity $\dot{\theta}_o$ is obtained by solving (4-27) and (4-28) to give

$$\dot{\theta}_o^{\,2} = \frac{2}{I_o} mg_m x_c (\cos \theta_o - \cos \overline{\theta}_o) \tag{4-30}$$

4.6.2 Pure Rotation About the Hinge

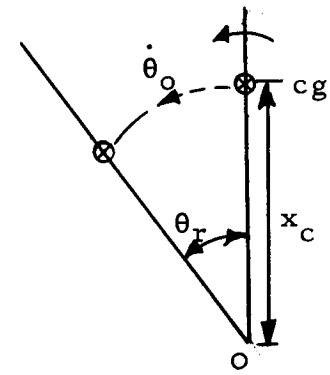

Assuming that at $\theta = 0$ the cg coincides with the centerline (local vertical) and the vehicle has an angular velocity $\dot{\theta}_o$ about the hinge, from the energy principle, it follows that at any position θ

$$\frac{1}{2} I_o \dot{\theta}_o^{\,2} + mg_m x_c = \frac{1}{2} I_o \dot{\theta}^2 + mg_m x_c \cos\theta. \qquad (4\text{-}31)$$

Thus

$$\dot{\theta}^2 = \frac{2}{I_o} mg_m x_c (1 - \cos\theta) + \dot{\theta}_o^{\,2}$$

or

$$\dot{\theta} = \sqrt{\frac{2}{I_o} mg_m x_c (1 - \cos\theta) + \dot{\theta}_o^{\,2}}. \qquad (4\text{-}32)$$

At $\theta = \theta_r$

$$\dot{\theta}_r = \sqrt{\frac{2}{I_o} mg_m x_c (1 - \cos\theta_r) = \dot{\theta}_o^{\,2}}. \qquad (4\text{-}33)$$

4.6.3 Plane Motion After Unlatching

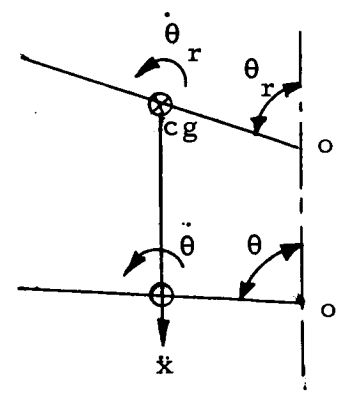

Assuming unlatching occurs at $\theta = \theta_r$, the vehicle will have plane motion. The plane motion can be represented by a rotation about the cg ($\dot{\theta}$) and a translation of cg as ($\dot{x}$). From the conservation of energy principle

$$mg_m x + \frac{1}{2} I_o \dot{\theta}_r^2 = \frac{1}{2} m\dot{x}^2 + \frac{1}{2} I_c \dot{\theta}^2 \qquad (4\text{-}34)$$

where the new quantity I_c is the mass moment of inertia about the cg.

Also, the translation of the cg is given by

$$\ddot{x} = g_m. \tag{4-35}$$

When

$$t = o,\ x = o,\ \dot{x} = \dot{x}_r,\ \text{and}\ \theta = \theta_r \tag{4-36}$$

Equation (4-35) gives

$$\int_{x_r}^{\dot{x}} d\dot{x} = \int_o^t g_m\, dt.$$

Thus

$$\dot{x} = g_m\, t + \dot{x}_r. \tag{4-37}$$

But it is known that at $t = 0$, $\theta = \theta_r$;

thus,

$$\dot{x}_r = x_c \sin \theta_r \dot{\theta}_r. \tag{4-38}$$

Further integration of (4-37) gives

$$x = \frac{g_m}{2} t^2 + \dot{x}_r\, t. \tag{4-39}$$

Substituting (4-37) and (4-13) into (4-34) the following expression is obtained:

$$\dot{\theta}^2 = \frac{I_o}{I_c} \dot{\theta}_r^2 - \frac{m}{I_c} \dot{x}_r^2$$

or

$$\dot{\theta} = \sqrt{\frac{I_o}{I_c} + \dot{\theta}_r^2 - \frac{m}{I_c} \dot{x}_r^2} \tag{4-40}$$

and

$$\theta = \int_{o}^{t} \sqrt{\frac{I_o}{I_c} \dot{\theta}_r^2 - \frac{m}{I_c} \dot{x}_r^2} \, dt + \theta_r .$$

Therefore

$$\theta = t \sqrt{\frac{I_o}{I_c} \dot{\theta}_r^2 - \frac{m}{I_c} \dot{x}_r^2} + \theta_r . \qquad (4\text{-}41)$$

Thus, for any dropping distance x, the instantaneous linear velocity and angular velocity can be obtained from Equations (4-37) and (4-40, and the angle of the vehicle with respect to the local vertical can be found from Equation (4-41). Figure 4-5 shows a sketch of the lunar roving vehicle in the stowed position, and Figure 4-6 shows the geometry of the vehicle at deployment position for $\overline{\theta}_r = 60^o$ when the Surveyor is landed on a 15° slope, either uphill or downhill.

Calculations are made for the following data:

$I_c = 1.248$ slug-ft^2

$x_c = 23.2$ in.

$I_o = (I_c + \frac{mx_c^2}{144})$ slug-ft^2

$\theta_v = 21^o$ (Figure 4-5)

$\overline{\theta}_r = 60^o$

$m = 3.1$ slugs

$g_m = 5.37$ ft/sec^2

ground slope $\theta_s = 15.$

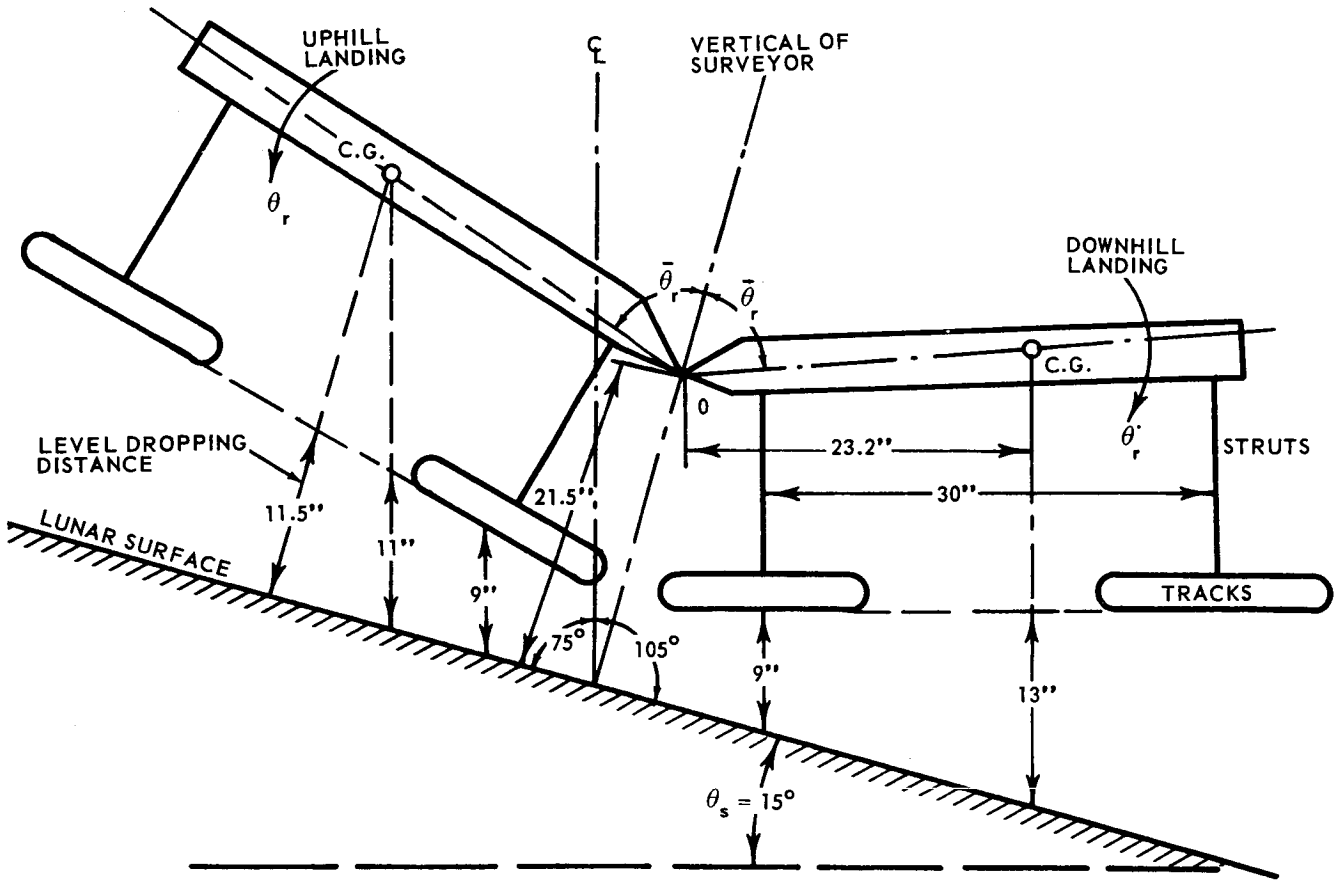

Figure 4-6 Deployment on 15° Slope, Uphill or Downhill

The results are shown in Figures 4-7 and 4-8. Given any dropping distance x within the plotted range, the orientation of the vehicle (θ), the angular velocity ($\dot{\theta}$), and the linear velocity ($\dot{x}$) can be found from these illustrations.

From the results obtained above, further study of the impact and overturning problems can be made.

4.6.4 Impact During Deployment Landing

The following assumptions are made:

1. Collision is elastic (which is highly conservative).

2. Difference of potential energy before and after impact is negligible.

3. Impulse of any finite external force is negligible.

Two quantities are defined:

1. Linear impulse

$$\hat{F} = \int_0^{\Delta t} F \, dt \tag{4-42}$$

2. Angular impulse

$$\hat{M} = \int_0^{\Delta t} M \, dt. \tag{4-43}$$

The symbols $\dot{\theta}$ and $\dot{x}$ refer to the state before impact, while $\dot{\theta}'$ and $\dot{x}'$ refer to the state after impact. The positive signs are for the arrows shown in the sketch. There are three unknowns for which three equations are needed.

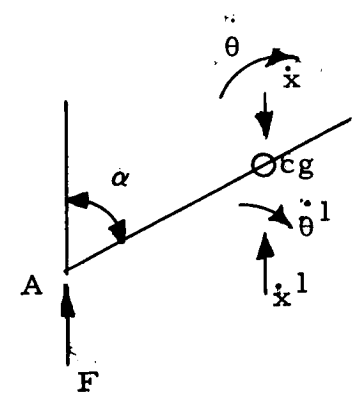

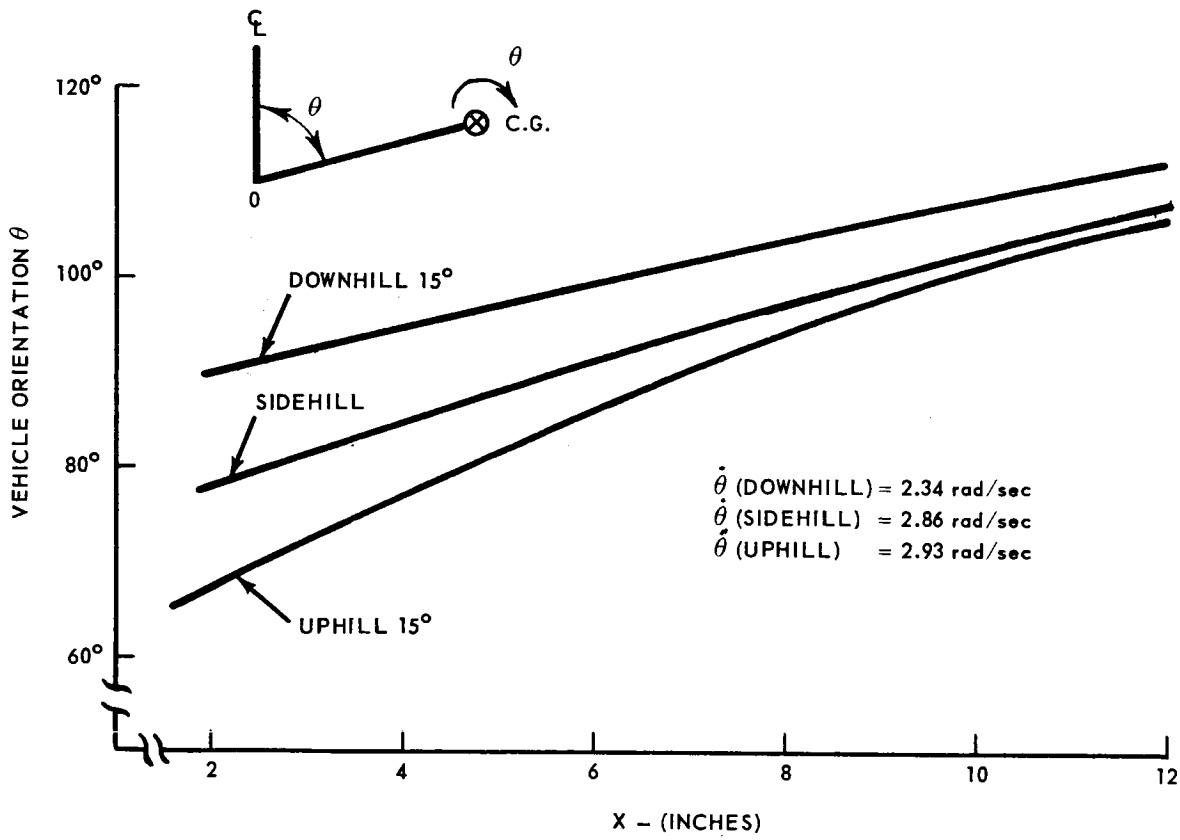

Figure 4-7 Orientation vs Vehicle Dropping Distance

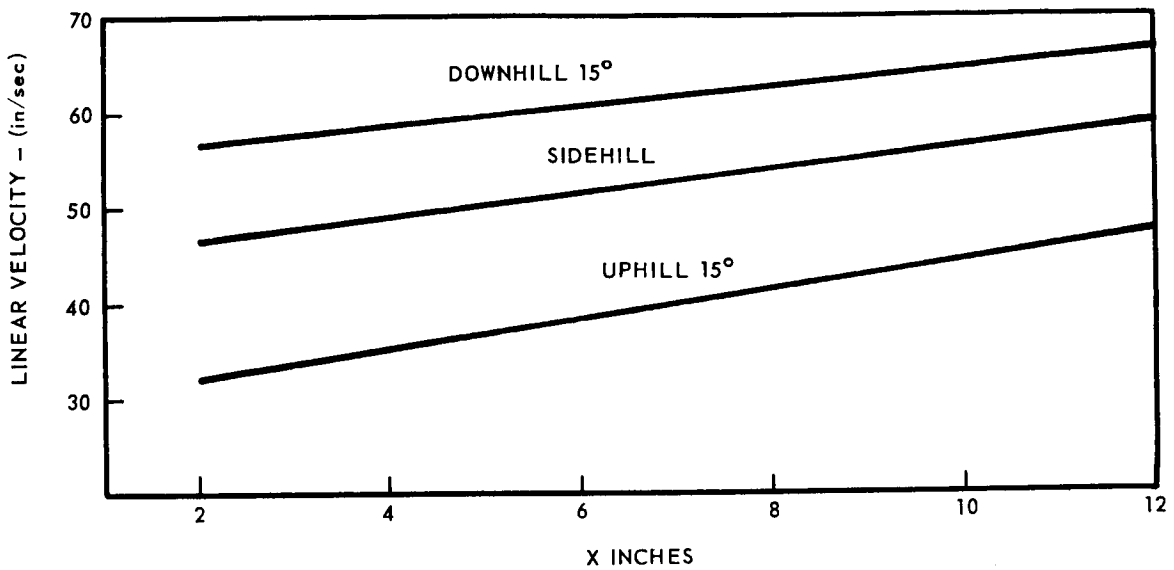

Figure 4-8 Linear Velocity vs Dropping Distance

From conservation of energy, the following expressions are derived:

$$\frac{1}{2} m\dot{x}^2 + \frac{1}{2} I_c \dot{\theta}^2 = \frac{1}{2} m\dot{x}'^2 + \frac{1}{2} I_c \dot{\theta}'^2. \tag{4-44}$$

From the linear impulse momentum principle

$$\hat{F} = m (\dot{x} + \dot{x}') \tag{4-45}$$

and from the angular impulse momentum principle

$$\hat{F} x_c \sin \alpha = I_c (\dot{\theta}' - \dot{\theta}). \tag{4-46}$$

Solving these equations results in the following expressions:

$$\dot{x}' = \frac{1}{I_c + m x_c^2 \sin^2 \alpha} \left[(I_c - m x_c^2 \sin^2 \alpha) \dot{x} - (2 I_c x_c \sin \alpha) \dot{\theta} \right] \tag{4-47}$$

$$\dot{\theta}' = \frac{1}{I_c + m x_c^2 \sin^2 \alpha} \left[2 m x_c \sin \alpha \dot{x} + (I_c - m x_c^2 \sin^2 \alpha) \dot{\theta} \right] \tag{4-48}$$

$$\hat{F} = m (\dot{x}' + \dot{x}) = \frac{2 I_c m}{I_c + m x_c \sin^2 \alpha} (\dot{x} - x_c \sin \alpha) \dot{\theta}. \tag{4-49}$$

Aircraft landing data[1] shows that the impulse is usually of an irregular parabolic shape with an impact time ranging up to 0.08 sec. Therefore, it is reasonable to assume a triangular shape for the impulse and to derive the impact force F for any arbitrary interval Δt.

Thus

$$\hat{F} = \int_0^{\Delta t} F \, dt = \frac{1}{2} F_m \Delta t$$

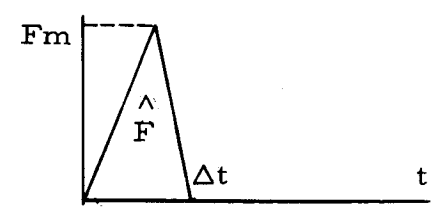

[1] See Harris and Crede, "Shock and Vibration Handbook", p. 9.1-9.11; also Biot and Bisplinghoff, "Dynamic Loads in Airplane Structures During Landing", NACA Wartime Report No. W-92, October 1944.

or

$$F_m = \frac{2\hat{F}}{\Delta t} \tag{4-50}$$

Substituting (4-49) into (4-50)

$$F_m = \frac{4 I_c m}{\Delta t (I_c + m x_c^2 \sin^2 \theta)} (\dot{x} - x_c \sin \theta)\dot{\theta} \tag{4-51}$$

Using the previous data, values of peak, impact force and velocities immediately after impact are obtained. Results are shown in Figures 4-9, 4-10, and 4-11. Since energy loss always accompanies impact, and since the actual vehicle is an elastic body rather than a rigid body, the actual impact force is much less than the calculated values. Figure 4-9 gives the impact to be 11 g for a 0.05-sec duration.

4.6.5 Landing Stability

The stability (overturning tendency) during SLRV landing can be examined from the results obtained in the above paragraphs. From the relationship between vehicle orientation θ and the dropping distance x (Figure 4-7) and from the geometry of deployment (Figure 4-6), the actual dropping distance and the orientation at impact can be determined. For the release angle chosen ($\overline{\theta}_r = 60^\circ$), the initial impact contact is always made at the front tracks. Table 4-1 shows the maximum and minimum possible dropping distances and corresponding vehicle orientation angle θ. The minimum distance is obtained if there is a 10-cm obstacle on the lunar surface.

TABLE 4-1

MAXIMUM AND MINIMUM DROPPING DISTANCE AND VEHICLE ORIENTATION ON LANDING OF THE ROVING VEHICLE

Front End Hit	Maximum		Minimum	
	x (in.)	θ	x (in.)	θ
Uphill 15°	7	88°	4.5	78.5°
Downhill 15°	11	110°	8.5	104.7°
Sidehill 15°	9.5	101°	6.5	93°

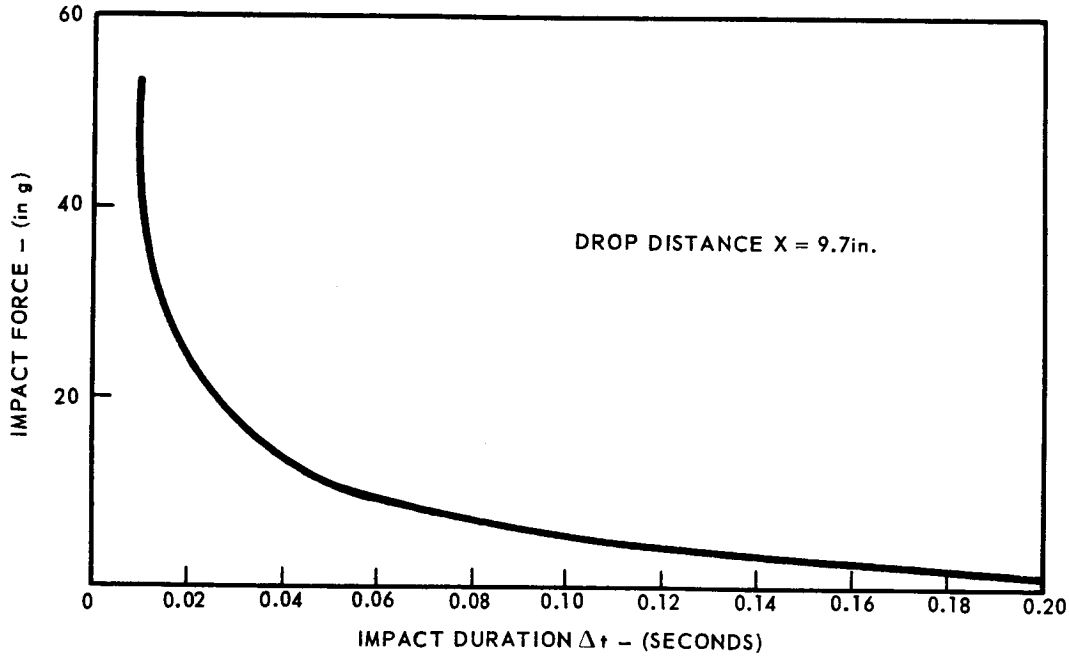

Figure 4-9 Impact Force During Lunar Landing of Roving Vehicle

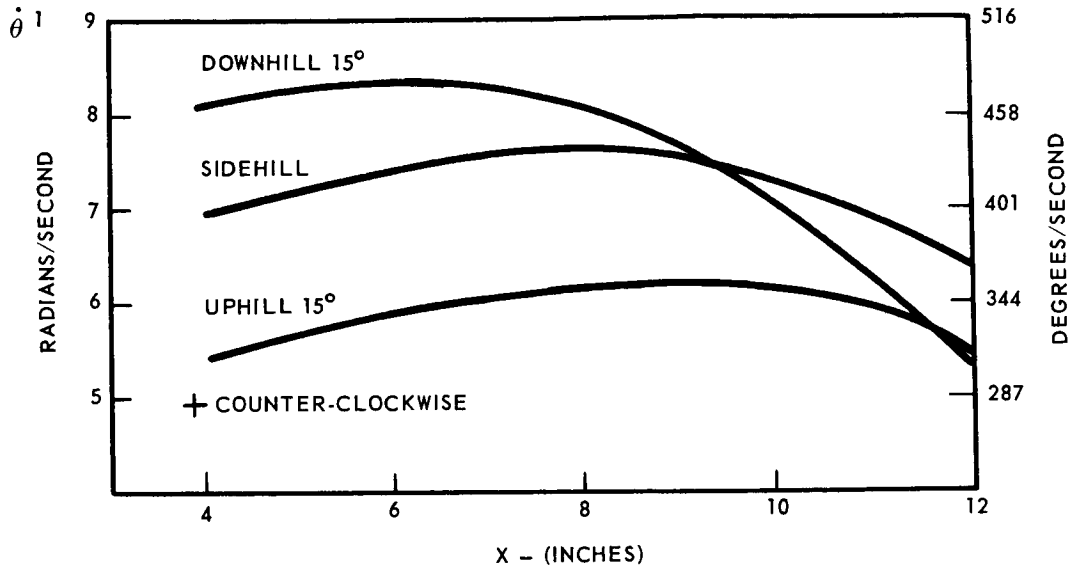

Figure 4-10 Angular Velocity After Impact
Front Tracks Hitting

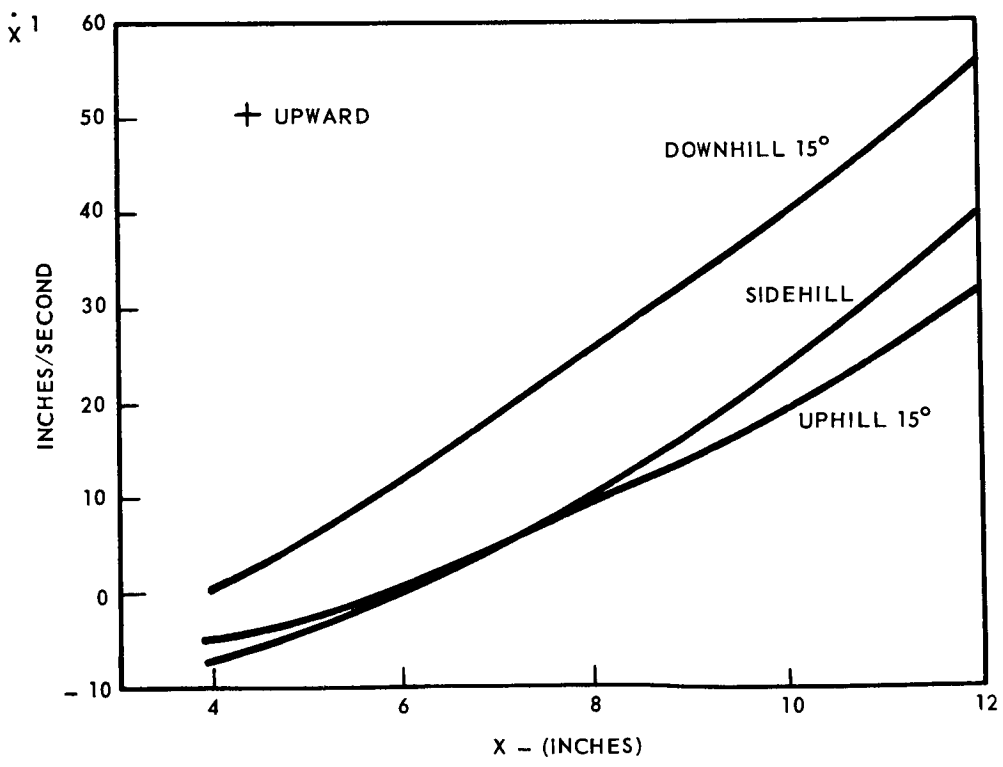

Figure 4-11 Linear Velocity After Impact,
Front Tracks Hitting

To define the criteria of overturning the geometry of the vehicle with respect to the local vertical is examined first. In Figure 4-12, all the angles shown are measured from the local vertical; θ and x are the quantities defined previously (Figure 4-7). Point C is the center of gravity; point A is the rear track; while point B is the front track. Overturning occurs if either $\overline{AC}$ or $\overline{BC}$ is aligned with the local vertical centerline. Thus, the vehicle is stable if for rear end hitting

$$0 < \alpha_1 < 180^\circ \tag{4-52}$$

for front end hitting

$$0 < \alpha_2 < 180^\circ \tag{4-53}$$

where α_1 and α_2 are the angles from the local vertical to $\overline{AC}$ and $\overline{BC}$, respectively. From Figure 4-12

$$\alpha_1 = \beta - \eta_1, \quad \alpha_2 = \beta + \eta_2.$$

From the geometry of the vehicle

$$\beta = \theta + 5^\circ$$

$$\eta_2 = 33^\circ, \quad \eta_2 = 38^\circ.$$

Thus

$$\alpha_1 = \theta - 28^\circ$$

$$\alpha_2 = \theta + 43^\circ$$

and expressions (4-52 and (4-53) become

$$\begin{aligned} 0 &< (\theta - 28^\circ) < 180^\circ \\ 0 &< (\theta + 43^\circ) < 180^\circ. \end{aligned} \tag{4-54}$$

If the angle θ upon impact satisfies these conditions, no overturning will occur.

Equations (4-54) are applied to the cases listed in Table 4-1. Since all the values of θ satisfy these two conditions, all the cases are stable during the first impact. The stability of the vehicle after the first rebound also can be studied by applying Equation (4-54). To accomplish this, the dynamics after rebound are studied first. Figure 4-13 shows the vehicle at two positions. The first position shows the vehicle ABDCE landed on the front tracks at B. The second position, represented by A'B'D'C'E' shows the vehicle about to strike the ground at rear tracks A' after rebound. Points C or C' represent the center of gravity of the vehicle.

From Figure 4-13, by applying the Law of Sines

$$\frac{y}{\sin a} = \frac{\overline{A'G}}{\sin b}$$

or

$$y = \frac{\sin a}{\sin b}\ \overline{A'G}. \tag{4-55}$$

From dynamics, the distance y can also be expressed as

$$y = \dot{y}t - \frac{g_m}{2}t^2 + y_o \tag{4-56}$$

where t is the travel time, y_o is the initial height, and $\dot{y}$ is the initial velocity. During the interval t, the vehicle rotates an angle $\Delta\theta$

$$\Delta\theta = \dot{\theta}t \tag{4-57}$$

where $\dot{\theta}$ is the angular velocity.

Referring to Figure 4-13, it can be seen that

$$\beta - \beta_f = \theta - \theta_f = \Delta\theta = \dot{\theta}t \tag{4-58}$$

and

$$\angle c = \Delta\theta = \dot{\theta}t. \tag{4-59}$$

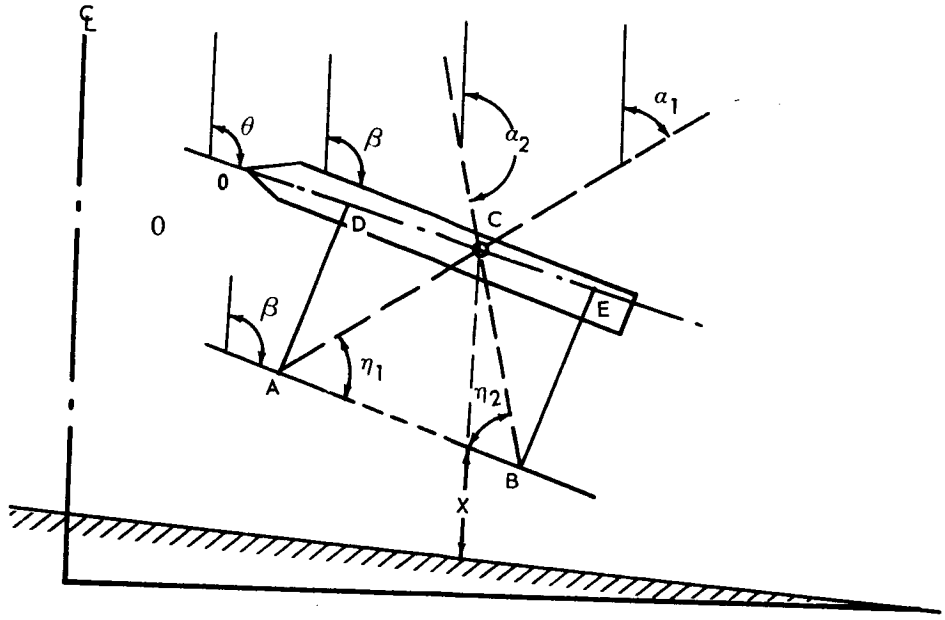

Figure 4-12 Geometry of Vehicle During Deployment

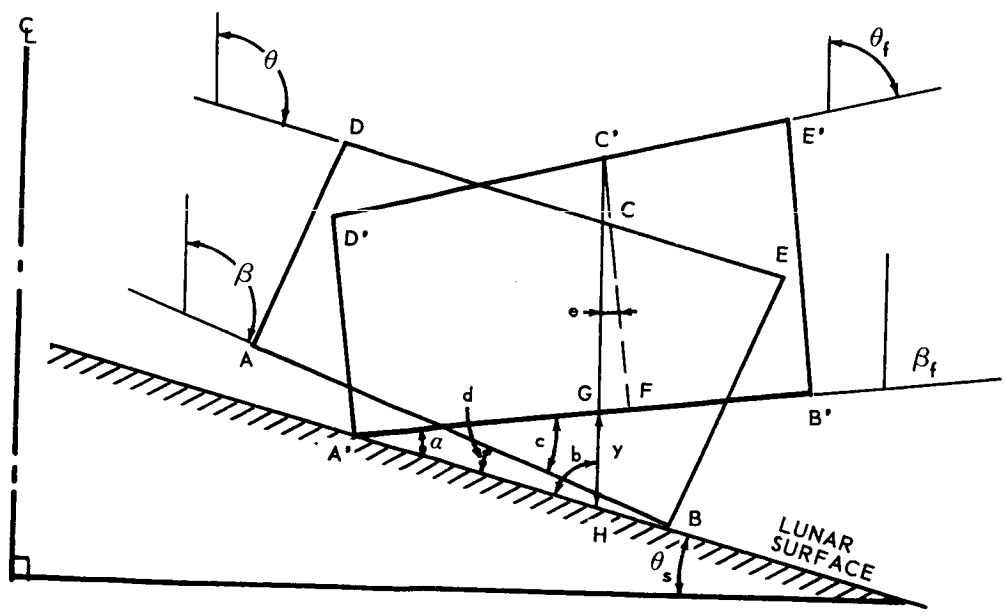

Figure 4-13 Geometry of Vehicle After Rebound

From the geometry

$$\angle b = 90^{\circ} - \theta_s \tag{4-60}$$

$$\angle d = \beta - (90^{\circ} + \theta_s) \tag{4-61}$$

$$\angle a = \angle c - \angle d = \dot{\theta}t - \beta + 90^{\circ} + \theta_s \tag{4-62}$$

$$\angle e = 90^{\circ} - \beta_f = 90^{\circ} (\beta - \dot{\theta}t) \tag{4-63}$$

$$\overline{GF} = \overline{C'_F} \tan e$$

$$\overline{A'G} = \overline{A'_F} - \overline{G_F} = \overline{A'_F} - \overline{C'_F} \tan e \tag{4-64}$$

Substituting Equations (4-60), (4-62), (4-63), and (4-64) into (4-55) yields

$$y = \frac{\sin (\dot{\theta}t - \beta + 90^{\circ} + \theta_s)}{\sin (90 - \theta_s)} \left[\overline{A'_F} - \overline{C'_F} \tan (90^{\circ} - \beta + \dot{\theta}t)\right] \tag{4-65}$$

Equating (4-56) and (4-65)

$$\dot{y}t - \frac{g_m}{2} t^2 + y_o = \frac{\sin (\dot{\theta}t - \beta + 90^{\circ} + \theta_s)}{\sin (90 - \theta_s)} \left[\overline{A'_F} - \overline{C'_F} \tan (90^{\circ} - \beta + \dot{\theta}t)\right] \tag{4-66}$$

Equation (4-66) can be solved for t. When t is obtained, $\Delta\theta$ can be obtained from Equation (4-57) and, thus, angle θ_f of the second impact can be obtained using Equation (4-58). Finally, the stability after rebound can be examined by applying conditions (4-54) to θ_f.

For the most severe case; i.e., downhill 15° deployment, maximum dropping case

where

$y = 11''$

$\theta = 110^{\circ}$ (Table 4-1)

$\dot{y} = 47.5$

$\dot{\theta} = 6.88$ rad/sec $= 395^{\circ}$/sec (Figure 4-10 and 4-11),

$\theta_s = 15^{\circ}$

$\beta = \theta + 5^{\circ} = 115^{\circ}$

$y_o = 2$ in.

$\overline{A'_F} = 17.7$ in., $\overline{C'_F} = 16$ in.

$g_m = 64.4$ in./sec^2

Equation (4-66) becomes

$$47.5t - 32.2t^2 + 2 = \frac{\sin(395t - 10^{\circ})}{\sin 75^{\circ}} \left[17.7 - 16\tan(395t - 25^{\circ})\right] \quad (4\text{-}67)$$

By trial and error, the solution of (4-67) is

$t = .069$ sec.

From (4-57), $\Delta\theta = 27.3^{\circ}$. From (4-58), $\theta_f = \theta - 27.3 = 110 - 27.3 = 82.7^{\circ}$. Applying conditions (4-54)

$\theta_f - 28 = 54.7^{\circ}$

$\theta_f = 43 = 125.7^{\circ}$

As $0 < 54.7^{\circ} < 180^{\circ}$ and $0 < 125.7^{\circ} < 180^{\circ}$, the vehicle is stable.

4.7 SUMMARY

The only mechanical changes made to the Surveyor Bus are those necessary for supporting and deploying the SLRV. Loads on the Surveyor space frame structure are analyzed on the basis of these modifications; however, the basic intent was to investigate feasibility and estimate the weight of the modifications. It is understood that structural integration problems between SLRV and Surveyor will be resolved at a later date, and further refinements are anticipated.

The auxiliary strut support and body lock to be used during the launch, transit, and landing phases for stabilizing the struts and vehicle body appears to be a workable device to the extent that a paper study can demonstrate feasibility. This area will require further development, including model testing to guarantee its reliability in meeting all design requirements.

As a result of the design and analysis accomplished in this section, it is believed that all of the requirements established for the deployment subsystem are met.

SECTION 5

FOLDING AND ERECTION MECHANISMS

The minimal storage space for the LRV on the Surveyor Spacecraft requires that all protrusive structures have the capability of being retracted. Also, in many instances such protrusive structures would not, without severe weight penalties, have the necessary stiffness to withstand the vibrational environment unless additional support is provided.

The items of primary concern are the TV camera and the steerable antenna. These subsystems will be attached to the SLRV by relatively long cantilevered arms. In their extended configuration they are incompatible with the stowage space limitations and the vibration environment. Both requirements are fulfilled by designing the support structures such that they can be retracted, clamped at a second support point, and released on command to unfold into the operational configuration.

5.1 TV CAMERA SUPPORT AND ERECTION MECHANISM

5.1.1 Description

To ensure adequate visibility for the TV camera, it is required that the lens be centrally located with respect to the SLRV y-axis at a height of about 35 inches above the ground. This requirement is met by attaching the camera to a mast located at the front of the SLRV (see Figure 5-1). The mast will be folded and locked to the vehicle during transit. Upon deployment of the vehicle to the lunar surface, a command signal will cause an explosive latch pin to release the spring loaded mast which will allow it to rotate to its erect position above the vehicle. The mast will then lock and firmly position the television camera approximately 35 inches above the lunar surface. A flange at the top of the mast provides the attachment point for the TV camera. The lower end terminates in a clevis joint designed to stradle the power spring. A positive lock and snubber are engaged by an extension to the mast. A locking mechanism is built into the shaft to hold the mast securely at the 90° position.

A redundant hard-stop is also provided past the 90° point. The complete camera lower support structure and associated erection equipment weighs 0.82 lb.

5.1.2 Actuation

Dual squibs to release the latch pin, and two positioning devices provide redundancy in the initiation and termination of erecting the camera to its final position. The power spring recommended will readily raise the camera. Loads imposed on the mast and the vehicle when the mast locks into its final position are less than those resulting from launch and, also, are not large enough to affect vehicle stability.

5.1.3 Design

Packaging in the stowed configuration, mechanical stresses during launch, and thermal effects after deployment are the major factors affecting the design of the mast. Mechanical and thermal considerations governed the selection of the support tube. Attention has been concentrated on providing the system with the highest possible natural frequency in the stowed configuration. This is important because of the severe vibration environment to which the system is subjected during powered flight. Because of the TV camera thermal requirements, a camera support structure consisting of a 0.005-inch gage stainless-steel tube about which phenolic fiberglas is wound, was investigated. The thickness of the latter material is 0.025 inches.

5.1.3.1 Dynamic Analysis

In order to demonstrate the capabilities of the structural system in meeting the conditions cited above, a preliminary dynamic analysis was conducted to provide structural loads.

The simplified mathematical model used for this investigation is the 3-deg. of freedom system illustrated in Figure 5-2. The mass stations used represent the following: (1) The structure and fittings of the smaller-diameter (2.5 in.) support tube section; and (2) the motors, fittings, the larger-diameter (3.2 in.) portion of the support tube, and the portion of the camera housing located between supports to the SLRV, and (3) the optics and electronics within the camera fittings and attachments, and the portion

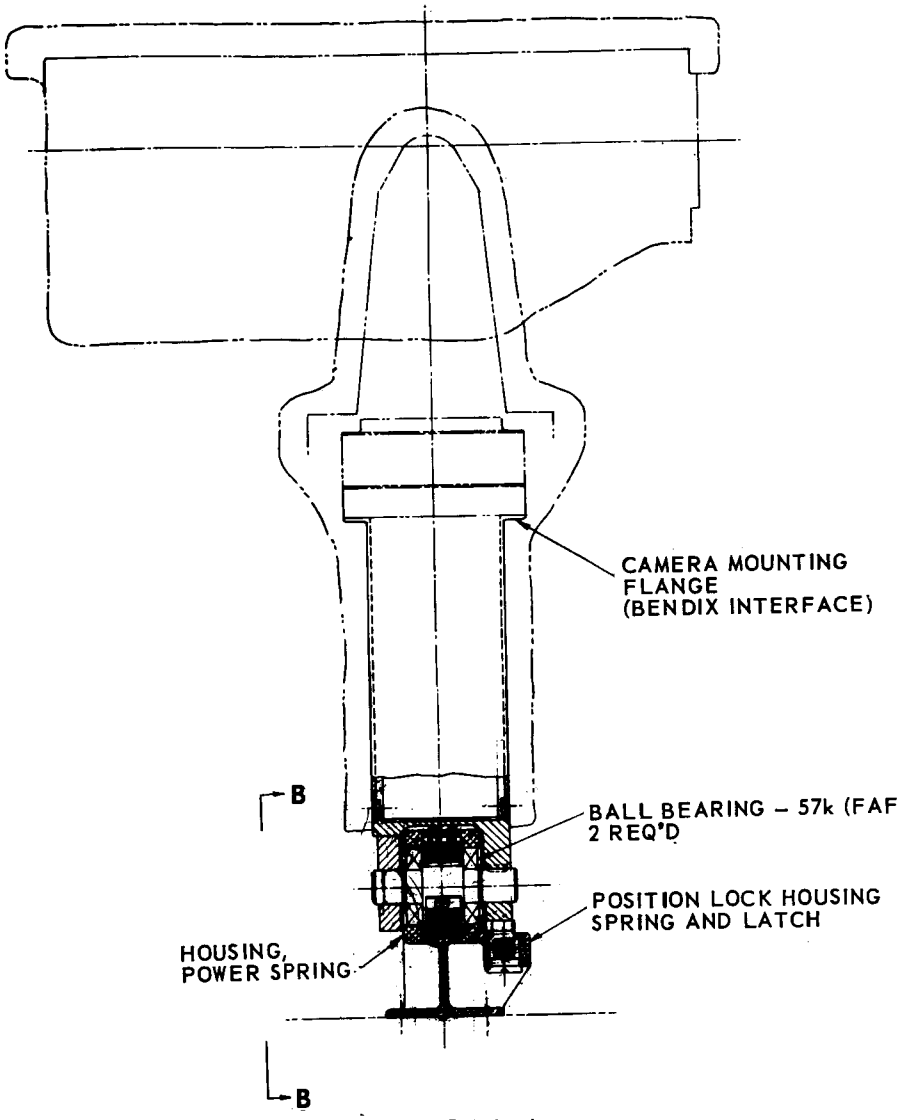

SECTION A–A
CAMERA MOUNT IN VERTICAL POSITION

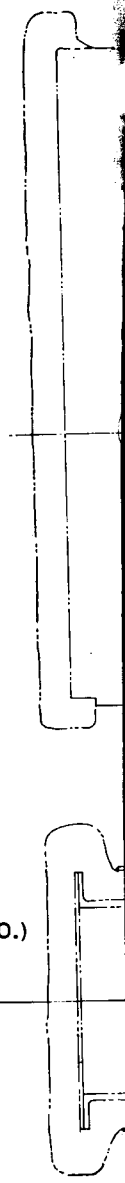

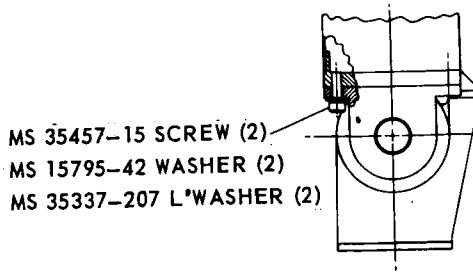

VIEW B–B

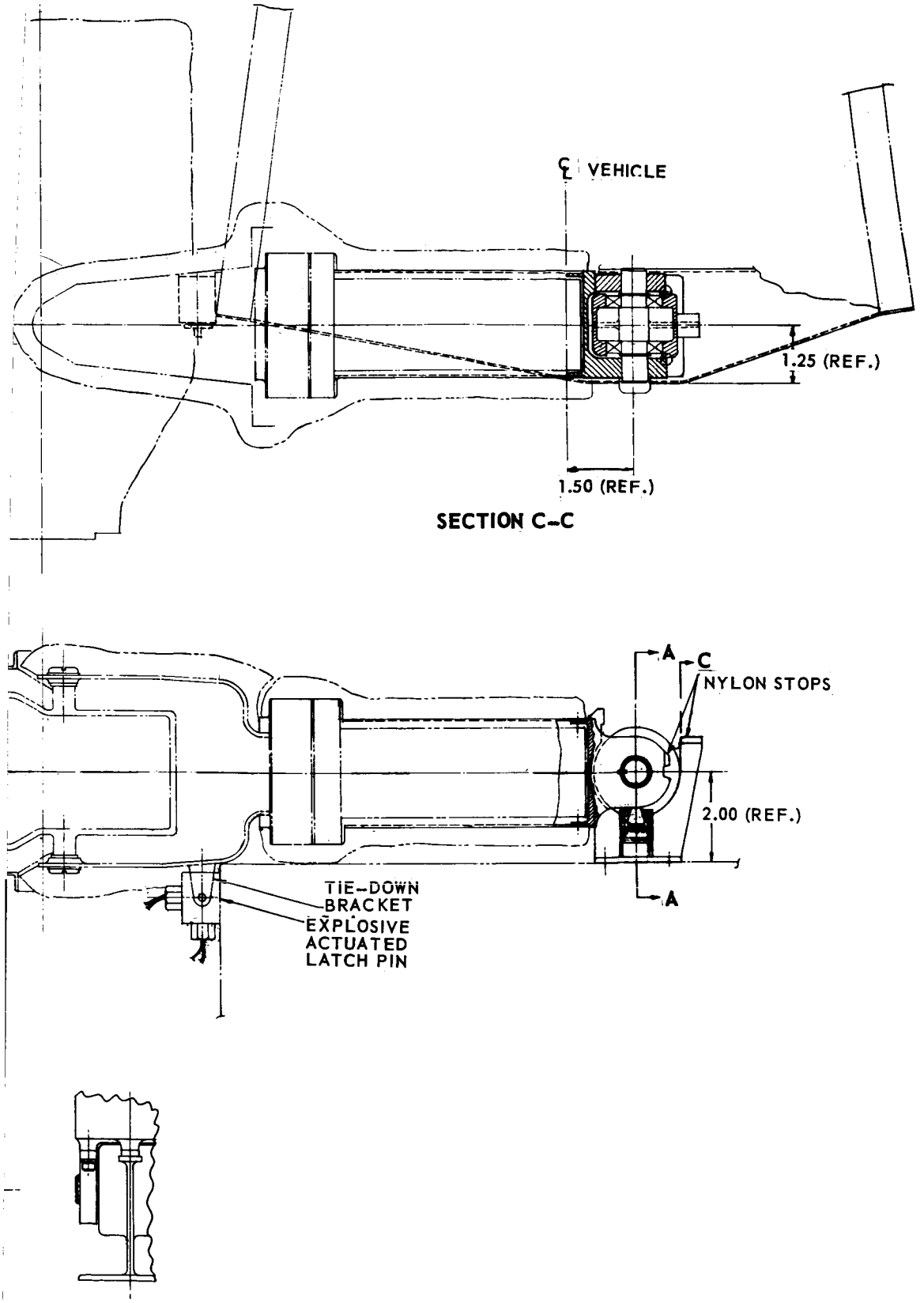

Figure 5-1 TV Camera Erection Mechanism

#2

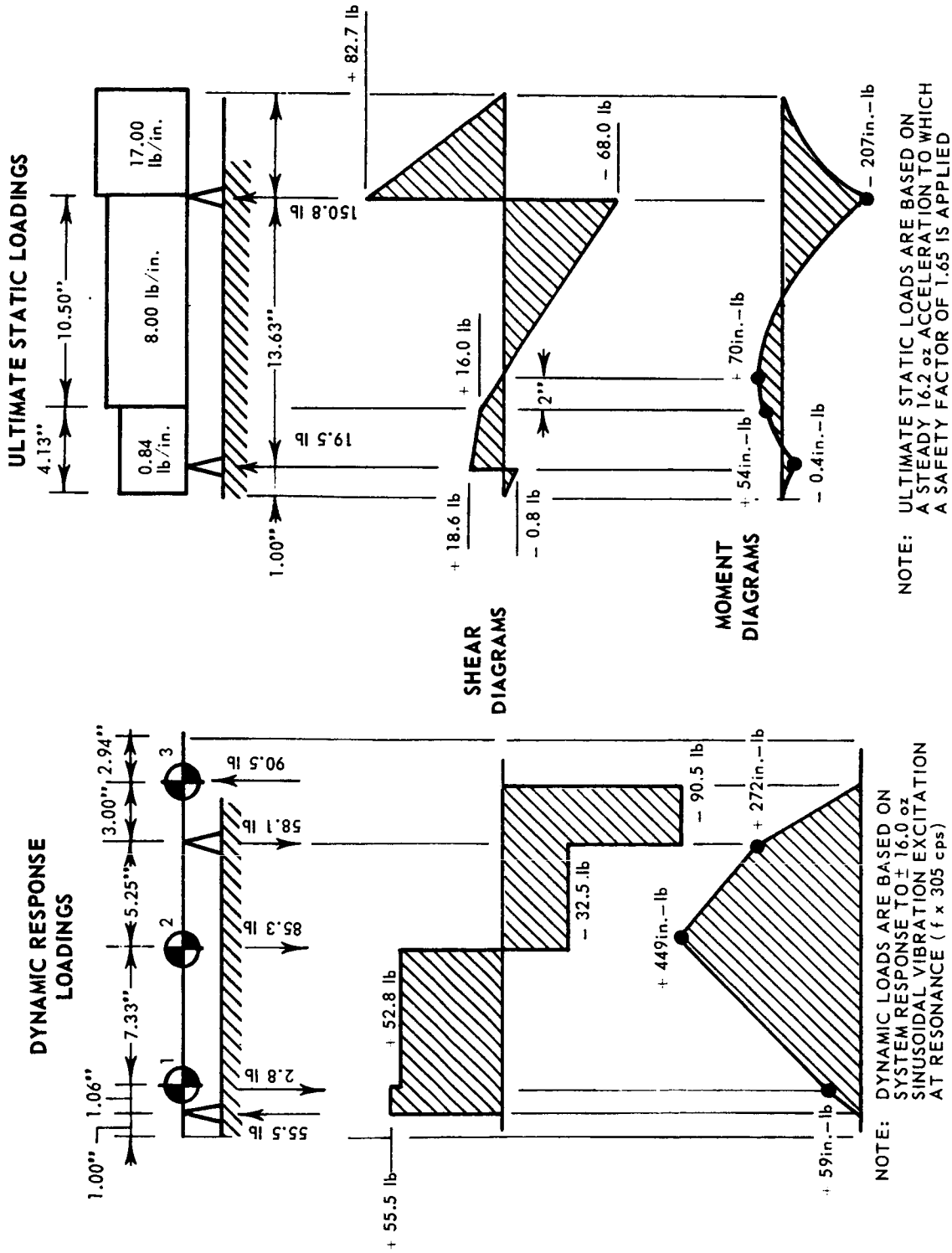

Figure 5-2 Ideal TV Camera System Design Loads

of the camera housing extending beyond the support. The camera support structure was idealized as a composite stainless-steel phenolic, fiberglas tube, whose gages are given above and whose length-diameter relationship is illustrated in Figure 5-3. The camera system is in its folded (stowed) configuration.

Using the simplified 3-deg. of freedom system, structural influence coefficients were determined for use in the vibration analysis. The first mode fundamental frequency was used to define system vibration characteristics and evaluate structural response to the environmental dynamic load. This procedure was used to verify the adequacy of the camera support tube diameters.

Dynamic analysis has shown that system response to the specified vibration environment (Section 3) would produce extremely high loadings. Adequate strength must be provided to prevent these loads from causing fatigue failure within the support structure.

For the system using composite stainless-steel phenolic, fiberglas tube, the fundamental bending frequency (of the stowed configuration) is 305 cps. The system displacements (Figure 5-3) at this fundamental resonance indicate that for foundation-induced excitations (i.e., from the vehicle structure), the modal momentum contributions of the Station (2) and Station (3) masses nearly cancel each other out. Since the modal momentum Station (1) mass is small, the system thus has a very small modal participation factor at its fundamental resonance.

System response to ± 16.0g sinusoidal vibration excitation at resonsance as illustrated in Figure 5-3 may be easily withstood by the analysis model system without loss of structural integrity. This condition would produce a total (rigid body plus fundamental mode) camera station response acceleration of +28.0 g; a motor station loading of +26.8 g and mounting section of the mast response acceleration of +21.9g. These levels are based on a resonance factor (Q) of 10. Since the phenolic fiberglas provides the system with a relatively high degree of damping, this resonance factor and hence the resulting dyanmic loadings are probably worse than the actual case. Since the damping increases with frequency, the response levels of higher modes of vibration would be considerably reduced.

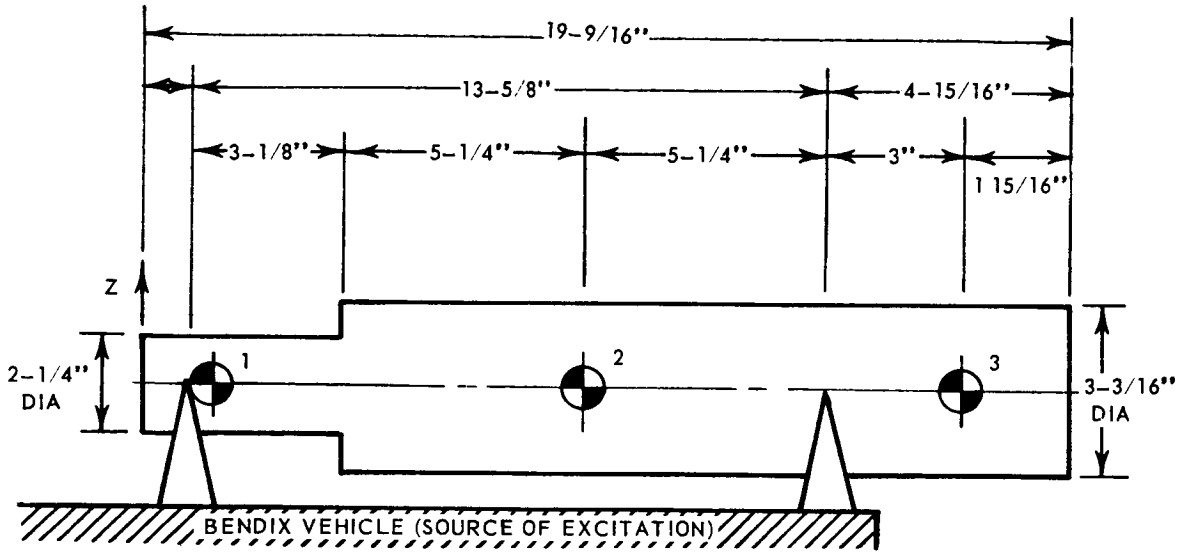

NOTE: STRUCTURE IS TAKEN AS HAVING A WALL THICKNESS OF 0.030 INCHES, OF WHICH 0.005 INCHES IS STAINLESS STEEL, AND 0.025 INCHES IS PHENOLIC-FIBERGLASS TAPE WRAPPED AROUND THE STAINLESS STEEL.

IDEALIZED SYSTEM WEIGHT, GEOMETRY AND FUNDAMENTALS

MASS STATION	ITEMS INCLUDED	EST. WT. (lb)	STATION (X) (INCHES)	NORMALIZED MODEL DISPLACEMENT * (in./in.)	TOTAL RESPONSE LOAD DUE TO SPEC. VIBRATION (X)
1	CAMERA SUPPORT TUBE; FITTINGS	0.13	2.06	− 0.658	∓ 21.9
2	CAMERA SUPPORT TUBE; FITTINGS MOTORS	3.18	9.38	− 0.891	∓ 26.8
3	OPTICS; ELECTRONICS; STRUCTURE; CONTROLS	3.23	16.63	+ 1.000	± 28.0

NOTE: SYSTEM FUNDAMENTAL BENDING FREQUENCY IS 305cps

Figure 5-3 Ideal TV Camera System Stowed Configuration

Ultimate static loadings were determined for the system. These were based on the specified 16.2 g steady-state acceleration which was increased by the margin of 1.65. These ultimate static loads are shown by Figure 5-2 where they are compared with the dynamic response loadings. The latter condition, as will be noted, is still more severe.

Using system dynamic response to vibration excitation as a source for design loading criteria, a preliminary stress analysis was conducted to estimate the required sizes of the structural members. Margins of safety of 1.65 under ultimate loading conditions were applied, since only stress levels at failure are available for classes of materials such as phenolic fiberglas. An ultimate strength of 40,000 psi was used. The stainless-steel tubing was considered capable of withstanding stresses up to 100,000 psi.

It was found that support tube thickness of 0.030 in. (0.005 in. of stainless steel and 0.025 in. of phenolic fiberglas) is in excess of that required by system stiffness and strength criteria. This wall thickness of 0.030 in. is being maintained to eliminate potential local buckling and crippling problems.

5.1.3.2 Thermal Analysis

The thermal adequacy of this design can be estimated by assuming that the TV camera, and the top of the Lunar Roving Vehicle operate at two different temperatures. If this occurs, two items are capable of conducting heat from the TV camera package; namely, the interconnecting cable, and the support structure itself. The cable length is about 58 in. This length results from the horizontal cable spiral twist of four turns which provides for the azimuth angular movement of $\pm 200^{\circ}$. The cable is comprised of a dual 25 (50 wires total) printed circuit cable, each wire is 0.005-in. thick and 0.010-in. wide. Assuming a temperature differential of 160°F (conservative estimate) approximately 0.04 watts will be lost through the cable.

Various combinations of structures were investigated. The best one in terms of thermal control is a 0.005-in. thick stainless-steel inner tube wrapped with 0.025 reinforced plastic. A thermal loss of about 0.17 watts is estimated for this structure at the assumed $\Delta T = 160^{\circ}$F. Together with the cable loss, total loss through the support structure is estimated to be less than 0.2 watts.

5.1.3.3 Overturning Moment

The moment produced at impact in the raised position (when the camera mast hits the stop) must be limited to about 200 in.-lb to prevent tipping the vehicle. For design purposes, the moment will be limited to 100 in.-lb. This constraint requires that the velocity not exceed 1/4 rad/sec if the mast is allowed to hit a hard stop. As an alternative, the energy can be dissipated in a snubber. The latter approach will result in more positive latching and is used to establish the terminal velocity:

$$\omega = \sqrt{2M\,\delta/J} \qquad (5\text{-}1)$$

where

M = resisting moment = 100 in.-lb

J = equivalent inertia of the camera at the end of the mast

δ = snubbing angle = 0.087 radians = 5 degrees

now

$$J = MR^2 = 4.05 \text{ in.-lb-sec}^2$$

where R is the radius of gyration.

Therefore,

$$\omega = 2.06 \text{ rad/sec.}$$

The snubbing action will take place within the latch travel which is designed to accommodate the 5° motion.

5.1.3.4 Spring Design

The spring energy to raise the camera at 2.06 rad/sec is shown below

$$\frac{1}{2} K (\theta^2 + 2\alpha\,\theta) = mgh + 1/2\, J\omega^2 = 27.2 \text{ in.-lb.} \qquad (5\text{-}2)$$

where θ and α are defined in Figure 5-4.

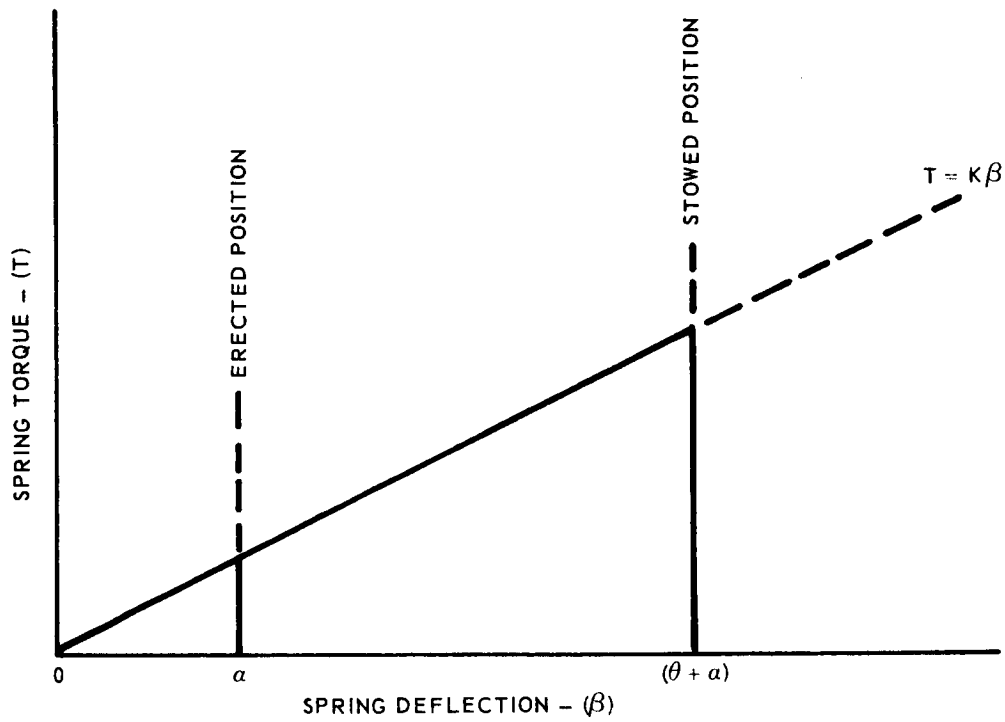

$$\text{ERECTION ENERGY} = \int_{\alpha}^{\theta+\alpha} K\beta \, d\beta$$

$$= 1/2K\,(\theta^2 + 2\alpha\theta)$$

α = PRELOAD ANGLE OF SPRING WHEN CAMERA MAST IS ERECTED

θ = ANGULAR MOVEMENT OF CAMERA MAST FROM STOWED TO ERECTED POSITIONS

Figure 5-4 Linear Torsion Spring Design

The spring moment in the stowed position must exceed the moment produced by the camera at the end of the mast, or 18.6 in.-lbs. Similarly a preload of at least 9.3 in.-lbs is necessary in the event the lock does not engage and the vehicle is listing at 30°. A spring with a rate of 8 in.-lb/radian preloaded 97° will meet these requirements.

5.2 DIRECTIONAL ANTENNA SUPPORT AND ERECTION MECHANISM

The function of the antenna mast is to deploy the 18-in. directional antenna and support it above the vehicle. The final position was selected to shift the vehicle center of mass to a desirable location as well as elevate the antenna for communication purposes.

A support mast attached to a pivot at the rear of the LRV at one end and incorporating a housing for the roll gimbal drive mechanism at the other is shown in Figure 5-5. The mast will be made of a 0.016-in. thick aluminum tube, 1 inch in diameter with 0.030-in. phenolic fiberglas wrapping. A spring mechanism will raise it to the final position in a two-step sequence described below. At the final position, a positive lock will secure the mast.

As the LRV leaves Surveyor, the antenna will be partially elevated and latched near the top of the vehicle. This maneuver, illustrated in Figure 5-5, will prevent damage to the antenna which could occur if the SLRV landed on the moon's surface with the antenna in the stowed position. Furthermore, delaying full antenna deployment with the intermediate latch eliminates the possibility of antenna damage due to striking the Surveyor.

The transition from the stowed position alongside the vehicle to the final position above the vehicle can be accomplished with the mast canted with respect to the axis of rotation at the mast support as shown in the auxiliary view in Figure 5-5. This geometry will permit single axis rotation and still satisfy the positioning requirements.

During transit to the moon, a tiedown lug attached close to the antenna center of mass will be fastened to the vehicle. A cradle-bracket, shown in Figure 5-5 at the top of the vehicle, will confine the lateral motion of the mast while stowed. Vertical motion will be minimized by pre-loading the mast laterally in the stowed position.

The tiedown lug and the intermediate stop will be secured with an explosive latch pin similar to Conax Corporation's Model L-2880. Dual squibs have been incorporated for reliability. The weight penalty for the redundant squib is about 2 oz per latch. When these latch pins are withdrawn, stored energy in the power spring (see Figure 5-5) will raise the antenna.

The initial phase of raising the antenna to the intermediate latch position requires insignificant lifting moment, since the vehicle is being deployed at that time and is actually falling away from the antenna. The spring size is, therefore, determined by the energy required to lift it 12 in. from the intermediate position to the vertical position during the phase of erection with enough momentum at that point to carry it over center and allow it to drop down into the lock.

Static requirements dictate that the spring torque at the intermediate position exceed the moment produced by the antenna on the mast.

The spring arrangement which will satisfy these requirements is computed by letting the stored energy (released in the excursion from the intermediate latch to the final lock) be equal to the kinetic energy at impact, plus the potential energy required to raise the antenna to its highest position less the potential energy recovered as the antenna is dropped into its final position:

$$\frac{1}{2} K (\theta^2 + 2\alpha\theta) = \frac{1}{2} J \omega_3^2 + mg (h_2 - h_1) - mg (h_2 - h_3) \qquad (5\text{-}3)$$

where the sketch and nomenclature shown below illustrate the mathematical model.

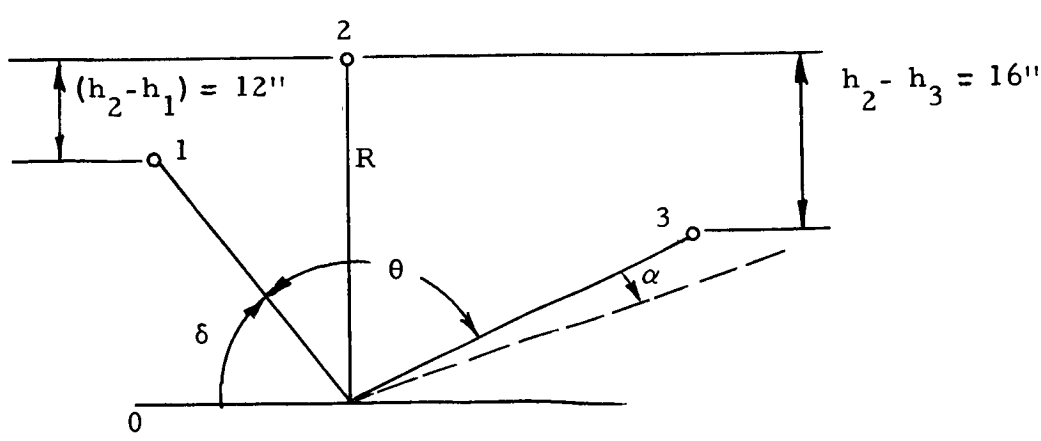

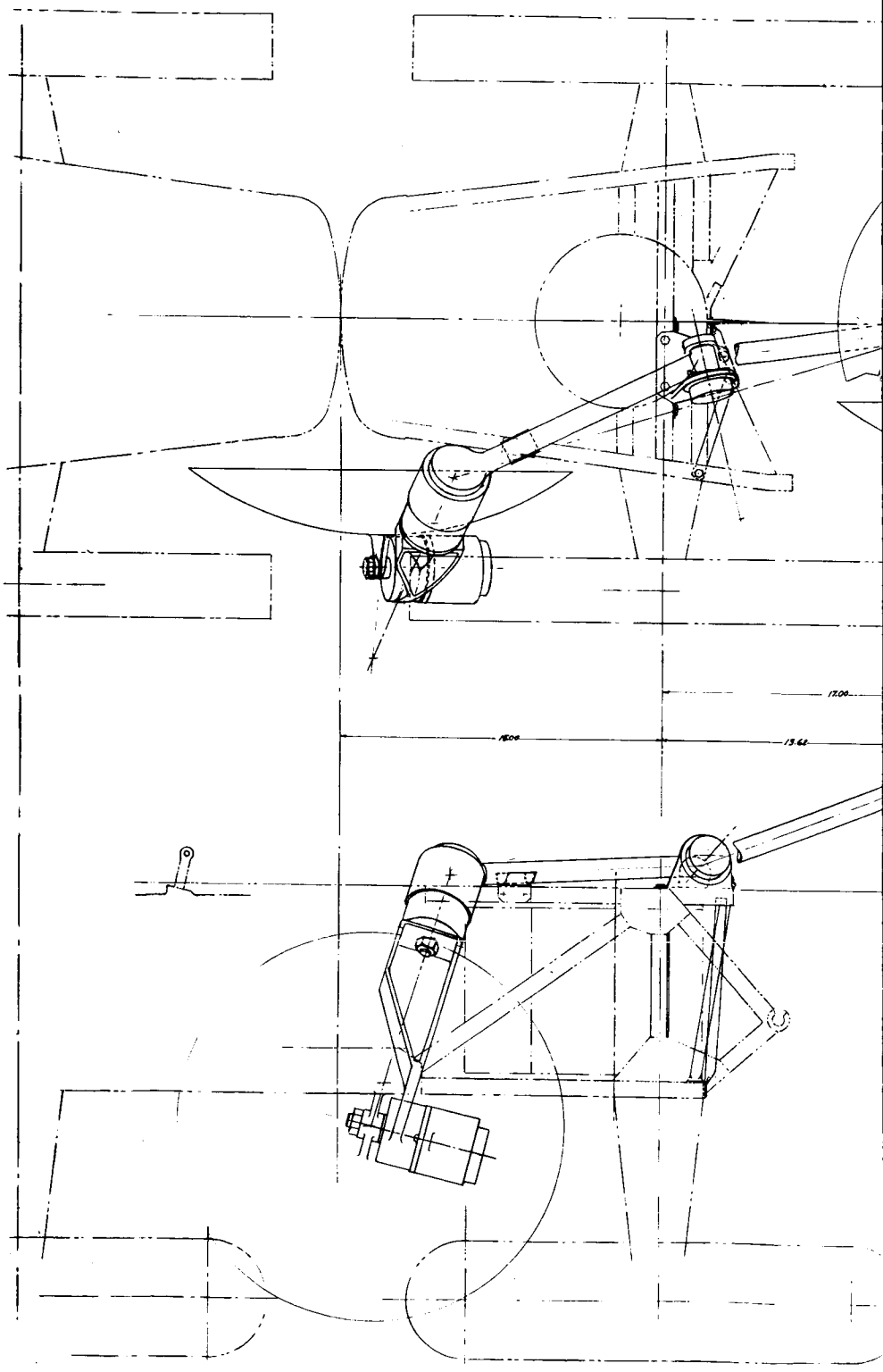

#1

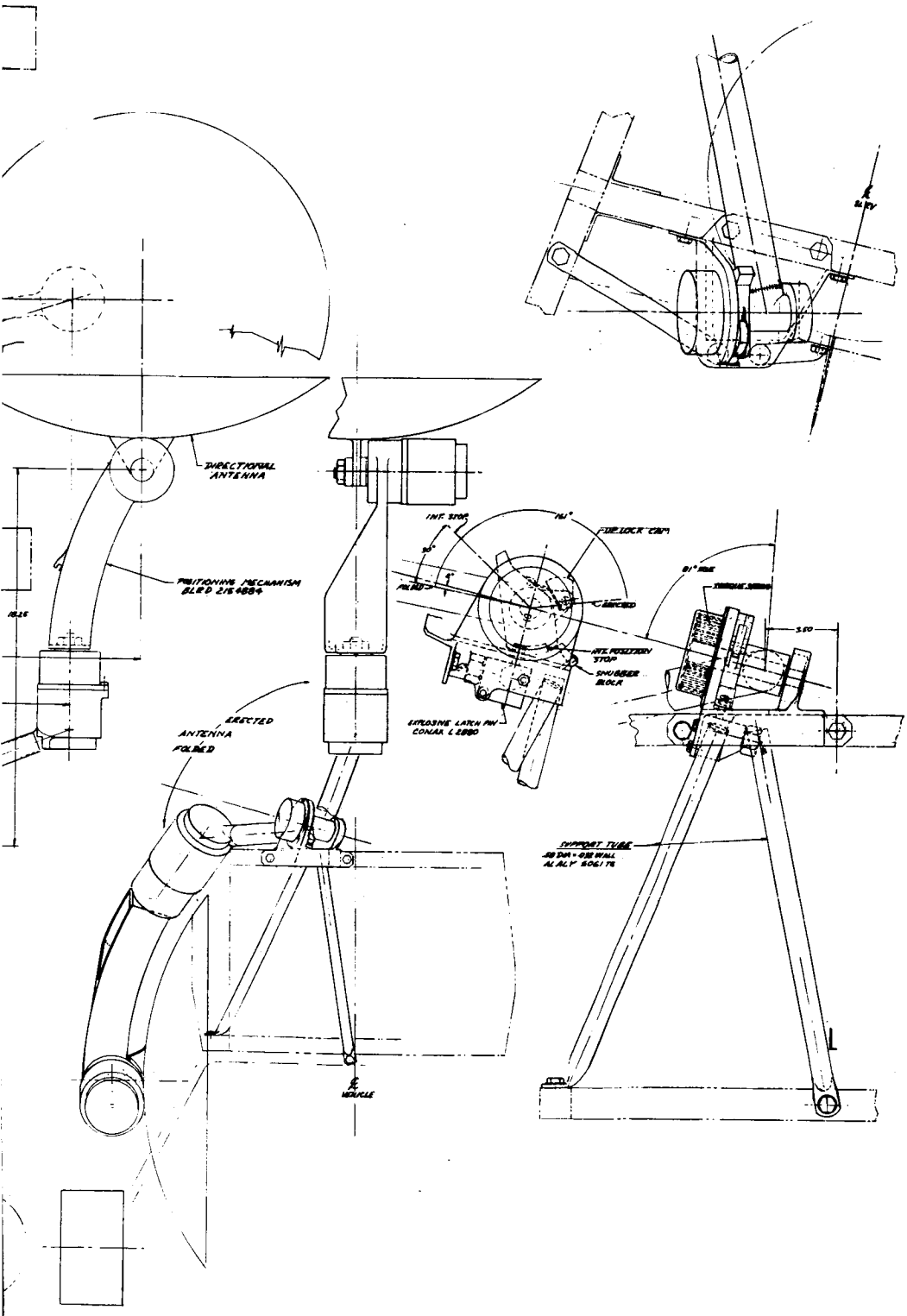

Figure 5-5 Antenna Support and Erection Assembly

Definitions:

0 = stowed position

1 = intermediate latch position

2 = vertical position

3 = final locked position

R = 24 in. (moment arm)

m = 8 lb/386 in/sec^2 (assume mass is concentrated at a point)

K = spring rate

θ = angular travel from intermediate stop to final position = 131°

α = spring preload angle when the mast is locked

δ = angular travel from stowed position to intermediate latch = 30°

J = Equivalent polar moment of inertia = mR^2 = 12 in. lb sec^2

ω = rotational velocity

h = elevation

If the angular velocity at impact is allowed to reach 2.5 rad/sec, then sufficient momentum will exist at the vertical position to carry the antenna past the highest point and into the lock. Using this value with the indicated weight and elevation values, the following energy storage requirement is obtained:

$$\frac{1}{2} K (\alpha^2 + 2\theta) = 32.5 \text{ in-lb} \qquad (5\text{-}3)$$

The static load that must be satisfied is:

$$K(\alpha + \theta) = mg\,R \cos \delta$$

$$K(\alpha + \theta) = 27.6 \text{ in-lb}$$

Since θ is defined as 131°, only the spring rate and the preload angle can be varied to store the required spring energy and meet static requirements. A spring with a rate of 8 in. lb/radian preloaded to 93° will produce a torque of 27.8 in-lb at the intermediate latch, and will store 42.3 in-lb energy at that point. This has the effect of increasing the terminal velocity from 2.5 rad/sec to 2.82 rad/sec.

The velocity at which the mast hits the intermediate latch can be conservatively estimated by assuming the stored energy is converted to kinetic energy (i.e., potential energy is neglected).

$$\frac{1}{2} J \omega_1^2 = \frac{1}{2} K (\delta^2 + 2\theta\delta + 2\alpha\delta)$$

$$\omega_1 = 1.62 \text{ rad/sec} \tag{5-4}$$

The maximum momentum at the mast hinge point is determined by equating the work performed in deflecting the mast to the kinetic energy of the assembly:

$$M\theta = \frac{1}{2} J \omega_1^2 \tag{5-5}$$

where M is the applied moment.

Angular deflection as a function of the applied moment is expressed in the flexure formula:

$$\theta = \frac{1}{2} \frac{Mr}{EI} \tag{5-6}$$

Combining Equations (5-5) and (5-6) results in the following:

$$M^2 = \frac{J\omega_1^2 EI}{r} \tag{5-7}$$

In this application,

$r = 0.50$ in., tube radius

$t_{AL} = 0.016$ in., aluminum thickness

$t_{FG} = 0.030$ in., fiberglas thickness

$I_{AL} = 0.0063$ in.^{4} aluminum tube area moment of inertia

$I_{FG} = 0.0118$ in.^{4} fiberglas wrap area moment of inertia

$E_{AL} = 10 \times 10^6$ psi, aluminum modulus of elasticity

$E_{FG} = 10 \times 10^5$ psi, fiberglas modulus of elasticity

It is estimated that EI for the composite mast will be at least 7.48×10^4 lb-in.^{2} Substituting into Equation (5-7) yields:

$$M = 310 \text{ in-lb.}$$

The stress in the aluminum tube is:

$$S_{AL} = \frac{Mr}{I_{AL} + \frac{E_{FG}}{E_{AL}} I_{FG}} .$$

Thus, at impact with the latch, $S_{AL} = 20,700$ psi. The stress in the fiberglas is 2,070 psi because its modulus of elasticity (proportional to stress for equal strains) is 1/10 that of aluminum.

Impact with a hard lock at 2.82 rad/sec would produce a stress level to 36,000 psi. which would not damage the mast but the corresponding moment of 540 in-lb would tip the vehicle. Therefore, a snubber has been added to dissipate part of the energy over the last 5° of travel and reduce the impact moment at the locking position to 150 in-lb. Sufficient energy will remain to carry the mast into the positive lock.

The coefficient of thermal expansion for aluminum is 12.6×10^{-6} in/in/^{o}F and for phenolic fiberglas; it is 17.1×10^{-6} in/in^{o}F. These values are so close that temperature-induced stresses can be neglected. The weight estimate for the mast mounting bracket, lock, latch, explosive latch pins and power spring totals 1.5 lbs.

SECTION 6

APOLLO SUPPORT SCIENTIFIC EXPERIMENTS

6.1 MAPPING AND SITE VERIFICATION

6.1.1 Photogrammetric Analysis

6.1.1.1 Geometric Considerations

If a photograph is considered as a central projection of the object space onto the photographic plane through the camera lens, it is evident that the directions to discrete points in the object space, with respect to the camera axes, can be computed from the measured coordinates of the image points. Without any additional data, this is all the information that can be obtained from a single photograph.

If, however, two photographs are available which have been obtained from different camera stations, and the same object point is imaged on both photographs, then two directions can be determined to one and the same point. The coordinates of such points may be computed provided that the orientation and location of the camera axes for each of the exposures is known with respect to a common reference system. This is the basis of intersection photogrammetry, which is used for the location of discrete points. However, one of the more important problems of intersection photogrammetry is that of identifying the corresponding images of an object, when that object has been photographed from widely separated viewpoints.

In the event that two photographs are taken of an area, such that the two camera stations are in close proximity to each other, a large portion of the photographed area is imaged on both pictures. These images may be viewed simultaneously, so that a stereoscopic model of the common area is constructed. Assuming that error free photography and reconstruction equipment is available, this is an exact model of the object space, the scale of which is determinate. Precise photogrammetric apparatus exists for the creation and measurement of such stereoscopic models. With these instruments it is possible to produce a map of the stereo model in a continuous

fashion, rather than from discrete points. Furthermore, the nature of the model is such that there is rarely any difficulty in identifying points which are common to the two photographs.

Performance Analysis

Since it is possible to consider the process of stereo photogrammetric mapping as if it were a continuous integration of photogrammetric intersections, the fundamental geometry is identical for both methods.

Consider a photograph which was taken when the focal plane was vertical. Let an orthogonal right-handed coordinate system be defined such that:

1. The origin is located at the perspective center of the camera

2. The positive y axis is directed toward the object space, and coincides with the optical axis

3. The positive z axis is upward.

Consider the plane which represents the positive photograph; i. e., that parallel to the x - z plane and located at a distance of +f from the origin, where f is equal to the focal length of the camera objective (see Figure 6-1).

The ray from any point P in the object space, intersects the positive plane at a point p; let the coordinates of this image point be x_p, y_p, z_p. (It is obvious that the value of y_p is equal to f, and that the corresponding coordinates in the negative plane are $-x_p$, $-f$, $-z_p$).

Denote the horizontal angle between the camera axis and the point P as α, and the vertical angle between the horizon plane and P at the perspective center as β. These angles may be determined from the measured image coordinates, according to the formulae

$$\tan \alpha = \frac{x}{y} = x_p/f \qquad (6\text{-}1)$$

and

$$\tan \beta = \frac{z}{y} = z_p \cdot \cos \alpha/f \qquad (6\text{-}2)$$

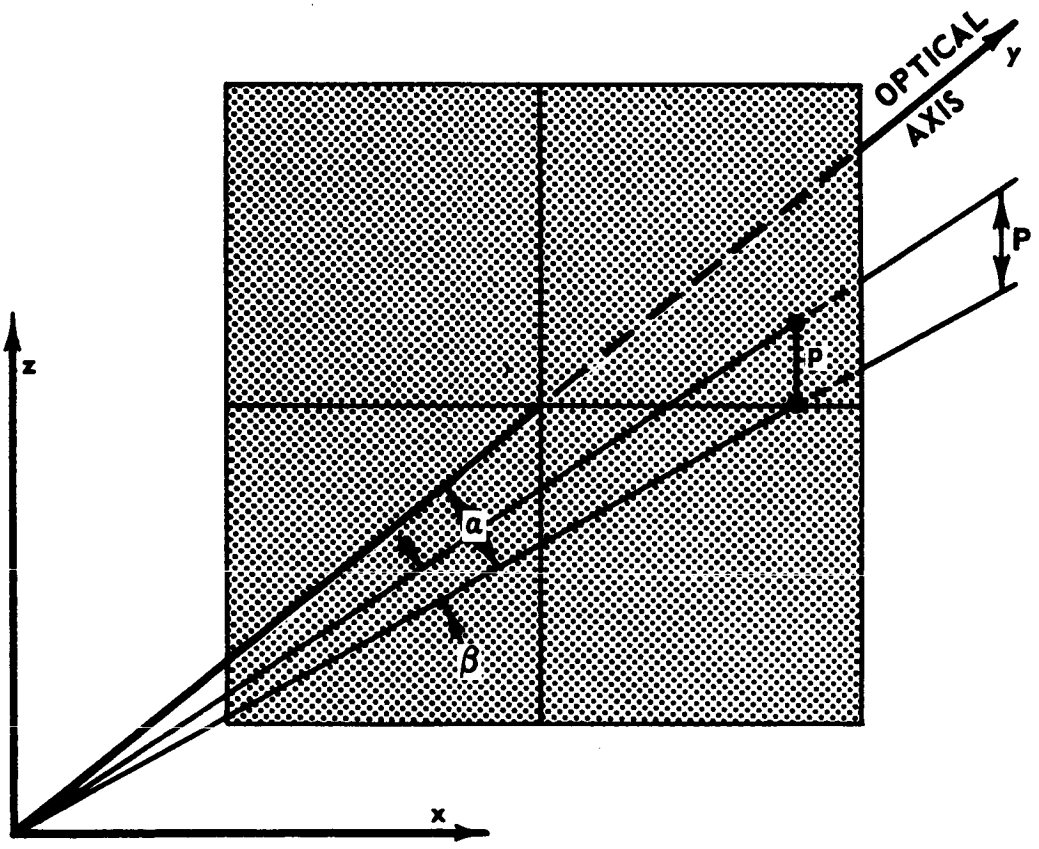

Figure 6-1 Angular Relationships for Leveled Photograph

If now the optical axis is depressed downward through an angle of $+\lambda$, the values of α and β are computed according to the formulae

$$\tan \alpha = x'/(f \cos \lambda + z' \sin \lambda) \tag{6-3}$$

and

$$\tan \beta = \cos \alpha (f \sin \lambda - z' \cos \lambda)/(f \cos \lambda + z' \sin \lambda) \tag{6-4}$$

where x' and z' are measured in an orthogonal coordinate system in the photographic plane such that:

1. The origin is located at the intersection of the optical axis and the included photo plane

2. The z' axis is defined by the intersection of the vertical plane passing through the optical axis with the photo plane, the positive direction being upward.

These formulae may be derived geometrically by considering Figure 6-2, or more directly by applying the matrix

$$\begin{bmatrix} 1 & 0 & 0 \\ 0 & \cos \lambda & -\sin \lambda \\ 0 & \sin \lambda & +\cos \lambda \end{bmatrix} \text{ to the coordinates } \begin{bmatrix} x' \\ f \\ -z' \end{bmatrix}$$

to yield

$$\begin{bmatrix} x \\ y \\ z \end{bmatrix} = \begin{bmatrix} x' \\ f \cos \lambda + z' \sin \lambda \\ f \sin \lambda - z' \cos \lambda \end{bmatrix} \tag{6-5}$$

which are then substituted into Equations (6-1) and (6-2).

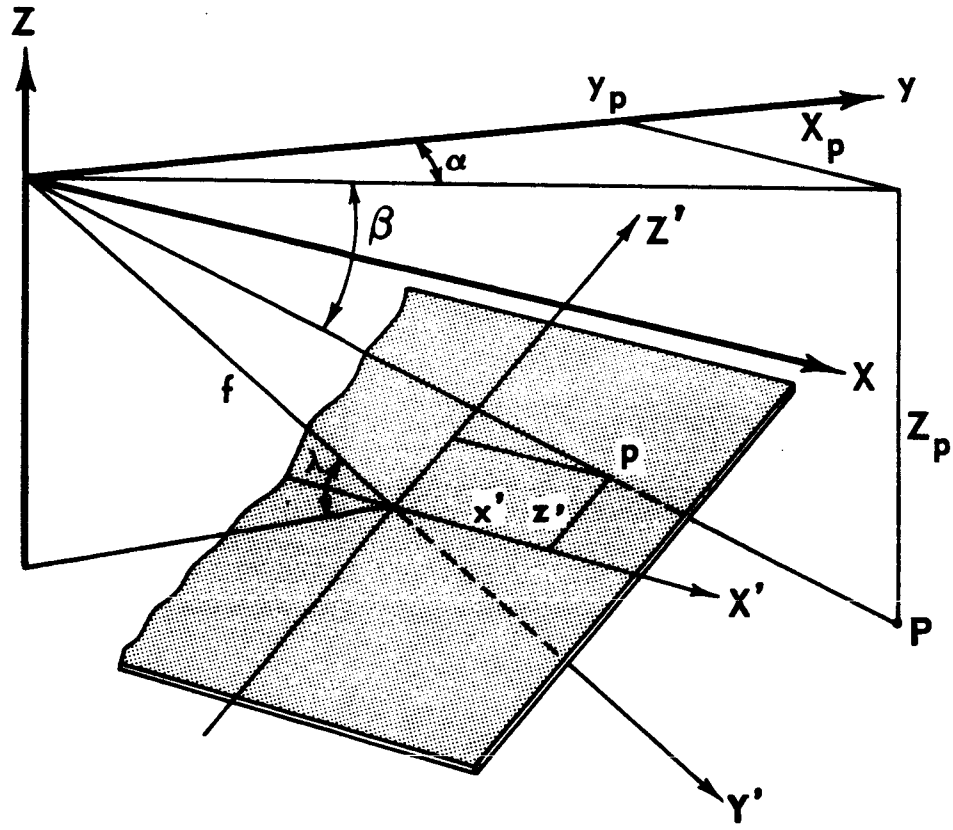

Figure 6-2 Angular Relationships for Inclined Photograph

In the event that a rotation of ψ exists around the camera optical axis, the correct values of x, y, and z to be used in Equations (6-1) and (6-2) may be obtained by applying another rotation matrix to the observed coordinates.

$$\begin{bmatrix} x \\ y \\ z \end{bmatrix} = \beta \begin{bmatrix} 1 & 0 & 0 \\ 0 & \cos\lambda & -\sin\lambda \\ 0 & \sin\lambda & +\cos\lambda \end{bmatrix} \begin{bmatrix} \cos\psi & 0 & \sin\psi \\ 0 & 1 & 0 \\ -\sin\psi & 0 & \cos\psi \end{bmatrix} \begin{bmatrix} x'' \\ f \\ -z'' \end{bmatrix} \qquad (6\text{-}6)$$

Where x'' and y'' are the measured image coordinates with respect to the photographic coordinate system. The resulting coordinates are:

$$\bar{P} = \begin{bmatrix} x \\ y \\ z \end{bmatrix} \begin{matrix} = \\ = \\ = \end{matrix} \begin{bmatrix} x'' \cos\psi - z'' \sin\psi \\ f\cos\lambda + z'' \cos\psi \sin\lambda + z'' \sin\psi \sin\lambda \\ f\sin\lambda - z'' \cos\psi \cos\lambda - x'' \sin\psi \cos\lambda \end{bmatrix} \qquad (6\text{-}7)$$

To determine the position of a point through photogrammetric intersection, it is not necessary to determine the angles α and β, per se. The rectangular coordinates will be computed from the measured photo coordinates x'', z'' of the point image. From the two camera stations located at the terminals of a base line, there are three possible cases of intersection. These are:

1. Camera axes normal to the base line, parallel but not necessarily horizontal

2. Camera axes averted with respect to the base line, parallel but not necessarily horizontal

3. Camera axes convergent with respect to the base line, non-parallel and not necessarily horizontal.

The third case is the most general and the first two may be derived from it. This situation is illustrated by Figure 6-3 in which the angles γ and δ are measured positive clockwise from the normal to the base line. The geometry yields the following equations for the rectangular coordinates of P.

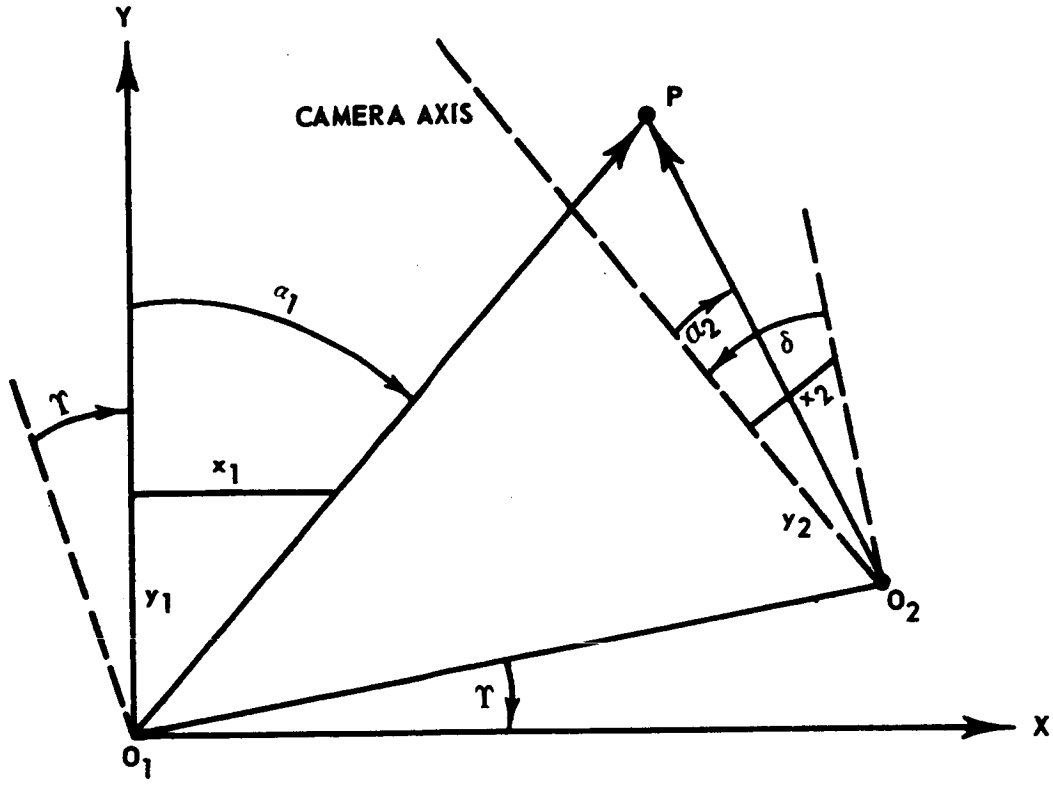

Figure 6-3 Intersection with Convergent Camera Axes

$$Y_P = \frac{by_1(y_2\cos\delta - x_2\sin\delta)}{(y_1y_2+x_1x_2)\sin(\gamma-\delta)+(x_1y_2-x_2y_1)\cos(\gamma-\delta)} \tag{6-8}$$

and

$$X_p = \frac{bx_1(y_2\cos\delta - x_2\sin\delta)}{(y_1y_2+x_1x_2)\sin(\gamma-\delta)+(x_1y_2-x_2y_1)\cos(\gamma-\delta)} \tag{6-9}$$

where b = base line length.

The elevation of P may be computed in two different ways as:

$$Z'_p = \frac{bz_1(y_2\cos\delta - x_2\sin\delta)}{(y_1y_2+x_1x_2)\sin(\gamma-\delta)+(x_1y_2-x_2y_1)\cos(\gamma-\delta)} + Z_1 \tag{6-10}$$

and

$$Z''_p = \left\{\frac{bz_2(y_2\cos\delta - x_2\sin\delta)}{(y_1y_2+x_1x_2)\sin(\gamma-\delta)+(x_1y_2-x_2y_1)\cos(\gamma-\delta)}\right\}\frac{y_1}{y_2} + \frac{bz_2}{y_2}\sin\gamma + Z_2 \tag{6-11}$$

To apply these formulae to a specific case in which the cameras are levelled, the values of ψ_1 and ψ_2 become zero. If only horizontal camera axis are considered, λ_1 and λ_2 are equal to zero.

Thus, the equation defining the rectangular coordinates of an intersected point may be summarized:

Case I - Parallel, horizontal camera axes, normal to base

$$Y_p = \frac{bf}{x+x_2} = \frac{bf}{p} \tag{6-12}$$

$$X_p = \frac{bx_1}{p} \tag{6-13}$$

$$Z'_p = \frac{Y_p z_1}{f} + Z_1 \tag{6-14}$$

$$Z''_p = \frac{Y_p z_2}{f} + Z_2 \tag{6-15}$$

where

p = image parallax

Case II - Parallel, horizontal camera axes, averted to base

$$Y_p = \frac{bf}{x_1 + x_2} \left(\cos \gamma - \frac{x_2}{f} \sin \gamma \right) \tag{6-16}$$

$$X_p = \frac{bx_1}{x_1 + x_2} \left(\cos \gamma - \frac{x_2}{f} \sin \gamma \right) \tag{6-17}$$

$$Z'_p = \frac{bx_1}{x_1 + x_2} \left(\cos \gamma - \frac{x_2}{f} \sin \gamma \right) + Z_1 \tag{6-18}$$

$$Z''_p = \frac{bz_2}{x_1 + x_2} \left(\cos \gamma - \frac{x_2}{f} \sin \gamma \right) + \frac{bz_2}{f} \sin \gamma + Z_2 \tag{6-19}$$

Case III - Convergent, horizontal camera axes

$$Y_p = bp \cdot K \tag{6-20}$$

$$X_p = bx_1 \cdot K \tag{6-21}$$

$$Z'_p = bz_1 K + Z_1 \tag{6-22}$$

$$Z''_p = bz_2 \left(K + \frac{\sin \gamma}{f}\right) + Z_2 \tag{6-23}$$

where

$$K = \frac{(f \cos \delta - x_2 \sin \delta)}{(f^2 + x_1 x_2) \sin (\gamma - \delta) + f (x_1 - x_2) \cos (\gamma - \delta)} \tag{6-24}$$

Thus far, the derivation has been concerned with computing in a local coordinate system. In order to transfer these values into map coordinates it is necessary to know the azimuth ρ of the optical axis. This is accomplished by applying an azimuthal rotation matrix directly to Equation (6-6) to yield:

$$\bar{P} \begin{bmatrix} \cos \rho & \sin \rho & 0 \\ -\sin \rho & \cos \rho & 0 \\ 0 & 0 & 1 \end{bmatrix} \begin{bmatrix} 1 & 0 & 0 \\ 0 & \cos \lambda & -\sin \lambda \\ 0 & \sin \lambda & \cos \lambda \end{bmatrix} \begin{bmatrix} \cos \psi & 0 & \sin \psi \\ 0 & 1 & 0 \\ -\sin \psi & 0 & \cos \psi \end{bmatrix} \begin{bmatrix} x'' \\ y'' \\ -z'' \end{bmatrix} \tag{6-25}$$

6.1.1.2 Error Coefficients

Since stereophotogrammetric techniques are not geometrically different from a sequence of continuous photogrammetric intersections, it is possible to analyze the mapping system in the general sense, which may then be modified according to the operational mode. There are three such modes which may be employed:

1. Stereophotogrammetric mode, using a fixed (split optics) base line

2. Stereophotogrammetric mode, using distinct camera stations, so that the base line is variable

3. Intersection photogrammetry.

For this analysis, the following error sources are considered:

1. Photo coordinate errors caused by:

   a. measuring apparatus

   b. identification errors

   c. limiting picture resolution.

2. Errors in the base line

3. Errors in the angular measurements of the television line of sight in the angles ψ, λ, and ρ

4. Errors in the camera station position

5. Errors in the calibrated focal length of lenses

6. Errors in the location of the intersection of the optical axis

7. Picture distortions:

   a. lens distortion

   b. non-linearity of scan lines.

Considering Equations (6-20) through (6-23) which describe the most general case of camera positions, the error in coordinate measurement may be written as: (e. g.)

$$\Delta X_p = \frac{\partial X_p}{\partial b} \Delta b + \frac{\partial X_p}{\partial x_1''} \Delta x_1'' + \frac{\partial X_p}{\partial y_1''} \Delta y_1'' + \frac{\partial X_p}{\partial z_1''} \Delta z_1'' + \frac{\partial X_p}{\partial \rho_1} \Delta \rho_1$$

$$+ \frac{\partial X_p}{\partial \lambda_1} \Delta \lambda_1 + \frac{\partial X_p}{\partial \psi_1} \Delta_{\psi 1} + \frac{\partial X_p}{\partial x_2''} \Delta x_2'' + \frac{\partial X_p}{\partial y_2''} \Delta y_2'' + \frac{\partial X_p}{\partial z_2''} \Delta z_2''$$

$$+ \frac{\partial X_p}{\partial \rho_2} \Delta \rho_2 + \frac{\partial X_p}{\partial \lambda_2} \Delta \lambda_2 + \frac{\partial X_p}{\partial \psi_2} \Delta \psi_2 + \frac{\partial X_p}{\partial \alpha_b} \Delta \alpha_b \qquad (6\text{-}26)$$

The individual error terms for Equation (6-26) are:

$$\frac{\partial X_p}{\partial b} \Delta b = \frac{X_p}{b} \Delta b = \frac{X_p}{b^2}\Big[(X_2 - X_1)(\Delta X_2 - \Delta X_1) + (Y_2 - Y_1)(\Delta Y_2 - \Delta Y_1) + (Z_2 - Z_1)(\Delta Z_2 - \Delta Z_1)\Big]\Delta b \tag{6-27}$$

$$\frac{\partial X_p}{\partial x_1''} \Delta x_1'' = X_p\left[\frac{a_{11}'}{x_1} - \frac{1}{D}\left((a_{21}' y_2 + a_{11}' x_2)\sin(\gamma - \delta) + (a_{11}' y_2 - a_{21}' x_2)\cos(\gamma - \delta)\right)\right]\Delta x_1'' \tag{6-28}$$

$$\frac{\partial X_p}{\partial y_1''} \Delta y_1'' = X_p\left[\frac{a_{12}'}{x_1} - \frac{1}{D}\left((a_{22}' y_2 + a_{12}' x_2)\sin(\gamma - \delta) + (a_{12}' y_2 - a_{22} x_2)\cos(\gamma - \delta)\right)\right]\Delta y_1'' \tag{6-29}$$

$$\frac{\partial X_p}{\partial z_1''} \Delta z_1'' = X_p\left[\frac{a_{13}'}{x_1} - \frac{1}{D}\left((a_{13}' x_2 + a_{23}' y_2)\sin(\gamma - \delta) + (a_{13}' y_2 - a_{23}' x_2)\cos(\gamma - \delta)\right)\right]\Delta z_1'' \tag{6-30}$$

$$\frac{\partial X_p}{\partial x''_2}\,\Delta x''_2 = X_p\left[\frac{a^2_{21}\cos\delta - a^2_{11}\sin\delta}{N} - \frac{1}{D}\left((a^2_{21}\,y_1 + a^2_{11}\,x_1)\sin(\gamma-\delta) + (a^2_{21}\,x_1 - a^2_{11}\,y_1)\cos(\gamma-\delta)\right)\right]\Delta x''_2 \tag{6-31}$$

$$\frac{\partial X_p}{\partial y''_2}\,\Delta y''_2 = X_p\left[\frac{a^2_{22}\cos\delta - a^2_{12}\sin\delta}{N} - \frac{1}{D}\left((a^2_{22}\,y_1 + a^2_{12}\,x_1)\sin(\gamma-\delta) + (a^2_{22}\,x_1 - a^2_{12}\,y_1)\cos(\gamma-\delta)\right)\right]\Delta y''_2 \tag{6-32}$$

$$\frac{\partial X_p}{\partial z''_2}\,\Delta z''_2 = X_p\left[\frac{a^2_{23}\cos\delta - a^2_{13}\sin\delta}{N} - \frac{1}{D}\left((a^2_{23}\,y_1 + a^2_{13}\,x_1)\sin(\gamma-\delta) + (a^2_{23}\,x_1 - a^2_{13}\,y_1)\cos(\gamma-\delta)\right)\right]\Delta z''_2 \tag{6-33}$$

$$\frac{\partial X_p}{\partial \rho_1}\,\Delta\rho_1 = X_p\left[\frac{\vec{\rho}_{11}\cdot\vec{p}_1}{x_1} - \frac{1}{D}\left(\begin{array}{l}(\vec{\rho}_{21}\cdot\vec{p}_1 y_2 + \vec{\rho}_{11}\cdot\vec{p}_1 x_2 - x_1 y_2 + x_2 y_1)\sin(\gamma-\delta)\\ + (\vec{\rho}_{11}\cdot\vec{p}_1 y_2 - \vec{\rho}_{21}\cdot\vec{p}_1 x_2 + y_1 y_2 + x_1 x_2)\cos(\gamma-\delta)\end{array}\right)\right]\Delta\rho_1 \tag{6-34}$$

$$\frac{\partial X_p}{\partial \rho_1}\,\Delta\lambda_1 = X_p\left[\frac{\vec{\lambda}_{11}\cdot\vec{p}_1}{x_1} - \frac{1}{D}\left(\begin{array}{l}(\vec{\lambda}_{21}\cdot\vec{p}_1\,y_2 + \vec{\lambda}_{11}\cdot\vec{p}_1\,x_2)\sin(\gamma-\delta)\\ + (\vec{\lambda}_{11}\cdot\vec{p}_1\,y_2 - \vec{\lambda}_{21}\cdot\vec{p}_1\,x_2)\cos(\gamma-\delta)\end{array}\right)\right]\Delta\lambda_1 \tag{6-35}$$

$$\frac{\partial X_p}{\partial \psi_1}\,\Delta\psi_1 = X_p\left[\frac{\vec{\psi}_{11}\cdot\vec{p}_1}{x_1} - \frac{1}{D}\left(\begin{array}{l}(\vec{\psi}_{21}\cdot\vec{p}_1\,y_2 + \vec{\psi}_{11}\cdot\vec{p}_1\,x_2)\sin(\gamma-\delta)\\ + (\vec{\psi}_{11}\cdot\vec{p}_1\,y_2 - \vec{\psi}_{21}\cdot\vec{p}_1\,x_2)\cos(\gamma-\delta)\end{array}\right)\right]\Delta\psi_1 \tag{6-36}$$

$$\frac{\partial X_p}{\partial \rho_2} \Delta\rho_2 = X_p \left[\frac{(\vec{\rho}_{22} \cdot \vec{p}_2 - x_2) \cos\delta - (\vec{\rho}_{12} \cdot \vec{p}_2 - y_2) \sin\delta}{N} \right. \tag{6-37}$$

$$\left. - \frac{1}{D} \left(\begin{array}{l} (\vec{\rho}_{22} \cdot \vec{p}_2 y_1 + \vec{\rho}_{12} \cdot \vec{p}_2 x_1 - x_1 y_2 + x_2 y_1) \sin(\gamma - \delta) \\ + (\vec{\rho}_{22} \cdot \vec{p}_2 x_1 - \vec{\rho}_{12} \cdot \vec{p}_2 y_1 + y_1 y_2 + x_1 x_2) \cos(\gamma - \delta) \end{array} \right) \right] \Delta\rho_2$$

$$\frac{\partial X_p}{\partial \lambda_2} \Delta\lambda_2 = X_p \left[\frac{\vec{\lambda}_{22} \cdot \vec{p}_2 \cos\delta - \vec{\lambda}_{12} \cdot \vec{p}_2 \sin\delta}{N} \right. \tag{6-38}$$

$$\left. - \frac{1}{D} \left(\begin{array}{l} (\vec{\lambda}_{22} \cdot \vec{p}_2 y_1 + \vec{\lambda}_{11} \cdot \vec{p}_2 x_1) \sin(\gamma - \delta) \\ + (\vec{\lambda}_{22} \cdot \vec{p}_2 x_1 - \vec{\lambda}_{11} \cdot \vec{p}_2 y_1) \cos(\gamma - \delta) \end{array} \right) \right] \Delta\lambda_2$$

$$\frac{\partial X_p}{\partial \psi_2} \Delta\psi_2 = X_p \left[\frac{\vec{\psi}_{22} \cdot \vec{p}_2 \cos\delta - \vec{\psi}_{12} \cdot \vec{p}_2 \sin\delta}{N} \right. \tag{6-39}$$

$$\left. - \frac{1}{D} \left(\begin{array}{l} (\vec{\psi}_{22} \cdot \vec{p}_2 y_1 + \vec{\psi}_{12} \cdot \vec{p}_2 x_1) \sin(\gamma - \delta) \\ + (\vec{\psi}_{22} \cdot \vec{p}_2 x_1 - \vec{\psi}_{12} \cdot \vec{p}_2 y_1) \cos(\gamma - \delta) \end{array} \right) \right] \Delta\psi_2$$

$$\frac{\partial X}{\partial \alpha_b} \Delta\alpha_b = \frac{-X_p}{N} (y_2 \sin\delta + x_2 \cos\delta) \Delta\alpha_b \tag{6-40}$$

$$\frac{\partial X}{\partial \alpha_b} \Delta\alpha_b = \frac{-X_p}{N} \left[(y_2 \sin\delta + x_2 \cos\delta) \left(\frac{\Delta X_2 - \Delta X_1}{(Y_2 - Y_1)} + \frac{(X_2 - X_1)\Delta Y_1 - (X_2 - X_1)\Delta Y_2}{(Y_2 - Y_1)^2} \right) \right] \tag{6-41}$$

Where $\bar{\rho}_{11}, \bar{\rho}_{12} \ldots \bar{\lambda}_{11}, \bar{\lambda}_{12} \ldots \bar{\psi}_{11}, \bar{\psi}_{12} \ldots$ are row vectors obtained by partial differentiation of the matrices $[\rho]$ $[\lambda]$ $[\psi]$ in Equation (6-25). The items $a_{11}, a_{12} \ldots a_{33}$ denote the rows and columns of that original matrix, the superscripts denoting the first or second camera station. The vector $[x'', y'', z'']$ is denoted by $\bar{\rho}$.

The corresponding error coefficients for Y_p and Z'_p are:

$$\frac{\partial Y_p}{\partial b} = \frac{Y_p}{b} \tag{6-42}$$

$$\frac{\partial Y_p}{\partial x''_1} = Y_p \left[\frac{a'_{21}}{y_1} - \frac{1}{D} \left((a'_{21} y_2 - a'_{11} x_2) \sin(\gamma - \delta) + (a'_{11} y_2 - a'_{21} x_2) \cos(\gamma - \delta) \right) \right] \Delta x''_1 \tag{6-43}$$

$$\frac{\partial Y_p}{\partial y''_1} = Y_p \left[\frac{a'_{22}}{y_1} - \frac{1}{D} \left((a'_{22} y_2 + a'_{12} x_2) \sin(\gamma - \delta) + (a'_{12} y_2 - a'_{22} x_2) \cos(\gamma - \delta) \right) \right] \Delta y''_1 \tag{6-44}$$

$$\frac{\partial Y_p}{\partial z''_1} = Y_p \left[\frac{a'_{23}}{y_1} - \frac{1}{D} \left((a'_{13} x_2 + a'_{23} y_2) \sin(\gamma - \delta) + (a'_{13} y_2 - a'_{23} x_2) \cos(\gamma - \delta) \right) \right] \Delta z''_1 \tag{6-45}$$

$$\frac{\partial Y_p}{\partial x''_2} = \frac{Y_p}{X_p} \cdot \frac{\partial X_p}{\partial x''_2} \tag{6-46}$$

$$\frac{\partial Y_p}{\partial y''_2} = \frac{Y_p}{X_p} \cdot \frac{\partial X_p}{\partial y''_2} \tag{6-47}$$

$$\frac{\partial Y_p}{\partial z''_2} = \frac{Y_p}{X_p} \cdot \frac{\partial X_p}{\partial z''_2} \tag{6-48}$$

$$\frac{\partial Y_p}{\partial \rho_1} = Y_p \left[\frac{\vec{\rho}_{21} \cdot \vec{p}_1}{y_1} - \frac{1}{D} \left(\begin{array}{l} (\vec{\rho}_{21} \cdot \vec{p}_1 y_2 + \vec{\rho}_{11} \cdot \vec{p}_1 x_2 - x_1 y_2 + x_2 y_1) \sin(\gamma - \delta) \\ + (\vec{\rho}_{11} \cdot \vec{p}_1 y_2 - \vec{\rho}_{21} \cdot \vec{p}_1 x_2 + y_1 y_2 + x_1 x_2) \cos(\gamma - \delta) \end{array} \right) \right] \tag{6-49}$$

$$\frac{\partial Y_p}{\partial \lambda_1} = Y_p \left[\frac{\vec{\lambda}_{21} \cdot \vec{p}_1}{y_1} - \frac{1}{D} \left(\begin{array}{l} (\vec{\lambda}_{21} \cdot \vec{p}_1 y_2 + \vec{\lambda}_{11} \cdot \vec{p}_1 x_2) \sin(\gamma - \delta) \\ + (\vec{\lambda}_{11} \cdot \vec{p}_1 y_2 - \vec{\lambda}_{21} \cdot \vec{p}_1 x_2) \cos(\gamma - \delta) \end{array} \right) \right] \tag{6-50}$$

$$\frac{\partial Y_p}{\partial \psi_1} = Y_p \left[\frac{\vec{\psi}_{21} \cdot \vec{p}_1}{y_1} - \frac{1}{D} \left(\begin{array}{l} (\vec{\psi}_{21} \cdot \vec{p}_1 y_2 + \vec{\psi}_{11} \cdot \vec{p}_1 x_2) \sin(\gamma - \delta) \\ + (\vec{\psi}_{11} \cdot \vec{p}_1 y_2 - \vec{\psi}_{21} \cdot \vec{p}_1 x_2) \cos(\gamma - \delta) \end{array} \right) \right] \tag{6-51}$$

$$\frac{\partial Y_p}{\partial \rho_2} = \frac{Y_p}{X_p} \cdot \frac{\partial X_p}{\partial \rho_2} \tag{6-52}$$

$$\frac{\partial Y_p}{\partial \lambda_2} = \frac{Y_p}{X_p} \cdot \frac{\partial X_p}{\partial \lambda_2} \tag{6-53}$$

$$\frac{\partial Y_p}{\partial \psi_2} = \frac{Y_p}{X_p} \cdot \frac{\partial X_p}{\partial \psi_2} \tag{6-54}$$

$$\frac{\partial Y_p}{\partial \delta} = \frac{\partial X_p}{\partial \delta} \cdot \frac{Y_p}{X_p} \tag{6-55}$$

$$\frac{\partial Z}{\partial b} = \frac{Z_p}{b} \tag{6-56}$$

$$\frac{\partial Z}{\partial x_1''} = Z_p \left[\frac{a_{31}}{z_1} - \frac{a_{21}}{y_1} - \frac{1}{D} \left(\begin{array}{l} (a_{21}' y_2 + a_{11}' x_2) \sin(\gamma - \delta) \\ + (a_{11}' y_2 - a_{21}' x_2) \cos(\gamma - \delta) \end{array} \right) \right] \tag{6-57}$$

$$\frac{\partial Z}{\partial y_1''} = Z_p \left[\frac{a_{32}}{z_1} - \frac{a_{22}}{y_1} - \frac{1}{D} \left(\begin{array}{l} (a_{22}' y_2 + a_{12}' x_2) \sin(\gamma - \delta) \\ + (a_{12}' y_2 - a_{22} x_2) \cos(\gamma - \delta) \end{array} \right) \right] \tag{6-58}$$

$$\frac{\partial Z}{\partial z_1''} = Z_p \left[\frac{-a_{33}}{z_1} + \frac{a_{23}}{y_1} - \frac{1}{D} \left(\begin{array}{l} (a_{13}' x_2 + a_{23}' y_2) \sin(\gamma - \delta) \\ + (a_{13}' y_2 - a_{23}' x_2) \cos(\gamma - \delta) \end{array} \right) \right] \tag{6-59}$$

$$\frac{\partial Z}{\partial x_2''} = \frac{Z_p}{X_p} \cdot \frac{\partial X}{\partial x_2''} \tag{6-60}$$

$$\frac{\partial Z}{\partial y_2'} = \frac{Z_p}{X_p} \cdot \frac{\partial X}{\partial y_2''} \tag{6-61}$$

$$\frac{\partial Z}{\partial z''_2} = \frac{Z_p}{X_p} \cdot \frac{\partial X}{\partial z''_2} \tag{6-62}$$

$$\frac{\partial Z_p}{\partial \rho_1} = Z_p \left[\frac{-\vec{\rho}_{21} \cdot \vec{p}_1}{y_1} - \frac{1}{D} \left(\begin{array}{l} (\vec{\rho}_{21} \cdot \vec{p}_1 \, y_2 + \vec{\rho}_{11} \cdot \vec{p}_1 \, x_2 - x_1 \, x_2 \, y_1) \sin(\gamma - \delta) \\ + (\vec{\rho}_{11} \cdot \vec{p}_1 \, y_2 - \vec{\rho}_{21} \cdot \vec{p}_1 \, x_2 + y_1 \, y_2 + x_1 \, x_2) \cos(\gamma - \delta) \end{array} \right) \right] \tag{6-63}$$

$$\frac{\partial Z_p}{\partial \lambda_1} = Z_p \left[\frac{\vec{\lambda}_{31} \cdot \vec{p}_1}{z_1} - \frac{\vec{\lambda}_{21} \cdot \vec{p}_1}{y_1} - \frac{1}{D} \left(\begin{array}{l} (\vec{\lambda}_{21} \cdot \vec{p}_1 y_2 + \vec{\lambda}_{11} \cdot \vec{p}_1 \, x_2) \sin(\gamma - \delta) \\ + (\vec{\lambda}_{11} \cdot \vec{p}_1 \, y_2 - \vec{\lambda}_{21} \cdot \vec{p}_1 x_2) \cos(\gamma - \delta) \end{array} \right) \right] \tag{6-64}$$

$$\frac{\partial Z_p}{\partial \psi_1} = Z_p \left[\frac{\vec{\psi}_{31} \cdot \vec{p}_1}{z_1} - \frac{\vec{\psi}_{21} \cdot \vec{p}_1}{y_1} - \frac{1}{D} \left(\begin{array}{l} (\vec{\psi}_{21} \cdot \vec{p}_1 \, y_2 + \vec{\psi}_{11} \cdot \vec{p}_1 \, x_2) \sin(\gamma - \delta) \\ + (\vec{\psi}_{11} \cdot \vec{p}_1 y_2 - \vec{\psi}_{21} \cdot \vec{p}_1 x_2) \cos(\gamma - \delta) \end{array} \right) \right] \tag{6-65}$$

$$\frac{\partial Z_p}{\partial \rho_2} = \frac{Z_p}{X_p} \cdot \frac{\partial X_p}{\partial \rho_2} \tag{6-66}$$

$$\frac{\partial Z_p}{\partial \lambda_2} = \frac{Z_p}{X_p} \cdot \frac{\partial X_p}{\partial \lambda_2} \tag{6-67}$$

$$\frac{\partial Z_p}{\partial \psi_2} = \frac{Z_p}{X_p} \cdot \frac{\partial X_p}{\partial \psi_2} \tag{6-68}$$

$$\frac{\partial Z_p}{\partial \alpha_b} = \frac{Z_p}{X_p} \cdot \frac{\partial X_p}{\partial \alpha_b} \tag{6-69}$$

$$\frac{\partial Z_p}{\partial \delta} = \frac{Z_p}{X_p} \cdot \frac{\partial X_p}{\partial \delta} \tag{6-70}$$

6.1.1.3 System Errors

The application of the formulae given in Section 6.1.1.2 to an analysis of the mapping system is dependent on the operational mode. The modifications for each mode are given below.

Mode I - Fixed Base Stereophotogrammetry

In this case, when using a split optics base line, the lines of sight are nominally parallel and normal to the base. Provided that no significant manufacturing errors are present, only small discrepancies between the corresponding angles λ_1 and λ_2, and ψ_1 and ψ_2, and ρ_1 and ρ_2 need to be considered.

Consequently, the analysis of mode I will be restricted to the following error sources:

1. Error (Δb) in the base length (b)
2. Error (Δf) in the focal length (f)
3. Error ($\Delta\alpha_b$) in the base line azimuth (α_b)
4. Errors ($\Delta\psi_1$ and $\Delta\psi_2$) in the depression angles ψ_1, ψ_2
5. Errors ($\Delta\lambda_1$ and $\Delta\lambda_2$) in the leveling angles λ_1, λ_2
6. Errors ($\Delta x''$, $\Delta z''$) in the measured image coordinates x'', z''
7. Error ($\Delta\delta$) in the convergence angle of the lines of sight δ
8. Errors in the SLRV position coordinates.

Mode II-Variable Base Stereophotogrammetry

All component errors will have to be considered in this case, although specific modification may be made:

1. The base length error, Δb, and base azimuth error $\Delta\alpha_b$, are considered to be functions of the terminal coordinate errors. For short base lines however, the error Δb may be considered to be the same as the error in the odometer readout.

2. The error in the lines of sight $\Delta\alpha_1$ and $\Delta\alpha_2$ may be combined into a single error in the angle of convergence associated with the base azimuth error, $\Delta\alpha_b$.

Image Measurement Errors

The errors incurred in measurement of image coordinates are caused by:

1. The precision of the measuring apparatus

2. The accuracy with which the point of intersection of the optical axis with the image plane may be recovered

3. The accuracy with which the usual optical distortions may be removed

4. The limiting resolution of the television system

5. The accuracy with which the nonlinearity effects of the television scan lines may be removed

6. The temporal and environmental variation of these items.

A standard error of ± 15 microns is assumed for the first three factors which are common to all photogrammetry.

The television system resolution is defined by the number of effective resolution elements over the vidicon format. If the format has the dimension a x a and the number of effective resolution elements is n, then the separation between corresponding edges of adjacent elements is:

$$\ell = \frac{a}{n}$$

A point object will be imaged as an element of dimension ℓ and thus is capable of being located to $\pm 0.5\ \ell$ at best. This corresponds to about 14μ on the 11 x 11 mm vidicon format at 512 total scan lines.

Controlling the television scan non-linearity to less than 1% would be extremely difficult. However, non-linearity is important only insofar as

one is not able to correct it by means of a reference reseau on the vidicon. For non-linearity correction in error by 0.25%, and a format size of a x a, the errors in the corrected point coordinates are

$$dx'' = \left(\pm \frac{a}{2} + x''_p\right) \frac{1}{400}$$

and

$$dy'' = \left(\pm \frac{a}{2} + z''_p\right) \frac{1}{400}$$

where x''_p and z''_p are the measured coordinates with respect to the intersection of the optical axis with the image plane, thus for a format size 11 x 11 mm these errors attain maximum values of $\pm$ 28 μ.

By compounding these errors with the resolution errors quadratically, one obtains the expected errors in the reduced coordinate measurements to be within the ranges shown in Figure 6-4.

The ability to measure coordinates on the television image with these anticipated accuracies was investigated by experiment. A series of photographs was taken on the lunar photometric model at Bendix Systems Division. One steroscopic pair was selected for processing at Raytheon into simulated television images of 400, 200, 150 and 100 elements; 2, 3, and 4 bits; and with and without Robert's Modulation. Samples of these television images are shown in Figures 6-5 and 6-6.

The parallaxes of 20 conjugate image points were measured by means of a Wild parallax bar and mirror stereoscope on both the original photographs and television images. The parallax errors for each set of television images were then computed from the measurements.

The results show that for all the 400-line images, the mean parallax errors are grouped about $\pm$ 41 μ. Assuming an rms combination, the uncertainty in the individual measurements is $\pm$ 29 μ. This is on the lower end of the analytically derived errors.

The method of encoding and bit levels appear to have only a second order effect on measurement errors.

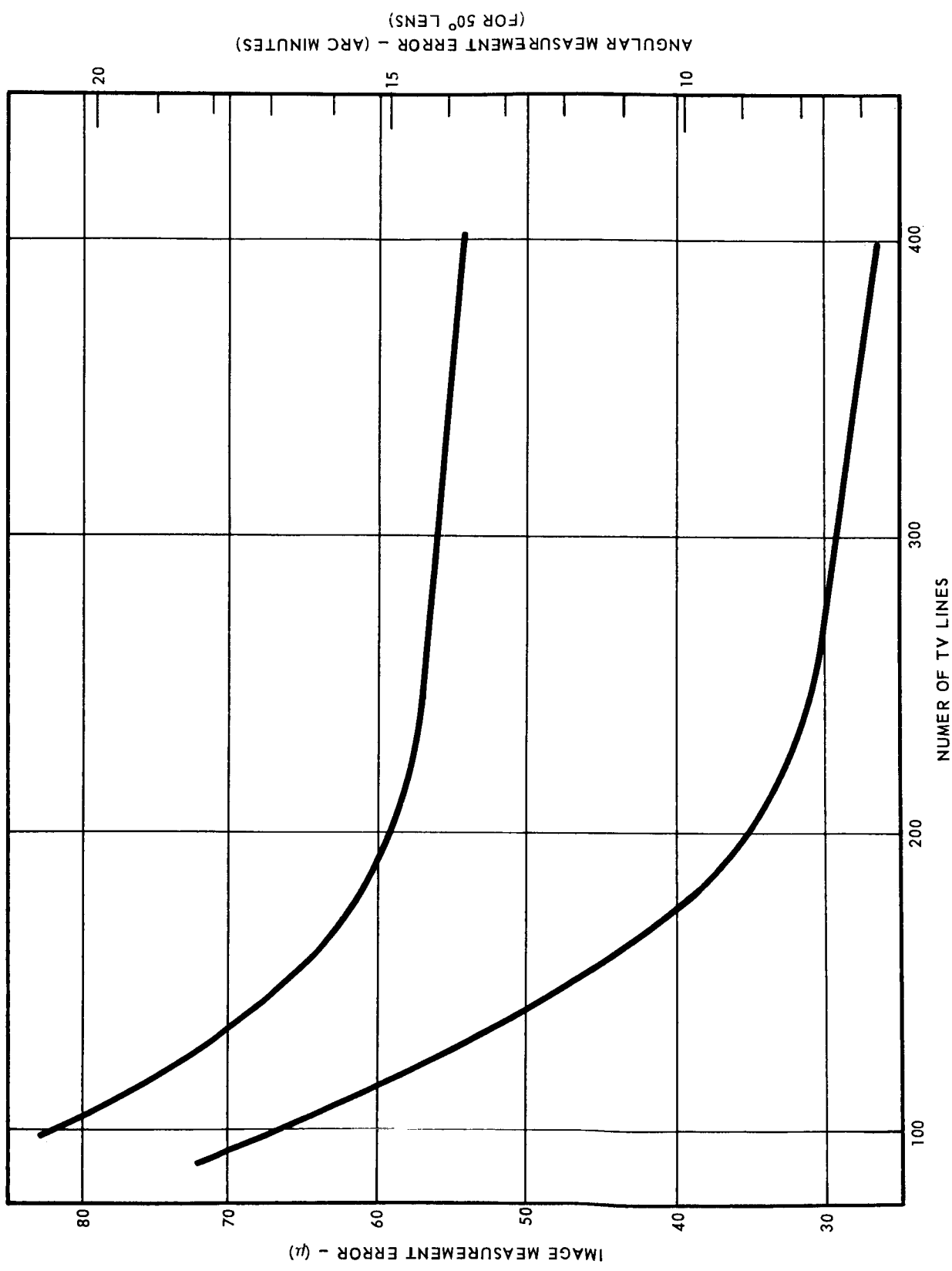

Figure 6-4 Image Measurement Error (11 x 11 Mm Format)

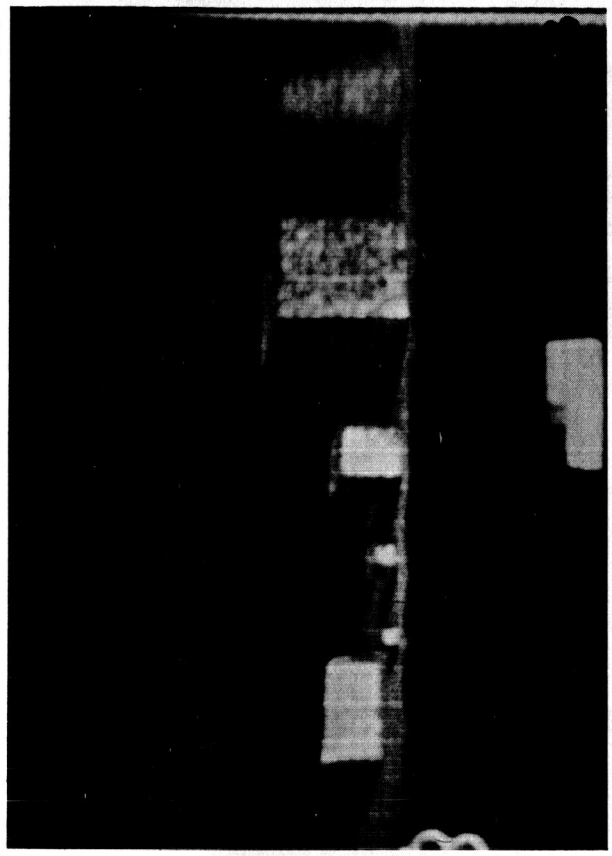

3-5

400 LINE, 3 BIT ROBERTS

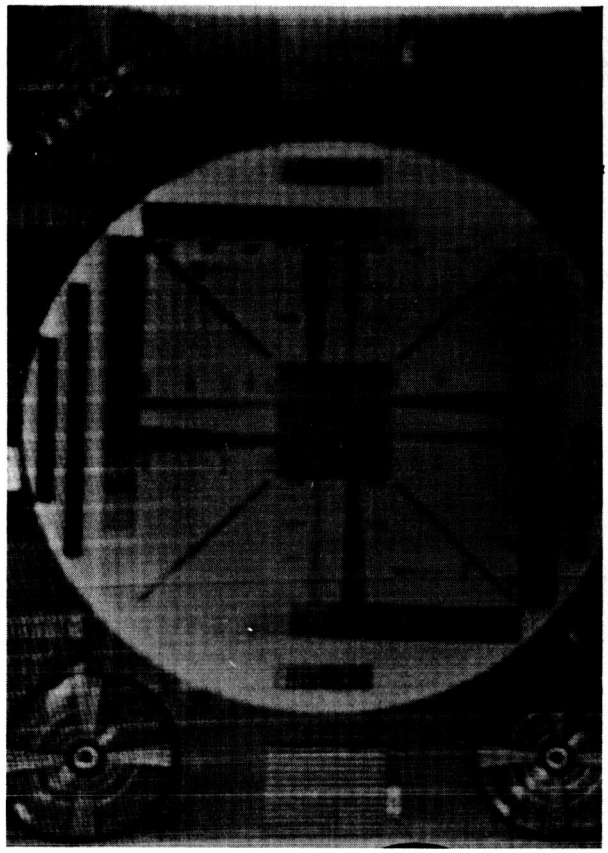

4-3

400 LINE, 4 BIT ROBERTS

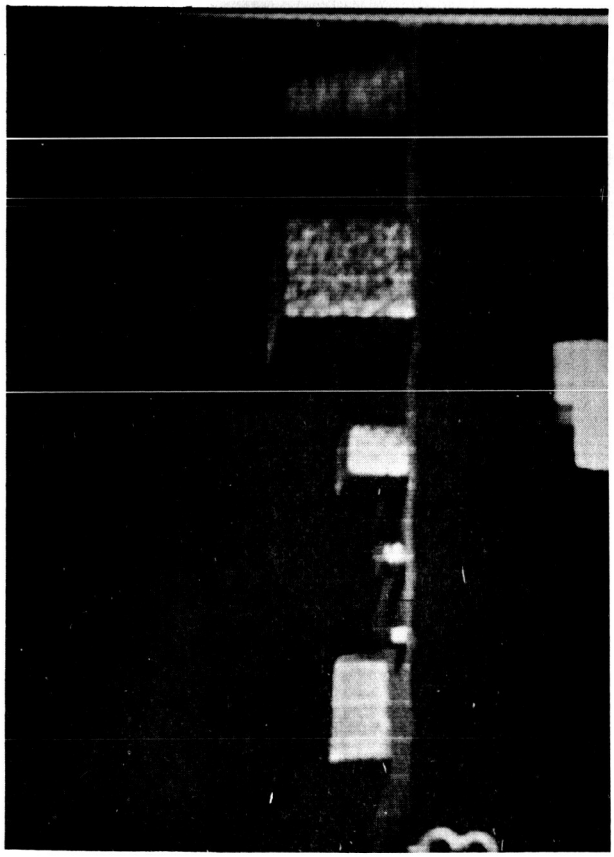

4-1

400 LINE, 4 BIT PCM

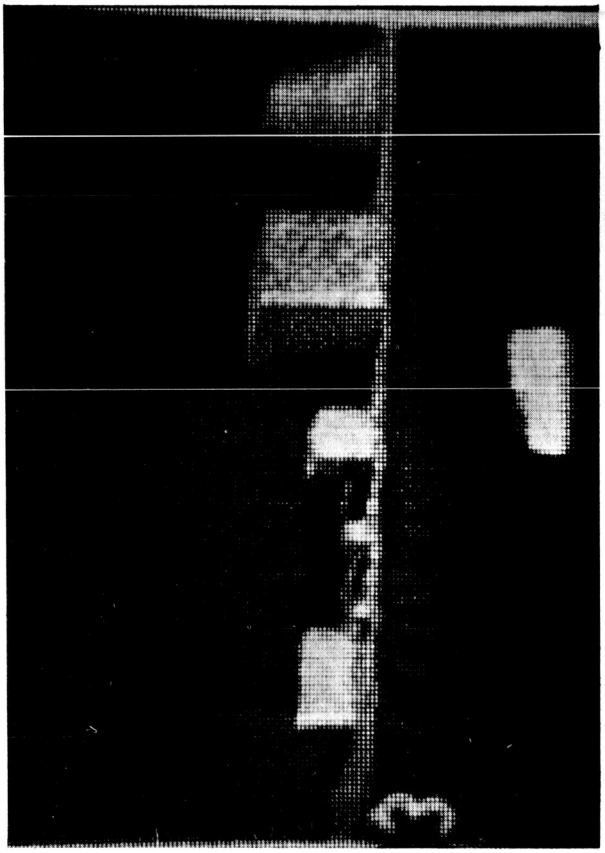

2-1

200 LINE, 3 BIT ROBERTS

Figure 6-5 Image Measurement Samples, (Sheet 1 of 2)

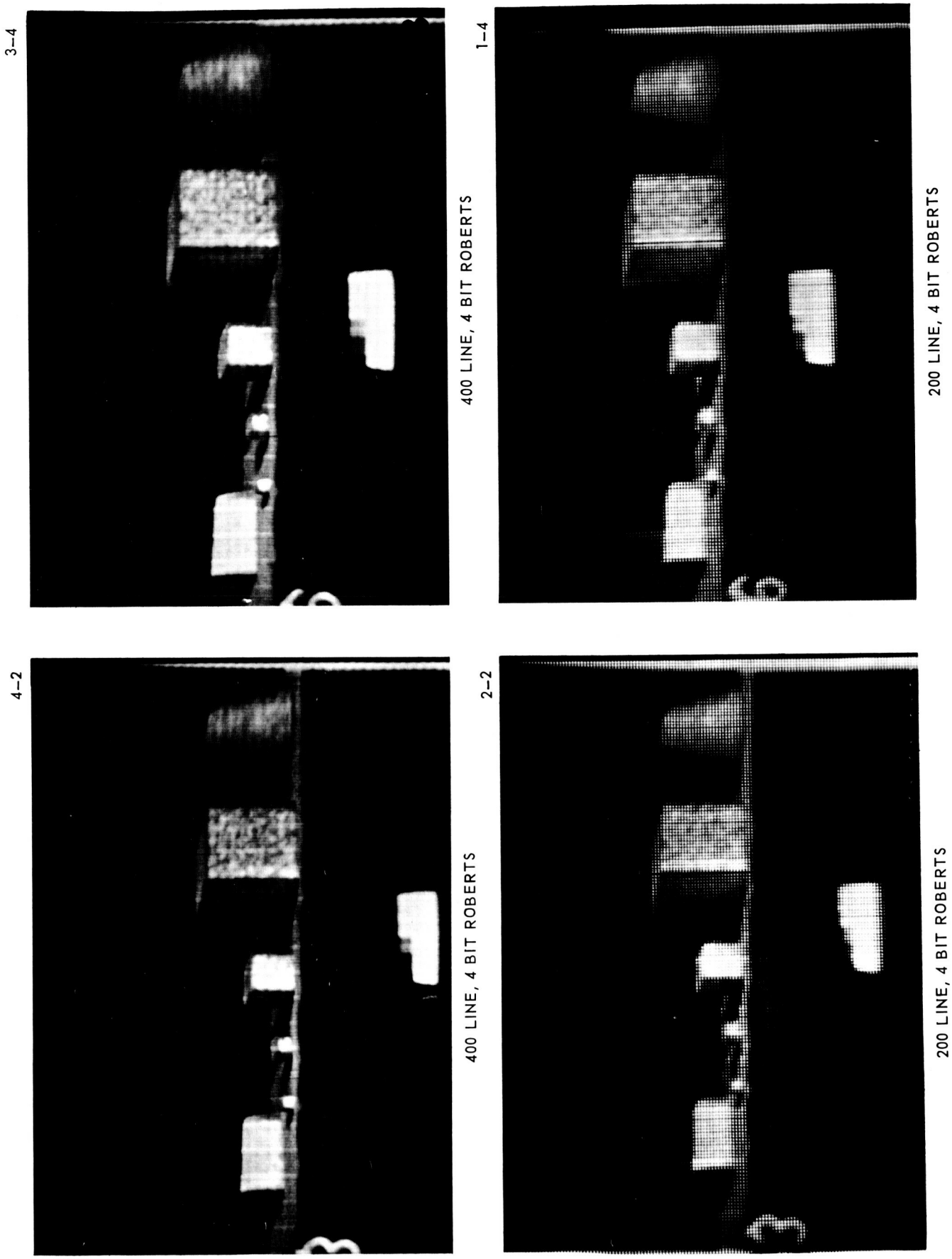

Figure 6-6 Image Measurement Samples, (Sheet 2 of 2)

For the 200-line television images, the results were significantly poorer. Only a small percentage of the conjugate image points could be positively identified and measured. No statistical significance can be attached to the few errors measured.

Images with fewer than 200 scan lines have no value for photogrammetry.

Measurement Errors in Object Space

Total system errors are now considered, assuming nominally leveled cameras, and that the azimuth errors $\Delta\rho_1$ and $\Delta\rho_2$ are combined into an azimuth error $\Delta\delta$ of the second camera station. For this case, the coefficients of each error term are listed in Table 6-1.

To each of these error coefficients are applied the following set of parametric values:

1. Base length error (Δb) = 3% b
2. Base length (b) = 3 m
3. Average image measurement error $\Delta z = \Delta x = 0.050$ mm
4. Focal length f = 13.62 mm
5. Angular measurement errors $\Delta\lambda = \Delta\psi = \psi\rho = 1/4^{\circ}$.

These then yield the following rms coordinate errors in measuring a point at 6 meters range, 50-cm elevation (the maximum tolerable obstacle size).

$$\Delta Z = \pm 4.8 \text{ cm}$$

$$\Delta Y = \pm 22 \text{ cm}$$

$$\Delta X = \pm 4.7 \text{ cm}$$

The resulting measurement errors appear to conform very closely to the system requirements particularly in x and z. The y measurement error

TABLE 6-1

COMPONENT ERRORS FOR NORMAL CASE, LINE SIGHT HORIZONTAL

Error Source	Error in X	Error in Y	Error in Z
Δb	$\frac{X}{b}\ \Delta b$	$\frac{Y}{b}\ \Delta b$	$\frac{Z}{b}\ \Delta b$
Δx_1	$X\left[\frac{1}{x_1} - \frac{1}{(x_1 - x_2)}\right]\Delta x_1$	$\frac{-Y}{(x_1 - x_2)}\ \Delta x_1$	$\frac{-Z}{(x_1 - x_2)}\ \Delta x_1$
Δx_2	$\frac{-X}{(x_1 - x_2)}\ \Delta x_2$	$\frac{-Y}{(x_1 - x_2)}\ \Delta x_2$	$\frac{-Z}{(x_1 - x_2)}\ \Delta x_2$
Δf	0	$\frac{Y\ \Delta f}{f}$	$\frac{Z\ \Delta f}{f}$
Δz_1	0	0	$\frac{Z\ \Delta z}{z}$
Δz_1	0	0	0
$\Delta\lambda_1$	$-X\ \frac{x_2 z_1}{f(x_1 - x_2)}\ \Delta\lambda_1$	$-Y\ \frac{x_2 z_1}{f(x_1 - x_2)}\ \Delta\lambda_1$	$-Z\ \frac{z_1 x_2}{f(x_1 - x_2)}\ \Delta\lambda_1$
$\Delta\lambda_2$	$-X\ \frac{x_2 z_2}{f(x_1 - x_2)}$	$-Y\ \frac{x_2 z_2}{f(x_1 - x_2)}\ \Delta\lambda_2$	$-Z\ \frac{x_2 z_2}{f(x_1 - x_2)}\ \Delta\lambda_2$
$\Delta\psi_1$	$-X\left[\frac{z_1}{x_1} - \frac{z_1}{(x_1 - x_2)}\right]\Delta\psi_1$	$-Y\ \frac{z_1}{(x_1 - x_2)}\ \Delta\psi_1$	$-Z\ \frac{z_1}{(x_1 - x_2)}\ \Delta\psi_1$
$\Delta\psi_2$	$-X\ \frac{z_2}{(x_1 - x_2)}\ \Delta\psi_2$	$-Y\ \frac{z_2}{(x_1 - x_2)}\ \Delta\psi_2$	$-Z\ \frac{z_2}{(x_1 - x_2)}\ \Delta\psi_2$
$\Delta\delta$	$X\ \frac{\left(f^2 + x_2^2\right)}{f(x_1 - x_2)}\ \Delta\delta$	$Y\ \frac{\left(f^2 + x_2^2\right)}{f(x_1 - x_2)}\ \Delta\delta$	$Z\ \frac{\left(f^2 + x_2^2\right)}{(f(x_1 - x_2)}\ \Delta\delta$

is considerably larger, however the effective slope is not particularly sensitive to y position errors. The effective slope (α) created by an obstacle is:

$$\tan \alpha = \frac{Z}{Y}$$

$$\therefore \frac{d\alpha}{dY} = \frac{Z}{Y^2 + Z^2}$$

Then over a 10-m base, an uncertainty of 22 cm in Y position of a 50-cm obstacle contributes only about 0.2° slope uncertainty.

In order to speed the computation of error values for various conditions the error coefficient curves, Figures 6-7 through 6-15 have been plotted. Figures 6-7 and 6-8 deal with the normal-horizontal axis case and the following illustrative example explains their use.

Let the conjugate points have the measured coordinates of $x_1 = +2$ mm, $z_1 = -1$ mm, $x_2 = -2$ mm, and $z_2 = -1$ mm; i.e., for a base of 1 m, Y = 3.4 m. Enter the graph using the value of the parallax 4 mm. Determine the ordinate at which the 4-mm abscissa intersects the hyperbola; i.e., 0.25. For an error of ± 50 μ in x_1 and x_2, errors in Y are 0.0426 meters; i.e., 4 cms. The intersection of the ordinate 0.25 with the line x or z = 1 mm, furnishes the abscissa of 0.45×10^{-2} on the scale $\Delta\psi$ (± 1° say) to yield the error of 0.015 m. Continue along this abscissa to the line indicating the field-of-view (50°) and traverse along the ordinate to the line x_2. Read the abscissa against the scale $\Delta\lambda / Y$, and multiply by Y $\Delta\lambda$ to yield the value $0.7 \times 10^{-3} \times 3.4 = 2.38 \times 10^{-3}$ m = 0.002 m. With a percentage error of 1% in the base length and 0.1% in the focal length, these errors yield the values of 0.034 and 0.003 m, respectively. $\Delta\delta$ of 1° yields an error of 0.0625 meters. Assuming that the errors due to $\Delta\psi_2$ and $\Delta\lambda_2$ are equal to those caused by $\Delta\psi$, and $\Delta\lambda_1$, the resulting coordinate error is:

$$\Delta Y = (225 + 225 + 1806 + 1806 + 4 + 4 + 9 + 1156)^{1/2} \times 10^{-3} \text{m} = \pm 7.27 \text{ cms}$$

The corresponding errors in X and Y are found by multiplying each Y error component by the ratios X/Y and Z/Y, respectively.

Figures 6-9 through 6-15 deal in a similar manner with the case of convergent images for a limited number of conveyance angles. These figures show error coefficients for a 50° lens. Similar curves are available for a 10° lens.

6.1.1.4 Obstacle Size From Photogrammetric Measurement

The true height dimension of an object (h) and its projected size on the image plane (δz) are related by

$$\frac{\delta z}{f} = \frac{h}{Y + f} \approx \frac{h}{Y}$$

or

$$h = \frac{Y \delta_z}{f}$$

where

Y = range to object

f = focal length

from which may be written

$$dh = \frac{\delta z}{f} dY + \frac{Y}{f} + \delta z - \frac{Y \delta_z}{f^2} df$$

Considering the error in focal length insignificant and substituting

$$Y = \frac{bf}{p}$$

$$dh = \frac{\delta z}{f} d \frac{bf}{p} + \frac{b}{p} d \delta z$$

$$= \frac{Y \delta_z}{f} \frac{df}{f} + \frac{db}{b} - \frac{dp}{p} + \frac{Y}{f} d \delta z$$

Again considering the error in focal length to be insignificant and substituting $\delta z = hf/Y$

$$dh = h \frac{db}{b} - \frac{dp}{p} + \frac{Y}{f} d \delta z$$

Considering each image measurement error to be in error by 50μ, the baseline by 3%, camera azimuth by 1/4°, a 5-m baseline measurement of an 18-cm obstacle at 20 m range yields a height uncertainty (dh) of ±2.1 cm.

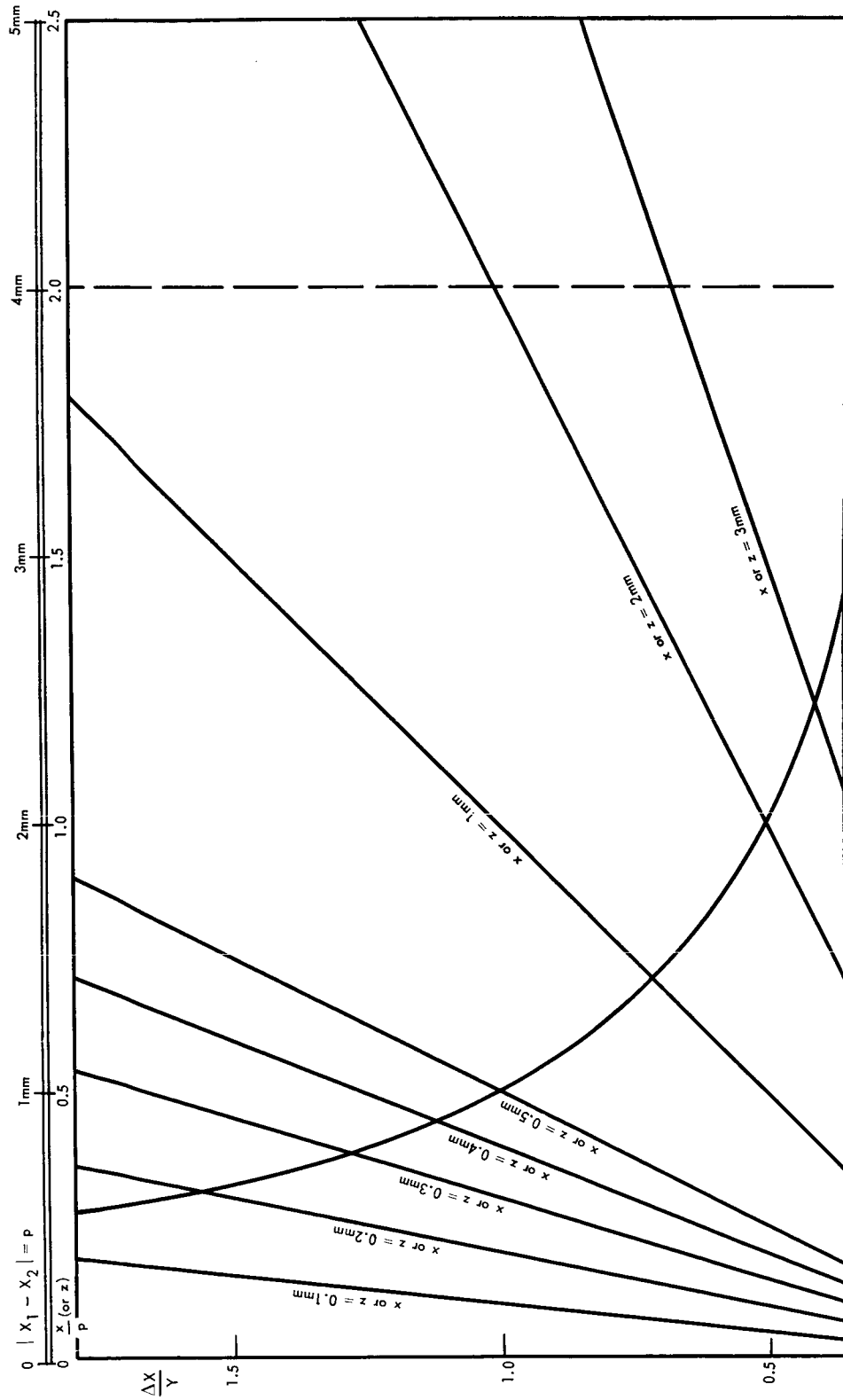
0
1mm
2mm
3mm
4mm
5mm
$|X_1 - X_2| = p$
$\frac{x}{p}$ (or z)
0
0.5
1.0
1.5
2.0
2.5
$\frac{\Delta X}{Y}$
1.5
1.0
0.5
x or z = 0.1mm
x or z = 0.2mm
x or z = 0.3mm
x or z = 0.4mm
x or z = 0.5mm
x or z = 1mm
x or z = 2mm
x or z = 3mm

#1

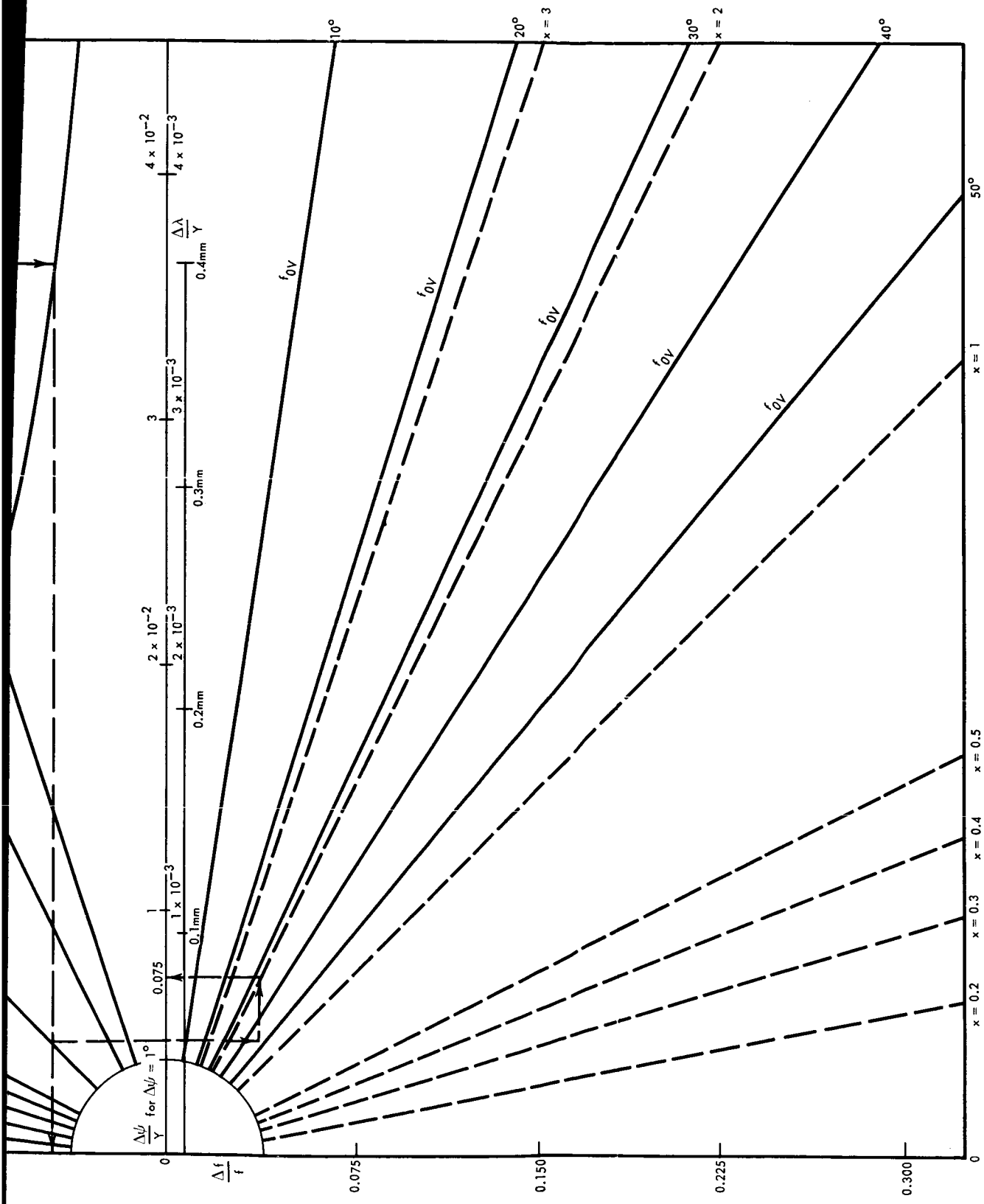

Figure 6-7 Error Coefficient for Normal Horizontal Case

#2

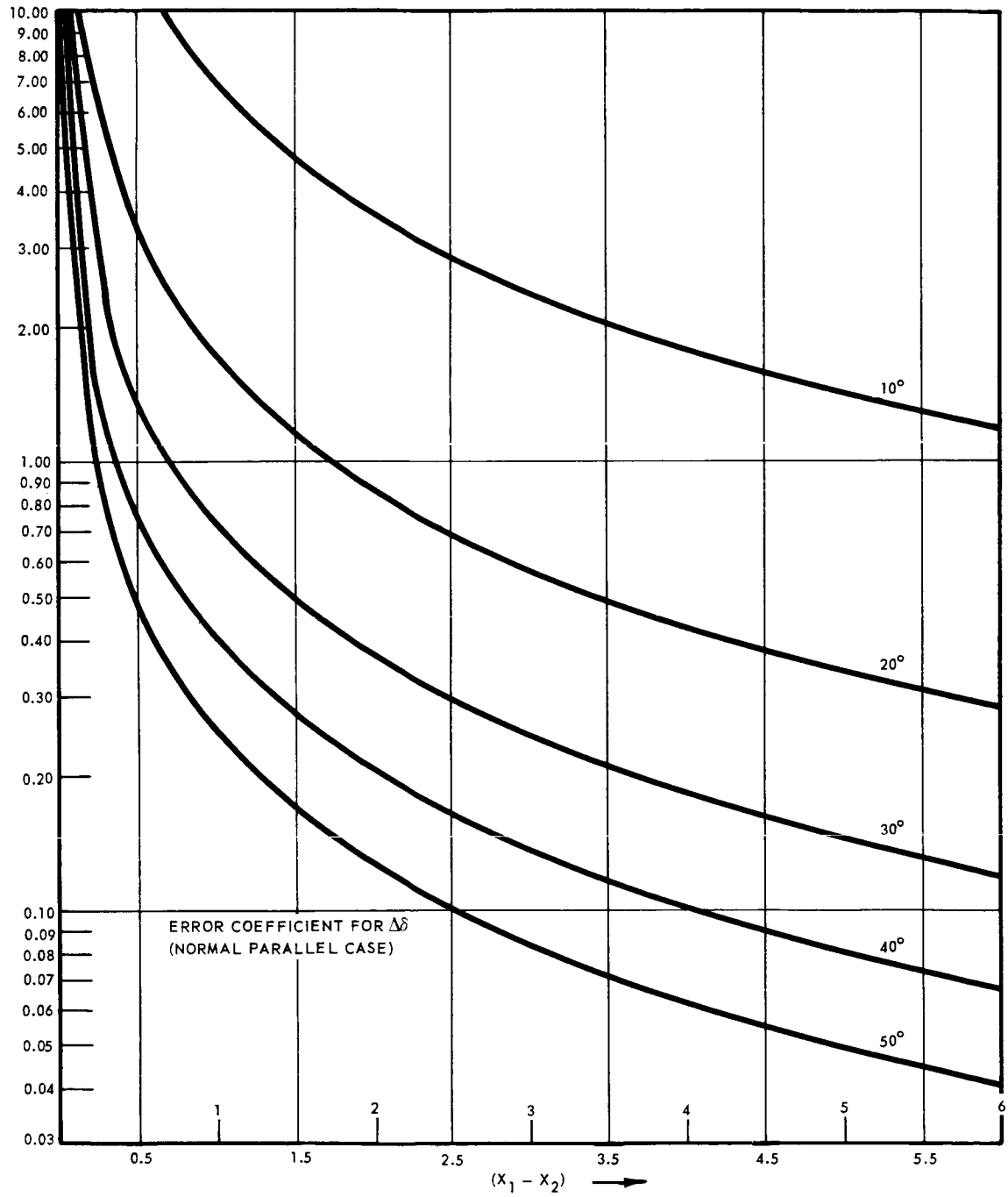

Figure 6-8 Evaluation of $\frac{\Delta \delta}{\gamma}$

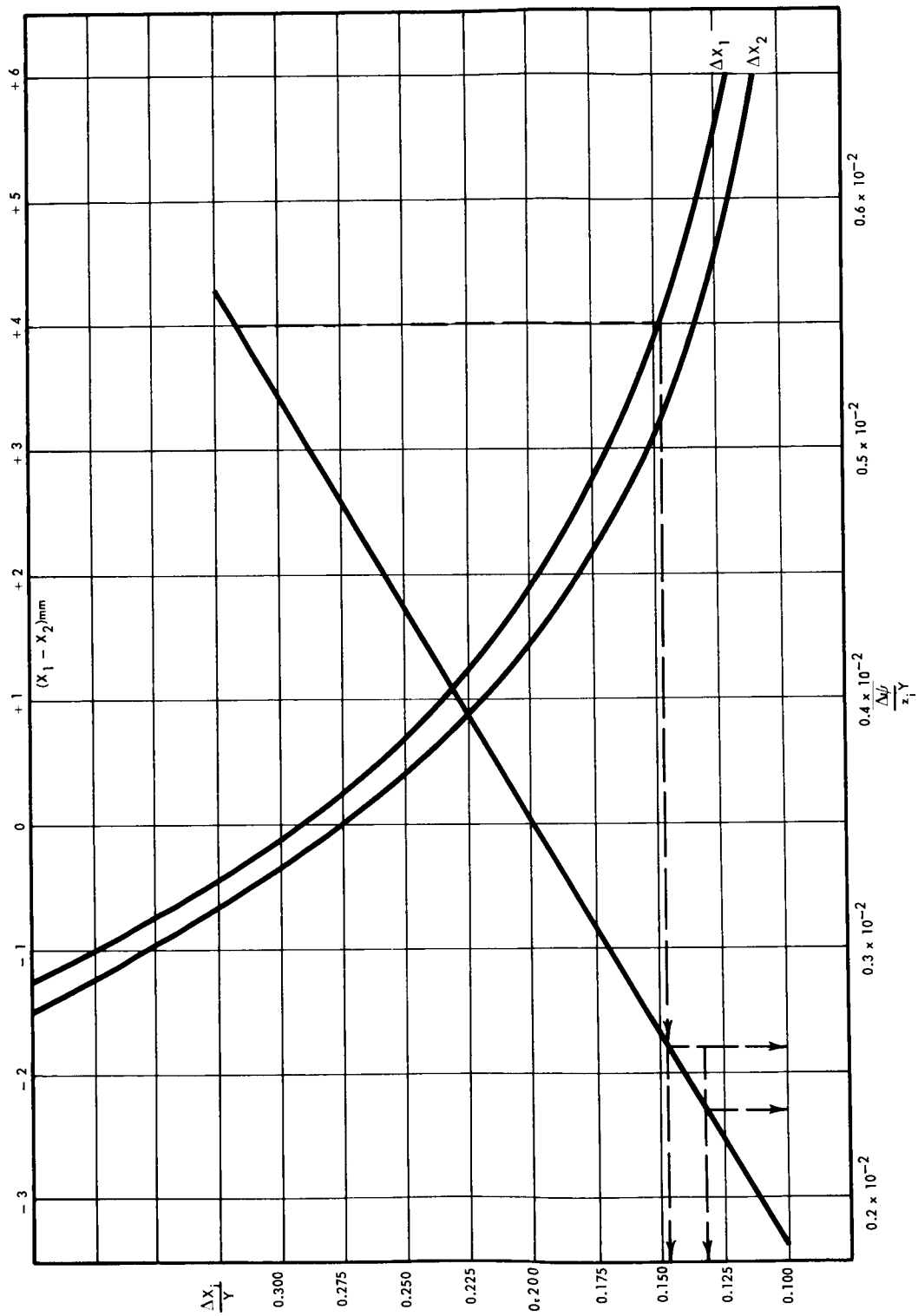

Figure 6-9 Error Coefficients of $\frac{\Delta Xi}{Y}$, $\frac{\Delta\psi}{Z_1 Y}$ for 50° Lens, 15° Convergence

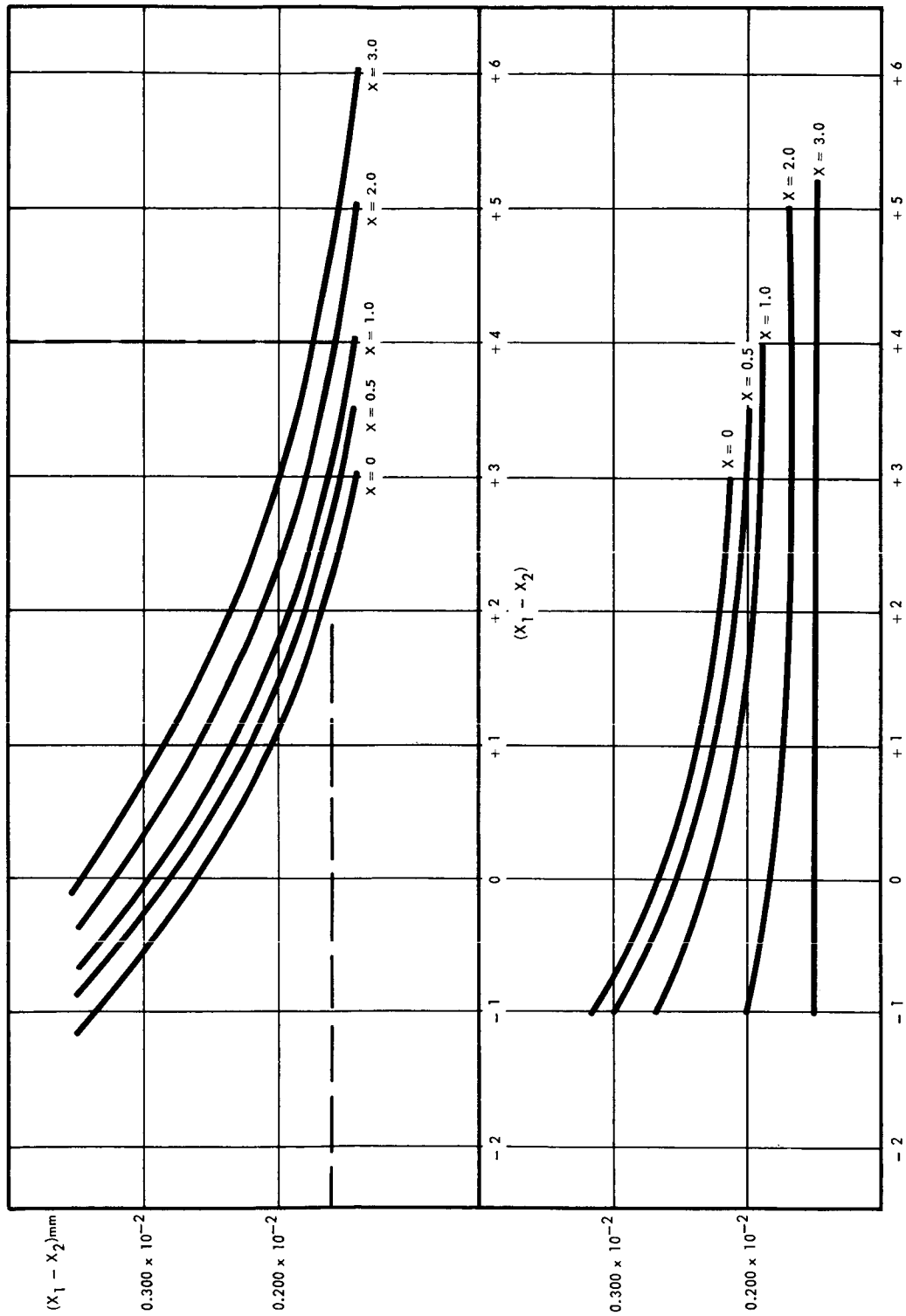

Figure 6-10 Error Coefficient $\frac{\Delta\lambda}{ZY}$ for 50° Lens, 15° Convergence

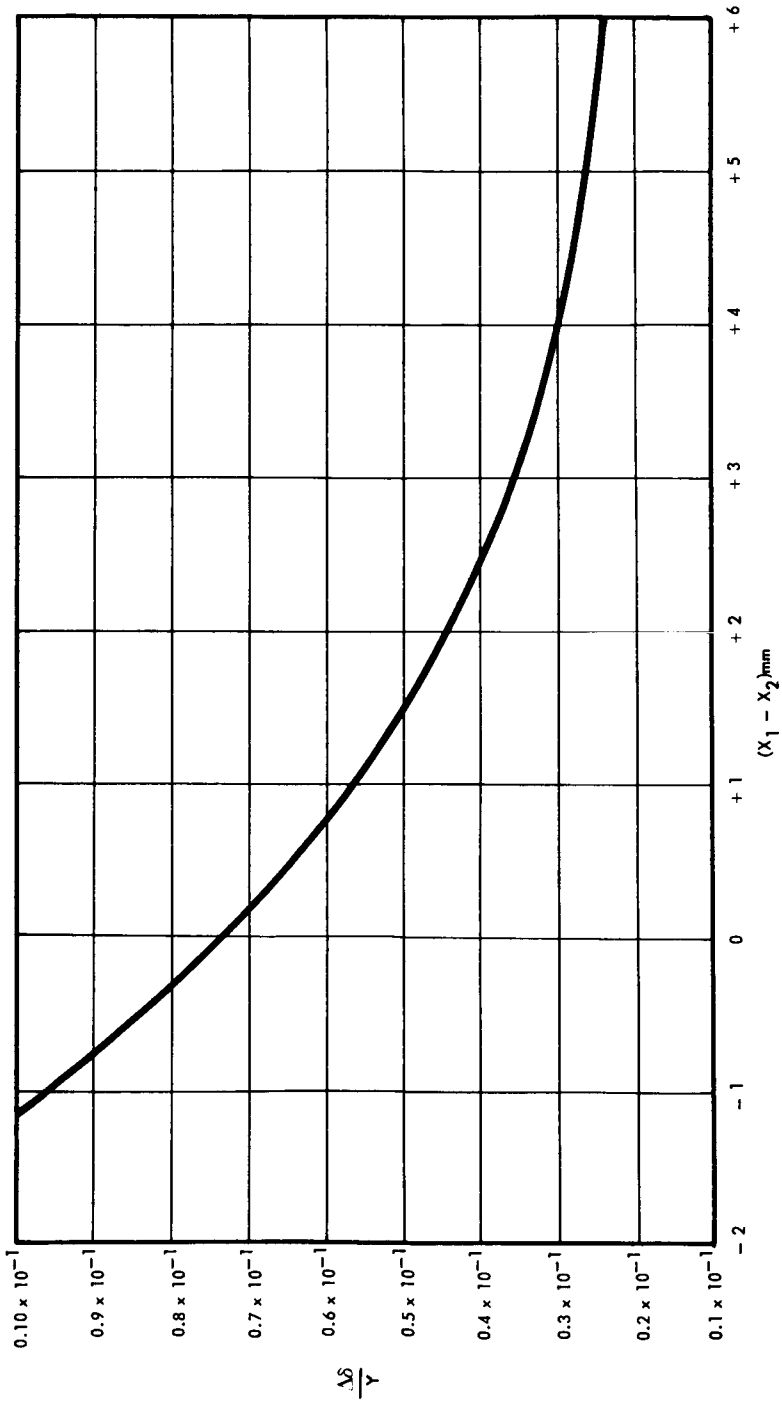

Figure 6-11 Error Coefficient $\frac{\Delta \delta}{Y}$ for 50° Lens, 15° Convergence

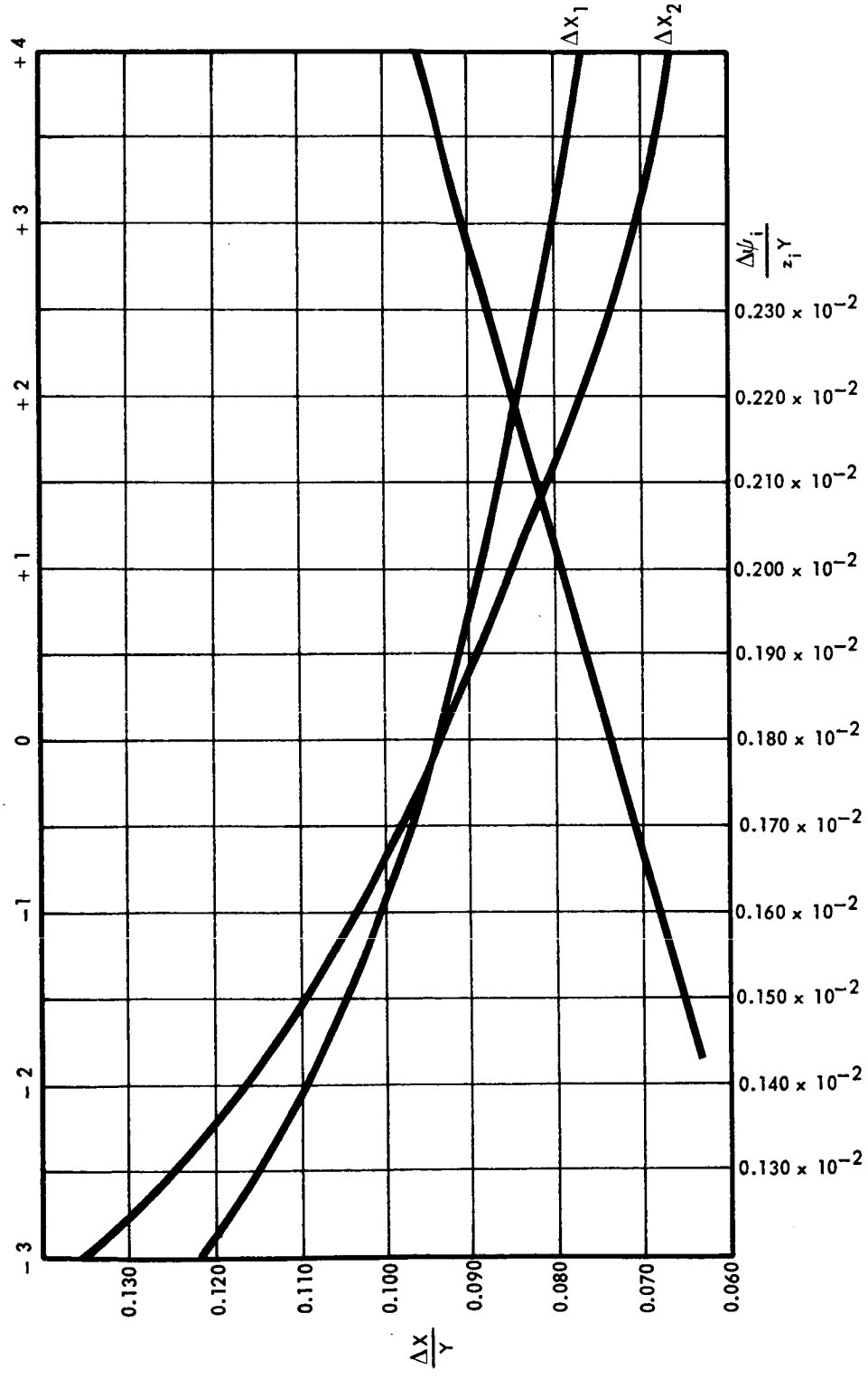

Figure 6-12 Error Coefficients of $\frac{\Delta X}{Y}$, $\frac{\Delta \psi i}{ZiY}$ for 50° Lens, 30° Convergence

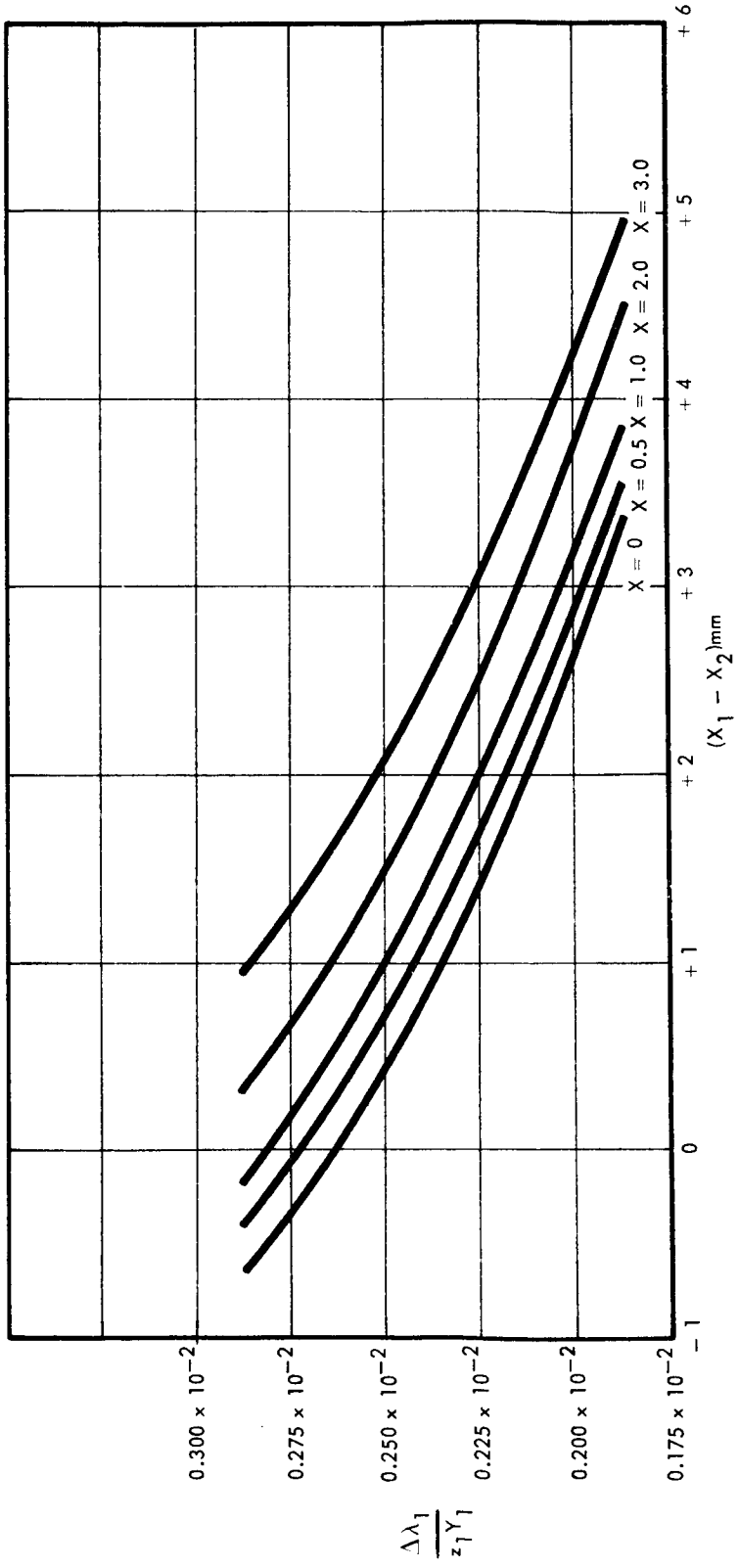

Figure 6-13 Error Coefficient of $\frac{\Delta \lambda i}{Z_1 Y_1}$ for 50° Lens, 30° Convergence

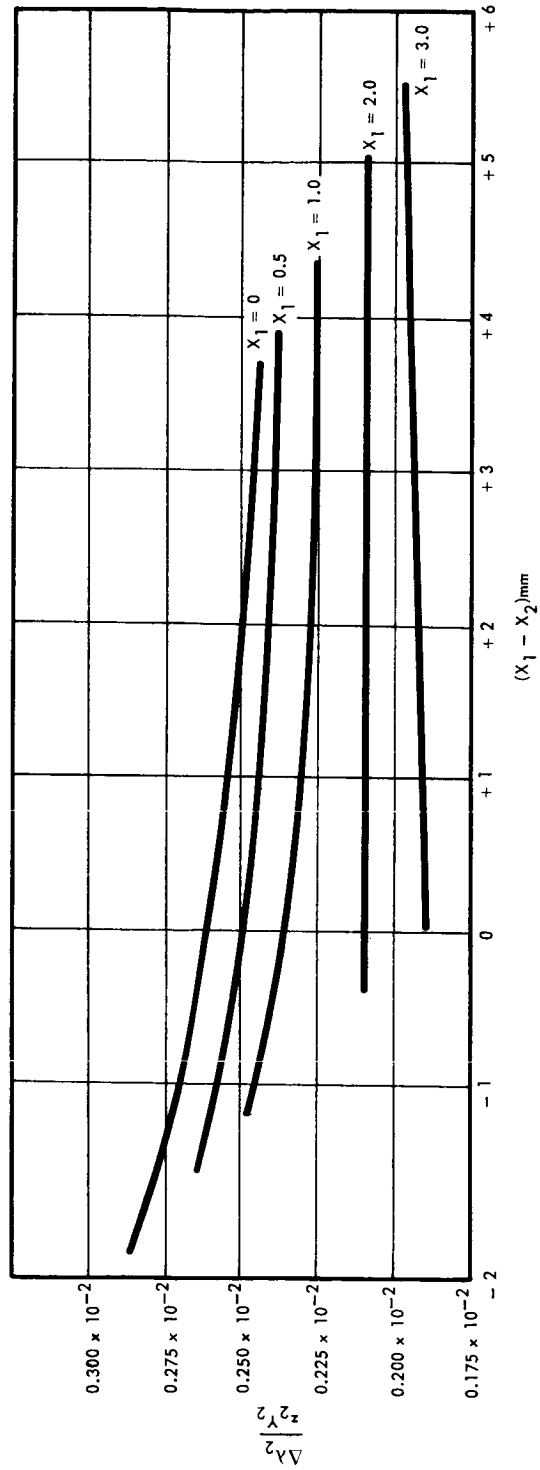

Figure 6-14 Error Coefficients of $\frac{\Delta\lambda_2}{Z_2 Y_2}$ for 50° Lens, 30° Convergence

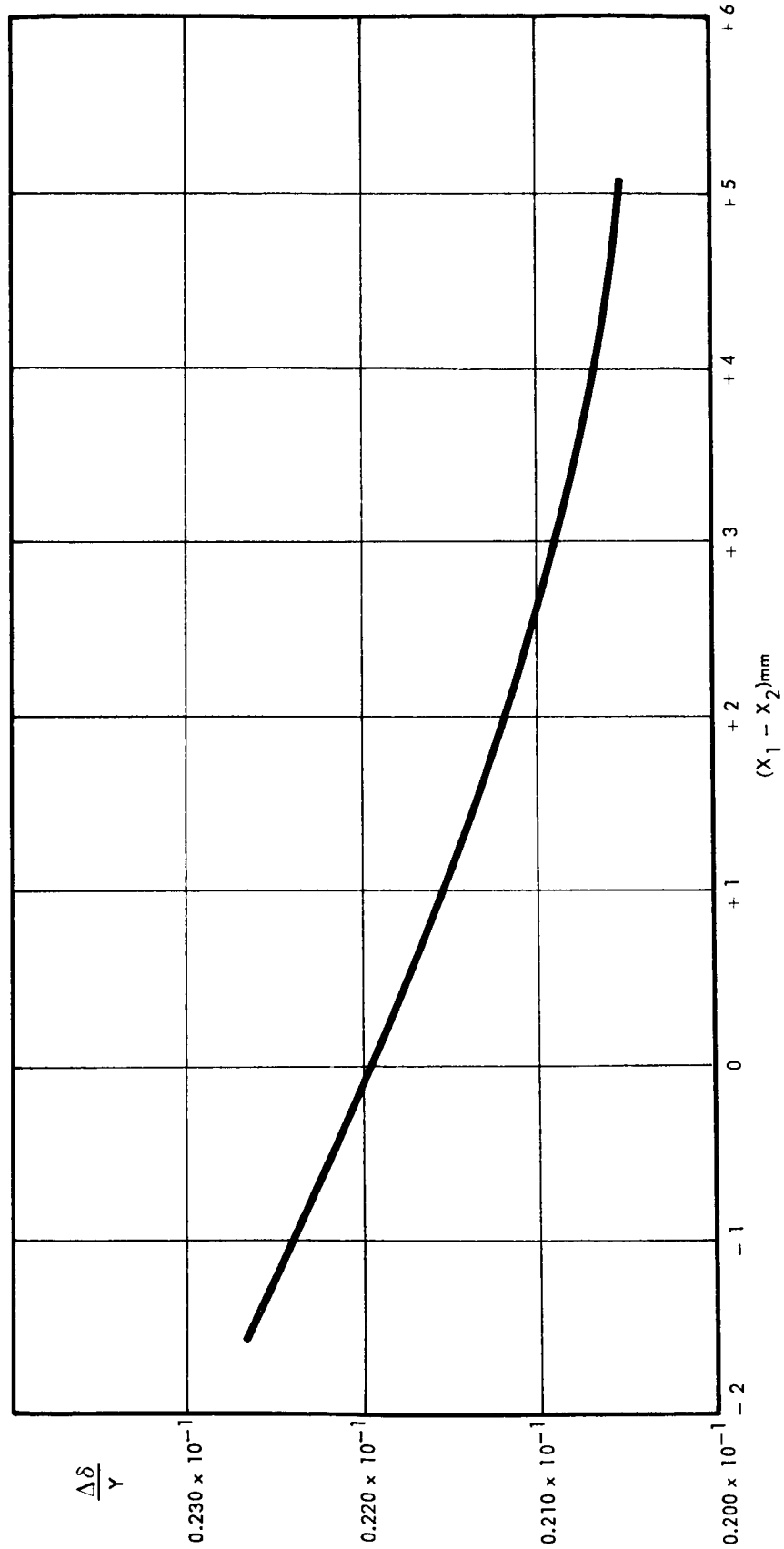

Figure 6-15 Error Coefficient of $\frac{\Delta\delta}{Y}$ for 50° Lens, 30° Convergence

6.1.1.5 Measuring Equipment

The model AP-2 stereoplotter will be used since it has the capability to handle high convergence angle images where as the simpler AP/C is restricted to a 10° maximum convergence.

The quality of the final map is dependent on correction of the image distortions caused by video non-linearities. Conventional stereophogrammetric instruments are at a serious disadvantage in handling complex image distortion, while the analytic stereoplotter can be readily compensated for these non-linearities.

The ability of the analytical stereoplotter to correct the image distortions will be exploited in the following manner: The image coordinates of the transmitted reseau will be measured and their deviation from linearity computed. From these deviations a best fit to a non-linearity function will be obtained and the coefficients determined. This non-linearity function, entered into the computer of the analytical plotter, corrects the measured image coordinates to true image coordinates as they are made.

6.1.2 Determination of Lunar Slopes by Photometric Technique

The photometric technique using the television camera as an absolute measurement photometer may be applied for the determination of lunar slopes under certain specific conditions of lunar illumination and vehicle orientation. Studies performed in support of the Phase I SLRV program (Figure 6-16) have demonstrated that with adequate calibration means and with parameter stability built into the television system, slopes of 8° or greater can be located and identified. This technique should be considered as a backup to the photogrammetric procedure and is intended to be used for photo interpretation of selected photographs for generating the required lunar maps. The accuracy determined with a closed circuit standard vidicon system is of the order of $\pm 5^{\circ}$ when the solar illuminance is at an incidence greater than 45° to the vertical and the slope is completely in the field-of-view. Further studies must be performed using a prototype model of the actual proposed slow-scan system since the pertinent parameters such as resolution, grey level rendition, shading, and charge readout rates will have a definite effect on the photometric capabilities. Extrapolation of the results obtained and the techniques developed during the laboratory studies leads to a postulation of a feasible mission profile and analysis procedure using the SLRV television subsystem and navigational sensor data. It will be assumed that the television sensor has a vidicon format with 512 x 512 picture elements and exhibits a minimum of 8 grey levels calibrated by means of a built-in step scale using solar illumination as the reference source.

6.1.2.1 Accuracy of Photometric Method

To determine the accuracy of slope measurement by the photometric method is complicated because of the complex nature of the lunar photometric function. The slope determination accuracy depends on 3 independent errors: the error in source angle determination (sun or earth sensor error); the error in auxiliary angle determination (gimbal read out error, vehicle slope error, etc.) and the error in the vidicon photometry. In addition, any variations in the albedo introduce errors, as does any deviation from the general photometric function. The two most significant sources of error are sun angle error and photometry error. The estimated sun sensor is of the order of $\pm 0.5^{\circ}$, which becomes the lower limit for slope error. The error in vidicon photometry will thus be the limiting factor in slope determination, and the less accurate the photometry, the less accurate the slope determination. For a given vidicon photometric accuracy, the error in apparent source angle (which is actually the unknown determined by this method) and hence the slope

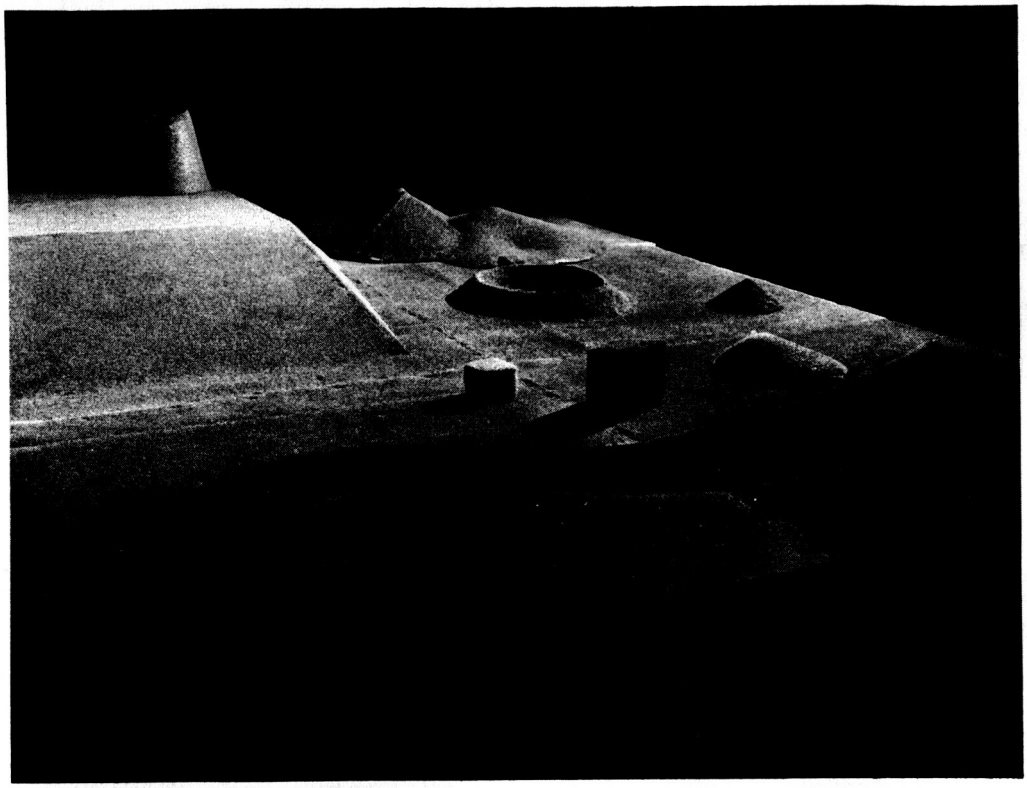

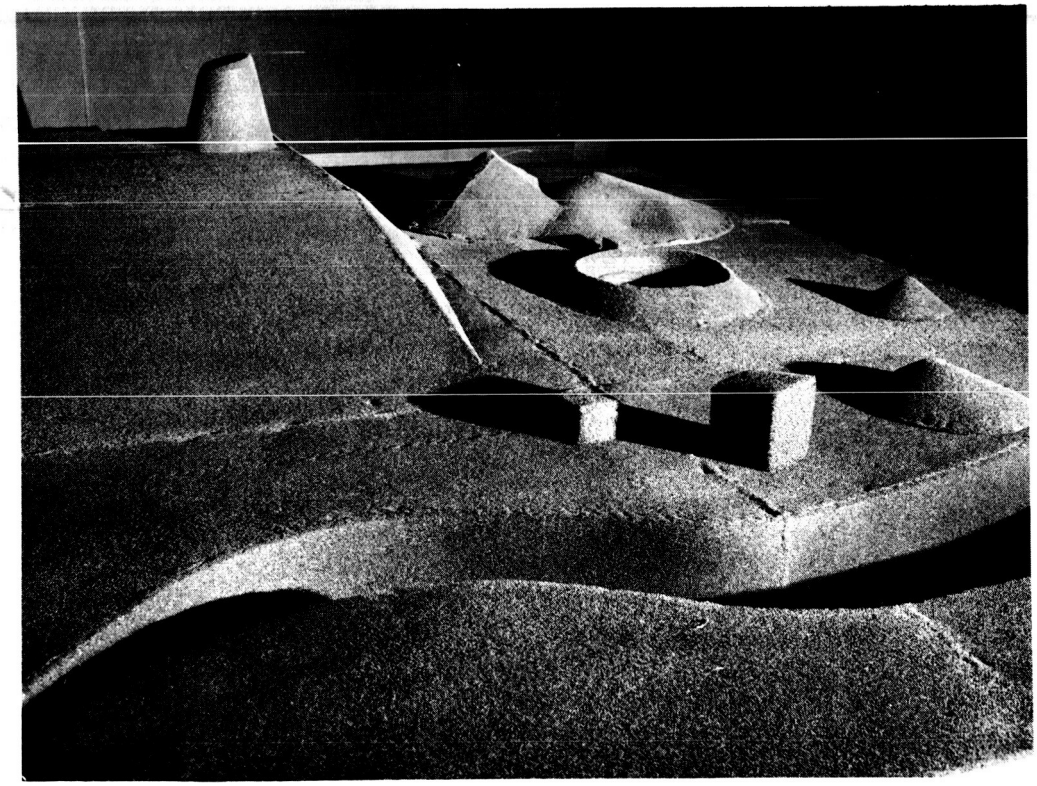

Figure 6-16 Lunar Photometric Simulation Model

error, is different for different values of i., ϵ, and a. This is because the photometric curves are very divergent at some angles, and very close to parallel at others. From the theoretical photometric function (Figure 6-17) and from the vidicon and photographic photometry of the Bendix simulation photometric material, the following accuracy estimates can be made:

LRV sensor angles are limited to a range of -90° and -45° to vertical and +45° to +90°.

Source Angles	Photometry Precision	Apparent Source Angle Accuracy
0° to 45° to vertical	± 10%	± 10°
	± 5%	± 7°
45° to 90° to vertical	± 10%	± 5°
	± 5%	± 3°

These are at present only rough estimates, based on limited laboratory data and approximate theoretical curves. More accurate estimates will require a more detailed analysis of re-computed photometric curves. The accuracy currently attainable by means of laboratory-type equipment is ± 10%. This means that the luminance of a surface can be determined to within ± 10% of the value as measured directly with a photoelectric luminance meter*, and the slope angle can be determined to within ± 10° during the middle half of the lunar day, and to within ± 5° during the first or last quarter of the lunar day. The use of more accurately calibrated luminance standards and meters would materially improve this stated accuracy, since direct photographic methods yielded photometric accuracy of ± 5%. A typical resultant curve of a vidicon photometry experiment is shown in Figure 6-18 for a 50° source incidence angle.

6.1.2.2 Parameter Effects

The parameter effects investigated during this program included horizontal and vertical shading, saturation, and any apparent inadequate erasure. The horizontal and vertical shading intensities were observed to vary by 15% across the monitor screen of the particular system examined,

* The meter used throughout these studies was of the type standardized for luminance measurements by the television and optical industries and manufactured by Photo Research Corporation, Hollywood, California.

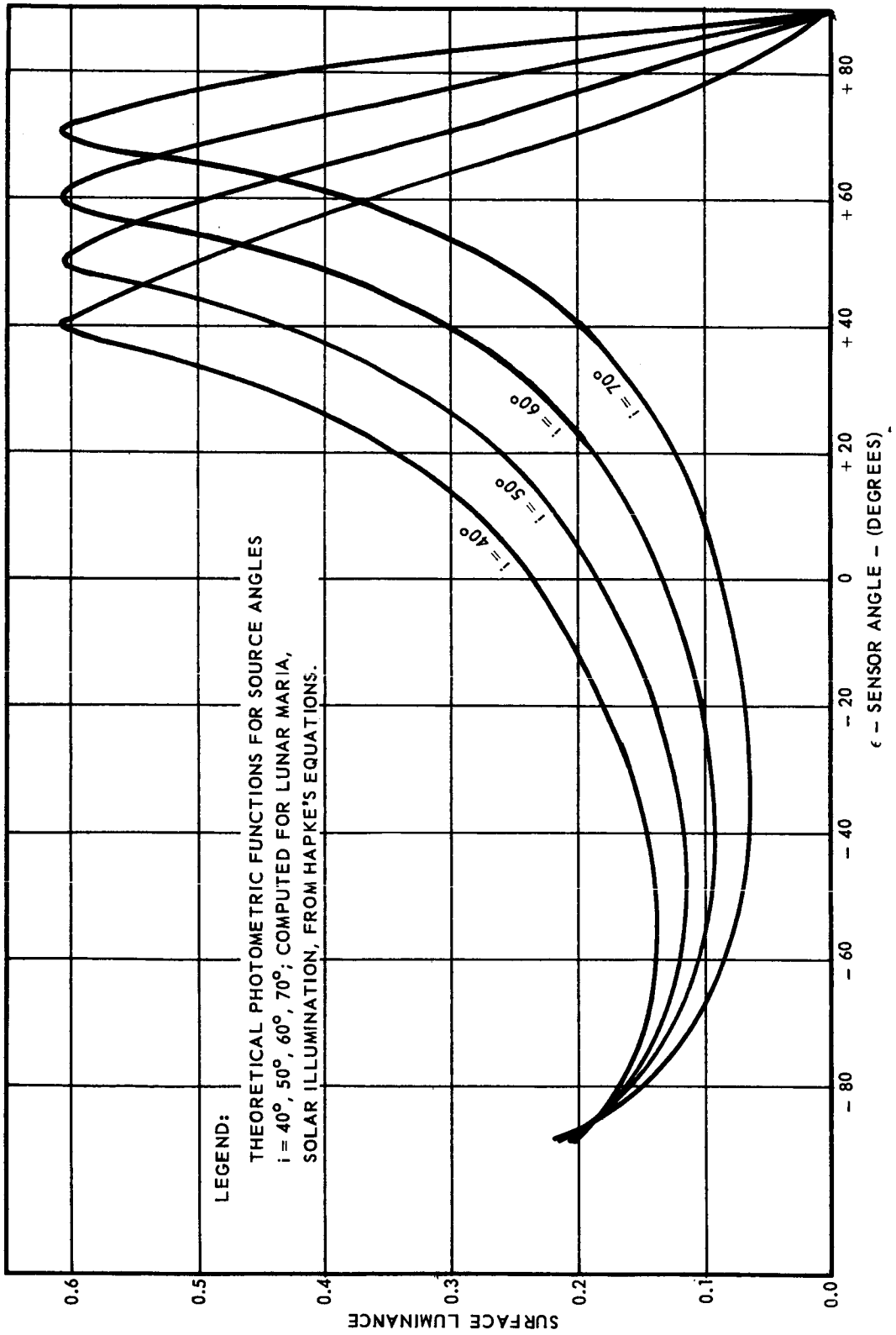

Figure 6-17 Theoretical Photometric Function

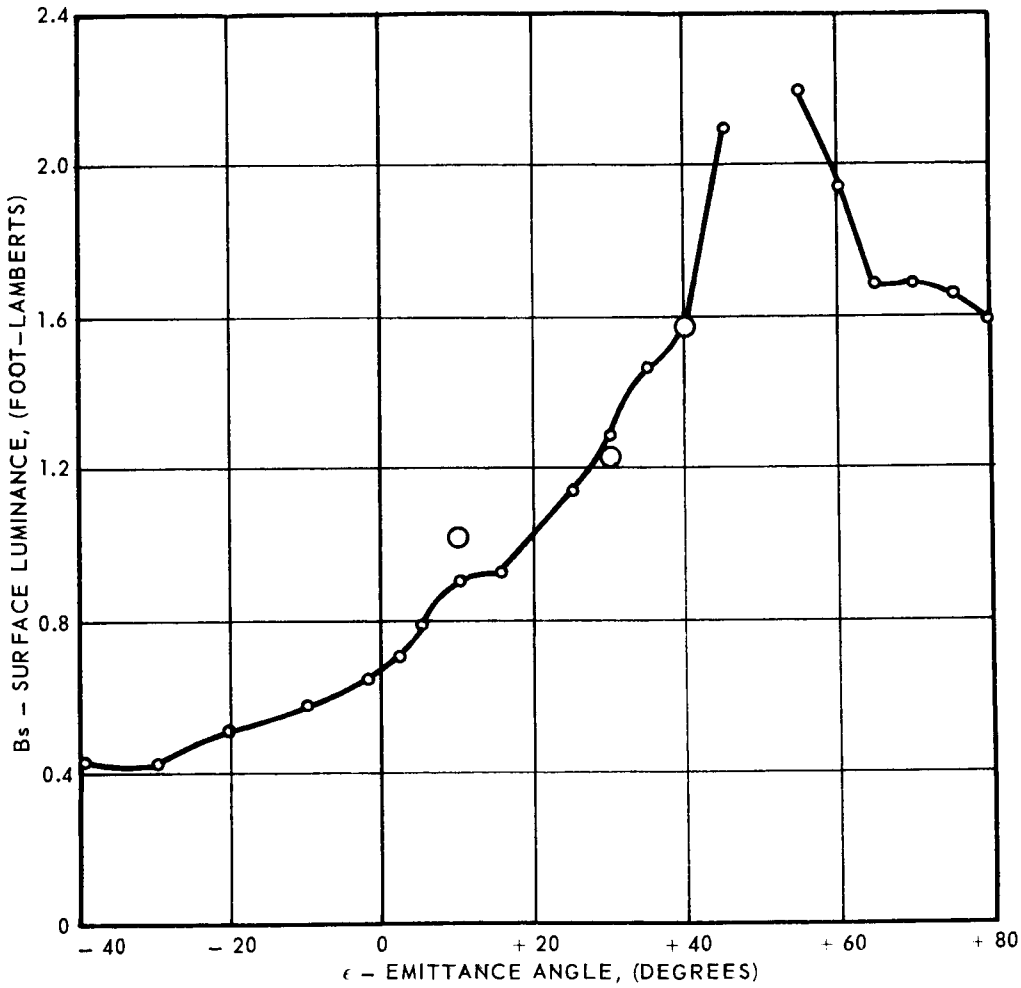

Figure 6-18 TV Photometry on Simulated Lunar Surface Material

which was a Kintel 20/20 model vidicon system. The effects of these variations were minimized by working in the central region of the screen, where the shading variations were reduced to approximately 2%. The shading also was reduced by judicious optimization of the vidicon sensitivity and contrast settings. The shading problem introduced by a slow-scan readout has not been investigated. Saturation effects may occur where variations in scene or calibration luminance exceed the available linear dynamic range. This will not be a problem in SLRV operation, since variations in lunar scene luminance within any one frame (excluding albedo and shadowing effects) will seldom exceed a factor of 40. One saturation problem which does occur unless properly accounted for is "bleeding" or "haloing" of the images. This effect was observed as a gradual decrease of intensity across an image boundary, extending to at least 10 lines away from the image. The brightest images of course produce the largest halo. Since the TV photometry is obtained by photographing the display and establishing a response curve by measuring image densities of the calibrated step wedge on the negative, relative to the base density, a zero level shift may be produced by the halo effect. The base density must be taken on the screen near the steps. This may be minimized by establishing the zero reference level near the darkest step, which has the least halo. The effect is due to internal reflections within the implosion shield and glass faceplate of the display tube and may be minimized by proper design of the CRT and photographic console.

Inadequate erasure did not present any problems in the photometry with the laboratory system, since exposures and intervals could be carefully controlled. The erasure control on the SLRV subsystem is also designed to eliminate this problem.

6.1.2.3 Calibration Reference Standard

The optimum type of luminance calibration standard is a regulated, uniformly back-illuminated set of neutral density steps, whose color is as closely matched as possible to the color of the source of scene illumination. Using visual photo-meters to calibrate a step wedge for vidicon photometry requires that the source of illumination for the step and for the scene be closely matched in color, otherwise the different responses of the photometer and the vidicon photocathode will produce considerable errors. The luminance increments used in the study program step wedges were approximately a factor of 2, giving a dynamic range

of 5.6 for a 6 step wedge. With a digital type format for data transmission, the calibration step increment should be chosen to be equal to the data increment, so that proper correlation of the grey levels can be made.

6.1.2.4 Response Characteristics

During the studies, a general method was developed for analysis of the photometric response characteristics of any vidicon or orthicon system. Using sets of calibrated steps, the vidicon monitor is photographed for various conditions of sensitivity, contrast and monitor brightness. The photographs are processed under carefully controlled procedures, and measured with the Jarrell-Ash Micro-densitometer. The resulting step wedge densities are plotted against the known step luminances, yielding a specific response curve for each set of control positions. By comparison of these response curves to the standard film-only response curve, and to each other, a quantitative analysis of system response is available. The region of linearity is easily established, and effects of saturation, compression and shading are evident. This type of analysis is absolutely necessary before accurate photometry over any range of scene luminance can be performed.

6.1.2.5 Photometric Functions

The final empirical photometric functions were established for Photo-mat (simulated lunar photometric material). These are shown in Figure 6-19 for source angles of $+40^{\circ}$, $+50^{\circ}$, $+60^{\circ}$, $+70^{\circ}$ to the vertical, and for sensor angles ranging from $+80^{\circ}$ to -50° to the vertical. These photometric curves were generated with a visual-type photometer, and correspond with the photometric curves generated photographically, and with later data taken with the P-R photoelectric photometer. The theoretical photometric functions for the lunar surface are shown in Figure 6-17. These curves were computed by a G-20 computer from Hapke's[1] equations assuming a mean local albedo of 0.078, a compaction parameter of +0.6 (typical of maria), and a solar illuminance of 13,100 foot-candles. A

[1] Hapke, (Journal of Geophysical Research, 68, 4571, 1963.)

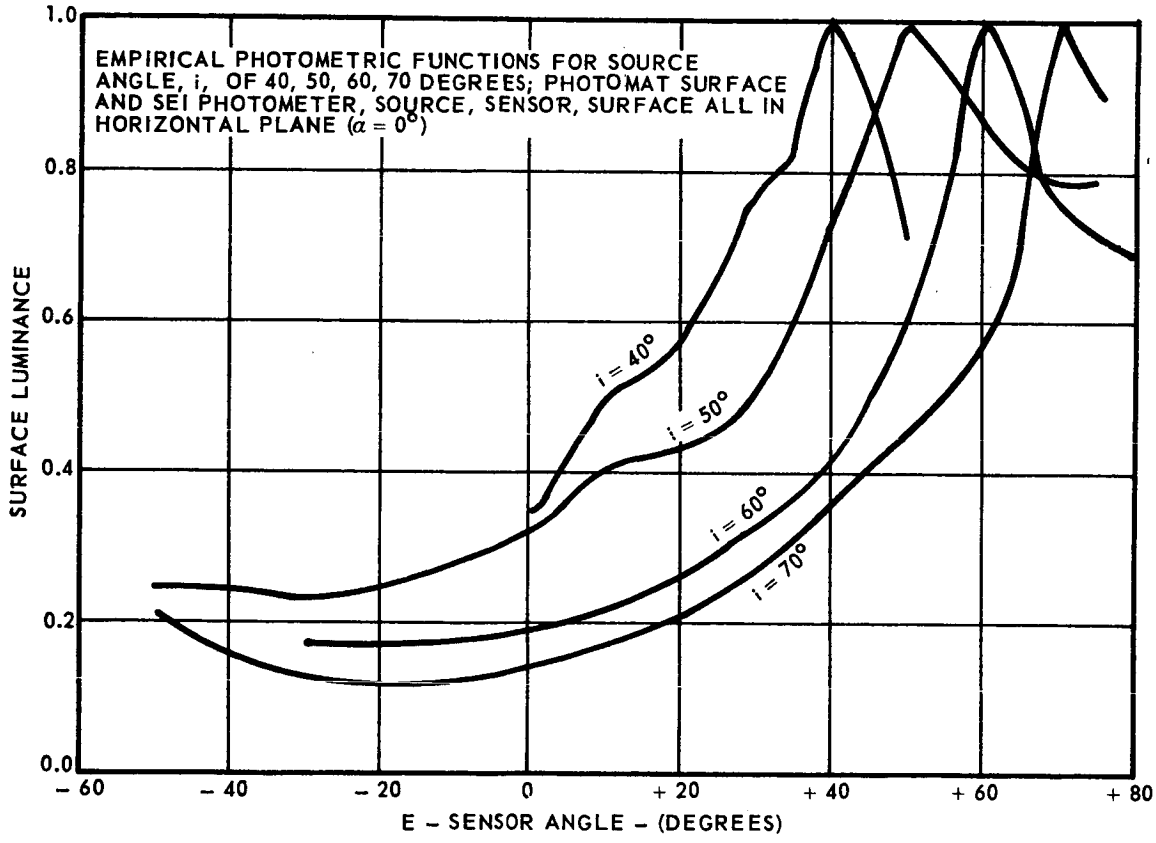

Figure 6-19 Empirical Photometric Function

comparison of the empirical photometric curve for photo-mat and the theoretical photometric curve is shown in Figure 6-20, for a source incidence angle of $+50^{\circ}$. The agreement is excellent between $\epsilon = +65^{\circ}$ and -40°, indicating that the photo-mat provides sufficient simulation for lunar photometric and other sensor studies.

6.1.2.6 System Requirements for SLRV Photometric Mission

Field-of-View, Focal Length Requirements

There are no inherent FOV limitations for the photometric mission. The photometric method could be used for any combination of FOV, as long as the image of the scene being viewed is articulated. The only limitation on the photometry mission is that any area whose slope is required must appear in two separate views. This can be accomplished in the process of vehicle guidance and mapping (as discussed in the mission profile) and application of the TV sensor.

Vidicon Resolution Requirements

There is no inherent minimum requirement on the resolution for television photometry. The average slope of an area could conceivably be determined whether it subtends 1-TV line as seen on an A-scope or the full field-of-view. In practice, a 10-line subtense would be a reasonable compromise for photometric purposes.

Vidicon Grey Scale and Dynamic Range Requirements

The instantaneous dynamic range as determined by an analysis of the highest luminance values in the LRV photometry mission is approximately 60. This represents the ratio of photo cathode illuminance produced from lunar highlights to that produced from the darkest surfaces elements, and assumes only small albedo variations. The number of grey levels required depends on the desired slope accuracy. From the practical vidicon experience gained during these studies, and from the anticipated problems of remote control, slow scan vidicons, a practical limit of vidicon photometer precision has been found to be $\pm 10\%$. The grey level steps were in ratios of 2:1 indicating that better results may be anticipated with the television system which articulates $\sqrt{2}$ steps on the standard RETMA test pattern.

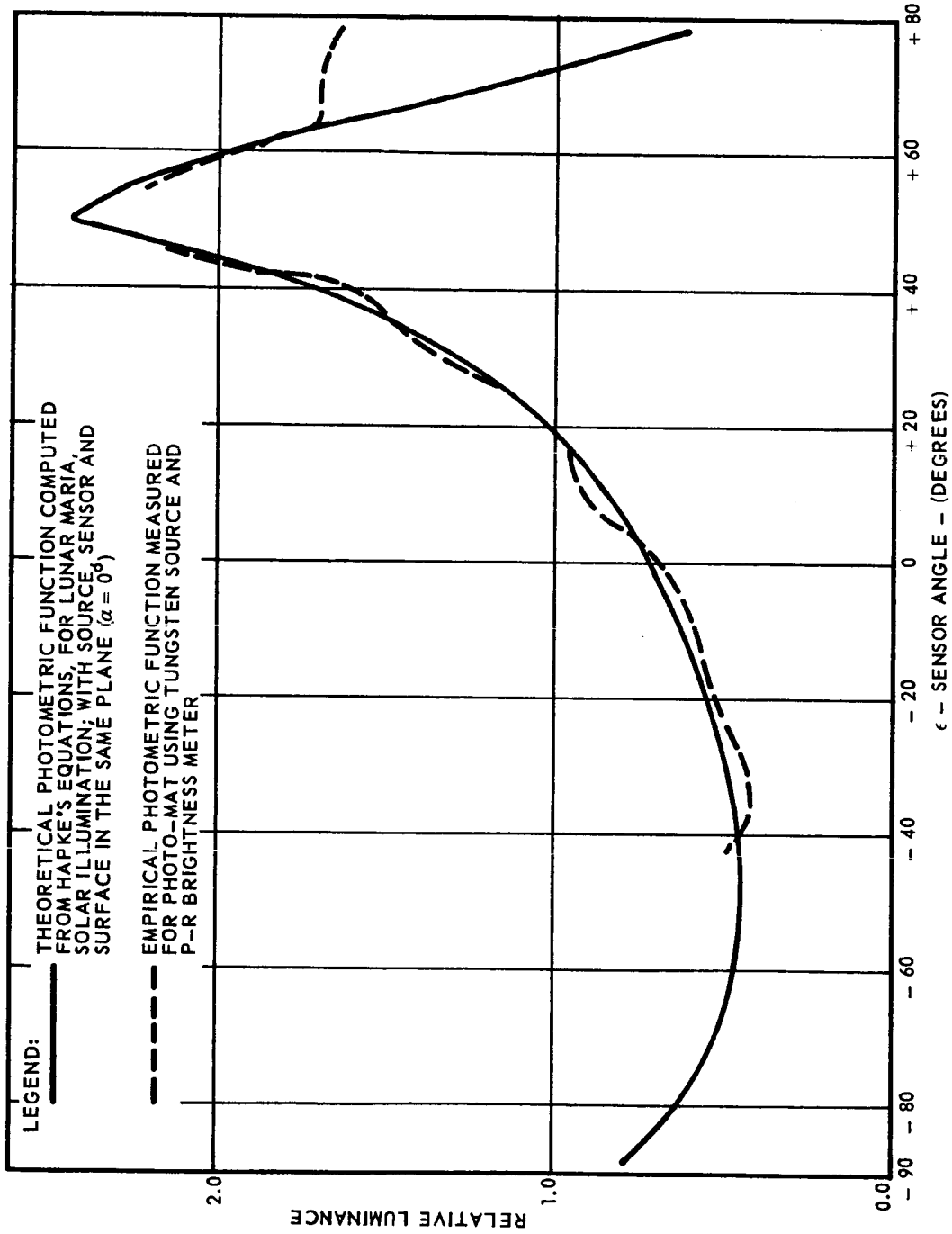

Figure 6-20 Photometric Functions for i = +50°

Vidicon Calibration Requirements

The SLRV vidicon calibration has two basic requirements: a dynamic range and grey scale range which equal that of the vidicon, and a fairly close color match to the source of lunar scene illumination. A simple method of meeting these requirements is the use of a passive sensor, using the sun as a source during the lunar day, and the earth as source during the lunar night. This system will be perfectly color matched to the observed scene, and will be automatically adjusted for the right calibration levels at all times. One proposed calibration device is shown in Figure 6-21, consisting of an opaque diffusing dome resting on an opaque diffusing wafer, a set of neutral density steps in a square array below the wafer, and a fiber optics light pipe or set of reflex mirrors. The calibration device may be placed in front of the TV optics in an unobscured position, so that it is fully illuminated by the sun (or earth). The diffusing dome and disc will produce a uniform illuminance falling on the set of neutral density wedges. The light from these wedges is carried by the fiber optics or mirrors to a corner of the optical field-of-view, where the elemental areas will be viewed during each exposure of the vidicon photo cathode to the lunar terrain. The system can be made small (2" x 2"), light-weight (2 ounces), and requires no power, and provides calibration over the full range of luminances anticipated during lunar day and night (see Table 6-2). The only additional data required is the value of the solar constant, and the earth illuminance, both of which should be accurately determined by 1965. The number of grey levels will depend on the required TV accuracy, with a minimum of eight and a maximum of 32 considered probable at present. A suggested calibration format is illustrated in Figure 6-21. The fiber optics can convert the square neutral density array into a rectangular array. This array will be positioned in the upper corner of the field, and should occupy a region of 20 lines high and 160 line elements wide. This allows a 20 x 20 line format for each step of an 8 step wedge. Any less than 10 lines will produce undesirable errors in the vidicon photometric calibration, although as few as 2 or 3 lines could be used with considerably less accuracy.

Supplementary Data Requirements

The supplementary data required for the completion of the SLRV photometry mission is summarized in Table 6-3. A set of constant parameters

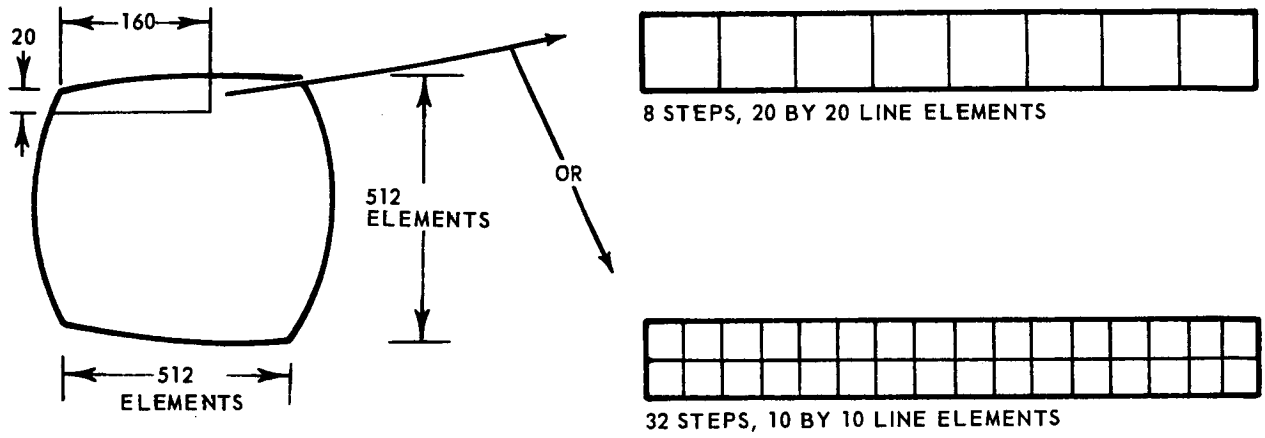

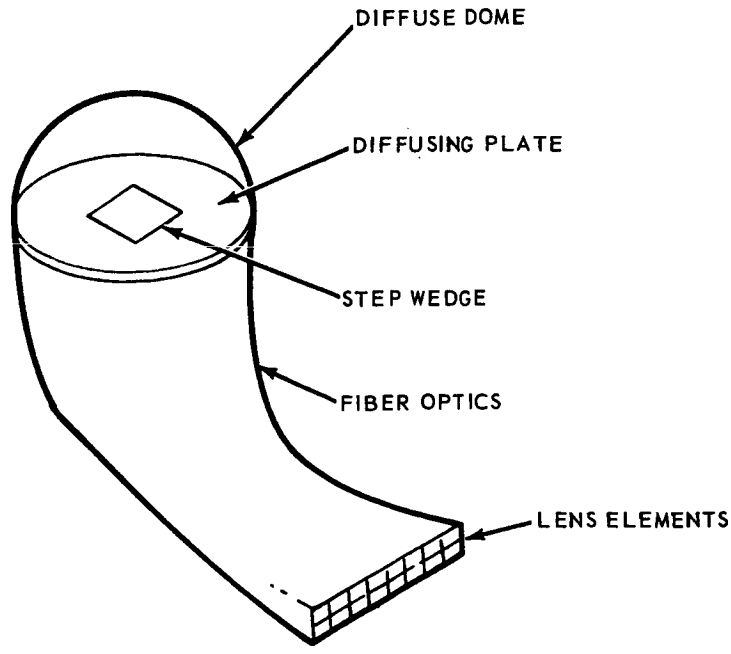

Figure 6-21 Vidicon Calibration Format

TABLE 6-2

REQUIRED INSTRUMENTATION

	LRV Vehicle	Earth Base Data Reduction Equipment
Type:	Calibration Standard	Computer + Display
Size:	2" x 2"	(Auxiliary: TV Monitor)
Weight:	2 oz	
Power:	0.0 w	
Location:	In front of vidicon optics	

will be determined before the LRV flight from previously gathered data. These constant parameters include the solar constant (and earthlight illuminance) the mean albedo, the specific photometric function, the transmittance and step densities of the calibration device, and the sensor constants such as relative aperture, elemental field-of-view, and the specific angular position in the field of view of the elemental segment under study for each lens system. In addition to these constant parameters, a set of variable parameters must be known; these include vehicle orientation and slope (to provide a set of reference axes; see Figure 6-22, the azimuth and elevation of the optical axis relative to the reference axes and the vidicon output signal level. These variable and constant parameters will be combined to compute i, ϵ, a and B (i, ϵ, a), which is then fitted to the photometric function to obtain i, the apparent sun angle at the surface element being viewed. The difference between i and i^1 yields the surface slope in the direction of the line-of-sight.

Additional Photoelectric Experiments

The SLRV vidicon system can be used for measurements of albedo if suitable absolute photometric calibration is supplied. The addition of polarizing and spectral filters will also provide the capability for polarimetric and colormetric analysis, but this cannot be accommodated within the 100-lb vehicle constraint.

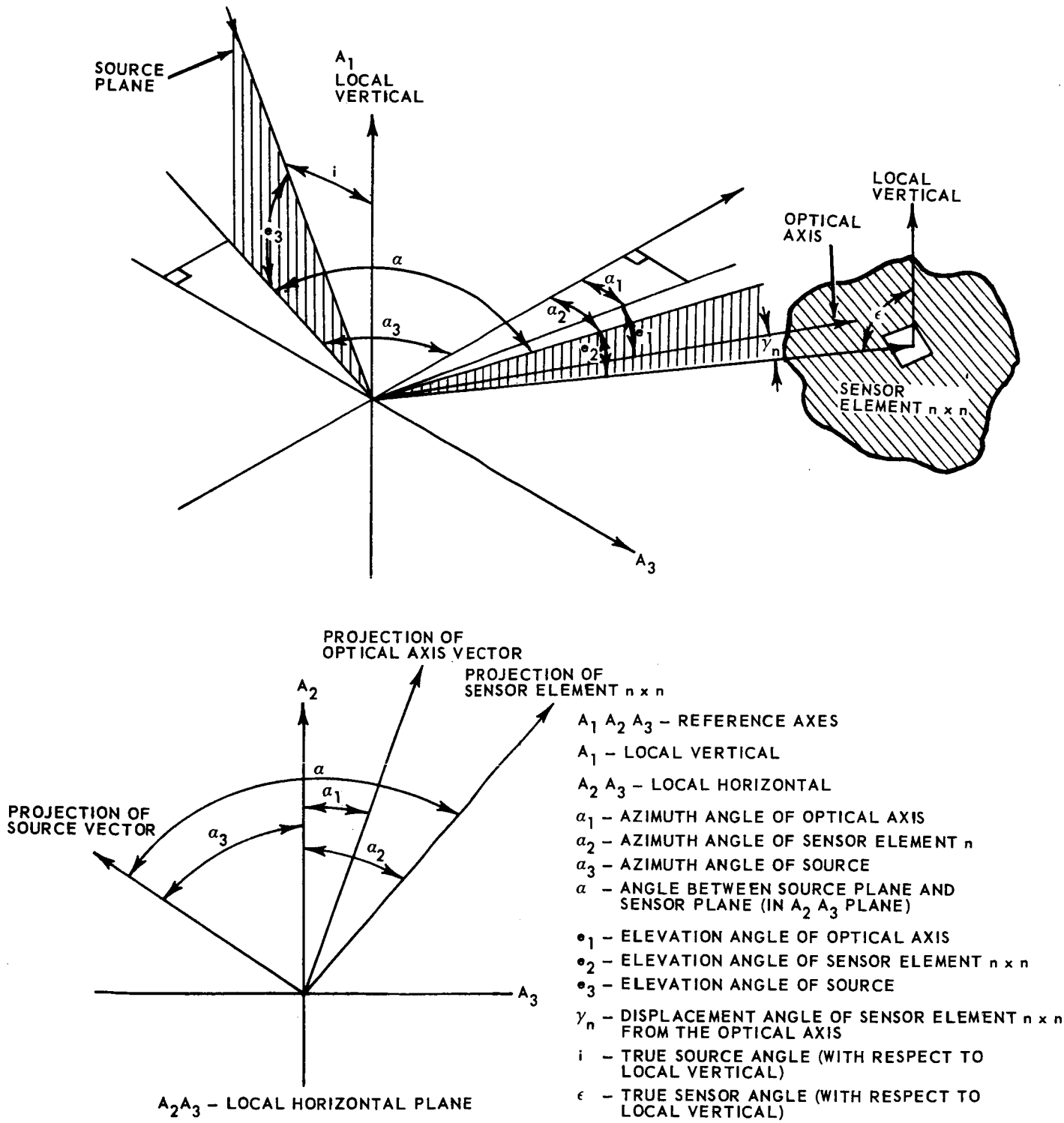

Figure 6-22 Photometric Reference Axes

TABLE 6-3

LRV PHOTOMETRY MISSION INPUT DATA REQUIREMENTS

	Parameter	Output
CONSTANTS	Solar constant (and earth-light illuminance) calibration step densities	Vidicon calibration
	Local albedo Local compaction parameter Sensor constants General photometric function Displacement angles with respect to optical axis	Photometric function for specific area
VARIABLES	Vehicle orientation and local slope	Reference axes (local vertical and vehicle axis)
	Optical axis orientation with respect to reference axes Displacement angles with respect to optical axis	ϵ (Sensor angle to local horizontal)
	Source angles with respect to reference axes	i (Source angle to local horizontal)
	Separation angle between source plane and sensor plane	a
	Vidicon photocathode signal	B (Relative scene luminances)

6.2 PENETROMETER

6.2.1 Summary

The penetrometer subsystem is shown schematically in Figure 6-23 and physically in Figure 6-24. The heart of the penetrometer mechanism is a preformed, longitudinally split, thin-walled tube which is flattened and rolled on a spool for storage with a minimum expenditure of weight and space. The conical penetrometer point, attaches to the tube, and carries a load cell to measure the force required to drive the probe into the lunar soil. The penetration depth is measured by monitoring the amount of tube which is payed-out at any point in the penetration process. The penetrometer has been designed in accordance with the SLRV design requirement to measure force versus penetration to a depth of 50 cm in a soil having a gradient of 8 psi per ft.

The tube is driven by a set of friction drive rolls which are powered through a spur gear train by a small permanent magnet DC motor. The tube is stored in its flattened state by winding it on a tube storage drum which is tensioned by a negator motor drive. The payout of the tube is monitored by an angular potentiometer which senses the rotation of the tube storage drum. A worm gear is used to reduce the angular rotation of the potentiometer to less than one turn for the entire travel of the tube (i.e., 76 cm). Cams mounted on the worm gear activate limit switches which control the extended and retracted positions of the penetrometer probe. The lead wires to the load cell are stored on a second drum, also driven by a lightweight negator motor. The penetrometer operates upon command with automatic controls to limit extension, retraction, and overload. An overload limit switch mounted in the load cell reverses the motor and retracts the tube in the event that a 10-lb penetrometer load is exceeded.

A block diagram of the SLRV penetrometer mechanism is shown in Figure 6-25.

The probe of the penetrometer mechanism is completely storable within the envelope dimensions of the mechanism until such a time as a soil bearing strength measurement is required.

Physical characteristics of the penetrometer subsystem are as follows:

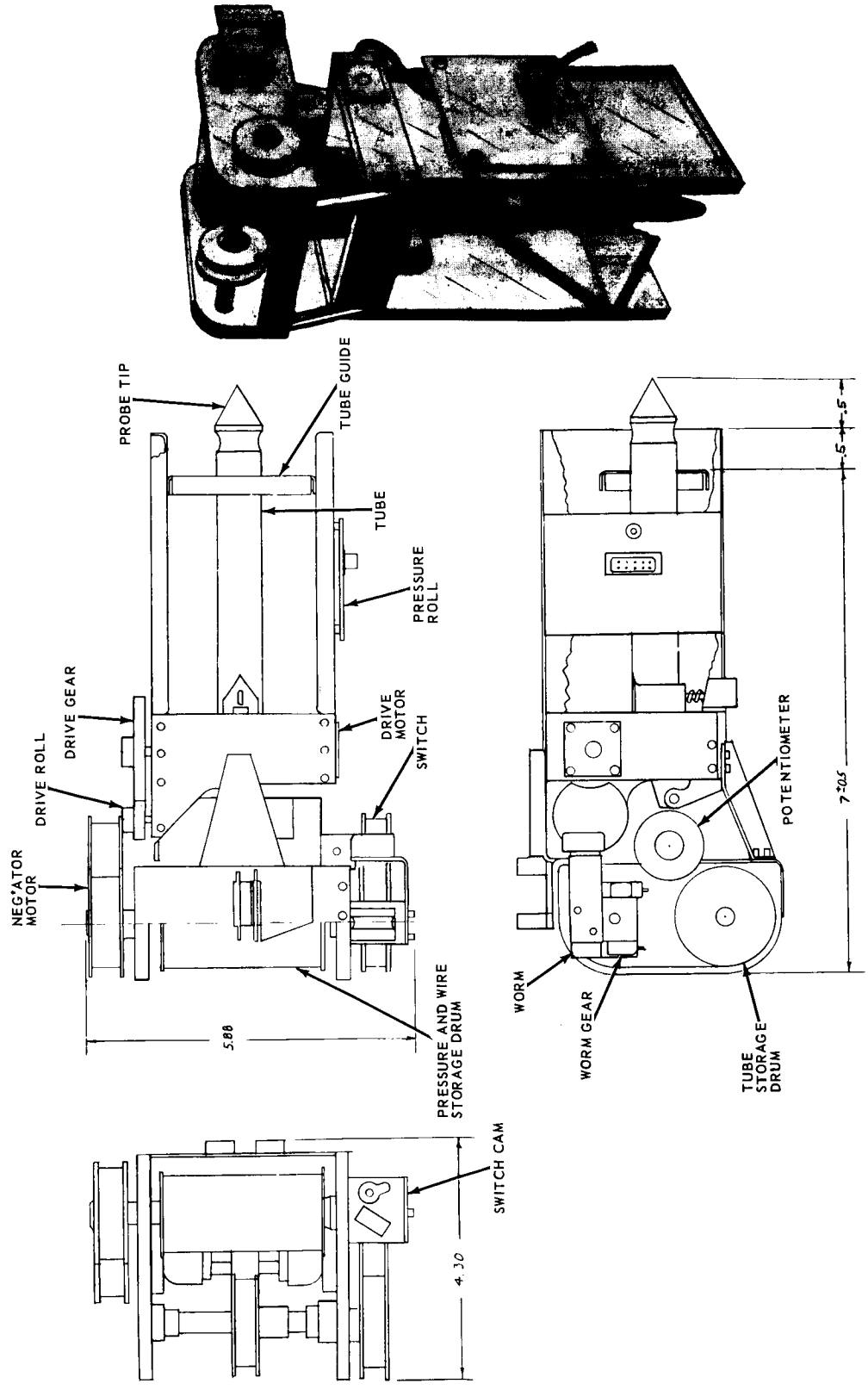

Figure 6-23 Penetrometer Schematic Diagram

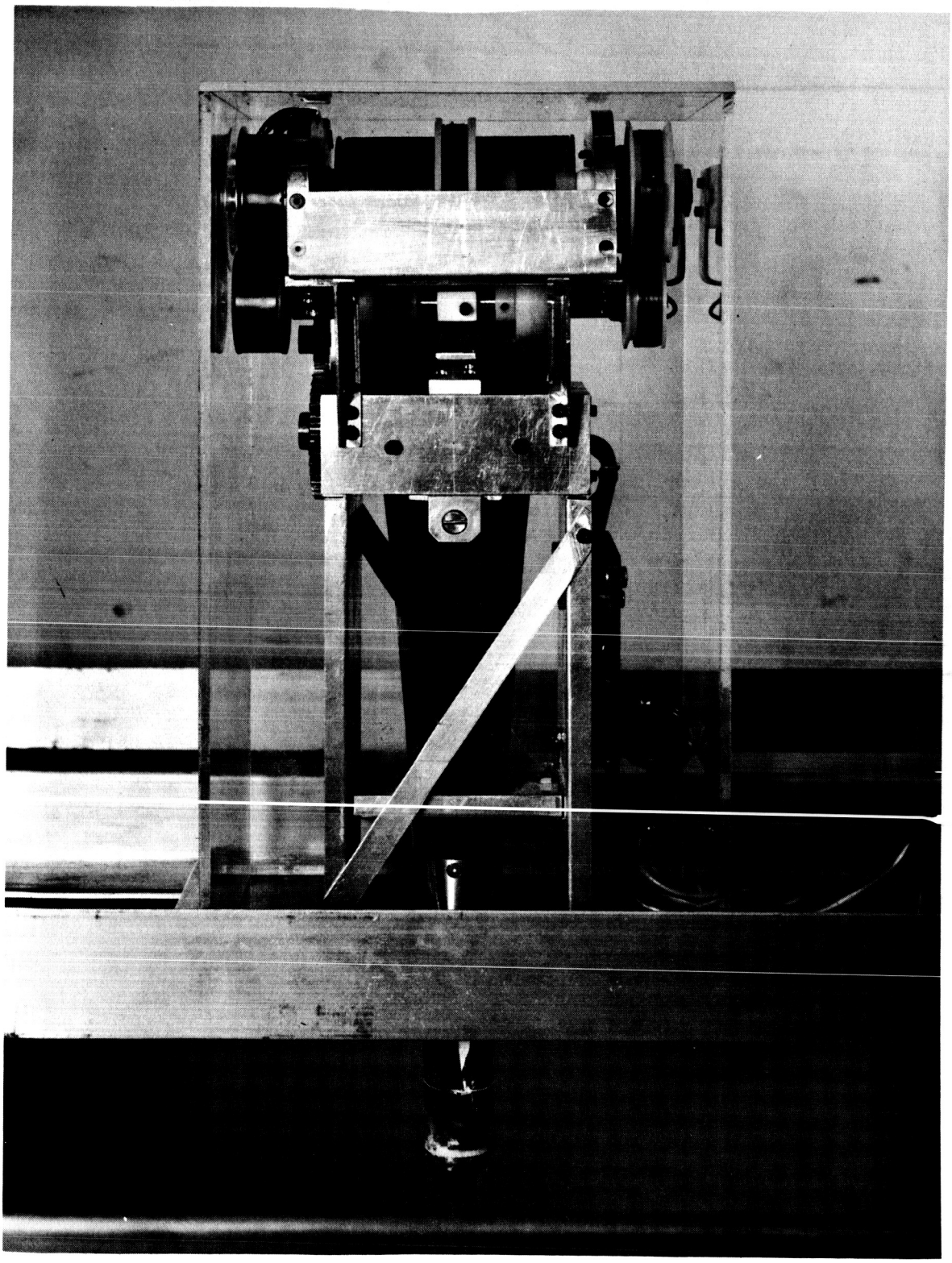

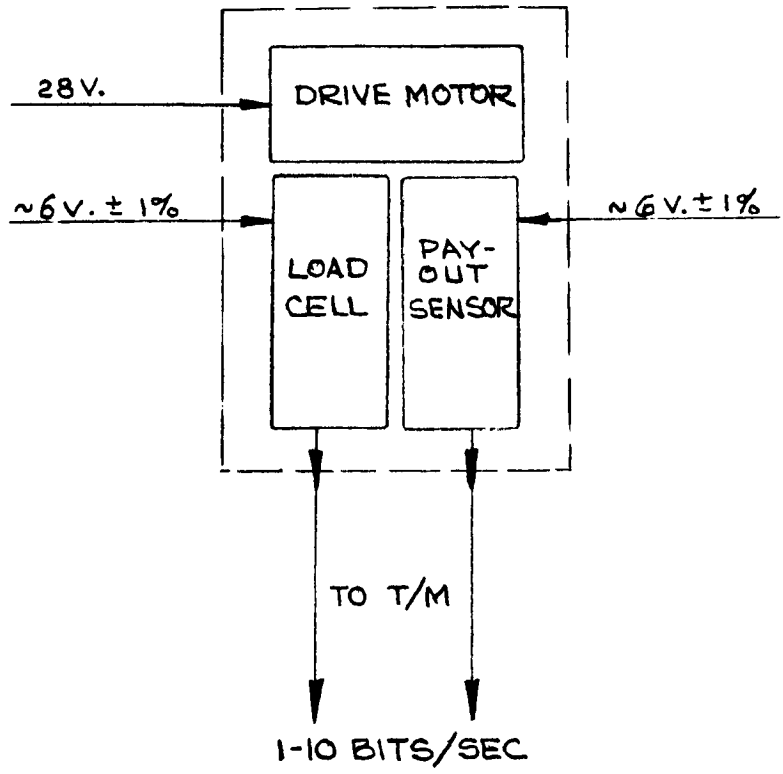

Figure 6-25 Penetrometer Block Diagram

1. Size

The maximum envelope dimensions for the penetrometer and related electronic equipment is 5-1/2 x 4-7/16 x 8 in.

2. Weight

Penetrometer weight as a design goal will not exceed 2.75 lbs

3. Power

The power requirements of the mechanism to fulfill the soil measurement function will not exceed 5 to 6 watts. Exact power levels are difficult to predict accurately since they depend on frictional effects. The power required for penetration into the soil is approximately 0.6 watts. The remainder of the power is associated with frictional losses.

4. Environmental Conditions

The penetrometer will be designed so that all equipment functions satisfactorily during or after exposure to the applicable environmental conditions of launch through lunar operation.

6.2.2 Operation

Upon receipt of the appropriate command signal, the penetrometer mechanism will be activated and the probe tube will be projected from the vehicle and into the soil. As the probe penetrates the soil, the load cell will sense the point of contact and the payout potentiometer will record the depth of penetration. At a depth of 20 in. a limit signal is generated which automatically withdraws the probe until a second limit signal is generated and the probe stops within the envelope dimensions of the mechanism. A safety factor in the form of a predetermined load setting is provided within the load sensing point to withdraw the probe in the event of an overload, to prevent damage to the probe or tipping of the vehicle. The rate of penetration and retraction will be 1/2 in./sec.

6.2.3 Interfaces

The following interfaces exist between the penetrometer subsystem and the SLRV or the ground control station.

6.2.3.1 Command Signal

The command signal required to initiate a single phase of operation of the penetrometer will be a 28-volt positive going pulse with a time duration of 10 milliseconds or greater. Two other command pulses will be necessary; one to provide an override signal to stop and retract the probe during the operation cycle and another to initiate the explosive charge destroying the tube in case of hang-up. Figure 6-26 is a circuit diagram of the penetrometer.

6.2.3.2 Voltage

The penetrometer mechanism requires two voltage supplies including one 28-volt supply for the DC motor and one regulated 6-volt supply for the instrumentation and control circuits.

6.2.3.3 Mechanical

The penetrometer package size is 5-1/2 in. wide by 4-7/16 in. deep by 8 in. high. The penetrometer is designed to rest on the bottom of the electronics compartment and to be fastened to the top plate of the compartment. A 0.825 in. diameter hole is provided in the bottom of the compartment to permit passage of the probe tube. This hole location is approximately on the centerline of the penetrometer package and near the center of gravity of the vehicle.

6.2.3.4 Data Transmission

The load and displacement signals generated by the penetrometer is sampled at a rate of 21 readings per second for each analog signal. The required accuracy for data transmission is 1/2 of 1 percent for both analog signals.

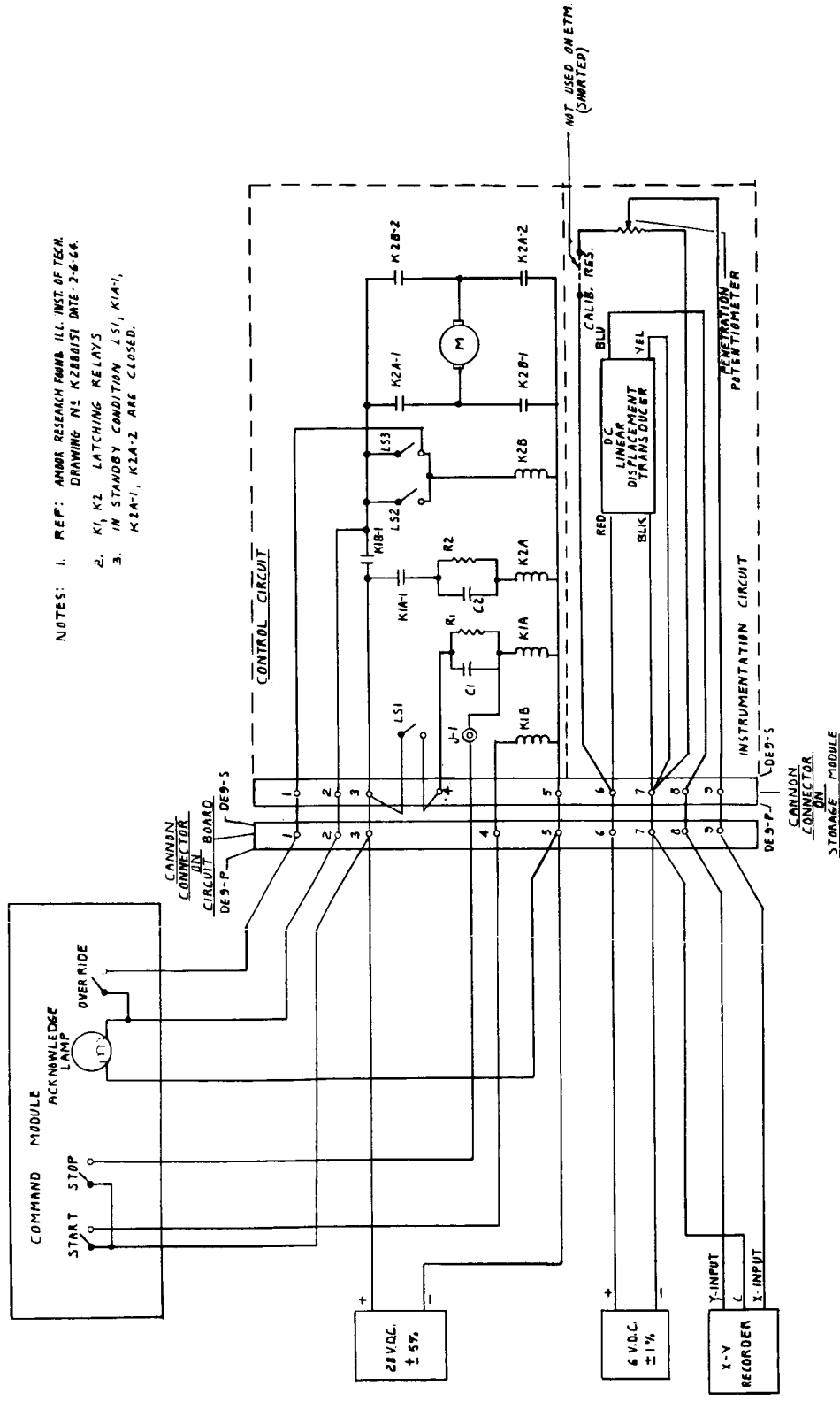

Figure 6-26 Penetrometer Circuit Diagram

6.2.3.5 Vehicle Constraints

The SLRV penetrometer will tolerate side loads up to 2 lb in the fully extended condition. To avoid damage to the penetrometer, the SLRV must be restricted to slopes which will not permit side loads of this two pound magnitude to develop (approximately 8° on a zero friction surface).

6.2.3.6 Safety Considerations

With the exception of one component, the penetrometer subsystem can be considered to be perfectly safe. The single component which represents a safety hazard in handling and installation is the linear charge and cutter assembly used to destroy the tube upon command. This explosively actuated device will be provided with safety features including shorts and safeties on both the charge and the firing circuit.

6.2.4 Parametric Studies

The component parameters of the penetrometer which were specifically investigated in a parametric study include:

1. Penetrometer tube geometry
2. Penetrometer tube material
3. Number and quality of component parts
4. Spacing between storage drums and drive rollers
5. Friction in the motor drive train
6. Friction in the mechanism
7. Velocity of the penetrometer probe
8. Vehicle restraints.

The results of parametric analysis (available on request) show that:

1. The penetrometer tube can be designed to withstand axial buckling loads far in excess of those required to penetrate the lunar soil

2. The limiting condition on the axial loads which can be developed is the weight of the SLRV

3. The penetrometer can be designed to operate in the velocity range from 1/2 to 1 in. per sec. The weight and size penalties associated with the higher velocities are minimal; however, the power penalities are more significant. It should be emphasized that a large portion (approximately 80%) of the power is absorbed by frictional losses in the penetrometer system.

4. Exact power levels are difficult to predict since they depend so strongly on frictional effects.

5. The penetrometer can be operated on a slope where side loads develop on the tube. The total range of maximum allowable slope extends from about 10 to 30°, depending upon the coefficient of friction and the vehicle constraints.

6. One of the most critical factors in the penetrometer design is the tube's fatigue life of the penetrometer tube which will influence its cycle life which is difficult to estimate.

7. The penetrometer weight can be maintained in the range from 2.75 to 3.00 earth pounds. The best area for potential weight reduction is in the selection of materials for the supporting structure.

8. The length of the penetrometer, based on a 3/4 in. diameter tube is estimated to be in the range from 7-5/8 to 8-3/8 in.

9. The system accuracy depends on load cell sensitivity and sampling rate. A load cell sensitivity of 1/2 percent of full scale (10 lb) and a sampling rate of from 5 to 20 readings per second should be sufficient for operation of the penetrometer in lunar soil at a velocity of 1/2 in. per sec.

10. The thermal analysis shows that the temperature of the penetrometer mechanism can be maintained within acceptable limits.

6.2.5 Preliminary Design

6.2.5.1 Description

The SLRV penetrometer is shown in Figure 6-23. The penetrometer includes the following modules:

1. Storage module
2. Power module
3. Probe tube module
4. Probe tip module
5. Tube housing module
6. Electronics package.

Each of these modules is described below as well as the necessary brackets and other components to assemble the modules into a complete unit.

Storage Module

The storage module contains all the necessary components for storing the probe tube and the lead wires which connect to the load cell. Also, the storage module serves as a mount for the potentiometer for recording the payload of the penetrometer tube. Finally, the storage module supplies the primary mounting points for the assembly of the entire penetrometer mechanism in the electronics compartment of SLRV.

The framework of the storage module consists of two flanged end plates, properly spaced on the right and left side of the storage assembly by two brackets and a tie bar. The tie bar is doweled and bolted to the flanges of the end plates to ensure proper alignment. Four holes are provided in the aft corners of the end plates for mounting of the entire penetrometer assembly in SLRV.

The probe tube storage drum is installed between the two end plates. A removable segment of this drum holds the end of the probe tube as it is wound onto the drum. Shaft extensions on the storage drum pass through bearing blocks mounted on each of the side plates. A negator spring power drum is mounted to the shaft extension which projects through the left-hand end plate. The payout potentiometer is coupled to the right-hand shaft extension through a worm gear reducing unit.

The bearing block which supports the right hand shaft extension, also serves as a mounting for the potentiometer. This single-turn potentiometer is equipped with a shaft extension on which two limit switch cams are mounted. As the tube storage drum revolves, the worm gear reducer turns the potentiometer shaft to automatically record the linear extension of the probe tube. The limit switch cams mounted on the potentiometer shaft are pre-set to control automatically the maximum extension and retraction lengths of the probe tube.

The lead wire storage drum is mounted directly below the tube storage drum. This drum stores the lead wires which carry the operating power and the output signal to the linear variable differential transformer (LVDT) located in the probe tip. The lead wires are guided through the probe tube and are payed out during the extension phase of operation and wound up on this drum during the retraction phase. The lead wire drum shaft rotates in bearings mounted on the right- and left-hand end plates. The right-hand end of the drum shaft extends through its bearing and serves as a mounting point for a second negator spring power drum.

Two stub shafts, mounted to the tie bar are used to center the two negator spring storage drums. Both of the negator spring motors serve to maintain tension on the probe tube and lead wires during the retraction phase of operation. With the probe tube in the fully retracted position, approximately 90 percent of the negator spring is wound on the storage drum. When the probe is extended, the rotation of the tube storage drum shaft causes the negator spring to be transferred from the storage drum to the power drum. If it is necessary to stop the tube extension, the inherent characteristic of the negator spring (to apply a constant torque on the power drum) maintains a tension on the tube or lead wires at their respective storage drums. This condition also exists during the retraction phase of operation as the negator spring, transferring from the power drum to the storage drum, tries to override the motor and always maintains tension on the tube and lead wires.

Two contoured tube rollers are mounted at an inboard location along the centerline of the two negator storage drums. These contoured rollers assist in forming the tube through the transition from a curved to a flat section as the probe tube is wound on the storage drum.

Power Module

The power module contains those components required for extension and retraction of the probe tube as well as a guide system to prevent any transverse movement of the probe tube during operation. The power module assembly is shown in Figure 6-27.

The basic framework of the power module is bolted and doweled to form a rigid, accurately aligned structure. A 27-volt DC motor is mounted on the left-hand wall of the power module. The shaft of the motor is connected to the shaft of the tube drive rollers through two spur gears which transmit the power and reduce the shaft speed. The tube drive shaft is supported by ball bearings which in turn are fitted into housing bolted to the side walls of the power module frame. A drive wheel is pinned to the center of the drive shaft. A pressure wheel is located on a separate shaft directly below the drive wheel to form a nip through which the tube is driven. The pressure wheel is ball bearing mounted and is spring loaded against the drive wheel with a normal force of approximately 100 lb. Although this normal force seems quite large, it is necessary to prevent any slippage of the drive wheel when the axial force on the probe tube approaches 10 lb.

Two probe tube guide assemblies are mounted to the right and left of the pressure wheel. These guide assemblies contain steel rollers which restrain the edges of the probe tube during operation and deter any transverse movement. The remainder of the probe tube guide assemblies are contoured to match the cross-section of the probe tube at this point and assist in proper forming of circular cross-sections further down the probe tube.

Probe Tube Module

The probe tube is considered as a complete module since it is fabricated as a unit. It is shown in Figure 6-28. The design analysis and trade-off studies have established the dimensions of the tube as 3/4 in. diameter with a wall thickness of 0.004 in. A manufacturing method for

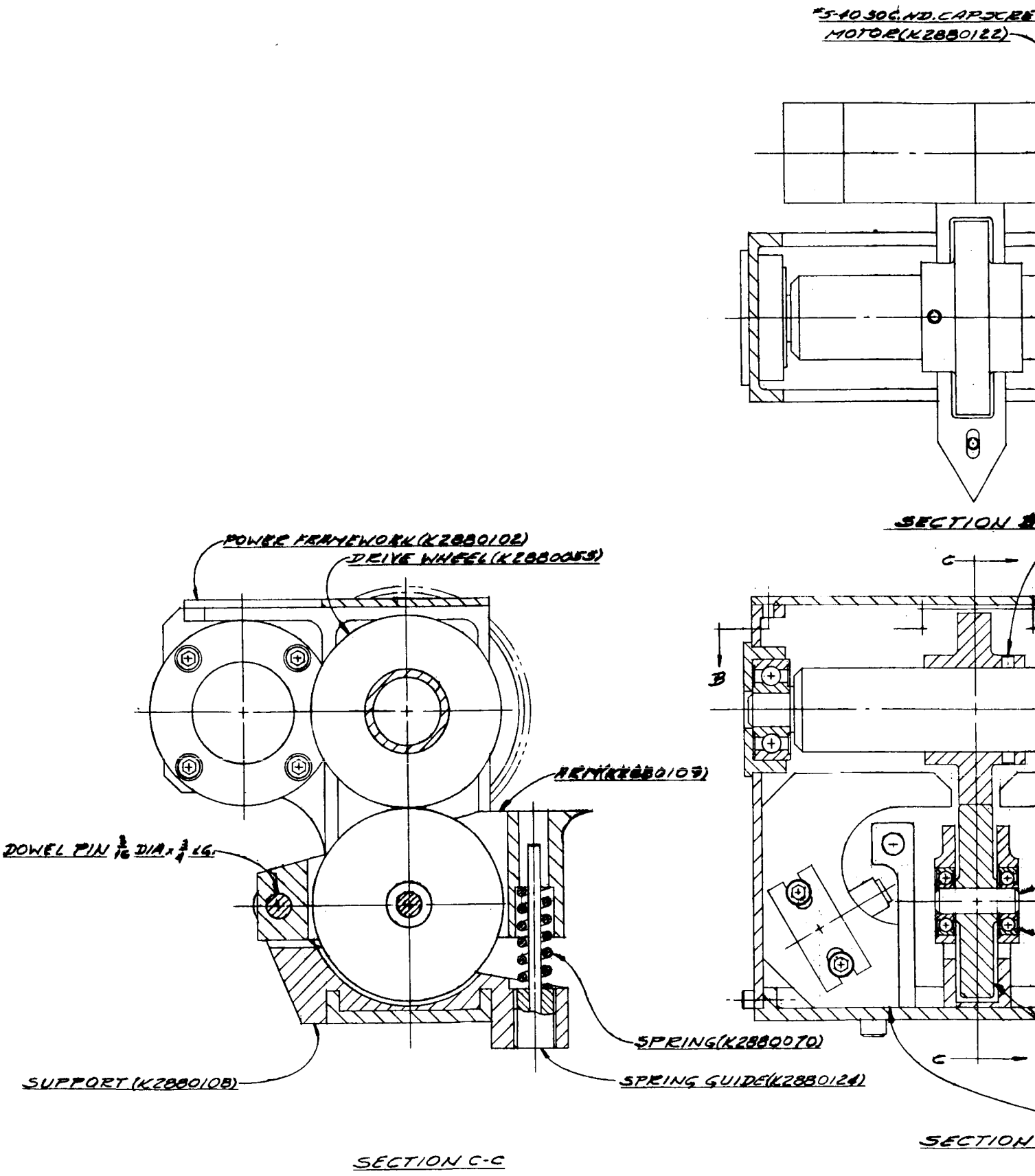
#5-40 SOC.HD.CAP SCREW
MOTOR (K2880122)
SECTION B
POWER FRAMEWORK (K2880102)
DRIVE WHEEL (K2880055)
ARM (K2880109)
DOWEL PIN 3/16 DIA x 3/4 LG.
SPRING (K2880070)
SUPPORT (K2880108)
SPRING GUIDE (K2880124)
SECTION C-C
SECTION

#1

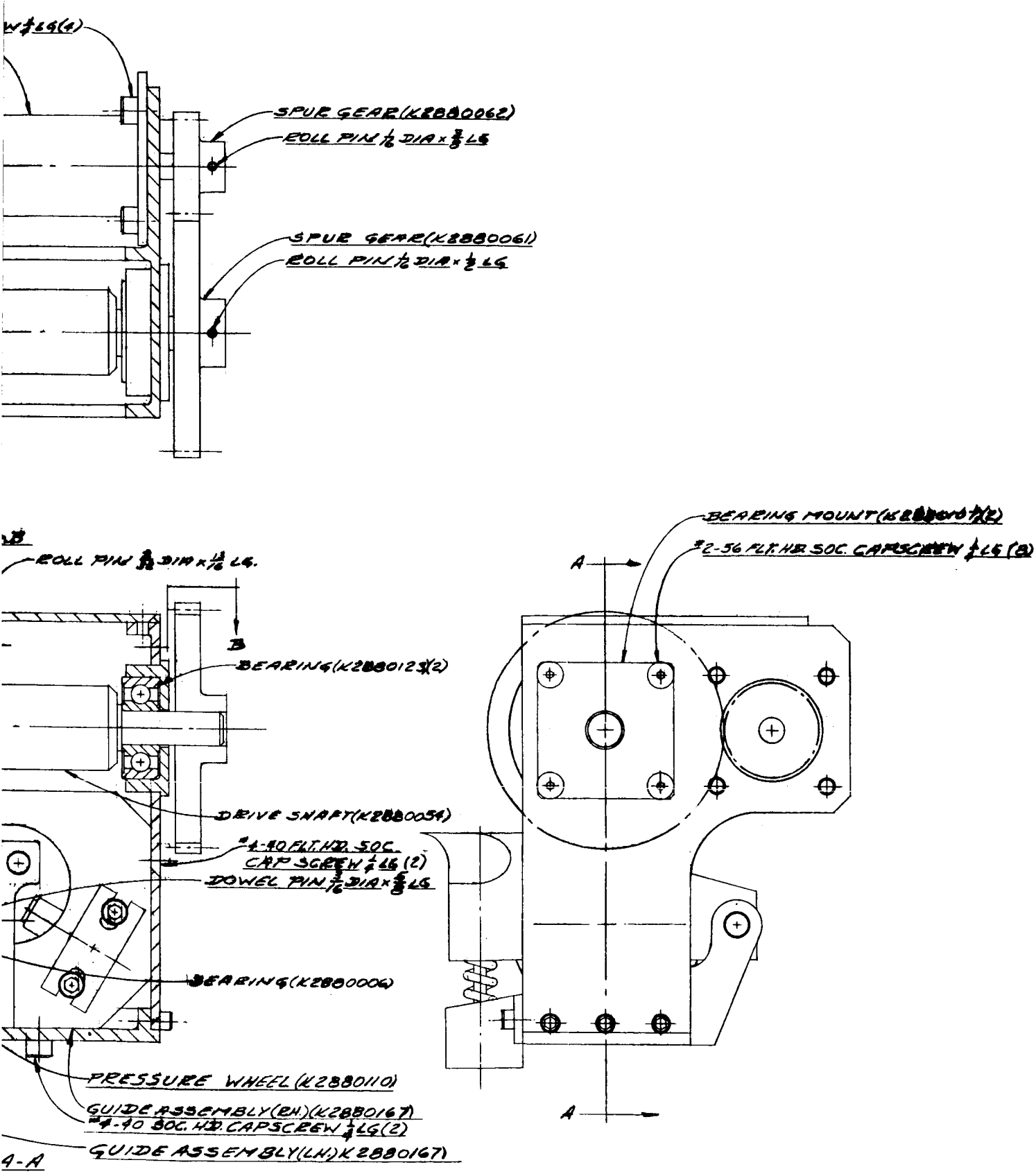

Figure 6-27 Power Module Assembly

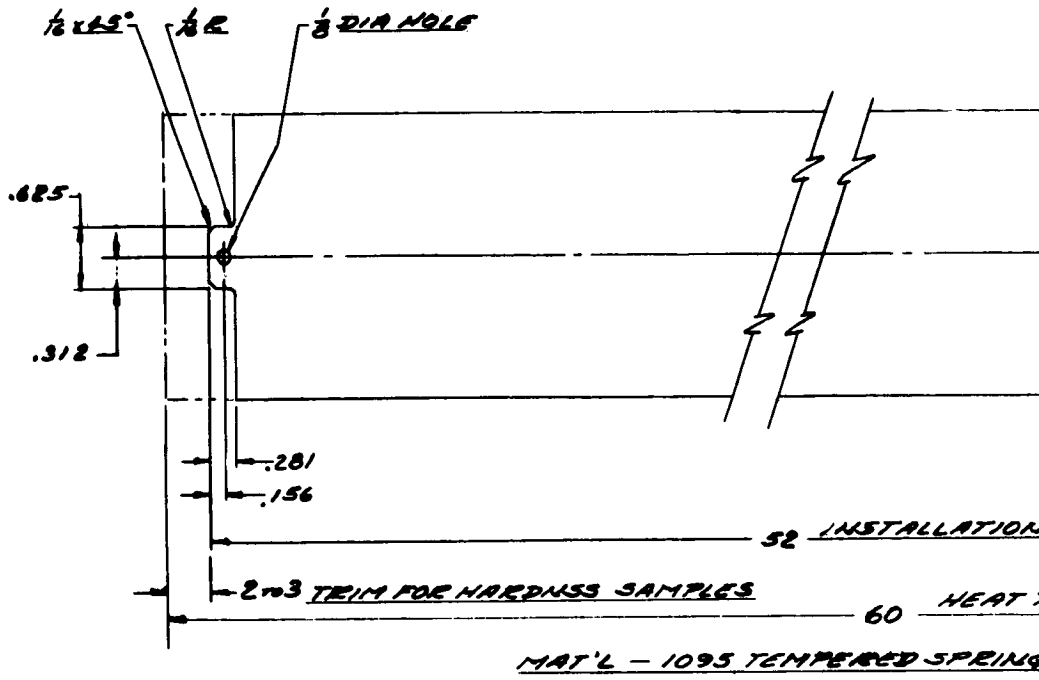

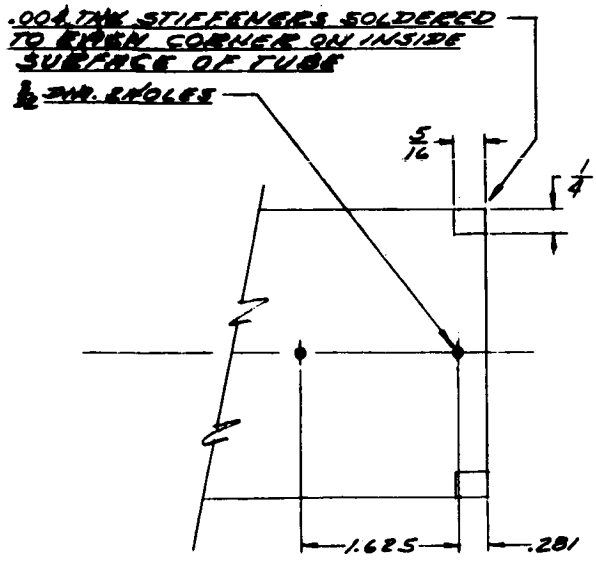

LOCATION OF 2 PROBE TIP MOUNTING HOLES

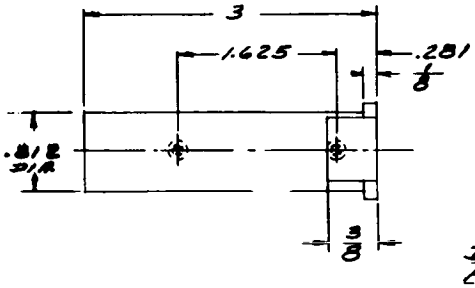

DRILL, TAP FOR #2-56 2 PLACES

PROBE TIP FIXTURE

#1

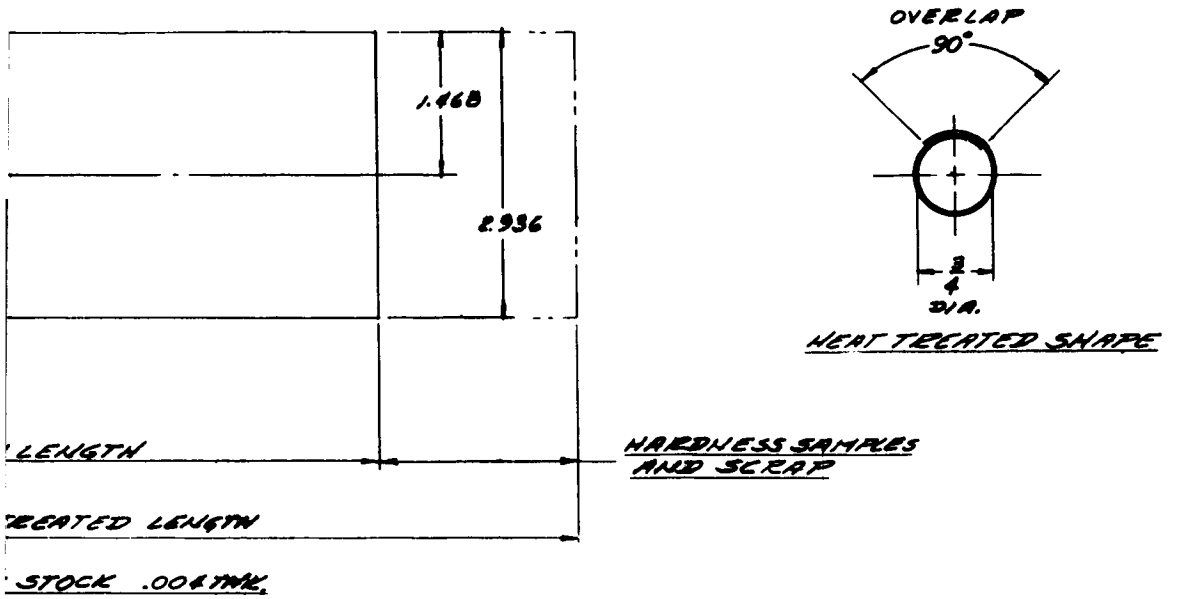

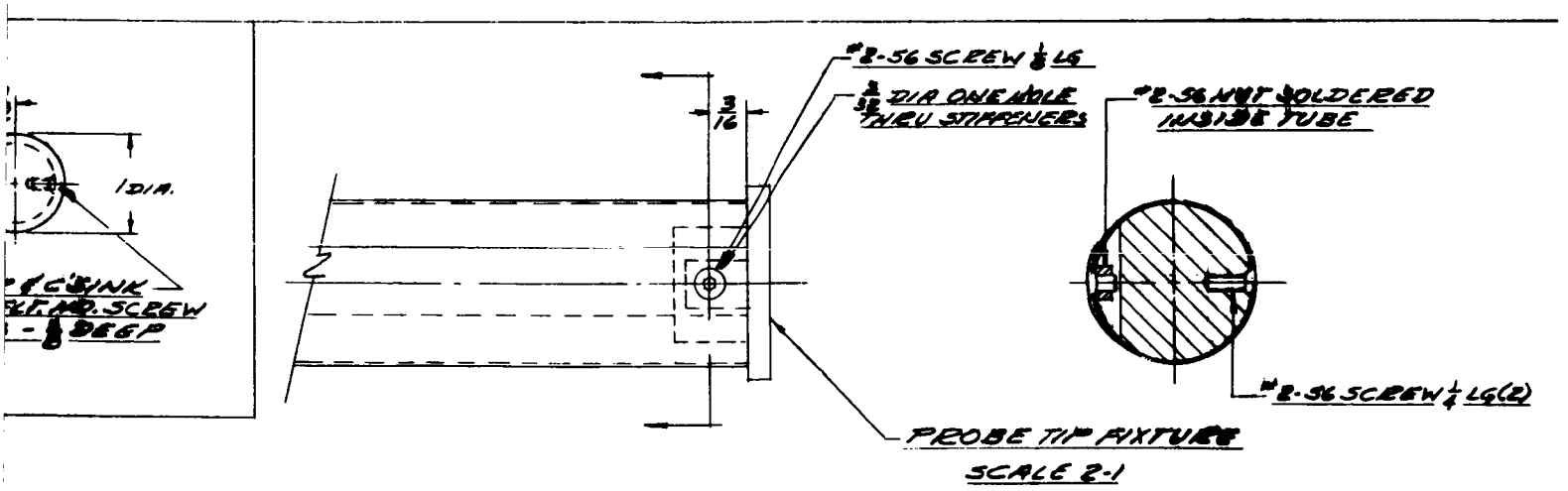

TUBE FINISHING OPERATIONS

1- INSERT PROBE TIP FIXTURE IN END OF TUBE & INSTALL (2) #2-56 SCREWS 1/4 LG. DO NOT TIGHTEN SCREWS COMPLETLY
2- LOCATE 3/32 HOLE - DRILL OR PUNCH THRU 2 LAYERS OF TUBE & 2 STIFFENERS
3- REMOVE TUBE & SOLDER #2-56 NUT AS SHOWN TO INSIDE OF TUBE
4- INSTALL TUBE ON FIXTURE - INSERT (2) 1/4 LG. SCREWS - C'SINK REMAINING HOLE FOR #2-56 FLT HD SCREW -
5- DRAW 3 SCREWS DOWN TIGHT TO FORM SMOOTH CONTOURED SEAT
6- REMOVE FIXTURE - INSTALL 1/8 LG SCREW IN NUT TO HOLD TUBE END CLOSED TUBE IS NOW READY FOR INSTALLATION IN PENETROMETER OR STORAGE

Figure 6-28 Probe Tube Module

forming and heat treating the tube has been developed. The final selection of material for the tube will depend upon the results of fatigue tests; hence, it can not be made at this time.

Probe Tip Module

The probe tip module (Figure 6-29) has three basic components: (1) a 60° cone point, (2) a load sensor, and (3) a limit switch. Since the speed of penetration into the lunar surface is relatively slow (1/2 in. per sec), a quasi-static load cell is adequate for measuring the force required to penetrate the soil. Two types of load cell designs have been considered. The first design incorporates a spring assembly of calibrated stiffness which permits a small movement of the conical penetrometer point relative to the end of the tube. By sensing this displacement (maximum 0.080 in.) with a linear variable differential transformer (LVDT) equipped with a solid-state oscillator and demodulator, an electrical signal ranging from 0 to 5 volts is obtained for a force ranging from 0 to 10 lb. At the 10-lb force level, the displacement of the conical tip is sufficiently large to trip a limit switch which reverses the motor and withdraws the penetrometer tube.

A second type of load sensor incorporating a proving ring inside a flat end probe tip is being considered. The proving ring acts in the same fashion as the helical springs; however, the proving ring gives more consistent performance and eliminates the need for bearings on the LVDT shaft. Pending further investigation, the LVDT will be used in the design.

Tube Housing Module

Under adverse operating conditions it may be possible for the penetrometer to malfunction in its extended position and affectively pin the roving vehicle to the lunar surface. A tube cut-off device has been designed and may be incorporated in the tube housing module. When activated, it will free the vehicle and abort the soil measurement segment of the mission.

The tube housing is conical at its forward end and, as it passes the probe tip, it flattens and widens out to follow the general contour of the probe tube. The mouth of the housing has a circular flange which rests on the inner face of the SLRV compartment. A segmented wiper which will readily conform to the contour of the probe tube is located immediately inside the mouth of the housing. The purpose of this guide is to remove the soil particles which might adhere to the tube during retraction.

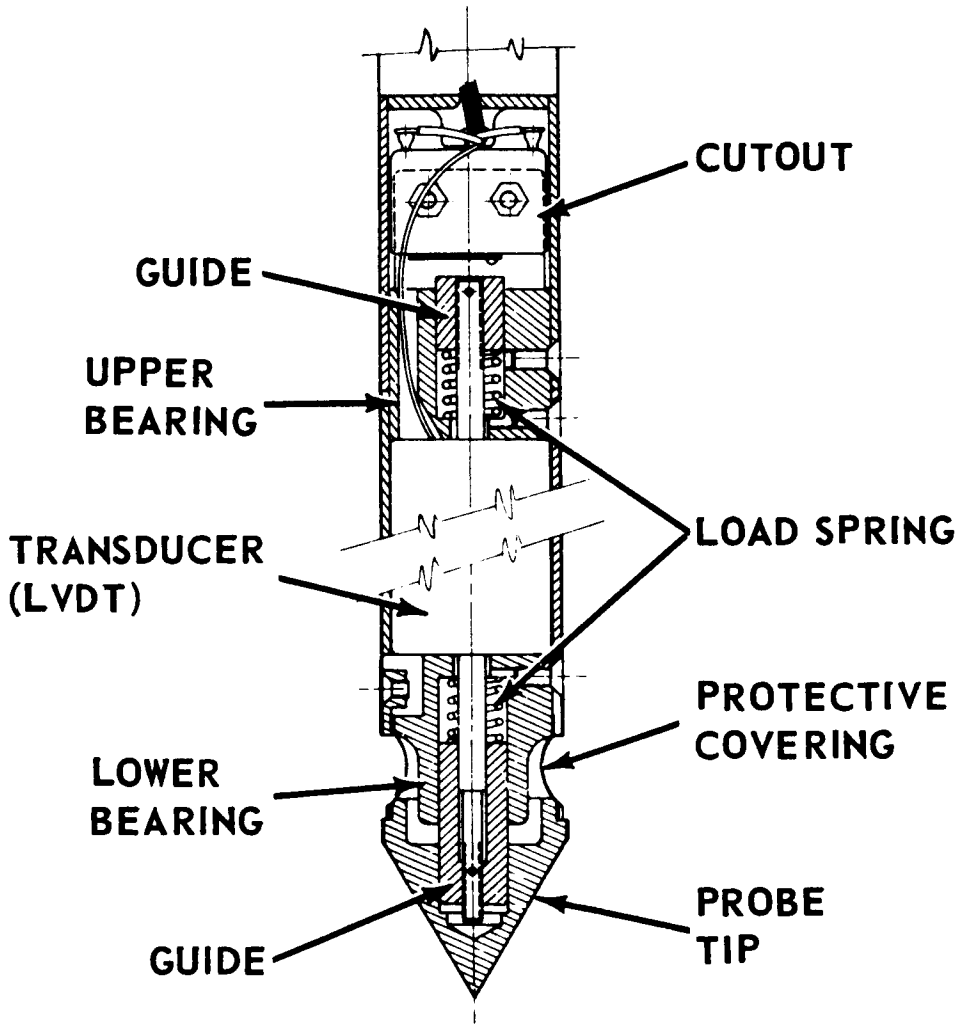

Figure 6-29 Probe Tip Assembly

Mounted behind the wiper is a probe tube cutter and its explosive actuator. The cutter is fabricated from carbide segments with a serrated knife edge designed to drive inward and shear the probe tube when the explosive charge is initiated. The explosive cutter actuator is a linear shaped charge which is relatively stable under impact loading. Detonation is initiated by an electric squib operating from a command signal. The actual shape and quantity of the charge required has not been determined.

A probe tube guide is mounted directly behind the tube cutter. The primary function of this guide is to prevent contact between the tube cutter and the tube. However the guide also serves as a blast shield in the event that the tube cutter must be actuated.

6.2.5.2 Materials and Component Selection

The selection of materials and components for the SLRV penetrometer is more critical from an operational and reliability viewpoint than for mechanical design. The lunar environment with its temperature extremes and its hard vacuum places such demands on the materials and components that they must be thoroughly analyzed and, if necessary, tested before being incorporated into the penetrometer. A tentative selection of materials and components is made for each module.

Storage Module

The framework of the storage module is currently designed with aluminum to establish the basic contours for unit strength and mounting capabilities. With the minimum internal dimensions established for functioning and the maximum external dimensions established for installation in the LRV, a secondary investigation will be undertaken on alternate materials. Glass reinforced plastic is one type of material which will be investigated in an attempt to further reduce the weight of the system. With proper selection of the matrix, resin glass reinforced plastics may perform satisfactorily in the lunar environment. However, its low modulus of elasticity may introduce deflection and stability problems.

The bearings in the storage module are of the sleeve type and are operated under relatively light loads. For this reason glass reinforced teflon bearings impregnated with a solid lubricant (molybdenum disulfide) have tentatively been selected.

Work hardened stainless steel appears to be the most suitable material for fabrication of the two negator springs. Further investigation of the spring materials will be made in conjunction with Hunter Spring Co., the major manufacturer of negator springs in the United States. Of particular importance is the problem of cold welding which the coiled material may experience in the lunar environment. Teflon coatings may be required on at least one face of the coil to avoid the tendency of cold welding.

The negator spring drums will be fabricated from either glass-reinforced plastic or teflon. If proper bakeout procedures are used these materials should prove satisfactory from both a weight and structural strength viewpoint.

The storage drum for the probe tube will probably be fabricated from aluminum and glass reinforced plastic. Aluminum will be used for the end caps and shafts, and glass reinforced plastic for the drum. This choice of materials will give a lightweight, structurally sound member to which the probe tube can be mounted without danger of cold welding.

The worm gear reduction unit which is placed between the storage drum shaft and the payout potentiometer is subjected to extremely light loads. For this reason plastic (teflon) and aluminum can be substituted for the more conventional steel and bronze gear components. Molybdenum disulfide will be employed to provide solid film lubrication of the gears.

Power Module

The structure framework for the power module must carry substantial loads due to the pressure required between the drive rollers. Hence, it appears the aluminum will be the most suitable material for this application.

A Globe MM type DC motor has been selected to drive the power module. Globe has indicated an operating life between 190 and 250 hours which appears suitable for a tentative selection. However, it is evident that this motor as well as a few other candidates must be thoroughly tested before making a final selection.

To prevent cold welding in the spur gear drive between the motor and the drive wheels, dissimilar materials must be employed where gears contact each other. The smaller of the two gears will be fabricated from stainless steel and the larger from a non-metallic such as teflon or reinforced plastic. It is anticipated that tests will be conducted to select the most suitable non-metallic material for this gear application.

Aluminum was used in the fabrication of the pressure and drive wheels in the prototype penetrometer. However, due to the possibility of cold welding to the probe tube these wheels must be coated with a non-metallic material. It is anticipated that a thin layer of alumina filled epoxy, approximately 0.005 to 0.010 in. thick around the circumference of both wheels, will be adequate. This composite material should resist creep and avoid any significant reduction in the coefficient of friction which may result from the presence of the polymeric materials at the interfaces.

The bearings in the power module carry considerable loads due to the normal force required between the pressure and drive rollers. For the preliminary design of the SLRV penetrometer, precision ball bearings with suitable solid film lubrication have been selected. However, this selection is quite tentative and further investigation in this area is in order.

The tube guides will be fabricated from a molybdenum disulfide impregnated teflon. This material exhibits a low coefficient of friction and should serve adequately as a guide material in the lunar environment providing proper bakeout procedures are employed to condition the teflon.

Probe Tube

Parametric studies were made of tube characteristics and the results are available on request. Chrome vanadium, silicon manganese, and 18-8 stainless steel are currently being considered as possible materials for the tube. Since the analysis of the tube life as a function of the materials fatigue properties depends strongly on the compressive stresses produced by the guide rollers, it will be necessary to determine the cyclic life experimentally. It is anticipated that cyclic life tests will be conducted with these three materials processed in different ways until the optimum combination of material and process are established.

Probe Tube Housing Module

The housing will be fabricated from glass reinforced plastic to provide a high strength yet lightweight structure. The guide mounted to the housing wall will be fabricated from molybdenum impregnated teflon to reduce the power loss due to friction. The tube wiper will be fabricated from a silicone rubber which will withstand the lunar environment while remaining flexible at the lower temperatures which it will encounter.

The segmented teeth for the explosive actuated tube cutter will probably be fabricated from tungsten carbide. However, the explosive to be used in the linear charge has not been selected at this date.

Probe Tip Assembly

The conical tip on the point of the penetrometer will be fabricated from aluminum. The aluminum should be sufficiently hard to resist the abrasion which will be encountered in the 4000 to 5000 operational cycles of the penetrometer. Although some wear of the sharp point on the probe tip will be encountered, the soil mechanics investigation (Section 6. 3) has shown that the rounding of the point will not significantly influence the accuracy of the soil measurements.

The probe tip housing is mounted behind the probe tip and contains the force sensor. This component will be fabricated from aluminum to facilitate mounting of the housing to the penetrometer tube.

The linear variable differential transformer (LVDT) sensor or force transducer requires a solid state oscillator and demodulator. These elements will be located in the electronics module mounted in the temperature controlled portion of the penetrometer. The mechanical design of the LVDT will include selection of suitable materials for the stake bobbin and potting compounds to operate in the lunar environment. Improved reliability of the transducer circuit can be obtained by reducing the number of components (essentially diodes) in the associated electronic circuit. This improved reliability would be accomplished at the expense of signal-to-noise ratio in the output signal. The final design thus becomes a compromise between the reliability of operation of the circuit and the signal-to-noise ratio of that signal. Two manufacturers can supply the modified transducer described above. They are, G. L. Collins Corp., and the Sanborn Co.

Electronics Package

The electronics package of the penetrometer subsystem consists primarily of the LVDT oscillator and demodulator, the switching circuit, the drive motor, and the penetration depth indicator. The LVDT unit will probably be procured as an entire unit from the manufacturer. The same situation holds for the drive motor. Thus, in these cases, the manufacturer's design, assembly, and material selection must be monitored. The switching circuit and potentiometer for depth indication will be fabricated from high reliability electronic components.

6.2.6 Engineering Prototype Penetrometer Tests

6.2.6.1 Performance Test Plan

An engineering prototype penetrometer was built and tested to establish its performance characteristics and contribute to the design.

The penetrometer was mounted on a skeleton frame which simulates the SLRV geometry, lunar weight, and spring constant.

6.2.6.2 Performance Test Results

In this section each of the seven tests will be described individually with particular emphasis on power requirements, probe velocity, time to achieve penetration and reproducibility.

Test Condition A - Full Probe Extension Zero Resistive Load

In this test the penetrometer was cycled four times to its maximum extended position (29 in.). The mechanism functioned properly in all four cases and the limit switches controlling both the extention and retraction phases of the operational cycle performed satisfactorily. The extension of the tube was plotted on the x axis of an x-y recorder and the records obtained are shown in Figure 6-30. By comparing markings on the tube with the depth indicated on the x-y recorder it was established that the potentiometer recording tube payout was functioning satisfactorily.

The time required for the tube to extend 29 in. was 102 ± 0.5 sec, the time required for retraction was 103 ± 1.5 sec, and the total time for the complete cycle was 205 ± 1 sec. The average probe velocity for the extension portion of the cycle was 0.284 in./sec and for the retraction portion of the cycle the average probe velocity was 0.282 in./sec.

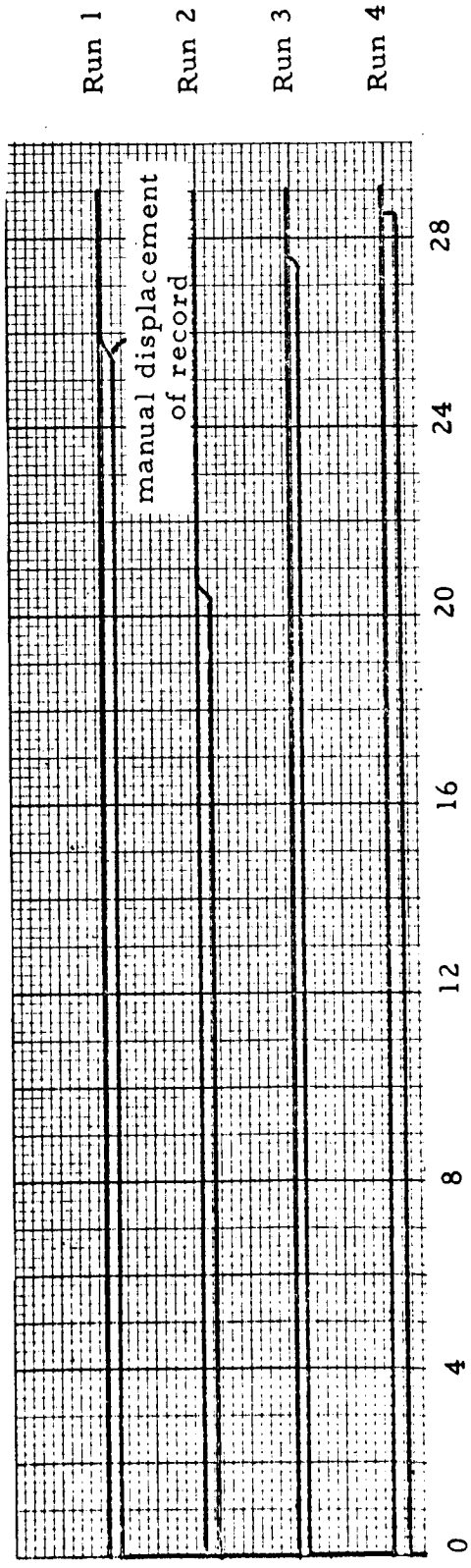

Figure 6-30 Probe Payout Records Obtained in Four Tests with No Resistive Load

The power required for operation during the extension and retraction phases of operation is shown in Figure 6-31. Approximately 2.70 watts and 2.49 watts are required during extension and retraction respectively. It should be emphasized here that this power is required to overcome friction in the drive mechanism. The delivery schedule did not permit a detailed experimental analysis of the friction losses in various components. However, it is believed that minor design changes could reduce the power losses due to friction by at least 25 percent.

Test Condition B - Partially Extended Contacting Infinite Resistive Load

In this test the penetrometer was cycled four times to a partially extended length where it encountered an infinite resistive load. The length of extension was varied according to the following schedule.

Run 1 - 26.7 in.

Run 2 - 21.4 in.

Run 3 - 14.4 in.

Run 4 - 8.4 in.

In all four test runs the penetrometer mechanism functioned properly and the overload switch mounted in the tip of the load cell performed satisfactorily. A graph of force as a function os position was recorded automatically on an x-y recorder during this series of four tests. These records which are reproduced in Figure 6-32 show clearly reproducibility in the activation of the overload protection system.

The time sequence data on the operating cycle and the average probe velocity is shown in Table 6-4. The average velocities achieved in test condition B were identical with those obtained in test condition A to within 0.004 in./sec. The power requirements for a typical test run are shown in Figure 6-33. This power-time curve is very similar to the curve shown in Figure 6-32 except for the peak power which was drawn as the tube was loaded to the overload limit.

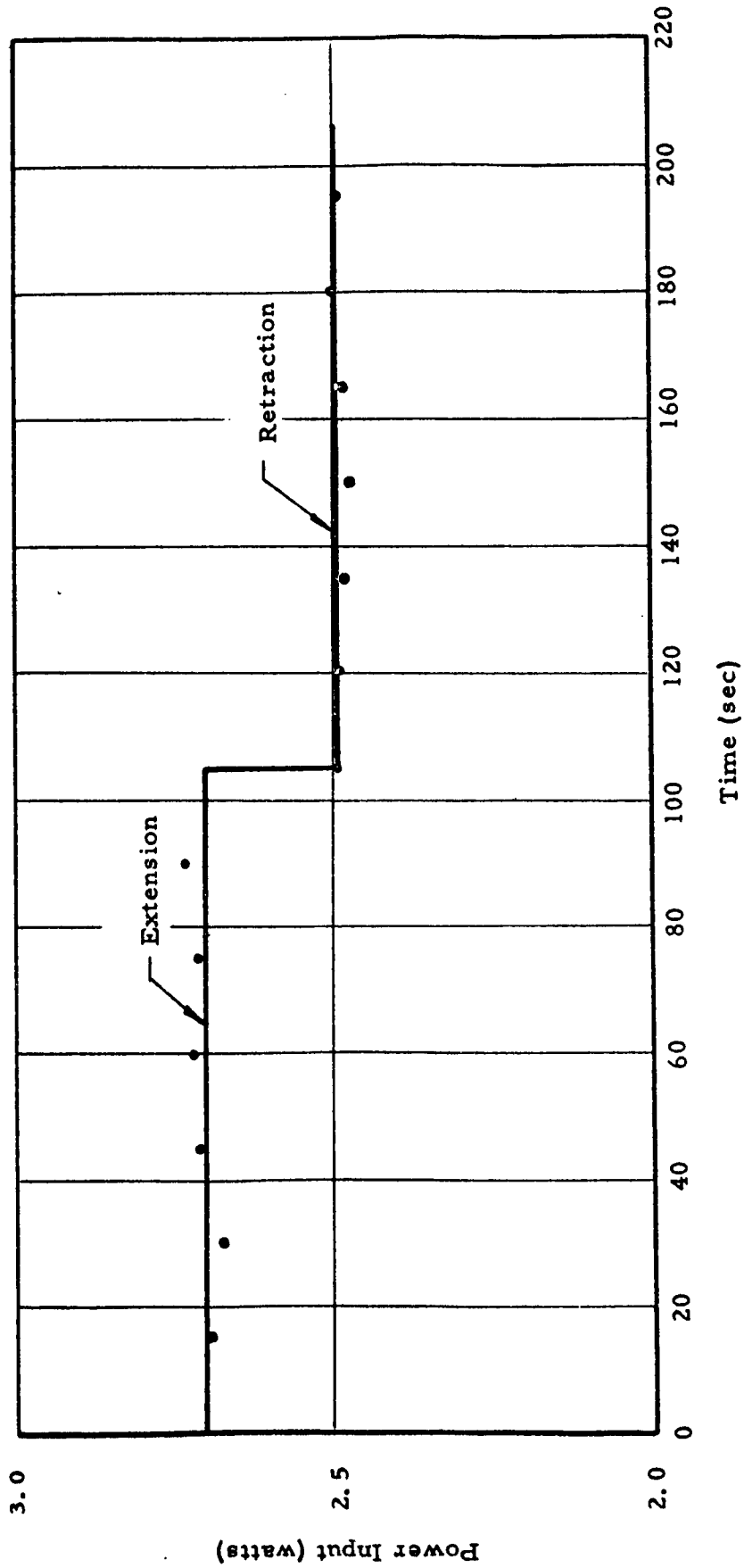

Figure 6-31 Typical Curves Showing Power Required During Extension and Retraction Phases of Operation, Test A, Run 1

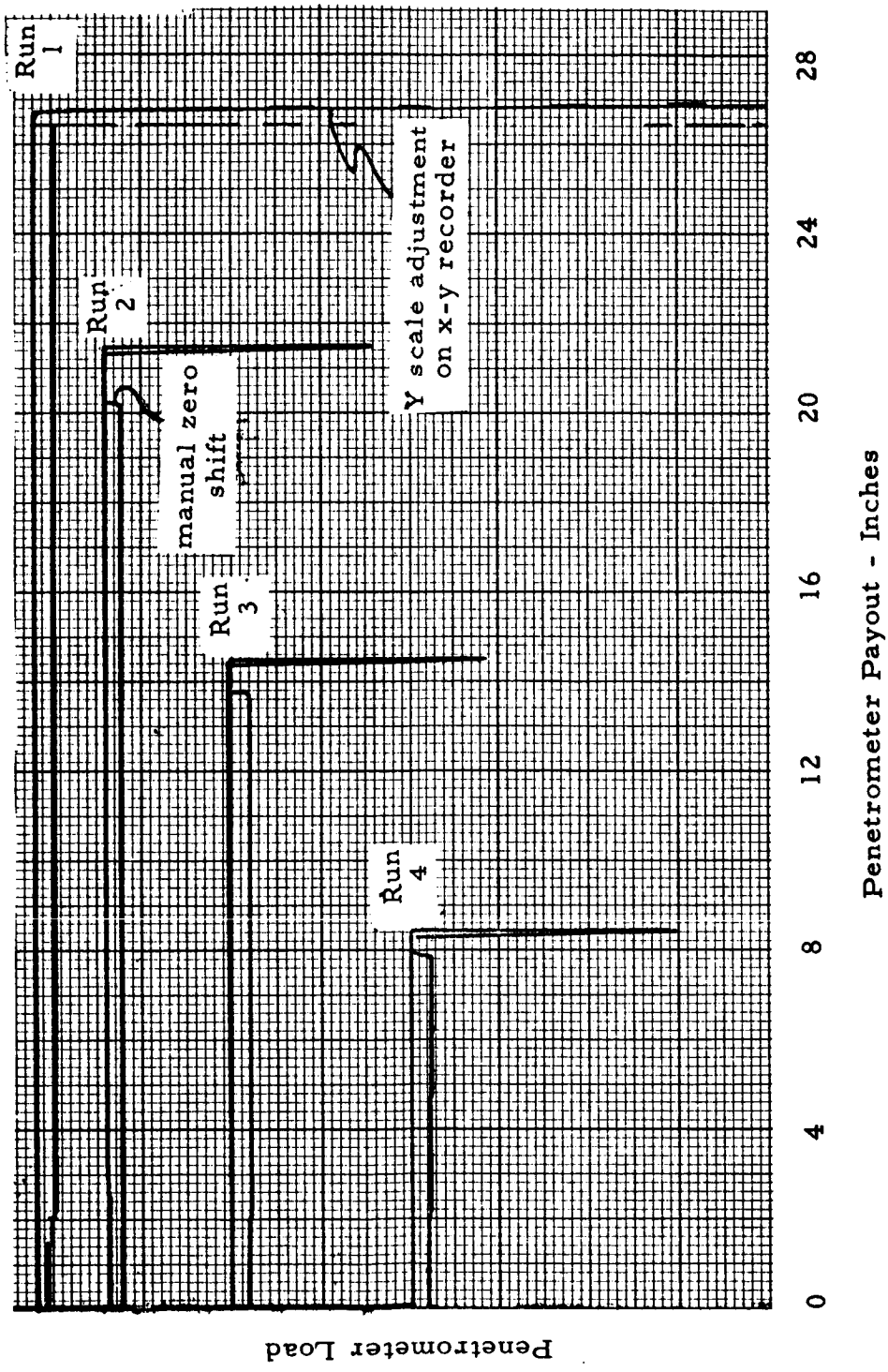

Figure 6-32 Load vs Penetrometer Payout Obtained in Four Test Runs under Loading Conditions (B)

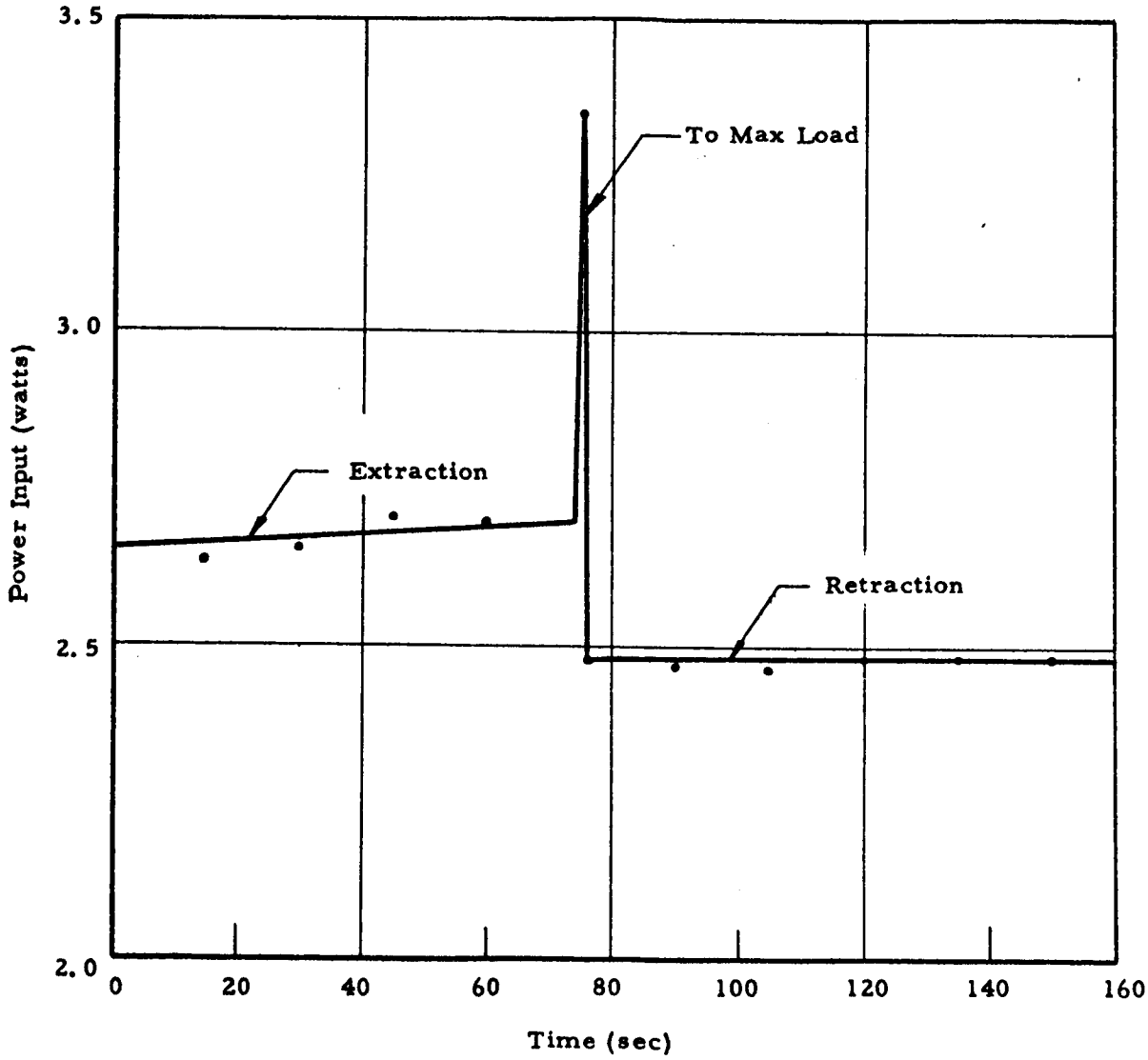

Figure 6-33 Typical Curve Showing Power Required During Extension and Retraction Phases of Operation, Test B, Run 2

TABLE 6-4

TIME, DISTANCE AND VELOCITY DATA OBTAINED IN TEST B

Run	T_E (sec)	T_R (sec)	T_T (sec)	$L_E = L_R$ (in.)	2_L (in.)	Average Velocity (in./sec)
1	95.5	94.5	190.0	26.7	53.4	0.281
2	76.0	76.5	152.5	21.4	42.8	0.281
3	52.0	51.0	103.0	14.4	28.8	0.280
4	31.5	28.0	59.5	8.4	16.8	0.282

Where

T_E .... Extension time

T_R .... Retraction time

T_T .... Total cycle time

L_E .... Extension length

L_R .... Retraction length

2_L .... Total cycle length

Test Condition C- Fully Extended Into Loose or Low Density Silica Flour

In this test the probe was cycled four times to its fully extended position into simulated lunar soil (atmospheric conditions). An adjustment of the spring controlling the pressure on the drive rollers was necessary on the first test run; however, after the adjustment of the drive roller pressure was made, the penetrometer functioned perfectly in the final three test runs. The penetrometer force which was recorded as a function of probe payout on an x-y recorder is shown in Figure 6-34. A comparison of the three records obtained indicates that the probe position could be established to within 0.05 to 0.1 in. Also, the force measurements appeared to be quite consistent when consideration was given to small variations in soil density which are inherent in this type of a test.

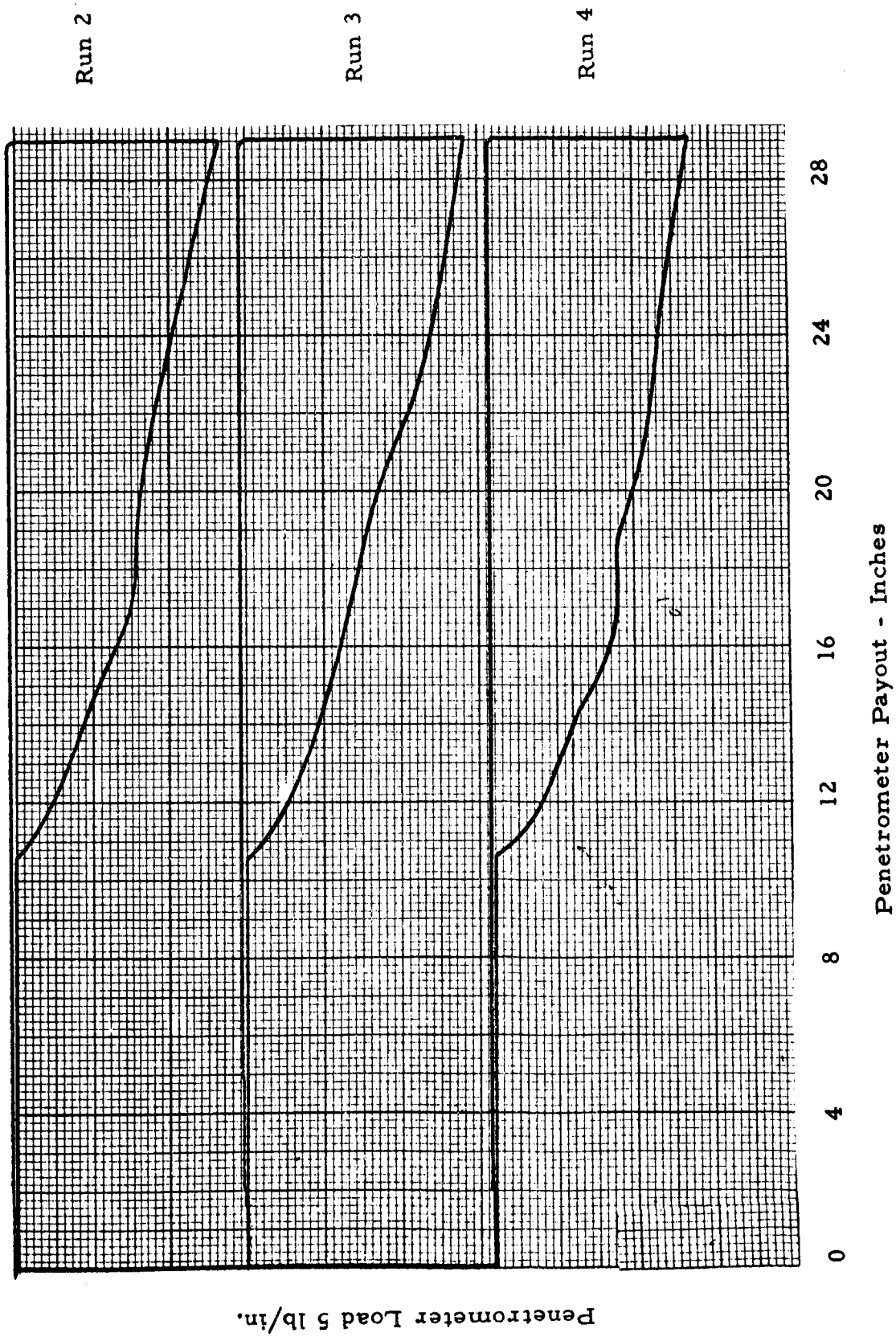

Figure 6-34 Load vs Penetrometer Payout Obtained in Three Test Runs under Loading Conditions (C)

Two of these penetrometer records (i.e., runs No. 2 and 3) were reduced in the form of F/A and X/C and compared to the results obtained in previous tests conducted with conventional flat-pad penetrometers. The comparison of the results obtained with the conical tip and with conventional penetrometers (presented in Figures 6-35 and 6-36) indicate that the results are very similar. The differences which exist can easily be attributed to variations in the soil sample.

The time sequence of operation of the penetrometer is presented in Table 6-5. The average velocity over the entire cycle was approximately 0.275 in./sec and the total time for cycling was about 211.5 seconds. These results should be compared with those obtained in test condition A where the average velocity was 0.283 in./sec and the total time for cycling was 205 sec. The resistive soil load ranged from 0 to about 7 lb during these tests and resulsted in a decrease of 0.008 in./sec in the average velocity of the peneteometer and an increase of 6.5 sec in the cycling time.

TABLE 6-5

TIME, DISTANCE AND VELOCITY DATA OBTAINED IN TEST C

Run	T_E (sec)	T_R (sec)	T_T (sec)	L_E (in.)	L_R (in.)	^2L (in.)	Average Velocity (in./sec)
2	107.5	103.5	211.0	29	29	58	0.276
3	107.5	103.5	211.0	29	29	58	0.276
4	109.0	103.0	212.0	29	29	58	0.274

Where

T_E .... Extension time

T_R .... Retraction time

T_T .... Total cycle time

L_E .... Extension length

L_R .... Retraction length

^2L .... Total cycle length

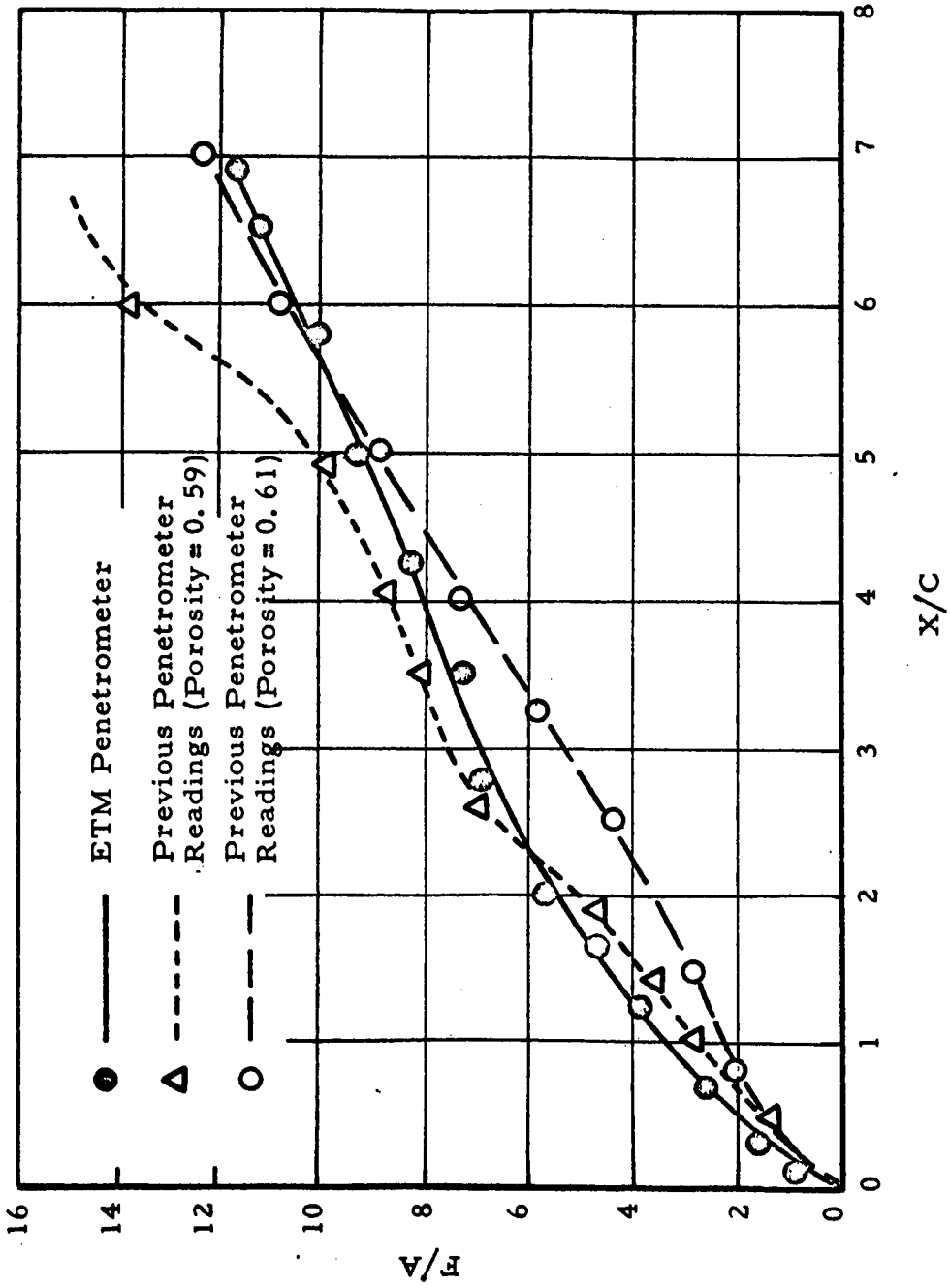

Figure 6-35 Force Per Unit Area vs Ratio of Penetration to Perimeter (F/A vs X/C), Run 2

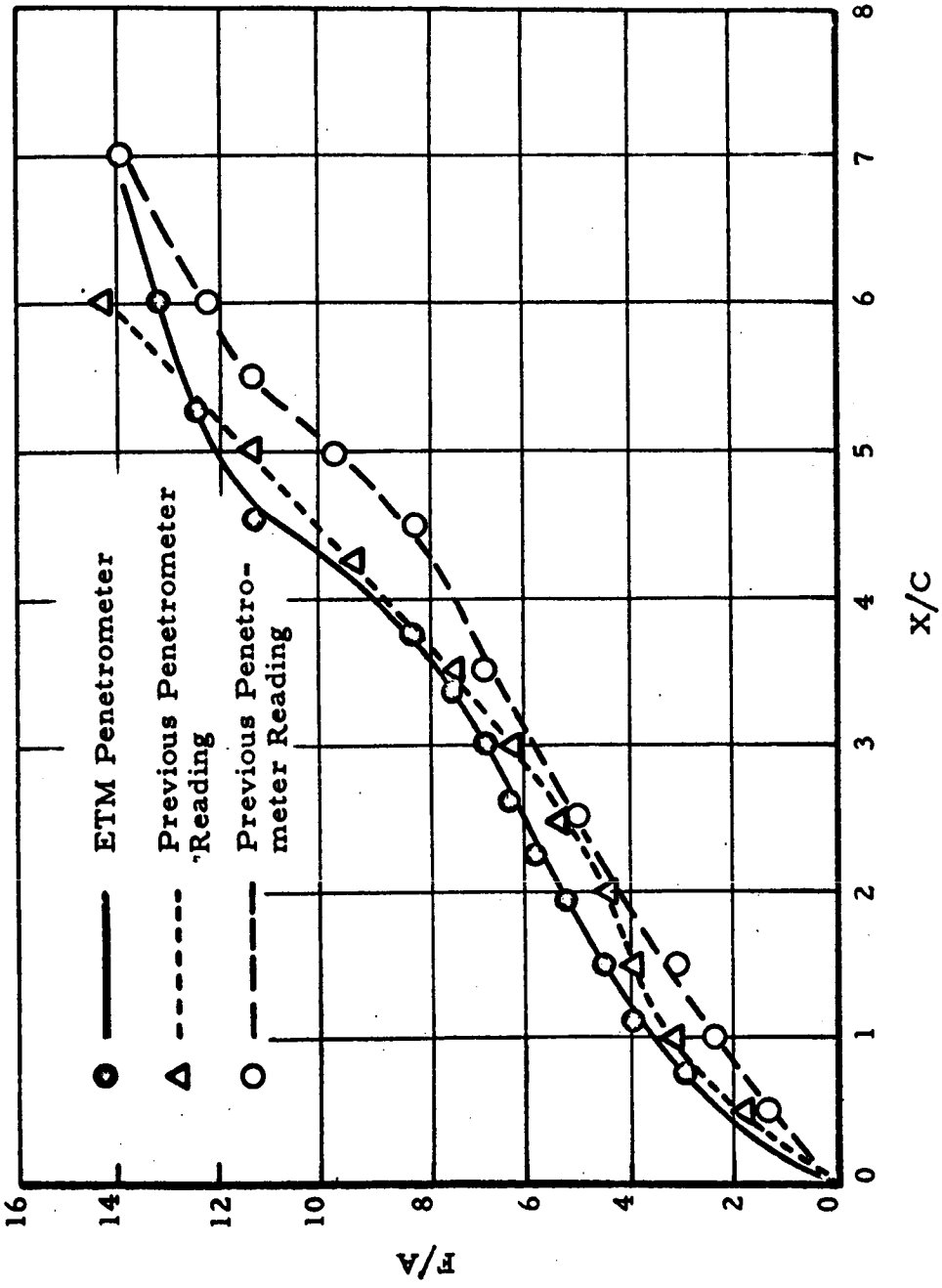

Figure 6-36 Force Per Unit Area vs Ratio of Penetration to Perimeter (F/A vs X/C), Run 3

The power input is presented as a function of time in Figure 6-37. The power required for free extension was about 2.9 watts; however, when the soil resistance was encountered the power increased almost linearly with penetration depth until a maximum of 3.7 watts was reached with the fully extended probe. Upon retraction, the required power decreased sharply to 2.59 watts. Little or no difference was noted in the power required for retraction from the hole and free retraction.

The power required for free extension and free retraction in this test was somewhat higher (0.1 to 0.2 watts) than the same power required in Test A. This difference can probably be attributed to a thin layer of soil which adhered to the outside wall of the tube and increased the friction losses at the wiper-guide located at the forward end of the penetrometer.

Test Condition D - Partially Extended Into High Density Silica Flour

In this test the penetrometer was cycled four times into a relatively well compacted silica flour-soil bed. The depth of penetration achieved before overloading the penetrometer at the 11.6 lb level was of the order of 1 to 1.5 in. Both the penetrometer driving mechanism and the overload protection device functioned satisfactorily. The force displacement records shown in Figure 6-38 indicate that the overload limit switch was activated at 11.6 lb ± 0.1 lb and that penetration occurred at payout distance of 10.25 ± 0.05 in.

The time sequence of operation and the average velocity of the probe is shown in Table 6-6. The results obtained for the time required to cycle appear to be consistent with those results achieved in earlier tests.

The power required to operate the penetrometer under these test conditions is shown in Figure 6-39. The power required for free extension is about 2.82 watts and that power required to achieve the 11.6 lb load in dense soil is about 3.58 watts. The retraction power required varies from 2.5 to about 2.6 watts. It is believed that this modest increase in power is due to soil accumulation on the forward guide and wiper as the probe is retracted.

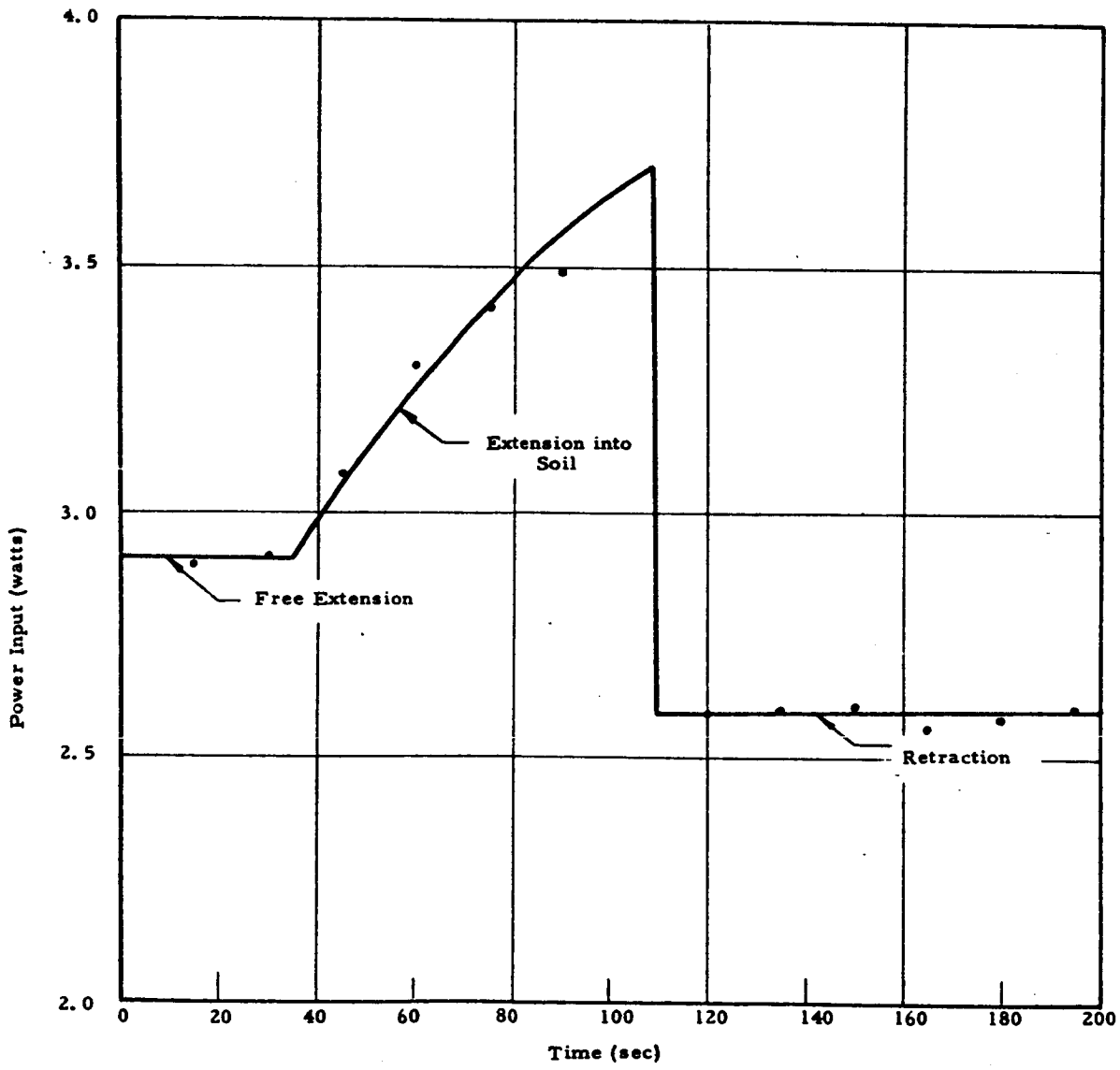

Figure 6-37 Typical Curve Showing Power Required During Extension and Retraction Phases of Operation, Test C, Run 4

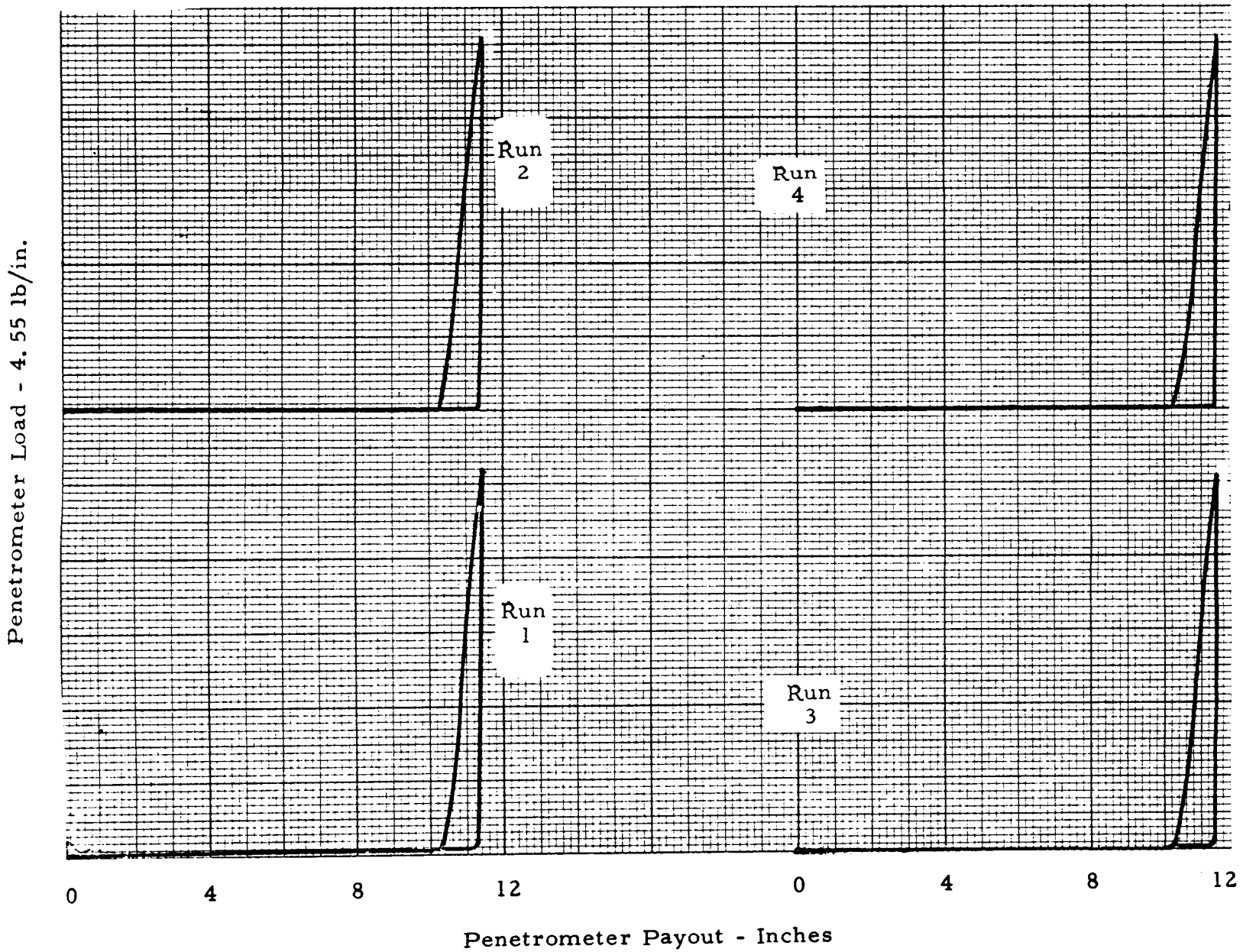

Figure 6-38 Load vs Penetrometer Payout Obtained in Four Test Runs under Loading Conditions (D)

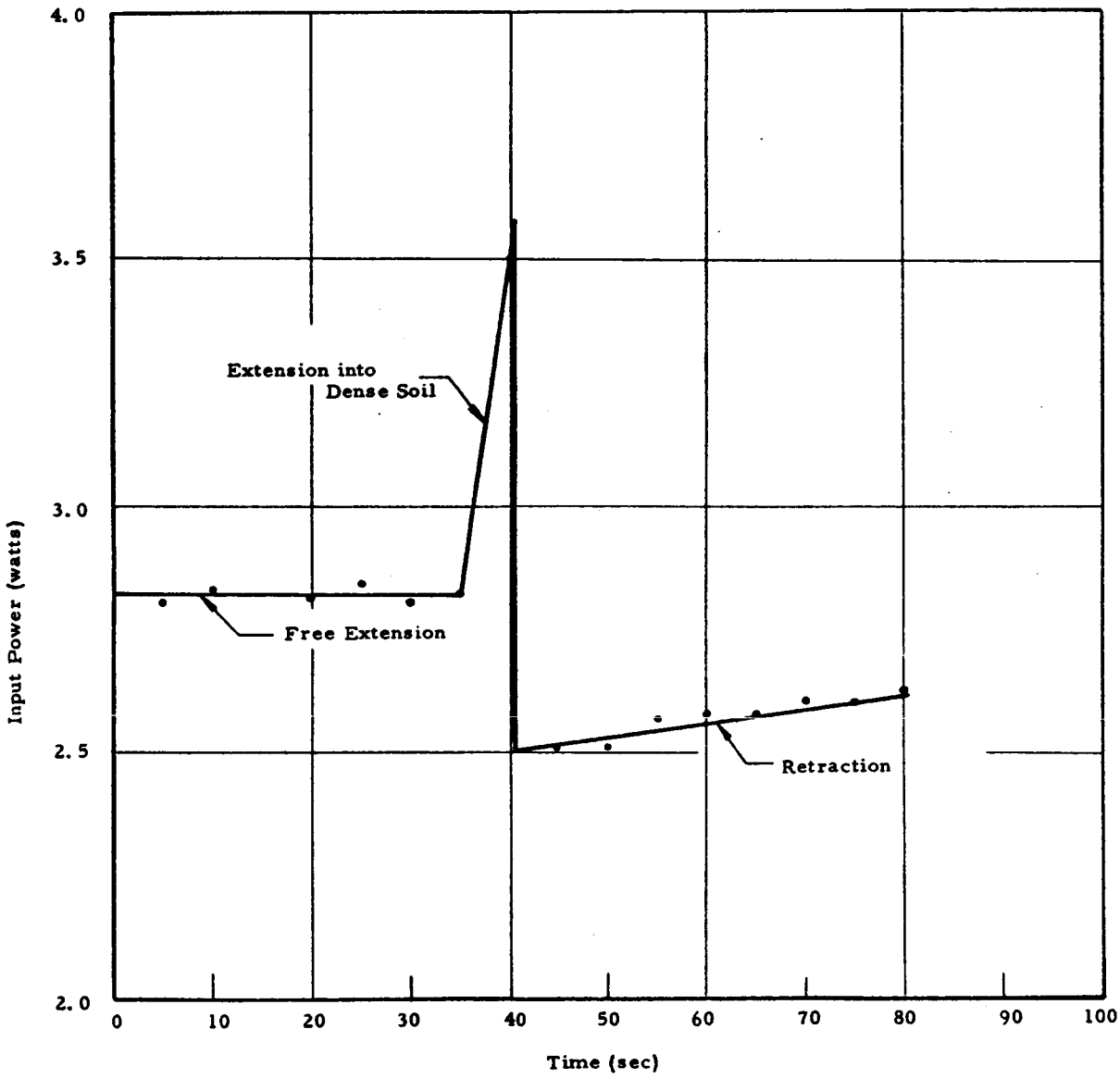

Figure 6-39 Typical Curve Showing Power Required During Extension and Retraction Phases of Operation, Test D, Run 3

TABLE 6-6

TIME, DISTANCE AND VELOCITY DATA OBTAINED IN TEST D

Run	T_E (sec)	T_R (sec)	T_T (sec)	L_E (in.)	L_R (in.)	w_L (in.)	Average Velocity (in./sec)
1	40.5	41.0	8.15	11.4	11.4	22.8	0.280
2	41.2	40.8	82.0	11.4	11.4	22.8	0.278
3	40.9	40.6	81.5	11.4	11.4	22.8	0.280
4	41.7	40.8	82.5	11.4	11.4	22.8	0.276

Where

T_E .... Extension time

T_R .... Retraction tine

T_T .... Total cycle time

L_E .... Extension length

L_R .... Retraction length

2_L .... Total cycle length

Test condition E - Partially Extended Into Silica Flour With a Layer of Randomly Dispersed Gravel

In this test the penetrometer was cycled four times into a soil bed containing a layer of randomly dispersed gravel located 10 in. below the surface of the soil. The gravel was irregular in size (approximately 1 in. in diameter) and was arranged only to the extent to ensure that the probe would be certain to contact one or more pieces of the gravel. In spite of this severe soil condition the penetrometer mechanism and its attendant overload protection device functioned quite adequately. The four records of penetrometer load as a function of payout shown in Figure 6-40 indicates that probe encountered a number of different conditions in the rock layer. For instance, in run 1, the drop off in load just prior to the peak load indicates a gross movement of the gravel under the penetrometer. Runs 2 and 4 indicate the solid nature of the gravel was moved approximately 2 in. before peak load could be obtained.

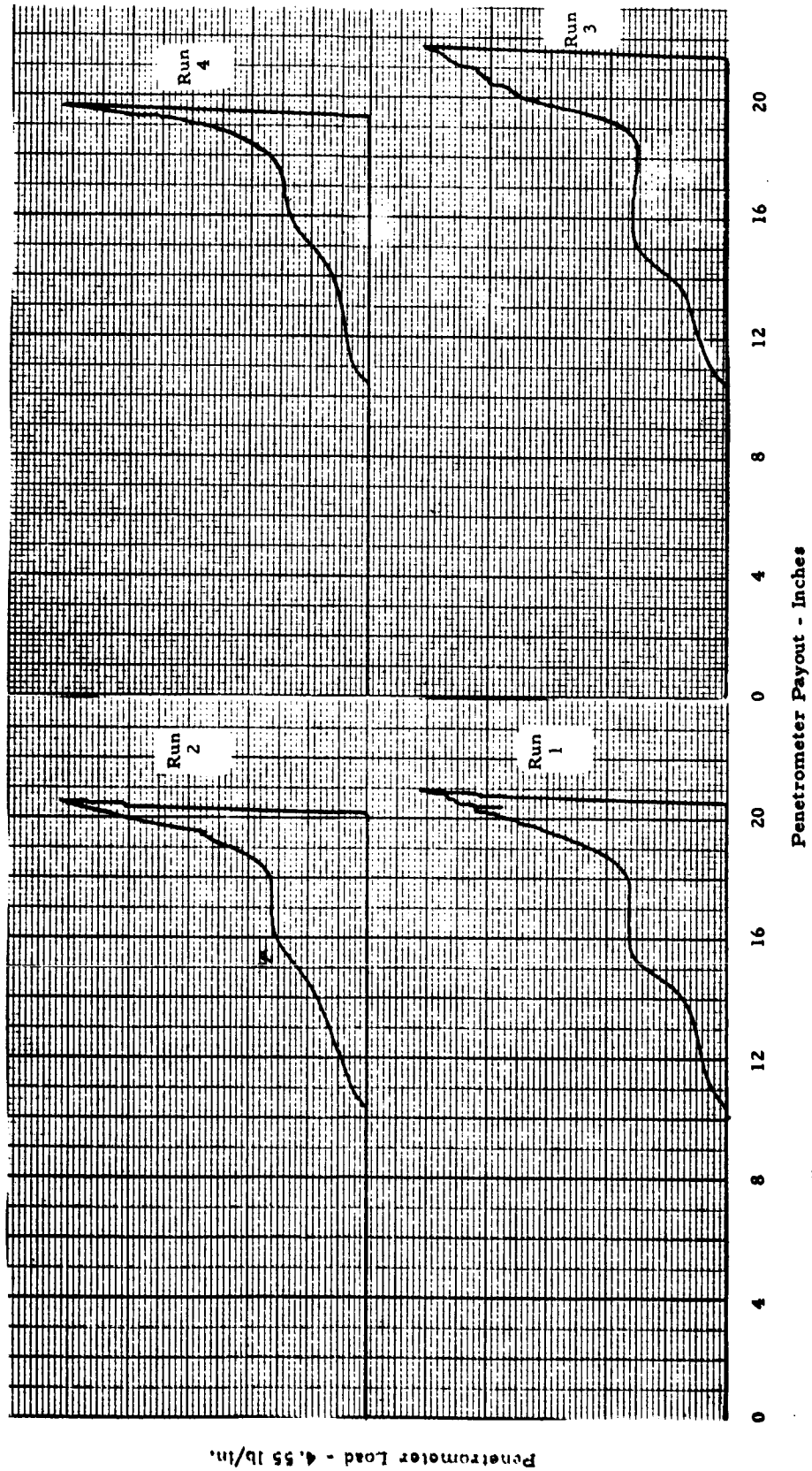

Figure 6-40 Load vs Penetration Payout Obtained in Four Test Runs under Loading Conditions (E)

The time sequence of the operation shown in Table 6-7 indicates a relative constant average velocity over the four test runs of 0.275 ± 0.001 in./sec. The time of operation for a given cycle is variable since the position of the gravel layer was not uniform. Overload at the gravel layer took place after payout distances ranging from 19.6 to 2.17 in.

TABLE 6-7

TIME, DISTANCE, AND VELOCITY DATA OBTAINED IN TEST E

Run	T_E (sec)	T_R (sec)	T_T (sec)	L_E (in.)	L_R (in.)	2_L (in.)	Average Velocity (in./sec)
1	78.0	74.0	152.0	20.9	20.9	41.8	0.276
2	76.5	73.0	149.5	20.5	20.5	41.0	0.274
3	80.4	77.6	158.0	21.7	21.7	43.4	0.275
4	72.5	70.0	142.5	19.6	19.6	39.2	0.275

Where

T_E .... Extension time

T_R .... Retraction time

T_T .... Total cycle time

L_E .... Extension length

L_R .... Retraction length

2_L .... Total cycle length

The power requirements for operation of the penetrometer into these soil conditions are shown in Figure 6-41. The free extension power was approximately 2.78 watts which increased to 3.65 watts as the soil and gravel was encountered. Upon retraction, the power dropped to 2.55 watts and then gradually increased as the tube was withdrawn to about 2.65 watts.

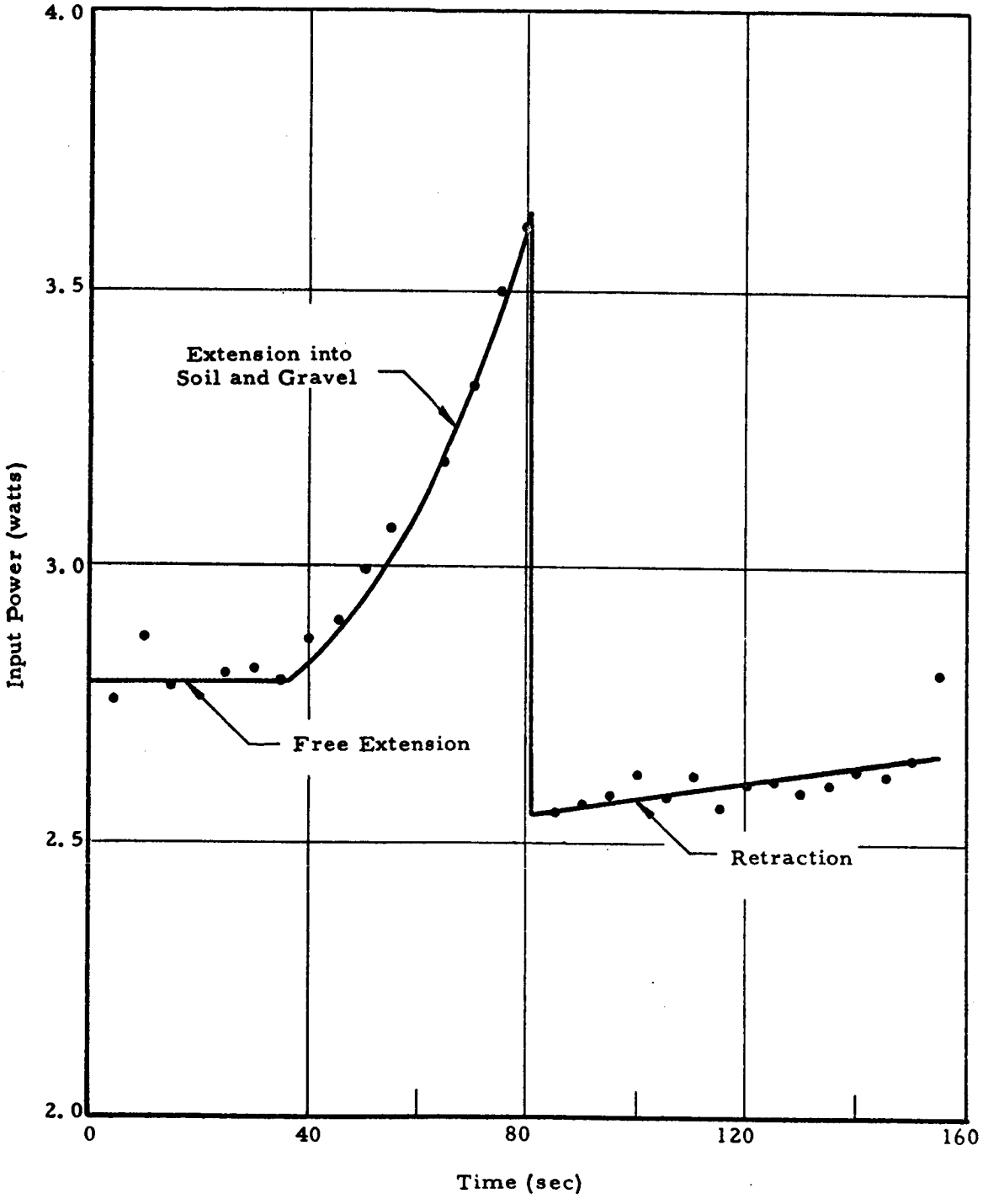

Figure 6-41 Typical Curve Showing Power Required During Extension and Retraction Phases of Operation. Test E. Run 3

Test Condition F - Operation on a 15° Slope

In this test, the skeleton frame supporting the penetrometer mechanism was mounted on a sheet of plywood inclined at a 15° angle with the surface of the soil bed. The penetrometer was cycled four times from this inclined position to observe if slippage would occur. On the first two tests with the aluminum skids of the skeleton frame against the plywood, no slippage occurred and the penetrometer was cycled to its full extension where a penetration force of 5 lbs was developed. The coefficient of friction between the vehicle and the wood surface was approximately 0.3 in these tests. Since no slippage of the skeleton frame could be observed, teflon tape was applied to the skids to attempt to lower the coefficient of friction. The penetrometer was again cycled to full extension at a peak load of 5 lbs and no slippage occurred. Teflon tape was then applied to the plywood to achieve a teflon on teflon friction condition. In the four tests a small slippage of about 1/16 of an inch was observed and the tube was side loaded; however, the penetrometer functioned adequately.

Test Condition G - Partially Extended Into a Soil (with Gravel Layer) with an Applied Side Load

In this test, the penetrometer was driven into the same soil bed as Test Condition E. After penetrating the soil for about 4 in. the penetrometer was stopped and a 1-lb side load was applied to the skeleton frame. Since the skeleton frame was placed on rollers and counterweighted to overcome friction, this 1-lb side load was transmitted directly to the tube. The penetrometer was restarted and driven into the gravel where it overloaded and retracted. Upon retraction, the side load produced a transverse motion of the skeleton frame and the penetrometer point plowed the surface of the soil for several inches. A force-payout record showing the performance of the penetrometer under these conditions is shown in Figure 6-42.

No measurements of power or time sequence were made during this test.

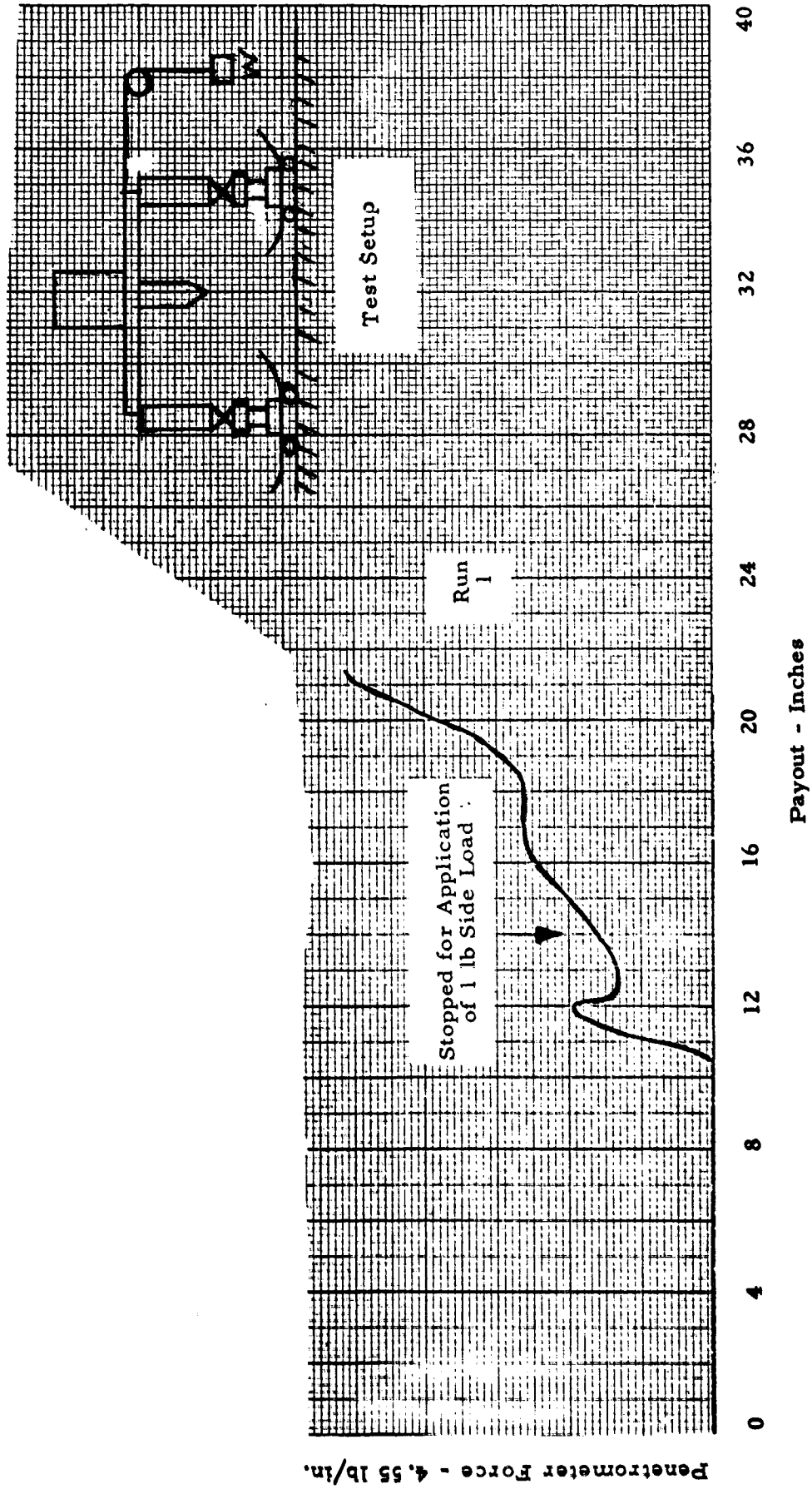

Figure 6-42 Load vs Penetrometer Payout Obtained in Test Conducted Under Loading Condition G

6.2.7 Modes of Partial Operation

An analysis of the penetrometer subsystem indicates that partial operation and some useful information can be obtained in the event of specific component failures. A fracture or major binding of the probe tube, a failure of the drive motor, or a failure of the drive rollers as well as non-operation of the electrical control and data-handling circuitry must be considered as catastrophic and cause to abort the experiment. However, failure of one or both of the sensors or the limit switches does not preclude the gathering of meaningful data if proper precautions are taken.

The partial modes of operation and possible results are summarzied in Table 6-8.

6.2.8 Conclusions

The prototype model of the penetrometer was tested under seven different conditions of loading through 25 cycles of operation. In only one case was it necessary to stop the penetrometer to make a minor adjustment with the driving rolls.* The extension and retraction control circuit functioned perfectly and the overload control circuit performed adequately under very adverse soil conditions. The tube was guided well and tracked perfectly. The lead wire and the tube storage mechanism functioned properly. The power required for free extension was between 2.7 and 2.8 watts with a peak power of about 3.6 watts at maximum load. During retraction power, requirements dropped to 2.5 to 2.6 watts. The average velocity of the probe ranged between 0.275 to 0.283 in./sec depending upon the loading conditions.

The soil penetration resistance data obtained during these tests compared well with the results obtained previously with a conventional penetrometer. Thus, it can be concluded that this mechanical design concept is a feasible approach for the SLRV penetrometer and that the data obtained can be resolved to the same accuracy as that normally employed in terrestrial soil mechanics.

---

* It should be noted that this penetrometer was not preadjusted before these performance tests. Delivery and test schedules did not permit complete adjustments of the overload switch and the drive roller pressure.

TABLE 6-8

MODES OF PARTIAL OPERATION

Failure Mode	Operating Procedure: Soft Soil	Operating Procedure: Hard Soil
LVDT and payout sensor fail	The operation time of the drive motor may be monitored to give go/no-go data. The payout limit switch will provide retraction control.	Monitoring of the drive motor will provide go/no-go data up to the point when the force is such as to activate the overload limit switch.
LVDT fails	Operation time and depth recording may be used to give go/no-go data.	Limit switches provide adequate control and safety features.
	Soft or Hard	
Payout sensor fails	Almost complete capability with payout information to accuracy of approximately 3 to 5% could be obtained by time monitoring of drive motor.	
Overload limit switch fails	Complte operational capability. Data must be monitored to prevent over-turning of vehicle. This will be provided by control from inclinometer output.	
Full-extension retract switch fails	Probe must be manually stopped and retracted before complete extension is made.	

6.3 BEARING STRENGTH EXTRAPOLATION STUDIES

6.3.1 Summary

The choice of using a penetrometer to determine the bearing strength of the lunar surface is based to a large extent on the fact that penetrometers have been used quite extensively in the field of soils engineering to obtain a measure of soil strength and, hence, are quite familiar to most engineers. Since little is known regarding the penetration resistance of "dust" or fine grained silt and since the major portion of all research on penetrometers is concerned with sand or clay soils, an experimental investigation was performed in order to demonstrate the validity of determining the bearing capacity of a soil type expected to be encountered on the lunar surface on the basis of penetrometer readings.

Load-penetration relationships were determined experimentally in simulated lunar soil for footings and penetrometers having various cone angles and rates of penetration. The correlation between the two was determined under atmospheric conditions and verified under vacuum levels of approximately 1×10^{-7} torr.

While the method of analysis which is presented is based on observations of only one material, the use of a penetrometer to determine the bearing capacity of soil such as is expected to exist on the lunar surface is shown to be quite satisfactory. Hence, in the event that larger grained soil (sand) is encountered on the lunar surface the penetrometer readings would still be meaningful.

It has been found that for a soil which derives its strength from apparent cohesive forces with a small angle of internal friction the factors derived from the penetrometer data are substantially independent of the footing size. Thus, it may be expected that the lunar soil which has been exposed to hard vacuum for long periods of time will have a large value of apparent cohesion and its bearing strength for large foot pads can be extrapolated. As more information concerning the nature of the lunar soil is obtained, this concept may be materially revised. The means for correlating the data and extrapolating to large foot pads is as follows:

1. Determine the force vs penetration relationship for the penetrometer

2. Replot this data in the form of x A/FC vs x/C to determine the constants a_p (the intercept) and b_p (the slope)

3. Using these values of a_p and b_p, determine $\alpha(d)$ and $\beta(d)$ by means of equations given later in this section

4. The force vs penetration relationship for the footing may then be determined using the values of α and β in the equation

$$F/A = \frac{x/C}{\alpha + \beta\, x/C} \quad . \qquad (6\text{-}71)$$

6.3.2 Soil Properties

The material comprising the lunar surface has been the subject of much controversy over the past few years. On the hypothesis that the surface is composed of a fine dust-like material, the soil chosen for the corollary experimentation was silica flour. This material is derived from finely ground Ottawa sand and is composed of quartz crystals which are almost pure silicon dioxide. It has a specific gravity of 2.64 and a grain size distribution as shown in Figure 6-43. Deposition of the soil by sifting will yield a maximum porosity of approximately 0.70 for small samples. However, deposition in large quantities as necessary for the bearing capacity experiments results in porosities ranging from 0.61 to 0.58. This decrease in porosity is due to increased overburden pressures and unavoidable disturbances of the container during preparation.

While it cannot be stated that this material has the same composition as the lunar soil it is believed that it is similar in nature to what exists on the moon, if it is indeed covered by a layer of dust. The possibility must be recognized that the surface material may exist in a fused state similar to a porous rock or vesicular lava. However, because of time limitations and the lunar model described in EPD-98, the silica flour has been used in a loose state for the experimental investigations.

6.3.2.1 Shear Strength

Direct shear tests were performed on the silica flour to determine the angle of internal friction and apparent cohesion by conventional methods of testing. Previous studies have shown that this resistance to displacement or "stiffness" is increased under vacuum.

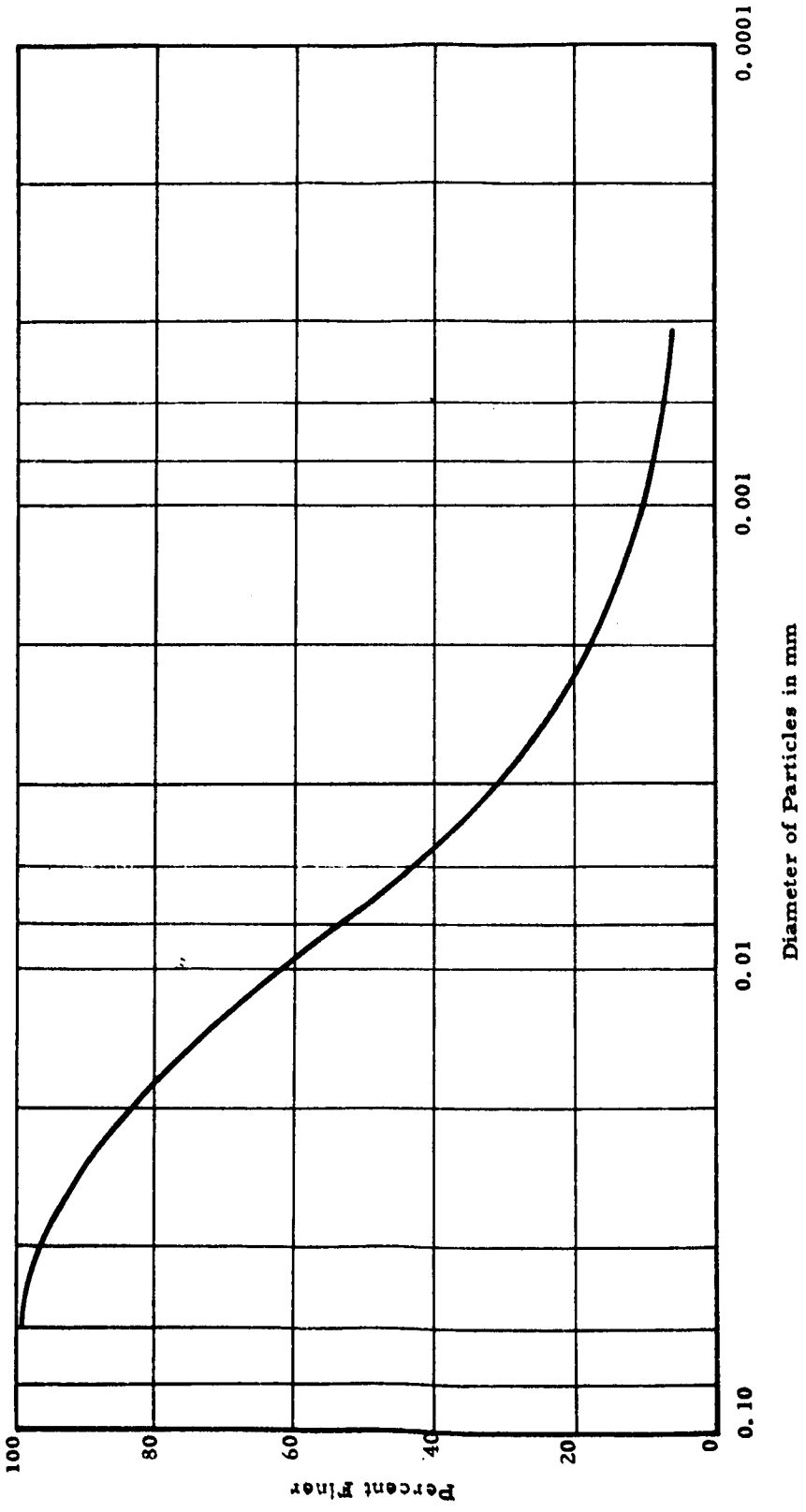

Figure 6-43 Grain Size Accumulation Curve for Silica Flour

The shear strength of a soil is given by the formula,

$$\tau = c + \sigma \tan \phi \qquad (6\text{-}72)$$

in which τ is the maximum shear stress that may be developed, σ is the normal stress on the plane of failure, c is the apparent cohesion and ϕ is the angle of internal friction. Use of Equation 6-72 permits values of ϕ and c to be determined graphically or analytically.

Experiments were performed on samples having various porosities and tan ϕ and c determined. It was found that the internal friction is not affected greatly by changes in porosity; however, porosity variation do influence the apparent cohesion appreciably. This influence is probably due to an increase in the interlocking of the soil grains at the low porosities.

The unconfined compressive strength of the soil may be determined from these shear strength parameters by the equation

$$q_u = \frac{2\ c}{\tan (45 - \phi\ 2)} \qquad (6\text{-}73)$$

in which q_u is the unconfined compressive strength and c and ϕ are the cohesion and angle of internal friction.

The effect of vacuum on the angle of internal friction and apparent cohesion of silica flour was determined in previous studies*. The effect of vacuum is to increase the shear strength substantially. The aforementioned increase in the "stiffness" of the soil under vacuum would also cause an increase in the penetration resistance. Thus, it is reasonable to assume that the bearing capacity of the lunar surface would be considerably greater than that of the same soil existing at the same porosity on earth.

6.3.2.2 Consolidation Characteristics

Consolidation tests were conducted to determine the effect of pore air on the consolidation characteristics of the silica flour.

Experiments were performed in atmosphere and under a low vacuum level of approximately 15 mm Hg using samples of two different initial void ratios for each condition. This vacuum level was sufficient

---

*E. Vey and J. D. Nelson, "Studies of Lunar Soil Mechanics", Final Report IITRI Project M272, NASA Contract NASr-65(02), July 1963.

to remove the major portion of the pore air but would not affect the shear strength or the stiffness due to the removal of adsorbed gas layers on the individual grains. The time necessary for the primary consolidation to take place was essentially the same under both atmosphere and vacuum, indicating a negligible effect of pore air.

The correlation derived under atmospheric conditions would be for a soil which derives its strength from both cohesion and internal friction (the major portion being due to friction). Although it has been seen that the shear strength of the soil may increase under vacuum, this shear strength will still be due to both cohesion and friction. Therefore, the relationships so derived between penetrometer readings and bearing capacity would be expected to be valid in both terrestrial and lunar environments.

6.3.3. Experimental Investigation in Atmosphere

6.3.3.1 Penetrometer Experiments

Experiments have been performed using the configurations of penetrometer head shape illustrated in Figure 6-44 and various rates of loading ranging from 0.49 in./sec to 0.073 in./sec. It should be noted that after withdrawal of the penetrometer, the soil around the hole caused by the penetration does not collapse.

Typical records of load cell output as a function of time are shown in Figure 6-45. It can be seen that the force on the penetrometer at the deeper regions of penetration does not follow a smooth curve. This is characteristic of penetration experiments in granular materials and is caused by the fact that during shear the particles move in discreet jumps rather than in a continuous motion. However, for purposes of analysis, the relationship between force and penetration may be treated as a smooth curve, as shown in Figure 6-46.

The curves in Figure 6-46 are for a representative number of tests using the three configurations of penetrometer tip. Except for some deviations at very shallow and deep penetrations, it is evident that the curves may be represented reasonably well by straight lines passing through the origin. Upon complete penetration of the point of the cone, the slope of these curves does not vary appreciably from one penetrometer to the other, and hence, the results obtained at depths greater than 5 cm are not

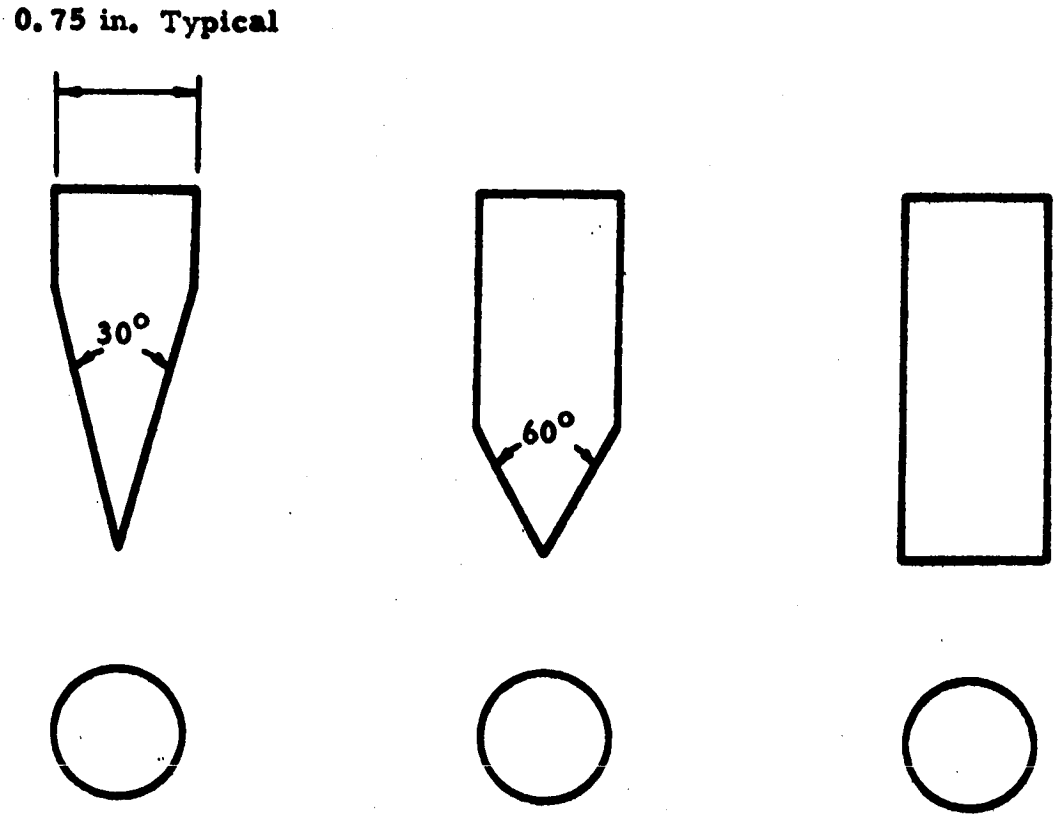

Figure 6-44 Penetrometer Tips Used

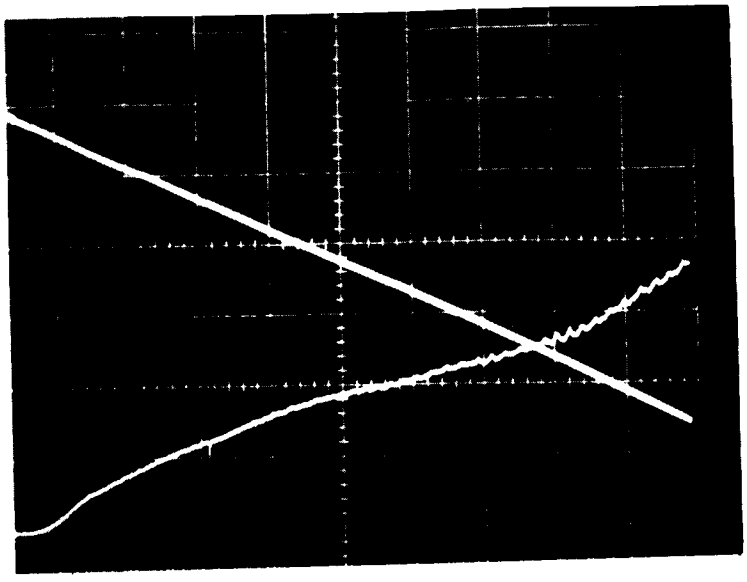

a) First Half of Record

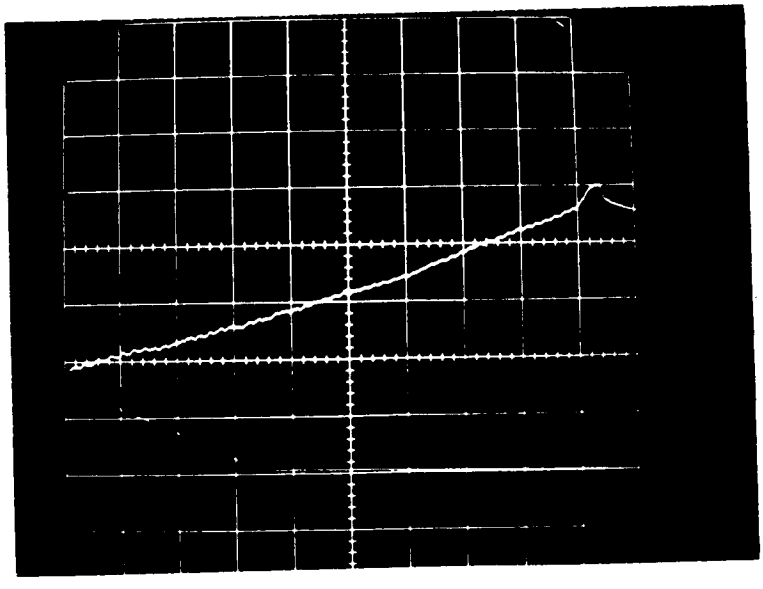

b) Second Half of Record

Figure 6-45 Typical Load Cell Output for Penetrometer Test in Atmosphere

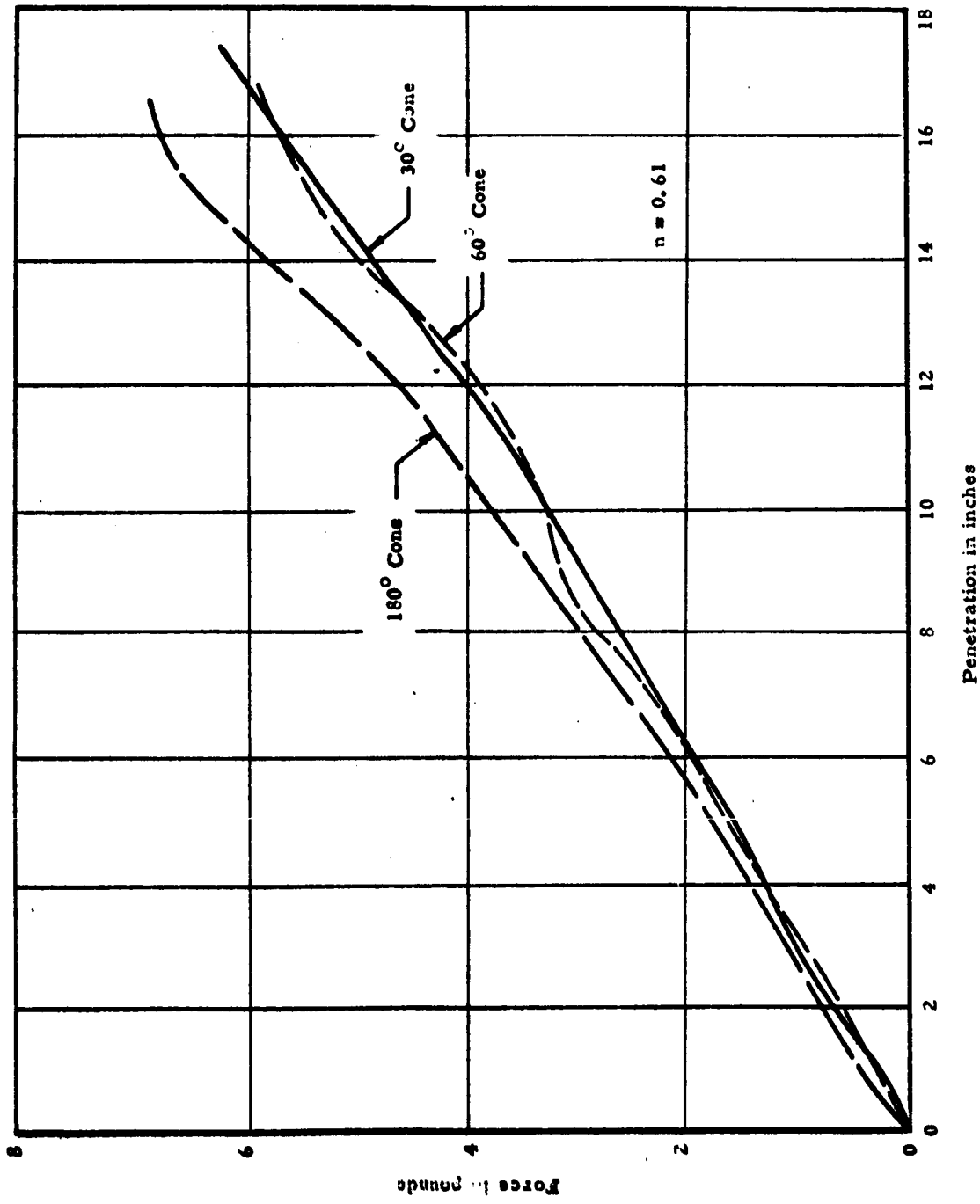

Figure 6-46 Force vs Penetration for Various Cone Angles

expected to vary significantly regardless of the angle of the cone point. In order to permit the application of the penetrometer over a wide range of materials and to effect penetration of a crusted surface (assuming the probability of the existence of a crust on the lunar surface) it is advantageous to employ a cone shape point. From the design viewpoint, however, it is desirable to use a large apex angle to reduce the overall length of the penetrometer package. On the basis of these two considerations, an apex angle of 60° was selected.

Figure 6-47 shows typical force vs penetration curves for the 60° cone at various rates of penetration, in which it is evident that the rate has a negligible effect on the results. This conclusion is in agreement with the results of the consolidation tests which showed a negligible effect of pore air on the time-consolidation characteristics.

6.3.3.2 Footing Experiments

The bearing capacities of footings have diameters of 1.5, 3.0, 6.0, 9.0 and 12.0 in. where determined experimentally, by two methods of load application (i.e., controlled stress and controlled strain). The controlled stress method consists of applying the load to the footing in increments and measuring the resulting penetration as a function of time. Typical results showing the deflection as a function of time for a 9-in. diameter footing are presented in Figure 6-48. Since this curve has the general shape of a hyperbola it is realistic to replot it in the form of t/Δ as a function of t, where t is the time and Δ is the penetration. This procedure yields a straight line function between t/Δ and t as indicated in Figure 6-49 and establishes the following relationship between t and Δ.

$$\Delta = \frac{t}{a + bt} \tag{6-73}$$

in which a and b are the intercept and slope of the curve presented in Figure 6-49.

It is clear from an inspection of Equation (6-73) that

$$\lim_{t \to \infty} \Delta = 1/b \tag{6-74}$$

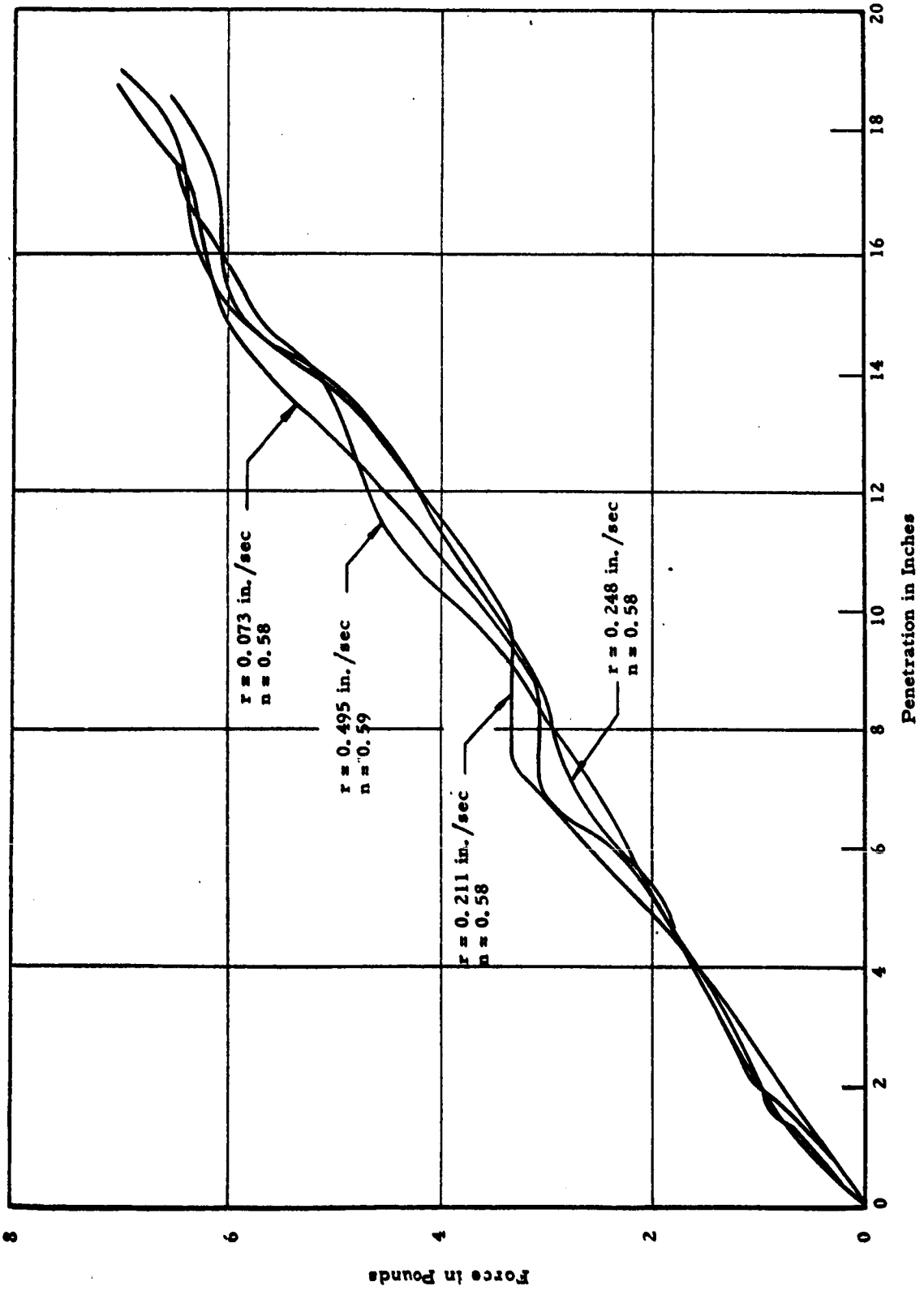

Figure 6-47 Force as a Function of Penetration for Various Rates of Penetration

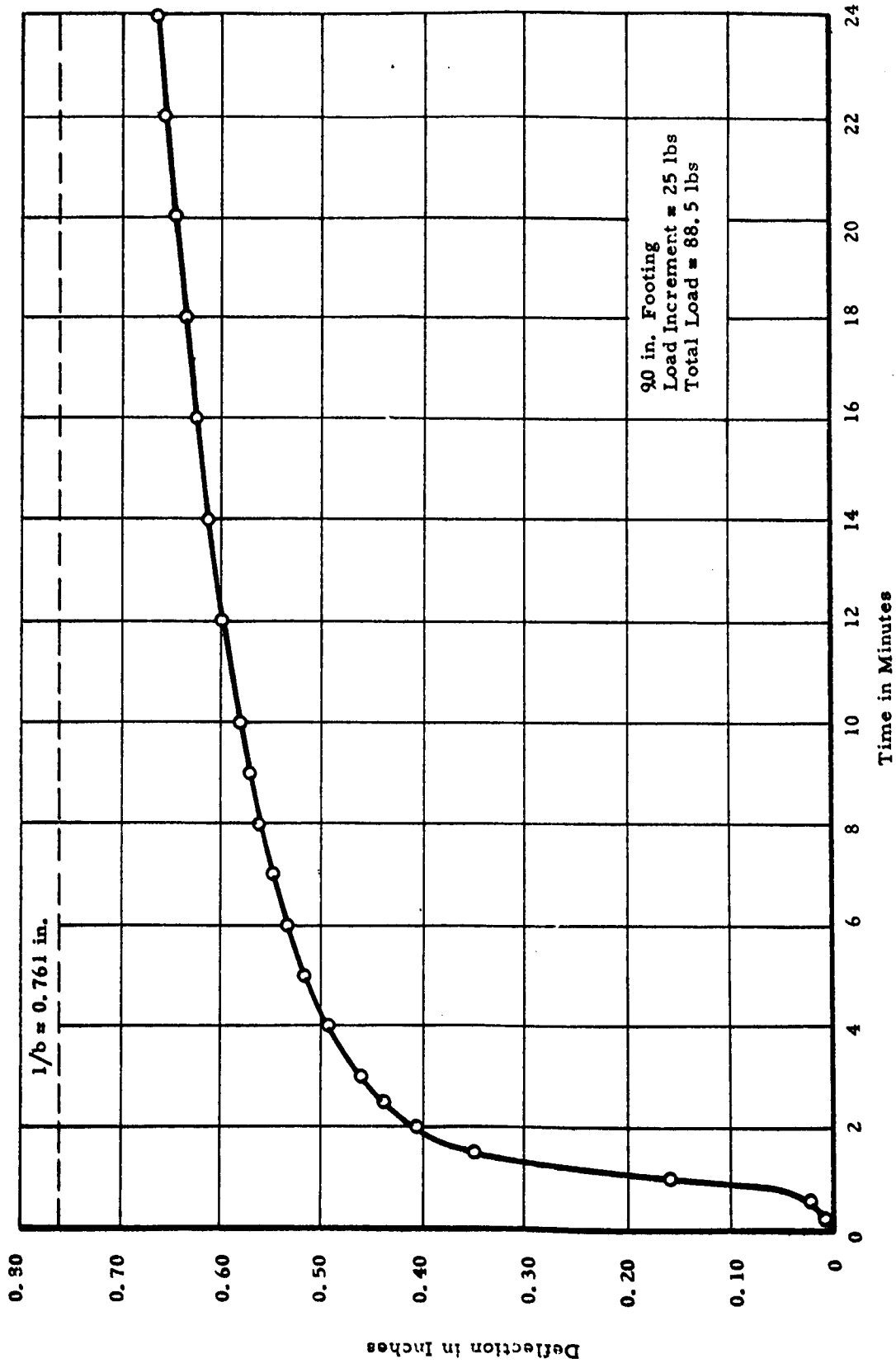

Figure 6-48 Penetration as a Function of Time

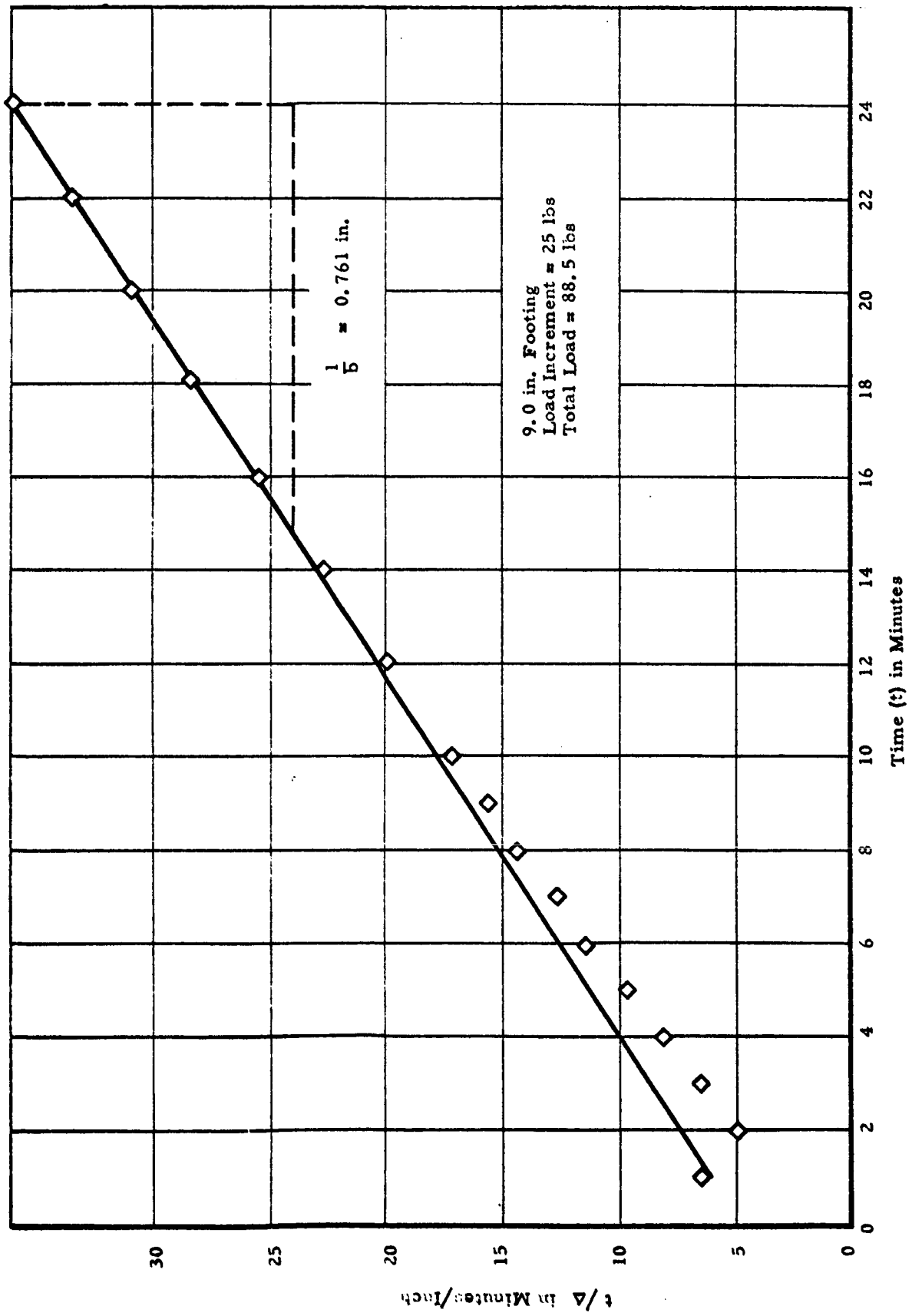

Figure 6-49 Time/Penetration as a Function of Time

and hence the maximum penetration obtained for long periods of loading is given by the values of 1/b. By repeating the constant stress footing experiment with different loads applied to the footing, it is possible to establish the relationship between maximum penetration and the load applied to the footing.

In these controlled stress studies, the load was applied to the footings by a pneumatic cylinder. With this system, loads could be applied concentrically to the footing over the entire loading range of interest in this investigation. The total load on the footing was monitored by means of a load cell between the footing and the piston.

The controlled strain test consists of forcing the footing into the soil at a constant rate and measuring the force on the footing as a function of the penetration. The footing was forced into the soil by a synchronous motor operating through a reducer. The rate of penetration was held constant at 0.071 in./min. The total force required was determined by mounting a force transducer between the drive unit and the footing.

Curves showing the bearing pressure on the footing as a function of the depth of penetration are shown in Figure 6-50. It can be seen that these curves may also be represented with reasonable accuracy by a straight line over a wide range as was also the case for the penetrometers. As might be expected, the slope of the curves for the larger footings is less than that for the smaller footings and for the penetrometer. However, it is evident from Figure 6-50 that for the lower values of penetration ($x < 6.0$ in.) the difference between the curves is small for the larger sized footings.

6.3.4 Penetrometer and Footing Tests in Vacuum

Penetrometer and footing experiments using the 60° cone penetormeter, 3-in. diameter footings and a 12-in. diameter footing were performed in a vacuum of 1×10^{-7} torr at ambient temperatures. The apparatus which was used in these experiments was similar to that used in the experiments in atmosphere.

The penetrometer experiments were performed at a rate of penetration of 0.32 in./sec. The footing experiments were performed using the controlled strain method of load application and a rate of penetration of 0.071 in./min. Due to limitations imposed by the vacuum chamber

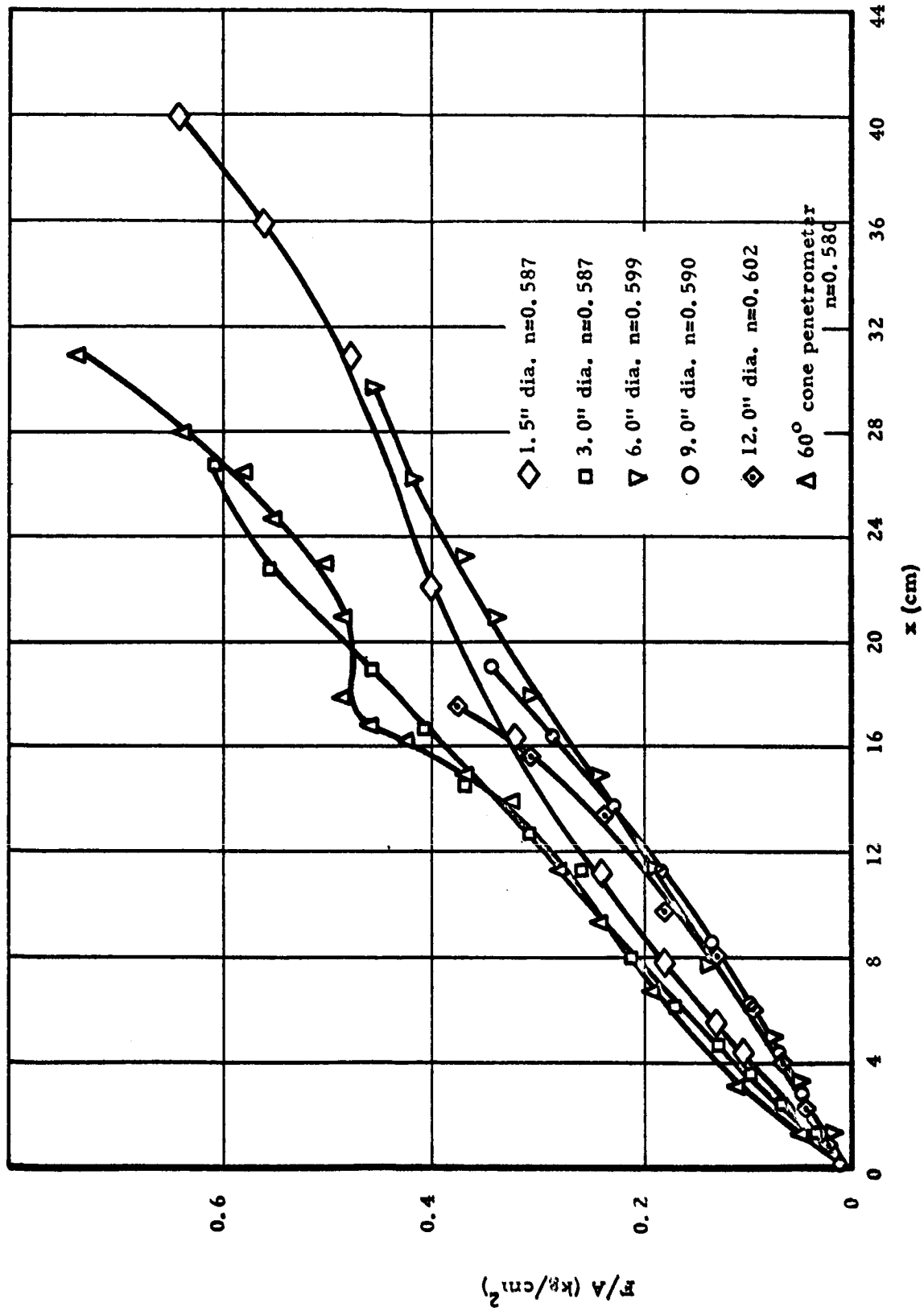

Figure 6-50 Bearing Pressure as a Function of Penetration for Footings

fixtures, the maximum penetration that could be effected was approximately 2 or 4 in. depending on the particular bellows being used. However, it is believed that penetrations of this magnitude are sufficient to demonstrate the validity of the scaling relationships.

The vacuum system which was used consisted of a 3-ft diameter by 4-ft high chamber mounted above a 35-in. diffusion pump. A chevron baffle was mounted between the chamber and the pump was cooled by liquid nitrogen to reduce backstreaming in the system.

The soil container was a stainless-steel bin 28 in. in diameter and 30 in. deep. A perforated false bottom was placed in the bin such as to provide a depth of soil of approximately 14 in. Holes were then drilled in the side of the soil bin below the false bottom. This arrangement allowed the gas to be pumped from the soil from both the top and the bottom of the sample and thus, aided in outgassing the soil in a shorter period of time.

The vacuum level was monitored using a Bayert-Alpert type ion gage. In all of the experiments the gage was outgassed just prior to conducting the test. Shortly after outgassing the gage, the pressure readings will generally be somewhat lower than the actual pressure in the system, and in these experiments the pressure was recorded at approximately 5×10^{-8} torr within the first few minutes after outgassing. However, the pressure readings leveled off between 9×10^{-8} and 1.1×10^{-7} torr in a period of approximately two hours. Thus, the chamber vacuum level may be considered to be 1.0×10^{-7} torr for all the experiments.

It has been found in previous studies that the vacuum which exists in the soil pores is not the same as that in the chamber, and may be several orders of magnitude less. Because the soil was outgassed from both the top and the bottom of the sample and the large diffusion pump (and hence, the large pumping speed) that was used, it would be expected that for a distance of 4 in. below the soil surface (the maximum penetration in any test) the actual pressure in the soil pores would not be expected to have been greater than 1×10^{-6} torr.

6.3.5 Results

6.3.5.1 Analysis of Data

Various methods of penetrometer data analysis were investigated in order to determine the one most suitable for use in interpreting the data obtained in this program. Extensive studies were performed in Europe[1, 2] to relate the shear strength of clays to the resistance to penetration by the cone. It was found that the results could be expressed by an equation of the form

$$F = k x^2 \tag{6-75}$$

in which F and x are the force and penetration respectively and k is a constant which depends upon the geometry of the cone and the properties of the soil being tested.

If one then assumes that the data obtained in this investigation may be represented by Equation (6-75), replotting the force vs penetration curves for the penetrometer in the form of F/x vs x should result in a straight line passing through the origin. Typical results of the data plotted in this form are shown in Figure 6-51. The equation of the line in Figure 6-51 for the larger values of penetration is given by

$$F/x = k \tag{6-76}$$

from which,

$$F = k x \tag{6-77}$$

Thus, it is evident that the relationship between force and penetration for this soil cannot be represented by Equation (6-75). In addition, this

1. S. Hansbo, "A New Approach to the Determination of the Shear Strength of Clay by the Fall-Cone Test", Royal Swedish Geotechnical Inst. Proc. No. 14, Stockholm, 1957.

2. A. W. Skempton and A. W. Bishop, "The Measurement of the Shear Strength of Soils", Geotechnique, Vol. 2, No. 2, 1950.

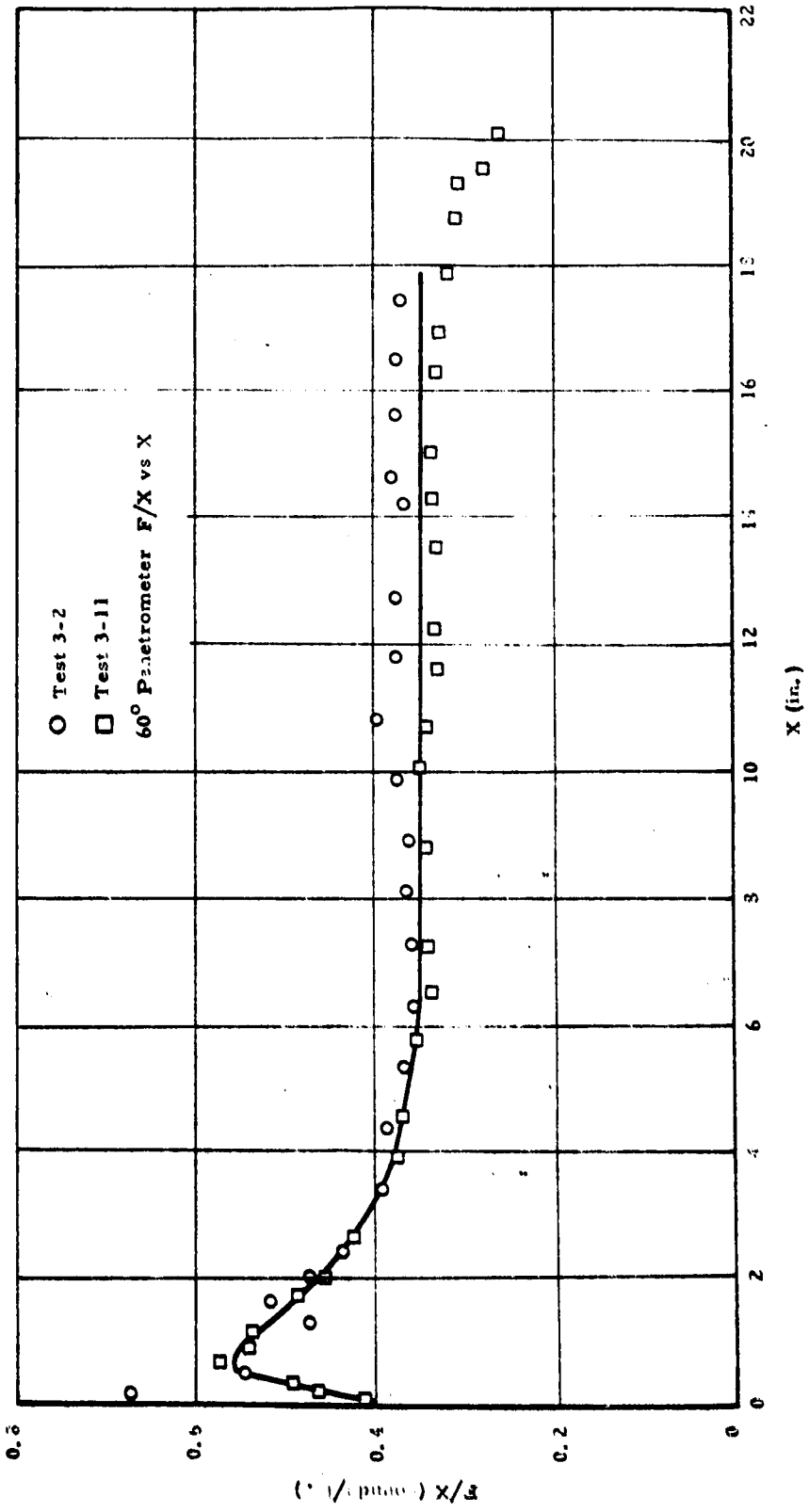

Figure 6-51 Force/Penetration (F/S) as a Function of Penetration (X)

relationship in the lower regions of penetration is somewhat more complex and cannot be represented by either Equations (6-75) or (6-77).

A number of other methods of analysis which have been used[1, 2] relate the force to the penetration by the equation

$$F = k x^m \tag{6-78}$$

in which k and m are constants depending on the soil properties and footing geometry. Equations (6-75) and (6-77) are merely particular cases for Equation (6-78) in which m is equal to 1 or 2. It has been shown that this method does not appear to be directly applicable to the silica flour.

Another method of analysis, which has been used quite successfully for both sand and clay soils, relates the force to the penetration by means of a hyperbola,[3] as was done in Section 6.3.1.1 of this report for the penetration-time curves. In this method, data were plotted in the form of the ratio xA/FC as a function of x/C in which F, x, A and C are the force, penetration, cross-sectional area, and circumference respectively. This form of representing the data resulted in a straight line relationship between the two ratios which was represented by the equation

$$\frac{xA}{FC} = a + b \frac{x}{C} \tag{6-79}$$

or

$$\frac{F}{A} = \frac{x/C}{a + b\, x/C} \tag{6-80}$$

in which a and b were constants depending only on the soil properties and were independent of the footing size in the case of clay soils.

1. R. Yong, "A Study of Settlement Characteristics of Model Footings on Silt", Proc. First Pan American Conference of Soil Mechanics and Foundation Engineering, Sept. 1959

2. M. G. Bekker, Theory of Land Locomotion, The University of Michigan Press, Ann Arbor, Michigan, 1956.

3. R. L. Kondner and R. J. Krizek, "Correlation of Load Bearing Tests on Soils", Proc. Highway Res. Board, Vol. 41, January, 1962.

Typical results of the penetrometer tests in the silica flour are shown in Figure 6-52 in the form of F/A as a function of x/C. For these data, the cross-sectional area and circumference were taken as the maximum values for the cone. Since A and C are both constants, the curves in Figure 6-52 are similar to the force vs penetration curves and for practical purposes may be represented by straight lines over a large portion of the curve. Replotting these curves in the form of xA/FC as a function of x/C results in the curves shown in Figure 6-53. In the region in which the cone point has not penetrated completely, the curves in Figure 6-53 have a steep negative slope (b_o), while the intercept (i.e., the ordinate at $x/C = 0$) is equal to $0/0$ and is not clearly defined; extrapolation of a straight line through the points in this region would result in an intercept (a_o) of a relatively large magnitude.

For $0.32 \leq x/C \leq$ approximately 2, the curve may be represented by a straight line having an intercept a, and a slope b, while in the region beyond this, the slope is very small and the curve may be represented by a straight horizontal line with an intercept a_2.

The equation for the force as a function of the penetration would be given by the equations,

$$\frac{F}{A} = \frac{x/C}{a_o - b_o\, x/C}, \quad 0 < x < 0.32 \qquad (6\text{-}81a)$$

$$\frac{F}{A} = \frac{x/C}{a_1 + b_1\, x/C}, \quad 0.32 < x < \text{approx. } 2 \qquad (6\text{-}81b)$$

$$\frac{F}{A} = \frac{x}{a_2\, C}, \quad \text{approx. } 2 < x \qquad (6\text{-}81c)$$

The shape of a curve represented by Equation (6-81) is shown in Figure 6-54.

In order to represent the force-penetration relationship of the penetrometer over a wide range of values of x/C it is necessary to use three different equations. However, Equation (6-81a) is valid only until the cone has penetrated completely and would not be directly applicable to the case of a footing on the soil. Also, larger sized footings would undoubtedly be designed such that the settlements would correspond to

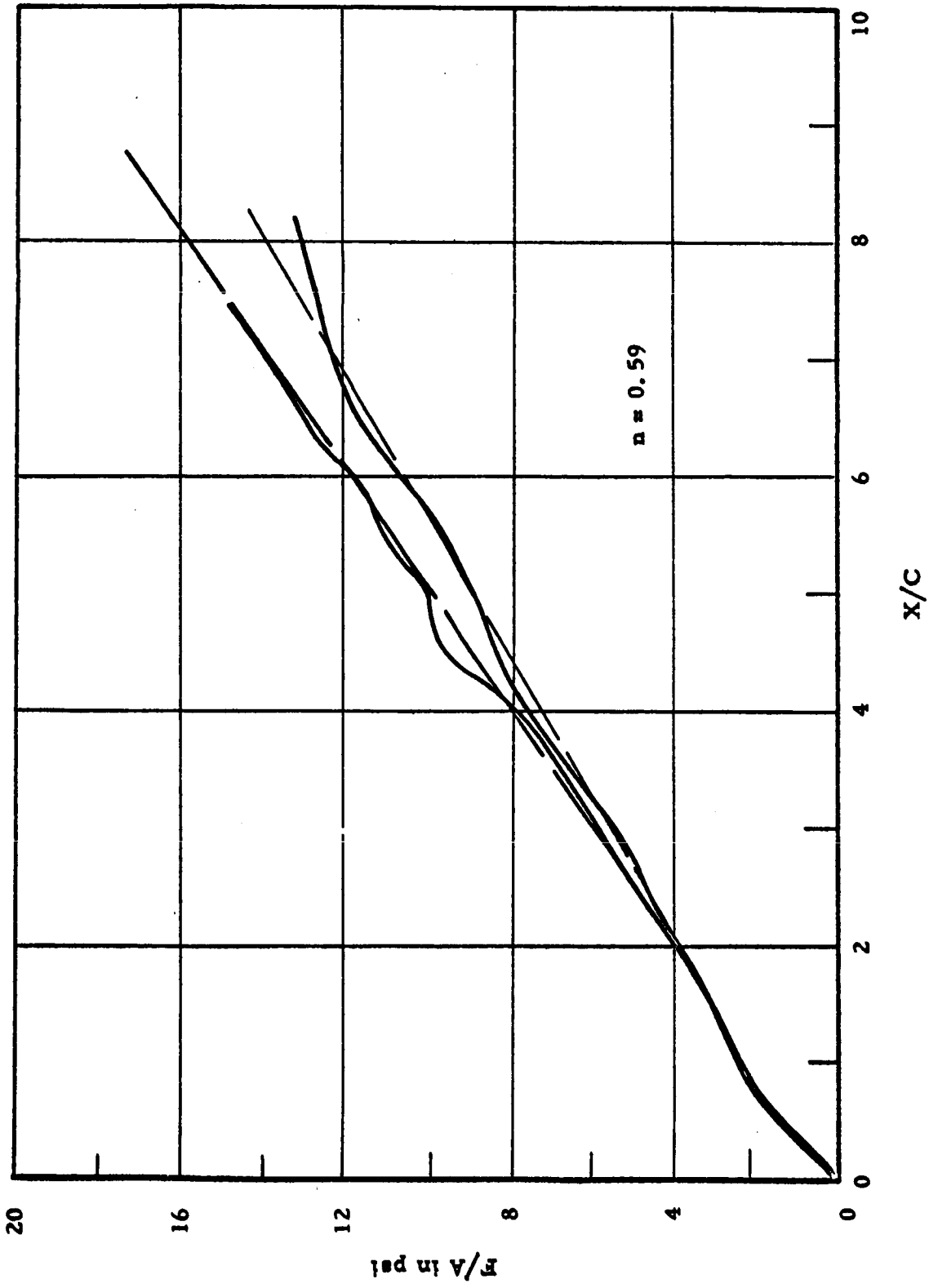

Figure 6-52 Typical F/A vs x/C Curves for 60° Penetrometer

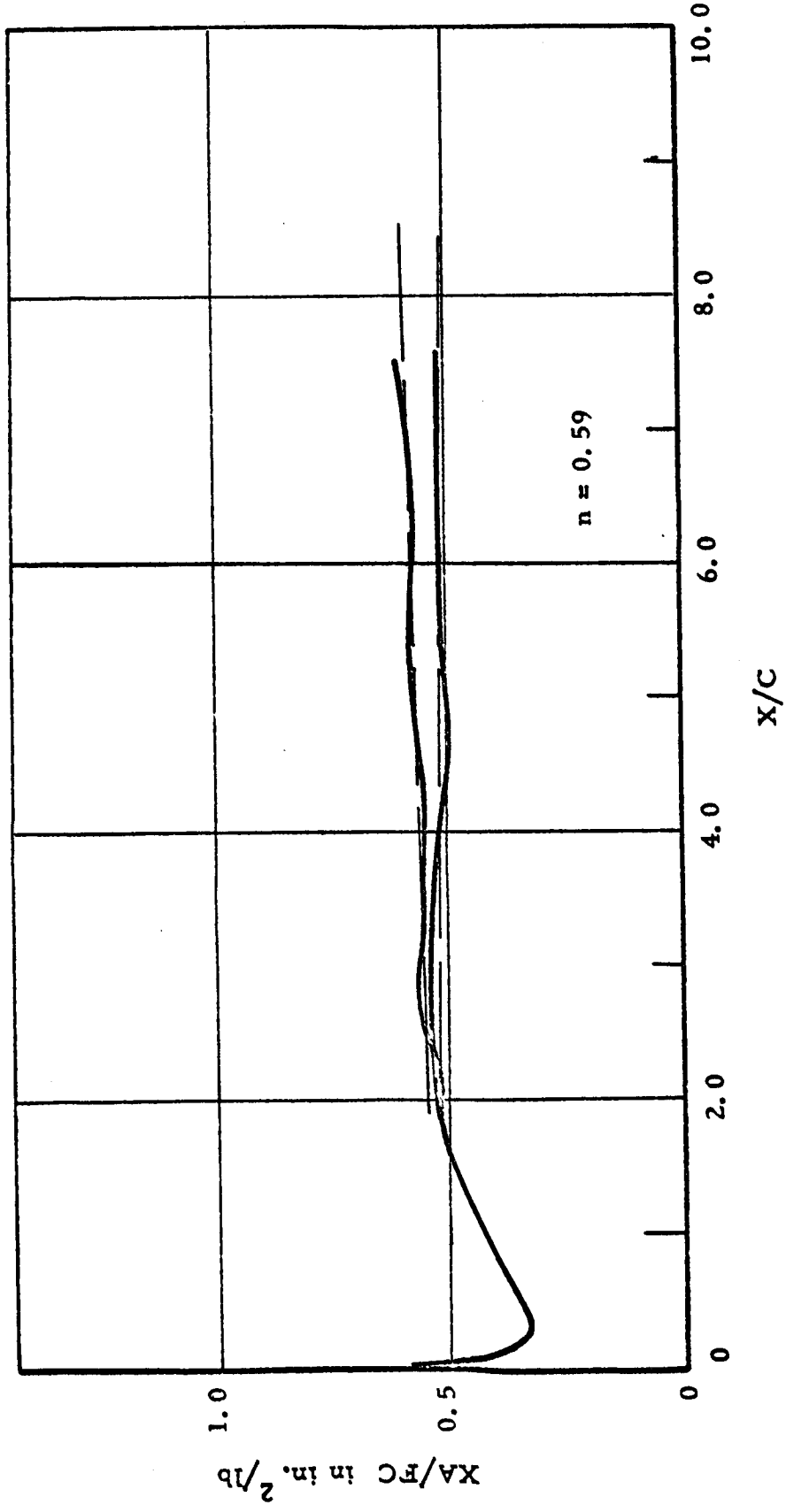

Figure 6-53 Typical XA/FC vs X/C Curves for 60° Penetrometer

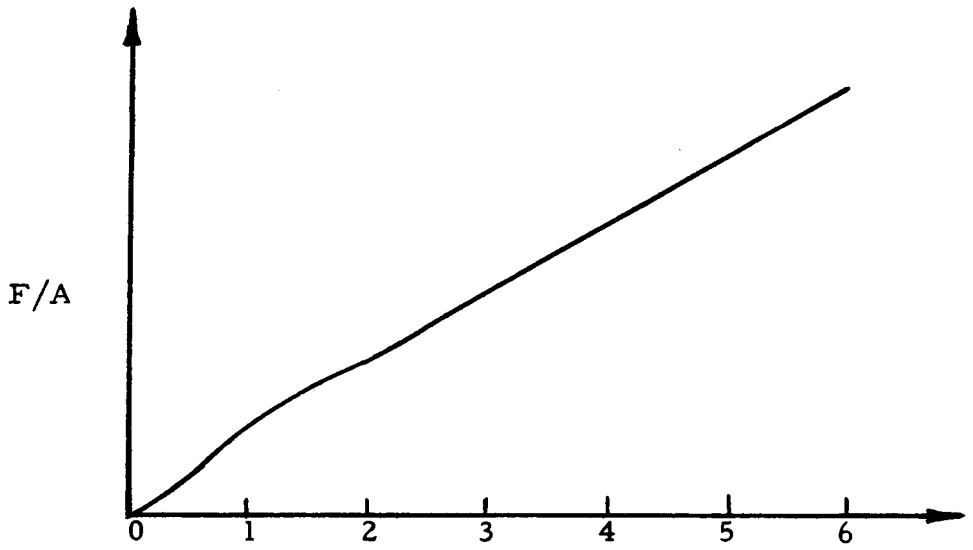

Figure 6-54 Graphical Representation of Equation

$x/C \rightarrow 2$. Therefore, Equation (6-81b) will be used in subsequent analyses to represent the relationship between force and penetration for the silica flour.

However, in order to correctly use Equation (6-81b) to predict the bearing capacity of a large sized footing, it is necessary to determine the constants a and b using a penetrometer having the same geometry as the footing (i.e. cone or flat end). Since it is desirable to use a cone penetrometer, it is necessary to have a correlation between the constants a and b for the 60° cone and those for the 180° cone.

The values obtained for a and b using both configurations of penetrometer tip in silica flour at various porosities were determined, and the values corresponding to the 60° cone (a_{60} and b_{60}) plotted as functions of those corresponding to the 180° cone (a_{180} and b_{180}). For the larger values of a and b (corresponding to high porosities) the values of a_{60} are somewhat greater than those of a_{180} while the values of b_{60} are less than those of b_{180}. In this region then, (which corresponds to soil having a low bearing strength) the error introduced by setting a_{60} equal to a_{180} would tend to compensate for that introduced by letting $b_{60}=b_{180}$.

The difference between the two will nevertheless be taken into account at a later point.

The values of a and b were determined using the 60° cone penetrometer in samples of silica flour having porosities ranging from 0.53 to 0.61 and plotted as functions of the porosity in Figure 6-55.

A greater number of points would allow one to reduce the scatter by statistical methods, but it appears from Figure 6-55 that the effect of changes in porosity appears to be primarily one of varying the value of b, while a appears to be constant throughout the range of porosities tested.

The values of a and b for the 180° cone were determined. They are quite similar to those in Figure 6-55.

The bearing capacities of the footings as determined by both methods of controlled stress and controlled strain showed that the method of testing has a negligible effect on the results. However, in the controlled stress test it was observed that if the increment of load was applied too quickly (i.e., approaching dynamic loading conditions) the resulting penetration was quite large. Thus, while the pore air effects are negligible under static conditions they are appreciable under dynamic conditions. Pore air effects under dynamic loading conditions have been presented and discussed in more detail elsewhere[1, 2] and will not be discussed further here.

The values of the constants a and b for the footing experiments were determined by plotting the data in the form of xA/FC vs x/C and are shown in Figure 6-56 and 6-57 as functions of the footing size. It is evident that these constants are not independent of the size of the footing.

---

1. E. Vey and J. D. Nelson, "Studies of Lunar Soil Mechanics", Second Quarterly Report on IITRI Project M272-Phase II, Dec. 30, 1963.

2. D. J. Roddy, J. B. Rittenhouse, and R. F. Scott, "Dynamic Penetration Studies in Crushed Rock Under Atmospheric and Vacuum Conditions", Technical Report No. 32-342, Jet Propulsion Laboratory, Pasadena, Calif., April 6, 1962.

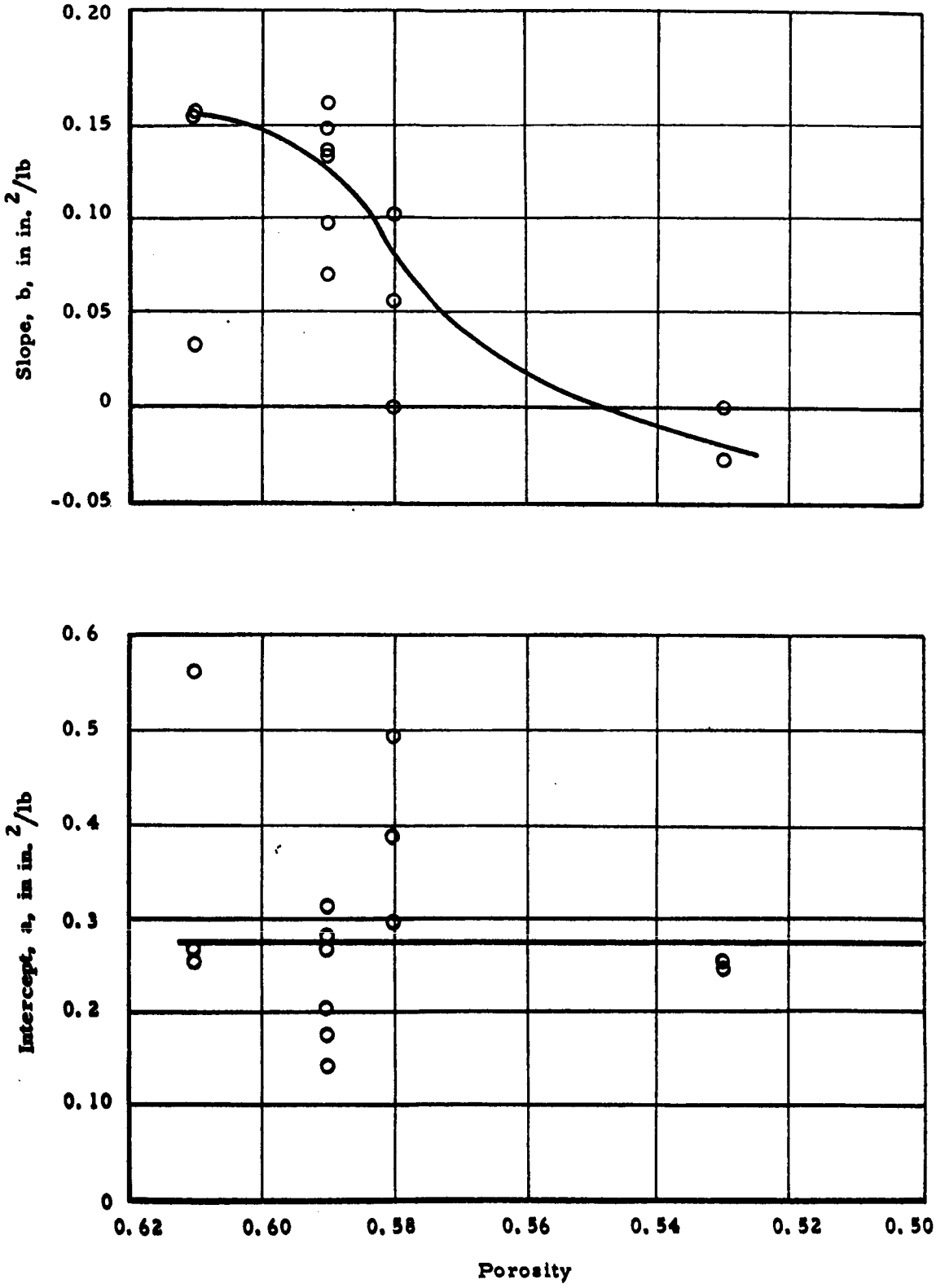

Figure 6-55 Slope and Intercept as Functions of Porosity (60° Cone)

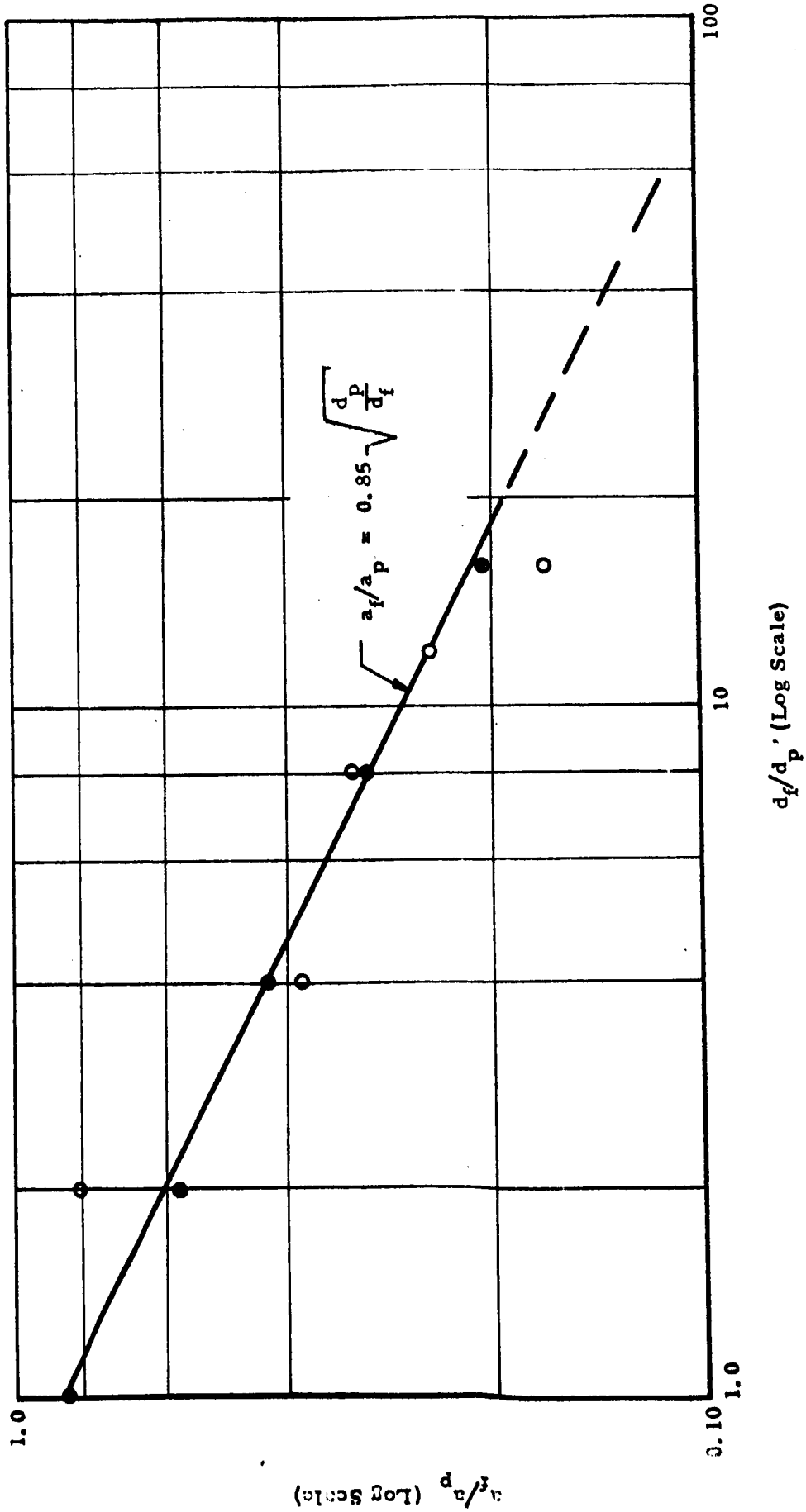

Figure 6-56 a_f/a_p as a Function of d_f/dp

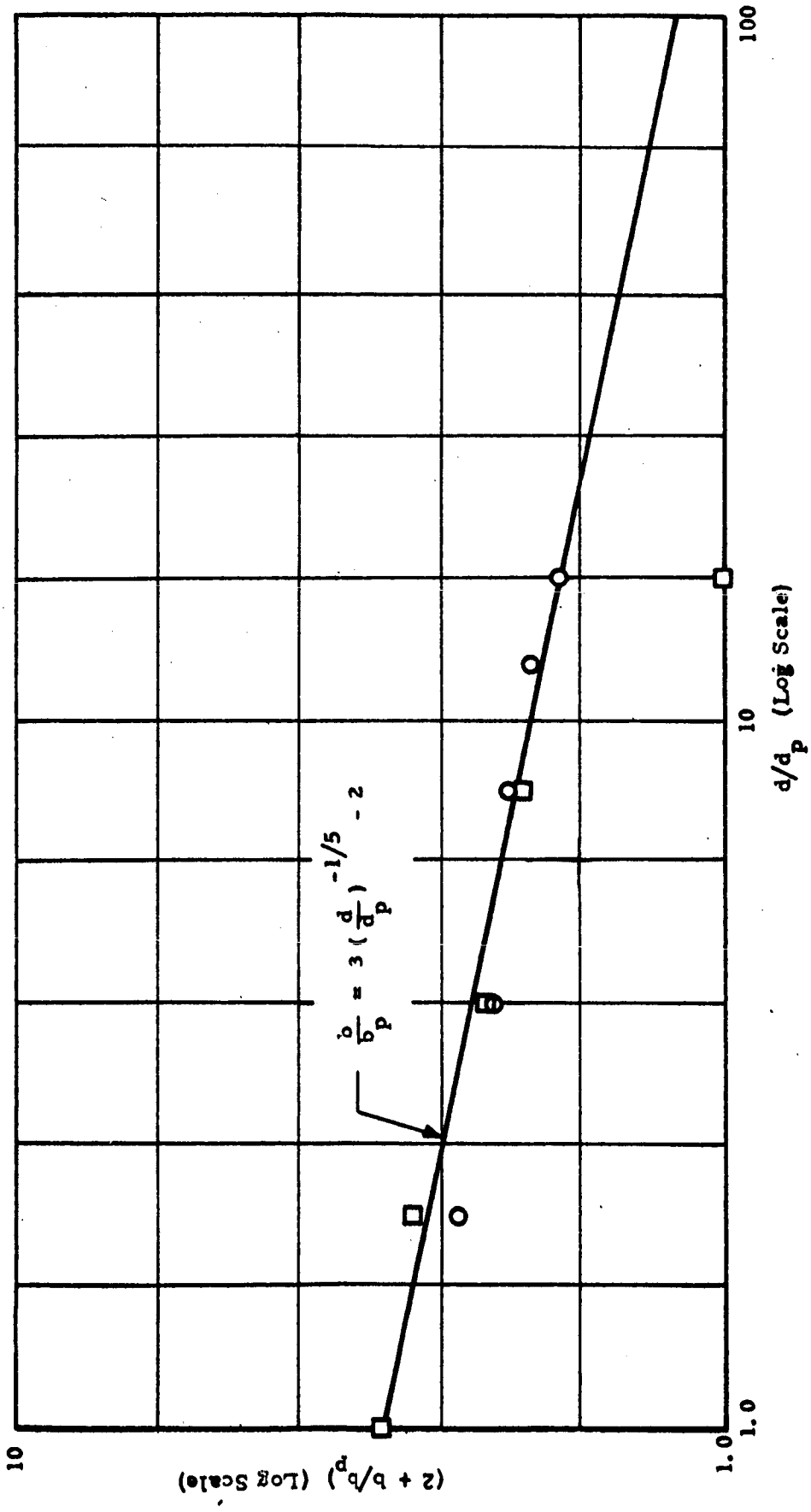

Figure 6-57 b/b_p as a Function of d/d_p

Thus, for the general case, Equation (6-81b) must be represented by the equation

$$\frac{F}{A} = \frac{x/C}{\alpha(d) + \beta(d)\, x/C} \tag{6-82}$$

in which $\alpha(d)$ and $\beta(d)$ are functions of the footing diameter and for this particular soil are given by

$$\alpha(d_f) = 0.85 \quad \frac{d_f}{d_f} \quad a_p \tag{6-83}$$

and

$$\beta(d_f) = 3 \quad \frac{d_f}{d_f}^{1/5} \quad -2 \quad b_p \tag{6-84}$$

in which the subscripts p and f denote penetrometer and footing respectively.

Since the values of a and b for the 180° penetrometer were used as the constants for a 0.75 in. diameter footing, the effect of penetrometer tip configuration is taken into account in Equation (6-83) and (6-84). This is evidenced by the coefficient 0.85 in Equation (6-83).

6.3.5.2 Scaling Relationships and Discussion of Results

As indicated by Figure 6-50, there appears to be no definite point at which a small increase in load on the footing would cause extreme increases in the penetration and, therefore, there is no definite value of the ultimate bearing capacity. Hence, the bearing capacity for any particular footing is actually represented by a curve showing the load on the footing as a function of the settlement.

This curve may be plotted in the form of the bearing pressure (F/A) as a function of the ratio of the depth of penetration to the footing perimeter, and has, in general, a shape as represented by one of the curves shown in Figure 6-58. Replotting this same data in the form of the quantity xA/FC as a function of x/C gives the straight line relationship between xA/FC and x/C as illustrated in Figure 6-59, resulting in the equation

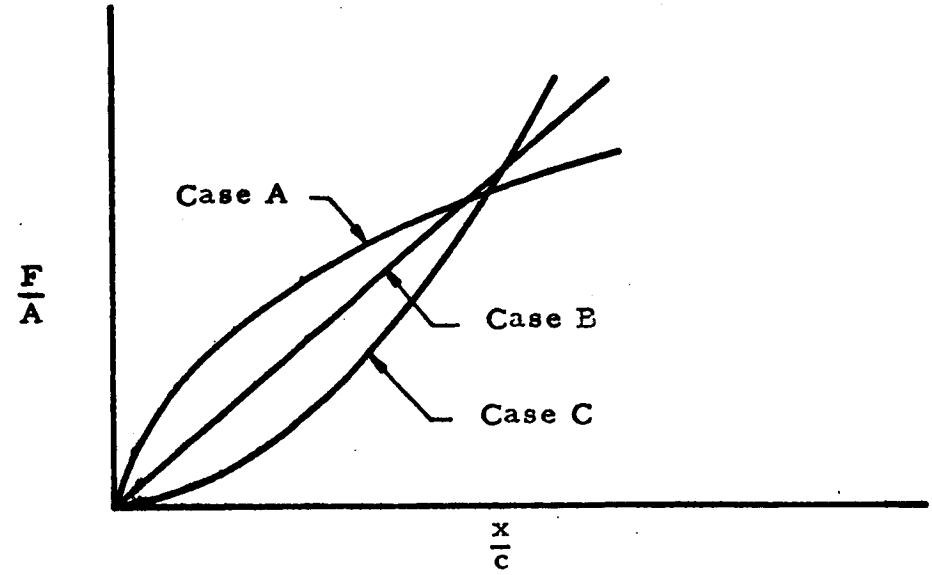

Figure 6-58 F/A vs X/C for General Case of Footing on Soil

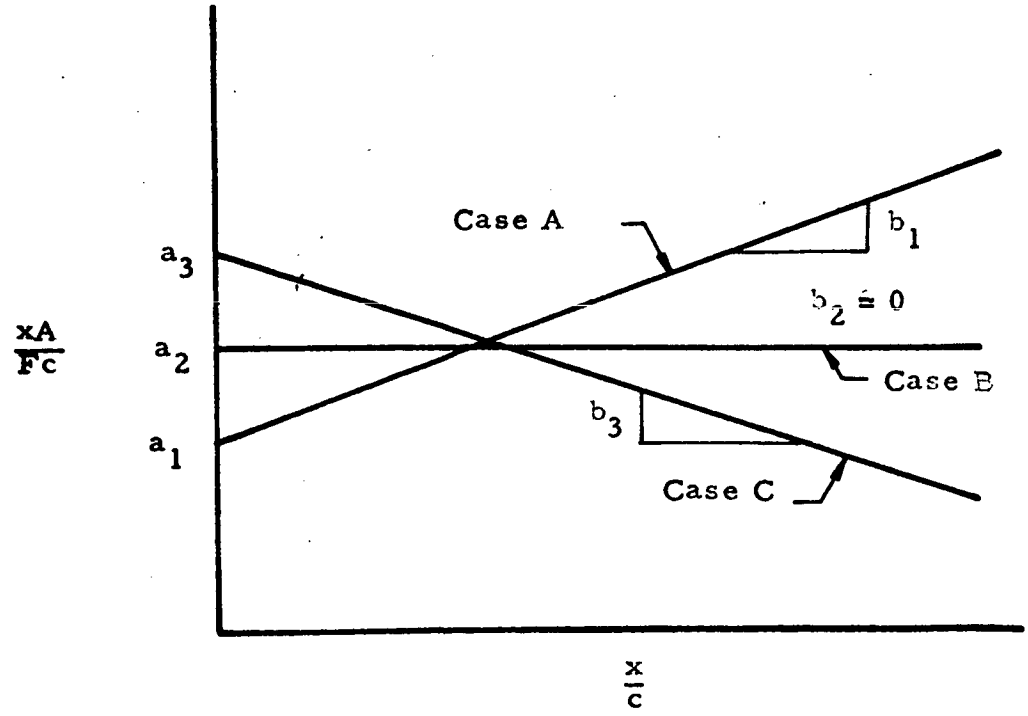

Figure 6-59 XA/FC vs X/C for General Case of Footing on Soil

$$F/A = \frac{x/C}{a + b\,x/C} \tag{6-85}$$

The physical significance of the constants a and b are then as follows. In all cases (A, B or C) the initial tangent modulus of the F/A vs x/C curve is given by the value of 1/a.

If $b > 0$, then the curve exhibits the form shown by case A in Figure 6-58, and

$$\lim_{x \to \infty} \frac{F}{A} = \frac{1}{b} \tag{6-86}$$

Thus, the ultimate bearing strength of the soil is represented by the value of 1/b.

If $b = 0$, (i.e. case B) then the equation of the curve is

$$\frac{F}{A} = \frac{x}{aC}$$

In this instance the bearing capacity increases linearly with x over the range of interest.

If $b < 0$ (i.e. case C) the equation takes the form

$$\frac{F}{A} = \frac{x/C}{a - \beta \frac{x}{C}} \tag{6-87}$$

where $\beta = -b$. This equation may be rewritten as

$$\frac{x}{C} = \frac{a\,F/A}{1 + \beta \frac{F}{A}} \tag{6-88}$$

Taking the limit of Equation (6-88) as $F/A \to \infty$

$$\lim_{f/A \to \infty} \frac{x}{C} = \frac{a}{\beta} \tag{6-89}$$

From Equation (6-89) it is clear that the maximum penetration of the footing in soil represented by case C is given by the value of a/β.

As was mentioned previously, it has been shown[1] that the load-settlement relationships of footings on sand and clay may be represented with reasonable accuracy by considering case A. For clay, the parameters a and b were found to be dependent upon the soil properties and the geometry of the footing, but were independent of the cross-sectional area, thus permitting one to predict the settlement of large footings from the results obtained from small sized footings. However, from the preceding analysis of the data it was seen that the load-settlement relationships of the silica flour may correspond to either of cases A, B or C.

For the larger sized footings (9 and 12 in. diameter) b has a small negative value (case C). Previous studies[2] have shown that in experiments where the size of the soil bin in relation to the footing is small, the container may have an appreciable effect on the results, and may cause a curvature as shown in case C. However, in a soil such as was used in these experiments, failure of the soil takes place primarily by consolidation, resulting in an increase in the stiffness of the soil below the footing with an increase in depth of penetration. Thus, a curve of the type shown in case C may be expected to be due to container effects and/or the manner in which failure of the soil takes place.

To study the container effects and the mode of failure of the soil, a limited number of experiments were performed in which the soil below the footing was observed during penetration. This was accomplished by using a narrow container in which one of the walls was made of glass.[3] A grid system was placed on the soil using silica flour which had been dyed black, in order to observe relative movement of the soil below the footing. Semicircular footings and penetrometers were then forced into the soil along the glass wall.

1. R. L. Kondner and R. J. Krizek, op. cit.
2. E. Vey and J. D. Nelson, op. cit.
3. E. T. Selig, "A Technique for Observing Structure-Soil Interaction", Materials Research and Standards, ASTM, Vol. I, No. 9, Sept. 1961.

Photographs of the soil were made at various penetrations using both a cone and flat end penetrometer and a 2 in. footing in loose silica flour and dense Ottawa sand. By comparing photographs of the sand with those of the silica flour, it was seen that the mode of failure is significantly different for the two materials. The upheaval of the soil surface near the edge of the penetrometer and footing in the dense sand indicate that failure was primarily by shear and that very little consolidation of the soil had taken place. On the other hand, the failure in the silica flour occurred primarily by consolidation of the soil, with some shear having taken place.

It is interesting to note that for both the flat end penetrometer and the footing, the soil directly below the penetrometer or footing compressed and was not displaced laterally. Therefore, when a sufficient amount of penetration had taken place, this compressed soil formed a wedge directly below the footing which is similar to the pointed tip on the cone penetrometer. Also, the failure of the soil below the 180° penetrometer was essentially the same as in the case of the 2 in. footing, indicating that scaling relationships developed using the 0.75 in. Diameter probe would be valid for larger sized footings.

By observing the lateral movement of the vertical grid lines in the soil relative to the reference grid lines, it appears that in order for the container to have no effect on the results of load bearing tests the ratio of container width to footing diameter should be approximately 3.5:1. Thus, a container 28 in. in diameter, as was used in these experiments, would be expected to influence the results of load bearing tests on footings having diameters of 8 in. or more. However, since the results for the 9.0 and 12.0 in. diameter footings correlate rather well with those for the 6.0 in. and smaller diameter footings and since these dimensions (9.0 in. and 12.0 in.) are not overly in excess of 8.0 in. it would be expected that the negative value of b is due primarily to the fact that the soil fails in compression rather than shear.

The bearing capacity of the footings were computed by Equation (6-81b) for the values of a_1 and b_1 equal to a and b_p (in which p denotes penetrometer values) and also be Equation (6-82). The results are shown in Figures 6-60 through 6-64 in the form of force vs penetration. Also shown are the bearing capacities determined by Equation (6-82) letting $\beta = 0$, and the actual experimentally determined points. The effect of footing size on a and b is clearly evident in that the curves using the values of a and b, obtained by the penetrometer, are quite conservative. However,

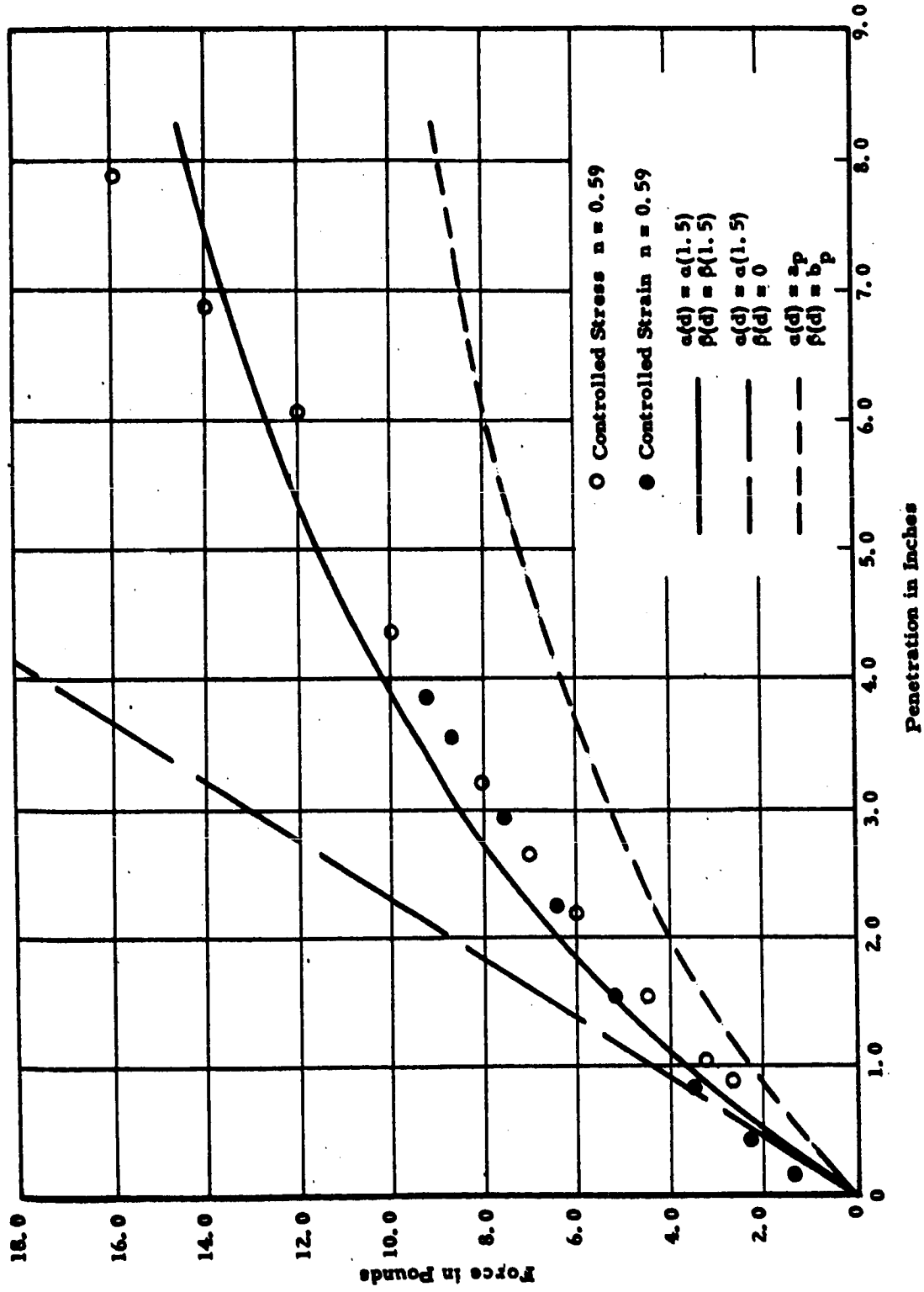

Figure 6-60 Computed and Actual Bearing Capacity of 1.5-Inch Footing

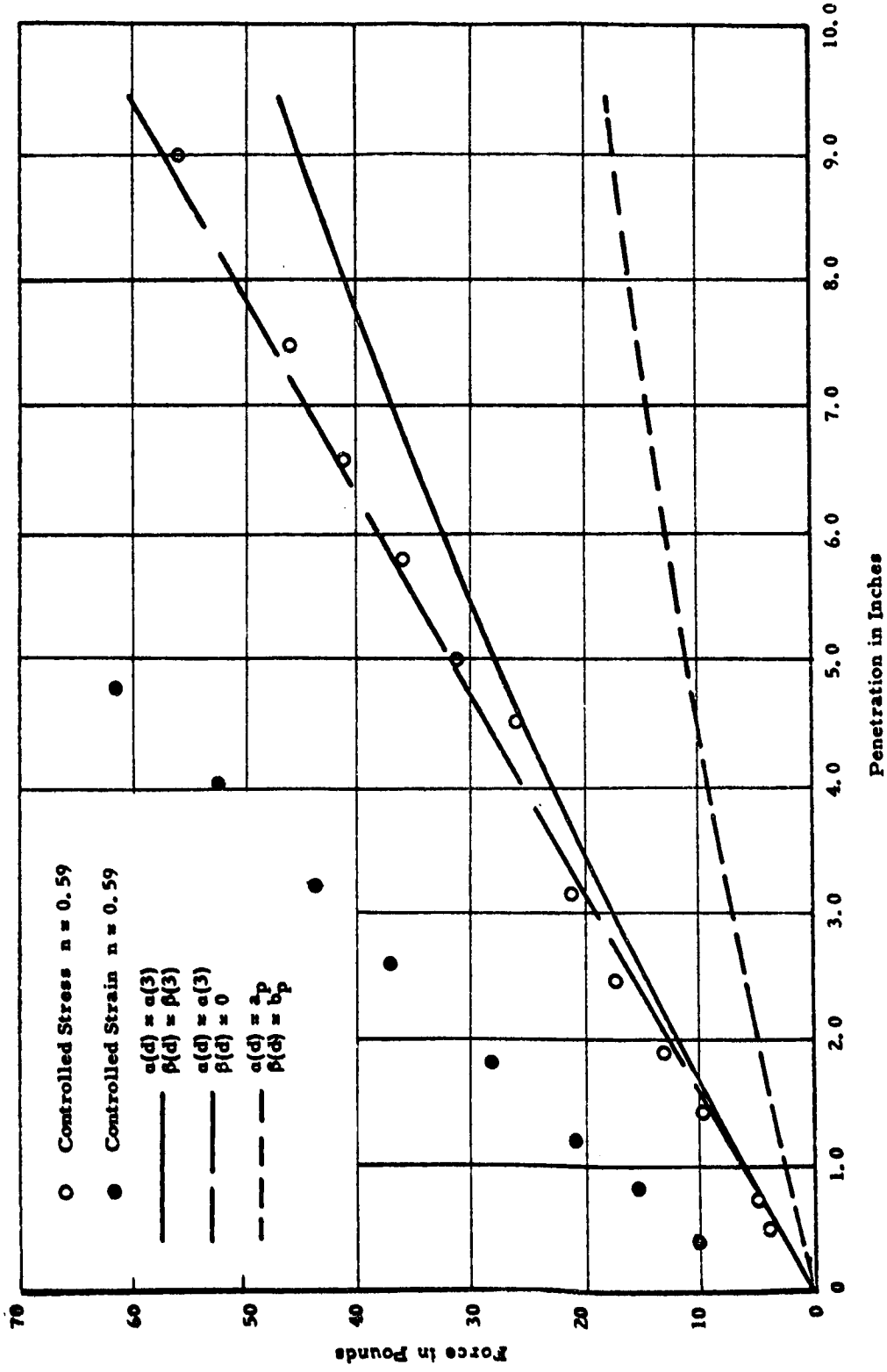

Figure 6-61 Computed and Actual Bearing Capacity of 3-Inch Footing

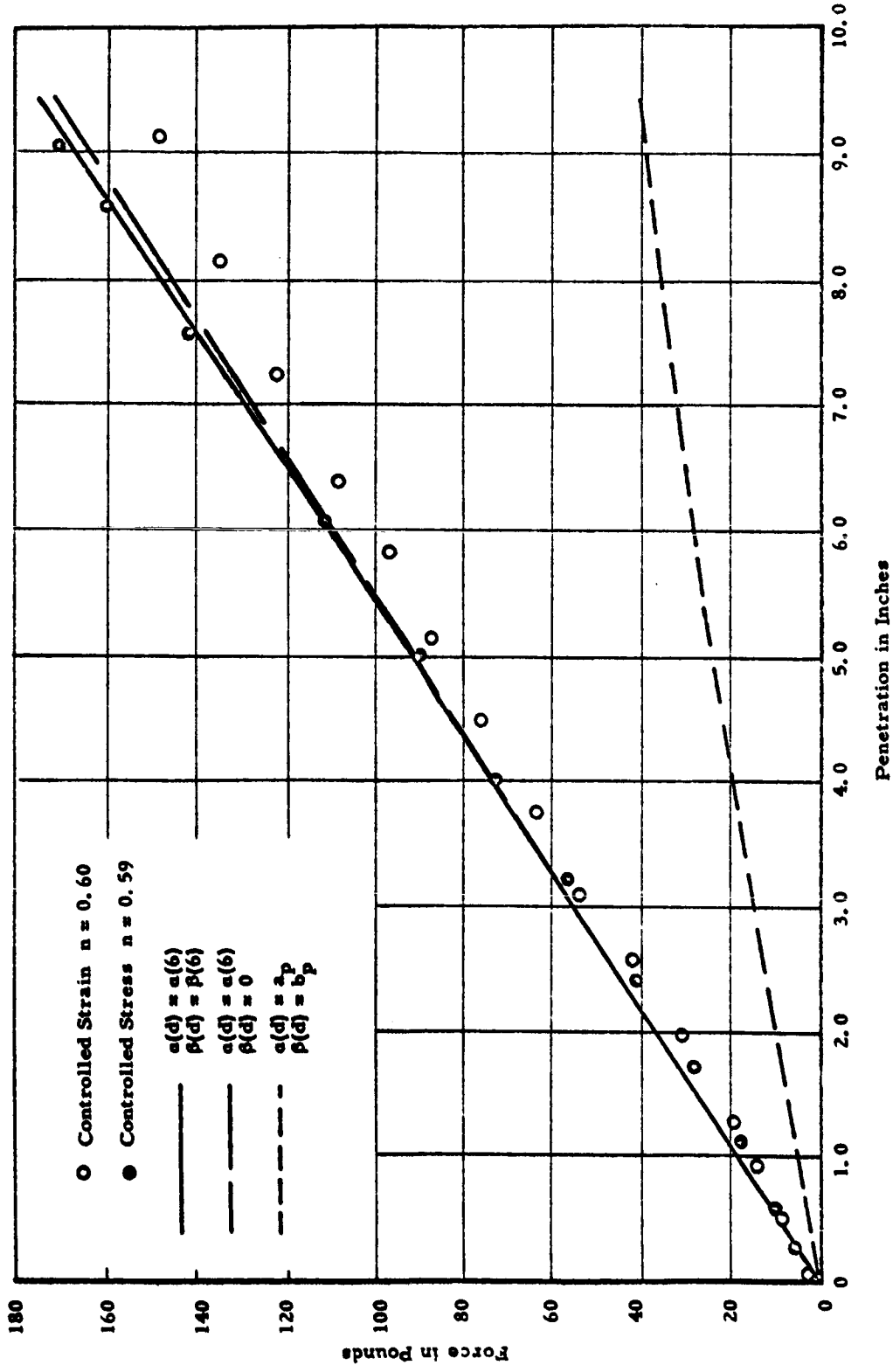

Figure 6-62 Computed and Actual Bearing Capacity of 6-Inch Footing

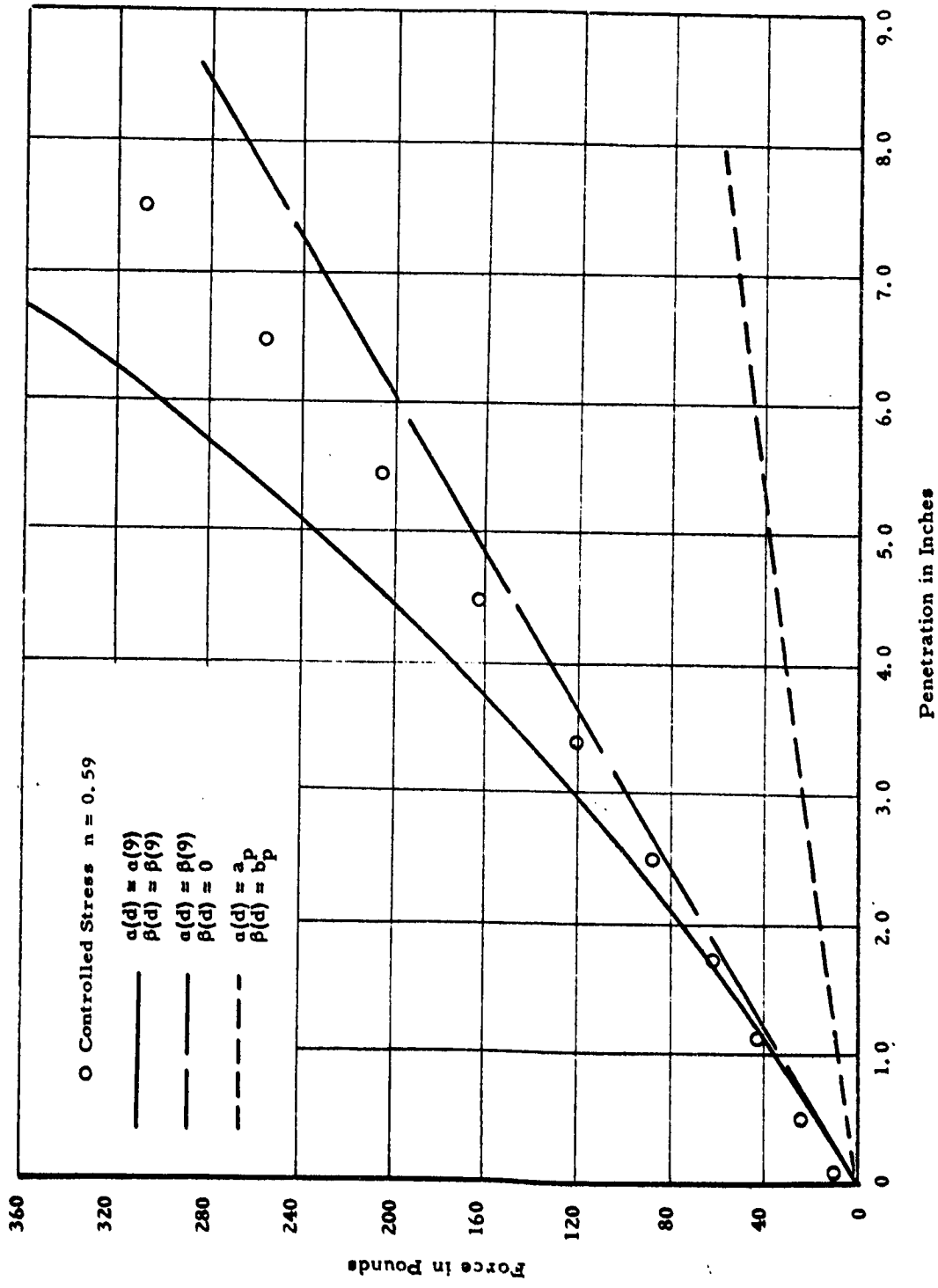

Figure 6-63 Computed and Actual Bearing Capacity of 9-Inch Footing

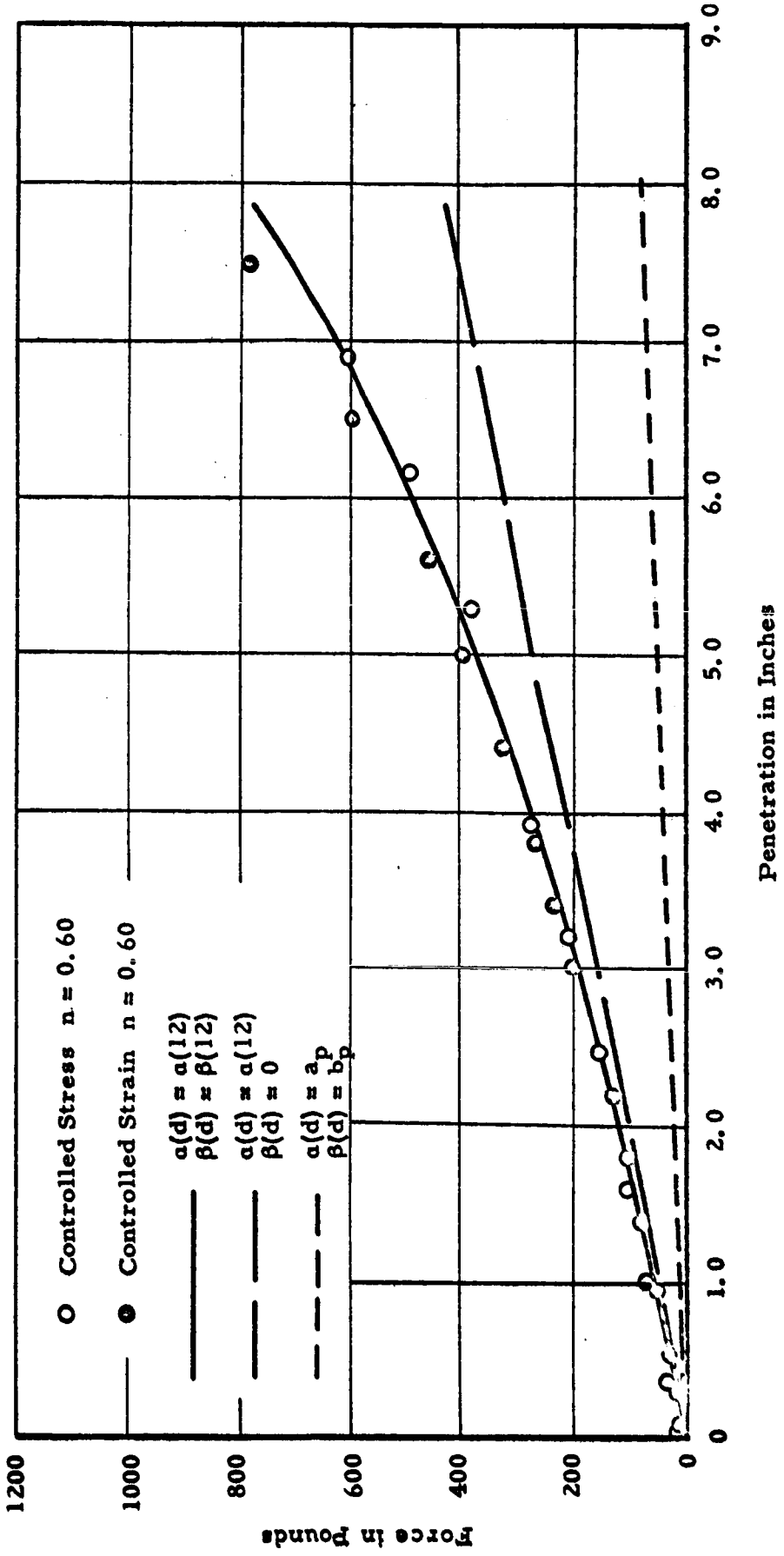

Figure 6-64 Computed and Actual Bearing Capacity of 12-Inch Footing

for the footings of 6 in. or greater, setting b = 0 results in a bearing capacity which is somewhat conservative. Although the data are somewhat limited, it would appear then that for larger sized footings the bearing capacity determined by Equation (6-82) and setting $\beta(d) = 0$ would be somewhat on the conservative side.

The consequences of letting $\beta = 0$ would depend on the amount of settlement that the footing is designed to undergo as illustrated below. For any particular footing the bearing capacities in each case would be given by

$$F_1/A = \frac{x/C}{\alpha + \beta\, x/C}$$

and

$$F_2/A = \frac{x}{\alpha C}$$

The ratio of F_1 to F_2 at any particular value of penetration, x, could then be expressed by equation

$$\frac{F_1}{F_2} = \frac{1}{1 + \frac{\beta}{\alpha}\,\frac{x}{C}} \qquad (6\text{-}90)$$

This equation is shown graphically in Figure 6-65 for various values of β/α.

From Equation (6-83) and (6-84) it is evident that as the size of the footing increases, the ratio of β/α decreases. However, as the footing size increases, the value of x/C corresponding to a particular value of x also decreases. Therefore, the amount of error which is introduced by letting $\beta = 0$ is highly dependent on the footing, size but for large footings having negative values of β, the bearing capacity computed by letting $\beta = 0$ would always be conservative.

The data obtained from the penetrometer experiments in vacuum were plotted in the form of F/A vs x/C as shown in Figure 6-66. It can be seen that the curve has the same general shape as for penetrometer tests in the atmosphere but, as may be expected, the force required to cause penetration is somewhat greater in the vacuum. These data were then

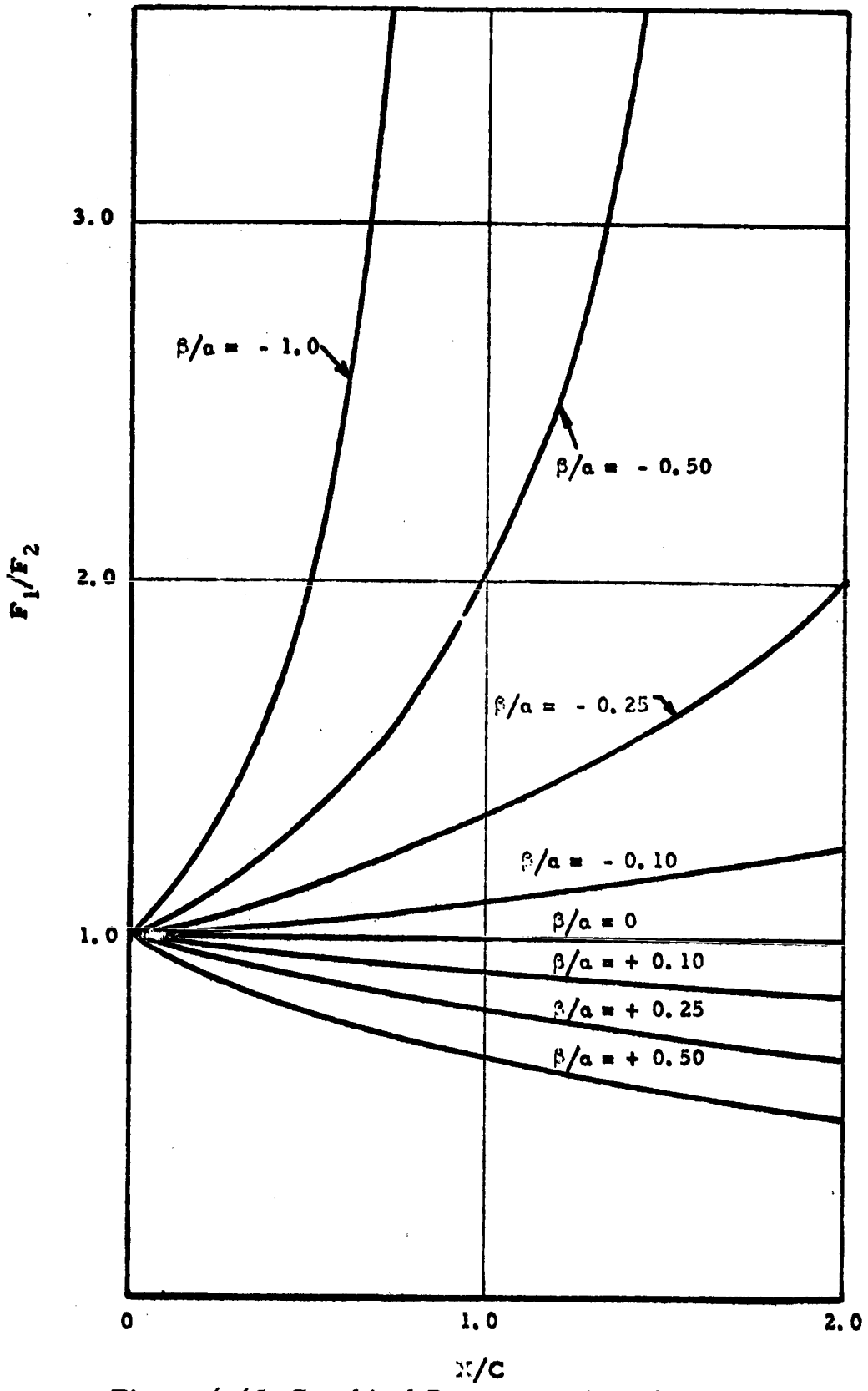

Figure 6-65 Graphical Representation of Equation

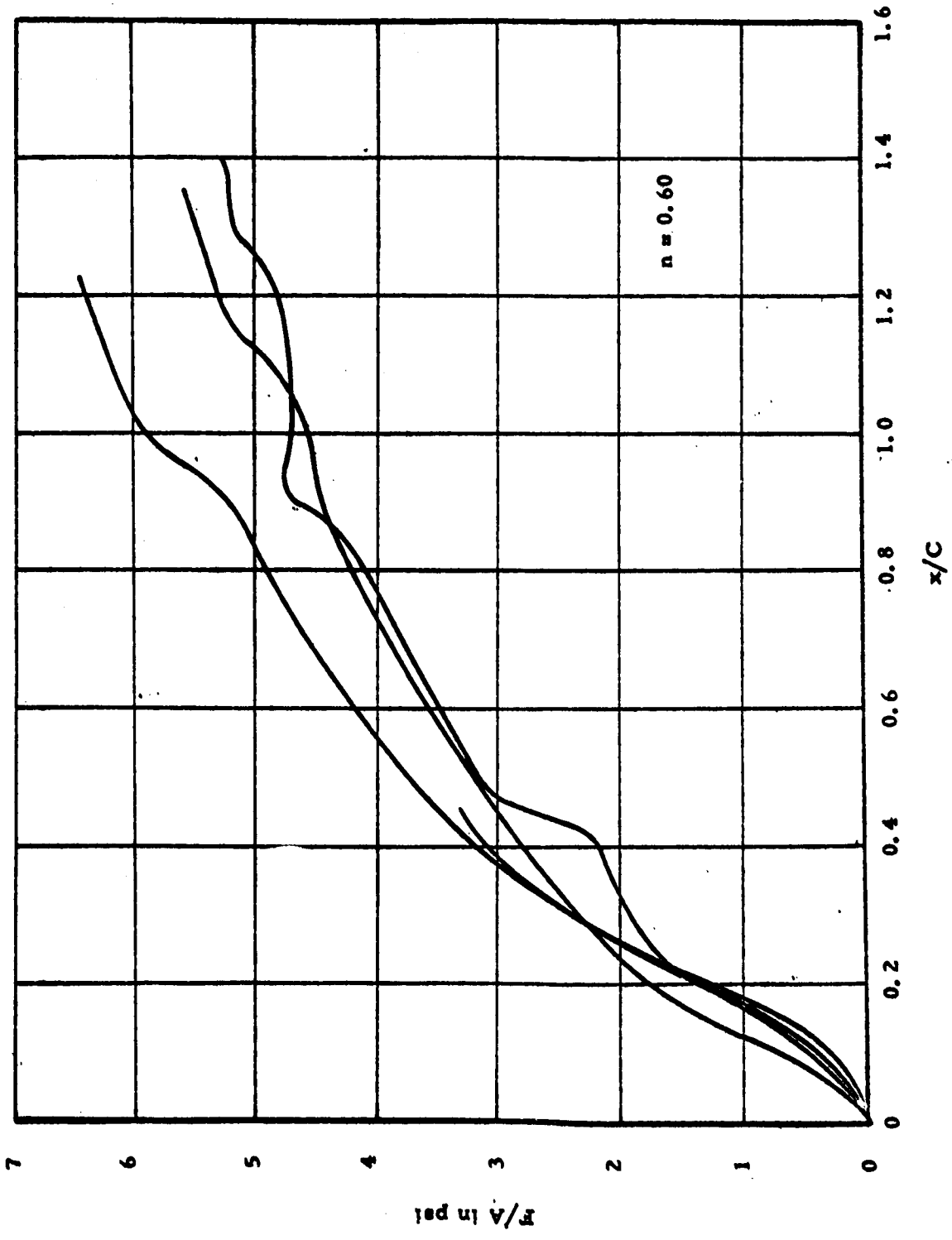

Figure 6-66 F/A vs X/C for Penetrometer Tests in Vacuum

replotted in the form of xA/FC vs x/C in Figure 6-67 and a value of a_p and b_p were determined as shown. The values of a_p and b_p were then used to predict the bearing capacities of the 3 in. and 12 in. diameter footings as was done previously for the experiments in the atmosphere. The computed bearing capacities are shown together with the actually measured points in Figures 6-68 and 6-69. The general shape of the measured force vs penetration curves for the footings is the same as was seen in the experiments in atmosphere. The distortion of the curve, defined by the measured points near the origin for the 12 in. footing, may be attributed to improper alignment of the footing relative to the soil surface caused by the feed-through port on the vacuum chamber. However, it is evident that the bearing capacities which were predicted on the basis of the values of α and β determined by Equations (6-83) and (6-84) are unconservative whereas the bearing capacities which were computed using a_p and b_p are not as conservative as was the case for the atmospheric experiments.

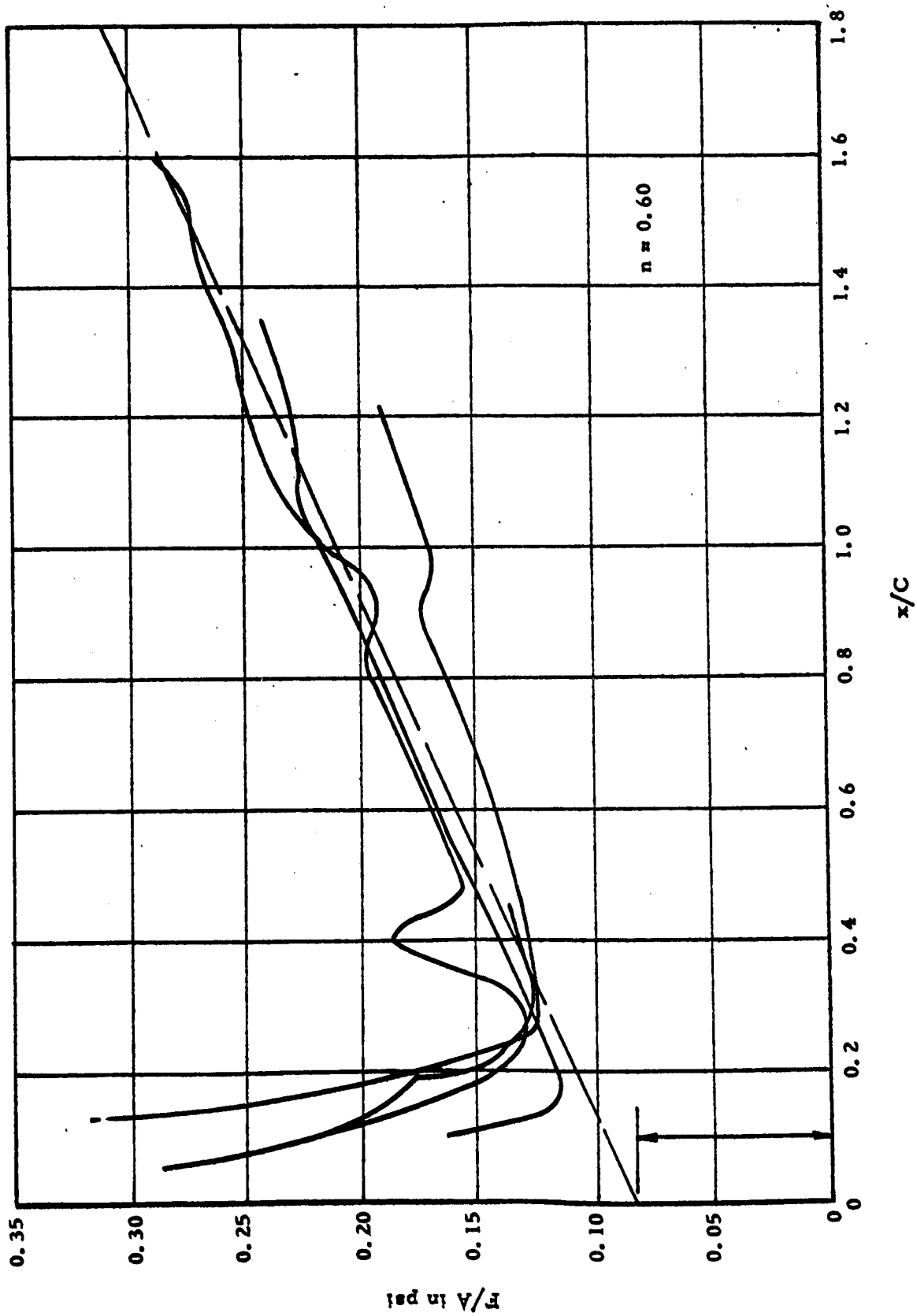

Figure 6-67 XA/FC vs X/C for Penetrometer Tests in Vacuum

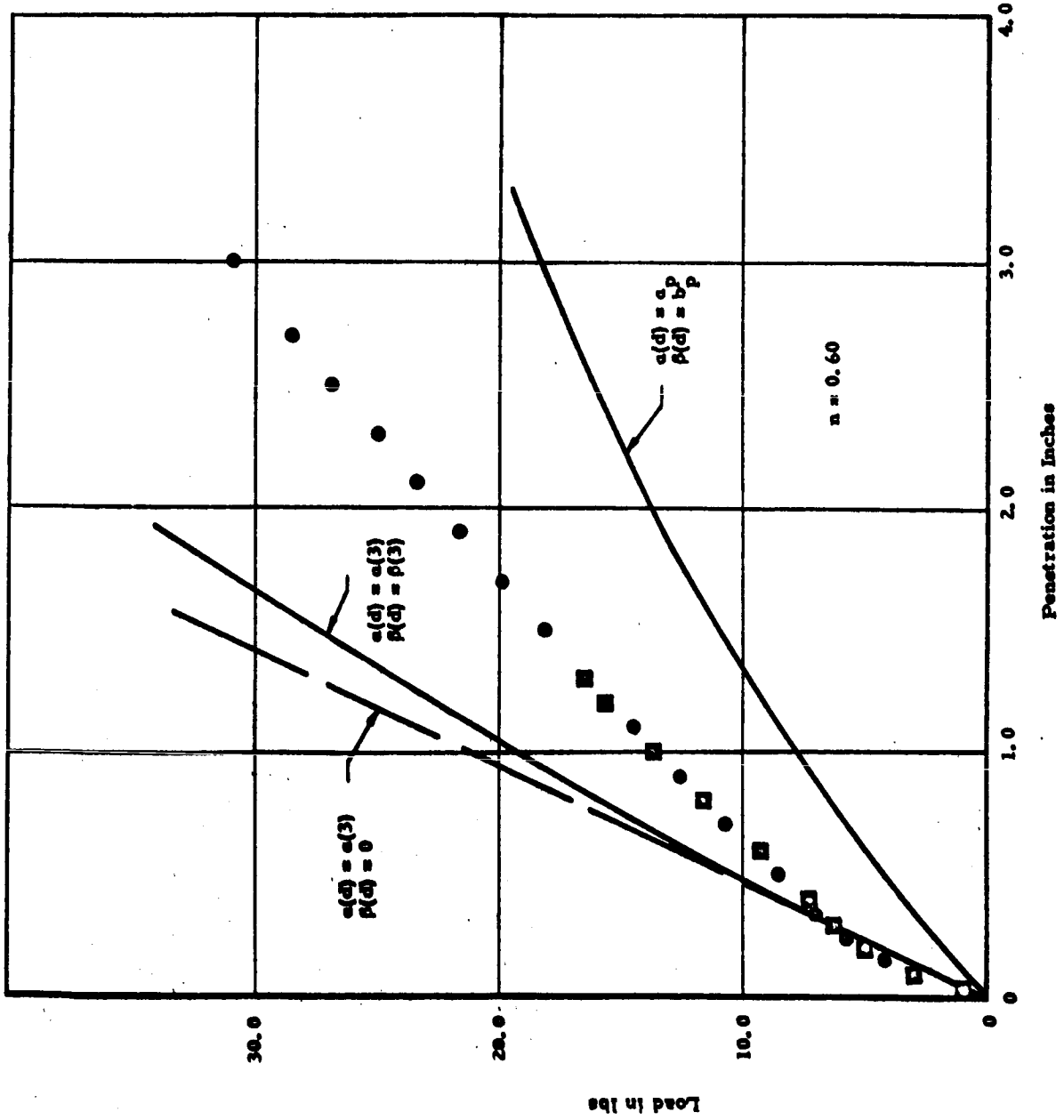

Figure 6-68 Actual and Computed Bearing Capacity of 3-Inch Footing in Vacuum

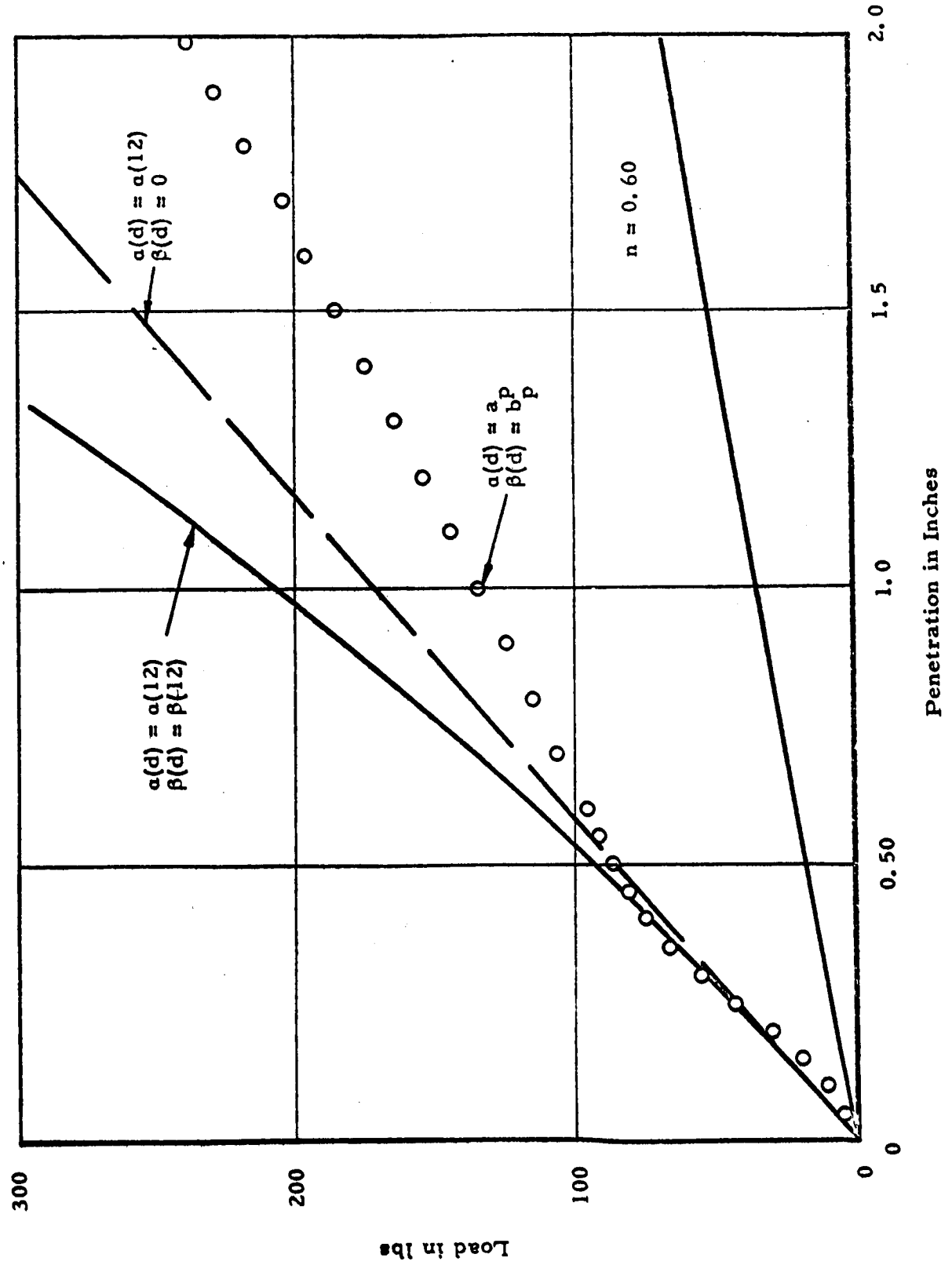

Figure 6-69 Actual and Computed Bearing Capacity of 12-Inch Footing in Vacuum

6.4 CORRELATION PROCEDURES FOR SURFACE PROPERTIES

Soil mechanics is an inexact science, even when the soil material parameters are well known. When practically nothing is known about the structural properties, as in the case with lunar surface materials, the task of determining bearing strength (for example) becomes one of using correlation procedures and as much data on properties of terrestrial soils as can be gathered. In addition to the data received from a penetrometer, in the form of the static force exerted topenetrate a known distance, the vehicle-soil interaction will be observed and analyzed by use of the odometer wheel, monitoring the driven track, and by direct observation with the television subsystem.

The two parameters to be determined from these data would be apparent sinkage of the driven track and slippage as determined by a comparison of the wheel and the track performance.

The motion resistance as a result of the soil has been related to the sinkage through the pressure-sinkage formula.

$$p = \frac{k_c}{b} + k_\phi \quad z^n \tag{6-91}$$

where

p = vertical component of soil pressure under the wheel

b = width of the wheel

z = sinkage

k_c, k_ϕ, n = soil parameters

If the work done in compacting the soil is considered equal to the resistance of the soil times the distance traveled, the resistance to motion, R, would then be

$$R = \frac{b}{n+1} \left[\frac{k_c}{b} + k_\phi\right] \quad z_o^{\,n+1} \tag{6-92}$$

which can be written in the form

$$R = k_o \; z^m \tag{6-93}$$

where

k_o = constant dependent upon the soil parameters k_c, k_ϕ and n

$m = n + 1$.

The equations presented above are for a flexible track or high-deflection elastic tire. However, the general form of the equations remains the same for a rigid track, the constants k_o and m being related to k_ϕ, k_c, and n in a somewhat different form. Determination of the power supplied to the tracks would allow the resistance to motion to be determined. However, only a portion of the power supplied will be applied to overcoming the motion resistance, the remainder being lost in slippage of the track. The efficiency of the system or that portion of the work applied toward motion of the vehicle, can be determined from the equation

$$E = \frac{FV_a}{P}$$

$$= \frac{F\,(1-i)V_t}{P} = (1 - i) \tag{6-94}$$

where

E = efficiency

F = drawbar pull

V_a = actual velocity of vehicle

V_t = theoretical velocity

P = input power

i = slip

The total power applied toward motion is then equal to (1 - i)P. Setting the total energy supplied equal to the work done in moving, the track gives

$$Rd = \int_{o}^{t_o} (1 - i) P \, dt \qquad (6\text{-}95)$$

where

t = time

d = distance traveled

from which the resistance to motion can be determined. This then allows the determination of the constants k_o and m for the particular track being used, upon determination of the sinkage and the slip of the track.